Homo-(4f) and Hetero-(3d-4f) metallic Complexes as Molecular Nanomagnets

By
PANKAJ KALITA

CHEM11201404007

National Institute of Science Education and Research, Bhubaneshwar, Odisha

A thesis submitted to the

Board of Studies in Chemical Sciences

In partial fulfillment of requirements

for the Degree of

DOCTOR OF PHILOSOPHY

of

HOMI BHABHA NATIONAL INSTITUTE

October, 2019

Homi Bhabha National Institute

Recommendations of the Viva Voce Committee

As members of the Viva Voce Committee, we certify that we have read the dissertation prepared by **Pankaj Kalita** entitled "**Homo-(4f) and Hetero-(3d-4f) metallic Complexes as Molecular Nanomagnets**" and recommend that it may be accepted as fulfilling the thesis requirement for the award of Degree of Doctor of Philosophy.
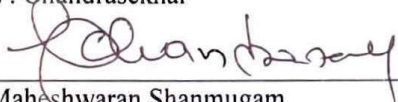
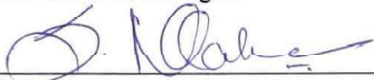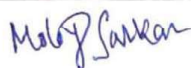|	
Chairman – Dr. U. Lourderaj	Date: 21·10·19
Guide / Convener – Prof. A. Srinivasan	Date: 21.10.19
Co-guide – Prof. V. Chandrasekhar	Date: 21|10|19
Examiner – Prof. Maheshwaran Shanmugam	Date:
Member 1 – Dr. V. Krishnan	Date: 21|10/2019
Member 2 – Dr. M. Sarkar	Date: 21|10|19
Member 3 – Dr. Pankaj V. Alone	Date: 21|10|19

Final approval and acceptance of this thesis is contingent upon the candidate's submission of the final copies of the thesis to HBNI.

I/We hereby certify that I/we have read this thesis prepared under my/our direction and recommend that it may be accepted as fulfilling the thesis requirement.

Date: 21\|10\|2019

Place: Jatni

<Signature>

<Signature>

Co-guide (if applicable)

i

STATEMENT BY AUTHOR

This dissertation has been submitted in partial fulfillment of requirements for an advanced degree at Homi Bhabha National Institute (HBNI) and is deposited in the Library to be made available to borrowers under rules of the HBNI.

Brief quotations from this dissertation are allowable without special permission, provided that accurate acknowledgement of source is made. Requests for permission for extended quotation from or reproduction of this manuscript in whole or in part may be granted by the Competent Authority of HBNI when in his or her judgment the proposed use of the material is in the interests of scholarship. In all other instances, however, permission must be obtained from the author.

Pankaj Kalita

DECLARATION

I, hereby declare that the investigation presented in the thesis has been carried out by me. The work is original and has not been submitted earlier as a whole or in part for a degree/diploma at this or any other Institution / University.

Pankaj Kalita

List of publications arising from the Thesis

A. Journal

a. Published:

*1. "Heterometallic Octanuclear $Ni^{II}_4Ln^{III}_4$ (Ln = Y, Gd, Tb, Dy, Ho, Er) Complexes Containing $Ni^{II}_2Ln^{III}_2O_4$ Distorted Cubane Motifs: Synthesis, Structure and Magnetic Properties", **Pankaj Kalita**, Joydeb Goura, Juan Manuel Herrera, Enrique Colacio and Vadapalli Chandrasekhar, *ACS Omega*, 2018, **3**, 5202–5211.

*2. "Homodinuclear $\{Ln^{III}_2\}$ (Ln^{III} = Gd^{III}, Tb^{III}, Ho^{III}, and Dy^{III}) Complexes: Field- Induced SMM Behavior of the Dy^{III} and Tb^{III} Analogues", **Pankaj Kalita**, Joydeb Goura, Juan Manuel Herrera Martínez, Enrique Colacio and Vadapalli Chandrasekhar, *Eur. Inorg. Chem.*, 2019, 212-220.

*3. "Pentagonal Bipyramidal Ln(III) Complexes Exhibiting Single-Ion Magnet Behaviour: A Rational Synthetic Approach for Rigid Equatorial Plane", Arun Kumar Bar, **Pankaj Kalita**, Jean-Pascal Sutter and Vadapalli Chandrasekhar, *Inorg. Chem.*, 2018, **57**, 2398-2401.

*4. "Low-coordinate mononuclear lanthanide complexes as molecular nanomagnets", Arun Kumar Bar, **Pankaj Kalita**, Mukesh Kumar Singh, Gopalan Rajaraman, Vadapalli Chandrasekhar, *Coord. Chem. Rev.*, 2018, **367**, 163-216.

*5. "Lanthanide (III)-Based Single-Ion Magnets", Atanu Dey, **Pankaj Kalita**, Vadapalli Chandrasekhar, *ACS Omega*, 2018, **3**, 9462-9475.

*6. "Mononuclear lanthanide complexes assembled from a tridentate NNO donor ligand: design of a Dy^{III} single-ion magnet", **Pankaj Kalita**, Amit Malakar,

Joydeb Goura, Subhashree Nayak, Enrique Colacio and Vadapalli Chandrasekhar, *Dalton Trans.*, 2019, **48**, 4857-4866.

b. Manuscripts under preparation

*1. "Pentagonal Bipyramidal Ln^{III} Complexes Containing Strong-field Axial Ligand: Field-induced SIM Behavior of the Dy^{III} Analogues", **Pankaj Kalita**, Arun Kumar Bar, Jean-Pascal Sutter, Vadapalli Chandrasekhar.

*2. "*Non*-planar Octanuclear {Ln$_8$} Complexes: Magneto-Caloric Effect in the {Gd$_8$} analogue", **Pankaj Kalita**, Joydeb Goura, Enrique Colacio, Alagar Srinivasan, and Vadapalli Chandrasekhar.

*3. "Mononuclear Ln^{III} complexes assembled from a bulky ^{Mes}Acac ligand: Luminescence and Magnetism", **Pankaj Kalita**, Prakash Nayak, Enrique Colacio, Alagar Srinivasan, and Vadapalli Chandrasekhar.

Pertaining to this thesis

c. Other publications:

1. "Heterometallic 3d-4f single molecule magnets containing diamagnetic metal ions", Amit Chakrabarty, Joydeb Goura, **Pankaj Kalita**, Abinash Swain, Gopalan Rajaraman, Vadapalli Chandrasekhar, *Dalton Trans.,* 2018, **47**, 8841-8864.

2. "Mononuclear Lanthanide Complexes: Energy-Barrier Enhancement by Ligand Substitution in Field-Induced Dy^{III} SIMs", Sourav Biswas, Kochan S Bejoymohandas, Sourav Das, **Pankaj Kalita**, Mundalapudi L P Reddy, Itziar Oyarzabal, Enrique Colacio, Vadapalli Chandrasekhar, *Inorg. Chem.*, 2017, **56**, 7985-7997.

3. "Reactivity Enhancement of a Diphosphene by Reversible N-Heterocyclic Carbene Coordination", Debabrata Dhara, **Pankaj Kalita**, Subhadip Mondal, Suriya Narayanan, Kaustubh Mote, Volker Huch, Michael Zimmer, Cem B Yildiz, David Scheschkewitz, Vadapalli Chandrasekhar, Anukul Jana, *Chem. Sci.*, 2018, **9**, 4235-4243.

4. "2, 6-(Diphenylmethyl)-Aryl-Substituted Neutral and Anionic Phosphates: Approaches to H-Bonded Dimeric Molecular Structures", Debdeep Mandal, Biswajit Santra, **Pankaj Kalita**, Nicolas Chrysochos, Amit Malakar, Ramakirushnan Suriya Narayanan, Sourav Biswas, Carola Schulzke, Vadapalli Chandrasekhar, Anukul Jana, *ChemistrySelect.*, 2017, **2**, 8898-8910.

5. "'Abnormal' Addition of NHC to a Conjugate Acid of CAAC: Formation of N-Alkyl Substituted CAAC", Anukul Jana, Debdeep Mandal, Ramapada Dolai, **Pankaj Kalita**, Ramakirushnan Suriya Narayanan, Ravi Kumar, Sebastian Sobottka, Biprajit Sarkar, Gopalan Rajaraman, Vadapalli Chandrasekhar, *Chem. Eur. J.*, 2018, **24**, 12722-12727.

6. "Stepwise Reversible Oxidation of N-Peralkyl-Substituted NHC–CAAC Derived Triazaalkenes: Isolation of Radical Cations and Dications", Debdeep Mandal, Ramapada Dolai, Nicolas Chrysochos, **Pankaj Kalita**, Ravi Kumar, Debabrata Dhara, Avijit Maiti, Ramakirushnan Suriya Narayanan, Gopalan Rajaraman, Carola Schulzke, Vadapalli Chandrasekhar, Anukul Jana, *Org. Lett.*, 2018, **19**, 5605-5608.

7. "Contrasting Reactivity of (Boryl)(Aryl) Lithium-Amide with Electrophiles: N-vs p-Aryl-C-Nucleophilic Substitution", Debabrata Dhara, Thangavel

Vijayakanth, Mithilesh Kumar Nayak, **Pankaj Kalita**, Boomishankar Ramamoorthy, Cem B Yildiz, Vadapalli Chandrasekhar, Anukul Jana, *Dalton Trans.*, 2018, **47**, 14411-14415.

8. "Neutral and anionic phosphate-diesters as molecular templates for the encapsulation of a water dimer", Vivek Gupta, Biswajit Santra, Debdeep Mandal, Shubhajit Das, Ramakirushnan Suriya Narayanan, **Pankaj Kalita**, D Krishna Rao, Carola Schulzke, Swapan K Pati, Vadapalli Chandrasekhar, Anukul Jana, *Chem. Commun.,* 2018, **54**, 11913-11916.

9. "Assembly of NHC-stabilized 2-hydrophosphasilenes from Si(IV) precursors: a Lewis acid–base complex", Debabrata Dhara, Debdeep Mandal, Avijit Maiti, Cem B Yildiz, **Pankaj Kalita**, Nicolas Chrysochos, Carola Schulzke, Vadapalli Chandrasekhar, Anukul Jana, *Dalton Trans.*, 2017, **45**, 19290-19298.

10. "Direct Access to 2-Aryl Substituted Pyrrolinium Salts for Carbon Center Based Radicals without Pyrrolidine-2-Ylidene alias cyclic (Alkyl)(Amino) Carbene (CAAC) as a Precursor", Debdeep Mandal, Sebastian Sobottka, Ramapada Dolai, Avijit Maiti, Debabrata Dhara, **Pankaj Kalita**, Ramakirushnan Surya Narayanan, Vadapalli Chandrasekhar, Biprajit Sarkar, Anukul Jana, *Chem. Sci.*, 2019, **10**, 4077-4081.

B. Conference

1. MTIC-XVI, 16th International Symposium on Modern Trends in Inorganic Chemistry 2015, 03-05 December at the Department of Chemistry, Jadavpur University, Kolkata, India.

2. Conference on Modern Trends in Molecular Magnets, MTMM-2016, 19-21 May at the Department of Chemistry, IIT Bombay, Mumbai, India.

3. "Ligand Substitution Triggered Energy Barrier Enhancement in Field-Induced Dy^{III} SIMs" **Pankaj Kalita**, Sourav Biswas, and Vadapalli Chandrasekhar, MTIC-XVII, 17th International Symposium on Modern Trends in Inorganic Chemistry 2017, 03-05 December at the Department of Chemistry, NCL Pune-IISER Pune-Pune University, Pune, India. (**Poster Presentation**)

4. "Multidentate Ligand Supported Lanthanide(III) Complexes", **Pankaj Kalita**, Arun Kumar Bar, Joydeb Goura, and Vadapalli Chandrasekhar, 1st International Symposium on Main-group Molecules to Materials (MMM) 28-31 October, 2018 at Department of Inorganic and Physical Chemistry, Indian Institute of Science, Bangalore, India. (**Poster Presentation**)

5. Indo-French School cum Conference on Magnetism of Molecular Systems, 26-30 November, 2018 at Department of Solid State and Structural Chemistry, Indian Institute of Science, Bangalore, India.

Pankaj Kalita

DEDICATED TO

MY PARENTS

AND

GRANDPARENTS....

ACKNOWLEDGEMENTS

*First and foremost, I would like to thank my thesis supervisor **Prof. A. Srinivasan** for his guidance, care, and support during the tenure of this Thesis.*

*I am extremely grateful to my thesis co-supervisor **Prof. V. Chandrasekhar** for his invaluable guidance, encouragement, and tremendous support to finish my research works in time. I am especially thankful to him for giving me the opportunity to pursue my research work in a peaceful and constructive environment. I am also thankful to Madam (**Mrs. Sudha Chandrasekhar)** for her care.*

*I am very thankful to **Prof. T. K. Chandrashekar**, senior professor, and ex-director, NISER, for his insightful suggestions and courage.*

*I would like to thank **Prof. U. Lourderaj**, the chairman of my doctoral committee and the other members **Dr. V. Krishnan**, **Dr. M. Sarkar**, **Dr. P. V. Alone** for their valuable suggestions and fruitful discussions.*

*I would also like to thank **Dr. S. Kar**, **Dr. H. S. Biswal**, **Dr. S. Nembenna**, **Dr. C. Gunanathan**, and **Dr. S. Barman** for teaching me in the PhD coursework and all the other faculty members in the School of Chemical Sciences, NISER.*

*I would like to extend my sincere gratitude to **Prof. E. Colacio**, University of Granada, Spain and **Prof. J.-P. Sutter**, CNRS LCC, Toulouse, France for their immense support and timely response in the magnetic measurements of my compounds.*

*I would like to thank **Dr. A. Jana**, TIFR, Hyderabad for his support, care and proving Lab infrastructure to work at TIFR, Hyderabad. I would also like to thank **Dr. A. Kumar**, Scientific Officer, SCS, NISER, for his kind help and suggestions throughout my stay at NISER, Bhubaneswar.*

Pankaj Kalita

CONTENTS

Summary

The work presented in this thesis primarily deals with the syntheses, structural characterization, and magnetic properties of (*i*) mononuclear 4f complexes, (*ii*) polynuclear 4f complexes, and (*iii*) polynuclear 3d-4f complexes. A variety of synthetic strategies have been employed to isolate these three different categories of complexes. The investigation of magnetic properties reveals the presence of single-molecule magnet (SMM) and single-ion magnet (SIM) behaviour in many of the complexes. The thesis begins with a general introduction concerning the recent advancements in this field in a comprehensive manner. The aim and objective of this thesis is also discussed here including the synthetic challenges associated with fine tuning the desired magnetic properties. Following this all the chapters in this thesis deal with the syntheses, structure, luminescence, and magnetic properties of the newly synthesized coordination compounds.

The mononuclear Ln(III) complexes discussed in this thesis are of three different types as described below:

(*i*) Pentagonal bipyramidal Ln(III) complexes with a pentadentate ligand that provides a rigid equatorial pentagonal plane. The axial sites in these complexes are occupied by chloride ligands. The Dy(III) derivative shows single-ion magnet behavior under an applied magnetic field. In order to verify the effect of axial ligand field on the magnetic properties of these complexes, one of the axial chloride ligand was replaced by alkyl/aryl phosphine oxide ligands. It was observed that this systematic variation enhanced the anisotropic energy barriers of the Dy(III) derivatives by a factor of 2-3.

(*ii*) A second family of mononuclear Ln(III) complexes were synthesized using a rigid coordination sphere build up by two tridentate NNO donor ligands. The two ligands with phenolate moieties in the rigid coordination sphere are in a *trans* disposition leading to a strong axial ligand field. Indeed, the Dy(III) derivative shows SIM behaviour under a biased magnetic field with an energy barrier of 70 K.

(*iii*) A third series of mononuclear Ln complexes were synthesized utilizing a different synthetic strategy. An acetyl acetone ligand having a bulky backbone was synthesized and further utilized to isolate five mononuclear Ln(III) complexes. The photophysical properties of the Eu(III) and Tb(III) derivatives were investigated. The magnetic properties of the Dy(III) derivative were studied which revealed a field induced SIM behaviour.

The second category of complexes investigated is polynuclear 4f complexes that were synthesized by employing an enolizable multidentate Schiff base ligand. Depending on the reaction conditions dinuclear and octanuclear complexes were isolated. The $\{Tb\}_2$ and $\{Dy\}_2$ derivatives were shown to be field-induced single-molecule magnets. The octanuclear complexes are neutral and isostructural. The magneto caloric effect (MCE) was studied for the Gd(III) derivative.

The third and final category of complexes presented in this thesis belongs to a family of heterometallic polynuclear 3d-4f complexes prepared by an unsymmetrical Schiff base ligand. The central metallic core of these heterometallic octanuclear $[Ni_4Ln_4]$ complexes is comprised of $[Ni_2Ln_2O_4]$ cubane subunits connected to each other by acetate and hydroxyl ligands. The magnetic studies reveal a ferromagnetic interaction between the lanthanide and the nickel ions. Also, the magneto caloric effect (MCE) was studied for the $[Ni_4Gd_4]$ derivative.

mode (no field sweeping).

Lists of Abbreviations

Acac	Acetyl acetone
Anal	Analysis
An	Actinides
Anhyd.	Anhydrous
ac	alternating current
Cy	Cyclohexyl
Calcd	Calculated
CShM	Continuous Shape Measurement
DMF	N, N-Dimethyl formamide
D	Zero-field splitting parameter
DAP	Diacetyl pyridine
dc	direct current
EA	Elemental Analysis
ESI-MS	Electrospray Ionization Mass Spectroscopy
ET	Energy Transfer
EtOH	Ethanol
g	Landé factor
H	Magnetic field
Ĥ	Heisenberg spin-Hamiltonian
HSAB	Hard Soft Acid Base
Hz	Hertz
IR	Infrared
IC	Internal Conversion
ISC	Intersystem Crossing
IVR	Internal Vibrational Relaxation
J	Total Spin and Orbital Angular Momentum
k_B	Boltzmann's constant
K	Kelvin
L	Ligand
L	Total Orbital Angular Momentum

LS	Russell-Saunders Coupling
Ln	Lanthanide
M	Magnetization
MPMS	Magnetic Property Measurement System
Me	Methyl group
Mes	Mesityl group
MeCN	Acetonitrile
MeOH	Methanol
NEt_3	Triethylamine
NMR	Nuclear Magnetic Resonance
OAc	Acetate
pXRD	powder X-ray diffraction
Ph	Phenyl group
P	Phosphorescence Emission
PPMS	Physical Property Measurement System
QTM	Quantum tunneling of magnetization
SOC	Spin-Orbit Coupling
SQUID	Superconducting quantum interference device
SCXRD	Single crystal X-ray diffraction
TGA	Thermogravimetric analysis
T	Temperature
T	Tesla
TM	Transition Metal
TA-QTM	Thermally assisted Quantum tunneling of Magnetization
T_B	Blocking temperature
UV	Ultraviolet
U_{eff}	Effective energy barrier
XRD	X-ray diffraction
μ_B	Bohr magneton
χ_M	Molar magnetic susceptibility
τ	Relaxation time

General Introduction

This thesis deals with the synthesis, structural characterization and magnetic studies of coordination complexes involving 3d and 4f metal ions. Many of the complexes were shown to be single-molecule magnets (SMMs) or single-ion magnets (SIMs) both of which belong to the class of molecular magnets or molecular nanomagnets. In the following an introduction to this subject is given. Towards the end of this chapter the objectives of this thesis are outlined.

1.1 Molecular Nanomagnets. Molecular nanomagnets are paramagnetic metal complexes that show magnet-like behaviour below a certain temperature.[1] Importantly such a magnetic behavior is a molecular phenomenon and is not due to intermolecular interactions.[1] Such systems have sizes in the nanoscale or lower and are of potential interest in many futuristic technological applications.[2] Classical bulk magnets are comprises of magnetic domains separated by the domain walls. The magnetic properties in classical magnetic systems originate from the nucleation, propagation, and annihilation of domain walls (Figure 1.1 (*left*)).[3] Unlike the classical magnets, in the case of molecular nanomagnets, single molecules behave as "magnetic domains". This is possible because such molecular systems possess uniaxial magnetic anisotropy of purely molecular origin that enables the magnetic moment of individual molecules to remain in the direction of applied magnetic field. Once magnetized in a particular direction, the magnetization relaxes very slowly upon removal of the external magnetic field. Thus, the slow relaxation of magnetization is realized by thermally activated (over the barrier) relaxation process. However, quantum effects such as

quantum tunneling of magnetization (QTM) shortcuts this energy barrier leading to fast relaxation see Figure 1.1 (*right*).[4]
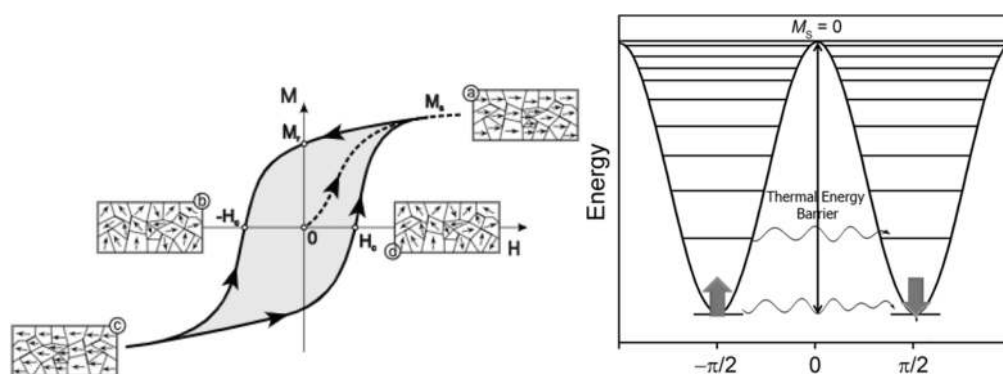
Figure 1.1. (*left*) A typical hysteresis loop of classical magnets (M_r: remnant magnetization; M_s: saturation magnetization; H_c: coercive field); (*right*) Double well potential diagram corresponding to single-molecule magnets (the x-axis represents the angle of magnetization and the wavy lines represents quantum tunneling). Figures are adapted from [3, 4b].

Similar magnetic behaviour can also be seen in the case of single-domain superparamagnetic nanoparticles. However, molecular nanomagnets offer various physical and chemical advantages over them.[5] These are as follows:

(*i*) Such molecular systems can be readily synthesized at ambient conditions using wet chemistry techniques.

(*ii*) The paramagnetic metal center(s) of individual molecules are enveloped in a diamagnetic shell of organic ligands which ensures that individual molecules do not interact with one another.

(*iii*) The organic moiety also provides an opportunity to fine tune the magnetic properties by modifying the ligand environment.

(*iv*) Such molecular systems are highly monodisperse in nature and soluble in most of the common organic solvents making them suitable candidates for thin film applications and surface deposition studies.

(*v*) Moreover, they possess well defined spin ground states and also show quantum tunneling of magnetization.

Molecular nanomagnets comprise of three categories: Single-Molecule Magnets (SMMs), Single-Ion Magnets (SIMs), and Single-Chain Magnets (SCMs). The potential candidates, synthetic designs, and the magnetic properties of each of these categories will be discussed in detail in this chapter. Before this, a brief overview about the different experimental techniques of characterizing molecular magnets and their quality check parameters is outlined below.

1.2 Experimental Characterization Techniques

Experimental characterization of molecular nanomagnets, in their powder or polycrystalline state, is usually realized with Superconducting Quantum Interference Device (SQUID) magnetometers. The two most common experimental characterization techniques are discussed below:

1.2.1 DC magnetometry. DC magnetic measurements on magnetic samples are performed applying a constant external magnetic field and the equilibrium magnetic moment is measured. After application of the external field the sample is considered to be in thermodynamic equilibrium such that sample relaxation time is smaller than the experimental time. The measurement of the field dependence of magnetization is usually performed at variable temperatures between 1.5 K and 300 K. It is a common practice to report the temperature variation of the magnetic susceptibility, χ, or its temperature product, χT. It is to note that the measurable property is the magnetization

(*M*) and the magnetic susceptibility is expressed as the ratio of magnetization vs field ($\chi = M/H$). At very high temperature, the χT value corresponds to the Curie constant representing the perfect paramagnetic behaviour. Fitting of the experimental χ (or χT) vs *T* plot valuable information can be gained regarding the nature of exchange interactions present in a system.

The most fundamental aspect of a magnet is the presence of a magnetic hysteresis loop in the *M* vs *H* plot. In classical magnets, magnetic hysteresis loops arise due to the irreversible growth of magnetic domains with the magnetic moments orienting in the same direction of the external field. In contrary, SMMs which are characterized by slow relaxation of magnetization and magnetic hysteresis loops are obtained due to the time required to sweep the field. Therefore in the DC measurements with a sweeping magnetic field, the magnetization of the ensemble of the molecules in the sample does not reach the equilibrium value giving rise to hysteresis loops in the experimental time-window. It is important to note that QTM has a peculiar effect on the shape of hysteresis loops. The presence of stepped hysteresis loops defines the presence of QTM i.e. fast relaxation at the corresponding magnetic field strength.[6] Most often, lanthanide ion SMMs are characterized by butterfly shape hysteresis loops resulting from significant quantum tunneling at zero applied magnetic field.[7]
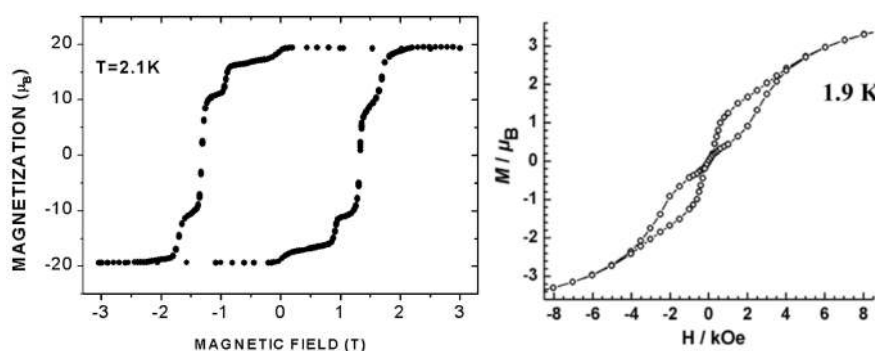
Figure 1.2. (*left*) Step-hysteresis of the Mn_{12} complex (**1.1**);[6] (*right*) Butterfly shape hysteresis of a mononuclear Dy^{III} complex, $[Dy(NSiMe_3)_3ClLi(THF)_3]$[7] (**1.2**).

1.2.2 AC magnetometry. The relaxation dynamics of majority of SMMs are typically faster than the field ramping as well as measurement time scales of conventional magnetometers.[1a] In order to study the magnetization dynamics conveniently, ac susceptibility measurements are performed using small oscillating magnetic fields with frequencies ranging from millihertz up to several tens of kilohertz.[8] The usefulness of this technique is that any molecule that shows slow relaxation can be detected from the observation of an imaginary component in the ac susceptibility signals in zero biased field or sometimes under a small biased dc magnetic field.[8] Generally, ac susceptibility measurements are represented in two different ways (*i*) in-phase (χ') and the out-of-phase (χ'') components plotted against temperatures (*T*) and (*ii*) in-phase (χ') and the out-of-phase (χ'') components plotted against the ac frequencies (*v*). Both the representations can be used to extract the relaxation times (τ) considering the maxima of the χ'' components that follows the relation, $\tau = 1/(2\pi v)$ at different temperatures. The extracted relaxation times (τ) are then plotted against the inverse of *T*. The Orbach relaxation which accounts for the relaxation of magnetization in the thermally activated regime directly correlates to the Arrhenius law, $\tau(T) = \tau_0 \exp(U_{eff}/k_B T)$. Here, U_{eff} is the effective energy barrier for magnetization reversal and τ_0 is a constant which represents average relaxation time in response to the thermal fluctuations. The value of U_{eff} is obtained from the slope of the semi logarithmic Arrhenius plot i.e. $\ln\tau$ vs T^{-1} (see Figure 1.3). The U_{eff} and τ_0 are considered as the quality check parameters reported for an SMM.
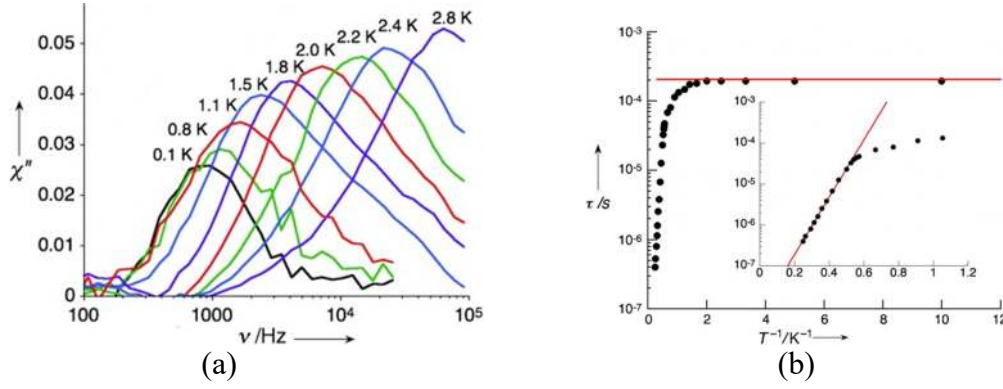
Figure 1.3. Plot of temperature-dependent χ'' components of ac susceptibility at different frequencies (a) and Arrhenius plot (b) for compound $[Mn_2(saltmen)_2(ReO_4)_2]$ (**1.3**) (saltmen^{2-} = N,N'-(1,1,2,2-tetramethylethylene)bis(salicylideneiminate). The best fit Arrhenius parameters are U_{eff} = 16 K and τ_0 = 8 x 10^{-9} s. At very low temperature, τ undergoes saturation and becomes independent to T. This feature is due to dominant QTM process. Reproduced from the ref [9]

The magnetization dynamics of SMMs in the ac susceptibility measurements can be well understood as follows.[1a, 10]

An ac magnetic field is defined as

$$H(t) = H_0 + h\cos(\omega t), \; \omega = 2\pi\nu \qquad (1)$$

Here H_0, is zero or nonzero constant indicating the zero- or nonzero-dc magnetic field in the same direction to the ac field h; h, is the amplitude of oscillating field, and ω, is the oscillating angular frequency of the ac field.

In ac susceptibility measurements, the measured susceptibility χ_{ac} is a complex value at given temperature and is given by

$$\chi_{ac} = \chi' + i\chi'' \qquad (2)$$

Here χ' and χ'' are the in-phase and is the out-of-phase susceptibilities respectively (Figure 1.4)

For a system having single relaxation process with just a single characteristic relaxation time (τ), the complex ac susceptibility can be derived by the Debye model is given by

$$\chi_{ac} = \chi_\infty + \frac{(\chi_0 - \chi_\infty)}{1+i\omega\tau} \tag{3}$$

The expression of χ' and χ'' are as follows

$$\chi' = \chi_\infty + \frac{(\chi_0 - \chi_\infty)}{1+\omega^2\tau^2} \tag{4}$$

$$\chi'' = \frac{(\chi_0 - \chi_\infty)\omega t}{1+\omega^2\tau^2} \tag{5}$$

where χ_0 represents the isothermal susceptibility when $\omega \to 0$ and χ_∞ represents the adiabatic susceptibility when. $\omega \to \infty$ (Figure 1.4)

In order to investigate the magnetic relaxation processes, $\chi''(\omega)$ is plotted against $\chi'(\omega)$. This plot is called Argand diagram which is similar to the Cole-Cole plot of dielectrics. By varying the frequency such that the relation $\omega\tau = 1$ holds, a maxima in χ'' and a declension in χ' curve is observed. Therefore, from the peak position of the χ'' curve ($\chi''_{max} = 1/2(\chi_\infty - \chi_0)$), the relaxation times (τ) can be obtained according to relation, $\tau = 1/\omega$.
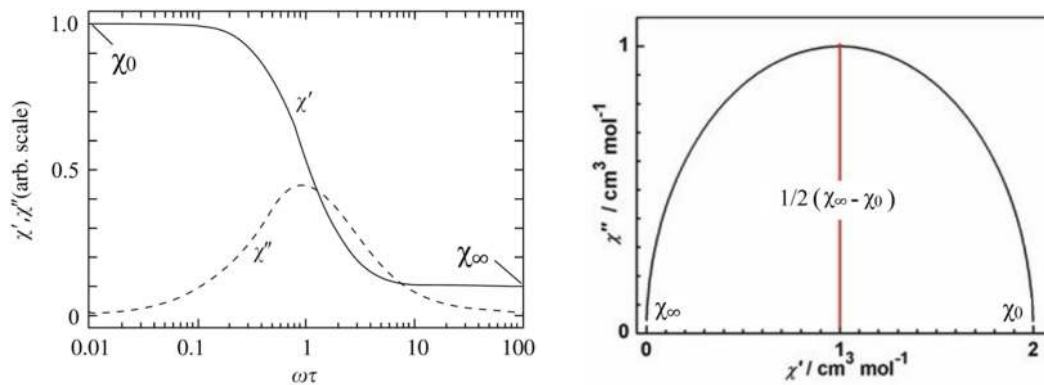
Figure 1.4. (*Left*) The in-phase (χ') and out-of-phase (χ'') ac components plotted against $\omega\tau$. (*Right*) the Argand diagram corresponding to a single-relaxation process having single-relaxation time.

However, in majority of instances a distribution of relaxation times are obtained. In that case eq.1 can be expressed as

$$\chi_{ac} = \chi_\infty + \frac{(\chi_0 - \chi_\infty)}{1+(i\omega\tau)^{(1-\alpha)}} \qquad (6)$$

The α parameter represents the width of the distribution i.e. $\alpha = 0$ represents a process corresponding to single relaxation time and $\alpha = 1$ corresponds to a process of infinite relaxation times. The Argand diagram involving only one relaxation process but having a narrow distribution of relaxation times follows complex mathematical expressions and the maximum of χ'' is expressed by the equation 7 from which the relaxation times can be extracted at different temperatures.

$$\chi''_{max} = \frac{1}{2} (\chi_\infty - \chi_0)\tan(\frac{\pi}{4}(1 - \alpha)) \qquad (7)$$

In the presence of more than one type of relaxation, the overall rate of relaxation follows a complex behaviour and is given by[11]

$$\tau^{-1} = \frac{B_1}{1+B_2 H^2} + AH^{n_1}T + CT^{n_2} + \tau_0^{-1}\left(\frac{U_{eff}}{k_B T}\right) \qquad (8)$$

Here, A, B, C, and τ_0 are constant parameters corresponding to QTM, direct, Raman, and Orbach relaxation processes, respectively; H denotes the applied field; T is the temperature; $n_1 = 4$ for Kramers and $n_1 = 2$ for non-Kramers doublets; and $n_2 = 7$ for the non-Kramers ions and $n_2 = 9$ for the Kramers ions.[11c] However, depending on the nature of phonons (acoustic and optical), n_2 may vary and a value of $n_2 \geq 4$ is equally relevant.[11c]

1.3 Quality Check Parameters

SMMs/SIMs are characterized by a double-well potential comprising of the various M_J or M_s states with a barrier height, U (see Figure 1.5). In the presence of an external magnetic field one of the lowest energy states in the double well potential gets

populated and even after removal of the magnetic field, this state remains populated, and the molecules experience an energy barrier represented by the double-well potential height for magnetization reversal to the equilibrium state below the blocking temperature, T_B. In practice, the thermal relaxations that defines the energy barrier, U_{eff} are accompanied by spin-lattice (Raman/direct) relaxations as well as QTM.[11b]
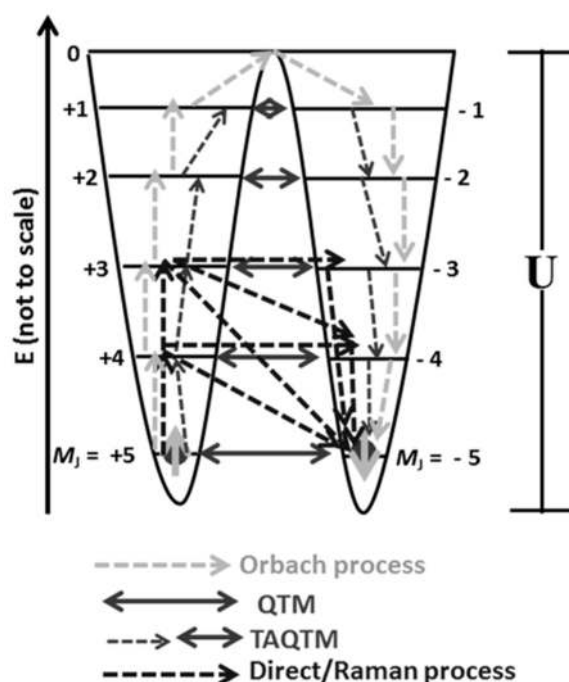
Figure 1.5. Schematic representation of a double well potential with barrier height, U. The most common mechanisms of magnetization relaxation are outlined. Adapted from [[11b]]

The assessment of SIMs/SMMs is done from the magnitude of U_{eff} and T_B (the blocking temperature). Therefore, a larger value of U_{eff} and T_B signifies the better quality of SIM/SMM. The experimental method of determination of U_{eff} was discussed in the section 1.2.1. Although large U_{eff} values are obtained in many 4f metal complexes, most often this is not directly translated to magnet like behaviour due to the presence of other prominent relaxation processes.[12]

Again, the magnitude of blocking temperature T_B, is subjected to the experimental methods and there are three experimental ways to determine it. One way of determining the T_B value is the ZFC-FC χ_M vs T plot. In this experiment, T_B is defined as the maximum temperature where a peak in the zero-field cooled (ZFC) χ_M vs T plot is obtained. It has to be noted that the magnitude of T_B in this case is dependent on the temperature sweep rate and the applied magnetic field. Another method is to determine the highest temperature at which an opening of magnetic hysteresis loop is observed at zero dc field. However, it is to be noted that the hysteresis loops are strongly sweep rate dependent of the applied magnetic field. Generally a higher sweep rate results in observation of hysteresis loops with measurable coercive field at higher temperature. The third method of determination of T_B is the temperature or frequency dependent ac susceptibility experiment and it is defined as the temperature corresponding to 100 s of the relaxation time. For example, the dimeric radical bridged complex, $[[(TMS)_2N]_2(thf)Tb]_2(\mu\text{-}\eta^2{:}\eta^2\text{-}N_2)\}$ (**1.4**) which shows a T_B value as 14 K follows all these three definitions (Figure 1.6).
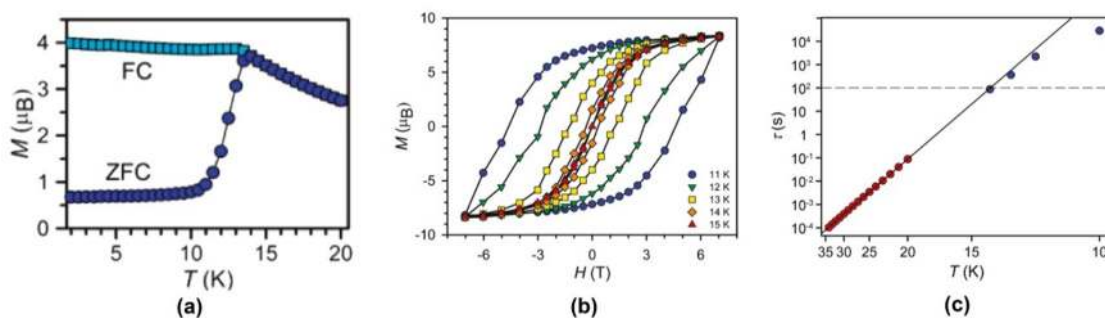
Figure 1.6. (a) ZFC-FC plot of **1.4** (sweep rate of 0.9 mT/s), (b) M-H plot of obtained for **1.4**, and (c) The relaxation times, τ plotted against T obtained from Cole-Cole plots for **1.4** from 11 to 15 K. Adapted with permission from the ref. [13].

With this background, we now move to describe the various types of molecular nanomagnets.

1.4 Single-Molecule Magnets (SMMs)

In 1990s, Sessoli and Gatteschi found that the dodecanuclear mixed-valence $[Mn_{12}]$ complex, $[Mn_{12}(CH_3COO)_{16}(H_2O)_4O_{12}]$ (**1.1**) (Figure 1.7 (*left*)) showed a slow magnetic relaxation of purely molecular in origin.[14] Although the molecular structure of this complex was known earlier, the unprecedented slow relaxation behaviour attracted the attention of scientific community. Thus, molecular complexes that show slow relaxation of magnetization and magnetic hysteresis below a certain temperature are now termed as Single-Molecule Magnets (SMMs). It is worth mentioning here that monometallic paramagnetic complexes that show similar magnetic behaviour are termed as Single-Ion Magnets (SIMs) and will be discussed in Section 1.5. In 1993, another interesting molecule $\{[(tacn)_6Fe_8(\mu_3\text{-}O)_2(\mu_2\text{-}OH)_{12}]Br_7(H_2O)\}Br$ (**1.5**) (where tacn = 1,4,7-triazacyclononane) was found to be a SMM (Figure 1.7 (*right*)).[15] Both the $\{Mn_{12}\}$ and $\{Fe_8\}$ complexes have a $S = 10$ spin ground state and also possess an *Ising* type magnetic anisotropy which generates an energy barrier that opposes magnetization reversal. Detailed magnetization studies revealed that magnetization relaxation in both the complexes occurs via a thermally activated pathway. However, in the case of the $\{Fe_8\}$ complex, below 0.3 K, the rate of relaxation becomes independent of temperature indicating relaxation via a quantum tunneling pathway. Soon after these discoveries, a large number of polynuclear 3d metal complexes were synthesized in order to observe SMM behavior, particularly at higher temperatures.
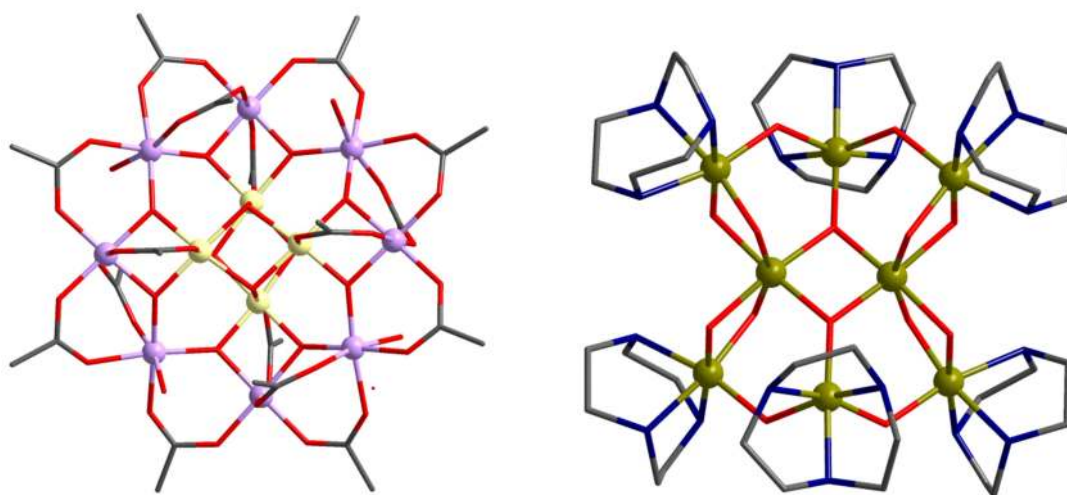
Figure 1.7. (*left*) Molecular structure of the {Mn$_{12}$} complex; Colour codes: C = charcoal black; O = red; Mn^{III} = lavender; Mn^{IV} = light yellow. (*right*) Molecular structure of the {Fe$_8$} complex. Colour codes: C = charcoal black; O = red; N = red Fe^{II} = lime. Reproduced with permission from refs [14c, 15]

In this section, various representative SMMs are described including their synthesis and magnetic properties.

1.4.1 3d Metal SMMs. The unique magnetic properties of polynuclear 3d metal complexes arise from two key parameters. These are (*i*) a large spin ground state (*S*) and (*ii*) a uniaxial (*Ising* type) magnetic anisotropy represented by –*D* (*D* is the zero field splitting parameter).[16] The combination of these two parameters leads to an anisotropic energy barrier given by

$$U = |D|S^2 \text{ for integer spin and}$$

$$= |D|(S^2 - 1/4) \text{ for half integer spin}$$

It is important to note here that the *D* value can be a -ve or a +ve quantity.[17] In the case of -ve *D*, the energy difference between *M*s = 0 and *M*s = ±*S*, denotes *U* i.e. the anisotropic energy barrier for magnetization reversal via thermaly activated pathway. In contrast, +ve *D* represents a situation where a non degenarate *M*s = 0 state

represents the ground state of the system of interest and therefore there is no barrier for magnetization reversal (Figure 1.8).[17] However, it is not very uncommon that some mononuclear Co^{II} complexes show slow relaxation process despite having +ve D value.[18] The plausible reasons for SIM behaviour in such monometallic systems may be due to (*i*) a field-induced bottleneck effect;[18b] (*ii*) the presence of a large easy-plane anisotropy barrier (large E parameter);[18a] or (*iii*) a dominant role of an optical acoustic Raman process. [18c]
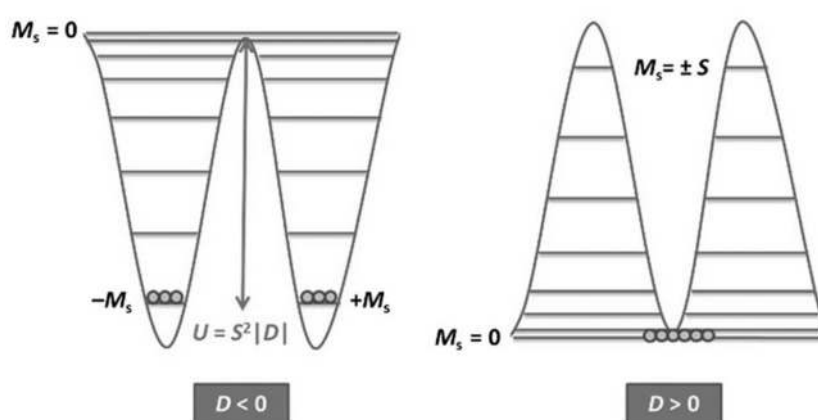
Figure 1.8. Double-well energy diagram for negative (*left*) and positive (*right*) D. Reproduced with permission from ref [17]

Another important parameter in polynuclear 3d metal complexes is the magnitude of exchange interaction between the metal ions, denoted by J. This parameter plays an important role in the isolation of the spin ground state from the excited states at a given temperature. Since the magnitude of exchange interaction in the case of 3d metal ions is quite large initial efforts of preparing SMMs relied on the synthesis of exchange coupled polynuclear 3d metal complexes with large S values. In this context, several polynuclear $Mn^{II/III}$ assemblies have been explored with S value ranging from 4 to 83/2.[19] The extremely high nuclearity polynuclear Mn^{III} complex, $[Mn^{III}_{84}O_{72}(OMe)_{24}(MeOH)_{12}(H2O)_{42}(OH)_6]$ (**1.6**) having $S = 83/2$ however showed a

poor energy barrier of 18 K (τ_0 = 5.7 x 10^{-9} s).[19g] Other polynuclear complexes also showed similar magnetic properties without much improvement in the enhancement of the overall energy barrier. Most strikingly, all the polynuclear 3d metal complexes are characterized by very small magnitude of the D parameter.[20] This is because the magnitude of $|D|$ is determined by the net contribution resulting from every local anisotropic metal centers present in the complex that often tends to cancel one another. Theoretical studies also reveal that D is inversely proportional to S^2, and therefore U_{eff} is virtually invariant with regards to increasing S.[21] These facts emphasize that enhancing S is not an efficient criterion to obtain good SMMs, and rather emphasis should be given to enhance the $|D|$ parameter. Therefore, mononuclear 3d metal complexes were synthesized and studied in order to manipulate the D parameter by modulating the coordination geometry around the metal center. These aspects will be discussed in section 1.4.1.

Although polynuclear 3d transition metal complexes are characterized by very low blocking temperatures (T_B) they are good examples of the bottom up synthetic approaches for the synthesis of molecular magnets. The syntheses of many 3d-metal based SMMs are mainly serendipity driven which depends on (*i*) metal ions, (*ii*) choice of ligands and (*iii*) the reaction conditions. The common metal ions used as spin carriers of 3d metal SMMs are V^{III},[22] Mn^{III},[23] $Mn^{II/III}$,[24] $Mn^{III/IV}$,[25] Fe^{II}/Fe^{III},[26] $Co^{II}/Co^{II/III}$,[27] and Ni^{II} metal ions[28]. The ideal ligand systems for the synthesis of multinuclear 3d metal complexes are the ones that can bind to multiple metal centers as well as being capable of propagating magnetic exchange interactions between paramagnetic metal ions at certain coordination modes and specific bond angles. Figure 1.9 demonstrates selected organic ligands that were used for the synthesis of polynuclear 3d metal complexes. In addition to ligands listed in Figure 1.9, several

monoatomic ligands such as O^{2-}, S^{2-}, F^-, Cl^-, etc., act as bridges to connect various metal ions enabling the stabilization of the polynuclear cluster. They are also efficient in enabling the transfer of magnetic exchange interactions by overlapping the magnetic orbitals of the metal centers.
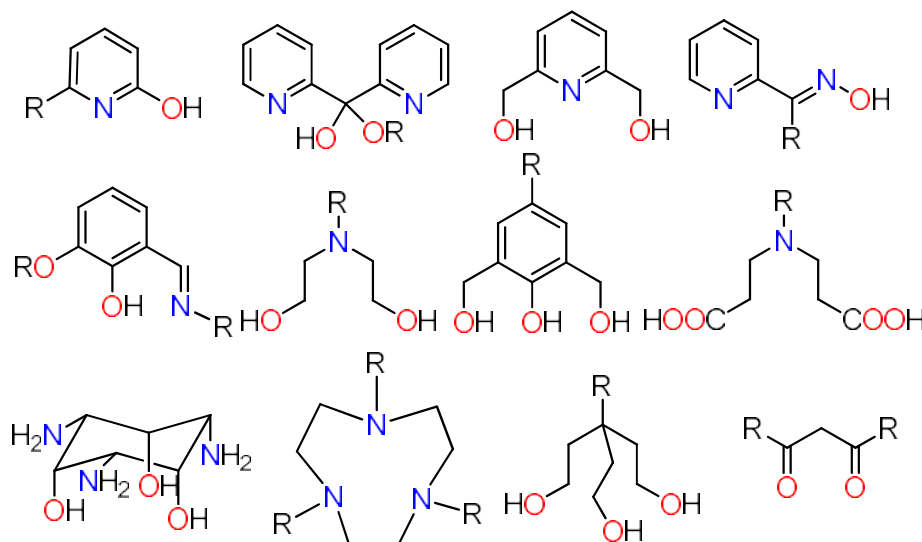
Figure 1.9. Selected ligands used for the synthesis of 3d-based SMMs. Here, R is H, alky/aryl groups and/or neutral donor groups (e.g. $-NH_2$, $-OMe$ etc.)

Since the discovery of Mn_{12} complex, the field of SMMs was dominated by metal complexes containing manganese ions. In particular, Mn^{III} ion (d^4) has been the most studied. This is because Mn^{III} ion in an octahedral crystal field undergoes Jahn-Teller distortion that results in a tetragonal elongation along the z-axis. A $^5B_1$ term that arises from the splitting of the ground ^5E term due to the distortion mixes with the excited states via 2nd order spin-orbit coupling (SOC) and stimulates a negative D value in most of the cases.[23] This was proved experimentally in the octahedral mononuclear Mn^{III} complex, $Ph_4P[Mn(opbaCl_2)(py)_2]$ (**1.7**) which showed a filed induced SIM behaviour with an energy barrier, U_{eff} = 18 K (H_{dc} = 1000 Oe).[29] The rational design of this ligand played a significant role in the isolation of this monometallic derivative in the axially elongated *pseudo* O_h geometry. The experimental data was fitted which

gave D = -3.27 cm^{-1}, E = 0.11 cm^{-1} for g = 1.99, confirming the presence of 2nd order SOC.

The iron-based SMMs are the second most studied family of SMMs just after the family of manganese-based SMMs. Iron in its +2 and +3 oxidation states provides four and five unpaired electrons in the high spin states and therefore suited for the synthesis of SMMs with high S value. However, the nature of the magnetic exchange interaction between two neighboring iron ions was found to be rarely ferromagnetic.[16a] Moreover, the iron storage protein which is considered as a magnetic nanoparticle attracted this ion in the bottom up synthesis of SMMs.[1c] Another metal ion that finds widespread application in SMMs/SIMs is the Co^{II} ion (d^7). The first Co^{II} based SMMs was reported by Christou and coworkers in the year 2002. Since then this metal ion has gained considerable attention in the field of SMMs. The 1st order spin-orbit coupling (λ for Co^{II} in octahedral field is –ve with the order of 170 cm^{-1}) [1b] accompanied with significant Jahn-Teller distortion makes this ion appealing in this field. Till date, the record of high energy barrier among the entire 3d metal ions is held by this ion (see Table 1.1 entry number 1). Ni-based SMMs are relatively small, although such systems are synthesized because of (*i*) ferromagnetic super-exchange interactions between neighboring nickel centers and (ii) ease of synthesis of a large number of multimetallic Ni^{II} clusters. Also, in an octahedral field Ni^{II} (d^8) ion is only weakly anisotropic as a result of second order spin-orbit coupling. Nevertheless, large ZFS values were obtained in mononuclear Ni^{II} complexes in certain coordination geometries (see Section 1.5.1). Selected examples of some of the best performing 3d metal SMMs (in terms of high U_{eff}) are tabulated in Table 1.1.

Table 1.1. Representative examples of high energy barrier 3d metal SMMs.

Sl. No.	Complex	U_{eff}^{exp} (cm^{-1})	T_B (K)	Sweep Rate (Oe/S^{-1})	Ref.
1	[Co$_4$(μ-NP^{t}Bu$_3$)$_4$][B(C$_6$F$_5$)$_4$] **(1.8)**	87	3.6	30	[30]
2	[Mn$_6$O$_2$(Et-sao)$_6$(O$_2$CPh(Me)$_2$)$_2$(EtOH)$_6$] **(1.9)**	60	4.5	1400	[31]
3	[Mn$_6$O$_2$(Et-sao)$_6$(O$_2$C$_{11}$H$_{15}$)$_2$(EtOH)$_6$] **(1.10)**	55.5	3.5	140	[32]
4	[Et$_3$NH][Co$_8$(chp)$_{10}$(O$_3$PPh)$_2$(NO$_3$)$_3$(Hchp)$_2$] **(1.11)**	58.4	4	140	[33]
5	[Mn$_{12}$O$_{12}$(O$_2$CCH$_2$Br)$_{16}$(H$_2$O)$_4$] **(1.12)**	52	3.6	20	[34]
6	[Mn$_{31}$O$_{24}$(OH)$_2$(OMe)$_{24}$(O$_2$CPh)$_{16}$(*rac*-hpm)$_2$] **(1.13)**	42	5	1400	[35]

^{t}Bu = tert-butyl; Et-saoH$_2$: 2-hydroxyphenylpropanone oxime; Hchp: 6-chloro-2-hydroxypyridine; hmpH: 2-Hydroxymethyl)pyridine

1.4.2 3d-4d/5d SMMs. The strategy of incorporating heavier transition metal ions in combination with the 3d metal ions has attracted attention due to the presence of diffused *d* orbitals in the latter.[36] The heavier transition metal ions (4d/5d) can facilitate substantial overlap between magnetic orbitals leading to stronger exchange interactions.[36] Also, the large spin-orbit coupling constant of the heavier transition metals ensures highly anisotropic *g* factors as well as unusually large zero-field splitting (ZFS) values in the complexes.[36] Moreover, their redox behaviour can be triggered electrochemically or photochemically which can be utilized for obtaining photo-magnets.[37]

The most promising synthetic design of obtaining 3d-4d/5d metal complexes is to employ a building block approach where predesigned metal building blocks of 4d and 5d ions are prepared with additional donor sites that can propagate into a multinuclear complex.[38] Some selected building blocks of 4d/5d metal ions are shown in Figure 1.10. From this figure it is evident that the cyanide ion, CN$^-$, is a promising bridging ligand and it is extensively used for the synthesis of 3d-4d/5d heterometallic

complexes.[38c, 39] Moreover, in the linear M–CN–M' coordination mode the nature of the exchange coupling between octahedral M and M' centers can be predicted depending on the nature of metal magnetic orbitals involved.[39a] The first 3d/4d (Mn^{II}/Mo^{III}) and 3d/5d (Mn^{II}/Re^{II}) CN-bridged SMMs were synthesized by Long and coworkers[39b] and Dunbar and coworkers[40], respectively (Figure 1.11). Table 1.2 shows a few representative examples of 3d-4d/5d SMMs. [41]
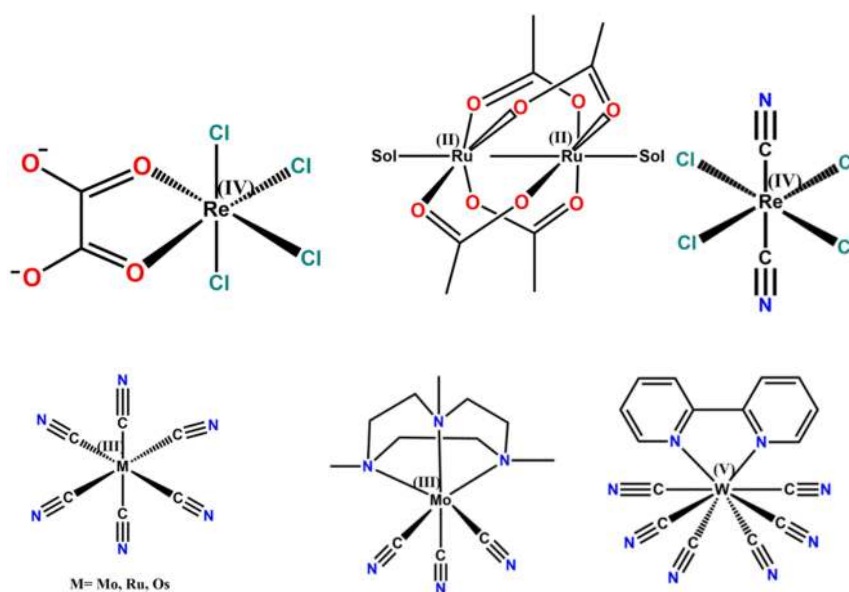
Figure 1.10. Selected 4d and 5d building blocks for the synthesis molecular magnets.[36]

Table 1.2. Representative examples of 3d-4d/5d metal SMMs.

Sl. No.	Complex	U_{eff}^{exp} (cm^{-1})	τ_0 (s^{-1})	D (cm^{-1})	Ref
1	$[(PY_5Me_2)_4Mn^{II}_4Re^{IV}(CN)_7](PF_6)_5$ (**1.14**)	47.3	2.4×10^{-8}	-0.44	[41a]
2	$[Ni\{Ni(bpy)(H_2O)\}_8\{W(CN)_8\}_6]$ (**1.15**)	47.3	1.5×10^{-13}	---	[41d]
3	$\{[W^V(bpy)(CN)_6]_2[Mn^{III}(L^!)]_2\}$ (**1.16**)	32.0	5.1×10^{-12}	-0.90	[41b]
4	$\{Co^{II}_9[W^V(CN)_8]_6 \cdot (CH_3OH)_{24}\}$ (**1.17**)	27.8	7.3×10^{-11}	---	[41c]
5	$[(PY_5Me_2)_4Ni^{II}_4Re^{IV}(CN)_7](PF_6)_5$ (**1.18**)	24.4	1.4×10^{-7}	-0.93	[41e]

PY₅Me₂: 2,6-bis(1,1-bis(2-pyridyl)ethyl)pyridine; bpy: bipyridine; L!: N,N'- bis(2-hydroxyacetophenylidene)-1,2-diaminopropane
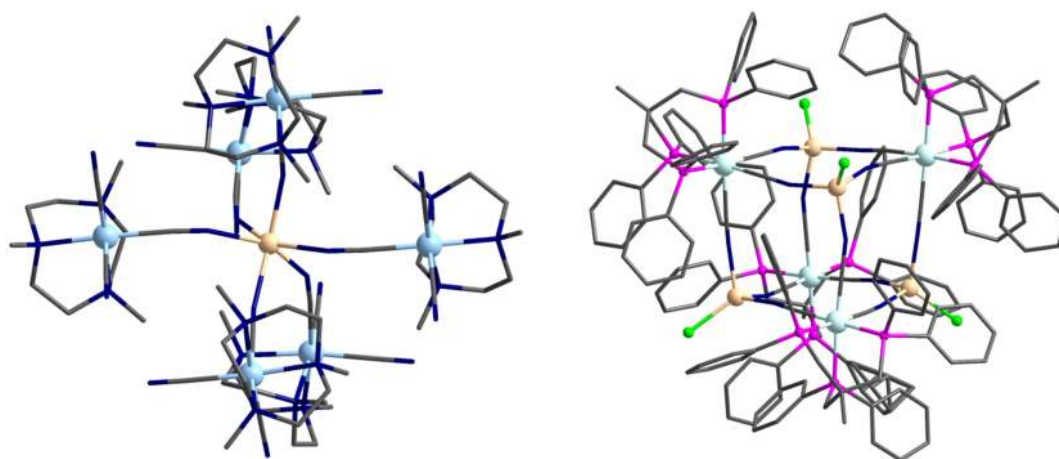
Figure 1.11. (*left*) Molecular structure of the {Mn^{II}/Mo^{III}} complex; Colour codes: C = charcoal black; N = blue; Mn^{II} = tan; Mo^{III} = pale blue. (*right*) Molecular structure of the {Mn^{II}/Re^{II}} complex. Colour codes: C = charcoal black; Cl = bright green; P = pink; N = blue; Mn^{II} = tan; Re^{II} = light turquoise. Adapted from refs [39b, 40]

1.4.3 4f Metal SMMs. The SMM behaviour in a 4f metal based complex was observed for the first time in 2003 by Ishikawa and coworkers.[42] They discovered that the monometallic Tb(III) *bis*-phthalocyanine complex, [Tb(Pc)$_2$]$^-$ (**1.19**) showed slow relaxation of magnetization with an energy barrier, U_{eff} = 330 K which was much greater than the observed U_{eff} values in the case of 3d metal complexes.[42] This discovery has triggered considerable interest in utilizing the 4f metal ions for the synthesis of SMMs operating at higher temperatures. It is worth noting that such monometallic 4f complex is termed as single-ion magnet or monometallic single-molecule magnet. These will be discussed separately in the section 1.5.2. In this section, SMMs containing two or more 4f metal ions will be discussed. The 4f electrons in lanthanides are deeply buried inside the [Xe] core and are largely shielded by the 5s and 5p orbitals from the ligand field.[43] This leads to extremely small Ln···Ln magnetic exchange interactions, mediated by the bridging organic ligand (in the order of 10 cm^{-1}) and the magnetic coupling is mediated by dipolar interactions.[10,

[20, 44] It has also been observed that the U_{eff} values in polynuclear Ln^{III} complexes are much larger than the magnitude of exchange interaction between the metal centers.[44b] This suggests that the strength and symmetry of the local crystal field plays the key role in determining the nature of magnetic relaxations in polynuclear 4f metal complexes.[45] The poor Ln···Ln exchange interactions results in poor quality of hysteresis loops and the coercive fields are found to be zero or close to zero at zero external field. This is because at the zero field even though there is an energy barrier for magnetization reversal the under-barrier quantum tunneling of magnetization (QTM) relaxation process is significantly operating.[10] This obscures their potential use in information storing devices. Therefore, the prime synthetic challenge associated with designing polynuclear Ln^{III} complexes is to enhance magnetic exchange interactions in order to reduce QTM effects. Figure 1.12 represents some selected ligands for the synthesis of multimetallic Ln^{III} complexes.
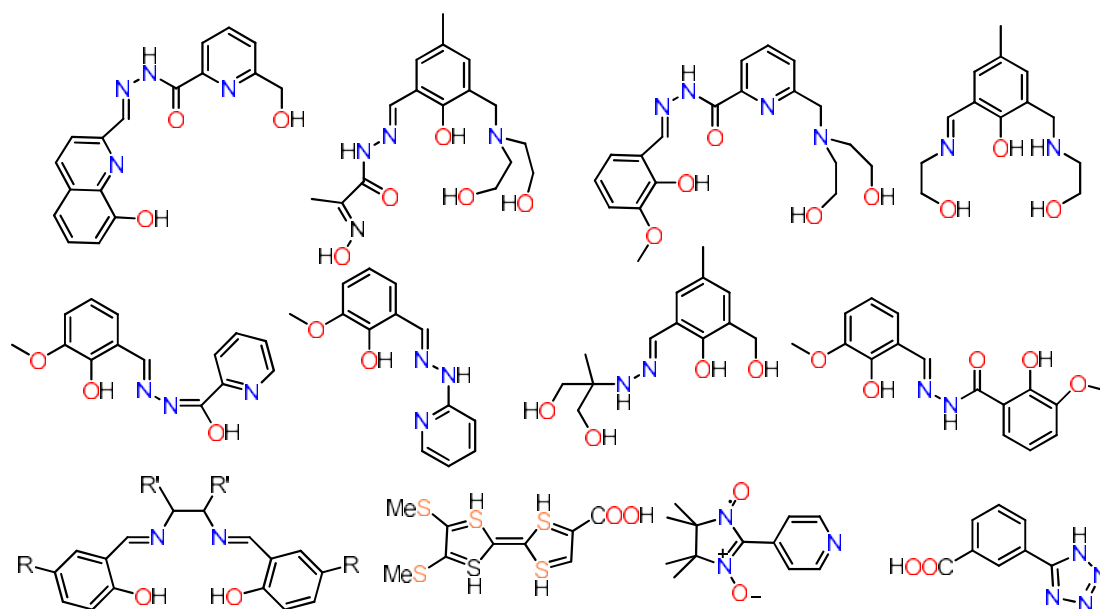
Figure 1.12. Selected multidentate ligands used for the synthesis of multimetallic Ln^{III} complexes.[10]

The smallest family of polynuclear lanthanide metal complexes is the dinuclear Ln^{III} complexes where magnetic exchange interactions can be studied explicitly.[44b, 46] They also serve as the simplest models to understand the single-ion relaxations vs molecular relaxations. Long and co-workers discovered that the N_2^{3-} radical bridged terbium complex, **1.4** ($[Tb_2(N_2)\{N(TMS)_2\}_4(thf)_2]^-$) shows a very strong coupling between the Ln^{III} ions and the N_2^{3-} bridge ($J = -27$ cm^{-1}, obtained from the Gd$_2$ derivative).[13] The SMM behavior for this complex revealed a very high energy barrier ($U_{eff} = 327$ K) with magnetic hysteresis observable up to 14 K.[13] This example infers that strong exchange coupled interactions diminishes the fast relaxation processes at zero field rendering only the thermally activated relaxation process. Apart from radical bridged dinuclear Ln^{III} complexes several other bridges have also been studied and it stands out that delocalized radical[47], aromatic ring[48] and S-bridged ligand[49] are very effective to promote exchange interactions between lanthanide centers.
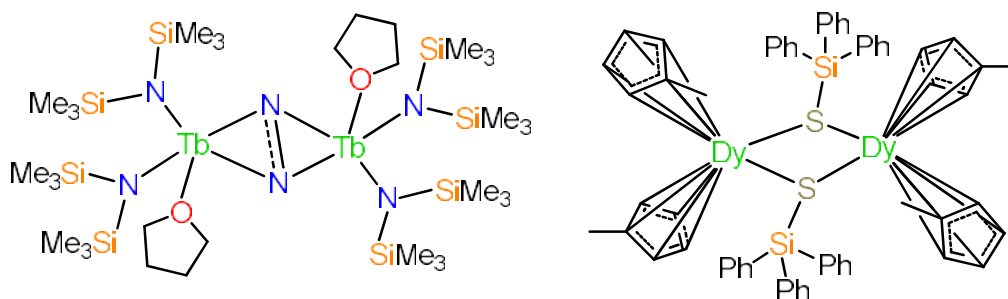
Figure 1.13. The line diagrams of N_2^{3-} radical bridged Tb^{III} complex **1.4** (*left*) and sulfur-bridged Dy^{III} complex, $[\{Cp'_2Dy(\mu\text{-}SSiPh_3)\}_2]$ (**1.20**) (*right*)

The next higher nuclearity i.e. the trinuclear Ln^{III} complexes showed new and interesting magnetic phenomenon such as spin chirality in the Dy$_3$ triangle.[50] The triangular Dy$_3$ complex shows a non-magnetic ground state resulting from the toroidal arrangement of magnetic anisotropic axes. This discovery leads to a new arena of

Single-Molecule Toroids (SMTs) based on the toroidal magnetic moments of ground

doublets. This behaviour is shown by polynuclear cyclic lanthanide systems.[51]
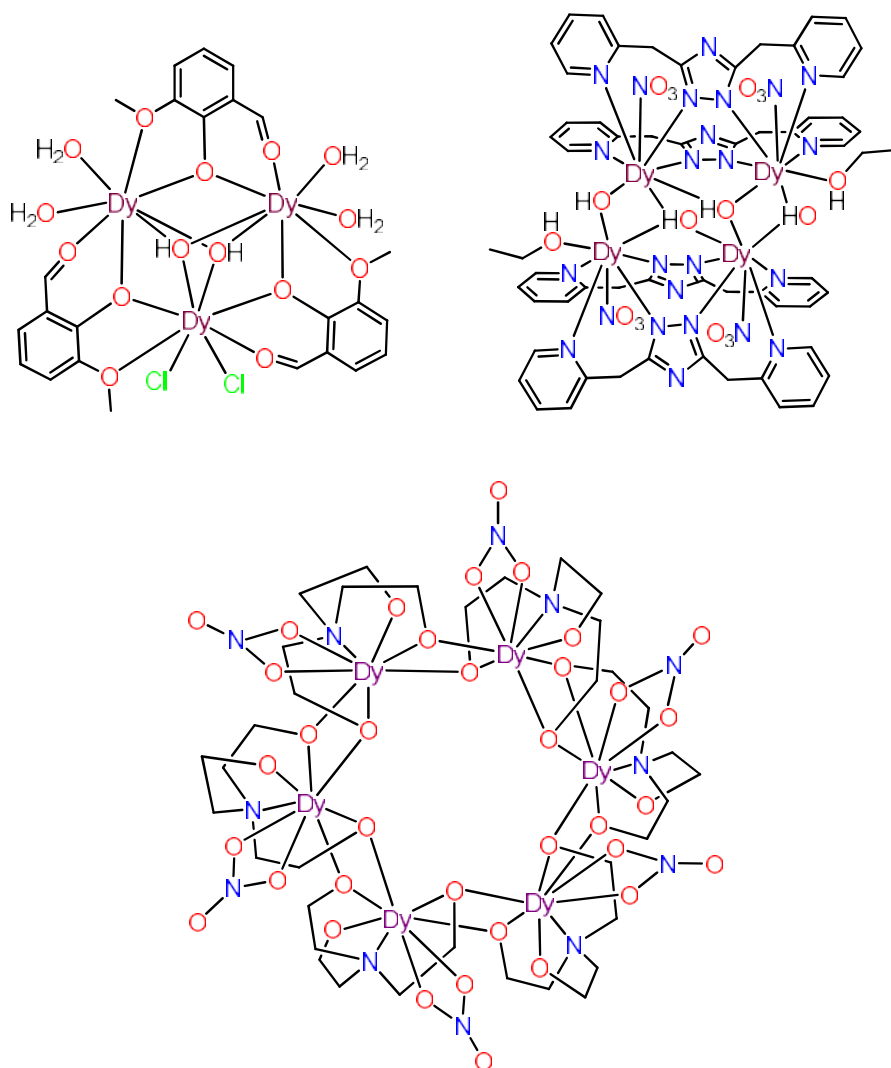
Figure 1.14. Cyclic multinuclear Dy^{III} complexes having toroidal magnetic moments.

The higher nuclearity 4f systems were targeted in order to enhance magnitude of U_{eff}

by maximizing the total spin ground state. This was particularly observed in the

strongly coupled 4f systems.[52] Two very interesting polynuclear 4f SMMs are

[Dy$_4$K$_2$O(O^{t}Bu)$_{12}$] (**1.21**) and [Dy$_5$O(O^{i}Pr)$_{13}$] (**1.22**) that show high energy barriers of

U_{eff} = 481 and 368 cm^{-1} respectively owing to extensive metal ligand interactions.[52a]

[52b] In addition, it was observed that suitable arrangement of the magnetic anisotropy

axes at the different magnetic sites effectively enhances the magnetic properties. However, controlling the magnetic anisotropy in polynuclear complexes is extremely difficult and synthetically challenging. Nevertheless, synthetic designs based on multidentate ligand approach, organometallic approach, and building block approach appear to be the effective routes for the synthesis of multimetallic 4f metal complexes.[10, 44a, 53] Apart from novel magnetic properties, the high nuclearity lanthanide complexes also possess a wide range of aesthetic core structures: tetranuclear (linear, grids, Y-shaped, cubanes, seesaw tetramers, rhombus),[54] pentanuclear (pyramid, goblet, butterfly),[55] hexanuclear (linked-triangles, wheel, propeller),[56] heptanuclear (disc, *non*-planar),[57] octanuclear (christmas-stars, cyclooctadiene, butterfly),[58] and so on[59]. Table 1.3 summarizes the magnetic properties a few selected SMMs based on high nuclearity 4f metal complexes.[60]

Table 1.3. Representative examples of 4f metal SMMs.

Sl. No.	Complex	$U_{\text{eff}}^{\text{exp}}$ (cm^{-1})	τ_0 (s^{-1})	T_B (K)	Sweep Rate (Oe/S^{-1})	Ref.
1	[Cp*$_2$Dy(μ-Fp)]$_2$ (**1.23**)	662	1.7 x 10^{-12}	6.2	20	[60e]
2	[Dy(μ-OH)(DBP)$_2$(THF)]$_2$ (**1.24**)	524	3.5 x 10^{-12}	8	200	[60b]
3	[Dy(L$^\$$)$_2$(phen)(μ_2-OH)(μ_2-H$_2$O)]$_n$ (**1.25**)	457	6.16 x 10^{-13}	6	300	[60a]
4	[Dy$_3$(Iba)$_8$(btaH)$_2$(ClO$_4$)(H$_2$O)$_5$]$_n$ (**1.26**)	280	4.37 x 10^{-11}	1.8	-	[60c]
5	[Er^{III}$_2$(COT'')$_3$] (**1.27**)	231	5.7 x 10^{-10}	12	22	[60f]
6	[Ho$_5$O(O^{i}Pr)$_{13}$] (**1.28**)	278	1.5 x 10^{-9}	---	---	[60d]

Fp = CpFe(CO)$_2$; DBP$^-$ = 2,6-di-tert-butylphenolate); COT'' = 1,4-bis(trimethylsilyl)-cyclooctatetraenyl dianion; HL$^\$$ = 4-nitrobenzoic acid; IbaH = isobutyric acid and btaH = benzotriazole;

1.4.4 5f Metal SMMs. The heavier multimetallic 5f complexes have been less explored compared to the polynuclear 4f metal complexes. The 5f metal complexes were sought due to the fact that unlike 4f orbitals the radial distribution of 5f orbitals are diffuse in nature that leads to significantly better overlap with ligands and hence greater covalent character and therefore stronger exchange coupling.[61] In addition, 5f ions possess greater spin-orbit coupling implying the presence of inherent magnetic anisotropy.[44a, 62] However, it has to be kept in mind that actinide elements are radioactive and require sophisticated facilities to handle them. Therefore, magnetic studies are limited to ^{238}U compounds as it is the most abundant and comparatively stable isotope of uranium.[62] Besides ^{238}U complexes, only a handful of mononuclear/polynuclear transuranic complexes are known to be SMMs.[62] Figure 1.15 shows the structures of two well-known multinuclear actinide SMMs.
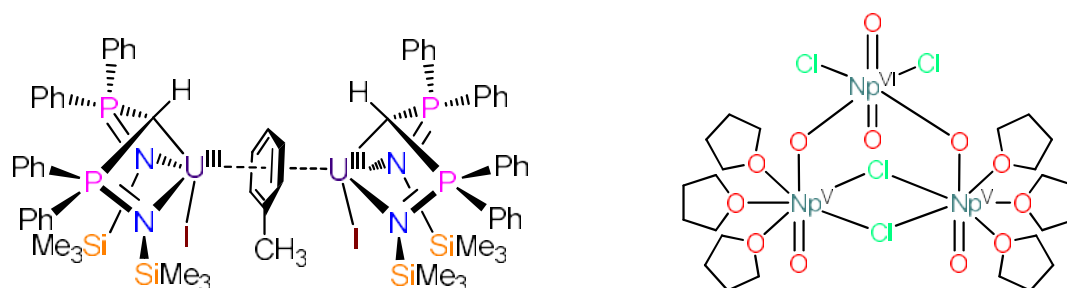
Figure 1.15. (*left*) Line diagram of delocalized arene-bridged dinuclear complex, [U$^{\mathrm{III}}$$_2$($\mu$-C$_6H_5CH_3$)(HBIPM$^{\mathrm{TMS}}$)$_2I_2$][63] (**1.29**) which is a SMM under a biased field of 0.1 T. (*right*) The transuranium mixed-valent [Np$^{\mathrm{VI}}$Np$^{\mathrm{V}}$$_2O_6$($\mu$-Cl)$_2Cl_2(THF)_6$][61] (**1.30**) complex showed SIM behavior with U_{eff} = 140 K (H_{dc} = 0 Oe) (the coupling constant for the Np$^{\mathrm{V}}$···Np$^{\mathrm{VI}}$ pairs is J = -7.5 cm^{-1}).

1.4.5 3d-4f Metal SMMs. Lanthanide metal ions although having an inherent single-ion anisotropy are poised to possess temperature independent zero field QTM in the molecular complexes.[64] As discussed in the section 1.2.2, 4f-4f exchange interactions are very weak and therefore magnetic relaxation in a polynuclear 4f complex is of single-ion in nature and therefore QTM cannot be avoided. However, this effect is less pronounced in the strongly exchange coupled polynuclear 3d metal complexes. Therefore, 3d metals ions are combined with the 4f metal ions in order to quench QTM and enlarge the barrier heights.[65] The 3d-4f magnetic interactions may also increase the ground spin state by ferromagnetic exchange coupling interactions.[66] Moreover, the magnetic anisotropy offered by some 3d metal ions in some specific coordination geometry can lead to the enhancement of the overall magnetic anisotropy and to larger U_{eff} values (see Table 1.4). The first time a substantial ferromagnetic coupling between 3d and 4f metal ion was observed was in the trinuclear complex, $[Cu^{II}Gd^{III}(L^{\#})_2(H_2O)_3][(Cu^{II}(L^{\#}))(ClO_4)]$ **(1.31)** (where $L^{\#}$ = [N, N'-ethylenebis(salicylaldiminato) and J_{Cu-Gd} = +12.23 cm^{-1}) which opened the interest for hetrerometalic 3d-4f complexes in molecular magnetism.[67] With the developments in the synthetic protocols many other heterometallic 3d-4f complexes have been synthesized with interesting magnetic properties.[68] Apart from magnetism, polynuclear complexes featuring both 3d metal and 4f metal ions in the same molecule are potentially useful in the fields of optics,[69] adsorption and storage,[70] and in catalysis[71]. In addition, toroidal magnetic moments are also now realized in the case of cyclic heterometallic 3d-4f complexes.[72]

From a synthetic point of view 3d and 4f metals ions have different binding requirements. This is due to the differences in charge/size ratio of these ions. In general, it has been observed that lanthanide ions are oxophilic. Using this preference

of lanthanide ions it is possible to arrive at heterometallic assemblies by mixing 3d ions, 4f ions and a ligand that provides specific sites of binding for both (Figure 1.16).[68d]
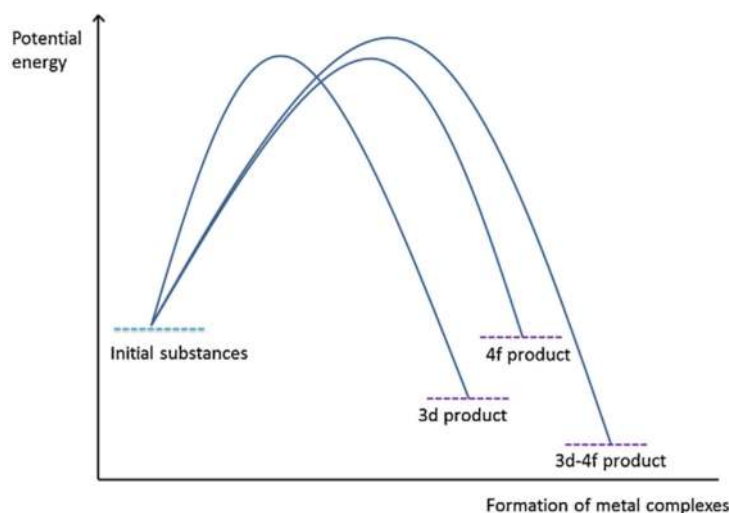
Figure 1.16. Qualitative model showing the relative energy levels of possible products. Adapted from ref [[68d]]

In order to tackle this, multi-pocket compartmental ligands having specific coordination pockets with *O*-donor and *N*-donor atoms capable of binding simultaneously to both 3d and 4f metal ions are used for the synthesis of heterometallic 3d-4f complexes. In addition, suitable co-ligands are also employed in many instances to assist the formation of the heterometallic complexes. Figures 1.17 and 1.18 show selective multi-pocket ligands and co-ligands (with binding modes) used in the synthesis of heterometallic 3d-4f complexes.
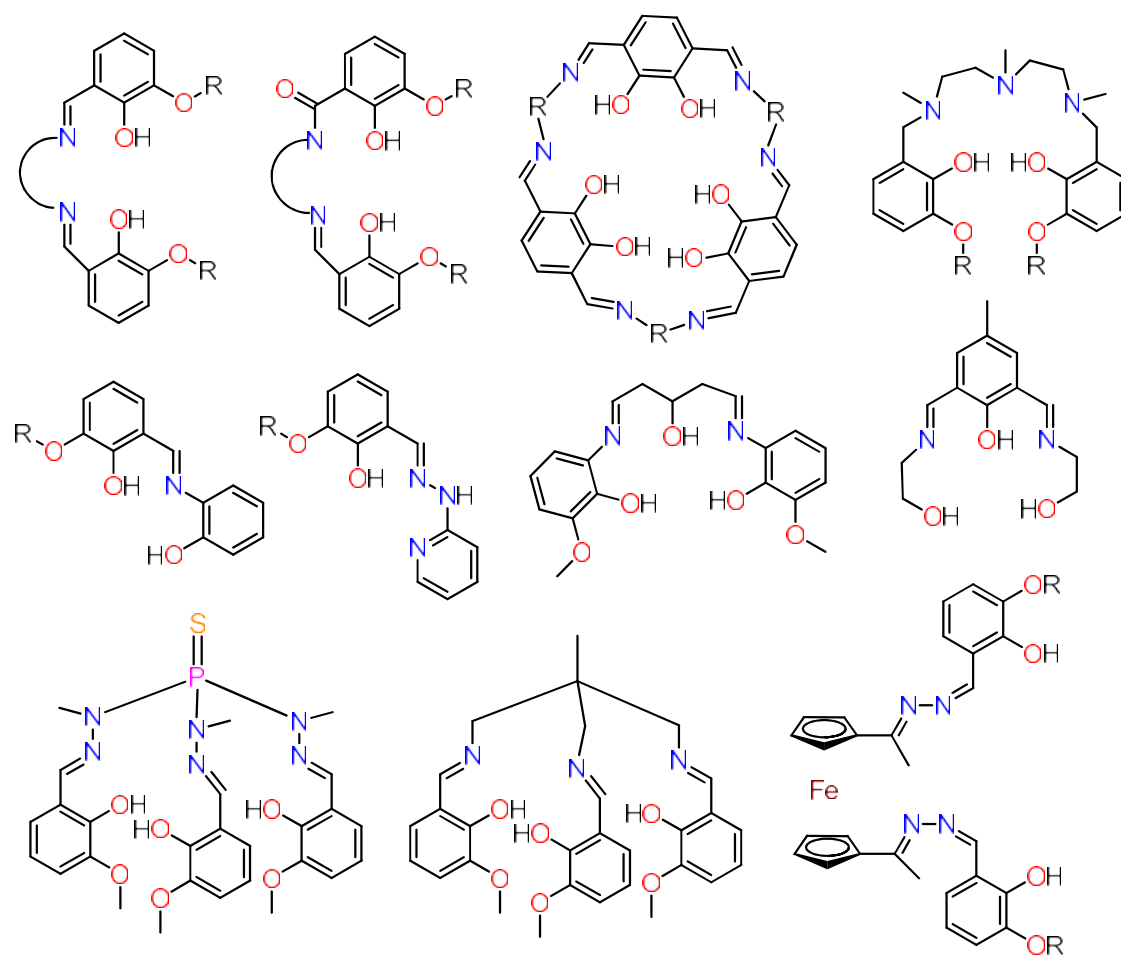
Figure 1.17. Selected multi-pocket ligands (here R is alkyl group)
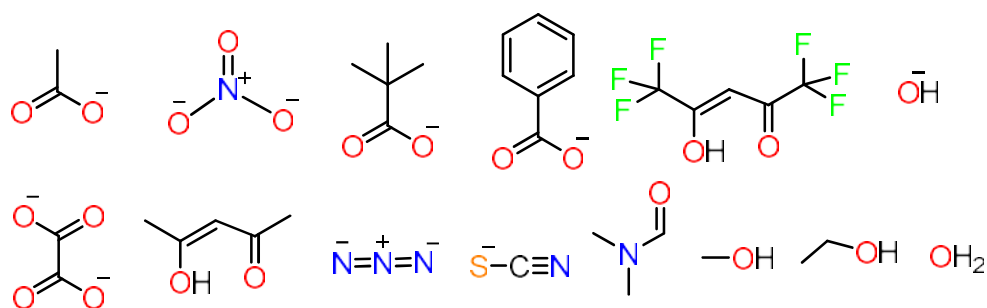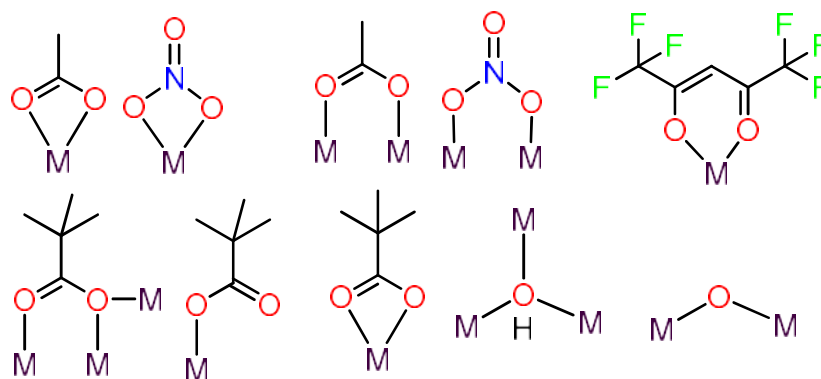
Figure 1.18. Selected co-ligands and their binding modes

Utilizing such ligands, a numerous of 3d-4f complexes have been isolated with varied nuclearity/topologies such as binuclear,[73] linear and non-linear trinuclear,[74] propeller,[75] butterfly,[76] and cubane shaped tetranuclear,[77] defect dicubane hexamer,[78], windmill[79] and so on[77, 80]. Among all the different classes of 3d-4f complexes, the linear trimeric complex, $[Co_2Dy(L^{Br})_2(H_2O)]NO_3$ (**1.32**) (where L^{Br} = 2,2',2"-(((nitrilotris(ethane-2,1-diyl))tris(azanediyl))tris(methylene))tris-(4-bromophenol))) features the highest energy barrier of magnetization reversal, U_{eff} = 600 K (Table 1.4, Figure 1.19).[81] This complex possesses very large single-ion anisotropy at the Dy^{III} site due to axially compressed pentagonal bipyramidal geometry. In addition, the two asymmetric 6-coordinate Co^{II} are connected at opposite sides of the Dy(III) ion in a linear topology (Figure 1.19). In this study, it was also observed that loss of the crystallizing solvent H_2O molecules changes the U_{eff} barrier (>100 cm^{-1} increase) significantly.
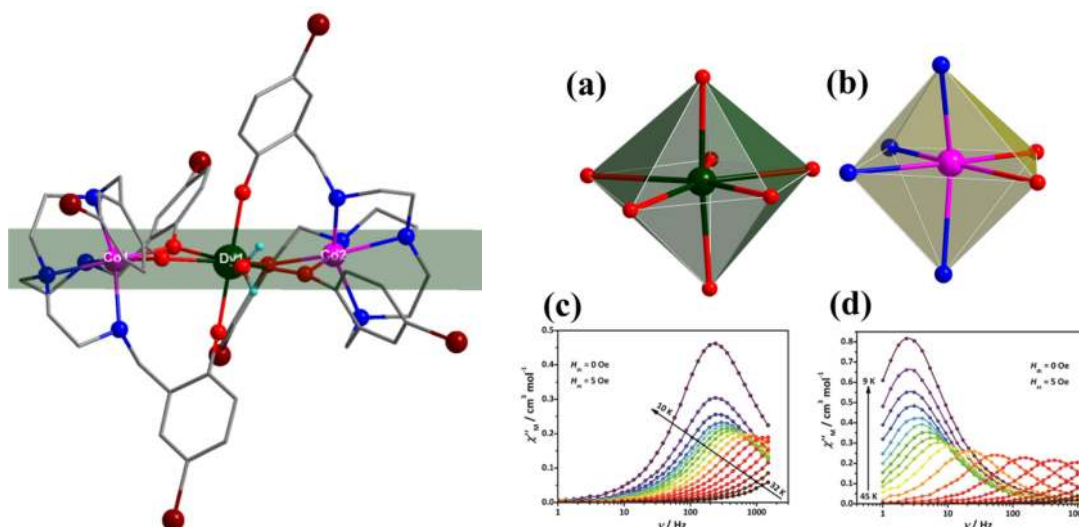
Figure 1.19. (*left*) Molecular structure of complex **1.32**. (*right*) coordination geometry of Dy^{III} (a), coordination geometry of Co^{II} (b), in phase and out of phase susceptibility of complex **1.32** (c and d). Adapted and reproduced with permission from ref [81].

The first family of Co^{II}-Ln^{III} SMMs was synthesized by Chandrasekhar and co-workers and this is the second most investigated family among all the 3d-4f complexes. A tripodal ligand (Figure 1.20) derived from the condensation of (S)P[N(Me)NH$_2$]$_3$ and *o*-vanillin was utilized to synthesize a linear Co^{II}-Ln^{III}-Co^{II} system (Figure 1.20). Interestingly, the Co^{II}-Gd^{III}-Co^{II} (**1.33**) derivative showed slow relaxation of magnetization below 8 K with U_{eff} = 27 K under a zero biased field.[82]
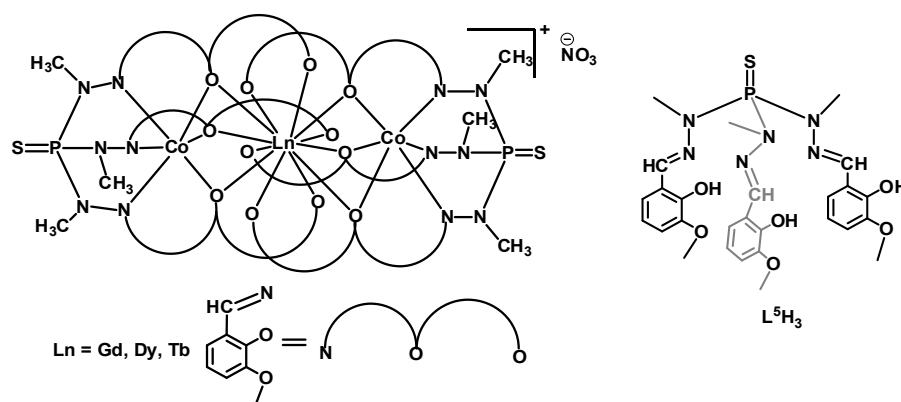
Figure 1.20. Line diagram of linear Co^{II}-Ln^{III}-Co^{II} complexes.

Although majority of 3d-4f complexes that have been investigated possess paramagnetic 3d metal ions[81, 83], interesting magnetic properties were also observed in 3d-4f metal complexes having diamagnetic 3d metal ions.[84] Most importantly it was observed that the diamagnetic metal ions alters the electron density distribution of coordinating ligands surrounding the lanthanide ion and enhances the magnetic properties. Further insight was gained in the theoretical calculations particularly on the Zn^{II}-Ln^{III} complexes which revealed that the diamagnetic metal ion increases the negative charge on the *oxo* center of the Zn–O–Ln bridging unit thereby helping in stabilizing the ground state of the Ln metal ions.[83a, 85] Table 1.4 summarizes the magnetic properties of selected heterometallic 3d-4f complexes.

Table 1.4. Magnetic properties of selected heterometallic 3d-4f complexes with high U_{eff} values.

Sl. No.	Complex	Topology	U_{eff}^{exp} (K)	τ_o	Ref.
paramagnetic 3d ion					
1	$[Co_2Dy(LBr)_2(H_2O)]NO_3$ (**1.34**)	linear	522	1.8×10^{-10}	[81]
			600	1.4×10^{-11}	
2	$[Fe_2Dy(L)_2(H_2O)](ClO_4)_2H_2O$ (**1.35**)	non linear	459	1.1×10^{-10}	[83a]
3	$Dy_2Co_2L_{10}(bipyridine)_2$ (**1.36**)	linear	118	1.8×10^{-11}	[83b]
	$Dy_2Co_2L_{10}(bipyridine)_2$ (**1.37**)	tetramer	105	1.8×10^{-11}	
4	$[Cr^{III}_2Ln^{III}_2(OMe)_2(O_2CPh)_4(mdea)_2(NO_3)_2]$ (**1.38**)	Coplanar rhombic	87.84	2.1×10^{-7}	[83c]
5	$[Cr_4Dy_4(\mu\text{-}F_4)(\mu_3\text{-}OMe)_{1.25}(\mu_3\text{-}H)_{2.75}(O_2CPh)_8(mdea)_4]$ (**1.39**)	Square grid	55	---	[83d]
with Zn^{II} ion					
9	$[Zn_2Dy(L)_2(MeOH)]$ (**1.40**)	linear	305	---	[86]
8	$[Zn_2(L^1)_2DyCl_3]\cdot2H_2O$ (**1.41**)	linear	299	7.4×10^{-11}	[85b]
7	$[ZnCl(\mu\text{-}L)Dy(\mu\text{-}L)ClZn]PF_6$ (**1.42**)	arc shape	186	4.98×10^{-10}	[85c]

10	[(LZnBr)$_2$Dy(H$_2$O)](ClO$_4$) (**1.43**)	linear	149	9.8×10^{-9}	[85a]

H$_2$L = N,N'-dimethyl-N,N'-bis(2-hydroxy-3-formyl-5-bromo-benzyl)ethylenediamine; L1 = N,N'-bis(3-methoxysalicylidene)phenylene-1,2-diamine;bipy = bipyridine; mdea = N-methyl-diethanolamine

1.5 Single-Ion Magnets (SIMs). The discovery of slow magnetic relaxation in the monmetallic 4f complex in 2003 has gained considerable interest in the magnetic properties of mononuclear derivatives. This class of magnets is known as single-ion magnets (SIMs). Thus, a monometallic paramagnetic complex showing the features of SMMs is termed as a single-ion magnet (SIM). The potential candidates of SIMs are 3d metal ions, 4f metal ions and as shown recently, also 5f metal ions. The synthetic strategies and magnetic properties of complexes prepared from these metal ions is outlined below.

1.5.1 3d Metal SIMs. The 3d metal ions are characterized by (*i*) small magnetic moments; (*ii*) small anisotropy due to intrinsically little spin-orbit coupling constants; and (*iii*) large LFSE (ligand field splitting energy) which effectively quenches the orbital contributions of the total magnetic momentum require to create magnetic anisotropy.[11a, 17] These make 3d metal ions comparatively less effective as high performance SIMs. Nevertheless, monometallic 3d metal based SIMs are of growing interest owing to the fact that large magnetic anisotropy can be induced in such complexes by employing specific ligand field environments.[87] 3d-metal based SIMs has gained interest in 2010 after the discovery of slow magnetic relaxation in the high spin Fe^{II} complex, K[(TPA^{Mes})Fe] (**1.44**) (H$_3$TPA^{Mes} = tris((5-mesityl-1Hpyrrol-2-yl)methyl)amine) with U_{eff} = 60.4 K (H_{dc} = 1000 Oe). Here, the metal is in a trigonal pyramid geometry with one axial position is occupied by the bulky mesityl substituents of the TPA ligand.[88] Although the complex has a large *Ising* magnetic

anisotropy with D = -9.6 cm^{-1}, it was observed that presence of significant transverse anisotropy components causes significant QTM in zero field which was observed as the dominant relaxation pathway (E).

Since then, a number of Fe-containing complexes with oxidation states +3, +2 and +1 have been investigated. Although examples of Fe^{III} based SIMs are rare, a few pentagonal bipyramidal complexes are found to be SIMs. Interestingly, the first five coordinate Fe^{III} complex, [(PNP)FeCl$_3$] (**1.45**) (PNP = N[2-P(CHMe$_2$)$_2$-4-methylphenyl]$_2$) showed a spin crossover (SCO) from S = 5/2 to 3/2 states (below 80 K) as well as SIM behaviour with U_{eff} = 46 K under zero dc field.[89] Moreover, several Fe^{II} complexes have been investigated with coordination numbers ranging from 2 to 8 but none of them are zero field SIMs. However, interestingly, the linear two-coordinate Fe^{II} complex [Fe^{II}(N(SiMe$_3$)(Dipp)$_2$)] (**1.46**) showed a high energy barrier with U_{eff} = 181 cm^{-1} (H_{dc} = 500 Oe).[90] These two-coordinate Fe^{II} complexes attest to the fact that lowering the coordination number weakens the effects of ligand filed and promotes spin-orbit coupling due to the regeneration of orbital angular momentum. Finally, the first linear two coordinate Fe^{I} complex (Fe^{I} is a Kramers ion with S = 7/2), [K(crypt-222)][Fe(C(SiMe$_3$)$_3$)$_2$] (**1.47**) showed a high spin reversal barrier among all the Fe-based SIMs (Table 1.5). These results suggest that mononuclear 3d metal complexes with low coordination numbers with a half-integer spin are good candidates for showing SIM behavior.

Another interesting and extensively studied candidate of SIM is cobalt. Co^{II}-based SIMs are of considerable interest particularly due to the strong 1st order spin orbit coupling interactions. Interestingly, the first octahedral Co^{II} SIM was [Co(SCN)$_2$(4-dzbpy)] (**1.48**) (dzbpy is diazobenzylpyridine) complex reported by Koga and co-workers in 2003.[91] This system showed a U_{eff} = 89 K and blocking temperature of 3.5

K. Thus by far, majority of Co^{II} SIMs with *Ising* magnetic anisotropy have been reported in complexes with coordination number of 5.[92] In fact, coordination number higher than five typically possess significant easy plane anisotropy (+ve D value).[92] Till date, the mononuclear two coordinate Co^{II} complex, Co(C(SiMe$_2$ONaph)$_3$)$_2$ (**1.49**) (where Me is methyl and Naph is a naphthyl group) has the highest energy barrier of magnetization reversal of magnitude, U_{eff} = 450 cm^{-1} among all other 3d SMMs (Figure 1.21(a)).[93] In this complex, the sufficiently weak ligand field leads to a *non*-Aufbau (d$_{x2-y2}$, d$_{xy}$)^3(d$_{xz}$, d$_{yz}$)^3(d$_{z2}$)^1 electron configuration which was confirmed by magnetic data as well as ab initio calculations. Previously, the two-coordinate Co^{II} imido complex, **1.50** (Figure 1.21 (b)) had the record of high U_{eff} barrier of magnitude 413 cm^{-1}.[94] This complex features a highly covalent Co≡N core responsible for the observation of SIM behaviour under zero biased field with high U_{eff}.
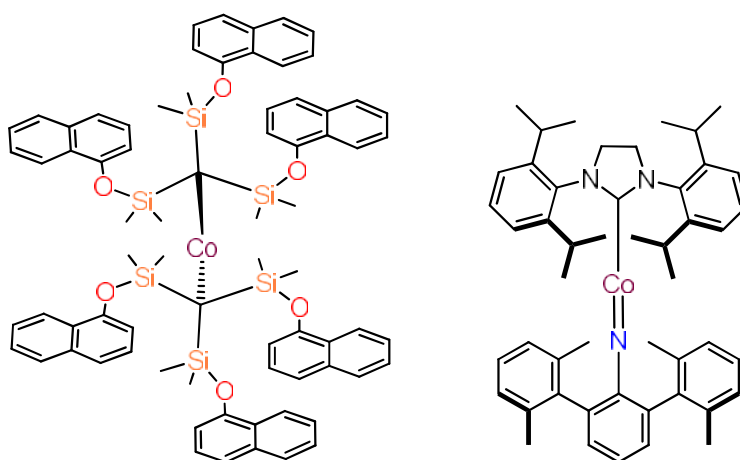
Figure 1.21. The line diagrams of complex **1.49** (left) and complex **1.50** (right)

The effect of ligands having heavy donor coordinating atoms on the magnetic anisotropy was reported in a series of *pseudo*-tetrahedral Co^{II} complexes by Dunbar et al.[95] This study showed that heavy donor atoms (soft bases) with large SOC parameter enhance the magnetic anisotropy of the 3d metal complexes (Figure 1.22).
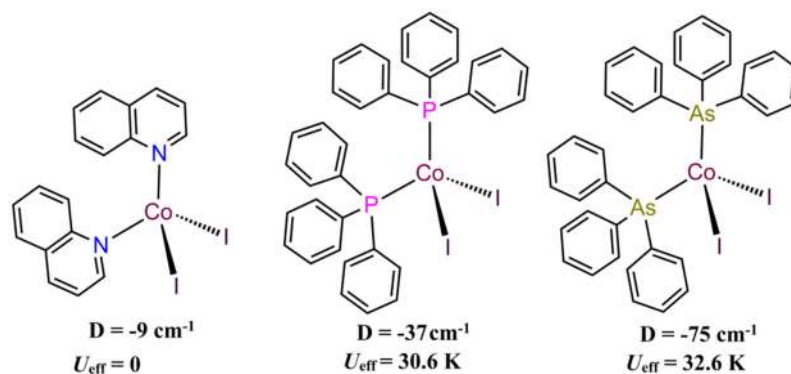
Figure 1.22. Line diagrams of *pseudo*-tetrahedral Co^{II} complexes including the magnetic parameters.

Although Co^{II} and $Fe^{I/II/III}$ based systems has dominated the field of 3d SIMs, there are exciting reports of other SIMs based on Mn^{III}, $Ni^{I/II}$, and very recently Cr^{II} ions in the literature.[96] All the SIMs based on Mn^{III} ions were reported with an axially elongated O_h coordination geometry with no 1st order spin orbit coupling interaction. Therefore the energy barriers of manganese-SIMs are limited by small D value. Till now, the largest D value was obtained for an axially elongated Mn^{III} with D = -4.73 cm^{-1}. The complex $[Mn^{III}(dibenzoylmethanido)_2(pyridine)_2](ClO_4)$ (**1.51**) showed the highest energy barrier of 18.5 cm^{-1} (H_{dc} = 1500 Oe) among the manganese based SIMs,.[29] On the other hand, only one low spin tetrahedral Mn^{IV} complex, $[PhB(^{Mes}Im)_3Mn^{IV}N]$ (**1.52**) (where ^{Mes}Im = mesityl imidazole) with S = 1/2 was reported to show slow relaxation of magnetization owing to a Raman relaxation process (n = 2.93). [97]

For nickel based monometallic systems, the octahedral complex $[Ni^{II}(pydc)(pybhm)] \cdot H_2O$ (**1.53**) (pydc=pyridine-2,6-dicarboxylate, pybhm=2,6-bis(hydroxymethyl) pyridine) show SIM behaviour for the first time with U_{eff} = 14.7 cm^{-1} (H_{dc} = 2000 Oe).[98] A negative D value of magnitude -13.7 cm^{-1} was observed in this complex. An interesting trigonal bipyramidal $[Ni(Me-DABCO)_2Cl_3][ClO_4]$ (**1.54**) (Me-DABCO = 1-methyl-4-aza-1-azoniabicyclo[2.2.2]octanium) complex was

recently characterized by Murrie and co-workers. high field EPR measurement revealed a large D value -535 cm^{-1} as a result of minimization of the Jahn-Teller distortion in a rigid trigonal bipyramid geometry.[96b] In spite of this, the effective barrier in this complex is found to be much smaller (U_{eff} = 19.3 cm^{-1}). Also, a linear [Ni^{I}(6-Mes)$_2$]Br (**1.55**) (6-Mes = 1,3-*bis*(2,4,6-trimethylphenyl) 3,4,5,6-tetrahydropyrimidin-2-ylidene) was observed to be a SIM.[96a] The magnetic anisotropy in this complex results from the 1st order spin orbit coupling interaction which gives U_{eff} = 11.8 cm^{-1} (H_{dc} = 600 Oe)

The cu-doped apatite inorganic materials [A$_{10}$(PO$_4$)$_6$(Cu^{III}$_x$(OH)$_{1-x-y}$)$_2$] (A = Sr (**1.56**), Ba (**1.57**), Ca (**1.58**)), comprising of Cu^{I} ($S = 0$) and Cu^{III} ($S = 1$) ions, were observed to be SIMs with high D values up to 600 cm^{-1}.[99] The magnetic anisotropy in this case arises from a linear arrangement of O–Cu–O$^-$ anions.

Recently, Cr^{II} ($S = 2$) based complexes have been explored as candidates of 3d based SIMs. Two such examples are [Cr^{II}(N(SiMe$_3$)$_2$)$_2$(pyridine)$_2$] (**1.59**) and [Cr^{II}(N(SiMe$_3$)$_2$)$_2$(thf)$_2$] (**1.60**) that show field-induced slow relaxation effective barriers U_{eff} = 6.3 and 8.2 cm^{-1} respectively.[96d]

Finally, the magnetic properties of a few selected 3d-metal SIMs are summarized in Table 1.5.

Table 1.5. Magnetic properties of selected 3d SIMs

Sl. No.	Complex	D (cm^{-1})	T_B (sweep rate/Oe s^{-1})	U_{eff}^{exp} (cm^{-1})	τ_o (s)	Ref.
1	[K(crypt-222)][Fe(C(SiMe$_3$)$_3$)$_2$] (**1.47**)	---	6.5 (20)	226	1.3 x 10^{-9}	[100]
2	[(sIPr)Co^{II}NDmp] (**1.50**) [(IPr)Co^{II}NDmp] (**1.61**) [(cyIPr)Co^{II}NDmp] (**1.62**)	---	---	413 297 288	1.2 x 10^{-10} 7.5 x 10^{-11} 8.4 x 10^{-10}	[94]
3	Ba$_{10}$(PO$_4$)$_6$(Co$^{II}_{0.3}$OH$_{0.4}$)$_2$ (**1.57**)	---	1.8 (50)	387	2.7 x 10^{-11}	[101]
4	Sr$_{10}$(PO$_4$)$_6$(Co$^{II}_{0.05}$O$_{1-y}$ H$_{0.9-2y-\delta}$)$_2$ (**1.56**)	---	1.8 (20)	254	6 x 10^{-10}	[102]
5	(HNEt$_3$)$_2$[Co^{II}(pdms)$_2$] (**1.63**)	-115	1.8 (500)	118	3.89 x 10^{-8}	[103]
6	[Ni^{II}(MDABCO)$_2$Cl$_3$]ClO$_4$ (**1.54**)	-535	---	19.3 (2 kOe)	3.1 x 10^{-8}	[96b]
7	Fe[N(SiMe$_3$)(Dipp)]$_2$ (**1.46**)	---	---	181	1 x 10^{-11}	[90]
8	(PMe$_3$)$_2$FeCl$_3$ (**1.64**)	-50	4 (200)	81	1.1 x 10^{-10}	[89]
9	[Na(THF)$_6$][Co^{II}(OAr)$_3$] (**1.65**)	-85.4	---	26 (1.5 kOe)	3.04 x 10^{-8}	[104]
10	*cis*-[Co^{II}(dmphen)$_2$(NCS)$_2$] (**1.66**)	+98 ($E = +8.4$)	1.3 (700)	16.2 (1 kOe)	4.37 x 10^{-7}	[18a]

pdms: 1,2-bis(methanesulfonamido)benzene; OAr⁻ : 2,6-di-tert-butylphenoxo ;dmphen : 2,9-dimethyl-1,10-phenanthroline.

1.5.2 4f Metal SIMs. In the previous section 1.4.3, the important features of 4f metal ions and the nature of exchange interaction was discussed. In this section the single-ion magnetic features of 4f metals ions and the effect of crystal field will be discussed. Lanthanide ions possess high spin ground states and inherent magnetic anisotropy resulting from unquenched orbital angular momentum of 4f orbitals.[11b, 44b, 64] Notably, the Eu^{III} (4f^6) ion has $J = 0$ (J is the total angular momentum quantum number) results in a non-magnetic ground state and Gd^{III} (4f^7) possesses magnetically an almost isotropic ground state (Table 1.6). All the other remaining Ln^{III} ions could be considered as suitable candidates for the synthesis of SIMs. In particular, the Dy^{III} ion is endowed with the largest free-ion magnetic moment resulting from the combination of a high J value ($J = 15/2$) and a large g-factor ($g_J = 4/3$) among all its

congeners. This makes the Dy^{III} ion very appealing in the arena of Ln^{III}-based molecular nanomagnets and consequently a numerous dysprosium derivatives behaves as SIMs/SMMs.

Table 1.6. SOC ground term symbols for Ln^{III} ions

Ln(III)	Ce	Pr	Nd	Pm	Sm	Eu	Gd
f^n	f^1	f^2	f^3	f^4	f^5	f^6	f^7
Term symbol	$^2F_{5/2}$	$^3H_4$	$^4I_{9/2}$	$^5I_4$	$^6H_{5/2}$	$^7F_0$	$^8S_{7/2}$
Free ion g-value	6/7	4/5	8/11	3/5	2/7	0	2
Ln(III)	**Tb**	**Dy**	**Ho**	**Er**	**Tm**	**Yb**	
f^n	f^8	f^9	f^{10}	f^{11}	f^{12}	f^{13}	
Term symbol	$^7F_6$	$^6H_{15/2}$	$^5I_8$	$^4I_{15/2}$	$^3H_6$	$^2F_{7/2}$	
Free ion g-value	3/2	4/3	5/4	6/5	7/6	8/7	

In order to understand the electronic states of the Ln^{III} ions, a crude energy level diagram of the various electronic energy states of Dy^{III} ion is given in the Figure 1.23.[11b] The electronic states arising from the electronic repulsions within the 4f orbitals can be deduced following the Russel-Saunders (R-S) coupling scheme (Figure 1.23). The other electronic effects in the case of Ln^{III} ions are assumed as perturbation to the electronic states obtained from the R-S coupling scheme. At first, the electronic states undergo splitting into different J levels due to strong SOC. It has to be noted that the strength of SOC in the case Ln^{III} ions is comparatively larger than the crystal field effects. In a non-spherical crystal field each of the J states will further split into several M_J (where $M_J = 2J + 1$) electronic states. For the non-Kramers ions i.e. J with integer value, the degeneracy of M_J level is lifted in low symmetric environment by the crystal field. On the contrary, for the Kramers ions i.e., J with a half-integer value, the degeneracy remains the same following the Kramers double degeneracy theorem.

But, the double degeneracy can be lifted by the application of an external magnetic field irrespective of the nature of J. This is the Zeeman effect. Moreover, the presence of nuclear spins can further split each of the Zeeman lines into closely spaced energy states by hyperfine interaction but it is usually weak.
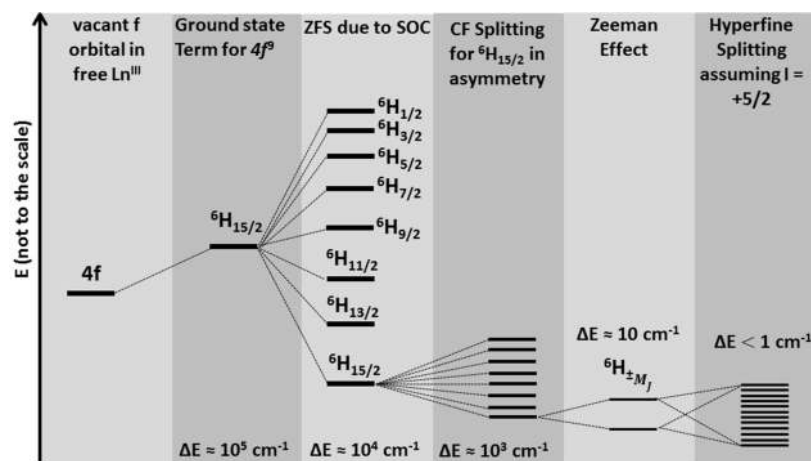
Figure 1.23. A representative energy level diagram of the various electronic states originated from 4f orbital of the Dy^{III} ion *via* perturbations through (from left to right) electron-electron repulsion, SOC, CF interactions, Zeeman effect (under ~ 1T dc field) and electron-spin-nuclear-spin coupling (hyperfine coupling), respectively. Figure and Caption adapted from ref [11b]

With the knowledge of electronic states of Ln^{III} ions, now comes the design of ligand field that are to be targeted for the observation best magnetic properties. In view of the realization of the importance of single-ion anisotropy for assembling molecular magnets, Long and coworkers have suggested a qualitative method to maximize the single-ion anisotropy of lanthanide ions in a molecular complex.[105] The spatial distribution of f electrons in the different 4f orbitals leads to an anisotropic charge density. A quadrupole approximation was used to calculate the basis shapes of the 4f electron distribution for the Ln^{III} ions corresponding to the ground J state. The calculated shapes are obtained as prolate (axially elongated), oblate (equatorially

expanded), or isotropic (spherical) as shown in Figure 1.24 (a).[105] The angular dependence of the total 4f charge density for the different M_J states of the ground J manifold was also calculated. The authors hypothesized that an axial crystal field stabilizes the oblate shaped lanthanide ions while an equatorial crystal field stabilizes the prolate-shaped lanthanide ions by minimization of the electron charge densities between the lanthanide ions and the ligands and ensuring that the highest M_J state is obtained as the ground state.
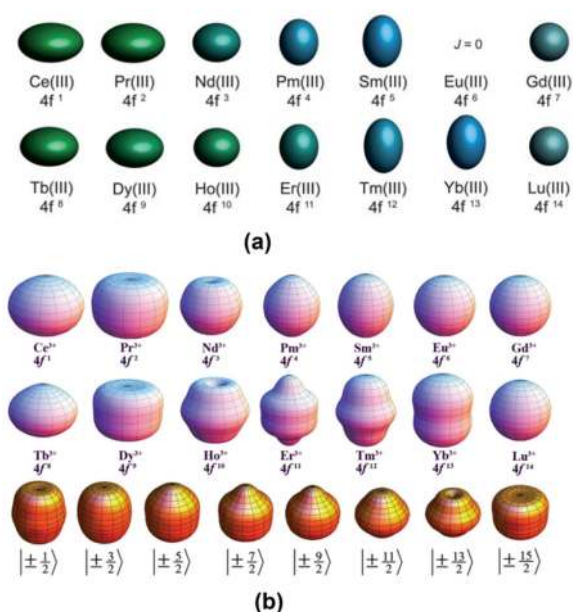
Figure 1.24. (a) Quadrupole approximations of the 4f electronic distribution for the Ln^{3+} ions. (b) The first two rows are the anisotropy of the electron-density distribution of Ln^{3+} ions in their *Ising*-limit state. The final row shows the transition of electron density distribution from prolate (M_J = 1/2) to oblate (M_J = 15/2) in the Dy^{III} ion. Reproduced with permission from the refs [105, 106]

Jiang and co-workers have also calculated the electrostatic potential surfaces of the 4f elements corresponding to the highest M_J state of the ground J state with more rigorous mathematical treatment. The basic shapes obtained are shown in Figure 1.24 (b).[106] They also calculated the electron-density distribution of Dy^{III} and the results

show a gradual transition of electron density distribution from typical prolate ($M_J = \pm 1/2$) to oblate.

The Ln^{III} ions have rich coordination chemistry with coordination number ranging from 3 to 12.[107] It is worth mentioning here that air stable Ln^{III} complexes prefer high coordination numbers usually 8-12, due to large ionic radii and strong ionic bonding. However, many of the Ln^{III} complexes especially the Dy^{III} containing mononuclear complexes showed interesting magnetic properties at unusual coordination environments.[108] Among the different synthetic strategies that are there, the organometallic approach stands out to be the most effective way of stabilizing Ln^{III} ions in unusual coordination environments in order to extract the desired magnetic properties. Using the organometallic ligand approach, Layfield and co-workers recently reported the Dy^{III} metallocene complex $[(Cp^{iPr5})Dy(Cp^*)][BPh_4]$ (**1.67**) (Cp^{iPr5} = penta-iso-propylcyclopentadienyl; Cp^* = pentamethyl cyclopentadi-enyl) (Figure 1.25 (a)).[109] This complex shows U_{eff} barrier of magnitude 1541 cm^{-1}. Interestingly, this complex holds the record of the highest magnetization blocking temperature of T_B = 80 K among all other reported SMMs/SIMs. Previously, an analogous mononuclear Dy^{III} metallocene complex, $[Dy(Cp^{ttt})_2][B(C_6F_5)_4]$ (**1.68**) (where Cp^{ttt} = {$C_5H_2{}^tBu_3$-1,2,4} and ^tBu = $C(CH_3)_3$) (Figure 1.25 (b)) showed a high U_{eff} barrier of magnitude 1837 K and hysteresis loops up to 60 K. [110]
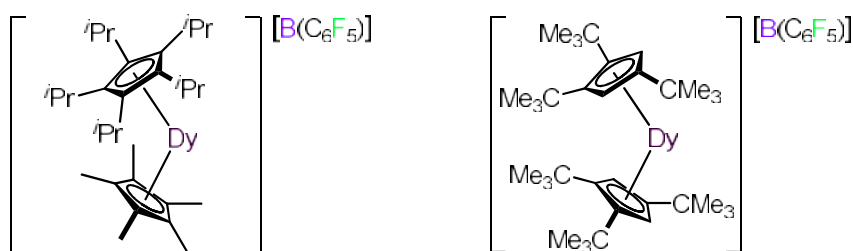
Figure 1.25. Line diagram of complex **1.67** (a) and complex **1.68** (b).

In order to have a magneto structural correlation in Dy^{III} metallocene cations, Long and co-workers synthesized a series of Dy^{III} metallocenium cations, $[Dy(Cp^{iPr4R})_2][B(C_6F_5)_4]$ (R = H (**1.69**), Me (**1.70**), Et (**1.71**), ^iPr (**1.72**)) Figure 1.26.[111] In this study it was observed that the variation of the substituents leads to substantial changes in the molecular structures. The sterically encumbered cyclopentadienyl ligands help promoting larger L–Dy–L (L is the Cp ring) angles and longer Dy–C distances. Dynamic magnetization studies revealed that the magnetic relaxation barrier increases with an increase in the L–Dy–L angle and decrease in the Dy–C distance (Figure 1.26).

Cp-Dy-Cp (°)	147.2	156.6	161.1	162.1
Dy-Cp (Å)	2.290	2.298	2.302	2.340
U_{eff} (cm⁻¹)	1285	1468	1380	1334
T_B (K)	17	62	59	56
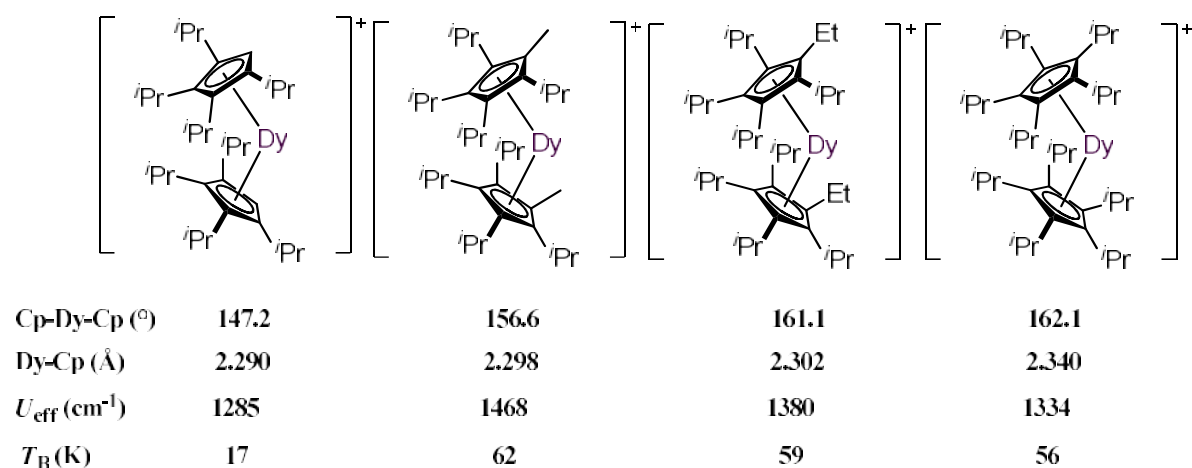
Figure 1.26. Line diagram of Dy^{III} metallocenium salts including a magneto-structural correlation observed in these complexes. The counter anion in all the cases is the $[B(C_6F_5)]^-$.

Apart from Dy^{III} metallocenes, interesting magnetic properties were also observed in the 7-coordinate pentagonal bipyramidal and the 8-coordinate square antiprism Dy^{III} complexes (see Table 1.7). The magnetic properties of a few SIMs based on Ln^{III} metal ion is tabulated in the Table 1.7.[112]

Table 1.7. Magnetic properties of selected Ln^{III} SIMs

Sl. No.	Complex	Hysteresis	T_B (sweep rate/Oe s^{-1})	U_{eff}^{exp} (cm^{-1})	τ_o	Ref.
1	[Dy(O^{t}Bu)$_2$(py)$_5$] (**1.73**)	yes	8.8 (12)	1261	1.17 x 10^{-12}	[112a]
2	[Dy(bbpen)Br] (**1.74**)	yes	14 (200)	712	4.21x10^{-12}	[112b]
	[Dy(bbpen)Cl] (**1.75**)	yes	8 (200)	492	9.46 x 10^{-11}	
	[Tb(Pc)(Pc-Oph)] (**1.76**)	yes	2 (---)	652	1.1 x 10^{-11}	[112l]
3	[Dy(BIPM^{TMS})$_2$]$^-$ (**1.77**)	yes	10 (300)	565	5.65 x 10^{-13}	[112c]
				501	1.11 x 10^{-12}	
4	[(^{t}BuPO(NH^{i}Pr)$_2$)$_2$Dy(H$_2$O)$_5$] [I$_3$] (**1.78**)	yes	30 (200)	511	1.56 x 10^{-12}	[113]
5	[Dy(OPCy$_3$)$_2$(H$_2$O)$_5$]Br$_3$ (**1.79**)	yes	20 (200)	377	2.0 x 10^{-11}	[112d]
	[Dy(OPCy$_3$)$_2$(H$_2$O)$_5$]Cl$_3$ (**1.80**)		11 (200)	328	8.7 x 10^{-12}	
6	[DyCl$_2$(NCN)(THF)$_2$] (**1.81**)	yes	1.9 (---)	233	6 x 10^{-10}	[112e]]
7	[(C$_5$H$_5$BMe)Er(COT)] (**1.82**)	yes	8 (19)	300	5.5 x 10^{-12}	[112f]
	[(C$_5$H$_5$BH)Er(COT)] (**1.83**)		6 (19)	259	5.3 x 10^{-12}	
8	[Er(Cp*)(COT)] (**1.84**)	yes	1.8 (9.2)	224	8.17 x 10^{-11}	[112g]
				136	3.13 x 10^{-9}	
9	[Nd(W$_5$O$_{18}$)$_2$]$^{9-}$ (**1.85**)	no	---	51.4 (1 kOe)	3.55 x 10^{-10}	[112h]
10	[Ho(CyPh$_2$PO)$_2$(H$_2$O)$_5$][I$_3$] (**1.86**)	yes	3 (1400)	237	1.7 x 10^{-11}	[112i]
11	[Tm (COT)(Tp)] (**1.87**)	no	---	90 (2 kOe)	4.7 x 10^{-7}	[112j]
12	[Yb(trensal)] (**1.88**)	no	---	38 (2 kOe)	1.5 x 10^{-8}	[112k]

H$_2$bbpen = N,N'-bis(2-hydroxybenzyl)-N,N'-bis(2-methylpyridyl)ethylenediamine);

BIPM^{TMS}H$_2$ = H$_2$C(PPh$_2$NSiMe$_3$)$_2$; NCN: 2,6-(2,6-C$_6$H$_3$R$_2$N$_5$CH)$_2$-C$_6$H$_3$]$^-$; COT: Cyclooctatriene; Tp: hydrotris(1-pyrazolyl)borate; H$_3$trensal is 2,2',2"-tris(salicylideneimino)trimethylamine.

1.5.3 5f Metal SIMs. As discussed in section 1.4.4, the relative strengths of SOC and repulsive electron-electron interaction are very closer in the case of 5f metal ions and therefore neither the R-S coupling scheme nor the *jj* coupling (weak electron-electron interaction) seems reasonable to describe the electronic energy states. In order obtain

a realistic picture of the energy states both the two interactions must be considered at the same time.[44a] In addition, the presence of non-negligible covalency of the metal-ligand interaction in actinides offers an advantage in generating strong exchange interactions, but also makes the rational design of monmetallic actinide complexes highly challenging compared to the lanthanide or transition metal complexes.[114] Therefore, the combination of large magnetic anisotropy along with the covalency of metal ligand interactions makes the magnetic properties of such systems very complex to study.[114]

Till date, SIM behaviour was observed only for $U^{III/V}$ and transuranic Np^{IV} and Pu^{III} ions (see Table 1.8). Among them, the majority of An-SIMs are based on the Kramers's ion U^{III} ($^5F_3$, $J = 9/2$). Most importantly, the $5f^3$ configuration of U^{III} can be compared to an oblate single-ion anisotropy such as Tb^{III} [$4f^8$] or Dy^{III} [$4f^9$] ions, therefore an axial ligand environment in combination with strong SOC can stabilize the spin alignment preferentially along the molecular anisotropy axis. SIM behaviour was first observed in the mononuclear U^{III} complex, [U{Ph$_2$B(pz)$_2$}$_3$] (**1.89**) (Figure 1.27) with a U_{eff} barrier of magnitude 29 K under zero applied biased field. Compared to U^{III} SIMs, U^V SIMs are less explored due to (*i*) comparatively smaller *J* value and (*ii*) disproportion tendency towards U^{IV} and U^{VI} in aqueous environments.[115] Nevertheless, the mono-oxo U^V complex, [UO(Tren^{TIPS})] (**1.90**) (Figure 1.27) shows SIM behavior with U_{eff} barrier of magnitude 21.5 K (1000 Oe). The magnetic properties of selected An-SIMs are summarized in Table 1.8.[116]
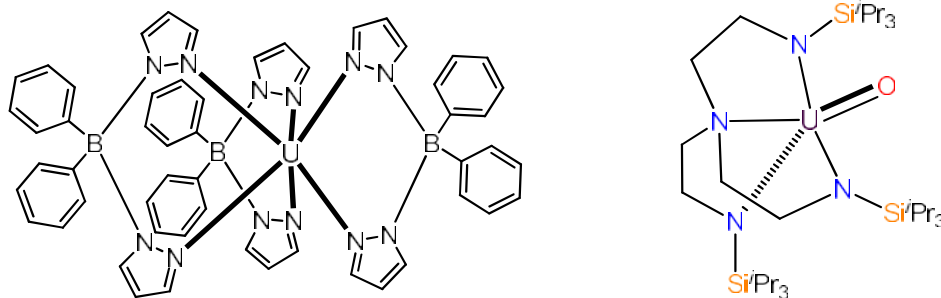
Figure 1.27. Line diagram of trigonal prismatic complex **1.89** (*left*) and trigonal bipyramidal complex **1.90** (*right*)

Table 1.8. Magnetic properties of selected Actinide SIMs

Sl. No.	Complex	H_{dc} (Oe)	U_{eff}^{exp} (cm^{-1})	τ_o	Ref.
1	[Pu(Tp)$_3$] (**1.91**)	0	18.3	2.9 x 10^{-7}	[116d]
2	[U(Bc^{Me})$_3$] (**1.92**)	1500	33	1.0 x 10^{-7}	[116f]
3	[U(N(TMS)$_2$)$_3$] (**1.93**)	2000	22	1.0 x 10^{-11}	[116c]
4	[U(Tp^{Me2})$_2$]I (**1.94**)	500	21	1.8 x 10^{-7}	[116b]
5	[U^V(O)(Tren^{TIPS})] (**1.90**)	1000	15	2.6 x 10^{-7}	[116a]
6	[Np(COT)$_2$] (**1.95**)	5000	28	1.1 x 10^{-5}	[116e]

Tp$^-$: hydrotris-(pyrazolyl)borate; Bp^{Me}: dihydrobis(methylpyrazolyl)borate Tp^{Me2}: hydrotris(3,5-dimethylpyrazolyl)borate; Tren^{TIPS}={N(CH$_2$CH$_2$NSiiPr$_3$)$_3$}$^{3-}$

1.6 Single-Chain Magnets (SCMs). The previous sections were focused on the magnetic properties of systems that can be considered essentially as zero-dimensional. The exciting magnetic properties shown by SMMs and SIMs have led to the exploration of one-dimensional magnets that are connected by a network of interactions. SCMs are characterized by magnetically isolated 1D polymeric chains that exhibit slow relaxation of magnetization below the blocking temperature, T_B.[117] The noticeable difference in the spin dynamics of SCMs and a 1D polymeric material is that the former requires an *Ising*-type interaction while the latter needs isotropic

interaction.[118] Clerác and other research groups have defined one dimensional *Ising* ferrimagnets that show slow magnetic relaxation similar to SMMs to be called SCMs.[117a] Therefore, the essential ingredients for a SCM are (*i*) strong uni-axial magnetic anisotropy of the spin carriers, (*ii*) non-zero interactions between the spin units along the chain, and (*iii*) small ratio of intrachain to interchain interactions.[119] Single-chain magnets has distinct advantages over SIMs/SMMs because the total energy barrier of spin reversal comprises of magnetic anisotropy energy barrier plus the correlation energy arising due to strong intra-chain exchange coupling.[120]

The spin dynamics of 1D *Ising* chain can be predicted by the Glauber model.[118] However, in real systems the rigorous conditions for *Ising*-type states are difficult to observe. Therefore, an anisotropic Heisenberg chain model is used for the description of real SCMs.[118, 121] For nearly defect-free chains the activation energy barrier is given by

$$\Delta_\tau = \Delta_A + 2\Delta_\xi \text{ (for an effectively infinite size regime)}$$

$$= \Delta_A + \Delta_\xi \text{ (for an finite size regime)}$$

Here, Δ_A is the magnetic anisotropy energy barrier and Δ_ξ is the correlation energy (see Figure 1.28). A noticeable difference between the *Ising* model (Glauber dynamics) and the anisotropic Heisenberg model is that the total spin (S) of each and every magnetic unit causes a anisotropic energy barrier ($\Delta_A = |D|S^2$) as in the case of SMMs.[121b] Therefore, Δ for the reversal of magnetization in the case of SCMs is affected not only by the magnetic anisotropy of the spins but also their intra-chain magnetic interactions.

$\Delta_{\text{Glauber}} = 2\Delta_{\xi}$

↑↑↑↑↓↑↑↑↑↑↑↑ (infinite chain)

$\Delta_{\text{Glauber}} = \Delta_{\xi}$
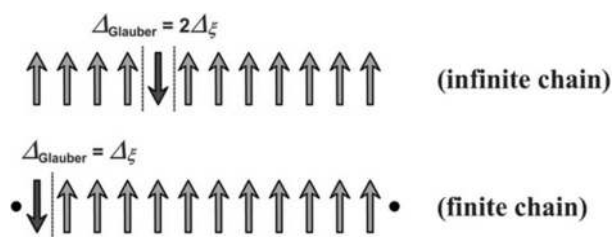
•↓↑↑↑↑↑↑↑↑↑↑↑• (finite chain)

Figure 1.28. Schematic representations of a single-spin-flip in infinite and finite chains. Adapted from ref. [121b]

In the year 2001, Cannesi and co-worker found that the helical Co^{II} derivative, [Co(hfac)$_2$(NITPhOMe)] (**1.96**) (Figure 1.29) (NITPhOMe = 4'-methoxy-phenyl-4,4,5,5-tetramethylimidazoline-1-oxyl-3-oxide) showed a high magnetization at low temperature. In fact, the system behaves as a 1D ferrimagnet due to the antiferromagnetic coupling between the organic radical and the high-spin Co^{II} center.[122] A very strong *Ising* magnetic interaction ($J = 224$ K) was observed between the spin of cobalt and radical and the Zeeman component of the two spins parallel to the trigonal axis. The ac and dc susceptibility measurements reveal an energy barrier, $\Delta_{\tau} = 154$ K and a stepped hysteresis loops similar to SMMs. The SCM properties in the Co^{II} NITPhOMe series can be tuned by modifying the bridging nitronyl nitroxide ligand. For example, *p*-butoxyphenyl substituted chains exhibit long-range order below 45 K and a high magnetic coercivity of 5.2 T at 6 K while pyrene-substituted derivatives show massive Δ_{τ} values of almost 400 K.[123] Following the discovery in 2002, Clerác and coworkers reported a heterometallic 1D compound formed by an assembly of trinuclear species (Mn–Ni–Mn) with a Ni^{II}–Mn^{III} AFM interaction ($J = 21$ K).[124] For this compound hysteresis loops were observed below 3.5 K. Further, magnetization dynamics revealed slow magnetic relaxation with an energy barrier 154 cm^{-1}. The authors also reported a large family of {Mn$_2$Ni} SCMs by finely modifying the precursor building units.[125] There are now many reports of one dimensional

polymeric complexes exhibiting SCM behaviour involving various metal combinations such as 3d-3d′,[126] 3d-4d,[127] 3d-5d,[128] 3d-4f,[129] and heterotrimetallic complexes[130]. The magnetic properties of a few selected SCMs are given in Table 1.9.[123b, 131]
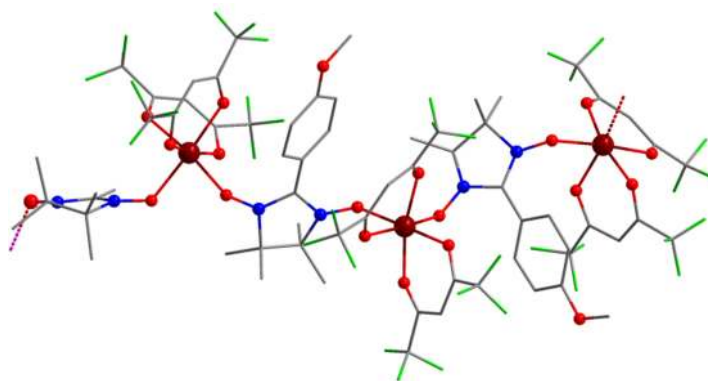
Figure 1.29. Molecular structure of a single chain of **1.96**. Adapted from ref [[122]]

Table 1.9. Magnetic properties of few selected SCMs

Sl. No.	Complex	J (cm^{-1})	T_B (K)	Δ_τ (K)	τ_0	Ref.
1	[Co(hfac)$_2$NaphNN]$_n$ (**1.97**)	-162 ($J_{M\text{-rad}}$)	13.2	398	4 x 10^{-12}	[[131a]]
2	[Co(hfac)$_2$PyrNN]$_n$ (**1.98**)	-161 (2$J_{M\text{-rad}}$)	14	369	7 x 10^{-10}	[[123b]]
3	[Fe(L‡)(N$_3$)]$_n$ (**1.99**)	2.8 ($J_{Fe\text{-Fe}}$)	7	124	4.8 x 10^{-12}	[[131b]]
4	{[UO$_2$(Me-saldien)][Mn(NO$_3$)-(Py)2]}$_n$ (**1.100**)	---	---	122	6.2 x 10^{-12}	[[131c]]
5	(Ph$_4$P)[Co^{II}(3-Methyl pyridine)$_{2.7}$(H$_2$O)$_{0.3}$W^V(CN)$_8$]n (**1.101**)	19.5 ($J_{Co\text{-W}}$)	10	252 / 169	1.5× 10^{-13} / 4.6 x 10^{-10}	[[131d]]
6	[Dy(hfac)$_3$(NIT-C6H4OPh)]$_n$ (**1.102**)	---	---	69	1.9 x 10^{-12}	[[131e]]
7	[{Cr(L^{N3O2Ph})(CN)$_2$}Fe(H$_2$L^{N3O2NH2})]·PF6 (**1.103**)	2.68 ($J_{Fe\text{-Cr}}$)	2	113	1.6 x 10^{-11}	[[131f]]
8	(NMe$_4$)$_2$[L‡FeCl$_2$]$_n$ (**1.104**)	-81 ($J_{M\text{-rad}}$)	---	55	3.9 x 10^{-12}	131g

NaphNN: 1-naphthyl nitronylnitroxide; PyrNN: 1-pyrenyl nitronylnitroxide L‡H$_2$: 2,5-dichloro-3,6-dihydroxy-1,4-benzoquinone; Me-saldien: Methyl salicyldimine.

1.7 Luminescence of Lanthanide Complexes

Although this thesis mainly deals with the magnetic properties of 3d-4f and 4f complexes we have also carried out studies on the photophysical properties of some complexes. This section gives a brief over view on this aspect of the lanthanide complexes. Luminescent lanthanide complexes are of considerable interest and have been investigated in the fields of biomedical analyses and imaging,[132] solid state lighting and display,[133] and as chemosensors[134]. The luminescence of lanthanides arising from f-f transitions has characteristic sharp line spectra and longer lifetimes.[43] The line-like spectra arises due to the shielding of 4f orbitals by the filled 5s and 5p orbitals while the long lifetimes result due to the Laporte forbidden f-f transitions. The forbidden f-f transitions also lead to weak absorption coefficients with molar absorption coefficients typically less than 3 M^{-1} cm^{-1}.[135] Therefore, direct excitation leads to poor emission properties. However, the emission properties can be enhanced considerably by employing chromophores that can act as antennas for light absorption. The chromophore sensitized lanthanide light emission is known as the "antenna effect" (Figure 1.30 (*top*)).[136] A Jablonski diagram depicting the different process that occurs during sensitized emission is shown in the Figure 1.30 (*bottom*).[43]
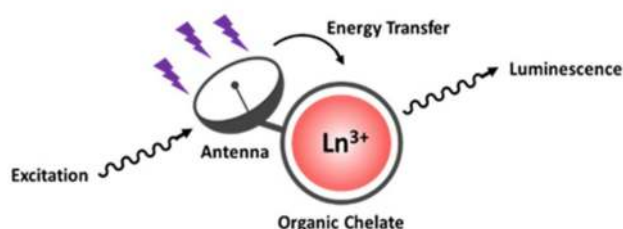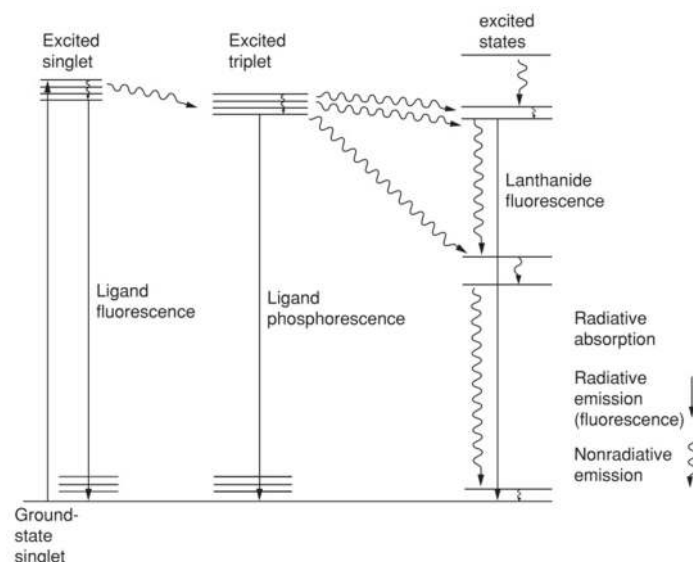
Figure 1.30. (*top*) Schematic representation of the "antenna effect". (*bottom*) Jablonski diagram corresponding to sensitized lanthanide emission. Adapted from refs [136, 43]

It is important to note that quantum yields of sensitized lanthanide emissions are highly dependent on the nature of antenna. Thus, the choice of the antenna is of paramount importance to observe efficient emission. The antenna must possess some characteristics features such as (*i*) an aromatic (or hetero-aromatic) highly π conjugated system characterized by high efficiency of light absorption, (*ii*) high efficiencies of intersystem crossing and energy transfer processes, and (*iii*) the triplet excited state being at least 1850 cm^{-1} higher than the lowest emitting levels of the Ln^{III} cation.[136-137] It is important to note that H_2O molecules can effectively deactivate the excited states of lanthanides in the form of vibrational energy transfer.[43, 137] The coordination of H_2O molecules around the Ln center can be minimized utlizing multidentate chelating ligands appended with the antenna moiety have been employed. Figure 1.31 depicts selected organic ligands that act as antenna.[136-137]
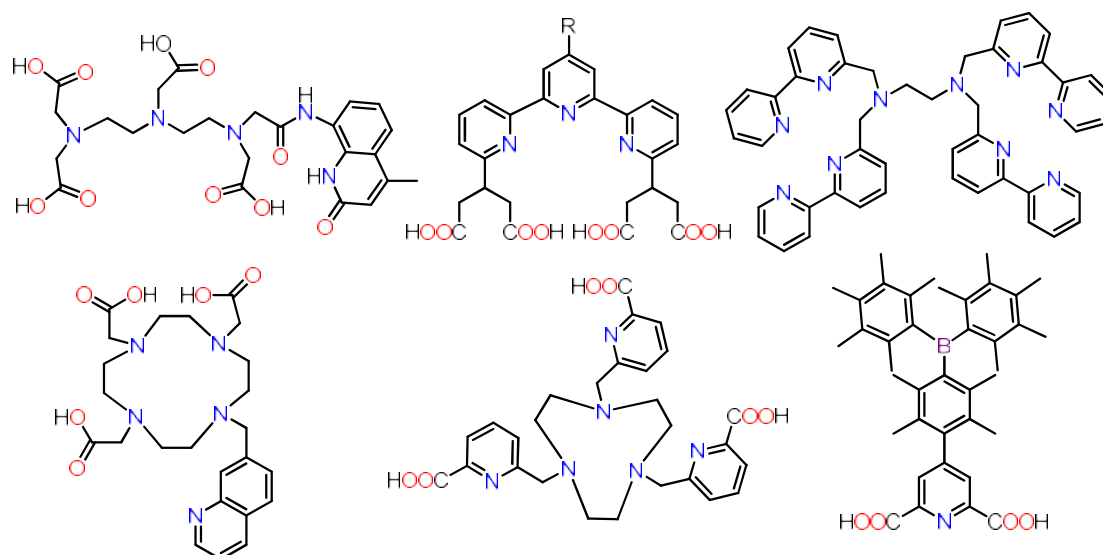
Figure 1.31. Selected multidentate ligands appended with antenna moiety.

Many lanthanide cations in the lanthanide series are capable of showing emissions over a wide spectral range from UV (Gd[III]) to visible (orange (Sm[III]), red (Eu[III]), yellow (Dy[III]), green (Tb[III]) and blue (Tm[III]) to the NIR (Yb[III], Nd[III] and Er[III]) region.[135-138] The ones that show emission in the visible region have lighting and luminescent imaging applications.[139] The triplet energy state of typical organic ligands lies slightly higher in energy compared to the first excited states of the Tb[III] and Eu[III] cations, and therefore can exhibit characteristic strong metal-centered fluorescence.[140] In the case of Tb[III] ion the emissions lines corresponds to $^5D_4 \rightarrow {}^7F_n$ (n = 6-0) transitions being $^5D_4 \rightarrow {}^7F_5$ the strongest one, while in case of Eu[III], ion $^5D_0 \rightarrow {}^7F_n$ transitions are observed (n = 4-0).[43] It is worth noting here that the intensity and splitting pattern of certain transitions in the emission spectra of Eu[III] and Tb[III] complexes could give an illustration about the lanthanide ion environment.[43]

1.8 Aim and Objective of this Thesis

The preceding discussion gives a glimpse of the recent developments in the field of molecular nanomagnetism. The field has been growing rapidly in the recent years in

terms of observing magnetic behaviour with very large energy barriers and magnetic hysteresis loops above liquid nitrogen temperatures. Till now, the 4f-based molecules especially the mononuclear complexes are found to be the dominating candidates among all others. The present research work primarily focuses on the various strategies of isolating homonuclear 4f-based metal complexes. Special efforts have been given towards the isolation of mononuclear Ln^{III} complexes by employing multi-/bidentate chelating ligands. The thesis also includes the utilization of compartmental ligands designed for the synthesis of heterometallic 3d-4f complexes. The key features of this research work are briefly outlined below.

1) A rational design of multidentate ligand systems has been demonstrated for the exclusive isolation of mononuclear pentagonal bipyramidal Ln^{III} complexes. A synthetic strategy involving fine tuning the magnetic properties by axial ligand substation was achieved and is discussed in detail.

2) To offer an axial crystal field in mononuclear Ln^{III} complexes, a chelating ligand has been prepared with a phenolate moiety. The *trans* disposition of two phenolate moieties in the complexes exerted sufficient axial crystal field so that the Dy^{III} complex behaves as a field-induced SIM.

3) The control of coordination number/geometry in mononuclear Ln^{III} complexes has been achieved by employing a flexible sterically hindered acetylacetonato ligand. Interesting magnetic and luminescent properties were observed in this series of mononuclear complexes.

4) A multidentate enolizable Schif base ligand was designed and utilized to afford homometallic dinuclear and polynuclear Ln^{III} complexes bridged by enolate *O* atoms. Synthesis, structure and magnetic properties of these complexes are discussed.

5) A compartmental ligand having *O*-donor and *N*-donor sites has been utilized to synthesize a series of homometallic 3d-4f complexes and their magnetic properties were studied.

The aforementioned topics are described in the subsequent chapters of this thesis.

1.9 References

1 (a) D. Gatteschi, R. Sessoli and J. Villain, Molecular Nanomagnets, Oxford University Press, 2006; (b) O. Kahn, Molecular magnetism, VCH-Verlag, Weinheim, New York, 1993; (c) S. G. (Ed.), Molecular Nanomagnets and Related Phenomena, Springer-Verlag Berlin Heidelberg, 2015.

2 (a) R. Vincent, S. Klyatskaya, M. Ruben, W. Wernsdorfer and F. Balestro, Nature, 2012, 488, 357-360; (b) M. Urdampilleta, S. Klyatskaya, J. P. Cleuziou, M. Ruben and W. Wernsdorfer, Nat. Mater., 2011, 10, 502-506; (c) F. Luis, A. Repollés, M. J. Martínez-Pérez, D. Aguilà, O. Roubeau, D. Zueco, P. J. Alonso, M. Evangelisti, A. Camón, J. Sesé, L. A. Barrios and G. Aromí, Phys. Rev. Lett., 2011, 107, 117203-117207; (d) L. Bogani and W. Wernsdorfer, Nat. Mater., 2008, 7, 179-186.

3 R. L. Carlin and A. J. v. Duyneveldt, Magnetic Properties of Transition Metal Compounds, Springer-Verlag Berlin Heidelberg, 1977.

4 (a) D. Gatteschi and R. Sessoli, Angew. Chem. Int. Ed., 2003, 42, 268-297; (b) R. Bagai and G. Christou, Chem. Soc. Rev., 2009, 38, 1011-1026.

5 D. Gatteschi and R. Sessoli, J. Magn. Magn. Mater., 2004, 272-276, 1030-1036.

6 G. Christou, D. Gatteschi, D. N. Hendrickson and R. Sessoli, MRS Bull., 2011, 25, 66-71.

7 A. J. Brown, D. Pinkowicz, M. R. Saber and K. R. Dunbar, Angew. Chem. Int. Ed., 2015, 54, 5864-5868.

8 D. Martien, Introduction to: AC susceptibility, Quantum Design, USA.

9 H. Miyasaka, R. Clérac, W. Wernsdorfer, L. Lecren, C. Bonhomme, K.-i. Sugiura and M. Yamashita, Angew. Chem. Int. Ed., 2004, 43, 2801-2805.

10 J. Tang and P. Zhang, Lanthanide Single Molecule Magnets, Springer-Verlag Berlin Heidelberg, 2015.

11 (a) G. A. Craig and M. Murrie, Chem. Soc. Rev., 2015, 44, 2135-2147; (b) A. K. Bar, P. Kalita, M. K. Singh, G. Rajaraman and V. Chandrasekhar, Coord. Chem. Rev., 2018, 367, 163-216; (c) A. Dey, P. Kalita and V. Chandrasekhar, ACS Omega, 2018, 3, 9462-9475.

12 (a) E. Moreno-Pineda, L. E. Nodaraki and F. Tuna, Molecular Nanomagnets Based on f-Elements, Elsevier Inc. , 2018 ; (b) S. T. Liddle and J. van Slageren, Chem. Soc. Rev., 2015, 44, 6655-6669.

13 J. D. Rinehart, M. Fang, W. J. Evans and J. R. Long, J. Am. Chem. Soc., 2011, 133, 14236-14239.

14 (a) R. Sessoli, D. Gatteschi, A. Caneschi and M. A. Novak, Nature, 1993, 365, 141-143; (b) A. Caneschi, D. Gatteschi, R. Sessoli, A. L. Barra, L. C. Brunel and M. Guillot, J. Am. Chem. Soc., 1991, 113, 5873-5874; (c) R. Sessoli, H. L. Tsai, A. R. Schake, S. Wang, J. B. Vincent, K. Folting, D. Gatteschi, G. Christou and D. N. Hendrickson, J. Am. Chem. Soc., 1993, 115, 1804-1816.

15 C. Delfs, D. Gatteschi, L. Pardi, R. Sessoli, K. Wieghardt and D. Hanke, Inorg. Chem., 1993, 32, 3099-3103.

16 (a) G. Aromí and E. K. Brechin, Synthesis of 3d Metallic Single-Molecule Magnets in Single-Molecule Magnets and related Phenomena: Structure and bonding, Springer-Verlag Berlin Heidelberg, 2006, vol. 122, pp. 1-67; (b) F. Neese and D. A. Pantazis, Faraday Discuss., 2011, 148, 229-238.

17 J. M. Frost, K. L. M. Harriman and M. Murugesu, Chem. Sci., 2016, 7, 2470-2491.

18 (a) J. Vallejo, I. Castro, R. Ruiz-García, J. Cano, M. Julve, F. Lloret, G. De Munno, W. Wernsdorfer and E. Pardo, J. Am. Chem. Soc., 2012, 134, 15704-15707; (b) J. M. Zadrozny, J. Liu, N. A. Piro, C. J. Chang, S. Hill and J. R. Long, Chem. Commun., 2012, 48, 3927-3929; (c) E. Colacio, J. Ruiz, E. Ruiz, E. Cremades, J. Krzystek, S. Carretta, J. Cano, T. Guidi, W. Wernsdorfer and E. K. Brechin, Angew. Chem. Int. Ed., 2013, 52, 9130-9134; (d) S. Gómez-Coca, A. Urtizberea, E. Cremades, P. J. Alonso, A. Camón, E. Ruiz and F. Luis, Nat. Commun., 2014, 5, 4300-4307.

19 (a) J. M. Clemente-Juan, E. Coronado, A. Forment-Aliaga, A. Gaita-Ariño, C. Giménez-Saiz, F. M. Romero, W. Wernsdorfer, R. Biagi and V. Corradini, Inorg. Chem., 2010, 49, 386-396; (b) A. J. Tasiopoulos, W. Wernsdorfer, K. A. Abboud and G. Christou, Inorg. Chem., 2005, 44, 6324-6338; (c) C. J. Milios, R. Inglis, A. Vinslava, R. Bagai, W. Wernsdorfer, S. Parsons, S. P. Perlepes, G. Christou and E. K. Brechin, J. Am. Chem. Soc., 2007, 129, 12505-12511; (d) S. Maheswaran, G. Chastanet, S. J. Teat, T. Mallah, R. Sessoli, W. Wernsdorfer and R. E. P. Winpenny, Angew. Chem. Int. Ed., 2005, 44, 5044-5048; (e) R. Inglis, S. M. Taylor, L. F. Jones, G. S. Papaefstathiou, S. P. Perlepes, S. Datta, S. Hill, W. Wernsdorfer and E. K. Brechin, Dalton Trans., 2009, 9157-9168; (f) T. C. Stamatatos, K. A. Abboud, W. Wernsdorfer and G. Christou, Angew. Chem. Int. Ed., 2007, 46, 884-888; (g) A. J. Tasiopoulos, A. Vinslava, W. Wernsdorfer, K. A. Abboud and G. Christou, Angew. Chem. Int. Ed., 2004, 43, 2117-2121; (h) M. Murugesu, M. Habrych, W. Wernsdorfer, K. A. Abboud and G. Christou, J. Am. Chem. Soc., 2004, 126, 4766-4767; (i) O. Waldmann, A. M. Ako, H. U. Güdel and A. K. Powell, Inorg. Chem., 2008, 47, 3486-3488.

20 C. J. Milios and R. E. P. Winpenny, Cluster-Based Single-Molecule Magnets in Single Molecule Magnets and related Phenomena: Structure and Bonding, ed. D. M. P. Mingos, Springer-Verlag Berlin Heidelberg, 2014, vol. 164, pp. 1-100.

21 O. Waldmann, Inorg. Chem., 2007, 46, 10035-10037.

22 (a) Z. Sun, D. N. Hendrickson, Z. Sun, C. M. Grant, S. L. Castro and G. Christou, Chem. Commun., 1998, 721-722; (b) S. L. Castro, Z. Sun, C. M. Grant, J. C. Bollinger, D. N. Hendrickson and G. Christou, J. Am. Chem. Soc., 1998, 120, 2365-2375.

23 (a) S. G. Sreerama and S. Pal, Inorg. Chem., 2002, 41, 4843-4845; (b) M. D. Godbole, O. Roubeau, R. Clérac, H. Kooijman, A. L. Spek and E. Bouwman, Chem. Commun., 2005, 3715-3717; (c) E. K. Brechin, Chem. Commun., 2005, 5141-5153.

24 (a) S. M. Taylor, R. D. McIntosh, J. Rezé, S. J. Dalgarno and E. K. Brechin, Chem. Commun., 2012, 48, 9263-9265; (b) S. K. Langley, B. Moubaraki, K. J. Berry and K. S. Murray, Dalton Trans., 2010, 39, 4848-4855; (c) P. King, W. Wernsdorfer, K. A. Abboud and G. Christou, Inorg. Chem., 2005, 44, 8659-8669.

25 (a) D. J. Price, S. R. Batten, B. Moubaraki and K. S. Murray, Polyhedron, 2007, 26, 305-317; (b) C.-L. Zhou, Z.-M. Wang, B.-W. Wang and S. Gao, Dalton Trans., 2012, 41, 13620-13625.

26 (a) J.-D. Compain, P. Mialane, A. Dolbecq, I. M. Mbomekallé, J. Marrot, F. Sécheresse, E. Rivière, G. Rogez and W. Wernsdorfer, Angew. Chem. Int. Ed., 2009, 48, 3077-3081; (b) R. Bagai, W. Wernsdorfer, K. A. Abboud and G. Christou, J. Am. Chem. Soc., 2007, 129, 12918-12919; (c) A. K. Boudalis, B. Donnadieu, V. Nastopoulos, J. M. Clemente-Juan, A. Mari, Y. Sanakis, J.-P. Tuchagues and S. P. Perlepes, Angew. Chem. Int. Ed., 2004, 43, 2266-2270; (d) A. K. Boudalis, J.-M. Clemente-Juan, F. Dahan and J.-P. Tuchagues, Inorg. Chem., 2004, 43, 1574-1586;

(e) H. Oshio, N. Hoshino and T. Ito, J. Am. Chem. Soc., 2000, 122, 12602-12603; (f) G. W. Powell, H. N. Lancashire, E. K. Brechin, D. Collison, S. L. Heath, T. Mallah and W. Wernsdorfer, Angew. Chem. Int. Ed., 2004, 43, 5772-5775.

27 (a) M. Ibrahim, Y. Lan, B. S. Bassil, Y. Xiang, A. Suchopar, A. K. Powell and U. Kortz, Angew. Chem. Int. Ed., 2011, 50, 4708-4711; (b) A. Ferguson, A. Parkin, J. Sanchez-Benitez, K. Kamenev, W. Wernsdorfer and M. Murrie, Chem. Commun., 2007, 3473-3475; (c) Q. Chen, M.-H. Zeng, Y.-L. Zhou, H.-H. Zou and M. Kurmoo, Chem. Mater., 2010, 22, 2114-2119; (d) T. Shiga, T. Matsumoto, M. Noguchi, T. Onuki, N. Hoshino, G. N. Newton, M. Nakano and H. Oshio, Chem. Asian J., 2009, 4, 1660-1663.

28 (a) S. T. Ochsenbein, M. Murrie, E. Rusanov, H. Stoeckli-Evans, C. Sekine and H. U. Güdel, Inorg. Chem., 2002, 41, 5133-5140; (b) G. Aromí, S. Parsons, W. Wernsdorfer, E. K. Brechin and E. J. L. McInnes, Chem. Commun., 2005, 5038-5040; (c) R. Biswas, Y. Ida, M. L. Baker, S. Biswas, P. Kar, H. Nojiri, T. Ishida and A. Ghosh, Chem. Eur. J., 2013, 19, 3943-3953; (d) A. Bell, G. Aromí, S. J. Teat, W. Wernsdorfer and R. E. P. Winpenny, Chem. Commun., 2005, 2808-2810.

29 J. Vallejo, A. Pascual-Álvarez, J. Cano, I. Castro, M. Julve, F. Lloret, J. Krzystek, G. De Munno, D. Armentano, W. Wernsdorfer, R. Ruiz-García and E. Pardo, Angew. Chem. Int. Ed., 2013, 52, 14075-14079.

30 K. Chakarawet, P. C. Bunting and J. R. Long, J. Am. Chem. Soc., 2018, 140, 2058-2061.

31 C. J. Milios, A. Vinslava, W. Wernsdorfer, S. Moggach, S. Parsons, S. P. Perlepes, G. Christou and E. K. Brechin, J. Am. Chem. Soc., 2007, 129, 2754-2755.

32 C. J. Milios, R. Inglis, R. Bagai, W. Wernsdorfer, A. Collins, S. Moggach, S. Parsons, S. P. Perlepes, G. Christou and E. K. Brechin, Chem. Commun., 2007, 3476-3478.

33 S. J. Langley, M. Helliwell, R. Sessoli, P. Rosa, W. Wernsdorfer and R. E. P. Winpenny, Chem. Commun., 2005, 5029-5031.

34 N. E. Chakov, S.-C. Lee, A. G. Harter, P. L. Kuhns, A. P. Reyes, S. O. Hill, N. S. Dalal, W. Wernsdorfer, K. A. Abboud and G. Christou, J. Am. Chem. Soc., 2006, 128, 6975-6989.

35 P. Abbasi, K. Quinn, D. I. Alexandropoulos, M. Damjanović, W. Wernsdorfer, A. Escuer, J. Mayans, M. Pilkington and T. C. Stamatatos, J. Am. Chem. Soc., 2017, 139, 15644-15647.

36 X.-Y. Wang, C. Avendaño and K. R. Dunbar, Chem. Soc. Rev., 2011, 40, 3213-3238.

37 (a) T. Mahfoud, G. Molnár, S. Bonhommeau, S. Cobo, L. Salmon, P. Demont, H. Tokoro, S.-I. Ohkoshi, K. Boukheddaden and A. Bousseksou, J. Am. Chem. Soc., 2009, 131, 15049-15054; (b) Y. Arimoto, S.-i. Ohkoshi, Z. J. Zhong, H. Seino, Y. Mizobe and K. Hashimoto, J. Am. Chem. Soc., 2003, 125, 9240-9241; (c) S.-i. Ohkoshi, S. Ikeda, T. Hozumi, T. Kashiwagi and K. Hashimoto, J. Am. Chem. Soc., 2006, 128, 5320-5321.

38 (a) D. Pinkowicz, R. Podgajny, B. Nowicka, S. Chorazy, M. Reczyński and B. Sieklucka, Inorg. Chem. Front., 2015, 2, 10-27; (b) D. Pinkowicz, H. I. Southerland, C. Avendaño, A. Prosvirin, C. Sanders, W. Wernsdorfer, K. S. Pedersen, J. Dreiser, R. Clérac, J. Nehrkorn, G. G. Simeoni, A. Schnegg, K. Holldack and K. R. Dunbar, J. Am. Chem. Soc., 2015, 137, 14406-14422; (c) E. J. Schelter, F. Karadas, C.

Avendano, A. V. Prosvirin, W. Wernsdorfer and K. R. Dunbar, J. Am. Chem. Soc., 2007, 129, 8139-8149.

39 (a) L. M. C. Beltran and J. R. Long, Acc. Chem. Res., 2005, 38, 325-334; (b) J. J. Sokol, A. G. Hee and J. R. Long, J. Am. Chem. Soc., 2002, 124, 7656-7657.

40 E. J. Schelter, A. V. Prosvirin and K. R. Dunbar, J. Am. Chem. Soc., 2004, 126, 15004-15005.

41 (a) D. E. Freedman, D. M. Jenkins, A. T. Iavarone and J. R. Long, J. Am. Chem. Soc., 2008, 130, 2884-2885; (b) J. H. Yoon, J. H. Lim, H. C. Kim and C. S. Hong, Inorg. Chem., 2006, 45, 9613-9615; (c) Y. Song, P. Zhang, X.-M. Ren, X.-F. Shen, Y.-Z. Li and X.-Z. You, J. Am. Chem. Soc., 2005, 127, 3708-3709; (d) J. H. Lim, J. H. Yoon, H. C. Kim and C. S. Hong, Angew. Chem. Int. Ed., 2006, 45, 7424-7426; (e) J. M. Zadrozny, D. E. Freedman, D. M. Jenkins, T. D. Harris, A. T. Iavarone, C. Mathonière, R. Clérac and J. R. Long, Inorg. Chem., 2010, 49, 8886-8896.

42 N. Ishikawa, M. Sugita, T. Ishikawa, S.-y. Koshihara and Y. Kaizu, J. Am. Chem. Soc., 2003, 125, 8694-8695.

43 S. Cotton, Lanthanide and Actinide Chemistry, John Wiley & Sons, Ltd, 2006.

44 (a) R. A. Layfield and M. Murugesu, in Lanthanides and Actinides in Molecular Magnetism, Wiley-VCH Verlag GmbH & Co. KGaA, 2015; (b) D. N. Woodruff, R. E. P. Winpenny and R. A. Layfield, Chem. Rev., 2013, 113, 5110-5148.

45 (a) J.-L. Liu, Y.-C. Chen and M.-L. Tong, Chem. Soc. Rev., 2018, 47, 2431-2453; (b) L. Ungur and L. F. Chibotaru, Phys.Chem. Chem. Phys., 2011, 13, 20086-20090.

46 F. Habib and M. Murugesu, Chem. Soc. Rev., 2013, 42, 3278-3288.

47 S. Demir, J. M. Zadrozny, M. Nippe and J. R. Long, J. Am. Chem. Soc., 2012, 134, 18546-18549.

48 K. L. M. Harriman, J. J. Le Roy, L. Ungur, R. J. Holmberg, I. Korobkov and M. Murugesu, Chem. Sci., 2017, 8, 231-240.

49 F. Tuna, C. A. Smith, M. Bodensteiner, L. Ungur, L. F. Chibotaru, E. J. L. McInnes, R. E. P. Winpenny, D. Collison and R. A. Layfield, Angew. Chem. Int. Ed., 2012, 51, 6976-6980.

50 (a) J. Tang, I. Hewitt, N. T. Madhu, G. Chastanet, W. Wernsdorfer, C. E. Anson, C. Benelli, R. Sessoli and A. K. Powell, Angew. Chem. Int. Ed., 2006, 45, 1729-1733; (b) D. I. Plokhov, A. I. Popov and A. K. Zvezdin, Phys. Rev. B, 2011, 84, 224436-224444.

51 (a) L. Ungur, S.-Y. Lin, J. Tang and L. F. Chibotaru, Chem. Soc. Rev., 2014, 43, 6894-6905; (b) P.-H. Guo, J.-L. Liu, Z.-M. Zhang, L. Ungur, L. F. Chibotaru, J.-D. Leng, F.-S. Guo and M.-L. Tong, Inorg. Chem., 2012, 51, 1233-1235; (c) L. Ungur, S. K. Langley, T. N. Hooper, B. Moubaraki, E. K. Brechin, K. S. Murray and L. F. Chibotaru, J. Am. Chem. Soc., 2012, 134, 18554-18557.

52 (a) R. J. Blagg, L. Ungur, F. Tuna, J. Speak, P. Comar, D. Collison, W. Wernsdorfer, E. J. L. McInnes, L. F. Chibotaru and R. E. P. Winpenny, Nat. Chem., 2013, 5, 673-678; (b) R. J. Blagg, C. A. Muryn, E. J. L. McInnes, F. Tuna and R. E. P. Winpenny, Angew. Chem. Int. Ed., 2011, 50, 6530-6533.

53 R. A. Layfield, Organometallics, 2014, 33, 1084-1099.

54 (a) Y.-N. Guo, G.-F. Xu, P. Gamez, L. Zhao, S.-Y. Lin, R. Deng, J. Tang and H.-J. Zhang, J. Am. Chem. Soc., 2010, 132, 8538-8539; (b) M. U. Anwar, L. K. Thompson, L. N. Dawe, F. Habib and M. Murugesu, Chem. Commun., 2012, 48, 4576-4578; (c) S. Xue, Y.-N. Guo, L. Zhao, P. Zhang and J. Tang, Dalton Trans., 2014, 43, 1564-1570; (d) S. Das, A. Dey, S. Biswas, E. Colacio and V. Chandrasekhar, Inorg. Chem., 2014, 53, 3417-3426; (e) J. Goura, J. P. S. Walsh, F. Tuna and V. Chandrasekhar,

Inorg. Chem., 2014, 53, 3385-3391; (f) V. Chandrasekhar, S. Hossain, S. Das, S. Biswas and J.-P. Sutter, Inorg. Chem., 2013, 52, 6346-6353.

55 (a) J.-Y. Ge, J. Ru, F. Gao, Y. Song, X.-H. Zhou and J.-L. Zuo, Dalton Trans., 2015, 44, 15481-15490; (b) G. Wang, Y. Wei and K. Wu, Dalton Trans., 2016, 45, 12734-12738; (c) H. Tian, L. Zhao, H. Lin, J. Tang and G. Li, Chem. Eur. J., 2013, 19, 13235-13241.

56 (a) B. Hussain, D. Savard, T. J. Burchell, W. Wernsdorfer and M. Murugesu, Chem. Commun., 2009, 1100-1102; (b) R. J. Holmberg, C.-J. Kuo, B. Gabidullin, C.-W. Wang, R. Clérac, M. Murugesu and P.-H. Lin, Dalton Trans., 2016, 45, 16769-16773; (c) S. K. Langley, B. Moubaraki, C. M. Forsyth, I. A. Gass and K. S. Murray, Dalton Trans., 2010, 39, 1705-1708.

57 (a) J. Goura, J. P. S. Walsh, F. Tuna and V. Chandrasekhar, Dalton Trans., 2015, 44, 1142-1149; (b) J. W. Sharples, D. Collison, E. J. L. McInnes, J. Schnack, E. Palacios and M. Evangelisti, Nat. Commun., 2014, 5, 5321-5326.

58 (a) V. Chandrasekhar, P. Bag and E. Colacio, Inorg. Chem., 2013, 52, 4562-4570; (b) S. Bala, M. S. Bishwas, B. Pramanik, S. Khanra, K. M. Fromm, P. Poddar and R. Mondal, Inorg. Chem., 2015, 54, 8197-8206; (c) D. I. Alexandropoulos, A. Fournet, L. Cunha-Silva, A. M. Mowson, V. Bekiari, G. Christou and T. C. Stamatatos, Inorg. Chem., 2014, 53, 5420-5422.

59 (a) X. Xu, L. Zhao, G.-F. Xu, Y.-N. Guo, J. Tang and Z. Liu, Dalton Trans., 2011, 40, 6440-6444; (b) X. Li, Q. Liu, J. Lin, Y. Li and R. Cao, Inorg. Chem. Commun., 2009, 12, 502-505; (c) X. Guo, G. Zhu, F. Sun, Z. Li, X. Zhao, X. Li, H. Wang and S. Qiu, Inorg. Chem., 2006, 45, 2581-2587; (d) L. Huang, L. Han, W. Feng, L. Zheng, Z. Zhang, Y. Xu, Q. Chen, D. Zhu and S. Niu, Cryst. Growth Des., 2010, 10, 2548-2552; (e) X. Gu and D. Xue, Inorg. Chem., 2007, 46, 3212-3216.

60 (a) X. Zhang, S. Liu, V. Vieru, N. Xu, C. Gao, B.-W. Wang, W. Shi, L. F. Chibotaru, S. Gao, P. Cheng and A. K. Powell, Chem. Eur. J., 2018, 24, 6079-6086; (b) J. Xiong, H.-Y. Ding, Y.-S. Meng, C. Gao, X.-J. Zhang, Z.-S. Meng, Y.-Q. Zhang, W. Shi, B.-W. Wang and S. Gao, Chem. Sci., 2017, 8, 1288-1294; (c) G.-J. Zhou, Y.-S. Ding and Y.-Z. Zheng, Dalton Trans., 2017, 46, 3100-3104; (d) R. J. Blagg, F. Tuna, E. J. L. McInnes and R. E. P. Winpenny, Chem. Commun., 2011, 47, 10587-10589; (e) T. Pugh, N. F. Chilton and R. A. Layfield, Angew. Chem. Int. Ed., 2016, 55, 11082-11085; (f) J. J. Le Roy, L. Ungur, I. Korobkov, L. F. Chibotaru and M. Murugesu, J. Am. Chem. Soc., 2014, 136, 8003-8010.

61 N. Magnani, E. Colineau, R. Eloirdi, J. C. Griveau, R. Caciuffo, S. M. Cornet, I. May, C. A. Sharrad, D. Collison and R. E. P. Winpenny, Phys. Rev. Lett., 2010, 104, 197202-197205.

62 K. R. Meihaus and J. R. Long, Dalton Trans., 2015, 44, 2517-2528.

63 D. P. Mills, F. Moro, J. McMaster, J. van Slageren, W. Lewis, A. J. Blake and S. T. Liddle, Nat. Chem., 2011, 3, 454-460.

64 J. Tang and P. Zhang, Lanthanide Single-Ion Molecular Magnets in Lanthanide Single Molecule Magnets, eds. J. Tang and P. Zhang, Springer Berlin Heidelberg, Berlin, Heidelberg, 2015, pp. 41-90.

65 (a) F. Pointillart, K. Bernot, R. Sessoli and D. Gatteschi, Chem. Eur. J., 2007, 13, 1602-1609; (b) R. E. P. Winpenny, Chem. Soc. Rev., 1998, 27, 447-452; (c) J. Rinck, G. Novitchi, W. Van den Heuvel, L. Ungur, Y. Lan, W. Wernsdorfer, C. E. Anson, L. F. Chibotaru and A. K. Powell, Angew. Chem. Int. Ed., 2010, 49, 7583-7587.

66 G. Cosquer, F. Pointillart, Y. Le Gal, S. Golhen, O. Cador and L. Ouahab, Chem. Eur. J., 2011, 17, 12502-12511.

67 A. Bencini, C. Benelli, A. Caneschi, R. L. Carlin, A. Dei and D. Gatteschi, J. Am. Chem. Soc., 1985, 107, 8128-8136.

68 (a) J. W. Sharples and D. Collison, Coord. Chem. Rev., 2014, 260, 1-20; (b) L. Rosado Piquer and E. C. Sañudo, Dalton Trans., 2015, 44, 8771-8780; (c) H. Li, Z.-J. Yao, D. Liu and G.-X. Jin, Coord. Chem. Rev., 2015, 293-294, 139-157; (d) K. Liu, W. Shi and P. Cheng, Coord. Chem. Rev., 2015, 289-290, 74-122.

69 (a) S. V. Eliseeva, I. P. Golovach, V. S. Liasotskyi, V. P. Antonovich, S. Petoud and S. B. Meshkova, J. Lumin., 2016, 171, 191-197; (b) L. Aboshyan-Sorgho, M. Cantuel, S. Petoud, A. Hauser and C. Piguet, Coord. Chem. Rev., 2012, 256, 1644-1663.

70 B. Zhao, P. Cheng, X. Chen, C. Cheng, W. Shi, D. Liao, S. Yan and Z. Jiang, J. Am. Chem. Soc., 2004, 126, 3012-3013.

71 F. Evangelisti, R. Moré, F. Hodel, S. Luber and G. R. Patzke, J. Am. Chem. Soc., 2015, 137, 11076-11084.

72 (a) J. Wu, X.-L. Li, M. Guo, L. Zhao, Y.-Q. Zhang and J. Tang, Chem. Commun., 2018, 54, 1065-1068; (b) K. R. Vignesh, S. K. Langley, A. Swain, B. Moubaraki, M. Damjanović, W. Wernsdorfer, G. Rajaraman and K. S. Murray, Angew. Chem. Int. Ed., 2018, 57, 779-784.

73 M. Ferbinteanu, T. Kajiwara, K.-Y. Choi, H. Nojiri, A. Nakamoto, N. Kojima, F. Cimpoesu, Y. Fujimura, S. Takaishi and M. Yamashita, J. Am. Chem. Soc., 2006, 128, 9008-9009.

74 (a) V. Chandrasekhar, B. M. Pandian, J. J. Vittal and R. Clérac, Inorg. Chem., 2009, 48, 1148-1157; (b) H.-R. Wen, P.-P. Dong, S.-J. Liu, J.-S. Liao, F.-Y. Liang and C.-M. Liu, Dalton Trans., 2017, 46, 1153-1162.

75 A. K. Chaudhari, B. Joarder, E. Rivière, G. Rogez and S. K. Ghosh, Inorg. Chem., 2012, 51, 9159-9161.

76 J. Li, R.-M. Wei, T.-C. Pu, F. Cao, L. Yang, Y. Han, Y.-Q. Zhang, J.-L. Zuo and Y. Song, Inorg. Chem. Front., 2017, 4, 114-122.

77 X.-Q. Zhao, Y. Lan, B. Zhao, P. Cheng, C. E. Anson and A. K. Powell, Dalton Trans., 2010, 39, 4911-4917.

78 L. Zhao, J. Wu, H. Ke and J. Tang, Inorg. Chem., 2014, 53, 3519-3525.

79 D. I. Alexandropoulos, K. M. Poole, L. Cunha-Silva, J. Ahmad Sheikh, W. Wernsdorfer, G. Christou and T. C. Stamatatos, Chem. Commun., 2017, 53, 4266-4269.

80 (a) X.-J. Kong, Y.-P. Ren, W.-X. Chen, L.-S. Long, Z. Zheng, R.-B. Huang and L.-S. Zheng, Angew. Chem. Int. Ed., 2008, 47, 2398-2401; (b) C. Papatriantafyllopoulou, T. C. Stamatatos, C. G. Efthymiou, L. Cunha-Silva, F. A. A. Paz, S. P. Perlepes and G. Christou, Inorg. Chem., 2010, 49, 9743-9745.

81 J.-L. Liu, J.-Y. Wu, G.-Z. Huang, Y.-C. Chen, J.-H. Jia, L. Ungur, L. F. Chibotaru, X.-M. Chen and M.-L. Tong, Sci. Rep., 2015, 5, 16621-16629.

82 V. Chandrasekhar, B. M. Pandian, R. Azhakar, J. J. Vittal and R. Clérac, Inorg. Chem., 2007, 46, 5140-5142.

83 (a) J.-L. Liu, J.-Y. Wu, Y.-C. Chen, V. Mereacre, A. K. Powell, L. Ungur, L. F. Chibotaru, X.-M. Chen and M.-L. Tong, Angew. Chem. Int. Ed., 2014, 53, 12966-12970; (b) F.-H. Zhao, H. Li, Y.-X. Che, J.-M. Zheng, V. Vieru, L. F. Chibotaru, F. Grandjean and G. J. Long, Inorg. Chem., 2014, 53, 9785-9799; (c) S. K. Langley, D. P. Wielechowski, B. Moubaraki and K. S. Murray, Chem. Commun., 2016, 52, 10976-10979; (d) K. R. Vignesh, S. K. Langley, K. S. Murray and G. Rajaraman, Chem. Eur. J., 2017, 23, 1654-1666.

84 A. Chakraborty, J. Goura, P. Kalita, A. Swain, G. Rajaraman and V. Chandrasekhar, Dalton Trans., 2018, 47, 8841-8864.

85 (a) J. P. Costes, S. Titos-Padilla, I. Oyarzabal, T. Gupta, C. Duhayon, G. Rajaraman and E. Colacio, Chem. Eur. J., 2015, 21, 15785-15796; (b) W.-B. Sun, P.-F. Yan, S.-D. Jiang, B.-W. Wang, Y.-Q. Zhang, H.-F. Li, P. Chen, Z.-M. Wang and S. Gao, Chem. Sci., 2016, 7, 684-691; (c) I. Oyarzabal, J. Ruiz, E. Ruiz, D. Aravena, J. M. Seco and E. Colacio, Chem. Commun., 2015, 51, 12353-12356.

86 J.-L. Liu, Y.-C. Chen, Y.-Z. Zheng, W.-Q. Lin, L. Ungur, W. Wernsdorfer, L. F. Chibotaru and M.-L. Tong, Chem. Sci., 2013, 4, 3310-3316.

87 (a) F. Shao, B. Cahier, N. Guihéry, E. Rivière, R. Guillot, A.-L. Barra, Y. Lan, W. Wernsdorfer, V. E. Campbell and T. Mallah, Chem. Commun., 2015, 51, 16475-16478; (b) R. Ruamps, L. J. Batchelor, R. Guillot, G. Zakhia, A.-L. Barra, W. Wernsdorfer, N. Guihéry and T. Mallah, Chem. Sci., 2014, 5, 3418-3424; (c) S. Gomez-Coca, E. Cremades, N. Aliaga-Alcalde and E. Ruiz, J. Am. Chem. Soc., 2013, 135, 7010-7018.

88 D. E. Freedman, W. H. Harman, T. D. Harris, G. J. Long, C. J. Chang and J. R. Long, J. Am. Chem. Soc., 2010, 132, 1224-1225.

89 X. Feng, S. J. Hwang, J.-L. Liu, Y.-C. Chen, M.-L. Tong and D. G. Nocera, J. Am. Chem. Soc., 2017, 139, 16474-16477.

90 J. M. Zadrozny, M. Atanasov, A. M. Bryan, C.-Y. Lin, B. D. Rekken, P. P. Power, F. Neese and J. R. Long, Chem. Sci., 2013, 4, 125-138.

91 S. Karasawa, G. Zhou, H. Morikawa and N. Koga, J. Am. Chem. Soc., 2003, 125, 13676-13677.

92 A. K. Bar, C. Pichon and J.-P. Sutter, Coord. Chem. Rev., 2016, 308, 346-380.

93 P. C. Bunting, M. Atanasov, E. Damgaard-Møller, M. Perfetti, I. Crassee, M. Orlita, J. Overgaard, J. van Slageren, F. Neese and J. R. Long, Science, 2018, 362, eaat7319.

94 X.-N. Yao, J.-Z. Du, Y.-Q. Zhang, X.-B. Leng, M.-W. Yang, S.-D. Jiang, Z.-X. Wang, Z.-W. Ouyang, L. Deng, B.-W. Wang and S. Gao, J. Am. Chem. Soc., 2017, 139, 373-380.

95 M. R. Saber and K. R. Dunbar, Chem. Commun., 2014, 50, 12266-12269.

96 (a) R. C. Poulten, M. J. Page, A. G. Algarra, J. J. Le Roy, I. López, E. Carter, A. Llobet, S. A. Macgregor, M. F. Mahon, D. M. Murphy, M. Murugesu and M. K. Whittlesey, J. Am. Chem. Soc., 2013, 135, 13640-13643; (b) K. E. R. Marriott, L. Bhaskaran, C. Wilson, M. Medarde, S. T. Ochsenbein, S. Hill and M. Murrie, Chem. Sci., 2015, 6, 6823-6828; (c) A. Pascual-Álvarez, J. Vallejo, E. Pardo, M. Julve, F. Lloret, J. Krzystek, D. Armentano, W. Wernsdorfer and J. Cano, Chem. Eur. J., 2015, 21, 17299-17307; (d) Y.-F. Deng, T. Han, Z. Wang, Z. Ouyang, B. Yin, Z. Zheng, J. Krzystek and Y.-Z. Zheng, Chem. Commun., 2015, 51, 17688-17691.

97 M. Ding, G. E. Cutsail Iii, D. Aravena, M. Amoza, M. Rouzières, P. Dechambenoit, Y. Losovyj, M. Pink, E. Ruiz, R. Clérac and J. M. Smith, Chem. Sci., 2016, 7, 6132-6140.

98 J. Miklovič, D. Valigura, R. Boča and J. Titiš, Dalton Trans., 2015, 44, 12484-12487.

99 P. E. Kazin, M. A. Zykin, W. Schnelle, C. Felser and M. Jansen, Chem. Commun., 2014, 50, 9325-9328.

100 J. M. Zadrozny, D. J. Xiao, M. Atanasov, G. J. Long, F. Grandjean, F. Neese and J. R. Long, Nat. Chem., 2013, 5, 577-581.

101 P. E. Kazin, M. A. Zykin, L. A. Trusov, A. A. Eliseev, O. V. Magdysyuk, R. E. Dinnebier, R. K. Kremer, C. Felser and M. Jansen, Chem. Commun., 2017, 53, 5416-5419.

102 P. E. Kazin, M. A. Zykin, W. Schnelle, Y. V. Zubavichus, K. A. Babeshkin, V. A. Tafeenko, C. Felser and M. Jansen, Inorg. Chem., 2017, 56, 1232-1240.

103 Y. Rechkemmer, F. D. Breitgoff, M. van der Meer, M. Atanasov, M. Hakl, M. Orlita, P. Neugebauer, F. Neese, B. Sarkar and J. van Slageren, Nat. Commun., 2016, 7, 10467-10474.

104 Y.-F. Deng, T. Han, B. Yin and Y.-Z. Zheng, Inorg. Chem. Front., 2017, 4, 1141-1148.

105 J. D. Rinehart and J. R. Long, Chem. Sci., 2011, 2, 2078-2085.

106 S.-D. Jiang and S.-X. Qin, Inorg. Chem. Front., 2015, 2, 613-619.

107 Z. B. E. C. Huang, Rare Earth Coordination Chemistry: Fundamentals and Applications, John, Wiley & Sons (Asia) Pte Ltd, 2010.

108 (a) N. F. Chilton, Inorg. Chem., 2015, 54, 2097-2099; (b) L. Ungur and L. F. Chibotaru, Inorg. Chem., 2016, 55, 10043-10056.

109 F.-S. Guo, B. M. Day, Y.-C. Chen, M.-L. Tong, A. Mansikkamäki and R. A. Layfield, Science, 2018, 362, 1400-1403.

110 C. A. P. Goodwin, F. Ortu, D. Reta, N. F. Chilton and D. P. Mills, Nature, 2017, 548, 439-442.

111 K. Randall McClain, C. A. Gould, K. Chakarawet, S. J. Teat, T. J. Groshens, J. R. Long and B. G. Harvey, Chem. Sci., 2018, 9, 8492-8503.

112 (a) Y.-S. Ding, N. F. Chilton, R. E. P. Winpenny and Y.-Z. Zheng, Angew. Chem. Int. Ed., 2016, 55, 16071-16074; (b) J. Liu, Y.-C. Chen, J.-L. Liu, V. Vieru, L. Ungur, J.-H. Jia, L. F. Chibotaru, Y. Lan, W. Wernsdorfer, S. Gao, X.-M. Chen and

M.-L. Tong, J. Am. Chem. Soc., 2016, 138, 5441-5450; (c) M. Gregson, N. F. Chilton, A.-M. Ariciu, F. Tuna, I. F. Crowe, W. Lewis, A. J. Blake, D. Collison, E. J. L. McInnes, R. E. P. Winpenny and S. T. Liddle, Chem. Sci., 2016, 7, 155-165; (d) Y.-C. Chen, J.-L. Liu, L. Ungur, J. Liu, Q.-W. Li, L.-F. Wang, Z.-P. Ni, L. F. Chibotaru, X.-M. Chen and M.-L. Tong, J. Am. Chem. Soc., 2016, 138, 2829-2837; (e) Y.-N. Guo, L. Ungur, G. E. Granroth, A. K. Powell, C. Wu, S. E. Nagler, J. Tang, L. F. Chibotaru and D. Cui, Sci. Rep., 2014, 4, 5471-5477; (f) Y.-S. Meng, C.-H. Wang, Y.-Q. Zhang, X.-B. Leng, B.-W. Wang, Y.-F. Chen and S. Gao, Inorg. Chem. Front., 2016, 3, 828-835; (g) S.-D. Jiang, B.-W. Wang, H.-L. Sun, Z.-M. Wang and S. Gao, J. Am. Chem. Soc., 2011, 133, 4730-4733; (h) J. J. Baldoví, J. M. Clemente-Juan, E. Coronado, Y. Duan, A. Gaita-Ariño and C. Giménez-Saiz, Inorg. Chem., 2014, 53, 9976-9980; (i) Y.-C. Chen, J.-L. Liu, W. Wernsdorfer, D. Liu, L. F. Chibotaru, X.-M. Chen and M.-L. Tong, Angew. Chem. Int. Ed., 2017, 56, 4996-5000; (j) Y.-S. Meng, Y.-S. Qiao, Y.-Q. Zhang, S.-D. Jiang, Z.-S. Meng, B.-W. Wang, Z.-M. Wang and S. Gao, Chem. Eur. J., 2016, 22, 4704-4708; (k) K. S. Pedersen, J. Dreiser, H. Weihe, R. Sibille, H. V. Johannesen, M. A. Sørensen, B. E. Nielsen, M. Sigrist, H. Mutka, S. Rols, J. Bendix and S. Piligkos, Inorg. Chem., 2015, 54, 7600-7606; (l) C. R. Ganivet, B. Ballesteros, G. de la Torre, J. M. Clemente-Juan, E. Coronado and T. Torres, Chem. Eur. J., 2013, 19, 1457-1465.

113 S. K. Gupta, T. Rajeshkumar, G. Rajaraman and R. Murugavel, Chem. Sci., 2016, 7, 5181-5191.

114 C. A. Gaggioli and L. Gagliardi, Inorg. Chem., 2018, 57, 8098-8105.

115 Z. G. Lada, E. Katsoulakou and S. P. Perlepes, Synthesis and Chemistry of Single-molecule Magnets in Single-Molecule Magnets: Molecular Architectures and Building Blocks for Spintronics, Wiley-VCH Verlag GmbH & Co. KGaA, 2019.

116 (a) D. M. King, F. Tuna, J. McMaster, W. Lewis, A. J. Blake, E. J. L. McInnes and S. T. Liddle, Angew. Chem. Int. Ed., 2013, 52, 4921-4924; (b) J. T. Coutinho, M. A. Antunes, L. C. J. Pereira, H. Bolvin, J. Marçalo, M. Mazzanti and M. Almeida, Dalton Trans., 2012, 41, 13568-13571; (c) F. Moro, D. P. Mills, S. T. Liddle and J. van Slageren, Angew. Chem. Int. Ed., 2013, 52, 3430-3433; (d) N. Magnani, E. Colineau, J. C. Griveau, C. Apostolidis, O. Walter and R. Caciuffo, Chem. Commun., 2014, 50, 8171-8173; (e) N. Magnani, C. Apostolidis, A. Morgenstern, E. Colineau, J.-C. Griveau, H. Bolvin, O. Walter and R. Caciuffo, Angew. Chem., 2011, 123, 1734-1736; (f) K. R. Meihaus, S. G. Minasian, W. W. Lukens, S. A. Kozimor, D. K. Shuh, T. Tyliszczak and J. R. Long, J. Am. Chem. Soc., 2014, 136, 6056-6068.

117 (a) C. Coulon, V. Pianet, Matias Urdampilleta and R. Cle´rac, Single-Chain Magnets and Related Systems in Single Molecule Magnets and Related Phenomenon: Structure and Bonding, 2015; (b) L. Bogani, A. Vindigni, R. Sessoli and D. Gatteschi, J. Mater. Chem., 2008, 18, 4750-4758.

118 C. Benelli and D. Gatteschi, Single Chain Magnet and More in Introduction toMolecular Magnetism: From Transition Metals to Lanthanides, VCH Verlag GmbH & Co. KGaA, Germany, 2015.

119 S. Dhers, H. L. C. Feltham and S. Brooker, Coord. Chem. Rev., 2015, 296, 24-44.

120 T. D. Harris, M. V. Bennett, R. Clérac and J. R. Long, J. Am. Chem. Soc., 2010, 132, 3980-3988.

121 (a) K. S. Pedersen, A. Vindigni, R. Sessoli, C. Coulon and R. Clérac, Single-Chain Magnets in Molecular Magnetic Materials: Concepts and Applications, Wiley-VCH Verlag GmbH & Co. KGaA, 2017; (b) W.-X. Zhang, R. Ishikawa, B. Breedlove and M. Yamashita, RSC Adv., 2013, 3, 3772-3798.

122 A. Caneschi, D. Gatteschi, N. Lalioti, C. Sangregorio, R. Sessoli, G. Venturi, A. Vindigni, A. Rettori, M. G. Pini and M. A. Novak, Angew. Chem. Int. Ed., 2001, 40, 1760-1763.

123 (a) N. Ishii, Y. Okamura, S. Chiba, T. Nogami and T. Ishida, J. Am. Chem. Soc., 2008, 130, 24-25; (b) M. G. F. Vaz, R. A. A. Cassaro, H. Akpinar, J. A. Schlueter, P. M. Lahti and M. A. Novak, Chem. Eur. J., 2014, 20, 5460-5467.

124 R. Clérac, H. Miyasaka, M. Yamashita and C. Coulon, J. Am. Chem. Soc., 2002, 124, 12837-12844.

125 (a) A. Saitoh, H. Miyasaka, M. Yamashita and R. Clérac, J. Mater. Chem., 2007, 17, 2002-2012; (b) H. Miyasaka, R. Clérac, K. Mizushima, K.-i. Sugiura, M. Yamashita, W. Wernsdorfer and C. Coulon, Inorg. Chem., 2003, 42, 8203-8213.

126 X.-B. Li, Y. Ma and E.-Q. Gao, Inorg. Chem., 2018, 57, 7446-7454.

127 T. S. Venkatakrishnan, S. Sahoo, N. Bréfuel, C. Duhayon, C. Paulsen, A.-L. Barra, S. Ramasesha and J.-P. Sutter, J. Am. Chem. Soc., 2010, 132, 6047-6056.

128 Y.-Z. Zhang, B. S. Dolinar, S. Liu, A. J. Brown, X. Zhang, Z.-X. Wang and K. R. Dunbar, Chem. Sci., 2018, 9, 119-124.

129 (a) M.-X. Yao, Q. Zheng, K. Qian, Y. Song, S. Gao and J.-L. Zuo, Chem. Eur. J., 2013, 19, 294-303; (b) J. Xie, H.-D. Li, M. Yang, J. Sun, L.-C. Li and J.-P. Sutter, Chem. Commun., 2019, 55, 3398-3401.

130 D. Visinescu, A. M. Madalan, M. Andruh, C. Duhayon, J.-P. Sutter, L. Ungur, W. Van den Heuvel and L. F. Chibotaru, Chem. Eur. J., 2009, 15, 11808-11814.

131 (a) R. A. A. Cassaro, S. G. Reis, T. S. Araujo, P. M. Lahti, M. A. Novak and M. G. F. Vaz, Inorg. Chem., 2015, 54, 9381-9383; (b) Y.-Q. Wang, Q. Yue and E.-Q. Gao, Chem. Eur. J., 2017, 23, 896-904; (c) L. Chatelain, F. Tuna, J. Pécaut and M. Mazzanti, Chem. Commun., 2015, 51, 11309-11312; (d) R.-M. Wei, F. Cao, J. Li, L.

Yang, Y. Han, X.-L. Zhang, Z. Zhang, X.-Y. Wang and Y. Song, Sci. Rep., 2016, 6, 24372-24379 ; (e) K. Bernot, L. Bogani, A. Caneschi, D. Gatteschi and R. Sessoli, J. Am. Chem. Soc., 2006, 128, 7947-7956; (f) C. Pichon, N. Suaud, C. Duhayon, N. Guihéry and J.-P. Sutter, J. Am. Chem. Soc., 2018, 140, 7698-7704; (g) J. A. DeGayner, K. Wang and T. D. Harris, J. Am. Chem. Soc., 2018, 140, 6550-6553.

132 J.-C. G. Bünzli, Chem. Rev., 2010, 110, 2729-2755.

133 J. Feng and H. Zhang, Chem. Soc. Rev., 2013, 42, 387-410.

134 J.-C. G. Bünzli and C. Piguet, Chem. Soc. Rev., 2005, 34, 1048-1077.

135 A. Thibon and V. C. Pierre, Anal. Bioanal. Chem., 2009, 394, 107-120.

136 M. L. Aulsebrook, B. Graham, M. R. Grace and K. L. Tuck, Coord. Chem. Rev., 2018, 375, 191-220.

137 L. Armelao, S. Quici, F. Barigelletti, G. Accorsi, G. Bottaro, M. Cavazzini and E. Tondello, Coord. Chem. Rev., 2010, 254, 487-505.

138 V. Bulach, F. Sguerra and M. W. Hosseini, Coord. Chem. Rev., 2012, 256, 1468-1478.

139 E. G. Moore, A. P. S. Samuel and K. N. Raymond, Acc. Chem. Res., 2009, 42, 542-552.

140 (a) K. P. Zhuravlev, V. A. Kudryashova and V. I. Tsaryuk, J. Photochem. Photobiol., B, 2016, 314, 14-21; (b) S. Dasari and A. K. Patra, Dalton Trans., 2015, 44, 19844-19855; (c) E. R. Souza, J. H. S. K. Monteiro, I. O. Mazali and F. A. Sigoli, J. Lumin., 2016, 170, 520-527; (d) K. Senthil Kumar, B. Schäfer, S. Lebedkin, L. Karmazin, M. M. Kappes and M. Ruben, Dalton Trans., 2015, 44, 15611-15619; (e) S. Pandya, J. Yu and D. Parker, Dalton Trans., 2006, 2757-2766; (f) A. R. Ramya, S. Varughese and M. L. P. Reddy, Dalton Trans., 2014, 43, 10940-10946.

Pentagonal Bipyramidal Ln[III] Complexes Exhibiting Single-Ion Magnet Behaviour: A Rational Synthetic Approach for Rigid Equatorial Plane

ABSTRACT: A pentadentate chelating ligand is utilized for the facile synthesis of air-stable pentagonal bipyramidal Ln[III] complexes with a rigid equatorial plane. The static and dynamic magnetic properties of the complexes were studied. The Dy[III] analogue exhibits single-ion magnet behaviour with $U_{eff}/k_B = 70$ K under an applied magnetic field, $H_{dc} = 500$ Oe. The single-ion magnet behaviour is further confirmed by ac magnetic susceptibility investigation on a magnetically diluted sample.

2.A.1 INTRODUCTION

Molecule-based nanomagnets possess huge prospects in the next generation technology.[1] The discovery of single-ion magnet behaviour in phthalocyanine-sandwiched Ln[III] mononuclear complexes by Ishikawa *et al.[2]* has triggered a tremendous research interest in the arena of molecule-based magnetism associated with Ln[III] ions.[3] Strong magnetic anisotropy and a large spin ground state endow the Ln[III] complexes, especially the Dy-analogues,[3d, 3k] with slow magnetic dynamics provided the Ln[III] ions are in an appropriate crystal-field (CF) environment.[3a-k, 4] Recent advances reveal that Ln[III]-based complexes with low-coordination numbers and high CF symmetry are expected to exhibit promising single-molecule magnet (SMM) behaviour.[5] However, it is worth mentioning that the Ln[III] ions prefer large coordination numbers (8-10) and variable coordination geometry owing to large ionic size and highly shielded valence (4f) orbitals.[4, 6] Therefore, it is a challenge to

synthetic chemists to control low-coordination with desired geometry in Ln^{III}-based complexes.

Realization of the topologies (prolate/oblate) of the electrostatic potential surfaces corresponding to the magnetic ground states of the Ln^{III} ions provides a straightforward rationale for Ln^{III}-based single-ion magnets (SIMs).[3a, 7] For example, the highest magnetic ground states for the Dy^{III} ion ($M_J = \pm15/2$) incorporate an oblate-like electrostatic potential surface.[3a, 7] Therefore, the coordination environments providing very strong axial CF and weak equatorial CF stabilize these magnetic ground states with large magnetization blockade barriers.[5f, 8] In addition to these, a high axial CF symmetry suppresses the quantum tunnelling of magnetization (QTM) and consequently, enhances the effective energy barrier for magnetization reversal (U_{eff}) and blocking temperature (T_B).[5f]

Ab initio calculations predict high U_{eff} values for Dy^{III} ion in pentagonal bipyramidal (PBP) coordination geometry owing to high axial CF symmetry.[5f] Moreover, PBP complexes with a rigid equatorial plane and kinetically labile ligands at apical positions seem to be one of the promising building blocks towards rational synthesis of multi-metallic SMMs.[9] In such building blocks, CF symmetry does not change upon association and the apical CF strength could be chemically tuned to tailor the slow magnetic dynamics. But, unlike 3d transition metal ions,[9c] PBP geometry is less common in Ln^{III}-based coordination complexes.[6a] Figure 2.A.1 shows a schematic representation of reported transition metal based PBP complexes with pentadentate chelating ligands. Remarkably, several Ln^{III} complexes with PBP geometry are reported as SMMs[10] displaying U_{eff} as high as 828 cm^{-1}.[10a] Keeping in mind that PBP Ln^{III} complexes are excellent candidates of SMMs, we have utilized a pentadentate chelating ligand (H$_4$L) for the synthesis of (Et$_3$NH)[(H$_2$L)LnCl$_2$] (Ln = Tb^{III}; **2.A.1**,

Dy^{III}; **2.A.2**, Dy^{III}/Y^{III}; **2.A.3**) complexes. The synthesis, structural characterization and magnetic properties of the complexes are discussed in this chapter.

R = Ph; M = Fe; X = Cl; m = 0
R = Ph; M = Fe; X = MeOH/H$_2$O; m = 2
R = biPh; M = Fe; X = Cl/MeOH; m = 1
R = biPh; M = Co; X = MeOH/NO$_3$; m = 1
R = NH$_2$; M = Fe; X = Cl; m = 0
R = NH$_2$; M = Ni; X = H$_2$O; m = 2
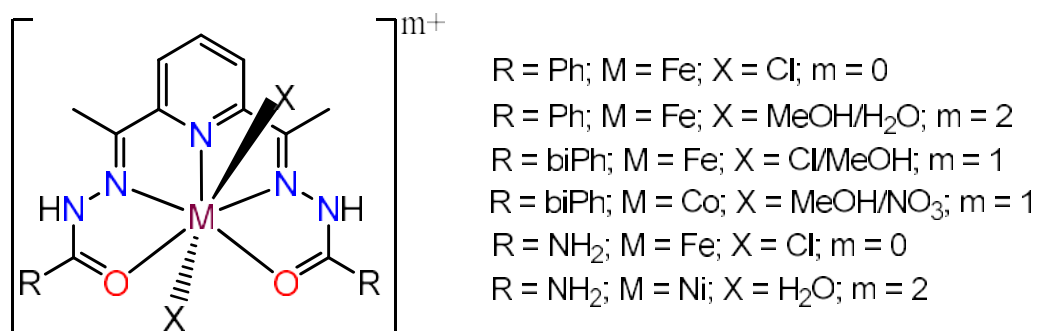
Figure 2.A.1. Schematic representation of a few mononuclear hepta-coordinate transition metal complexes.

2.A.2 EXPERIMENTAL SECTION

2.A.2.1 Materials and Methods. All the general reagents and solvents used for the syntheses were obtained from commercial sources and were used as received without further purification. Diacetyl pyridine (DAP), EtOH, and hydrated lanthanide chlorides were obtained from Sigma Aldrich Chemical Co. (India). Salicyloyl hydrazide was obtained from Spectrochem Pvt. Ltd., Mumbai, India. The organic ligand 2,6-diacetylpyridine *bis*-salicylhydrazone (H$_4$L) was synthesized following reported procedure.[11]

2.A.2.2 Instrumentation. Fourier transform infrared (FT-IR) spectroscopy was performed with a Perkin-Elmer spectrum RX-1 FT-IR spectrometer. Elemental analyses were performed with a Perkin-Elmer 2400 series II instrument. UV-Vis spectroscopic studies were carried out with Perkin-Elmer L-750 UV-Vis NIR instrument. Mass spectrometric analysis was performed with Bruker micrOTOF-Q II

Mass instrument. Powder X-ray diffraction study was performed on finely ground polycrystalline material with Bruker D8 Advance Powder X-ray diffractometer.

2.A.2.3 Magnetic Measurements. Magnetic properties were investigated on polycrystalline solid samples of the complexes mixed with grease. Magnetic susceptibility measurements were carried out with a Quantum Design MPMS-5S SQUID susceptometer. The magnetic measurements were performed on freshly filtered polycrystalline materials. The polycrystalline powders were mixed with grease and put in gelatin capsules. The dc measurements were conducted from 300 to 2 K at 1 kOe and the data were corrected for the diamagnetic contribution of the sample holder, grease and sample by using Pascal's tables.[6b] The field dependence of the magnetization was measured at several temperatures between 2 and 7 K with dc magnetic field up to 5 T. Preliminary ac susceptibility experiments for **2.A.1** and **2.A.2** were performed at various frequencies ranging from 1 to 1500 Hz with an ac field amplitude of 3 Oe. The ac susceptibility was investigated under an oscillating ac field of 3 Oe over the frequency range of 1 to 1500 Hz.

2.A.2.4 X-ray Crystallography. Single crystals suitable for X-ray diffraction were coated with oil and mounted onto the goniometer. The X-ray crystallographic data were obtained at low temperature (150 K for **2.A.1** and 100 K for **2.A.2** and **2.A.3**) from a Bruker Kappa Apex-II single crystal X-ray diffractometer (MoKα radiation source) and equipped with an Oxford Cryosystem. The structures were solved by direct methods using ShelXS and refined by means of least-square procedures on F^2 using the WinGX16 version.[12] The scattering factors for all the atoms were used as listed in the International Tables for X-ray Crystallography.[13] Absorption correction was performed using a multi-scan procedure. All the non-hydrogen atoms were refined anisotropically. When it was possible, the H atoms were located in a

difference map, but those attached to carbon atoms were repositioned geometrically. The H atoms were initially refined with soft restraints on the bond lengths and angles to regularise their geometry and U~iso~(H) (in the range 1.2-1.5 times U~eq~ of the parent atom), after which the positions were refined with riding constraints. For compound **2.A.3**, the Dy population was determined by positional disorder treatments. The single crystals of **2.A.1** are weakly diffracting, this results in weakly diffracting high angle data and hence the completeness is low. However, the formation of the complex can be convincingly realized from the data.

2.A.2.5 Synthesis of 2.A.1-2.A.3. Syntheses of all the complexes were performed under aerobic conditions following the same procedure described below:

The organic ligand 2,6-diacetylpyridine *bis*-salicylhydrazone (H_4L; 1 eq.) was suspended in 30 mL of absolute EtOH. To it an ethanolic solution of $LnCl_3·6H_2O$ (30 mL; 1 eq.) was added. The reaction mixture was refluxed for 1 h under stirring followed by cooling down to room temperature. The solvent was reduced to ~ 40 mL under reduced pressure. To this yellow reaction mixture NEt_3 (2 eq.) was added slowly under constant stirring to obtain a transparent, dark yellow solution, which was stirred further at room temperature for 10 min before it was filtered off. Diethyl ether was layered over the filtrate and kept undisturbed for two days to obtain rectangular, bright yellow crystals. The supernatant was filtered off. The crystalline materials were washed with diethyl ether and air-dried to obtain yellow crystalline solids. The stoichiometry of the reactants, yields of the products and the experimental characterization data of **2.A.1**-**2.A.3** are given below.

(Et₃NH)[(H₂L)TbCl₂] (**2.A.1**). H_4L (0.2 g, 0.4635 mmol), $TbCl_3·6H_2O$ (0.174 g, 0.4616 mmol), and NEt_3 (130 μL, 0.9289 mmol) were used. Yield: 0. 199 g, 57% (based on Tb). M.P.: > 250 °C. IR (cm^{-1}): υ_{O-H} = 3344 (bs); $\upsilon_{C=O}$ = 1582 (vs) and 1513

(vs); $\upsilon_{C=N}$ = 1526 (vs). UV-Vis (r.t., EtOH, 0.1 mM): λ_{max} (nm) = 251 and 400. ESI-MS: m/z = 624.15 and 632.08. Elemental analysis (%) calcd for $C_{29}H_{35}N_6O_4Cl_2Tb$: C 45.74; H 4.63; N 11.04; Found: C 45.37; H 4.47; N 10.81.

(Et₃NH)[(H₂L)DyCl₂] (**2.A.2**). H_4L (0.2 g, 0.4635 mmol), $DyCl_3 \cdot 6H_2O$ (0. 174 g, 0.4616 mmol), and NEt_3 (130 μL, 0.9289 mmol) were used. Yield: 0. 225 g, 64% (based on Dy). M.P.: > 250 °C. IR (cm⁻¹): υ_{O-H} = 3402 (bs); $\upsilon_{C=O}$ = 1586 (vs) and 1522 (vs); $\upsilon_{C=N}$ = 1526 (vs). UV-Vis (r.t., EtOH, 0.1 mM): λ_{max} (nm) = 251 and 400. ESI-MS: m/z = 628.05, 637.02 and 663.03. Elemental analysis (%) calcd for $C_{29}H_{35}N_6O_4Cl_2Dy$: C 45.53; H 4.61; N 10.99; Found: C 45.27; H 4.57; N 10.71.

(Et₃NH)[(H₂L)Y₀.₉₄Dy₀.₀₆Cl₂] (**2.A.3**). H_4L (0.2 g, 0.4635 mmol), $YCl_3 \cdot 6H_2O$ (0.162 g, 0.4352 mmol), $DyCl_3 \cdot 6H_2O$ (0.011 g, 0.0292 mmol), and NEt_3 (130 μL, 0.9289 mmol) were used. Yield: 0.201 g 62%. Elemental analysis (%) calcd. for $C_{29}H_{35}N_6O_4Cl_2Y_{0.94}Dy_{0.06}$: C 50.05; H 5.03; N 12.08; Found: C 49.97; H 5.01; N 11.89.

2.A.3 RESULTS AND DISCUSSION

2.A.3.1 Synthetic Aspects. Ligand design plays a crucial role in the isolation of PBP mononuclear lanthanide complexes. The initial efforts of synthesis relied on serendipity driven synthesis where seven monodentate ligands were sufficient enough to fulfil the coordination requirement around the Ln^{III} in a PBP geometry. Very few synthetic methods were based on rational design involving pre-designed multidentate ligands which can give exclusively PBP complexes. However, all these complexes are unlikely to retain the PBP geometry upon chemical alteration within the coordination sphere. To develop a rational synthetic strategy we have employed a pentadentate chelating ligand and synthesized mononuclear PBP Ln^{III} complexes with the general

formula $(Et_3NH)[(H_2L)Ln^{III}Cl_2]$ (where Ln = Tb (**2.A.1**), Dy (**2.A.2**), $Y_{0.94}Dy_{0.06}$ (**2.A.3**) and H_4L = 2,6-diacetylpyridine *bis*-salicylhydrazone). The ligand renders a rigid pentagonal equatorial plane around the Ln ions (Scheme 2.A.1). All the complexes could be synthesized upon treatment of the ligand with one equivalent of the corresponding hydrated lanthanide trichloride salt $(LnCl_3 \cdot xH_2O)$ followed by treatment with two equivalents triethylamine under aerobic condition in an ethanol solvent medium.
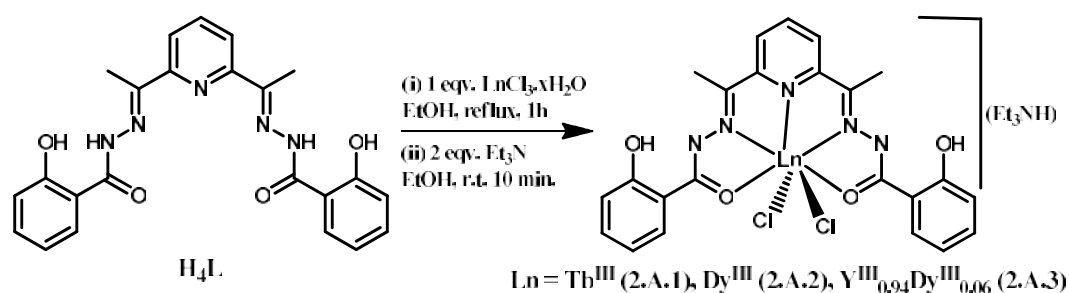
Scheme 2.A.1. Syntheses of the complexes **2.A.1-2.A.3**.

The solution state stability of the complexes is obtained by Electrospray Ionization Mass Spectrometry (ESI-MS) studies. ESI-MS of **2.A.1** displayed two intense peaks at m/z = 624.15 and 632.08 corresponding to $[(H_2L)TbCl + H^+]^+$ and $[(L)Tb + 2Na^+]^+$ molecular fragments (Figure 2.A.2 (top)). ESI-MS of **2.A.2** displayed three intense peaks at m/z = 628.05, 637.02, and 663.03. The first two peaks corresponds to $[(H_2L)DyCl + H^+]^+$ and $[(L)Dy + 2Na^+]^+$ molecular fragments respectively (Figure 2.A.2 (bottom)). The intense peak appearing around m/z = 663, is attributed to the molecular ion peak corresponding to $[(H_2L)Dy^{III}Cl_2]^-$ fragment supported by the simulated isotopic distribution patterns (Figure 2.A.3).
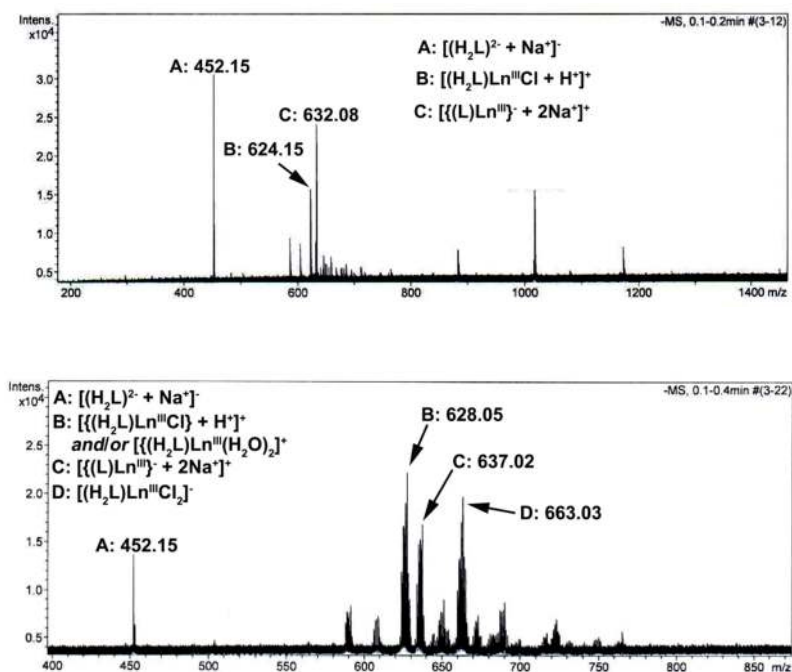
Figure 2.A.2. ESI-MS spectra of **2.A.1** (*top*), **2.A.2** (*bottom*)
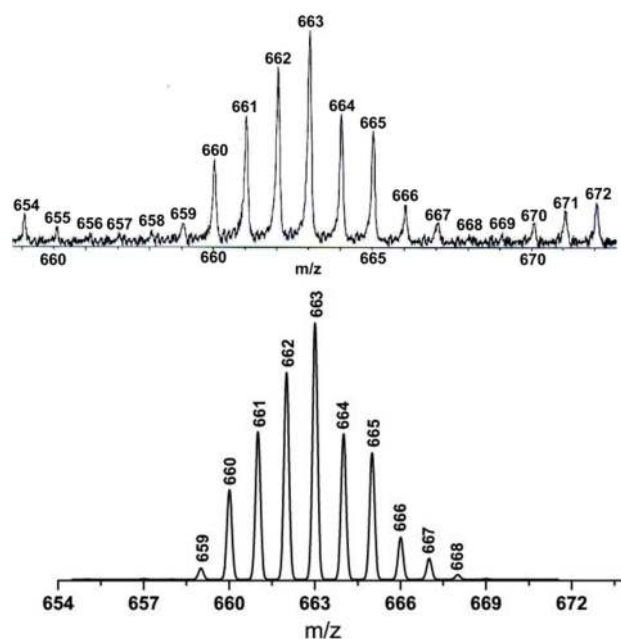
Figure 2.A.3. The experimental (*top*) and simulated (*bottom*) isotropic distribution pattern corresponding to the molecular ion peak for **2.A.2**.

The room temperature UV-Vis absorption spectra of the free ligand and the corresponding lanthanide metal complexes **2.A.1-2.A.3** were recorded in EtOH solution of concentration 10^{-4} mol L^{-1} (Figure 2.A.4). The absorption spectrum of the free ligand shows two bands in the range of 250-450 nm. The lowest energy transition is observed at 360-430 nm due to the $n \rightarrow \pi^*$ transitions of the carbonyl chromophore. The intra-ligand $\pi \rightarrow \pi^*$ transition of the free ligand was observed at 325 nm. Upon metalation these bands were red shifted to slightly higher wavelengths (251 and 400 nm respectively) consistent with coordination of the ligand to the metal center.
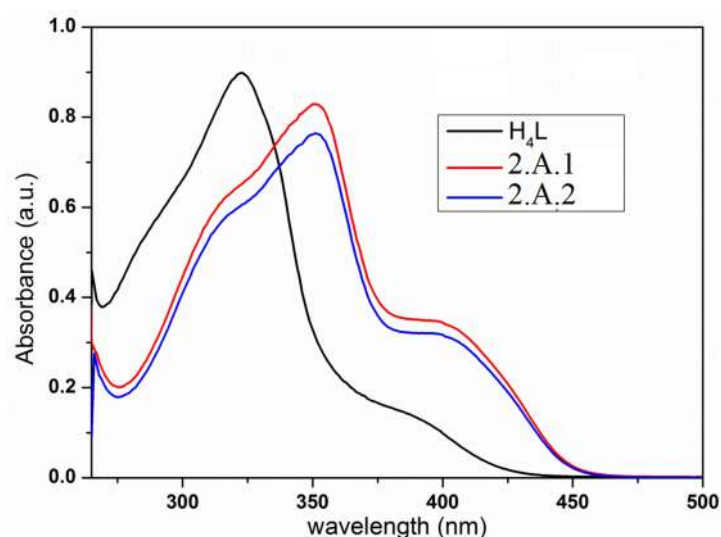
Figure 2.A.4. UV-Vis spectra (in EtOH, 0.1 mM, r.t.) of H_4L (*black*), **2.A.1** (*red*) and **2.A.2** (*blue*).

2.A.3.2 Molecular Structures. The molecular structures of **2.A.1-2.A.3** were analyzed by the single crystal X-ray diffraction studies. All the complexes crystalized in the orthorhombic crystal system in the Cmc2$_1$ space group. Crystallographic data and refinement parameters of **2.A.1-2.A.3** are given in Table 2.A.1.

Table 2.A.1. Crystallographic data and refinement parameters of **2.A.1-2.A.3**.

	2.A.1	2.A.2	2.A.3
Empirical formula	$C_{29}H_{35}N_6O_4Cl_2Tb_1$	$C_{29}H_{35}N_6O_4Cl_2Dy_1$	$C_{29}H_{35}N_6O_4Cl_2Y_{0.94}Dy_{0.06}$
M_w (g mol^{-1})	761.46	765.04	695.32
Temperature	150(2) K	100(2) K	100(2) K
Wavelength	0.71073 Å	0.71073 Å	0.71073 Å
Crystal system	Orthorhombic	Orthorhombic	Orthorhombic
Space group	Cmc2(1)	Cmc2(1)	Cmc2(1)
Unit cell dimensions	a = 18.898(3) Å b = 14.929(3) Å c = 11.3643(15) Å $\alpha = \beta = \gamma = 90°$	a = 18.856(2) Å b = 14.9492(15) Å c = 11.3389(11) Å $\alpha = \beta = \gamma = 90°$	a = 18.7683(8) Å b = 14.8966(8) Å c = 11.1603(5) Å $\alpha = \beta = \gamma = 90°$
Volume (Å^3)	3206.2(9)	3196.2(6)	3120.2(3)
Z	4	4	4
Density (calculated)	1.567 mg/m^3	1.446 mg/m^3	1.481 mg/m^3
Absorption coefficient	2.415 mm^{-1}	2.536 mm^{-1}	2.114 mm^{-1}
F(000)	1508	1325	1430
Crystal size (mm^3)	0.11 x 0.07 x 0.07	0.14 x 0.08 x 0.07	0.19 x 0.11 x 0.08
Theta range for data collection	1.738 to 20.877°.	2.160 to 28.338°	2.170 to 31.049°
Reflections collected	5836	15508	33179
Independent reflections	1476 [R_{int} = 0.0618]	3897 [R_{int} = 0.0327]	4449 [R_{int} = 0.0741]
Completeness (θ)	99.8 % (20.877°)	99.9 % (25.242°)	99.8 % (31.049°)
Refinement method	Full-matrix least-squares on F^2	Full-matrix least-squares on F^2	Full-matrix least-squares on F^2
GOF on F^2	0.941	0.878	0.991
Final R indices [I>2sigma(I)]	R$_1$ = 0.0401, wR$_2$ = 0.0932	R$_1$ = 0.0229, wR$_2$ = 0.0554	R$_1$ = 0.0299, wR$_2$ = 0.0597
R indices (all data)	R$_1$ = 0.0450, wR$_2$ = 0.0962	R$_1$ = 0.0273, wR$_2$ = 0.0581	R$_1$ = 0.0385, wR$_2$ = 0.0619
$R_1 = \sum|F_0 - F_c|/\sum F_0$; $wR_2 = \sum[w(F_0^2 - F_0^2)]^2/[w(F_0^2)^2]^{\frac{1}{2}}$			
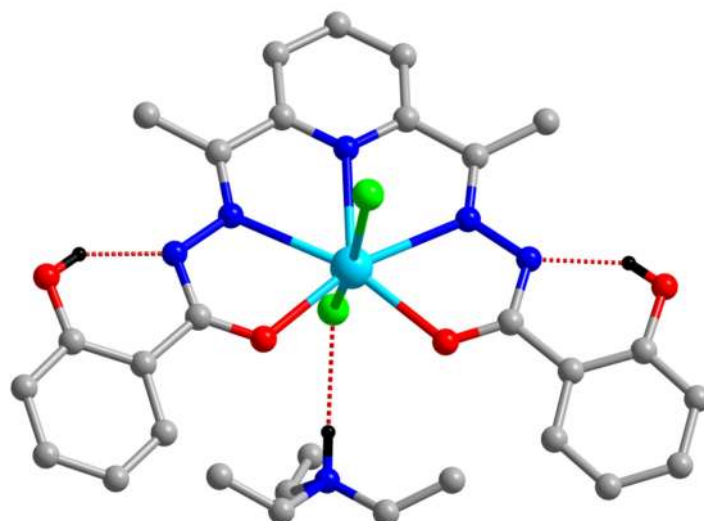
Figure 2.A.5. Single crystal X-ray structure of **2.A.2**. H atoms except selected ones are omitted for clarity. Colour codes: N = blue; O = red; green = Cl; C = grey; Dy = cyan and H = black

Figure 2.A.5 depicts single crystal X-ray structure of **2.A.2** as the representative example, while the molecular structures of **2.A.1** and **2.A.3** are portrayed in the Figures 2.A.6-2.A.7. The cationic core of **2.A.2** is seven-coordinated and comprises of one pyridyl N, two imino N and two carboxy O atoms of the ligand chelating the Dy^{III} ion and generating a coplanar equatorial coordination environment with a *pseudo* pentagonal geometry (O–Dy–N$_{im}$ angle = 65.63°; N$_{py}$–Dy–N$_{im}$ angle = 65.02° and O–Dy–O angle = 98.69°). The equatorial Dy–O/N bond distances lie in the range of 2.26-2.45 Å, confirming the penta-coordination. The remaining two apical positions are occupied by Cl$^-$ ligands completing the seventh coordination environment around the Ln ion. The average Dy–Cl bond distance and Cl–Dy–Cl bond angle are in the range of 2.64 Å and 166.32° respectively. One of the two Cl$^-$ ligands is H-bonded to the triethyl ammonium counter cation leading to stabilization of the monocationic core (Figure 2.A.5). Selected bond distance and bond angle parameters of **2.A.1-2.A.3** are given in Table 2.A.2.
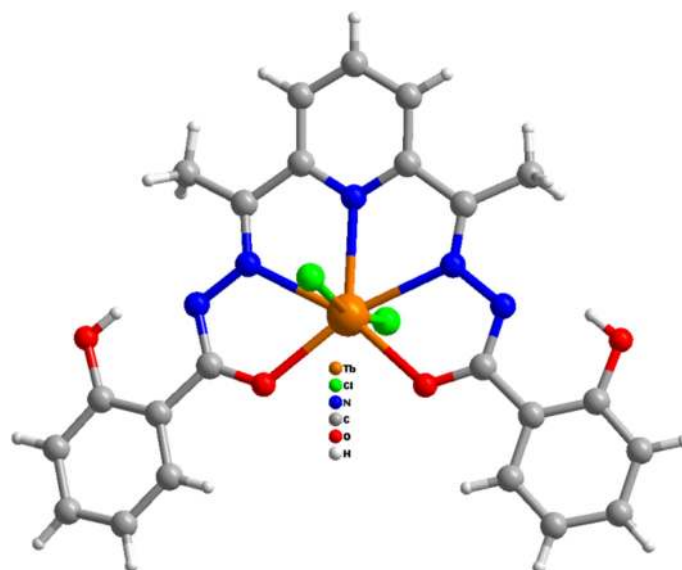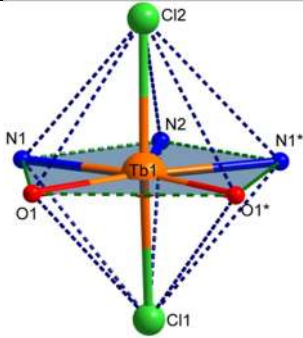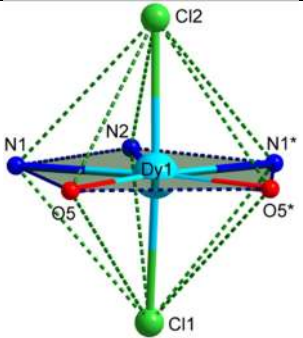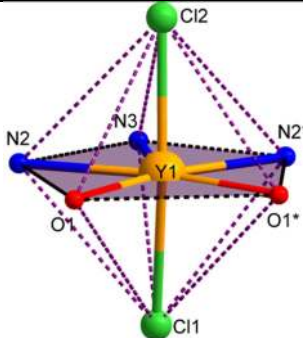
Figure 2.A.6. The molecular structures of **2.A.1**. The counter cations (Et₃NH) are removed for clarity. The colour codes are as presented in the inset legends.
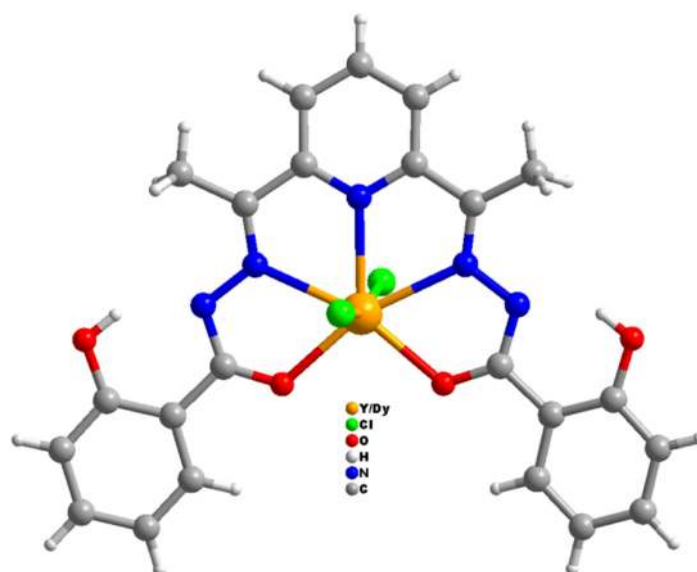
Figure 2.A.7. The molecular structures of **2.A.3**. The counter cations (Et₃NH) are removed for clarity. The colour codes are as presented in the inset legends.

Table 2.A.2. Selected bond lengths (Å) bond angles (°) of **2.A.1-2.A.3**.

Complex	Bond distance (Å)	Bond angle (°)
PBP geometry of Tb1 in **2.A.1**	Tb1–O1……2.281(10) Tb1–O1*…..2.281(10) Tb1–N1……2.456(13) Tb1–N1*…..2.456(13) Tb1–N2……..2.455(19) Tb1–Cl1…......2.625(6) Tb1–Cl2…......2.694(7)	O1–Tb1–O1*……....100.3(5) O1–Tb1–N2……….129.9(3) O1*- Tb1-N2……..129.8(3) O1–Tb1–Cl1……….94.0(3) N2–Tb1–Cl1………..84.3(5) N2- Tb1-Cl2……....81.7(5) N1*–Tb1–Cl1……...87.6(3) O1–Tb1–N1*……...165.5(4) Cl1–Tb1–Cl2……..166.1(2)
PBP geometry of Dy1 in **2.A.2**	Dy1–O5*…2.264(3) Dy1–O5…..2.264(3) Dy1–N1…..2.446(4) Dy1–N1*…2.446(4) Dy1–N2…..2.446(5) Dy1–Cl1….2.607(2) Dy1–Cl2....2.681(2)	O5*–Dy1–O5…..98.66(16) O5–Dy1–Cl1……94.61(10) N1–Dy1–Cl1……87.48(10) N1*–Dy1–Cl1…..87.48(10) N1–Dy1–Cl2……86.75(10) O5–Dy1–Cl1……94.61(10) Cl1-Dy1-Cl2…166.32(6) N1–Dy1–N2……65.02(9) O5*–Dy1–Cl2…94.29(10)
PBP geometry of Y1 in **2.A.3**	Y1–O1*…....2.252 (2) Y1–O1…......2.253(2) Y1–N3……..2.437(3) Y1–N2*…....2.441(2) Y1–N2…....2.441(2) Y1–Cl2……2.602(11) Y1–Cl1…......2.666 (11)	O1*–Y1–O1…...98.03(10) O1*–Y1–N2*…...65.75(7) O1*–Y1–N2…...163.77(7) N2–Y1–Cl2……..87.59(6) O1–Y1–Cl2…….94.55(6) N2–Y1–Cl2……...87.59(6) N3–Y1–Cl1……...81.28(9) Cl2–Y1–Cl1……165.85(3) N3–Y1–N2………65.23(5)

*symmetry transformations used to generate equivalent atoms: -x+2, y, z

The continuous shape measures analyses using SHAPE programme[14] reveals distorted pentagonal bipyramidal geometry with D_{5h} (*pseudo*) CF symmetry around the Ln^{III} ions in **2.A.1-2.A.3** (Table 2.A.3, Figure 2.A.8). The smallest value of the deviation geometric parameter corresponds to the plausible coordination geometry. All the complexes crystallize without any co-crystallized solvent. The solid state phase purity of the complex **2.A.3** was confirmed by powder X-ray diffraction studies (Figure 2.A.9). Solid state packing diagrams display that the shortest intermolecular Ln···Ln distance is ~ 7.6 Å (Figure 2.A.10). Interestingly, there is essentially no short contact between these two closest molecules which could provide magnetic superexchange pathway.[9b] The purity of the bulk samples of all the complexes was confirmed by elemental (CHN) analyses.

Table 2.A.3. The deviation geometric parameters as calculated from the Continuous Shape Measures using SHAPE program for different probable coordination geometries with seven coordination number around the Ln centers of **2.A.1-2.A.3**.

Ln	**PBPY-7**	JPBPY-7	CTPR-7	COC-7	JETPY-7	HPY-7	HP-7
Tb (**2.A.1**)	**1.345**	6.878	7.457	9.156	24.058	24.433	33.326
Dy (**2.A.2**)	**1.210**	6.725	7.276	8.971	24.222	24.910	33.613
Y/Dy (**2.A.3**)	**1.159**	6.653	7.330	9.079	24.319	24.901	33.495

PBPY-7: Pentagonal bipyramid (D_{5h}); JPBPY-7: Johnson pentagonal bipyramid J13 (D_{5h});

CTPR-7: Capped trigonal prism (C_{2v}); CTPR-7 Capped trigonal prism (C_{2v});

COC-7: Capped octahedron (C_{3v}); JETPY-7: Johnson elongated triangular pyramid J7 (C_{3v});

HPY-7 Hexagonal pyramid (C_{6v}); HP-7 : Heptagon (D_{7h})
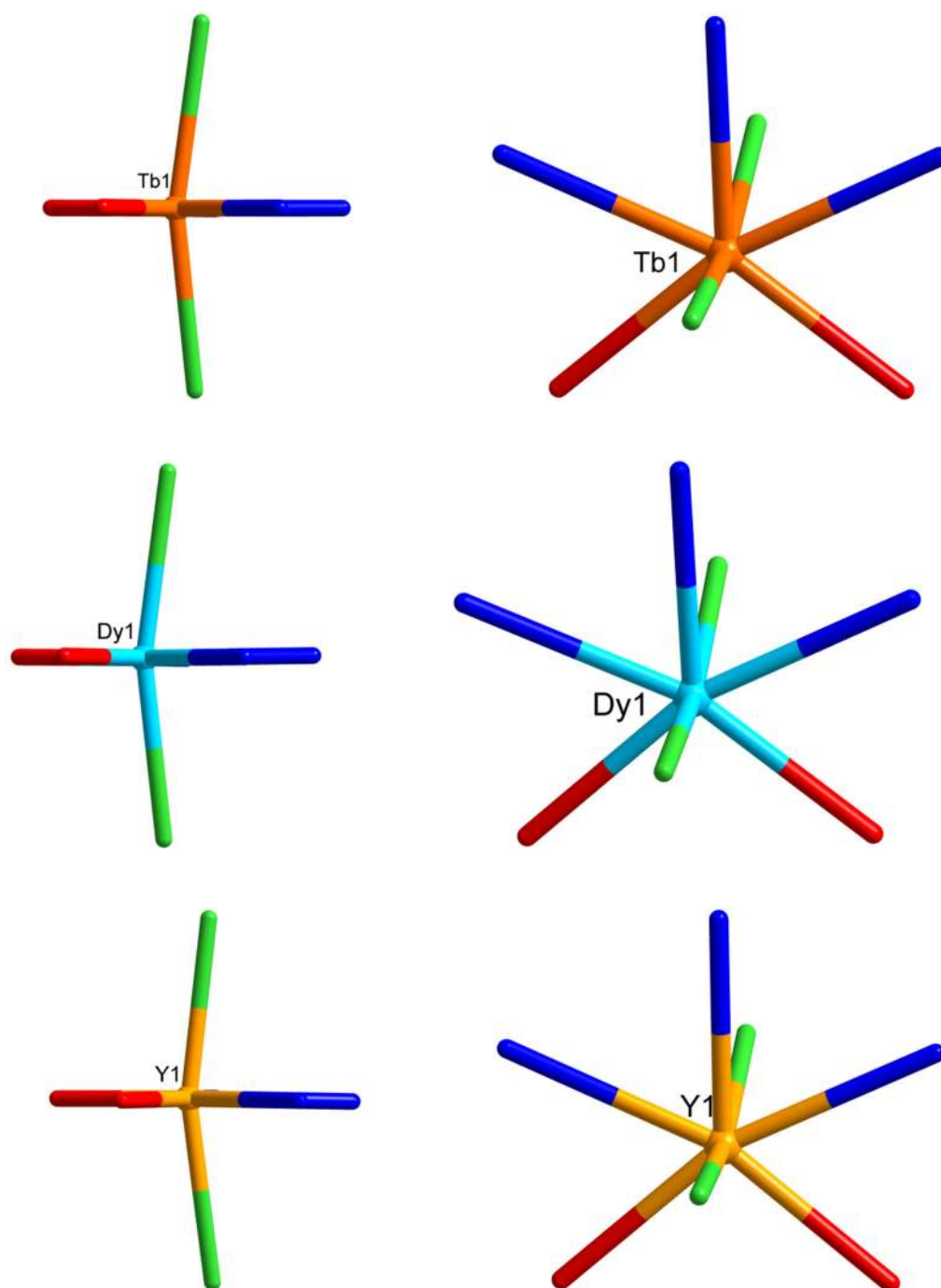
Figure 2.A.8. *Capped-sticks* models of the coordination environments around the Ln ions in the single crystal X-ray structures of **2.A.1** (Ln = Tb, *top*), **2.A.2** (Ln = Dy, *middle*) and **2.A.3** (Ln = $Y_{0.94}Dy_{0.06}$, *bottom*) depicting the coplanarity of the equatorial planes (side view: *left-hand side* and top view: *right-hand side*). Colour codes: N = blue; O = red; green = Cl; Tb = bronze; Dy = cyan and $Y_{0.94}Dy_{0.06}$ = brass.
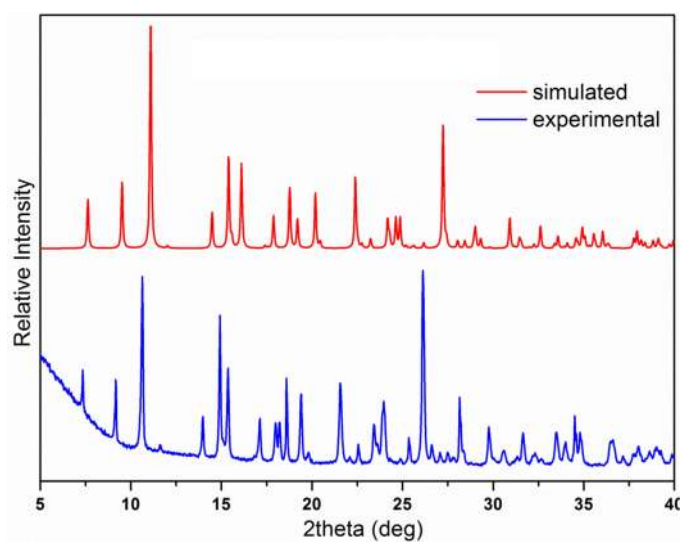
Figure 2.A.9. Calculated (red) and experimental (blue) pXRD patterns of complex **2.A.3**.
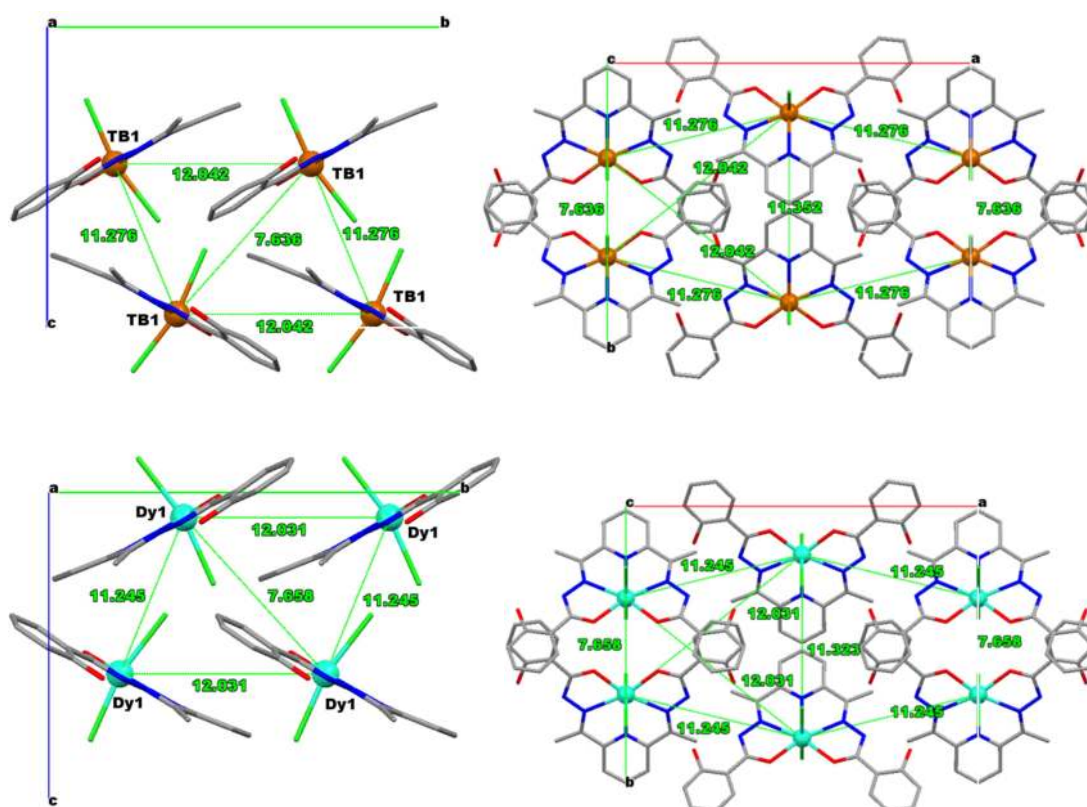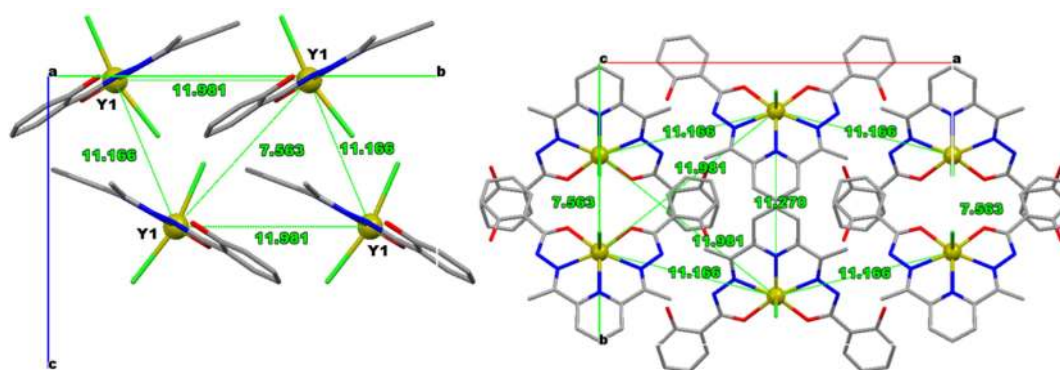
Figure 2.A.10. Unit cell contents in the solid state packing of the complexes viewed along crystallographic ***a*** (*left-hand side*) and ***c*** (*right-hand side*) axes. The inter Ln···Ln distances of the neighbor molecules are highlighted (values are in Å unit). The Et$_3$NH counter cations and H atoms are omitted for clarity. Colour codes: C = light gray; N = blue; O = red; Cl = green; Tb = bronze; Dy = cyan and Y$_{0.94}$Dy$_{0.06}$ = brass.

2.A.3.3 Magnetic properties. The temperature dependent magnetic susceptibilities of **2.A.1**-**2.A.2** were studied in the temperature range 2-300 K and are presented as $\chi_M T$ vs T plots in Figure 2.A.11. The measured room temperature (300 K) $\chi_M T$ values (12.2 (**2.A.1**) and 14.5 (**2.A.2**) cm^3 mol^{-1} K) are in good agreement with the expected values 11.82 (with $S = 3$, $g_J = 3/2$ for Tb^{III} in **2.A.1**) and 14.17 (with $S = 5/2$, $g_J = 4/3$ for Dy^{III} in **2.A.2**) cm^3 mol^{-1} K) for one magnetically isolated Ln^{III} ion. On cooling, the $\chi_M T$ values remain more or less same well up to ~150 K, followed by a rapid decrease upon further cooling (Figure 2.A.11). Such decrease can be ascribed to the depopulation of the Starks sublevels (crystal-field effect) of the anisotropic Ln^{III} ions.
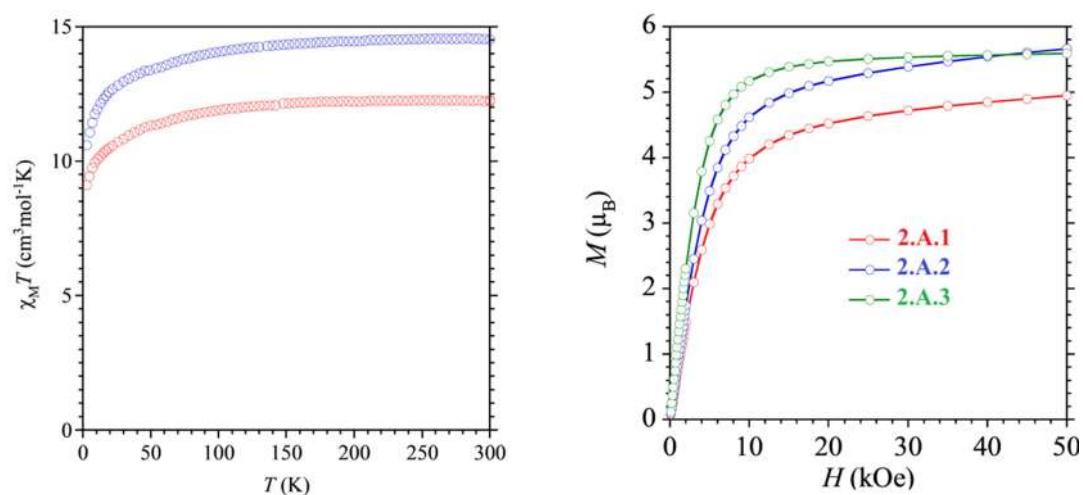
Figure 2.A.11. (*left*) Temperature dependent magnetic susceptibilities (open circles) of **2.A.1** (red) and **2.A.2** (blue). (*right*) Field dependent magnetizations (open circles) of **2.A.1** (red), **2.A.2** (blue), and **2.A.3** (green) at 2 K within the field range of 0-5 T. The solid lines are eye-guides only.

The field dependent magnetizations for **2.A.1**-**2.A.3** have been recorded in the field range of 0-5 T (Figure 2.A.11 and Figure 2.A.12). At low temperature (2 K) and high field (5 T), the magnetization values are observed to be 5 (**2.A.1**) and 5.6 (**2.A.2** and **2.A.3**) μ_B, which agree well with the generally observed values for magnetically exchange-free Ln^{III} ions (Tb^{III} in **2.A.1**, and Dy^{III} in **2.A.2** and **2.A.3**). Notably, the magnetization values rise steeply upon increasing the field at lower field regions and start to attenuate within the field range of 0.1-0.2 T in the temperature range 2-5 K (Figure 2.A.12).
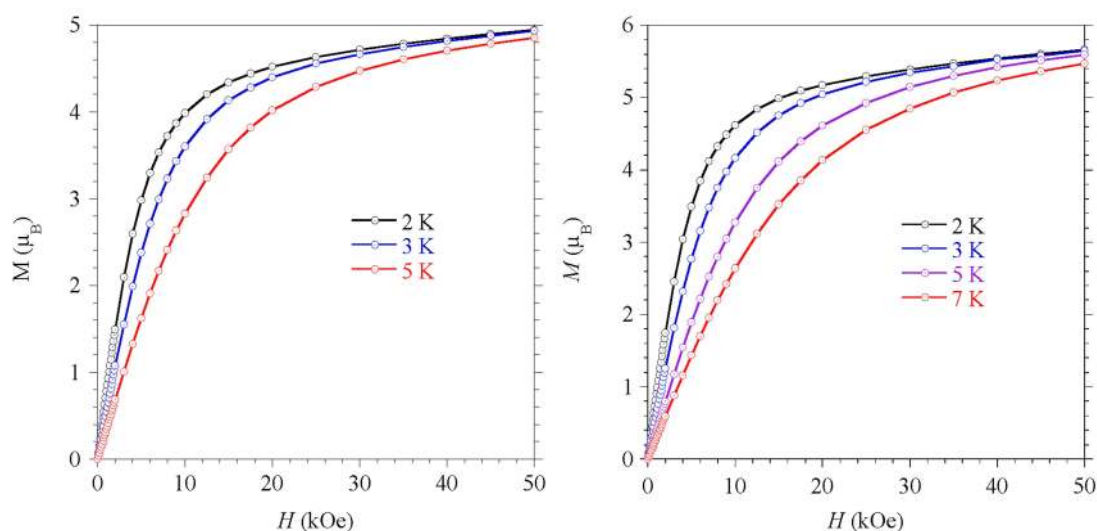
Figure 2.A.12. Field dependence of the magnetization (open circles), *M* vs *H*, for **2.A.1** (*left*) and **2.A.2** (*right*). The solid lines are eye-guides only.

The direction of the magnetic anisotropy axis of Dy^{III} ion in **2.A.2** was calculated by the MAGELLAN software (Figure 2.A.13).[15] The results show that the anisotropy axis of the Dy^{III} ion passes close to the Cl–Dy–Cl bonds and it is perpendicular to the pentagonal plane of the chelating ligand. The deviation angle of Cl–Dy–Cl bonds from the anisotropy axis is ~7.192°.
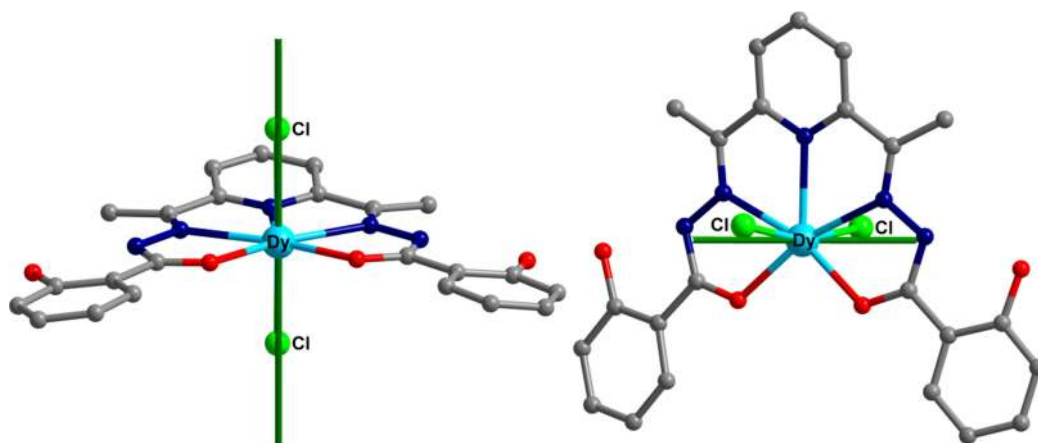
Figure 2.A.13. Quantitative calculation of the anisotropic axis orientation of **2.A.2** (solid green lines) using the electrostatic Chilton's method. *Left*: side view and *Right*: top view.

To probe the slow relaxation of the magnetization, dynamic (ac) magnetic susceptibility studies were carried out in the temperature range 2-25 K, in the absence and presence of applied static fields. No out-of-phase ac susceptibility (χ''_M) was detected for the Tb^{III} analogue (**2.A.1**) (Figure 2.A.14). On the other hand, a distinct maximum in χ''_M vs T plot was observed at around 14 K for the Dy^{III} analogue (**2.A.2**) in zero field (Figure 2.A.14) with an additional prominent feature found at lower temperatures. This latter contribution was drastically reduced upon application of a dc field.
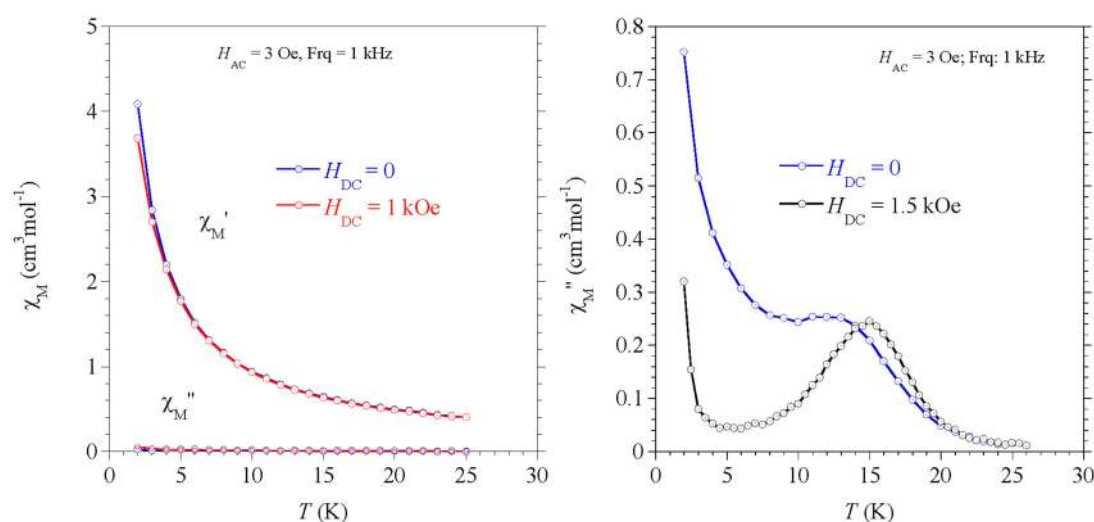
Figure 2.A.14. Temperature dependence of the ac susceptibility (with 3 Oe ac field and 1 kHz frequency) for **2.A.1** (*left*) and **2.A.2** (*right*) within the temperature range 2-25 K in zero field and with applied dc field. The solid lines are eye-guides only.

The detailed ac magnetic susceptibility study carried out for **2.A.2** with an applied dc field of 1.5 kOe yielded well-defined χ''_M maxima spanning over 7-16 K within the frequency domain 25-1500 Hz (Figure 2.A.15). Analysis of the Cole-Cole plots between 7.5 and 16 K revealed a narrow width of the distribution of the relaxation time, suggesting a single relaxation process operative for **2.A.2** within this temperature range (Figure 2.A.16 and Table 2.A.4 for the α values). But upon moving

further towards lower temperatures, the α values rapidly increased. Such low temperature behavior is indicative of additional fast relaxation mechanisms that are likely to result from dipolar interactions between the paramagnetic centers and hyperfine interactions.[9b]
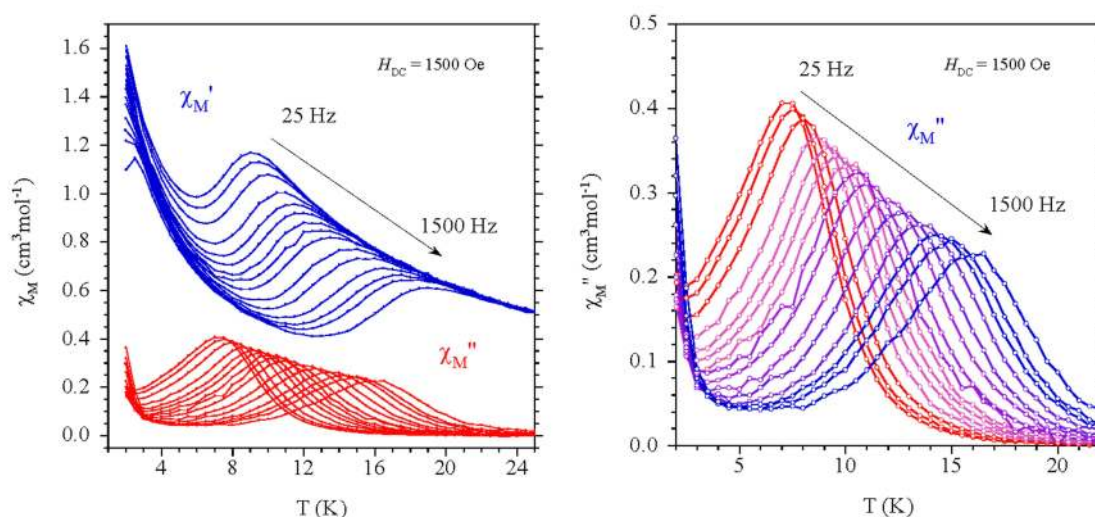
Figure 2.A.15. Variable frequency (25-1500 Hz) temperature-dependent ac magnetic susceptibilities (open circles) within the temperature range 2-25 K for **2.A.2** at 1.5 kOe dc and 3 Oe ac fields. The solid lines are eye-guides only.
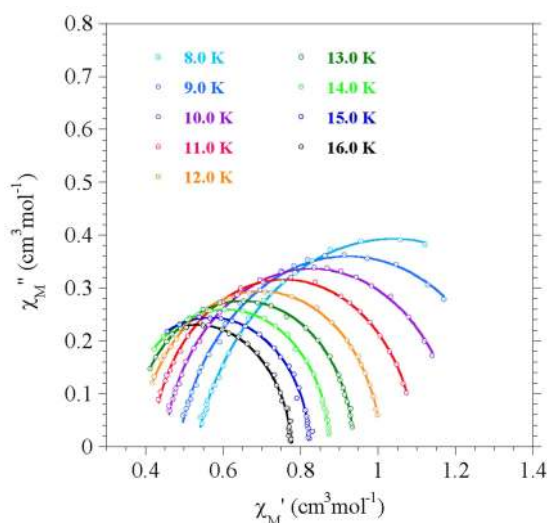
Figure 2.A.16. Cole-Cole plots for **2.A.2** showing experimental (circles) and best fit (solid lines). The best fit parameters are tabulated in Table 2.A.4.

Table 2.A.4. The best fit parameters deduced from Cole-Cole plots for **2.A.2**.

T	χ_T	χ_S	α
7.5	1.64 (3)	0.563 (3)	0.17 (1)
8.0	1.54 (2)	0.530(10)	0.161(8)
8.5	1.42(1)	0.514(3)	0.11(1)
9.0	1.358(9)	0.485(1)	0.122(8)
9.5	1.275(5)	0.466(1)	0.093(6)
10.0	1.210(4)	0.447(1)	0.080(6)
10.5	1.150(2)	0.433(1)	0.057(5)
11.0	1.098(1)	0.416(1)	0.048(4)
11.5	1.054(1)	0.369(3)	0.046(5)
12.0	1.0078(7)	0.386(1)	0.035(3)
12.5	0.973(1)	0.369(3)	0.038(8)
13.0	0.9377(8)	0.363(3)	0.0268(6)
13.5	0.9053(4)	0.350(2)	0.024(4)
14.0	0.8756(4)	0.338(3)	0.022(4)
14.5	0.8498(8)	0.329(8)	0.02(1)
15.0	0.825(2)	0.30(1)	0.03(1)
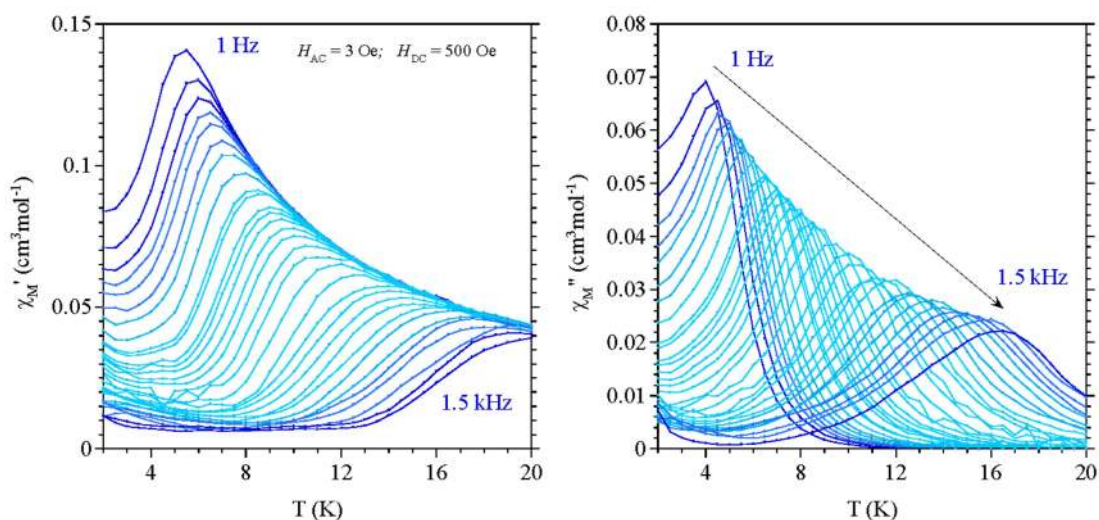
Figure 2.A.17. Temperature dependence of the magnetic ac susceptibility (χ'_M, left; χ''_M, right) for different frequencies (1-1500 Hz) within the temperature range 2-20 K for **2.A.3** at 500 Oe dc and 3 Oe ac fields. The solid lines are eye-guides only.

To reduce such contributions and confirm the molecular origin of the slow magnetization dynamics of Dy^{III} ion in this pentagonal bipyramid coordination environment, we have considered the Y^{III} analogue with 6% Dy^{III} site populations, $(Et_3NH)[(H_2L)Y_{0.94}Dy_{0.06}Cl_2]$ (**2.A.3**), in which the Y^{III} and Dy^{III} centers have the same coordination environment as for **2.A.2**. Field dependent magnetization study for **2.A.3** at 2 K (Figure 2.A.11) confirmed the relative Dy atom population and revealed a sharper increase of the magnetization for low fields as compared to **2.A.2**. Ac magnetic susceptibility studies were carried out under H_{dc} = 500 Oe to suppress a small tail in χ''_M appearing below 3 K. The χ''_M vs T plots for different frequencies (1-1500 Hz) lead to well-defined maxima in the temperature range 4-17 K (Figure 2.A.17). Analysis of the Cole-Cole plots for **2.A.3** yielded small α values between 4.5-15.5 K (Figure 2.A.18 and Table 2.A.5), in agreement with a single relaxation mechanism within this temperature window.
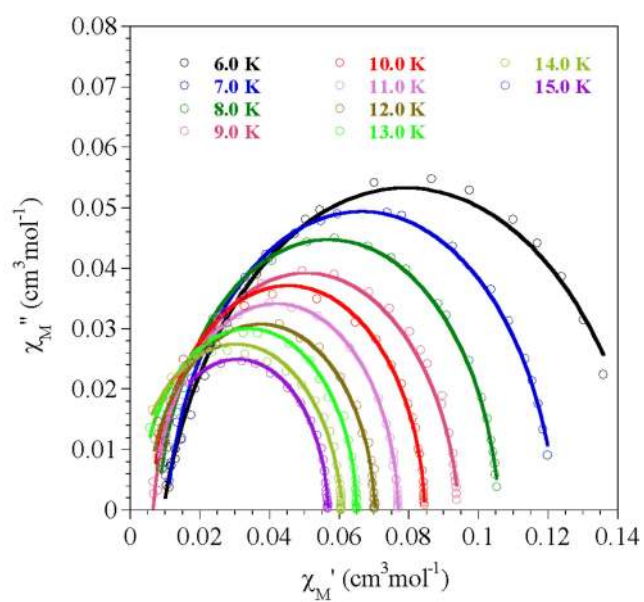
Figure 2.A.18. Cole-Cole plots for **2.A.3** showing experimental (circles) and best fit (solid lines). The best fit parameters are tabulated in Table 2.A.5.

Table 2.A.5. The best fit parameters deduced from Cole-Cole plots for **2.A.5**.

T	χ_T	χ_S	α
4	0.233	0.011	0.31
5.0	0.193	0.010	0.25
5.5	0.162	0.0126	0.17
6.0	0.149	0.0094	0.16
6.5	0.134	0.010	0.12
7.0	0.1222	0.010	0.08
7.5	0.1136	0.0074	0.08
8.0	0.1059	0.0080	0.06
8.5	0.1001	0.0076	0.05
9.0	0.0944	0.0065	0.07
9.5	0.0890	0.0066	0.03
10.0	0.08456	0.0062	0.03

10.5	0.08061	0.0042	0.04
11.0	0.07690	0.0069	0.016
11.5	0.07363	0.0072	0.016
12.0	0.07037	0.0047	0.04
12.5	0.0676	0.00035	0.026
13.0	0.0650	0.0027	0.023
13.5	0.0629	0.0004	0.07
14.0	0.0608	0.0002	0.07
14.5	0.0585	0.0048	0.015
15.0	0.0568	0.0048	0.02
15.5	0.0545	0.0023	0.016

The relaxation times for temperatures between 4 and 16 K were obtained by modeling the respective frequency dependence of χ''_M with the extended Debye model; results are plotted as τ vs $1/T$ in Figure 2.A.19 together with the relaxation times obtained for **2.A.2** (with applied field). Both sets of data match well with each other confirming the molecular origin of the relaxation behavior. They exhibit a linear variation above 10 K likely to result from a thermally activated relaxation process. The analysis of the linear variation for **2.A.3** with the Arrhenius law, $\tau = \tau_0 \exp(U_{eff}/k_B T)$, gave $U_{eff}/k_B = 70$ K with $\tau_0 = 1.9 \times 10^{-6}$ s.
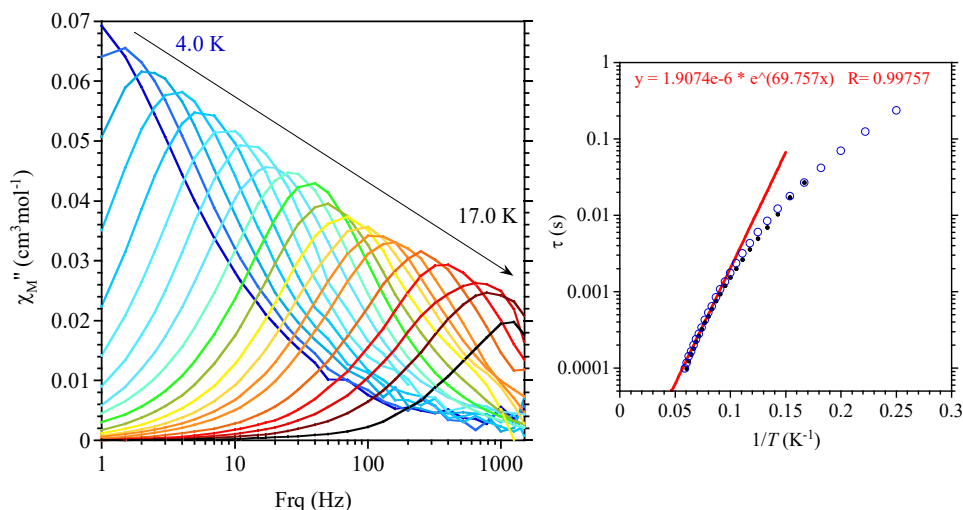
Figure 2.A.19. *Left:* Frequency dependence of the out-of-phase magnetic susceptibility (χ''_M) for **2.A.3** at different temperatures between 4 and 17 K under H_{dc} = 500 Oe (solid lines are eye-guides only). *Right*: semi-logarithmic plot of the relaxation time as the function of inverse temperature for **2.A.1** (dots) and **2.A.3** (open circles); the red line is the best fit of the exponential equation to the linear variation found between 10 and 16 K.

Attempts to simulate $\tau = f(T)$ throughout 2-17 K region considering concomitant contributions of an Orbach and a Raman process, or Raman and direct processes lead to poor fitting for the low temperature part even when possible relaxation by QTM was considered (Figure 2.A.20). But contribution of such an alternative process cannot be discarded. These results clearly support the occurrence of a slow relaxation of the magnetization for the Dy^{III} derivative.
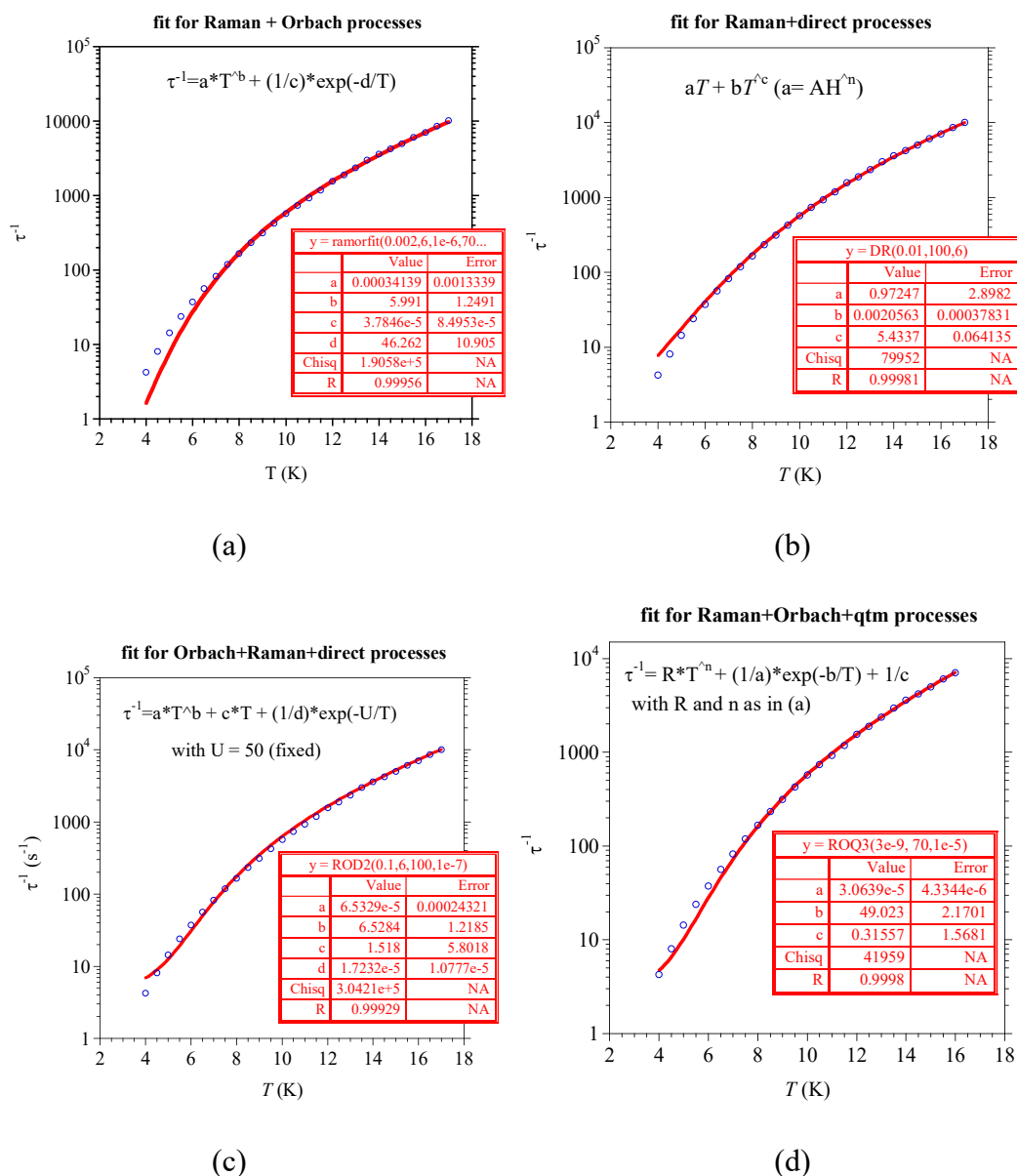
Figure 2.A.20. The temperature dependence of the relaxation time constants (τ; open circles) for **2.A.3** within the temperature 4-17 K. The solid lines are the attempted best fits to $\tau = f(T)$ considering simultaneous contributions of (a) Orbach and a Raman process, (b) Raman and direct processes, or (c) Orbach, Raman and direct processes. Addition of a contribution from QTM did not improve the fits for the lower temperatures (see the plot d).

2.A.4 CONCLUSIONS

In conclusion, Ln[III] complexes with pentagonal bipyramid coordination geometry were readily obtained using the pentadentate 2,6-diacetylpyridine *bis*-salicylhydrazone ligand, thus making controlled access to such hepta-coordinated species straightforward. The non-coordinating phenol groups of the pentadentate ligand used here stabilizes the molecular complexes through intramolecular H-bonding interactions. Moreover, due to the presence of these bulky peripheral groups, the Ln[III] centers are mutually far apart in solid state. Consequently, the observed slow magnetization dynamics are purely of molecular origin. With simple chloride ligands in the apical positions, the Dy[III] analogue exhibits single-ion magnet behavior. The lower effective energy barrier for magnetization reversal compared to a few reported pentagonal bipyramid Dy[III]-based SIMs[9] most certainly stems from weaker axial CF and stronger equatorial CF in **2.A.2.** Interestingly, mass spectrometric analysis indicates stability of the equatorial coordination environments and lability of the axial coordination sites. Therefore, the axial ligand fields could be chemically tuned without changing CF symmetry around the Ln[III] ions. This also provides an excellent opportunity to use these complexes, especially the Dy[III] analogues, as robust magnetic building-blocks towards the construction of multi-metallic high-performance SMMs. Further chemical modifications in these complexes were achieved via ligand substitution at the axial sites and will be discussed in the second part of this chapter.

2.A.5 REFERENCES

1 (a) F. Troiani and M. Affronte, *Chem. Soc. Rev.*, 2011, **40**, 3119-3129; (b) P. C. E. Stamp and A. Gaita-Arino, *J. Mater. Chem.*, 2009, **19**, 1718-1730; (c) A. Ardavan and

S. J. Blundell, *J. Mater. Chem.*, 2009, **19**, 1754-1760; (d) M. Affronte, *J. Mater. Chem.*, 2009, **19**, 1731-1737.

2 N. Ishikawa, M. Sugita, T. Ishikawa, S. Y. Koshihara and Y. Kaizu, *J. Am. Chem. Soc.*, 2003, **125**, 8694-8695.

3 (a) J. D. Rinehart and J. R. Long, *Chem. Sci.*, 2011, **2**, 2078-2085; (b) L. Sorace, C. Benelli and D. Gatteschi, *Chem. Soc. Rev.*, 2011, **40**, 3092-3104; (c) D. N. Woodruff, R. E. Winpenny and R. A. Layfield, *Chem. Rev.*, 2013, **113**, 5110-5148; (d) P. Zhang, Y.-N. Guo and J. Tang, *Coord. Chem. Rev.*, 2013, **257**, 1728-1763; (e) H. L. C. Feltham and S. Brooker, *Coord. Chem. Rev.*, 2014, **276**, 1-33; (f) R. A. Layfield, *Organometallics*, 2014, **33**, 1084-1099; (g) S. T. Liddle and J. van Slageren, *Chem. Soc. Rev.*, 2015, **44**, 6655-6669; (h) K. L. Harriman and M. Murugesu, *Acc. Chem. Res.*, 2016, **49**, 1158-1167; (i) K. Liu, X. Zhang, X. Meng, W. Shi, P. Cheng and A. K. Powell, *Chem. Soc. Rev.*, 2016, **45**, 2423-2439; (j) Y.-S. Meng, S.-D. Jiang, B.-W. Wang and S. Gao, *Acc. Chem. Res.*, 2016, **49**, 2381-2389; (k) Y. N. Guo, G. F. Xu, Y. Guo and J. Tang, *Dalton Trans.*, 2011, **40**, 9953-9963; (l) G. Aromi, D. Aguila, P. Gamez, F. Luis and O. Roubeau, *Chem. Soc. Rev.*, 2012, **41**, 537-546; (m) K. Liu, W. Shi and P. Cheng, *Coord. Chem. Rev.*, 2015, **289-290**, 74-122.

4 (a) C. B. Dante Gatteschi, *Introduction to Molecular Magnetism: From Transition Metals to Lanthanides*, Wiley-VCH, 2015; (b) R. A. Layfield and M. Murugesu, *Lanthanides and Actinides in Molecular Magnetism*, Wiley VCH, 2015.

5 (a) R. Layfield, F.-S. Guo, B. Day, Y.-C. Chen, M.-L. Tong and A. Mansikamäkki, *Angew. Chem. Int. Ed. Engl.*, 2017, **56**; 11445-11449; (b) C. A. P. Goodwin, F. Ortu, D. Reta, N. F. Chilton and D. P. Mills, *Nature*, 2017, **548**, 439-442; (c) N. F. Chilton, C. A. P. Goodwin, D. P. Mills and R. E. P. Winpenny, *Chem. Commun.*, 2015, **51**, 101-103; (d) N. F. Chilton, *Inorg. Chem.*, 2015, **54**, 2097; (e) K. L. M. Harriman, J. L.

Brosmer, L. Ungur, P. L. Diaconescu and M. Murugesu, *J. Am. Chem. Soc.*, 2017, **139** 1420–1423; (f) L. Ungur and L. F. Chibotaru, *Inorg. Chem.*, 2016, **55**, 10043-10056; (g) L. Ungur and L. F. Chibotaru, *Phys. Chem. Chem. Phys.*, 2011, **13**, 20086-20090.

6 (a) J.-C. G. Bünzli, *J. Coord. Chem.*, 2014, **67**, 3706-3733; (b) O. Kahn, *Molecular Magnetism*, Willey VCH, 1993.

7 S.-D. Jiang and S.-X. Qin, *Inorg. Chem. Front.*, 2015, **2**, 613-619.

8 (a) K. S. Pedersen, L. Ungur, M. Sigrist, A. Sundt, M. Schau-Magnussen, V. Vieru, H. Mutka, S. Rols, H. Weihe, O. Waldmann, L. F. Chibotaru, J. Bendix and J. Dreiser, *Chem. Sci.*, 2014, **5**, 1650-1660; (b) Y. S. Meng, Y. Q. Zhang, Z. M. Wang, B. W. Wang and S. Gao, *Chem. Eur. J.*, 2016, **22**, 12724–12731; (c) Y. N. Guo, G. F. Xu, W. Wernsdorfer, L. Ungur, Y. Guo, J. Tang, H. J. Zhang, L. F. Chibotaru and A. K. Powell, *J. Am. Chem. Soc.*, 2011, **133**, 11948-11951; (d) T. Pugh, V. Vieru, L. F. Chibotaru and R. A. Layfield, *Chem. Sci.*, 2016, **7**, 2128-2137.

9 (a) A. K. Bar, N. Gogoi, C. Pichon, V. M. Goli, M. Thlijeni, C. Duhayon, N. Suaud, N. Guihery, A. L. Barra, S. Ramasesha and J. P. Sutter, *Chem. Eur. J.*, 2017, **23**, 4380-4396; (b) A. K. Bar, C. Pichon, N. Gogoi, C. Duhayon, S. Ramasesha and J.-P. Sutter, *Chem. Commun.*, 2015, **51**, 3616-3619; (c) A. K. Bar, C. Pichon and J.-P. Sutter, *Coord. Chem. Rev.*, 2016, **308**, 346-380 and the references therein.

10 (a) J. Liu, Y. C. Chen, J. H. Jia, J. L. Liu, V. Vieru, L. Ungur, L. F. Chibotaru, Y. Lan, W. Wernsdorfer, S. Gao, X. M. Chen and M. L. Tong, *J. Am. Chem. Soc.*, 2016, **138**, 5441-5440; (b) Y.-C. Chen, J.-L. Liu, Y. Lan, Z.-Q. Zhong, A. Mansikkamäki, L. Ungur, Q.-W. Li, J.-H. Jia, L. F. Chibotaru, J.-B. Han, W. Wernsdorfer, X.-M. Chen and M.-L. Tong, *Chem. Eur. J.*, 2017, **23**, 5708-5715; (c) L. Zhang, J. Jung, P. Zhang, M. Guo, L. Zhao, J. Tang and B. Le Guennic, *Chem. Eur. J.*, 2016, **22**, 1392-1398; (d) S. K. Gupta, T. Rajeshkumar, G. Rajaraman and R. Murugavel, *Chem.*

Commun., 2016, **52**, 7168-7171; (e) Y.-S. Ding, N. F. Chilton, R. E. P. Winpenny and Y.-Z. Zheng, *Angew. Chem. Int. Ed. Engl.*, 2016, **55**, 16071-16074; (f) X. C. Huang, M. Zhang, D. Wu, D. Shao, X. H. Zhao, W. Huang and X. Y. Wang, *Dalton Trans.*, 2015, **44**, 20834-20838; (g) J.-L. Liu, Y.-C. Chen, Y.-Z. Zheng, W.-Q. Lin, L. Ungur, W. Wernsdorfer, L. F. Chibotaru and M.-L. Tong, *Chem. Sci.*, 2013, **4**, 3310-3316.

11 (a) C. Pelizzi and G. Pelizzi, *J. Chem. Soc., Dalton Trans.*, 1980, 1970-1973; (b) C. Pelizzi, G. Pelizzi and F. Vitali, *J. Chem. Soc., Dalton Trans.*, 1987, 177-181; (c) A. Bonardi, C. Carini, C. Merlo, C. Pelizzi, G. Pelizzi, P. Tarasconi, F. Vitali and F. Cavatorta, *J. Chem. Soc., Dalton Trans.*, 1990, 2771-2777.

12 (a) L. J. Farrugia, *J. Appl. Cryst..*, 2012, **45**, 849-854; (b) L. J. Farrugia, *J. Appl. Cryst..*, 1999, **32**, 837-838; (c) L. J. Farrugia, *WinGX, version 1.65.04, Department of Chemistry, University of Glasgow, Glasgow, Scotland, 2003*.

13 *International Tables for X-ray Crystallography*, Vol. IV, Kynoch Press, Birmingham, England, 1974.

14 M. C. Llunell, D.; Cirera, J.; Alemany, P.; Alvarez, S., *Shape program, version 2; Universitat de Barcelona: Barcelona, Spain*, 2010.

15 N. F. Chilton, D. Collison, E. J. McInnes, R. E. Winpenny and A. Soncini, *Nat. Chem.*, 2013, **4**, 2551-2557.

Pentagonal Bipyramidal Ln^{III} Complexes Containing Strong-field Axial Ligands: Field-induced SIM Behavior of the Dy^{III} Analogues

ABSTRACT: A series of pentagonal bipyramidal (PBP) Ln^{III} complexes, [(L)Ln^{III}(R$_3$PO)Cl] (Ln = Gd (**2.B.1**), Tb (**2.B.2**), Dy (**2.B.3**), Er (**2.B.5**); R = cyclohexyl and Dy (**2.B.4**); R = phenyl) were prepared by the utilization of a pentadentate chelating ligand (H$_2$L) that provides the basal pentagonal plane. A phosphine oxide ligand and one chloride ligand occupy the axial sites of the pentagonal bipyramid. The molecular structures of these complexes reveal a comparatively strong bonding interaction between the Ln and O atom of phosphine oxide ligand in one of the axial sites. The coordination geometry around the Ln^{III} center was analyzed with the SHAPE programme that revealed a pentagonal bipyramidal geometry. Dynamic magnetization studies revealed that the Dy^{III} analogues are field-induced single-ion magnets with energy barriers, U_{eff}/k_B = 204 K (**2.B.3**) and 241 K (**2.B.4**) respectively.

2.B.1 INTRODUCTION

There has been a significant renaissance in the chemistry of the *rare earth* elements because of their applications in catalysis[1], photophysical properties[2] and in magnetic materials[3]. In recent years lanthanide-[4] and some actinide complexes[5] are finding increasing utility as molecular magnets (single-molecule- and single-ion magnets, SMMs and SIMs). These molecular systems, once magnetized, retain their magnetization even after the removal of the external magnetic field and are characterized by a slow reversal of magnetization below certain temperatures.[6] This is because in SMMs, on application of a magnetic field, a double-well potential

comprising of the various M_J or M_S states with an energy barrier (U_{eff}) is generated which prevents the reversal of magnetization below certain temperatures (the blocking temperature, T_B).[7] Various relaxation mechanisms including quantum tunneling are prevalent to allow the magnetization to be lost.[8]

The evidence of SMM behaviour in a molecular Tb[III] complex, where the Tb is sandwiched by two phthalocyanine ligands, was first reported by Ishikawa and co-workers.[9] One of the intrinsic features of the lanthanide elements is that the 4f electrons are deeply buried inside the [Xe] core and are considerably shielded by the 5s and 5p electrons. This results in an almost unquenched orbital angular momentum (L) which couples with the spin angular momentum (S) giving rise to the total angular momentum, J.[10] Unlike transition metal ions the magnitude of spin-orbit coupling in the case of 4f metal ions is comparatively much larger than the crystal field and which splits the ground $^{2S+1}L_J$ term into different J multiplets. Although the crystal field effects are small, it has significant impact in removing the degeneracy of the ($2J + 1$) M_J microstates corresponding to each of the J multiplets. Since the dynamics of magnetization relies on the relative energies of the ground J manifold therefore a suitable crystal field renders the requirement of large splitting between the energy levels giving rise to high energy barrier for magnetization reversal.[11]

Soon after this discovery many mononuclear Ln[III] complexes were reported to be SMMs with high energy barriers (U_{eff}) and high blocking temperatures (T_B).[12] Among various types of lanthanide complexes, the mononuclear complexes are of considerable interest as they provide a very good understanding on the influence of the ligand field on the observed magnetic properties. A recent report by Layfield and co-workers revealing that the [Dy(Cp^{ttt})$_2$] (Cp^{ttt} = C$_5$H$_2^t$Bu$_3$-1,2,4) complex has the

highest blocking temperature of 80 K has further spurred activity in this area of mononuclear Ln^{III} complexes.[13]

Although ligand fields are much smaller compared to spin-orbit coupling among lanthanide complexes, ironically the former happen to be the most decisive in controlling the performance of SMMs/SIMs. The spatial distribution of the electrons in the different 4f orbitals leads to inherent anisotropic shapes in the Ln^{III} ions (except Gd, Eu La, and Lu). Based on an electrostatic argument Rinehart and Long have proposed a qualitative model that assists in the designing of SMMs/SIMs.[14] According to this theory an axial ligand field stabilizes the oblate-shaped Ln^{III} ions while a prolate-shaped Ln^{III} ion requires an equatorial ligand field because such a ligand field minimizes the electrostatic repulsion between the ligands and the metal center and maximizes the molecular magnetic anisotropy. Using this cue a large number of monometallic Ln^{III} complexes were prepared with interesting magnetic properties.[15] Among them the *pseudo*-linear pentagonal bipyramidal complexes with strong axial ligand field and weak equatorial ligand field stand out as the most effective system for the observation of high energy barriers of magnetization reversal.[16]

We have been utilizing various types of multidentate ligands for the synthesis of mononuclear Ln^{III} complexes. As discussed in Chapter 2.A.1 we have synthesized mononuclear pentagonal bipyramidal Ln^{III} complexes by employing a pentadentate chelating ligand that provides a rigid equatorial plane.[17] The axial sites in these complexes were occupied by the chloride ions which are considerably weak field ligands compared to *N*- and *O*-donors present in the ligand backbone. We have thoroughly studied the magnetic properties of the Dy^{III}, Tb^{III} and the diluted Dy^{III} (in an isostructural Y^{III} host) complexes which reveal the molecular origin of slow

magnetic relaxation in the Dy^{III} derivative with an energy barrier of magnetization reversal of 70 K.[17] To understand the role of the axial ligands in this system, we have now prepared a series of neutral mononuclear PBP complexes, $[(L)Ln^{III}(R_3PO)Cl]$ (Ln = Gd (**2.B.1**), Tb (**2.B.2**), Dy (**2.B.3**), Er (**2.B.5**); R = cyclohexyl and Ln = Dy (**2.B.4**); R = phenyl) where one phosphine oxide ligand replaces one of the two chloride ligands in the axial sites. Herein, we report the synthesis, structural characterization and magnetic properties of **2.B.1-2.B.5**.

2.B.2 EXPERIMENTAL SECTION

2.B.2.1 Materials and Methods. All the common reagents and solvents used for the syntheses were used as received from commercial sources. The organic ligand 2,6-diacetylpyridine was obtained from the TCI Chemicals (India) Pvt. Ltd. Hydrated lanthanide chlorides were obtained from the Sigma Aldrich Chemicals co. (India). Benzoic acid hydrazide and NEt_3 were obtained from the Spectrochem Pvt. Ltd. (India). The organic ligand 2,6-diacetylpyridine *bis*-benzoylhydrazone (H_2L) was synthesized following a reported procedure.[18]

2.B.2.2 Instrumentation. Fourier transform infrared (FT-IR) spectroscopy was performed with a Bruker FT-IR spectrometer. Elemental analyses of the compounds were obtained from a Euro Vector EA instrument (CHNS-O, Model EuroEA3000). Powder X-ray diffraction study was performed on finely ground polycrystalline material with Bruker D8 Advance Powder X-ray diffractometer.

2.B.2.3 Magnetic Measurements. Magnetic measurements for all the samples were carried out with a Quantum Design MPMS 5S SQUID magnetometer in the temperature range 2-300 K. The measurements were performed on polycrystalline samples. The crystalline powders of the complexes were mixed with grease (except

for Gd derivative) and put in gelatin capsules. The temperature dependences of the magnetization were measured in an applied field of 1 kOe and the isothermal field dependence of the magnetizations were collected up to 5 T. The molar susceptibility (χ_M) was corrected for sample holder, grease and for the diamagnetic contribution of all the atoms by using Pascal's tables. Ac susceptibility has been collected in zero field and with applied fields in the frequency range 1-1500 Hz.

2.B.2.4 X-ray Crystallography. The single crystal X-ray diffraction data of **2.B.1-2.B.5** were collected on a Rigaku Xtal LAB X-ray diffractometer system equipped with a CCD area detector and operated at 30 W power (50 kV, 0.6 mA) to generate MoKα radiation (λ = 0.71073 Å) at 120(2) K. Data were integrated using CrysAlis[Pro] software with a narrow frame algorithm.[19] Data were subsequently corrected for absorption by the program SCALE3 ABSPACK scaling algorithm.[19] All the structures were solved by the direct methods in ShelXT[20] and refined by the full-matrix least-squares method on F^2 (ShelXL-2014)[21] using the Olex-2 software.[22] All the non-hydrogen atoms were refined with anisotropic thermal parameters. All the hydrogen atoms were included in idealized positions and a riding model was used. All the mean plane analyses and crystallographic figures have been generated using the DIAMOND software (version 3.2k).[23] The crystal data and refinement parameters for **2.B.1-2.B.5** are summarized in Table 2.B.1 and Table 2.B.2.

Table 2.B.1. Crystallographic data and refinement parameters of **2.B.1-2.B.3**.

	2.B.1	2.B.2	2.B.3
Empirical formula	$C_{41}H_{52}Cl_1Gd_1N_5O_3P_1$	$C_{84}H_{116}Cl_2N_{12}O_8P_2Tb_2$	$C_{90}H_{124}Cl_2Dy_2N_{10}O_8P_2$
M_w (g/mol)	886.54	1872.56	1931.82
Temperature (K)	120.00(10)	120.00(10)	120(2)K
Crystal system	monoclinic	triclinic	Monoclinic
Space group	$P21/n$	P-1	$P21/c$
Unit cell lengths	a = 20.1164(5)	a = 10.0872(3)	a = 18.6952(5)

(Å)	b = 9.6283(2)	b = 18.3148(5)	b = 9.9898(3)
	c = 22.3601(6)	c = 23.4884(6)	c = 24.5545(7)
Unit cell angles (°)	$\beta = 113.594(3)$	$\alpha = 84.704(2)$ $\beta = 89.758(2)$ $\gamma = 83.504(2)$	$\beta = 91.430(2)$
Volume (Å^3)	3968.81(19)	4293.0(2)	4584.4(2)
Z	4	2	2
ρ_{cal} (g/cm^3)	1.484	1.449	1.399
Absorption coefficient (mm^{-1})	1.823	1.794	1.769 mm^{-1}
F(000)	1812.0	1924.0	1988.0
Crystal size (mm^3)	0.17 × 0.14 × 0.1	0.18 × 0.14 × 0.07	0.3 × 0.08 × 0.01
2θ range	5.5 to 58.818	5.244 to 49.998	5.412 to 57.664°
Reflections collected	62624	91078	53867
Index ranges	$-27 \leq h \leq 24$, $-11 \leq k \leq 12$, $-30 \leq l \leq 27$	$-11 \leq h \leq 11$, $-21 \leq k \leq 21$, $-27 \leq l \leq 27$	$-24 \leq h \leq 23$, $-13 \leq k \leq 8$, $-33 \leq l \leq 30$
Independent reflections	9730 [$R_{int} = 0.0382$]	15077 [$R_{int} = 0.0576$]	10841 [$R_{int} = 0.0587$]
Data/Restrain/Parameter	9730/0/471	15077/0/999	10841/0/518
GOF on F^2	1.031	1.159	1.040
Final R indices [I>2sigma(I)]	$R_1 = 0.0228$, $wR_2 = 0.0448$	$R_1 = 0.0492$, $wR_2 = 0.1197$	$R_1 = 0.0346$, $wR_2 = 0.0644$
R indices (all data)	$R_1 = 0.0289$, $wR_2 = 0.0465$	$R_1 = 0.0549$, $wR_2 = 0.1223$	$R_1 = 0.0571$, $wR_2 = 0.0704$

$R_1 = \sum |F_0 - F_c| / \sum F_0; \; wR_2 = \sum [w(F_0^2 - F_0^2)]^2 / [w(F_0^2)^2]^{\frac{1}{2}}$

Table 2.B.2. Crystallographic data and refinement parameters of **2.B.4** and **2.B.5**.

	2.B.4	2.B.5
Empirical formula	$C_{41}H_{34}Cl_1Dy_1N_5O_3P_1$	$C_{86}H_{116}Cl_2Er_2N_{10}O_8P_2$
M$_w$ (g/mol)	873.65	1885.24
Temperature (K)	120(2)	120.00(10)
Crystal system	triclinic	monoclinic
Space group	P-1	$P21/n$
Unit cell lengths (Å)	a = 8.8046(2) b = 11.5978(2) c = 18.9669(3)	a = 23.5494(8) b = 10.0618(3) c = 36.0847(11)
Unit cell angles (°)	$\alpha = 93.4930(10)$ $\beta = 101.8670(10)$ $\gamma = 103.418(2)$	$\beta = 94.409(3)$

Volume (Å^3)	1831.60(6)	8524.9(5)
Z	2	8
ρ_{cal} (gcm^{-3})	1.584	1.469
Absorption coefficient	2.203	2.116
F(000)	874.0	3864.0
Crystal size	0.34 × 0.11 × 0.09	0.21 × 0.12 × 0.09
2θ range	4.884 to 58.042	4.892 to 58.068
Reflections collected	27626	96210
Index ranges	-11 ≤ h ≤ 9, -15 ≤ k ≤ 15, -24 ≤ l ≤ 24	-30 ≤ h ≤ 32, -13 ≤ k ≤ 13, -45 ≤ l ≤ 44
Independent reflections	8459 [R_{int} = 0.0448]	19876 [R_{int} = 0.0840]
Data/Restrain/Parameter	8459/0/471	19876/0/999
GOF on F^2	1.055	1.026
Final R indices [I>2sigma(I)]	R_1 = 0.0293, wR_2 = 0.0648	R_1 = 0.0470, wR_2 = 0.0936
R indices (all data)	R_1 = 0.0348, wR_2 = 0.0668	R_1 = 0.0898, wR_2 = 0.1079
$R_1 = \sum |F_0 - F_c| / \sum F_0$; $wR_2 = \sum [w(F_0^2 - F_0^2)]^2 / [w(F_0^2)^2]^{\frac{1}{2}}$		

2.B.2.5 Synthesis of Complexes. The following general protocol was employed for the synthesis of complexes **2.B.1-2.B.5**.

The organic ligand, H_2L (1 eq.) was suspended in 30 mL of EtOH and cyclohexyl/phenyl phosphine oxide (1 eq.) was added to it. To this white cloudy solution, the respective $LnCl_3 \cdot 6H_2O$ (1 eq.) salts were added which results in a yellow solution. The reaction mixture was then heated under reflux conditions for 1 h and allowed to cool to room temperature. To this solution 2 eq. of NEt_3 was added and the solution further stirred at room temperature for 10 minutes. The solvent was evaporated to dryness and the resulting yellow precipitate was washed with diethyl ether. The dried yellow precipitate was then dissolved in 10 mL of EtOH and filtered. The filtrate was kept under vapor diffusion with diethyl ether to afford needle-shaped crystals suitable for X-ray crystallography after one week. The stoichiometry of the

reactants involved in each reaction, yield of the products, and their characterization data are provided below:

[(L)Gd(Cy$_3$PO)Cl] (**2.B.1**). H$_2$L (0.040 g, 0.100 mmol), GdCl$_3$·6H$_2$O (0.037 g, 0.100 mmol), Cy$_3$PO (0.030 g, 0.100 mmol), and Et$_3$N (28 μL, 0.200 mmol) were used. Yield: 0.053 g, 60% (based on Gd). M.P.: >250 °C. IR (KBr v/cm^{-1}): 3439(br), 3062(w), 2929(s), 2852(m), 1632(w), 1587(m), 1552(m), 1503(s), 1446(m), 1411(m), 1371(s), 1324(m), 1297(m), 1258(w), 1197(w), 1169(m), 1148(m), 1103(s), 1069(w), 1040(s), 987(w), 895(m), 854(w), 809(m), 744(m), 716(s), 679(s), 650(w), 534(m).Anal. Calcd for C$_{41}$H$_{54}$ClN$_5$O$_3$PGd (888.57): C, 55.42; H, 6.13; N, 7.88. Found: C, 55.21; H, 6.36; N, 7.61.

[(L)Tb(Cy$_3$PO)Cl] (**2.B.2**). H$_2$L (0.040 g, 0.100 mmol), TbCl$_3$·6H$_2$O (0.037 g, 0.100 mmol), Cy$_3$PO (0.030 g, 0.100 mmol), and Et$_3$N (28 μL, 0.200 mmol) were used. Yield: 0.059 g, 67% (based on Tb). M.P.: >250 °C. IR (KBr v/cm^{-1}): 3441(br), 3064(w), 2927(s), 2854(m), 1634(w), 1587(m), 1552(m), 1505(s), 1446(m), 1409(m), 1368(s), 1326(m), 1299(m), 1256(w), 1197(w), 1169(m), 1148(m), 1105(s), 1067(w), 1040(s), 987(w), 897(m), 856(w), 809(m), 744(m), 714(s), 679(s), 652(w), 532(m). Anal. Calcd for C$_{41}$H$_{54}$ClN$_5$O$_3$PTb (890.25): C, 55.31; H, 6.11; N, 7.87. Found: C, 55.02; H, 6.56; N, 7.75.

[(L)Dy(Cy$_3$PO)Cl] (**2.B.3**). H$_2$L (0.040 g, 0.100 mmol), DyCl$_3$·6H$_2$O (0.038 g, 0.100 mmol), Cy$_3$PO (0.030 g, 0.100 mmol), and Et$_3$N (28 μL, 0.200 mmol) were used. Yield: 0.061 g, 69% (based on Dy). M.P.: >250 °C. IR (KBr v/cm^{-1}): 3443(br), 3064(w), 2929(s), 2852(m), 1630(w), 1587(m), 1554(m), 1505(s), 1446(m), 1411(m), 1368(s), 1326(m), 1299(m), 1258(w), 1197(w), 1171(m), 1150(m), 1105(s), 1067(w), 1042(s), 989(w), 897(m), 854(w), 809(m), 744(m), 714(s), 679(s), 650(w), 532(m).

Anal. Calcd for $C_{41}H_{54}ClN_5O_3PDy$ (893.82): C, 55.09; H, 6.09; N, 7.84. Found: C, 54.85; H, 6.39; N, 7.71.

[(L)Y$_{0.88}$Dy$_{0.12}$(Cy$_3$PO)Cl] (**2.B.3'**). H_2L (0.040 g, 0.100 mmol), $DyCl_3 \cdot 6H_2O$ (0.005 g, 0.012 mmol), $YCl_3 \cdot 6H_2O$ (0.0267 g, 0.088 mmol), Cy_3PO (0.030 g, 0.100 mmol), and Et_3N (28 μL, 0.200 mmol) were used. Yield: 0.048 g, 68% (based on Y). Anal. Calcd for $C_{41}H_{54}Cl_1N_5O_3P_1Y_{0.88}Dy_{0.12}$: C, 60.04; H, 6.64; N, 8.54. Found: C, 59.91; H, 6.52; N, 8.39.

[(L)Dy(Ph$_3$PO)Cl] (**2.B.4**). H_2L (0.040 g, 0.100 mmol), $DyCl_3 \cdot 6H_2O$ (0.038 g, 0.100 mmol), Ph_3PO (0.028 g, 0.100 mmol), and Et_3N (28 μL, 0.200 mmol) were used. Yield: 0.064 g, 72% (based on Dy). M.P.: >250 °C. IR (KBr ν/cm^{-1}): 3429(br), 3054(w), 2919(s), 1632(w), 1587(m), 1552(m), 1499(m), 1438(m), 1409(m), 1366(s), 1325(m), 1297(m), 1258(w), 1160(w), 1122(m), 1093(m), 1067(s), 1044(w), 989(w), 897(m), 809(m), 744(m), 714(s), 691(m), 650(w), 540(m). Anal. Calcd for $C_{41}H_{54}ClN_5O_3PDy$ (893.82): C, 55.09; H, 6.09; N, 7.84. Found: C, 54.85; H, 6.39; N, 7.71.

[(L)Er(Cy$_3$PO)Cl] (**2.B.5**). H_2L (0.040 g, 0.100 mmol), $ErCl_3 \cdot 6H_2O$ (0.038 g, 0.100 mmol), Cy_3PO (0.030 g, 0.100 mmol), and Et_3N (28 μL, 0.200 mmol) were used. Yield: 0.065 g, 73% (based on Er). M.P.: >250 IR (KBr ν/cm^{-1}): 3447(br), 3068(w), 2929(s), 2852(m), 1636(w), 1587(m), 1554(m), 1505(s), 1446(m), 1413(m), 1366(s), 1326(m), 1299(m), 1260(w), 1199(w), 1169(m), 1152(m), 1107(s), 1067(w), 1044(s), 989(w), 897(m), 854(w), 809(m), 746(m), 714(s), 679(s), 650(w), 534(m). Anal. Calcd for $C_{41}H_{54}ClN_5O_3PEr$ (898.58): C, 54.80; H, 6.06; N, 7.79. Found: C, 54.65; H, 6.33; N, 7.53.

2.B.3 RESULTS AND DISCUSSION

2.B.3.1 Synthetic Aspects. The PBP geometry is regarded as one of the most promising coordination geometry around the Ln^{III} center that can bring axiality in the ground state of Ln^{III} ions provided the axial sites are occupied by comparatively strong donor ligands. In the previous chapter we have shown the synthesis of mononuclear pentagonal bipyramidal Ln^{III} complexes using a pentadentate chelating ligand which effectively provides a rigid equatorial plane. In those complexes, the two axial sites were occupied by Cl^- ligands which can be regarded as weak field ligands compared to the N- and O-donor atoms of the pentadentate chelating ligand. Theoretical studies accompanied by experimental evidences show that oblate shaped Ln^{III} ions show high energy barriers of magnetization in the PBP geometry when the axial sites are occupied by relatively strong donor ligands compared to the equatorial sites. Keeping this in mind we have chosen tri-alkyl/aryl phosphine oxides to replace the chloride ions in the axial sites. Accordingly, when we treated the ligand H_2L with lanthanide chlorides in the presence of phosphine oxides followed by addition of base we obtained neutral mononuclear $[(L)Ln^{III}(R_3PO)Cl]$ (Ln = Gd (**2.B.1**), Tb (**2.B.2**), Dy (**2.B.3**), Er (**2.B.5**); R = cyclohexyl and Dy (**2.B.4**); R = phenyl) complexes (Scheme **2.B.1**).
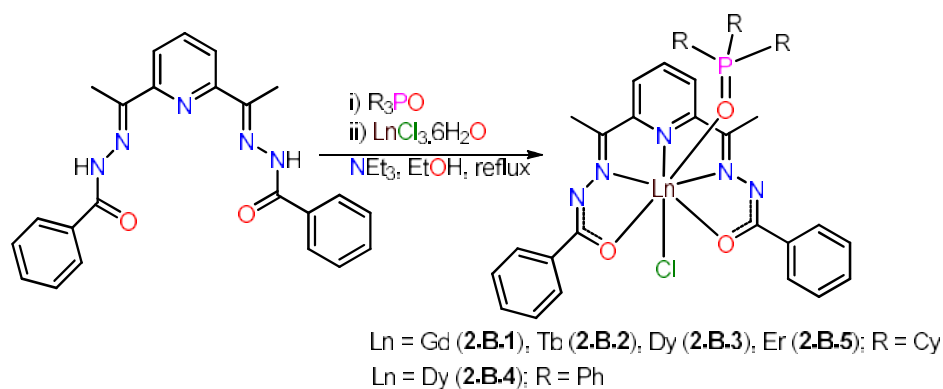
Scheme 2.B.1. Reaction scheme for the synthesis of **2.B.1-2.B.5**.

2.B.3.2 X-ray Crystallography. The complexes **2.B.1**, **2.B.3** and **2.B.5** crystallize in the monoclinic crystal system with $P2_1/c$ (for **2.B.3**) and $P2_1/n$ (for **2.B.1** and **2.B.5**) space groups whereas the complexes **2.B.2** and **2.B.4** crystallize in the triclinic crystal system with P-1 space group. The overall molecular structures of the complexes **2.B.1-2.B.5** are essentially identical. The molecular structure of complex **2.B.3** is shown in Figure 2.B.1, while those of **2.B.1**, **2.B.2**, **2.B.4** and **2.B.5** are given in the Figures 2.B.2-2.B.5. In view of the structural similarities present in the complexes we discuss below the molecular structures of complexes **2.B.3** and **2.B.4**.
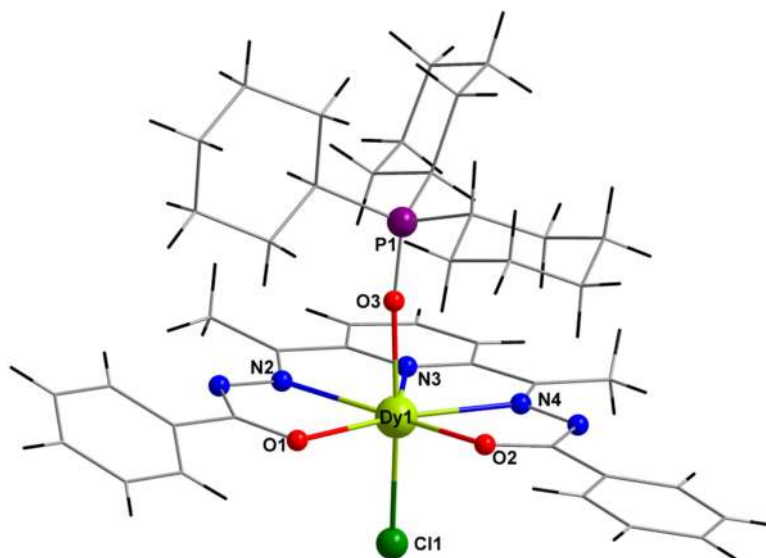
Figure 2.B.1. Molecular structures of complex **2.B.3**. Color codes: N = blue; O = red; green = Cl; C = grey; Dy = lime and H = black.

The complexes are formed by the coordination action of ligand *pyridyl* N atom, two *imino* N atoms, and two *carboxy* O atoms in the equatorial positions. One of the two axial sites is occupied by one chloride anion in both the complexes. The remaining axial site is occupied by one Cy₃PO ligand in the case of **2.B.3** and Ph₃PO ligand in the case of **2.B.4**. The ligand upon chelation with the Ln ions generates four *five*-membered rings revealing its excellent ability to

stabilize the Ln ions in its pentagonal coordination environment. The equatorial Dy–O/N bond distances are in the range of 2.259(2)-2.462(2) Å for **2.B.3** and 2.282(2)-2.456(2) Å for **2.B.4**. The Dy–O_{axial} bond distances are 2.237(2) for **2.B.3** and 2.275(2) for **2.B.4**. The Dy–Cl bond distances are 2.625(8) Å for **2.B.3** and 2.622(7) Å for **2.B.4**. Interestingly, the Dy–O_{axial} bond distance in both **2.B.3** and **2.B.4** are shorter compared to the Dy–$O_{equatorial}$ distances (Table 2.B.3) indicating the strong-field nature of the phosphine oxide ligand in comparison to the equatorial oxygen donor. The O_{phos}–Dy–Cl bond angles are 169.62(5)° for **2.B.3** and 174.07(5)° for **2.B.4**. The immediate coordination environment of the Ln^{III} ions were analyzed with Continuous Shape Measures using the SHAPE programme.[24] It reveals a distorted pentagonal bipyramid geometry around the Dy^{III} ions with D_{5h} (*pseudo*) CF symmetry (Table 2.B.4). The pentagonal bipyramidal geometry of the Dy^{III} ion in the complex **2.B.3** is shown in Figure 2.B.6 (c). The shortest intermolecular Ln···Ln distance in **2.B.3** is ~ 8.56 Å (Figure 2.B.7), while in **2.B.4** is ~ 8.80 Å (Figure 2.B.8) as revealed in the solid state packing diagram. The solid state phase purity of the complex **2.B.3'** (12% Dy^{III} sites diluted with an isostructural Y^{III} host) was confirmed by powder X-ray diffraction studies (Figure 2.B.9). The selected bond lengths and bond angles of complexes **2.B.1**-**2.B.5** are summarized in Table 2.B.3. The results of SHAPE measures calculations for all the complexes are given in Table 2.B.4.
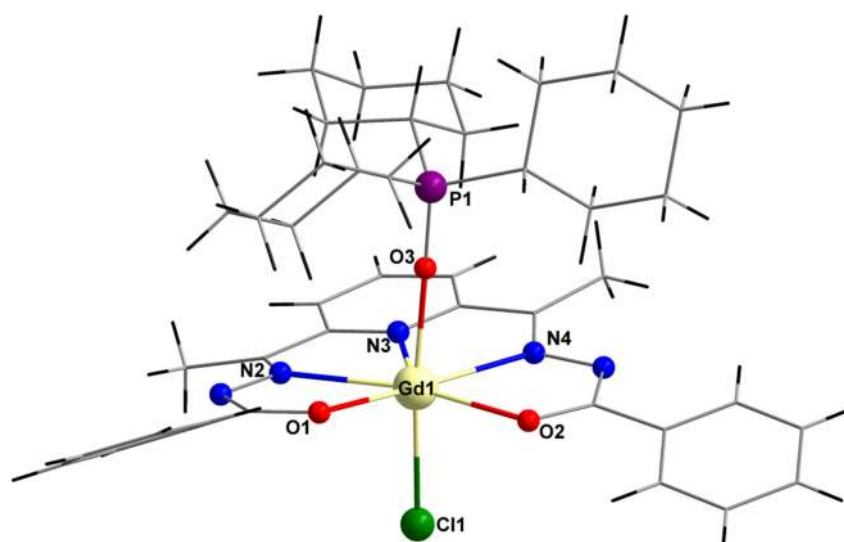
Figure 2.B.2. Molecular structure of complex **2.B.1**. Color codes: N = blue; O = red; green = Cl; C = grey; Gd = light yellow and H = black.
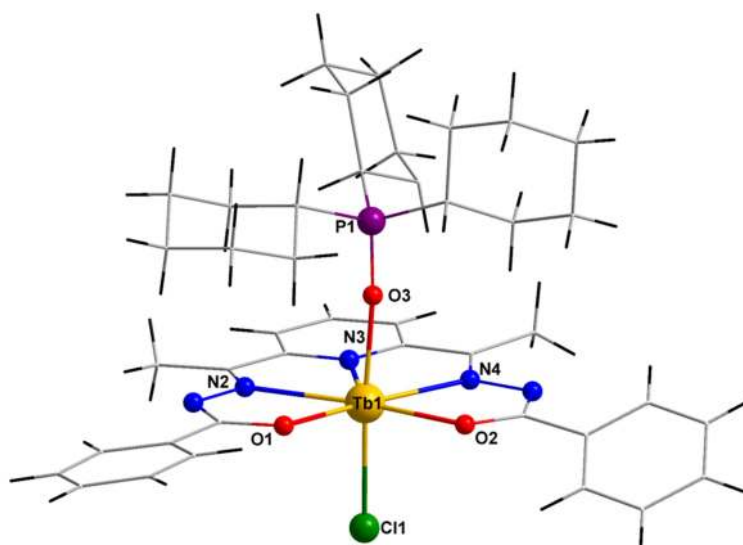
Figure 2.B.3. Molecular structure of complex **2.B.2**. Color codes: N = blue; O = red; green = Cl; C = grey; Tb = orange and H = black.
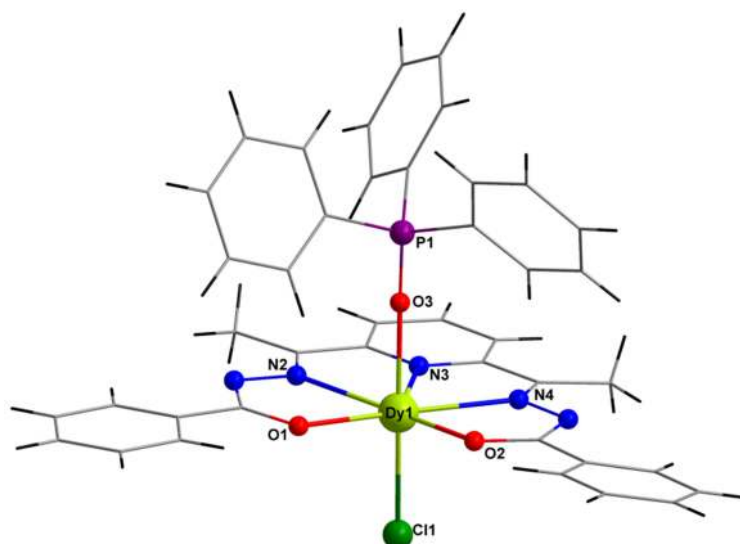
Figure 2.B.4. Molecular structure of complex **2.B.4**. Color codes: N = blue; O = red; green = Cl; C = grey; Dy = lime and H = black.
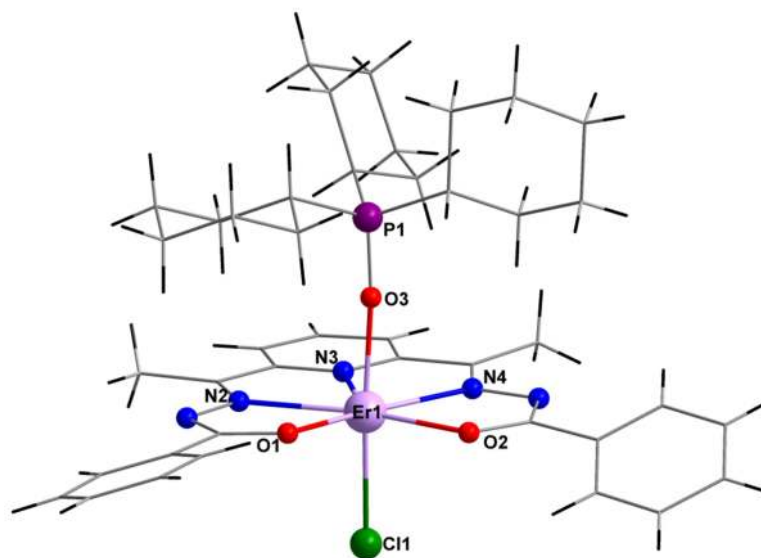
Figure 2.B.5. Molecular structure of complex **2.B.5**. Color codes: N = blue; O = red; green = Cl; C = grey; Er = lavender and H = black.

(a)

(b)

(c)

(d)

(e)
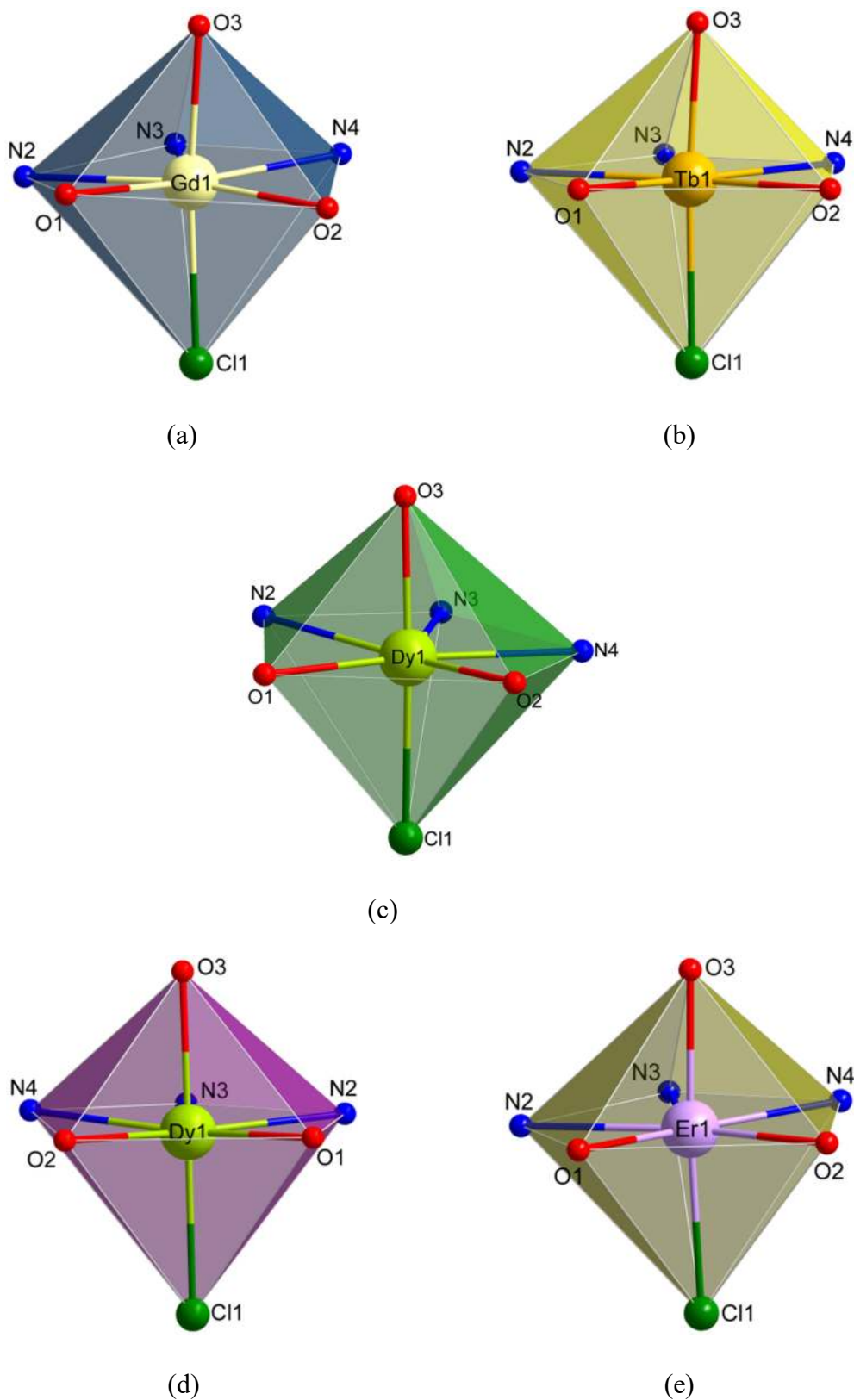
Figure 2.B.6. PBP coordination geometry of the Ln^{III} ions in **2.B.1** (a), **2.B.2** (b), **2.B.3** (c), **2.B.4** (d) **2.B.5** (e).

Table 2.B.3. Bond distance and Angle parameters of complexes **2.B.1-2.B.5**.

Bond lengths (Å)	Bond angles (°)			
Gd1–Cl1 2.645(5)	O1–Gd1–Cl1 97.10(3)	O1–Gd1–N3 126.15(4)		
Gd1–O1 2.330(12)	O1–Gd1–N2 63.55(5)	O1–Gd1–N4 167.95(5)		
Gd1–O2 2.313(12)	O2–Gd1–Cl1 87.60(3)	O2–Gd1–O1 105.63(4)		
Gd1–O3 2.271(13)	O2–Gd1–N3 128.20(5)	O2–Gd1vN2 167.59(5)		
Gd1–N3 2.510(15)	O2–Gd1–N4 64.78(5)	O3–Gd1–Cl1 174.67(3)		
Gd1–N2 2.522(15)	O3–Gd1–O1 87.87(5)	O3–Gd1–O2 89.22(5)		
Gd1–N4 2.480(15)	O3–Gd1–N3 91.00(5)	O3–Gd1–N2 96.12(5)		
	O3–Gd1–N4 84.82(5)	N3–Gd1–Cl1 87.61(3)		
	N3–Gd1–N2 63.08(5)	N2–Gd1–Cl1 87.84(4)		
	N4–Gd1–Cl1 89.96(4)	N4–Gd1–N3 63.68(5)		
Tb1–Cl1 2.622(12)	O1–Tb1–Cl1 93.57(10)	O1–Tb1–O2 102.50(13)		
Tb1–O1 2.291(3)	O1–Tb1–N4 167.36(13)	O1–Tb1–N3 128.57(13)		
Tb1–O2 2.306(3)	O1–Tb1–N2 64.66(14)	O2–Tb1–Cl1 90.53(10)		
Tb1–O3 2.228(4)	O2–Tb1–N4 65.20(13)	O2–Tb1–N3 128.85(13)		
Tb1–N4 2.472(4)	O2–Tb1–N2 167.16(14)	O3–Tb1–Cl1 175.22(9)		
Tb1–N3 2.500(4)	O3–Tb1–O1 91.19(13)	O3–Tb1–O2 87.95(13)		
Tb1–N2 2.495(4)	O3–Tb1–N4 85.66(13)	O3–Tb1–N3 88.25(13)		
	O3–Tb1–N2 92.04(13)	N4–Tb1–Cl1 89.59(10)		
	N4–Tb1–N3 63.65(13)	N4–Tb1–N2 127.62(14)		
	N3–Tb1–Cl1 89.18(10)	N2–Tb1–Cl1 90.44(10)		
Dy1–Cl1 2.625(8)	O2–Dy1–Cl1 93.19(5)	O2–Dy1–O1 100.23(7)		
Dy1–O1 2.272(2)	O2–Dy1–N3 130.25(7)	O2–Dy1–N2 165.17(7)		
	O2–Dy1–N4 65.59(7)	O3–Dy1–Cl1 169.62(5)		
	O3–Dy1–O1 92.19(7)	O3–Dy1–O2 90.35(7)		

Dy1–O2	2.259(2)	O3–Dy1–N3	84.83(7)	O3–Dy1–N2	91.41(7)
Dy1–O3	2.237(2)	O3–Dy1–N4	81.19(7)	N3–Dy1–Cl1	85.44(6)
Dy1–N3	2.462(2)	N3–Dy1–N2	64.57(7)	N2–Dy1–Cl1	87.67(6)
Dy1–N2	2.464(2)	O1–Dy1–Cl1	96.78(6)	O1–Dy1–N3	129.37(7)
Dy1–N4	2.448(2)	O1–Dy1–N2	65.00(7)	O1–Dy1–N4	164.10(7)
		N4–Dy1–Cl1	91.39(6)	N4–Dy1–N3	64.74(7)
		O2–Dy1–Cl1	94.12(5)	O2–Dy1–O1	100.00(6)
		O2–Dy1–N4	65.20(7)	O2-Dy1–N2	164.01(7)
Dy1–Cl1	2.622(7)	O2–Dy1–N3	129.84(7)	O3–Dy1–Cl1	174.07(5)
Dy1–O2	2.282(2)	O3–Dy1–O2	89.99(7)	O3–Dy1–O1	88.02(6)
Dy1–O3	2.276(2)	O3–Dy1–N4	88.02(7)	O3–Dy1–N2	83.31(7)
Dy1–O1	2.285(2)	O3–Dy1–N3	85.96(7)	O1–Dy1–Cl1	95.46(5)
Dy1–N4	2.456(2)	O1–Dy1–N4	164.67(7)	O1–Dy1–N2	65.38(7)
Dy1–N2	2.457(2)	O1–Dy1–N3	129.71(7)	N4–Dy1–Cl1	89.83(5)
Dy1–N3	2.467(2)	N4–Dy1–N2	128.73(8)	N4–Dy1–N3	64.71(8)
		N2–Dy1–Cl1	93.75(5)	N2–Dy1–N3	64.32(7)
		O1–Er1–Cl1	94.97(9)	O1–Er1–O2	97.78(11)
		O1–Er1–N3	130.69(11)	O1–Er1–N4	163.78(11)
Er1–Cl1	2.591(11)	O1–Er1–N2	65.83(12)	O3–Er1–Cl1	174.16(8)
Er1–O1	2.259(3)	O3–Er1–O1	90.83(11)	O3–Er1–O2	89.86(11)
Er1–O3	2.195(3)	O3–Er1–N3	86.83(12)	O3–Er1–N4	85.42(12)
Er1–O2	2.268(3)	O3–Er1–N2	91.81(12)	O2–Er1–Cl1	89.99(8)
Er1–N3	2.444(4)	O2–Er1–N3	131.42(11)	O2–Er1–N4	66.48(11)
Er1–N4	2.420(4)	O2–Er1–N2	163.55(12)	N3–Er1–Cl1	88.89(9)
Er1–N2	2.432(4)	N4–Er1–Cl1	89.16(9)	N4–Er1–N3	64.95(12)
		N4–Er1–N2	129.97(12)	N2–Er1–Cl1	89.99(9)
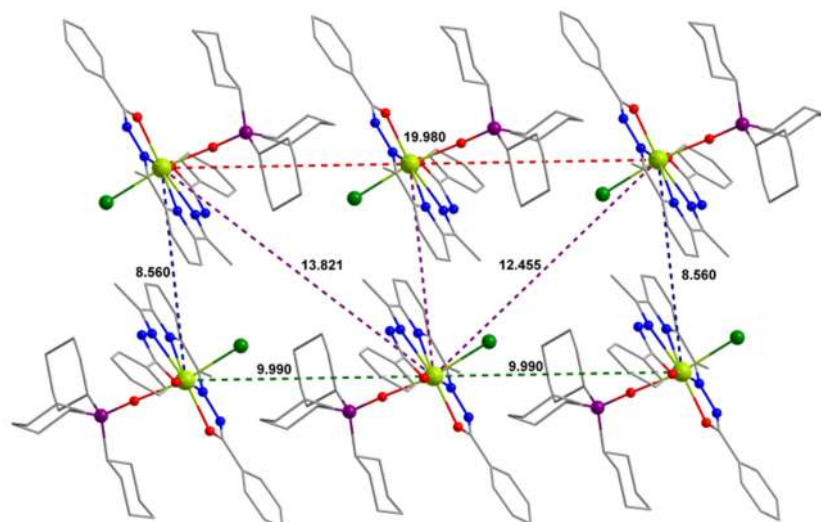
Figure 2.B.7. The solid state crystal packing diagram of complex **2.B.3**.
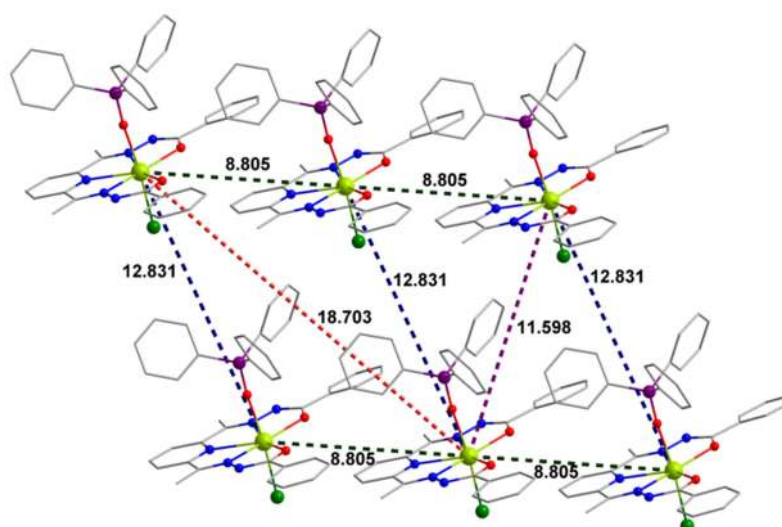
Figure 2.B.8. The solid state crystal packing diagram of complex **2.B.4**.

Table 2.B.4. Continuous Shape Measures (CShM) calculations for Ln^{III}.[24]

Complex	Structure[i]						
	HP-7	**HPY-7**	**PBPY-7**	**COC-7**	**CTPR-7**	**JPBPY-7**	**JETPY-7**
2.B.1	31.572	19.350	**2.233**	7.665	6.207	6.298	18.718
2.B.2	32.740	20.143	**1.732**	7.872	6.409	5.652	20.810
2.B.3	32.944	22.380	**1.446**	8.229	6.678	5.549	21.175

2.B.4	32.742	21.540	**1.505**	7.661	6.338	5.725	21.267
2.B.5	32.781	20.809	**1.353**	7.774	6.403	5.232	21.450

!HP-7: Heptagon (D_{7h}); HPY-7: Hexagonal pyramid (C_{6v}); PBPY-7: Pentagonal bipyramid (D_{5h}); COC-7: Capped octahedron (C_{3v}); CTPR-7: Capped trigonal prism (C_{2v}); JPBPY-7: Johnson pentagonal bipyramid J13 (D_{5h}); JETPY-7: Johnson elongated triangular pyramid J7 (C_{3v})
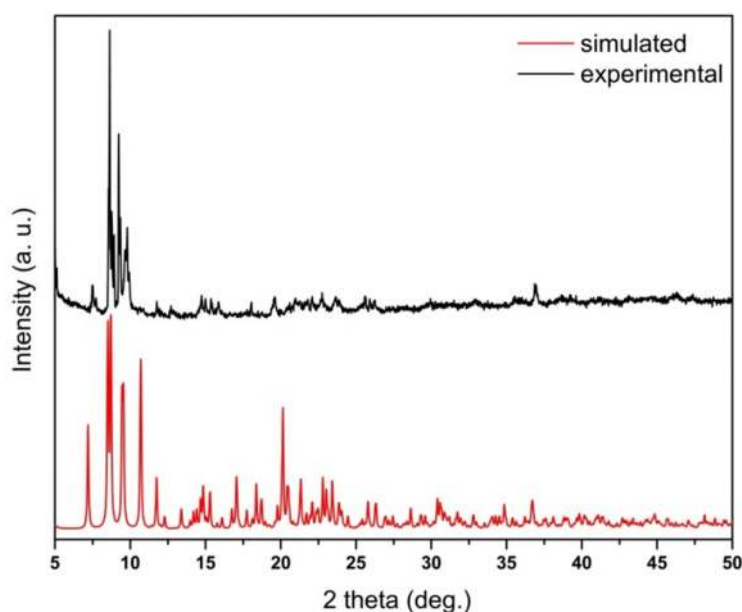
Figure 2.B.9. The experimental and simulated pXRD pattern of complex **2.B.3'**

2.B.3.3 Magnetic properties. The temperature dependence of the molar magnetic susceptibility (χ_M) for **2.B.1**-**2.B.3** and **2.B.5** are plotted as *T* in Figure 2.B.10 (*left*) and their field dependence of the magnetization behaviour is shown in Figure 2.B11. The corresponding behaviors for **2.B.4** are given in Figure 2.B.10 (*right*).
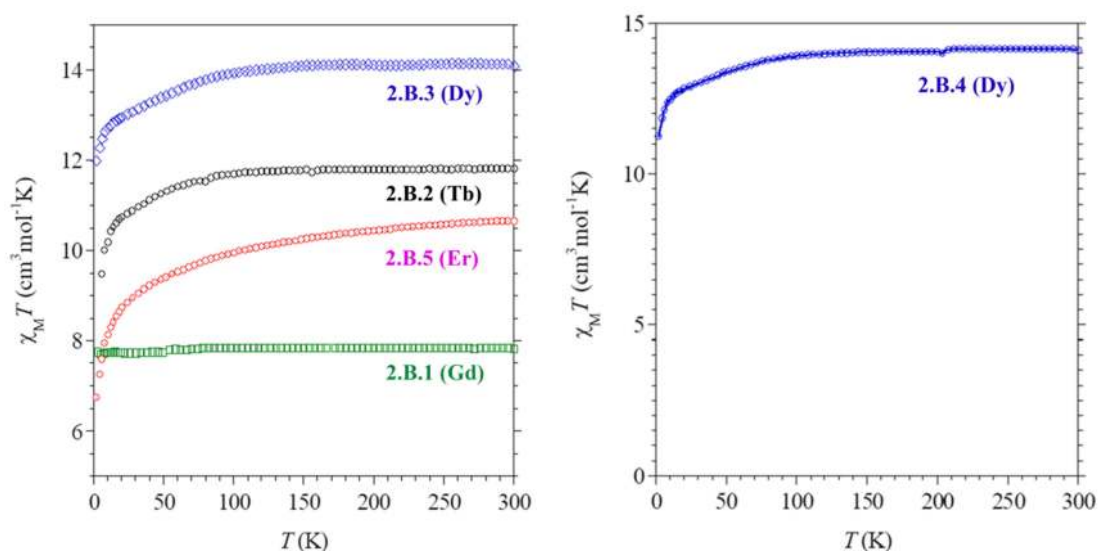
Figure 2.B.10. (*left*) Temperature dependence of the $\chi_M T$ product for compounds **2.B.1** (green), **2.B.2** (black), **2.B.3** (blue), and **2.B.5** (pink); (*right*) Temperature dependence of the χ_MT product for compound **2.B.4** (blue).

The values for $\chi_M T$ (in cm^3 mol^{-1} K) found at 300 K are 7.85 (Gd), 11.79 (Tb), 14.14 and 14.10 (Dy), and 10.65 (Er), in good accordance with the values expected for these ions (see Table 2.B.5). For the Tb, Dy, and Er derivatives the $\chi_M T$ slowly decreases as *T* is lowered in agreement with the anticipated crystal field effect. The absence of any contribution from intermolecular exchange interactions is confirmed by the perfect Curie behavior down to 2 K for Gd in **2.B.1** (Figure 2.B.10 green line). For the Tb and Dy derivatives, the field-dependent magnetization at 2-5 K show a fast rise at lower field regions and remain almost unchanged above 15 kOe (at 2 K) to reach 4.8 μ_B (**2.B.2**), 5.14 μ_B (**2.B.3**), and 5.09 μ_B (**2.B.4**) at high field (5 T) (Table 2.B.5).

(a)

(b)

(c)

(d)

(e)
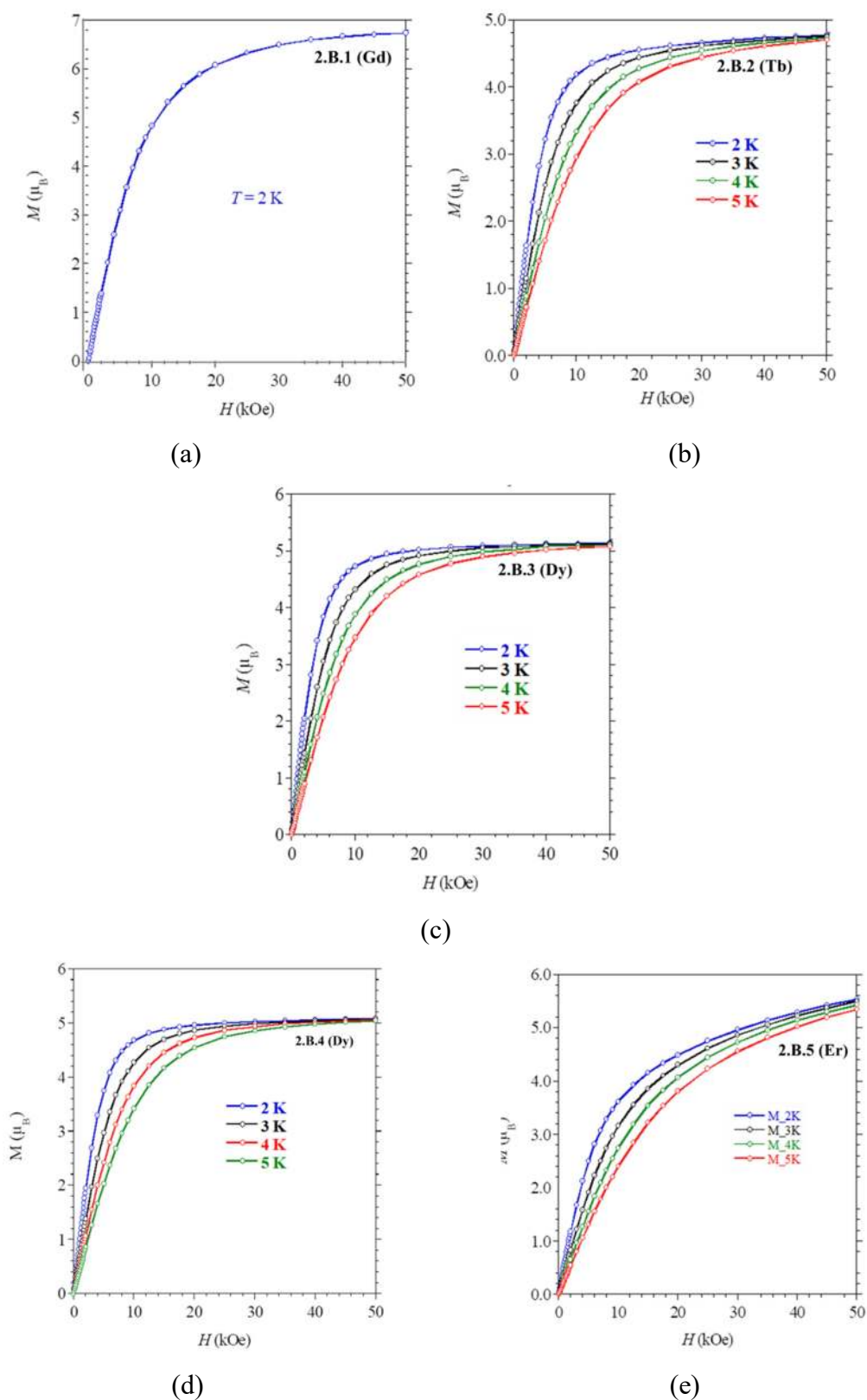
Figure 2.B.11. (a) Field dependence of magnetization for compound **2.B.1** at 2 K. (b-e) field dependence of magnetization for compounds **2.B.2-2.B.5** in the temperature range 2-5 K.

Table 2.B.5. Direct current magnetic data for the complexes **2.B.1-2.B.5**

compound	free-ion $\chi_M T$ values (cm³ K mol⁻¹)[a]	experimental $\chi_M T_{300K}$/ $\chi_M T_{2K}$ (cm³ K mol⁻¹)	experimental M value ($T = 2$ K, $H = 5$ T) (Nμ_B)	Theoretical M_{sat} value (Nμ_B)[b]
2.B.1	7.875	7.85/7.84	7.01	7
2.B.2	11.82	11.79/9.05	4.80	9
2.B.3	14.17	14.14/11.96	5.14	10
2.B.4	14.17	14.13/11.16	5.09	10
2.B.5	11.48	10.65/6.68	5.88	9

[a]$\chi_M T = \frac{N\beta^2}{3k}\{g_J^2 J(J + 1)$ [b]$M = NJg_J\mu_B$; $J = L + S$; $g_J = \frac{3}{2} + \frac{S_T(S_T+1)-L(L+1)}{2J(J+1)}$

To probe the slow relaxation of magnetization in compounds **2.B.2-2.B.5**, temperature and frequency dependent dynamic (alternating current, ac) magnetic susceptibility studies were carried out in the temperature range 2-25 K in zero field and with applied static fields. The Tb^{III} (**2.B.2**) and Er^{III} (**2.B.5**) derivatives did not show any out-of-phase component (χ''_M) down to 2 K at zero field and under an applied field of 1 kOe (the out-of-phase components of Er^{III} derivative is shown in Figure 2.B.12 (a) as a representative example). However, both the Dy^{III} complexes **2.B.3** and **2.B.4** exhibited a χ''_M signal but no maximum was observed above 2 K (Figure 2.B.12 (b) and (c)). Such a behavior was suggesting relaxation driven by QTM (blue plot) in the zero field. In order to suppress the QTM partially or fully dynamic studies were performed at different biased fields and found that applying static fields with $H_{dc} = 1$ kOe in **2.B.3** and $H_{dc} = 1.5$ kOe in **2.B.4** the QTM was suppressed. This is further confirmed in the case of **2.B.3** by an examination of the field dependence of τ at 8 K (Figure 2.B.12 (d)) that shows an increase for low applied fields up to 1 kOe where a plateau value is reached before decreasing again for fields above 2 kOe. This indicates

that the optimal field to quench QTM is 1 kOe. A detailed ac susceptibility investigation for Dy^{III} was therefore performed with $H_{dc} = 1$ kOe in the case of **2.B.3** and $H_{dc} = 1.5$ kOe in the case of **2.B.4**

(a)

(b)

(c)

(d)
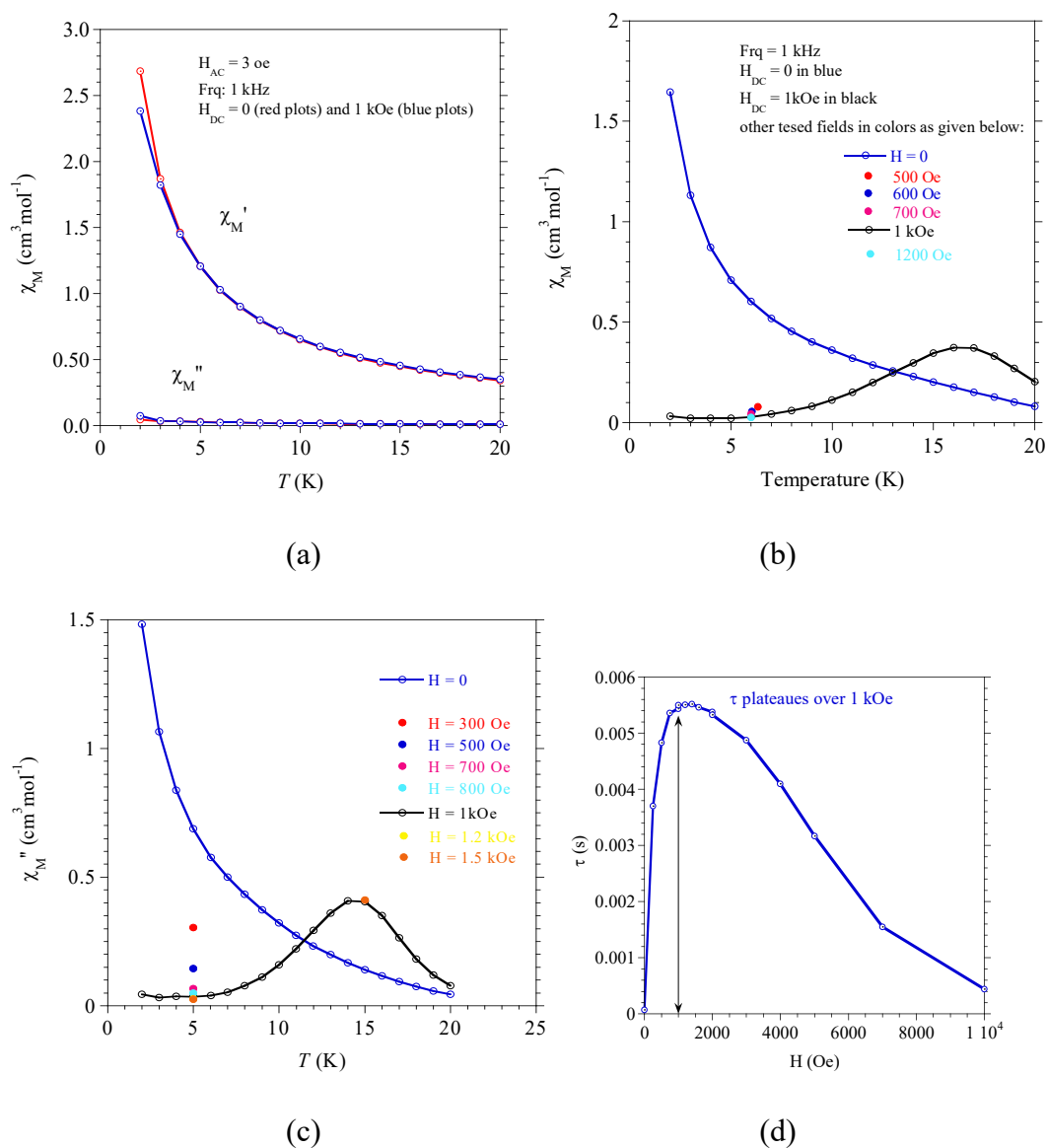
Figure 2.B.12. (a) Temperature dependence of the ac susceptibility plot for **2.B.5**; (b) Temperature dependence of the ac susceptibility plot for **2.B.3** at different biased fields; (c) Temperature dependence of the ac susceptibility plot for **2.B.4** at different biased fields; (d) field dependence of the relaxation time (τ) at 8 K for Dy derivative (**2.B.3**).

A full set of ac data for **2.B.3** was recorded in the temperature range 4 to 18 K for frequencies between 1 to 1500 Hz with $H_{ac} = 3$ Oe in an applied field of $H_{dc} = 1$ kOe (Figure 2.B.13) yielded well-defined maxima for χ''_M. The relaxation times have been assessed by fitting $\chi''_M = f(Frq)$ for different temperature with an extended Debye model and the best fit parameters are gathered in Table 2.B.6. The very small α parameter is indicative for a narrow distribution width for the relaxation time over the whole temperature domain suggesting that mainly one relaxation process is operative. The temperature dependence of the relaxation time, plotted in log scale in Figure 2.B.14, shows a linear variation between 18 and 10 K, which is the behavior anticipated for a thermally activated process (Orbach). Deviation from linearity for lower T indicates that other processes also come into play. Analysis of the behavior over the whole T range was obtained by summing the contributions of the Orbach, Raman, and direct processes ($\tau = \tau_0 \exp(U_{eff}/k_B T) + 1/(CT^n) + 1/(AT)$). The latter were required to reproduce the lower T behavior. Best fit gave a thermal energy barrier for magnetization reversal, $U_{eff}/k_B = 204 \pm 3$ K with $\tau_0 = (6 \pm 1) \times 10^{-9}$ s, C = 0.015 K^{-1} s^{-1}, n = 4.5, and A = -1.30 s^{-1}.
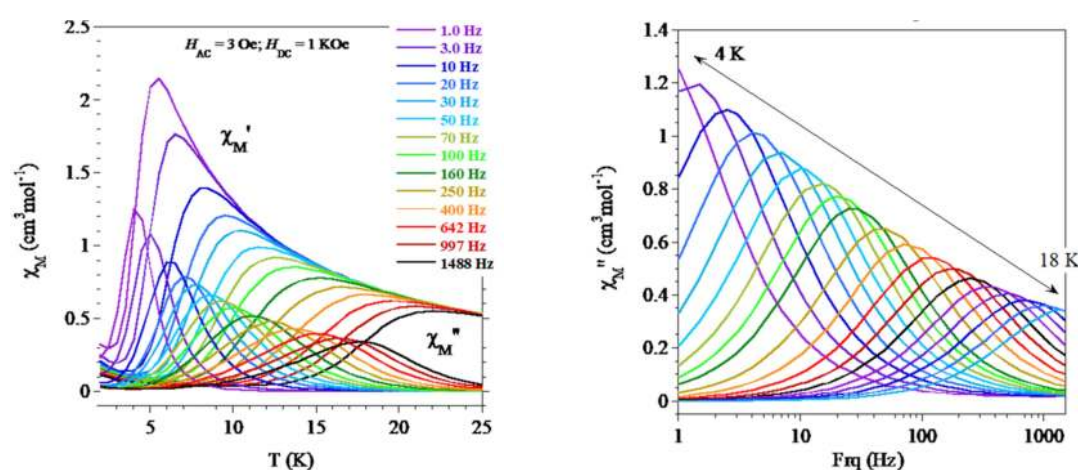
Figure 2.B.13. Temperature dependent of the ac susceptibility of **2.B.3** at variable frequency (*left*) and frequency dependent of the ac susceptibility at variable temperature (*right*) under an applied field of 1 kOe and 3 Oe ac fields.
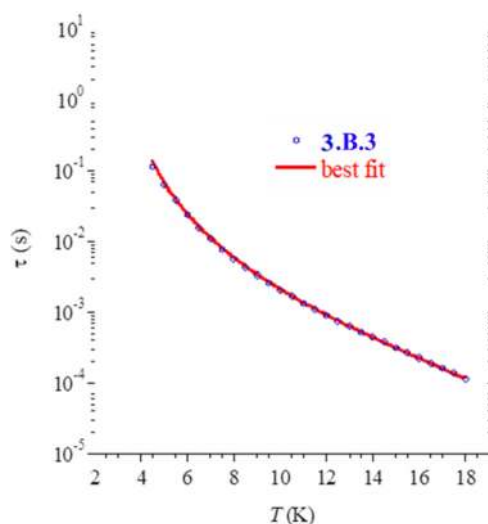
Figure 2.B.14. Experimental and calculated temperature dependence of τ plotted as $f(T)$ with best fit parameters.

Table 2.B.6. Best fit parameters for the analysis of the $\chi''_M = f(Frq)$ behaviors by an extended Debye model.

T (K)	χ_T	χ_S	τ (s)	α
4.5	5.71	3.29	0.11675	0.12
5.0	5.61	3.39	0.065181	0.12
5.5	5.52	3.47	0.038369	0.11
6.0	5.45	3.55	0.024021	0.10
6.5	5.38	3.61	0.015912	0.095
7.0	5.33	3.67	0.011003	0.088
7.5	5.28	3.72	0.007867	0.082
8.0	5.24	3.76	0.005804	0.078
8.5	5.20	3.80	0.004379	0.075
9.0	5.16	3.84	0.003369	0.073
9.5	5.13	3.87	0.002638	0.070
10.0	5.10	3.90	0.002096	0.068
10.5	5.07	3.93	0.001685	0.065
11.0	5.05	3.95	0.001365	0.065
11.5	5.02	3.97	0.001128	0.064
12.0	5.00	4.00	0.000905	0.063
12.5	4.98	4.01	0.00075741	0.060
13.0	4.97	4.03	0.0006327	0.059
13.5	4.95	4.05	0.00053185	0.057
14.0	4.94	4.06	0.00044954	0.056
14.5	4.92	4.08	0.00037815	0.056
15.0	4.91	4.09	0.00031952	0.055

15.5	3.90	3.10	0.00027045	0.055
16.0	3.88	3.11	0.00022847	0.052
16.5	3.87	3.13	0.00019351	0.050
17.0	3.86	3.14	0.0001633	0.048
17.5	4.35	3.65	0.00013939	0.042
18.0	3.84	3.16	0.00011626	0.041

To reduce the contributions of dipolar interactions and confirm the molecular origin of the slow magnetization dynamics of the Dy^{III} ion in this PBP coordination environment, we have considered the Y^{III} analogue with 12% Dy^{III} site populations, $[(L)Y_{0.85}Dy_{0.15}(Cy_3PO)Cl]$ (**2.B.3'**), in which the Y^{III} and Dy^{III} centers have the same coordination environments as that for **2.B.3**. The composition in Dy^{III} of the sample was determined to be 11.8 % by adjusting the M vs H behavior at 2 K to the one of the pure Dy complex (Figure 2.B.15 (*left*)). The phase purity of the complex **2.B.3'** was checked by powder X-ray diffraction studies as shown in the Figure 2.B.9.
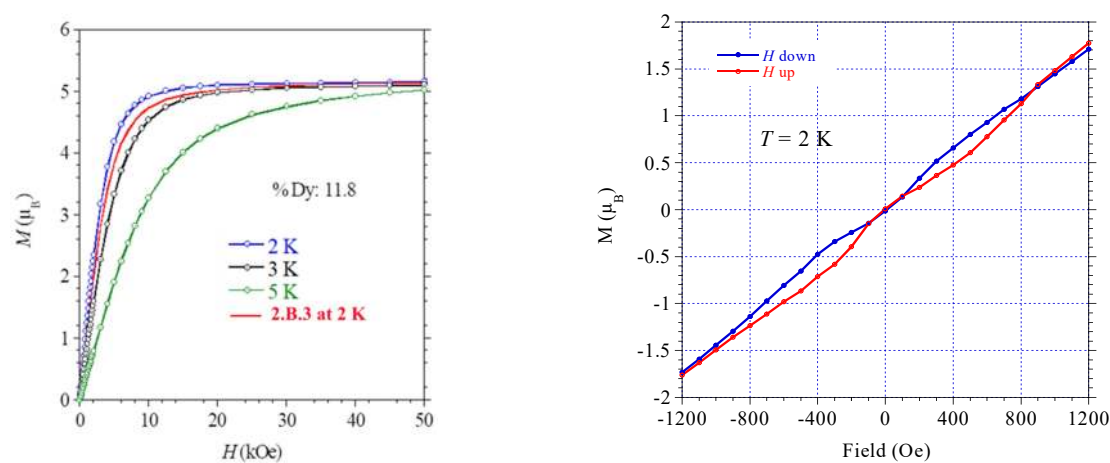
Figure 2.B.15. (*left*) $M = f(H)$ behavior for the Y/Dy sample at 2 K, 3 K, 4 K, and 5 K. The behavior for the pure Dy complex at 2 K is also shown. (*right*) Detail of the hysteresis loop observed at 2 K. Note that measurement has been performed in static-field mode (no field sweeping).

The diluted $Dy^{III}(Y^{III})$ complex (**2.B.3'**) exhibits a butterfly-shaped hysteresis loop at 2 K (Figure 2.B.15 (*right*)) with a merging of the magnetization for low fields (|H| < 100 Oe). Since the magnetization has been recorded with static field (not in sweeping field mode), the observation of a magnetic hysteresis loop implies a very slow relaxation at 2 K. This was confirmed from ac behaviors. The complex **2.B.3'** hereafter, gave very similar results (see Figure 2.B.16). For this sample however, a maximum was observed in the $\chi''_M = f(T)$ behavior in zero field but a QTM contribution was discernible at low temperature. This was suppressed upon applying a small dc field of 750 Oe. The temperature dependence of the relaxation times between 2 and 17.5 K (Figure 2.B.17 and Table 2.B.7) parallels that obtained for the pure Dy derivative **2.B.3**, and contributions of the Orbach, Raman, and direct processes had to be taken into account to reach a good modeling. Best fit to the experimental data yielded for **2.B.3'** (Y^{III}) $U_{eff}/k_B = 208 \pm 5$ K, $\tau_0 = (6 \pm 2) \times 10^{-9}$ s, C = 4.3×10^{-3} $K^{-1} s^{-1}$, n = 5.0, and A = -0.30 s^{-1} (Figure 2.B.17). The comparison of the behavior for **2.B.3** and its diluted form, **2.B.3'** (Y^{III}) shows that the observed behavior is clearly of molecular origin.
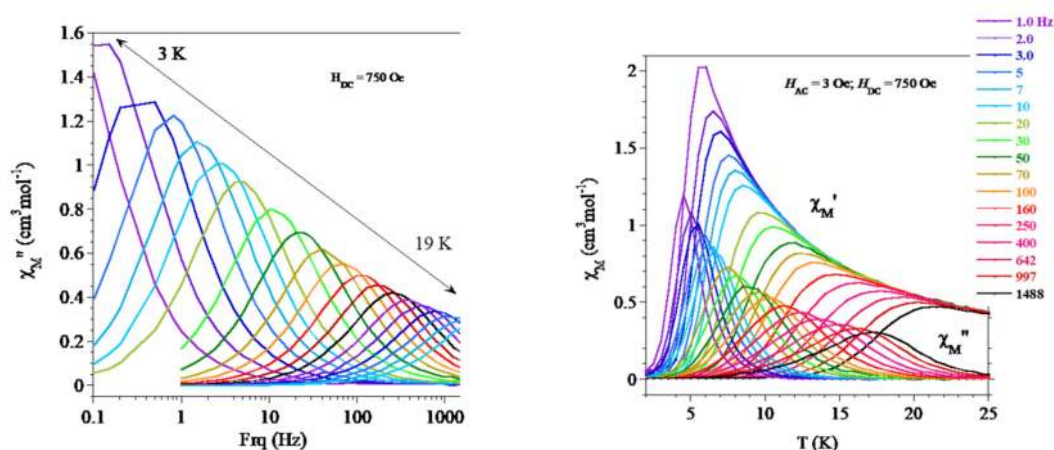
Figure 2.B.16. Frequency dependent of the ac susceptibility at variable temperature (*left*) and temperature dependent of the ac susceptibility at variable frequency and (*right*) of **2.B.3** under an applied field of 750 Oe and 3 Oe ac fields.
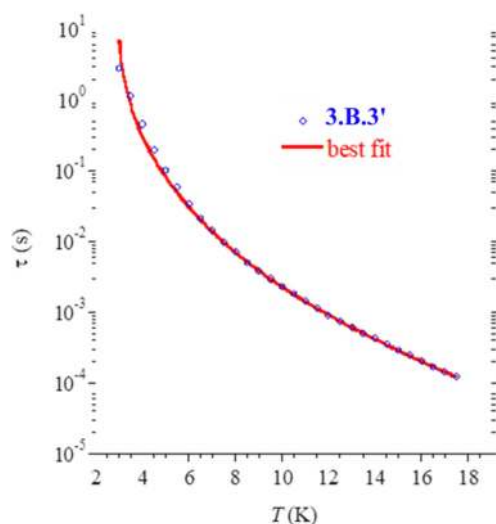
Figure 2.B.17. Experimental and calculated temperature dependence of τ plotted as $\tau = f(T)$ with best fit parameters.

Table 2.B.7. Best fit parameters of a Debye model to $\chi''_M = f(\text{Frq})$ for different T.

T (K)	χ_T	χ_S	τ (s)	α
4.0	5.825	3.175	0.166	0.16
4.5	5.6816	3.3184	0.080	0.11
5.0	5.5944	3.4056	0.04511	0.062
5.5	5.5049	3.4951	0.02776	0.064
6.0	5.4324	3.5677	0.0178	0.0558
6.5	5.3645	3.6355	0.01177	0.0573
7.0	5.3137	3.6863	0.00817	0.052
7.5	5.2669	3.7331	0.00577	0.048
8.0	5.2233	3.7767	0.00417	0.044
8.5	5.1878	3.8122	0.00306	0.034
9.0	5.1514	3.8486	0.00230	0.035
9.5	5.119	3.881	0.001747	0.037
10.0	5.0922	3.9078	0.001341	0.027
10.5	5.0658	3.9342	0.001049	0.032
11.0	5.0435	3.9565	0.000825	0.026
11.5	5.0224	3.9776	0.000656	0.023
12.0	5.001	3.999	0.000517	0.018
12.5	4.9822	4.0178	0.000421	0.023
13.0	4.9661	4.0339	0.0003419	0.020
13.5	4.9513	4.0487	0.0002823	0.011
14.0	4.9367	4.0633	0.000233	0.008
14.5	4.9235	4.0765	0.0001895	0.013
15.0	4.9127	4.0873	0.000156	0.01
15.5	4.9004	4.0996	0.000128	0.00006

The replacement of OPCy$_3$ for OPPh$_3$ in the apical position of Dy^{III} appeared to have no significant incidence on the magnetic behaviors; the ac susceptibility features for **2.B.4** (Figure 2.B.18 and Table 2.B.8) are very similar to that obtained for **2.B.3**. To reproduce the temperature dependence of the relaxation time for **2.B.4** required to consider contributions from Orbach, Raman and direct processes, best fit (using equation $\tau^{-1} = (1/\tau_0)\exp(-U_{\text{eff}}/k_B T) + (CT^n) + (AT)$) to the experimental behavior gave $U_{\text{eff}}/k_B = 241 \pm 7$ K, $\tau_0 = (2.3 \pm 0.9) \times 10^{-10}$ s, $C = (5.97 \pm 0.03) \times 10^{-3}$ K^{-1} s^{-1}, n = 5.1, and A = 0.2 ± 0.7 s^{-1} (Figure 2.B.19).
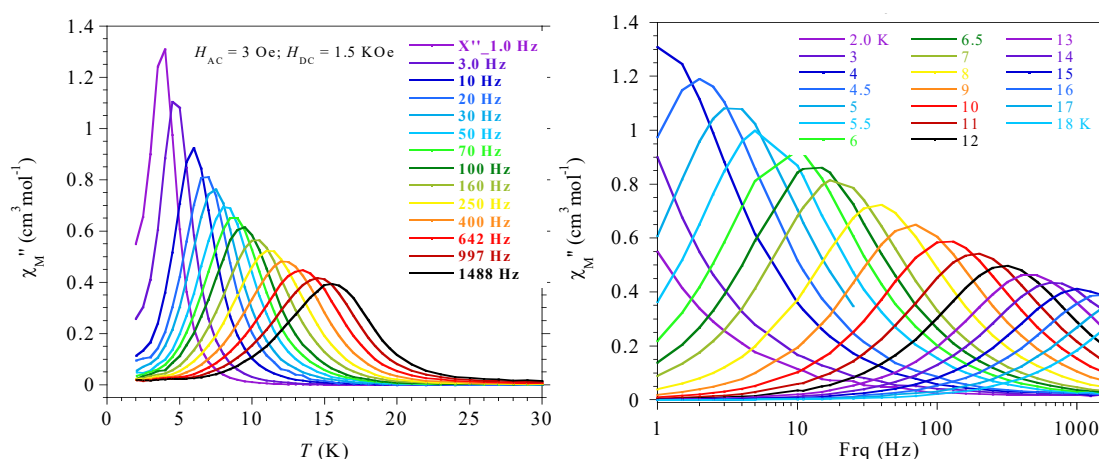
Figure 2.B.18. Temperature dependent of the ac susceptibility of **2.B.4** at variable frequency (*left*) and frequency dependent of the ac susceptibility at variable temperature (*right*) under an applied field of 1.5 kOe and 3 Oe ac fields.

Table 2.B.8. Best fit parameters of a Debye model to $\chi''_M = f(\text{Frq})$ for different T.

T (K)	χ_T	χ_s	τ (s)	α
4.0	5.825	3.175	0.166	0.16
4.5	5.6816	3.3184	0.080	0.11
5.0	5.5944	3.4056	0.04511	0.062
5.5	5.5049	3.4951	0.02776	0.064
6.0	5.4324	3.5677	0.0178	0.0558
6.5	5.3645	3.6355	0.01177	0.0573
7.0	5.3137	3.6863	0.00817	0.052
7.5	5.2669	3.7331	0.00577	0.048
8.0	5.2233	3.7767	0.00417	0.044

8.5	5.1878	3.8122	0.00306	0.034
9.0	5.1514	3.8486	0.00230	0.035
9.5	5.119	3.881	0.001747	0.037
10.0	5.0922	3.9078	0.001341	0.027
10.5	5.0658	3.9342	0.001049	0.032
11.0	5.0435	3.9565	0.000825	0.026
11.5	5.0224	3.9776	0.000656	0.023
12.0	5.001	3.999	0.000517	0.018
12.5	4.9822	4.0178	0.000421	0.023
13.0	4.9661	4.0339	0.0003419	0.020
13.5	4.9513	4.0487	0.0002823	0.011
14.0	4.9367	4.0633	0.000233	0.008
14.5	4.9235	4.0765	0.0001895	0.013
15.0	4.9127	4.0873	0.000156	0.01
15.5	4.9004	4.0996	0.000128	0.00006
16.0	4.89	4.11	0.0001045	0.0002
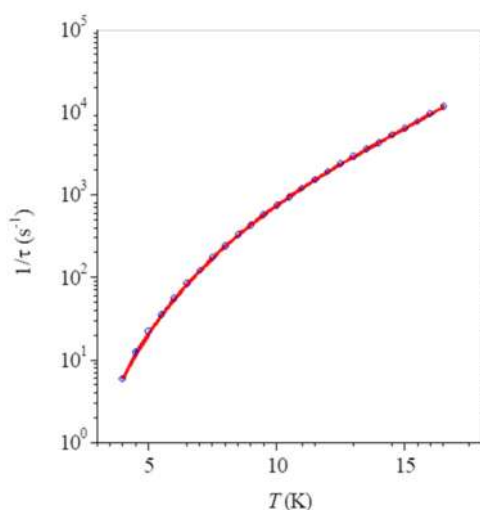
Figure 2.B.19. Relaxation time (τ) as a function of $\tau^{-1} = f(T)$ and its best fit.

It is satisfying to see that the energy barrier for magnetization reversal, U_{eff}/k_B, for the Dy^{III} complexes reported herein is significantly increased with respect to the homologue complex containing two Cl$^-$ ligands in the apical positions. This can be attributed to the stronger axial field due to the phosphine oxide ligands.

2.B.4 CONCLUSIONS

In conclusion, we have synthesized a series of mononuclear PBP Ln^{III} complexes with strong donor alkyl/aryl phosphine oxide ligands in the axial site. The molecular structures of these complexes were confirmed by single crystal X-ray diffraction studies. A close inspection of the PBP coordination geometries in these complexes revealed a strong bonding interaction between the Ln center and phosphine oxide ligands. The magnetization dynamics of the Dy^{III} derivatives were found to be strikingly different than that of the homologous Dy^{III} complex with two Cl$^-$ atoms in the apical positions. In this case, introduction of the phosphine oxide ligands in one of the axial sites enhances the energy barriers 2-3 fold in the Dy^{III} derivatives. The results of this work are consistent with the notion that strong-field axial ligands in pentagonal bipyramidal Ln^{III} complexes are conducive for good SMM Behavior. This effect would be further accentuated if the ligands in the equatorial position are very weak field.

2.B.5 REFERENCES

1 (a) J. R. Robinson, X. Fan, J. Yadav, P. J. Carroll, A. J. Wooten, M. A. Pericàs, E. J. Schelter and P. J. Walsh, *J. Am. Chem. Soc.*, 2014, **136**, 8034-8041; (b) S. Chen, D. Yan, M. Xue, Y. Hong, Y. Yao and Q. Shen, *Org. Lett.*, 2017, **19**, 3382-3385; (c) D. P. Halter, C. T. Palumbo, J. W. Ziller, M. Gembicky, A. L. Rheingold, W. J. Evans and K. Meyer, *J. Am. Chem. Soc.*, 2018, **140**, 2587-2594; (d) H. Nagae, R. Aoki, S.-n. Akutagawa, J. Kleemann, R. Tagawa, T. Schindler, G. Choi, T. P. Spaniol, H. Tsurugi, J. Okuda and K. Mashima, *Angew. Chem. Int. Ed.*, 2018, **57**, 2492-2496; (e) B. M. Schmidt, A. Pindwal, A. Venkatesh, A. Ellern, A. J. Rossini and A. D. Sadow, *ACS Catal.*, 2019, **9**, 827-838.

2 (a) J.-C. G. Bünzli, *Coord. Chem. Rev.*, 2015, **293-294**, 19-47; (b) Y. Hirai, T. Nakanishi, Y. Kitagawa, K. Fushimi, T. Seki, H. Ito and Y. Hasegawa, *Angew. Chem. Int. Ed.*, 2016, **55**, 12059-12062; (c) H. Wei, Z. Zhao, C. Wei, G. Yu, Z. Liu, B. Zhang, J. Bian, Z. Bian and C. Huang, *Adv. Funct. Mater.*, 2016, **26**, 2085-2096; (d) D. Kovacs, X. Lu, L. S. Mészáros, M. Ott, J. Andres and K. E. Borbas, *J. Am. Chem. Soc.*, 2017, **139**, 5756-5767; (e) X.-Z. Li, L.-P. Zhou, L.-L. Yan, D.-Q. Yuan, C.-S. Lin and Q.-F. Sun, *J. Am. Chem. Soc.*, 2017, **139**, 8237-8244; (f) I. Martinić, S. V. Eliseeva, T. N. Nguyen, V. L. Pecoraro and S. Petoud, *J. Am. Chem. Soc.*, 2017, **139**, 8388-8391; (g) S. Xiang, D.-X. Bao, J. Wang, Y.-C. Li and X.-Q. Zhao, *J. Lumin.*, 2017, **186**, 273-282; (h) Y. Qiao and E. J. Schelter, *Acc. Chem. Res.*, 2018, **51**, 2926-2936; (i) Y. Du, Y. Jiang, T. Sun, J. Zhao, B. Huang, D. Peng and F. Wang, *Adv. Mater.*, 2019, **31**, 1807062-1807070.

3 (a) K. Strnat, G. Hoffer, J. Olson, W. Ostertag and J. J. Becker, *J. Appl. Phys.*, 1967, **38**, 1001-1002; (b) R. Vincent, S. Klyatskaya, M. Ruben, W. Wernsdorfer and F. Balestro, *Nature*, 2012, **488**, 357-360; (c) D. N. Woodruff, R. E. P. Winpenny and R. A. Layfield, *Chem. Rev.*, 2013, **113**, 5110-5148; (d) E. Kiefl, M. Mannini, K. Bernot, X. Yi, A. Amato, T. Leviant, A. Magnani, T. Prokscha, A. Suter, R. Sessoli and Z. Salman, *ACS Nano*, 2016, **10**, 5663-5669; (e) Z. Zhu, M. Guo, X.-L. Li and J. Tang, *Coord. Chem. Rev.*, 2019, **378**, 350-364.

4 (a) J. T. Coutinho, B. Monteiro and L. C. J. Pereira, *6 - Ln(III)-based SIMs* in *Lanthanide-Based Multifunctional Materials*, eds. P. Martín-Ramos and M. Ramos Silva, Elsevier, 2018, pp. 195-231; (b) A. Dey, P. Kalita and V. Chandrasekhar, *ACS Omega*, 2018, **3**, 9462-9475; (c) J. Lu, M. Guo and J. Tang, *Chem Asian J*, 2017, **12**, 2772-2779; (d) J. Tang and P. Zhang, *Lanthanide Single Molecule Magnets*, Springer-Verlag Berlin Heidelberg 2015.

5 (a) K. R. Meihaus and J. R. Long, *Dalton Trans.*, 2015, **44**, 2517-2528; (b) N. Magnani and R. Caciuffo, *Inorganics*, 2018, **6**, 26-35; (c) J. T. Coutinho, M. Perfetti, J. J. Baldovi, M. A. Antunes, P. P. Hallmen, H. Bamberger, I. Crassee, M. Orlita, M. Almeida, J. van Slageren and L. C. J. Pereira, *Chem. Eur. J.*, 2019, **25**, 1758-1766; (d) D. M. King, P. A. Cleaves, A. J. Wooles, B. M. Gardner, N. F. Chilton, F. Tuna, W. Lewis, E. J. L. McInnes and S. T. Liddle, *Nat. Commun.*, 2016, **7**, 13773-13787; (e) L. Chatelain, F. Tuna, J. Pécaut and M. Mazzanti, *Chem. Commun.*, 2015, **51**, 11309-11312.

6 (a) R. A. Layfield and M. Murugesu, *Lanthanides and Actinides in Molecular Magnetism*, Wiley-VCH Verlag GmbH & Co. KGaA 2015; (b) S. E. Gao, *Molecular Nanomagnets and Related Phenomena*, Springer-Verlag Berlin Heidelberg, 2015; (c) D. Gatteschi, R. Sessoli and J. Villain, *Molecular Nanomagnets*, 2006.

7 C. Benelli and D. Gatteschi, *Introduction to Molecular Magnetism: From Transition Metals to Lanthanides*, Wiley-VCH.

8 E. Bartolomé, A. Arauzo, J. Luzón, J. Bartolomé and F. Bartolomé, *Magnetic Relaxation of Lanthanide-Based Molecular Magnets* in *Handbook of Magnetic Materials*, ed. E. Brück, Elsevier, 2017, vol. 26, pp. 1-289.

9 N. Ishikawa, M. Sugita, T. Ishikawa, S.-y. Koshihara and Y. Kaizu, *J. Am. Chem. Soc.*, 2003, **125**, 8694-8695.

10 (a) O. Kahn, *Molecular Magnetism*, Willey VCH, 1993; (b) S. A. Cotton, *Lanthanides and Actinides*, Macmillan, London, 1991.

11 (a) S. T. Liddle and J. van Slageren, *Chem. Soc. Rev.*, 2015, **44**, 6655-6669; (b) N. F. Chilton, *Inorg. Chem.*, 2015, **54**, 2097-2099; (c) L. Ungur and L. F. Chibotaru, *Inorg. Chem.*, 2016, **55**, 10043-10056; (d) J.-L. Liu, Y.-C. Chen and M.-L. Tong, *Chem. Soc. Rev.*, 2018, **47**, 2431-2453.

12 (a) B. M. Day, F.-S. Guo and R. A. Layfield, *Acc. Chem. Res.*, 2018, **51**, 1880-1889; (b) K. L. M. Harriman and M. Murugesu, *Acc. Chem. Res.*, 2016, **49**, 1158-1167; (c) A. K. Bar, P. Kalita, M. K. Singh, G. Rajaraman and V. Chandrasekhar, *Coord. Chem. Rev.*, 2018, **367**, 163-216.

13 F.-S. Guo, B. M. Day, Y.-C. Chen, M.-L. Tong, A. Mansikkamäki and R. A. Layfield, *Science*, 2018, **362**, 1400-1403.

14 J. D. Rinehart and J. R. Long, *Chem. Sci.*, 2011, **2**, 2078-2085.

15 (a) P. Zhang, L. Zhang, C. Wang, S. Xue, S.-Y. Lin and J. Tang, *J. Am. Chem. Soc.*, 2014, **136**, 4484-4487; (b) W.-B. Sun, P.-F. Yan, S.-D. Jiang, B.-W. Wang, Y.-Q. Zhang, H.-F. Li, P. Chen, Z.-M. Wang and S. Gao, *Chem. Sci.*, 2016, **7**, 684-691; (c) Y.-C. Chen, J.-L. Liu, W. Wernsdorfer, D. Liu, L. F. Chibotaru, X.-M. Chen and M.-L. Tong, *Angew. Chem. Int. Ed.*, 2017, **56**, 4996-5000; (d) S. K. Gupta and R. Murugavel, *Chem. Commun.*, 2018, **54**, 3685-3696.

16 (a) S. K. Gupta, T. Rajeshkumar, G. Rajaraman and R. Murugavel, *Chem. Sci.*, 2016, **7**, 5181-5191; (b) J. Liu, Y.-C. Chen, J.-L. Liu, V. Vieru, L. Ungur, J.-H. Jia, L. F. Chibotaru, Y. Lan, W. Wernsdorfer, S. Gao, X.-M. Chen and M.-L. Tong, *J. Am. Chem. Soc.*, 2016, **138**, 5441-5450; (c) Z. Jiang, L. Sun, Q. Yang, B. Yin, H. Ke, J. Han, Q. Wei, G. Xie and S. Chen, *J. Mater. Chem. C*, 2018, **6**, 4273-4280; (d) Y.-S. Ding, N. F. Chilton, R. E. P. Winpenny and Y.-Z. Zheng, *Angew. Chem. Int. Ed.*, 2016, **55**, 16071-16074.

17 A. K. Bar, P. Kalita, J.-P. Sutter and V. Chandrasekhar, *Inorg. Chem.*, 2018, **57**, 2398-2401.

18 C. Pelizzi and G. Pelizzi, *J. Chem. Soc., Dalton Trans.*, 1980, 1970-1973.

19 *CrysAlisPRO*, Oxford Diffraction UK Ltd., Yarnton, England.

20 G. M. Sheldrick, *Acta Cryst. A*, 2015, **71**, 3-8.

21 G. M. Sheldrick, *Acta Cryst. C*, 2015, **71**, 3-8.

22 O. V. Dolomanov, L. J. Bourhis, R. J. Gildea, J. A. K. Howard and H. Puschmann, *J. Appl. Cryst.*, 2009, **42**, 339-341.

23 K. Brandenburg and H. Putz, *DIAMOND*, Crystal Impact GbR, Bonn, Germany, version 3.2, 1997−2014.

24. (a) J. Cirera, E. Ruiz and S. Alvarez, *Organometallics*, 2005, **24**, 1556-1562; (b) *SHAPE: Continuous Shape Measures calculation*, Electronic Structure Group, Universitat de Barcelona, Spain, version 2.1, 2013.

Mononuclear Lanthanide Complexes Assembled from a Tridentate NNO Donor Ligand: Design of a Dy^{III} Single-Ion Magnet

ABSTRACT: The reaction of a tridentate *NNO* donor ligand, 4-nitro-2-((2-(pyridine-2-yl)hydrazono)methyl)phenol (HL) with lanthanide(III) nitrates in the presence of triethylamine afforded a new family of neutral mononuclear Ln^{III} complexes [Ln(NO$_3$)(L)$_2$(HOCH$_3$)] (Ln = Gd; (**3.A.1**), Tb; (**3.A.2**), Dy; (**3.A.3**), and Ho (**3.A.4**). The mononuclear complexes were structurally characterized by single crystal X-ray diffraction studies which revealed a spherical tricapped trigonal prism geometry with a *pseudo* D_{3h} symmetry around the Ln^{III} center. Static (dc) and dynamic (ac) magnetic studies have been performed on these complexes. Field-induced single-ion magnet behaviour was observed in the Dy^{III} analogue (diluted) with an effective energy barrier and pre-exponential parameters of U_{eff}/k_B = 68(2) K and τ_0 = 1.8 x 10^{-7} s, respectively.

3.A.1 INTRODUCTION

The observation of single-molecule magnet (SMM) behaviour in the lanthanide *bis*-phthalocyanine double-decker complexes, [LnPc$_2$]$^-$ (Ln = Dy^{III} and Tb^{III}; Pc = phthalocyanine)[1] has spurred interest in utilizing complexes containing 4f metal ions in molecular magnets.[2] A deeper analysis of the role of 4f metal ions in the field of molecular magnetism has revealed that the inherent unquenched spin-orbital angular momentum present in lanthanide ions can allow, particularly, ions such as Dy^{III}, Tb^{III}, Er^{III} and Ho^{III} to have large magnetic anisotropy, an important criterion in promoting SMM behavior.[3] Although crystal field effects are dominated by spin-orbit coupling in lanthanide complexes the former play a crucial and important role in perturbing the

energy levels in the resultant complexes as shown by Ishikawa in his pioneering work and as subsequently analyzed by others.[1b, 4] A seminal insight was provided by Long and co-workers who argued that the oblate electron density around Dy^{III} and Tb^{III} would need an axial crystal filed to harness and maximize the magnetic anisotropy while Er^{III} and Ho^{III} having a prolate electron density would need an equatorial crystal field.[5] A further qualitative analysis revealing that complexes possessing high axial symmetries such as $C_{\infty v}$, D_{4d}, S_8, D_{5h}, D_{6d}, and $D_{\infty h}$ etc. would be good candidates as molecular magnets has allowed rational design to take precedence over serendipity in preparing potential SMMs.[4c, 6] These developments have led to a spurt in the growth of mononuclear lanthanide complexes with an aim to achieve high blocking temperatures (T_B) and high energies of barrier (U_{eff}) for magnetization reversal. Recent reports on mononuclear Ln^{III} complexes show that large energy barriers for magnetization reversal and high blocking temperatures can be achieved by employing strong axial ligand fields with the *Ising*-type anisotropic lanthanides such as Dy^{III}.[7] Till date, the mononuclear dysprosium complex, $[(Cp^{iPr5})Dy(Cp^*)][B(C_6F_5)_4]$ has the highest blocking temperature of 80 K, among all other reported lanthanide based single-molecule magnets.[8] Also, there are some interesting reports on air-stable mononuclear lanthanide-based single molecule magnets having high energy barriers of magnetization reversal.[9] These recent advancements have triggered a fresh interest in utilizing the 4f ions in molecular magnetism.

We have been utilizing polydentate ligands for the preparation of hetero- (3d/4f) and homometallic lanthanide complexes as molecular magnets.[10] In the latter, we were able to tune the nuclearity of the complexes from the lowest possible to a highest of 21.[11] In the previous chapter we have shown that by using a rigid ligand that enforces an equatorial geometry we prepared a hepta-coordinate lanthanide complex,

[Et$_3$NH][(H$_2$L)Dy^{III}Cl$_2$] (where H$_4$L = 2,6-diacetylpyridine *bis*-salicylhydrazone), which was shown to be a single-ion magnet.[12] Encouraged by this we wished to design flexible polydentate ligands that can be used for preparing mononuclear lanthanide complexes. However, one of the difficulties with this approach is that often, multidentate ligands having phenolate/enolate and/or alkoxide functionalities are precisely those that are suitable to bind to lanthanide metal ions but are often unsuitable for isolation of mononuclear Ln^{III} complexes. To overcome this synthetic hurdle we reasoned that the introduction of an electron withdrawing substituent such as an –NO$_2$ group in the ligand backbone, might effectively reduce the bridging ability of the phenolate group and thereby increase the chances of isolating mononuclear complexes.

Accordingly, herein, we report the synthesis, structure and magnetic properties of a new family of mononuclear Ln^{III} complexes, Ln(NO$_3$)(L)$_2$(HOCH$_3$)]·xCH$_3$OH (Ln = Gd, (**3.A.1**); Tb, (**3.A.2**); Dy, (**3.A.3**); and Ho, (**3.A.4**)) utilizing a tridentate *NNO* donor ligand, 4-nitro-2-((2-(pyridine-2-yl)hydrazono)methyl)phenol (HL). These complexes were formed by the reaction of HL with lanthanide nitrates in the presence of triethylamine in methanolic medium. Interestingly, we have found that the same ligand that does not contain the –NO$_2$ group under similar reaction conditions produces [Dy$_5$(L)$_4$(NO$_3$)$_5$(HOMe)$_2$(O$_2$)$_2$(H$_2$O)$_4$]·(NO$_3$)$_2$·(H$_2$O)$_2$ complex (Figure 3.A.1), where the bridging coordination action of the phenolate group is clearly evident. Figure 3.A.2, displays other examples of 3d/4f and lanthanide complexes obtained by using ligands similar to those used in the present study.[13] This underscores the electronic effects that need to be built into ligands for modulating the nuclearity of complexes. The magnetic properties of **3.A.1-3.A.4** were studied and are discussed herein.
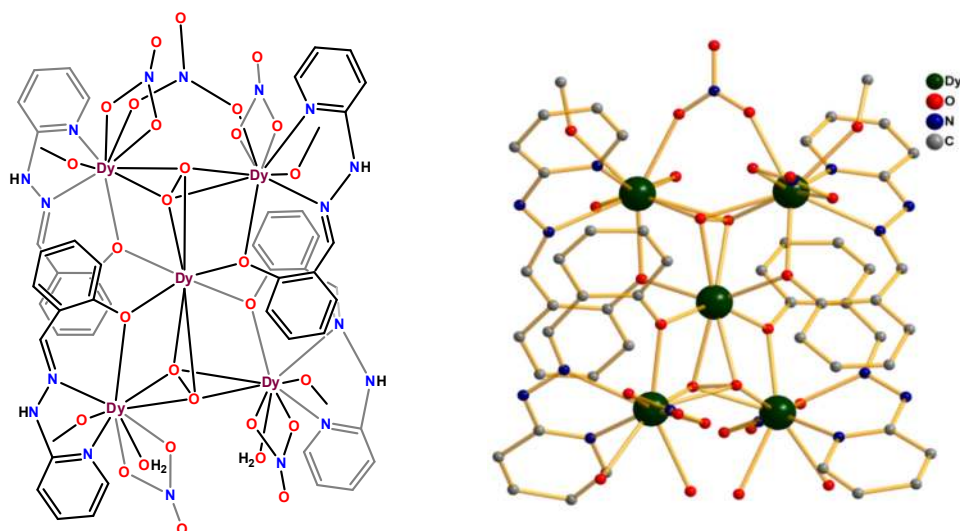
Figure 3.A.1. Line diagram (*left*) and Molecular structure (*right*) of the complex $[Dy_5(L)_4(NO_3)_5(HOMe)_2(O_2)_2(H_2O)_4]^{2+}$ (H-atoms and counter anions are omitted for clarity)
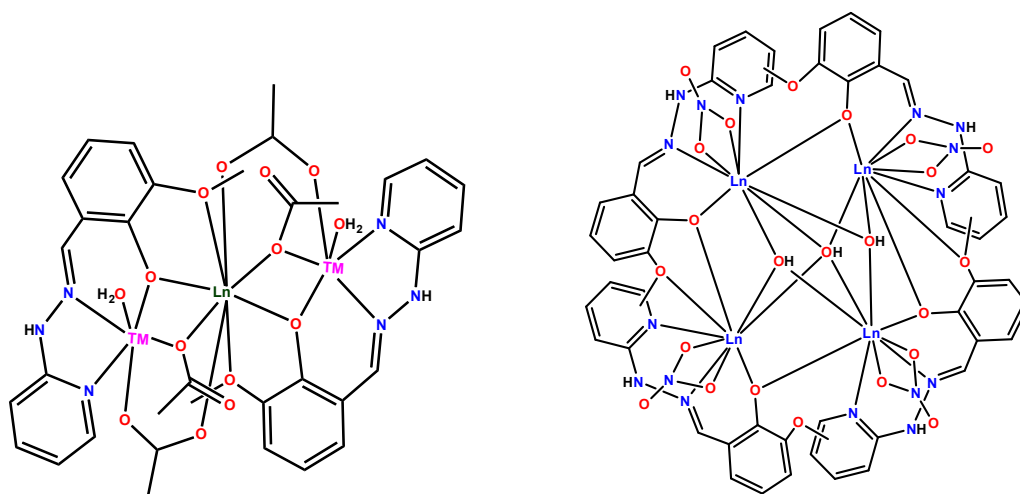
Figure 3.A.2. Bridging coordination action of phenolate ligand. A linear trimeric 3d-4f complex (*left*).[13b] A Ln$_4$ complex in a see-saw geometry (*right*).[13a]

3.A.2 EXPERIMENTAL SECTION

3.A.2.1 Materials and Methods. The solvents and other general reagents used in this work were received from commercial sources and used without further purification. 2-Hydroxy-5-nitrobenzaldehyde, 2-hydrazino pyridine, Gd(NO$_3$)$_3$·6H$_2$O,

$Tb(NO_3)_3 \cdot 5H_2O$, $Dy(NO_3)_3 \cdot 5H_2O$, $Ho(NO_3)_3 \cdot 5H_2O$ were obtained from the Sigma Aldrich Chemical Co. (India) and used as obtained. 2-Hydroxy benzaldehyde and NEt_3 were obtained from the Spectrochem Pvt. Ltd. (India). The ligand 4-nitro-2-((2-(pyridine-2-yl)hydrazono)methyl)phenol (HL) was prepared by an adaptation of a literature procedure.[14]

3.A.2.2 Instrumentation. Melting points were measured using a Stuart™ SMP10 melting point apparatus and are uncorrected. ^1H NMR and $^{13}C\{^1H\}$ NMR spectra were recorded on a Bruker Ascend-300 (^1H: 300 MHz; $^{13}C\{^1H\}$: 75 MHz) and were referenced to the resonances of the solvent used. IR spectra were recorded on a PerkinElmer FT-IR spectrometer. Mass spectra were recorded with a Bruker micrOTOF-Q II spectrometer. Elemental analyses of the compounds were obtained from a Euro Vector EA instrument (CHNS-O, model EuroEA3000). Powder X-ray diffraction data of all the complexes were collected with a Bruker D8 Advance X-ray Powder Diffractometer using CuKα radiation ($\lambda = 1.5418$ Å).

3.A.2.3 Magnetic Measurements. Direct (dc) and alternating (ac) current susceptibility measurements were performed with a Quantum Design SQUID MPMS XL-5 device. Ac experiments were performed using an oscillating ac field of 3.5 Oe and frequencies ranging from 1 to 1500 Hz. The experimental susceptibilities were corrected for the sample holder and diamagnetic contributions. Pellets of the different samples were cut into small pieces and placed in the sample holder to avoid any orientation of the microcrystals by the magnetic field.

3.A.2.4 X-ray Crystallography. Single crystal X-ray structural studies of **3.A.1** was performed on a Bruker Apex II CCD diffractometer system equipped with graphite-monochromated MoKα radiation ($\lambda_\alpha = 0.71073$ Å) at 100 K. The program SMART

was used for collecting frames of data, indexing reflections, and determining lattice parameters, and SAINT for integration of the intensity of reflections and scaling.[15] Absorption correction was performed by multi-scan method implemented in SADABS.[16] Space groups were determined using XPREP implemented in APEX2.[17] The single crystal X-ray diffraction data of **3.A.2**-**3.A.3** were collected on a Rigaku Xtal LAB X-ray diffractometer system equipped with a CCD area detector and operated at 30 W power (50 kV, 0.6 mA) to generate MoKα radiation ($\lambda = 0.71073$ Å) at 120 K for **3.A.3** and 173 K for **3.A.2** and **3.A.4** respectively. Data were integrated using CrysAlis[Pro] software with a narrow frame algorithm.[18] Data were subsequently corrected for absorption by the program SCALE3 ABSPACK scaling algorithm.[18] All the structures were solved by the direct methods in ShelXT[19] and refined by the full-matrix least-squares method on F^2 (ShelXL-2014)[20] using the Olex-2[21] software. All the non-hydrogen atoms were refined with anisotropic thermal parameters. All the hydrogen atoms were included in idealized positions, and a riding model was used. All the mean plane analyses and crystallographic figures have been generated using DIAMOND software (version 3.2k).[22]

3.A.4.5 Synthesis of Ligand HL. A methanolic solution of 2-hydrazino pyridine (600 mg, 5.45 mmol) was taken in a 100 ml round bottom flask and stirred for ten minutes. To it a methanolic solution of 2-hydroxy-5-nitro benzaldehyde (900 mg, 5.38 mmol) was added. The solution was then heated to reflux for 6 hours. During this time a yellow colored precipitate was obtained. After cooling, the precipitate was filtered out and washed with cold methanol followed by diethyl ether. The precipitate was finally dried under vacuum and the product was obtained in 92% yield (1.3 g). The melting point and other experimental characterization data are as follows: M.P.: 240 $^{\circ}$C. IR (KBr ν/cm^{-1}): 1606(s), 1520(m), 1482(m), 1442(s), 1348(s), 1303(s), 1170(m),

1096(m), 994(w), 924(m), 828(m), 772(m), 718(w), 638(w). ^{1}H NMR (DMSO-d_6, δ,

ppm): 11.09 (s, 1H, N-H), 8.49 (d, 1H, Ar-H), 8.25 (s, 1 H, imine H), 8.09 (dd, 1H,

Ar-H), 7.66-7.60 (m, 1H, Ar-H), 7.10 (d, 1H, Ar-H), 7.00 (d, 1H, Ar-H), 6.77-6.73

(m, 1H, Ar-H). ESI-MS (m/z) (M + H$^+$) = 259.0881.
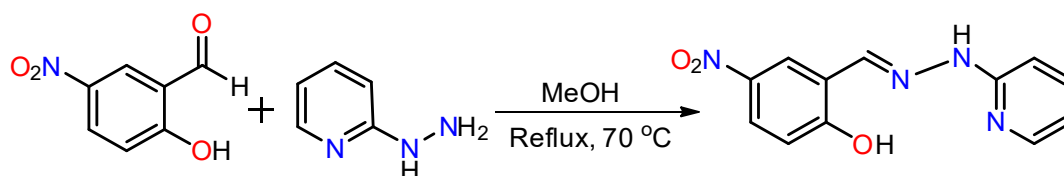
Scheme 3.A.1. Synthesis of the ligand HL.
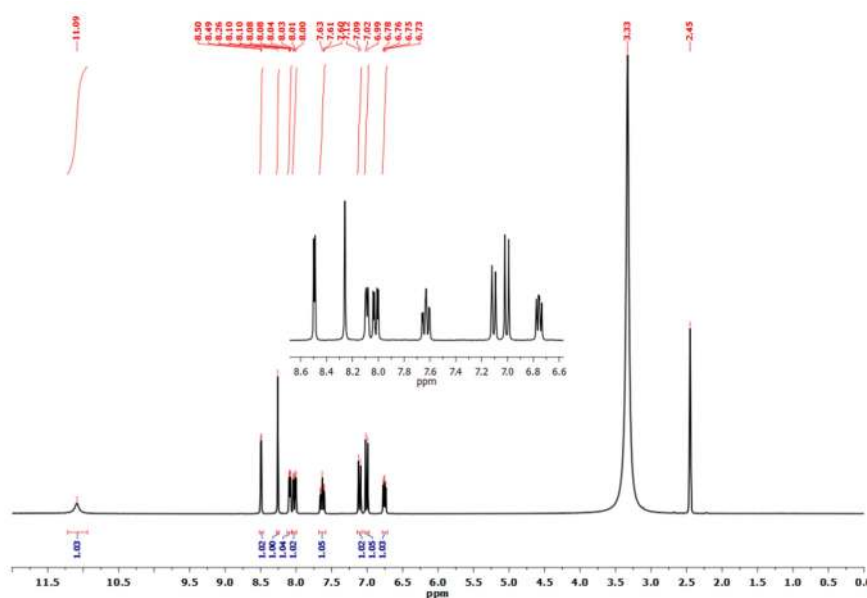
Figure 3.A.3. ^{1}H NMR spectra of ligand HL in DMSO-d_6 solvent. (The peaks

observed at 3.33 ppm and 2.45 ppm is due to the residual solvents)
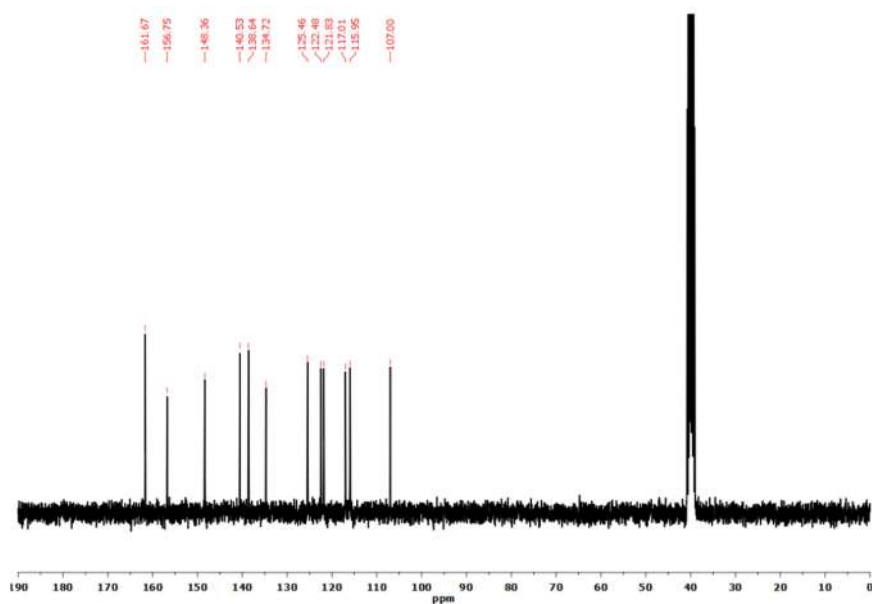
Figure 3.A.4. $^{13}C\{^1H\}$ NMR spectra of ligand HL in a DMSO-d_6 solvent. (The peak observed at 40 ppm is due to the residual solvent)
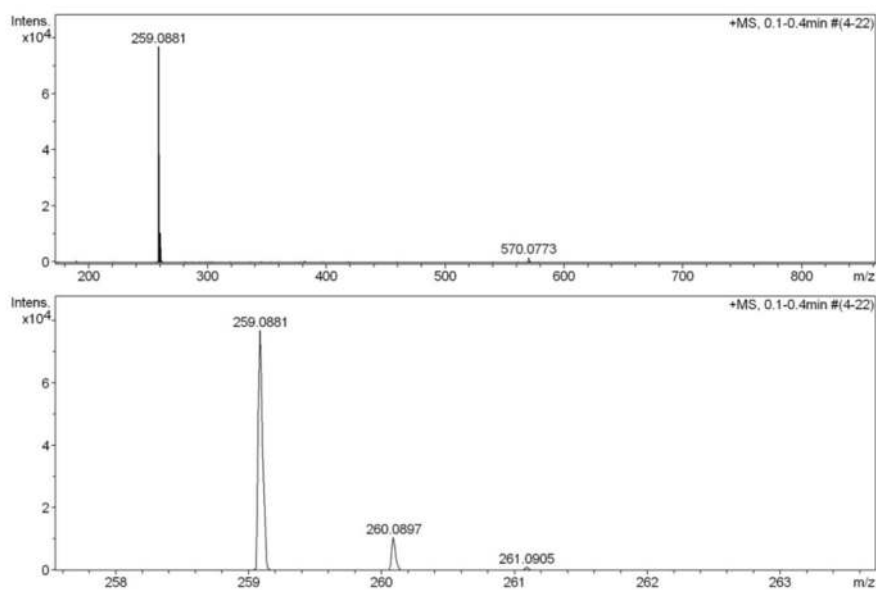
Figure 3.A.5. ESI-MS of ligand HL.

3.A.4.6 Synthesis of complexes 3.A.1-3.A.4. The following general synthetic protocol was used for the preparation of the metal complexes (**3.A.1-3.A.4**): a methanolic solution (5 mL) of $Ln(NO_3)_3 \cdot xH_2O$ (1 eq.) (n = 5 for **3.A.2-3.A.4** and 6 for

3.A.1) was added drop wise to a 15 mL methanolic solution containing a mixture of HL (1 eq.) and triethylamine (1 eq.) with constant stirring. The resultant deep orange colored solution was stirred further for 12 h. The volume of the solution was reduced to 10 mL, filtered, and kept undisturbed for crystallization under ambient conditions. Slow evaporation of the solvent afforded brick red, block-shaped crystals suitable for single crystal X-ray analysis after 2-3 days. The crystal structure analysis showed three MeOH molecules as solvent of crystallization and the magnetic measurements are analyzed accordingly. However, the elemental analyses do not agree with the presence of MeOH molecules, rather it matches quite well with water molecules. This is presumably due to the exchange of labile lattice solvent molecules with water under atmospheric conditions. The stoichiometry of the reactants involved in each reaction, yield of the products, and their characterization data are provided below.

[Gd(NO₃)(L)₂(HOCH₃)] (**3.A.1**). HL (0.060 g, 0.232 mmol), Gd(NO₃)₃·6H₂O (0.104 g, 0.232 mmol), and Et₃N (32 μL, 0.232 mmol)) were used. Yield: 0.082 g, 41% (based on Gd). M.P.: >250 °C. IR (KBr ν/cm⁻¹): 3445(br), 3284 (w), 3059 (w) 1619 (s), 1595(m), 1548(s), 1487(s), 1419(s), 1383(s), 1309(s), 1244(s), 1197(w), 1158(w), 1134(m), 1099(s), 999(m), 948(m), 897(m), 836(m), 764(m), 736(w), 709(m), 644(m), 550(w). Anal. Calcd (%) for $C_{25}H_{29}N_9O_{14}$ Gd (836.79): C, 35.88; H, 3.49; N, 15.06. Found: C, 35.28; H, 3.22; N, 15.38. ESI-MS m/z, ion (-ve mode): 796.0579, $[\{(L)_2Gd(NO_3)\}_2]^{2-}$

[Tb(NO₃)(L)₂(HOCH₃)] (**3.A.2**). HL (0.06 g, 0.232 mmol), Tb(NO₃)₃·5H₂O (0.101 g, 0.232 mmol), Et₃N (32 μL, 0.232 mmol) were used. Yield: 0.080 g, 40% (based on Tb). M.P.: >250 °C. IR (KBr ν/cm⁻¹): 3445(br), 3281(w), 3059(w) 1625(s), 1595(m), 1548(s), 1487(s), 1421(s), 1381(s), 1305(s), 1245(s), 1197(w), 1158(w), 1134(m), 1097(s), 999(m), 950(m), 895(m), 836(m), 764(m), 736(w), 709(m), 643(m), 554(w).

Anal. Calcd (%) for $C_{25}H_{29}N_9O_{14}Tb$ (765.75): C, 35.81; H, 3.49; N, 15.03. Found: C, 35.54; H, 3.41; N, 15.29. ESI-MS m/z, ion (-ve mode): 797.0359, $[(L)_2Tb(NO_3)_2]^-$.

[Dy(NO₃)(L)₂(HOCH₃)] (**3.A.3**). HL (0.060 g, 0.232 mmol), $Dy(NO_3)_3 \cdot 5H_2O$ (0.102 g, 0.232 mmol), Et_3N (32 μL, 0.232 mmol) were used. Yield: 0.086 g, 43% (based on Dy). M.P.: >250 °C. IR (KBr ν/cm^{-1}): 3451(br), 3282(w), 3059(w), 1619(s), 1597(m), 1552(s), 1489(s), 1419(s), 1383(s), 1309(s), 1246(s), 1197(w), 1158(w), 1132(m), 1097(s), 1001(m), 950(m), 897(m), 838(m), 773(m), 736(w), 711(m), 646(m), 553(w). Anal. Calcd (%) for $C_{25}H_{22}N_9O_{10}Dy$ (765.75): C, 35.66; H, 3.47; N, 14.97. Found: C, 35.88; H, 3.29; N, 15.55. ESI-MS m/z, ion (+ve mode): 678.0537, $[(L)_2Dy]^+$.

[Y₀.₈₅Dy₀.₁₅(NO₃)(L)₂(HOCH₃)] (**3.A.3'**). HL (0.060 g, 0.232 mmol), $Y(NO_3)_3 \cdot 6H_2O$ (0.075 g, 0.196 mmol), $Dy(NO_3)_3 \cdot 5H_2O$ (0.016 g, 0.036 mmol), Et_3N (32 μL, 0.232 mmol) were used. Anal. Calcd (%) for $C_{25}H_{29}N_9O_{19}Dy_{0.15}Y_{0.85}$ (805.25): C, 37.29; H, 3.63; N, 15.65. Found: C, 37.03; H, 3.51; N, 16.33.

[Ho(NO₃)(L)₂(HOCH₃)] (**3.A.4**). HL (0.060 g, 0.232 mmol), $Ho(NO_3)_3 \cdot 5H_2O$ (0.102 g, 0.232 mmol), Et_3N (32 μL, 0.232 mmol) were used. Yield: 0.079 g, 39% (based on Ho). M.P.: >250 °C. IR (KBr ν/cm^{-1}): 3443(br), 3284(w), 3059(w) 1621(s), 1595(m), 1548(s), 1487(s), 1421(s), 1381(s), 1305(s), 1244(s), 1197(w), 1158(w), 1134(m), 1097(s), 999(m), 950(m), 899(m), 836(m), 764(m), 736(w), 709(m), 642(m), 554(w). Anal. Calcd for $C_{25}H_{31}N_9O_{15}Ho$ (862.49): C, 34.81; H, 3.62; N, 15.24. Found: C, 34.61; H, 3.11; N, 15.24. ESI-MS m/z, ion: 679.0652, $[C_{24}H_{18}N_8O_6Ho]^+$. ESI-MS m/z, ion (+ve mode): 679.0551, $[(L)_2Ho]^+$.

3.A.3 RESULTS AND DISCUSSION

3.A.3.1 Synthetic Aspects. The coordination requirements of lanthanide metal ions can be met by utilizing polydentate ligands. In the current instance we prepared a tridentate *NNO* donor Schiff base ligand bearing a nitro group in the *para*-position of the phenolic moiety. This ligand when reacted with lanthanide nitrates in the presence of one equivalent of triethylamine resulted in the formation of mononuclear complexes. The presence of electron withdrawing group in the ligand backbone reduces the bridging ability of the phenoxide moiety and allowed us to isolate exclusively a new family of mononuclear complexes, $[Ln(NO_3)(L)_2(HOCH_3)]$. ($Ln =$ Gd, Tb, Dy, and Ho) (Scheme 3.A.2). The coordination of two ligands to the Dy^{III} ions could lead to a disposition of donor atoms where the phenoxide oxygen atoms, which should have the shortest Dy−O distances, would be located in (almost) opposite sides of the Dy^{III} coordination sphere. This donor distribution around the Dy^{III} ion would create an axial ligand field, which favors an axial ground Kramers doublet (KD) and then the SIM behaviour.
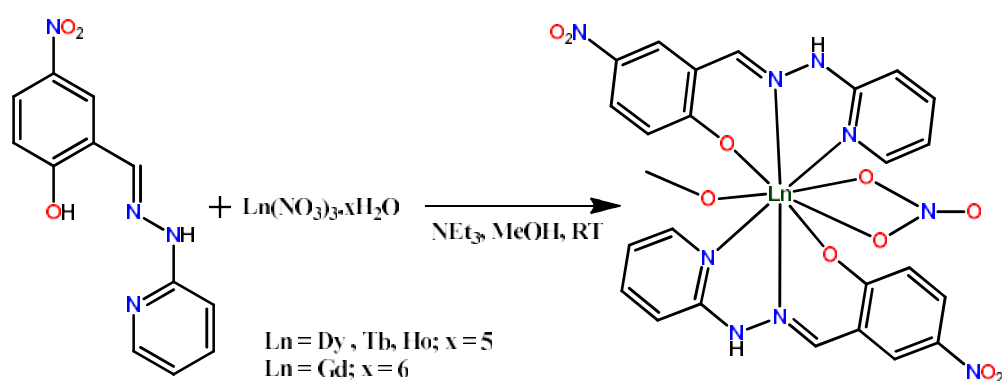
Scheme 3.A.2. Synthesis of the mononuclear complexes **3.A.1-3.A.4**.

The structural integrity of **3.A.1-3.A.4** in solution was investigated by carrying out ESI-MS studies in CH_3OH/CH_3CN solvent (1:1 v/v) which revealed the peaks at m/z:

796.0579, 797.0359, 678.0537, and 679.0652 corresponding to the mono-cationic/anionic species, $[\{(L)_2Gd(NO_3)\}_2]^{2-}$ (Figure 3.A.6), $[(L)_2Tb(NO_3)_3]^-$ (Figure 3.A.7), $[(L)_2Dy]^+$ (Figure 3.A.8), and $[(L)_2Ho]^+$ (Figure 3.A.9) respectively.

(a)

(b)

(c)
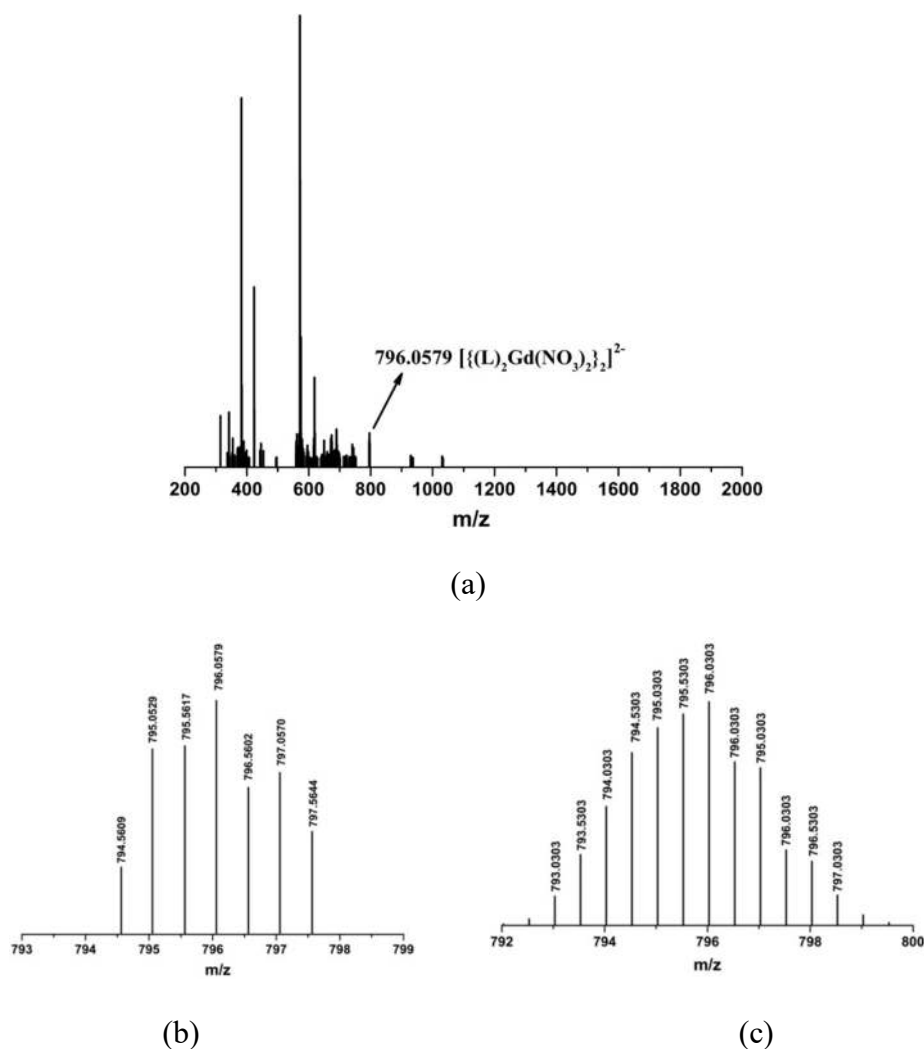
Figure 3.A.6. (a) Full range ESI-MS spectrum of complex **3.A.1**. (b) Experimental and (c) Simulated pattern of $[\{(L)_2Gd(NO_3)\}_2]^{2-}$.

(a)

(b)   (c)
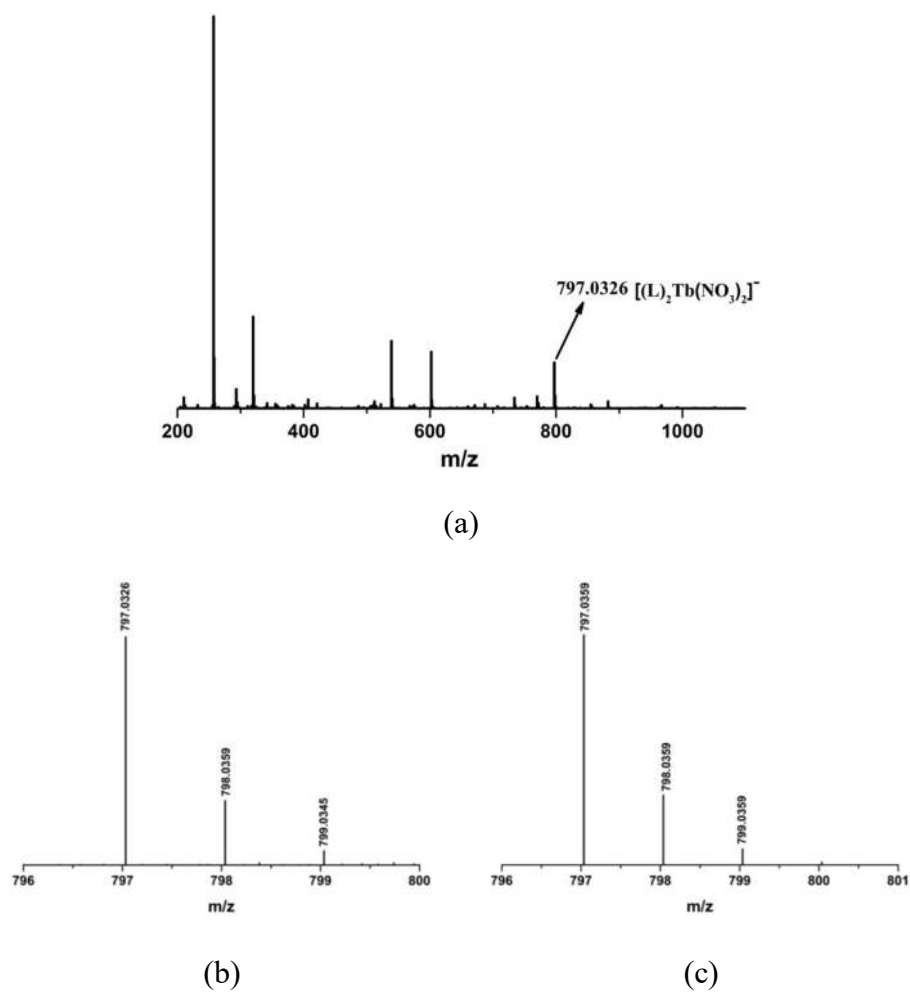
Figure 3.A.7. (a) Full range ESI-MS spectrum of complex **3.A.2**. (b) Experimental and (c) simulated mass spectral pattern of $[(L)_2Tb(NO_3)_3]^-$.

(a)

(b)   (c)
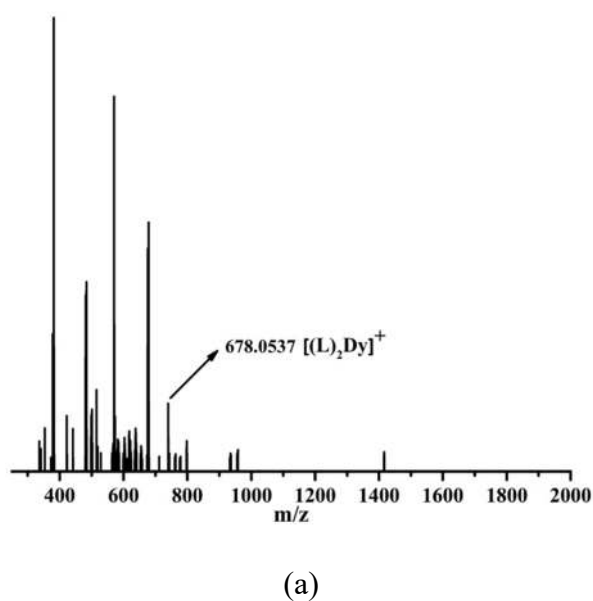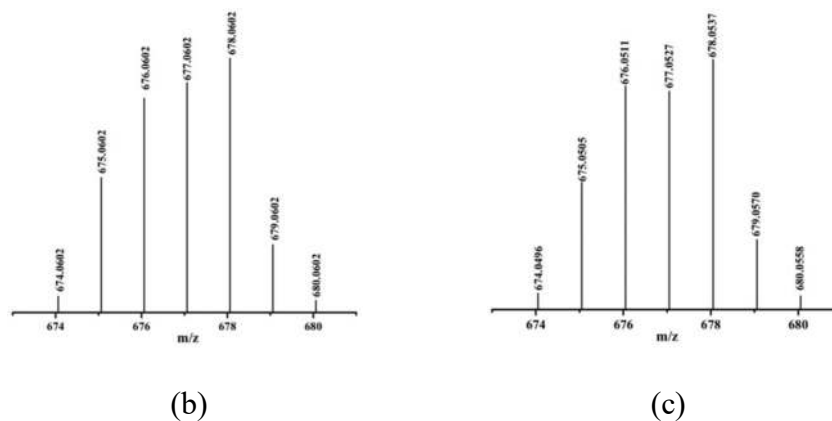
Figure 3.A.8. (a) Full range ESI-MS spectrum of complex **3.A.3**. (b) Experimental and (c) Simulated pattern of $[(L)_2Dy]^+$

679.0551 $[(L)_2Ho]^+$

(a)

(b)   (c)
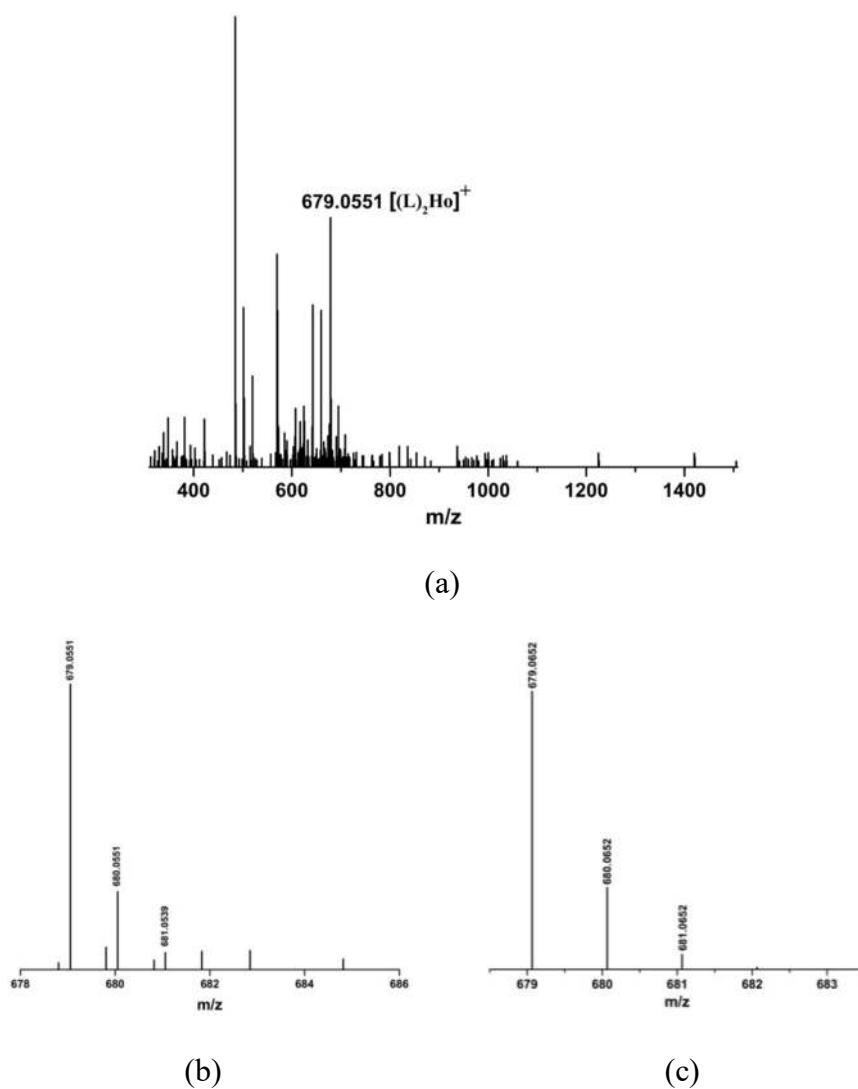
Figure 3.A.9. (a) Full range ESI-MS spectrum of complex **3.A.4**. (b) Experimental and (c) Simulated pattern of $[(L)_2Ho]^+$.

3.A.3.2 Molecular Structures. The molecular structures of the mononuclear lanthanide complexes **3.A.1**-**3.A.4** were confirmed by single crystal X-ray diffraction studies. The crystal data and refinement parameters for **3.A.1**-**3.A.4** are summarized in Table 3.A.1.

Table 3.A.1. Details of the data collection and refinement parameters for **3.A.1**-**3.A.4**

	3.A.1	**3.A.2**	**3.A.3**	**3.A.4**
Chemical formula	$C_{28}H_{34}GdN_9O_{13}$	$C_{28}H_{34}N_9O_{13}Tb$	$C_{28}H_{34}DyN_9O_{13}$	$C_{28}H_{34}HoN_9O_{13}$
M_w/g mol^{-1}	861.89	863.56	867.14	869.57
Crystal system	Triclinic	Triclinic	Triclinic	Triclinic
Space group	P-1	P-1	P-1	P-1
Temperature (K)	100(2)	173.00(10)	120.10(10)	172.99(10)
a, b, c (Å)	11.2570(4) 11.7166(4) 13.7355(5)	11.3219(3) 11.7730(3) 13.7532(4)	11.3165(3) 11.6740(4) 13.7042(2)	11.3398(4) 11.7893(4) 13.7166(3)
α, β, γ (°)	94.1350(10) 104.9910(10) 105.1770(10)	93.856(2) 105.196(3) 105.168(3)	94.491(2) 105.765(2) 105.073(3)	93.941(2) 105.350(3) 105.348(3)
V (Å^3)	1669.83(10)	1689.22(9)	1660.64(8)	1650.5(8)
Z	2	2	2	2
ρ_c/g cm^{-3}	1.714	1.698	1.734	1.713
μ (mm^{-1})	2.065	2.172	2.329	2.425
F (000)	866.0	868.0	870.0	872.0
Crystal size (mm)	0.2 × 0.15 × 0.12	0.19 × 0.13 × 0.09	0.3 × 0.22 × 0.06	0.15 × 0.10 × 0.08
2θ range (°)	4.238 to 56.812	5.642 to 57.988	5.132 to 52.998	5.66 to 57.904
Limiting indices	-15 ≤ h ≤ 15, -15 ≤ k ≤ 15, -18 ≤ l ≤ 18	-12 ≤ h ≤ 15, -15 ≤ k ≤ 14, -17 ≤ l ≤ 17	-13 ≤ h ≤ 14, -14 ≤ k ≤ 14, -17 ≤ l ≤ 17	-15 ≤ h ≤ 14, -15 ≤ k ≤ 15, -17 ≤ l ≤ 16
Reflections collected	25879	30176	31915	34416
Unique reflections	8367 [R_{int} = 0.0500]	7845 [R_{int} = 0.0528]	6862 [R_{int} = 0.0628]	7858 [R_{int} = 0.0380]
Completeness to θ	99.7 % (28.406°)	99.7 % (25.242°)	99.7 % (26.499°)	99.4 % (25.026°)
Refinement method	full-matrix least-squares on F^2	full-matrix least-squares on F^2	full-matrix least-squares on F^2	full-matrix least-squares on F^2

Data/Restraints/ Parameters	8367/4/474	7845/4/481	6862/10/470	7858/4/481
GOF on F^2	1.066	1.032	1.023	1.046
R indices (all data)	$R_1 = 0.0401$, $wR_2 = 0.0714$	$R_1 = 0.0314$, $wR_2 = 0.0594$	$R_1 = 0.0432$, $wR_2 = 0.0874$	$R_1 = 0.0258$, $wR_2 = 0.0470$
Final R indices [I >2σ (I)]	$R_1 = 0.0538$, $wR_2 = 0.0889$	$R_1 = 0.0275$, $wR_2 = 0.0582$	$R_1 = 0.0361$, $wR_2 = 0.0844$	$R_1 = 0.0230$, $wR_2 = 0.0479$
$\Delta\rho_{max}$, $\Delta\rho_{min}$ (e Å^{-3})	1.29, -0.78	1.35, -0.87	2.74, -1.24	0.57, -0.49
$R_1 = \sum|F_0 - F_c|/\sum F_0$; $wR_2 = \sum[w(F_0^2 - F_0^2)]^2/[w(F_0^2)^2]^{\frac{1}{2}}$				

All the complexes are neutral, isostructural and crystallized in the triclinic *P*-1 space group (Z = 2). In view of their structural similarity, we have chosen complex **3.A.3** as a representative example to elucidate the common structural features present in them. A perspective view of the molecular structure of **3.A.3** is shown in Figure 3.A.10, while those of **3.A.1**, **3.A.2**, and **3.A.4** are shown in the Figures 3.A.11-3.A.13.
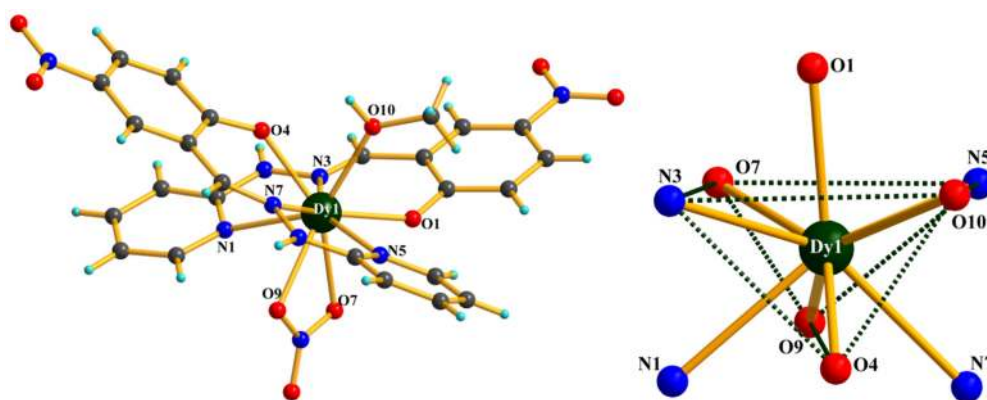
Figure 3.A.10. Molecular structure of complex **3.A.3** (*left*). The immediate coordination environment around dysprosium is shown in the right.

The mononuclear complex **3.A.3** is formed by the coordination action of two mono deprotonated ligands, [L]⁻, a nitrate anion and a methanol molecule. Both the tridentate [L]⁻s bind to the lanthanide center through the phenolate oxygen, the imino nitrogen and the pyridinic nitrogen. This results in the formation of a five-and a six-

membered ring containing the lanthanide center. The nitrate anion coordinates to the metal center through a chelating coordination mode. Finally, a neutral methanol molecule completes the coordination around the lanthanide. The overall coordination number around the lanthanide center is nine (4N, 5O) and the coordination geometry is spherical tricapped trigonal prism as confirmed by the SHAPE analysis.[23] The SHAPE analysis parameters of **3.A.1-3.A.4** are given in Table 3.A.2. The bond parameters around the lanthanide center of **3.A.3** are the following. *(1)* Involving [L]⁻: O1, O4; Dy−O average distance 2.279(3) Å; N1, N5; Dy−N average distance, 2.547(3) Å; N3, N7; Dy−N average distance, 2.530(3) Å, *(2)* The chelating nitrate ion: O7, O9; Dy−O average distance, 2.500(3) Å. *(3)* the solvent methanol: Dy−O10, 2.413(3) Å, (Figure 3.A.10 and Table 3.A.3). Selected bond distance and angle parameters of **3.A.1-3.A.4** are tabulated in Table 3.A.3.

Figure 3.A.11. Molecular structure of complex **3.A.1**.
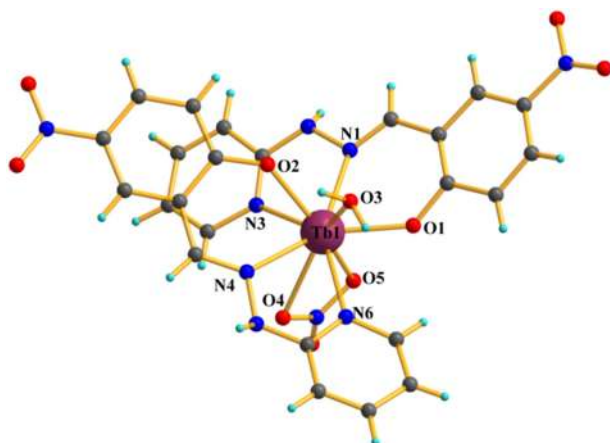
Figure 3.A.12. Molecular structure of complex **3.A.2**.
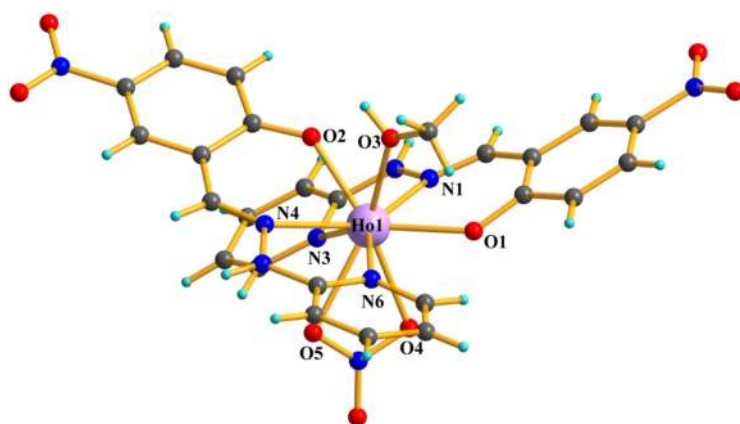
Figure 3.A.13. Molecular structure of complex **3.A.4**.

Table 3.A.2. Continuous Shape Measures (CShM) calculations for Ln^{III}

Complex_ Metal center	Structure[†]								
	JTC-9	JCCU -9	CCU -9	JCSA PR-9	CSAPR -9	JTCT PR-9	**TCTP R-9**	HH-9	MFF -9
3.A.1_Gd CShM	17.21 4	9.234	6.93 0	3.577	1.849	4.111	**1.520**	10.296	2.147
3.A.2_Tb CShM	16.27 4	9.613	7.98 9	2.811	2.051	4.027	**1.373**	10.340	2.135
3.A.3_Dy CShM	17.02 5	9.252	6.96 6	3.442	1.822	3.960	**1.488**	10.246	2.198
3.A.4_Ho CShM	17.01 6	9.307	7.07 2	3.414	1.793	3.894	**1.405**	10.338	2.154

†*JTC-9 = Johnson triangular cupola J3 (C_{3v}); JCCU-9= Capped cube J8 (C_{4v}); CCU-9 = Spherical-relaxed capped cube (C4v); JCSAPR-9 = Capped square antiprism J10 (C_{4v}); CSAPR-9 = Spherical capped square antiprism (C_{4v}); JTCTPR-9 = Tricapped trigonal prism J51 (D_{3h}); TCTPR-9 = Spherical tricapped trigonal prism (D_{3h}); HH-9 = Hula-hoop (C_{2v}); MFF-9 = Muffin (C_s)*

In the crystal, centrosymmetrically related molecules are hold together by two sets of complementary hydrogen bonds giving rise to a zigzag 1-D system with two different Dy···Dy distances along the chain (Figure 3.A.14). The first set involves one of the oxygen atoms of the nitro group and the coordinated methanol molecule with a donor-acceptor O···O distance of 2.801 Å. The second set, at the opposite side of the molecule, involves a methanol molecule and the oxygen atoms O7 and O1 belonging to the nitrate anion and phenoxide groups, respectively, and the N2 atom of the hydrazone group. In this trifurcated hydrogen bond, the O···O donor acceptor distances are 3.172 Å and 3.000 Å, respectively, and an N···O distance is 2.817 Å. These first and second set of hydrogen bonds give rise to Dy···Dy distances of 11.145 Å and 7.635 Å, respectively (see Figure 3.A.15). The other two methanol molecules of crystallization form a hydrogen bond between themselves with a O···O distance of 2.742 Å and one of them forms an additional hydrogen bonds with the O4 phenoxido oxygen atom with a O···O distance of 2.872 Å. The chains are isolated in the structure by the methanol molecules of crystallization with a shortest Dy···Dy inter-chain distance of 8.351 Å.
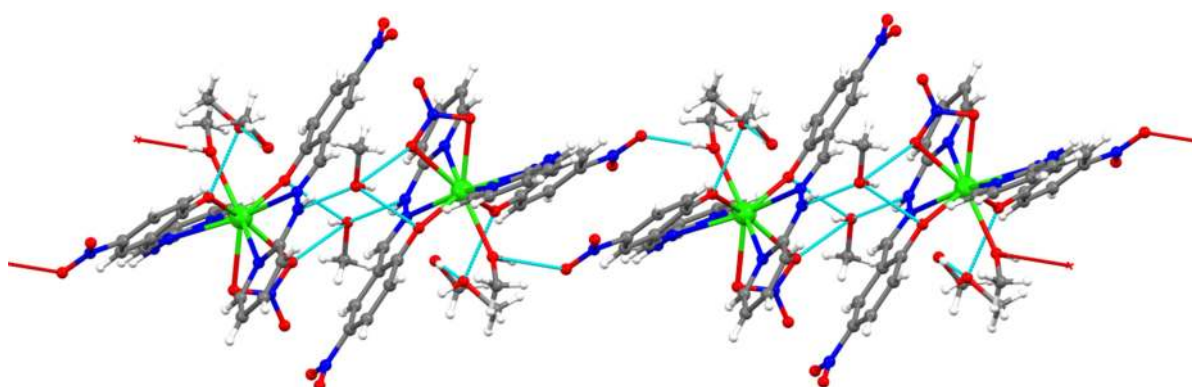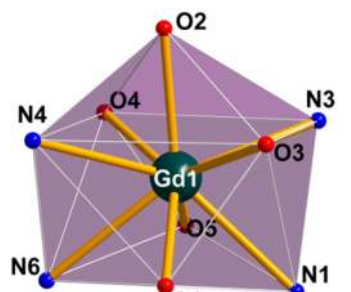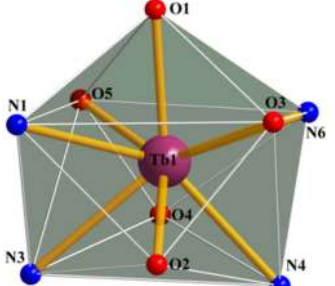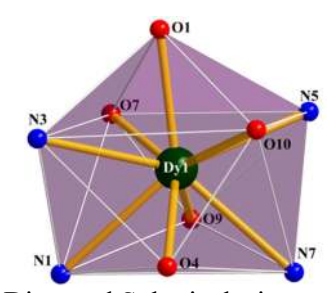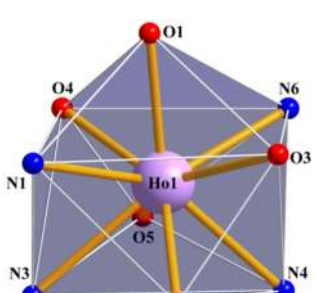
Figure 3.A.14. H-bonded one dimensional zigzag chain of complex **3.A.3**.
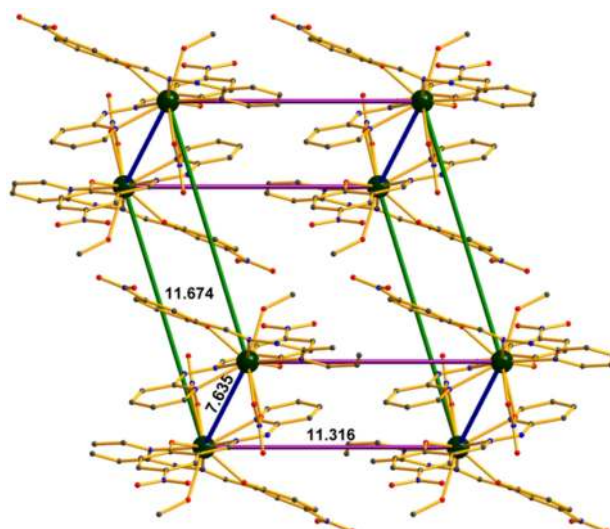
Figure 3.A.15. A perspective view (*c* direction) of the crystal packing diagram of complex **3.A.3**. (H atoms and interstitial solvent molecules are omitted for clear visibility)

Table 3.A.3. Selected bond lengths (Å) and angles (°) of complexes **3.A.1-3.A.4**

Coordination Geometry	Bond lengths (Å)		Bond angles (°)	
 Distorted Spherical tricapped trigonal prism geometry of *Gd1* in complex **3.A.1**	Gd1–O1	2.330(2)	O2–Gd1–N1	138.67(9)
	Gd1–O2	2.284(2)	O2–Gd1–N6	124.76(9)
	Gd1–O5	2.538(3)	O1–Gd1–N3	125.69(9)
	Gd1–O3	2.434(3)	O3–Gd1–N1	81.35(10)
	Gd1–O4	2.474(3)	O4–Gd1–O5	50.96(9)
	Gd1–N1	2.556(3)	O4–Gd1–N3	84.78(10)
	Gd1–N3	2.554(3)	O5–Gd1–N3	69.82(9)
	Gd1–N4	2.555(3)	O5–Gd1–N6	72.15(9)
	Gd1–N6	2.562(3)	N3–Gd1–N6	141.46(10)
	Gd1–N7	2.942(3)	N4–Gd1–N7	105.42(10)
			N1–Gd1–N7	92.92(10)
			N6–Gd1–N7	71.90(9)

Distorted Spherical tricapped trigonal prism geometry of *Tb1* in complex **3.A.2**	Tb1–O1	2.298(13)	O1–Tb1–O4	115.2(4)
	Tb1–O2	2.335(12)	O1–Tb1–O3	72.9(4)
	Tb1–N6	2.569(14)	O2–Tb1–N6	125.7(4)
	Tb1–N4	2.568(16)	O2–Tb1–O4	121.2(4)
	Tb1–N3	2.657(15)	N6–Tb1–N3	136.6(5)
	Tb1–O4	2.702(15)	N4–Tb1–N1	143.1(5)
	Tb1–O5	2.533(15)	N3–Tb1–O4	68.1(4)
	Tb1–N1	2.577(17)	O5–Tb1–N4	118.4(5)
	Tb1–O3	2.513(13)	N1–Tb1–N3	64.7(5)
			N1–Tb1–O4	119.5(5)
			O3–Tb1–N6	74.8(4)
			O3–Tb1–N4	81.1(4)
Distorted Spherical tricapped trigonal prism geometry of *Dy1* in complex **3.A.3**	Dy1−O1	2.256(3)	O1−Dy1−N7	138.54(11)
	Dy1−O4	2.302(3)	O4−Dy1−O9	117.89(10)
	Dy1−O10	2.413(3)	O4−Dy1−N9	134.75(10)
	Dy1−O9	2.550(3)	O10−Dy1−N3	93.75(11)
	Dy1−O7	2.448(3)	O10−Dy1−N9	153.33(10)
	Dy1−N5	2.535(3)	O7−Dy1−O9	51.05(10)
	Dy1−N7	2.530(3)	O7−Dy1−N5	83.38(11)
	Dy1−N3	2.530(3)	N3−Dy1−O9	123.71(11)
	Dy1−N1	2.559(4)	N7−Dy1−O9	67.89(11)
	Dy1−N9	2.931(4)	N5−Dy1−N9	75.79(11)
			O9−Dy1−N1	71.30(11)
			N1−Dy1−N9	71.45(11)
Distorted Spherical tricapped trigonal prism geometry of *Ho1* in complex **3.A.4**	Ho1–O2	2.290(10)	O1–Ho1–O4	71.3(4)
	Ho1–O3	2.397(10)	O1–Ho1–N4	138.5(4)
	Ho1–O5	2.524(10)	O2–Ho1–N6	127.0(4)
	Ho1–O1	2.258(9)	O3–Ho1–O5	142.2(3)
	Ho1–O4	2.437(10)	O3–Ho1–O4	143.6(3)
	Ho1–N7	2.903(15)	O4–Ho1–O5	51.0(3)
	Ho1–N6	2.513(12)	O4–Ho1–N7	25.9(3)
	Ho1–N3	2.538(12)	N1–Ho1–N6	147.8(4)
	Ho1–N4	2.517(10)	N1–Ho1–N3	64.7(4)
	Ho1 N1	2.505(11)	N6–Ho1–O5	69.7(4)
			N4–Ho1–N7	93.4(4)
			O5–Ho1–N7	25.2(3)

In order to study the magnetic properties of **3.A.3** under dilute conditions, an analogous complex **3.A.3'** was prepared with 15% Y^{III} sites replaced by Dy^{III} ions in the isostructural Y^{III} host. This is confirmed by the powder X-ray diffraction study which show good agreement of the experimental patterns of **3.A.3'** with the simulated patterns of **3.A.3** generated from the SCXRD data.
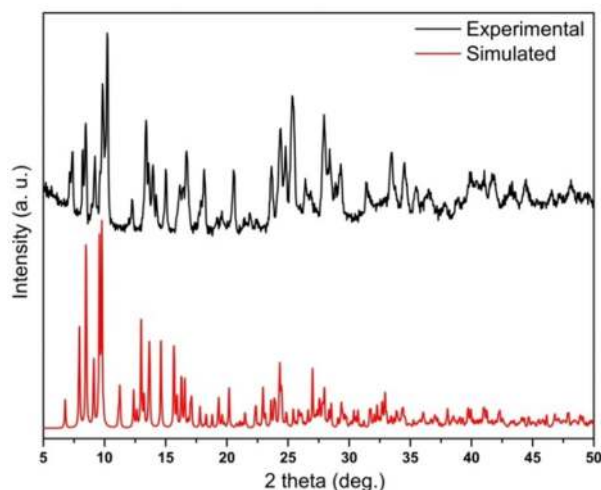
Figure 3.A.16. Powder XRD pattern of **3.A.3'** (The simulated pattern is obtained from SCXRD struture of **3.A.3**).

3.A.3.3 Magnetic properties. The dependence on temperature of $\chi_M T$ product for **3.A.1**-**3.A.4** (χ_M is the molar magnetic susceptibility per mononuclear Ln^{III} unit) in the 2-300 K temperature range was measured with an applied magnetic field of 0.1 T (Figure 3.A.17). At room temperature, the observed $\chi_M T$ values for **3.A.1**-**3.A.4** are close to those calculated for independent Ln^{III} ions in the free ion approximation (see Table 3.A.4). On cooling down, the $\chi_M T$ product for the Gd^{III} complex **3.A.1** remains almost constant until approximately 15 K and then decreases down to 2 K to reach a value of 7.51 cm^3 K mol^{-1}. This behaviour is probably due to the combined effects of very weak intermolecular dipolar interactions between the Gd^{III}, very small ZFS of the ground state, which sometimes is observed for this essentially isotropic ion, and

Zeeman effects. The field dependence of the magnetization at 2 K (Figure 3.A.18) shows a relatively rapid increase of the magnetization up to 2 T and then a linear increase to reach a value of 7.32 μ_B at 5 T, which is very close to the theoretical saturation value for a Gd^{III} ion with g = 2.0 (7 μ_B).
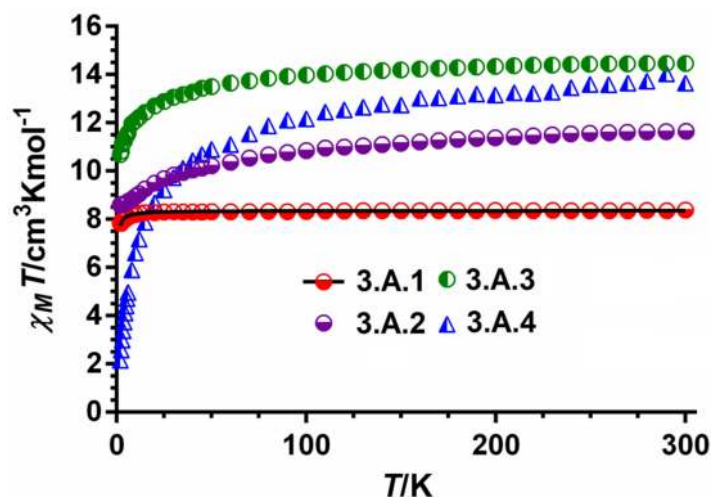
Figure 3.A.17. Temperature dependence of the $\chi_M T$ product for compounds **3.A.1**-**3.A.4**. The solid line represents the best fit of the experimental data.

Table 3.A.4. Direct current magnetic data for the complexes studied in this work.

Compound	Theoretical $\chi_M T_{300K}$ value (cm³ K mol⁻¹)ᵃ	Experimental $\chi_M T_{300K}$ / $\chi_M T_{2K}$ (cm³ K mol⁻¹)	Theoretical M_{sat} value (Nμ_B)ᵇ	Experimental M_{sat} value (T = 2 K, H = 5 T) (Nμ_B)
3.A.1	7.875	8.37/ 7.82	7	7.32
3.A.2	11.48	11.64/ 8.57	9	7.5
3.A.3	14.18	14.45 / 10.68	10	7.10
3.A.4	14.07	13.64 / 2.15	10	5.20
ᵃ$\chi_M T = \frac{N\beta^2}{3k}\{g_J^2 J(J+1)$ ᵇ$M = NJg_J\mu_B$; $J = L + S$; $g_J = \frac{3}{2} + \frac{S_T(S_T+1)-L(L+1)}{2J(J+1)}$				

The magnetic susceptibility and magnetization data of **3.A.1** were analyzed simultaneously with the following Hamiltonian:

$$H = -zJ'\langle S_z \rangle S_z + g\mu_B S_{Gd} B$$

Where $-zJ'\langle S_z \rangle S_z$ accounts for the intermolecular interactions by means of the molecular field approximation, g is the g factor, μ_B the Bohr magneton and B the applied magnetic field. The best fit of the magnetic properties by using the PHI program[24] afforded the following set of parameters: zJ' = -0.010(1) cm^{-1} and g = 2.060(1). These results show that, as expected, the intermolecular interactions are either dipolar or mediated by the network of hydrogen bonds along the chain and are very weak.

The $\chi_M T$ product of complexes **3.A.2-3.A.4** decreases steadily until approximately 25 K for **3.A.2** and **3.A.3** and 40 K for **3.A.4** and then more sharply down to 2 K. This behaviour is primarily due to the depopulation of the M_J sublevels of the Ln^{III} ions, which arise from the splitting of the ground term by the ligand field, as well as the possible existence of intermolecular dipolar interactions. As usual, this effect is more important for the Ho^{III} compound than for the Dy^{III} and Tb^{III} counterparts. The field dependence of the magnetization for these complexes at T = 2 K (Figure 3.A.18) exhibits a fast increase of the magnetization up to ~ 1 T for **3.A.2** and **3.A.3**, whereas for **3.A.4** the increase is rather slower. From 1 T the magnetization increases in a slower manner without reaching saturation at 5 T, which is more patent in the case of compound **3.A.4**. The fact that the magnetization values at the highest applied dc magnetic field of 5 T are rather lower than those calculated for three non-interacting Ln^{III} ions (Table 3.A.4) can be largely ascribed to crystal-field effects giving rise to significant magnetic anisotropy.[25]
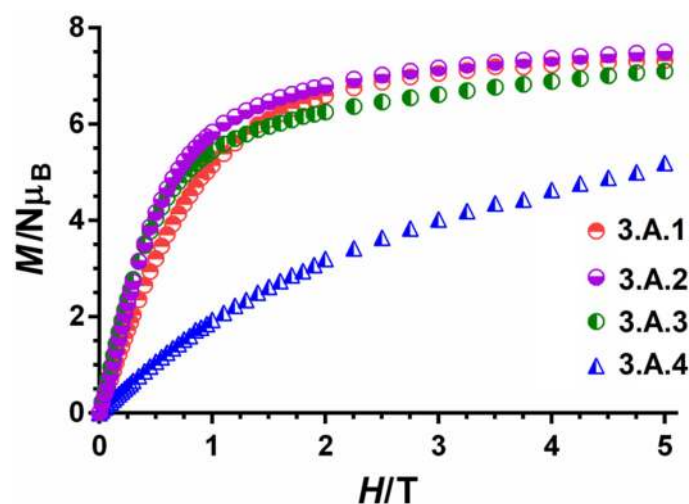
Figure 3.A.18. Field dependence of the magnetization at 2 K for complexes **3.A.1**-**3.A.4**.

It should be noted that the value of $\chi'_M T$ of **3.A.3** (χ'_M is the in-phase ac susceptibility, Figure 3.A.19) for the plateau at low temperature where all the lines are coincident is 14.1 cm^3 mol^{-1} K. This value agrees quite well with that expected for randomly oriented crystals of a mononuclear Dy^{III} complex with a $M_J = \pm15/2$ *Ising* ground Kramers doublet (12.5 cm^3 mol^{-1} K). Taking into account the presumable axiality of the ground Kramers doublet, we have calculated the direction of the anisotropy axes of the Dy^{III} ions by using the electrostatic Chilton's method.[26] The results show that the anisotropy axis of the Dy^{III} ion is located close to the Dy–O$_{phenoxide}$ bonds, which presents by far the shortest Dy–O distances (2.256 Å and 2.302 Å).
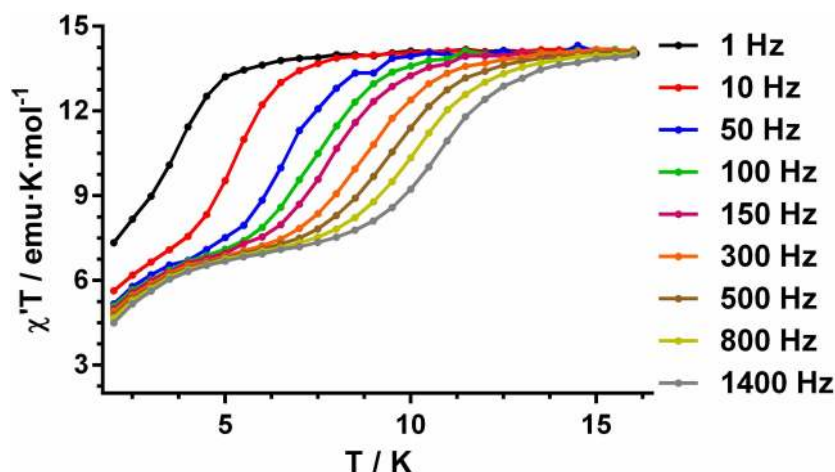
Figure 3.A.19. Temperature dependence of $\chi'_M T$ at different frequencies for **3.A.3**.

This orientation of the magnetic moment can be explained by taking into consideration the simple oblate-prolate model.[5] The 4f electron density of the $M_J = \pm 15/2$ ground Kramers doublet of the Dy^{III} center has an oblate disc shape, so that to reduce the repulsion with the atoms possessing the shortest Dy–O bond distance and, consequently, the largest negative charge (phenoxide oxygen atoms), the electron density disc is situated almost perpendicular to the Dy–O$_{phenoxide}$ bonds. Because of this, the resulting magnetic moment, which is perpendicular to the electron density disc, lies in the direction of the Dy–O$_{phenoxide}$ bonds (see Figure 3.A.20). The two Dy–O$_{phenoxide}$ bonds can be considered as located at opposite sides of the Dy^{III} ions with a O–Dy–O angle of 127°. This disposition creates a sufficient axial ligand field around the Dy^{III} ion as to lead to an axial ground KD doublet and SIM behaviour.[27] The largest axiality would be expected for an O–Dy–O bond angle of 180°.
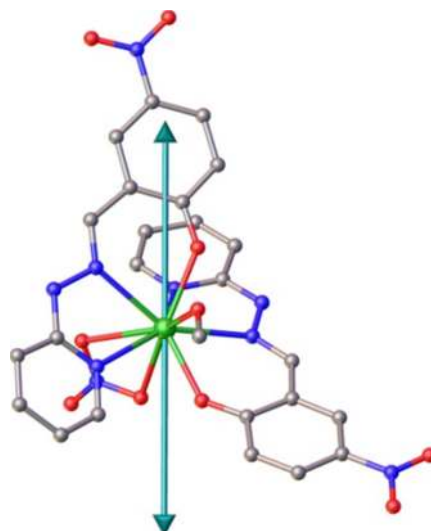
Figure 3.A.20. Quantitative calculation of the anisotropic axes orientation (green arrows) using the Chilton´s method.[26]

Within the unit cell, the molecules of **3.A.3** with the shortest Dy···Dy distances (7.635 Å) are related by a center of symmetry and consequently, the local anisotropy axes of the Dy^{III} ions are parallel to each other. In this case, orientation of the magnetic moments with respect to the line connecting the Dy^{III} ions (θ angle) determines the sign of the magnetic dipolar interaction.[28] This interaction can be calculated using the following Hamiltonian for the dipole-dipole interaction:[28]

$$H_{dip} = \frac{-\mu_o}{4\pi} \frac{\mu_i \mu_j}{r^3} (3cos^2\theta - 1)$$

where r is their distance, $\mu_{i,j}$ are the magnetic moments of centers i and j and μ_0 is the vacuum permittivity. This expression leads to antiferromagnetic coupling for angles between the magnetic moments and the molecular plane larger than 54.7° and ferromagnetic coupling for angles lower than 54.7°, respectively. From the above Hamiltonian, the dipolar contribution to the magnetic coupling can be expressed as:

$$J_{dip} = \frac{\mu_o}{4\pi} \frac{(g_J \beta)^2}{r^3} (3cos^2\theta - 1)$$

For compound **3.A.3**, with θ = 61.95° an antiferromagnetic interaction J_{dip} = -0.002 cm^{-1} can be calculated using the above expression. This very small value is not unexpected in view of the large distance between the neighboring Dy^{III} ions.
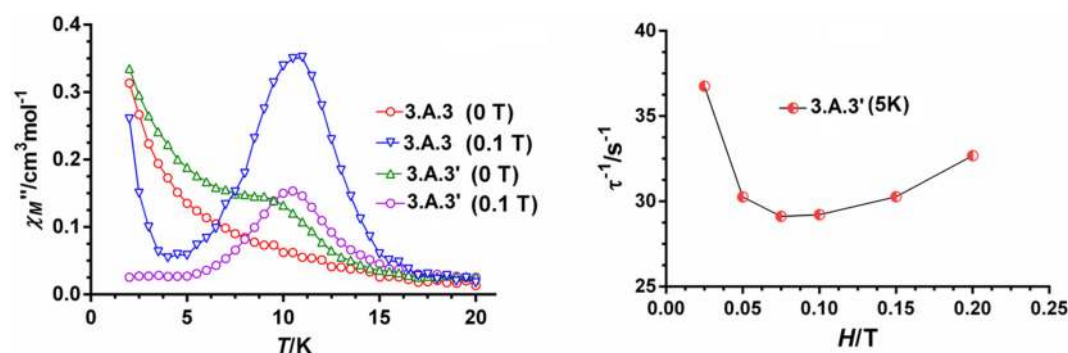
Figure 3.A.21. Temperature dependence of the out-of-phase χ''_M component of the ac susceptibility for **3.A.3** and **3.A.3'** at 1200 Hz and under zero and 0.1 T magnetic field (*left*). Field dependence of the relaxation time for **3.A.3'** at 5 K (*right*).

Preliminary temperature dependent dynamic ac magnetic susceptibility measurements at a frequency of 1200 Hz were carried out to know if these complexes exhibited slow relaxation of the magnetization and then SIM behaviour. Except for complex **3.A.3**, none of the complexes showed out-of-phase (χ''_M) signals at zero field above 2 K. Nevertheless, in the case of **3.A.3**, the out-of-phase (χ''_M) did not reach a maximum above 2 K (Figure 3.A.21). This behavior could be due to either (*i*) the anisotropy barrier for magnetization reversal is a too small as to trap the magnetization above 2 K, or (*ii*) the existence of a very fast resonant zero field quantum tunneling of the magnetization (QTM). When the ac measurements were carried out in the presence of a small external field of 1000 Oe to partly or fully quench QTM, only compound **3.A.3** showed out-of-phase (χ''_M) signals, which exhibited a maximum at 10.5 K (Figure 3.A.21). However, the appearance of a tail below 5 K, which increases in intensity down to 2 K, points out that QTM has not been fully suppressed and/or a

direct process occurs at very low temperature. This behaviour can be due to the existence of dipolar and/or hyperfine interactions opening new relaxation pathways for direct and QTM processes. The detailed temperature and frequency dependent ac measurements for **3.A.3** are shown in Figure 3.A.22.
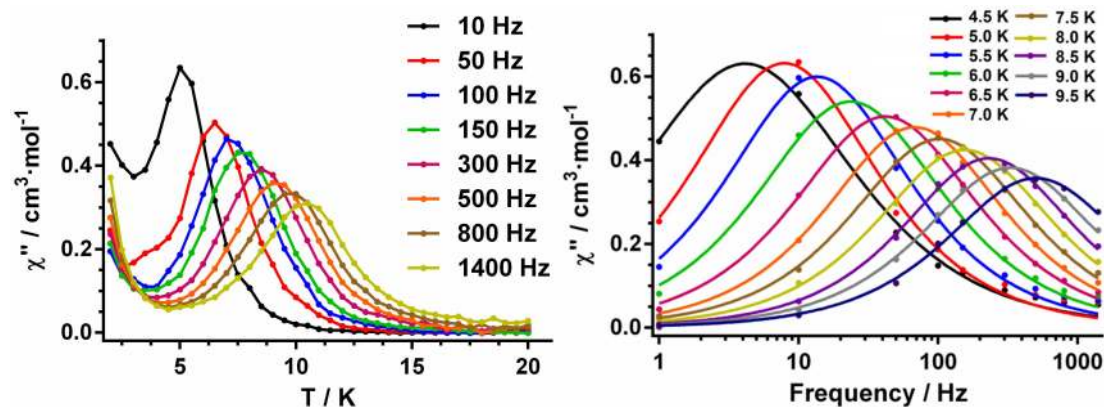
Figure 3.A.22. (*left*) Temperature dependence and (*right*) Frequency dependence of χ''_M for **3.A.3**.

In view of this and in order to suppress intermolecular dipolar interactions, we decided to prepare a magnetic diluted sample of **3.A.3** by substituting Dy^{III} ions by Y^{III} to achieve a Dy^{III}/Y^{III} molar ratio 15/85 (this ratio was estimated from the susceptibility and magnetization data for **3.A.3'** at room temperature compared to those for **3.A.3**). The temperature dependence of out-of-phase (χ''_M) at 1200 Hz and under zero field for **3.A.3'** shows a clear shoulder centered around 9 K and a tail below 8 K, thus pointing out that that even though the relaxation slows down after dilution, the QTM has not been fully suppressed. Moreover, when the results for **3.A.3** at 0.1 T are compared to those of **3.A.3'** at zero field, one realizes that the effect of the dilution appears to be less effective in suppressing QTM than the effect of the field. Bearing this in mind, the temperature dependence of out-of-phase (χ''_M) signal at 1200 Hz was measured under a static magnetic field of 0.1 T. The results indicate

that the maximum still appears at 10.5 K but the tail due to QTM at low temperature has almost disappeared. In light of this, the frequency and temperature dependence of the ac susceptibility measurements for **3.A.3'** were recorded in the presence of a small static magnetic field. To determine the optimal field, the frequency dependence of the out-of-phase (χ''_M) at 5 K was measured in the 0.025-0.20 T range. On increasing the field the relaxation time first increases in the 0.075 T-0.1 T field range due to the suppression of QTM process and then decreases for upper fields due to the contribution of a direct process. Considering this, the complete set of ac measurements on the diluted complex **3.A.3'** was carried out under a field of 0.1 T. The results show a strong frequency dependence of the ac susceptibility signals with maxima in the 10.5 (100 Hz)-5 K (10 Hz) temperature range (Figure 3.A.23). Moreover, the absence of a tail at low temperature points out the suppression of the QTM fast relaxation process.
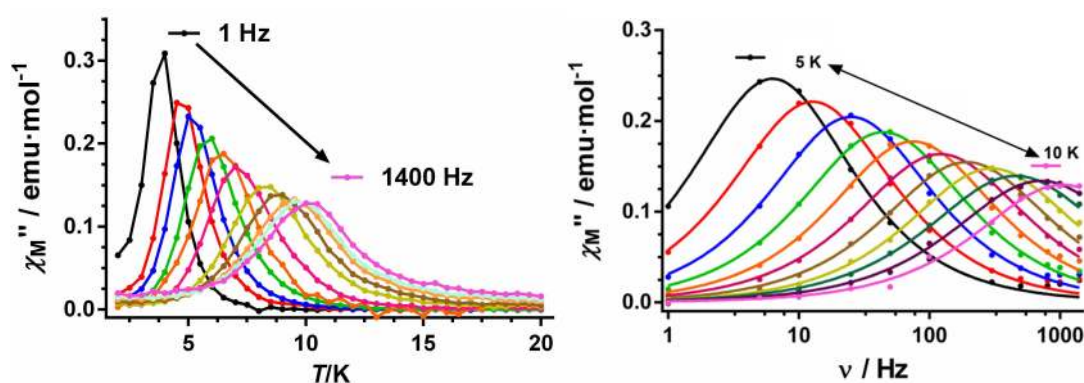
Figure 3.A.23. (*left*) Temperature dependence and (*right*) Frequency dependence of χ''_M for **3.A.3'**.

The relaxation times (τ) for **3.A.3'** were extracted from the fitting of the frequency dependence of χ''_M at each temperature to the generalized Debye model (Figure 3.A.24). The fit of the relaxation times to the Arrhenius equation in the 8-10 K temperature range afforded the following values of the effective energy barrier for the

reversal of the magnetization and the pre-exponential factor: $U_{eff}/k_B = 68(2)$ K. and τ_0 = 1.8·x 10^{-7} s. The deviation of the data from the Arrhenius law below 8 K is a clear sign that either the magnetic relaxation takes place through a relaxation process other than Arrhenius or there is co-existence of several competing relaxation processes. In the studied temperature range ($T > 4.5$ K) and at 0.1 T the direct and QTM relaxation processes for the magnetic diluted complex should be almost negligible, and therefore the relaxation times were fitted to the following equation:

$$\tau^{-1} = BT^n + \tau_0^{-1}\exp(-U_{eff}/k_BT)$$

which considers that Raman (first term) and Orbach processes (second term) contribute simultaneously to the relaxation of the magnetization. It should be noted that the relaxation times can be fitted to this equation using almost any value of U_{eff} and τ_0, including those extracted from the Arrhenius plot for the Orbach process. In view of this, we decided to fit the data to only a Raman relaxation process. A very good fit was obtained, affording the following parameter: $B = 0.00017(2)$ s^{-1} K^n and n = 7.58(5). This result indicates that the magnetization relaxation takes place only through a Raman process or this is the dominant process in the 4.5-10 K temperature range. It is worth mentioning that n = 9 is expected for Kramers ions like Dy^{III}.[29] Nevertheless, values between n = 2 and n = 7 are also realistic when both acoustic and optical phonons are active.[30] Similar values have been previously reported for other Dy^{III} containing complexes.[31] When the ac susceptibility data for **3.A.3** (Figure 3.A.24) and **3.A.3'** at 0.1 T are compared one realizes that the magnetization relaxation is slower for the former, which is not unexpected because suppression of the intermolecular dipolar interactions decreases the fast QTM. In keeping with this, the hypothetical effective energy barrier increases (from 56 K to 68 K) with the concomitant decrease of the flipping rate τ_0 (from 9.3 x 10^{-7} s^{-1} to 1.8·x 10^{-7} s^{-1}). As

for **3.A.3'**, the data for **3.A.3** in the 4.5-10 K can be very well fitted to Raman process with $B = 0.007(2)$ s^{-1} K^n and n $=$ 6.78(1). Therefore, the slowdown of the magnetization relaxation concomitantly decreases B and increase n.
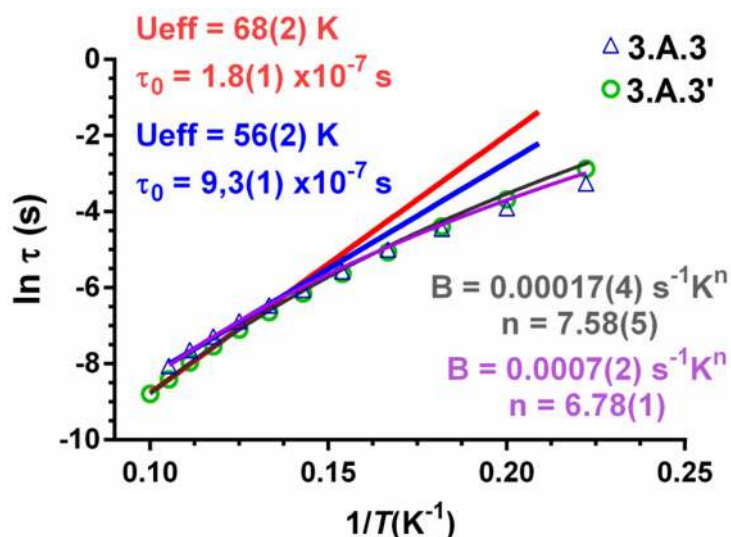
Figure 3.A.24. The red and blue lines represent the best fits of the experimental data to the Arrhenius equation whereas the black and violet lines correspond to the best fit to Raman relaxation process for complexes **3.A.3'** and **3.A.3**, respectively.

The fact that complexes **3.A.2** and **3.A.4** do not show slow relaxation is not unexpected taking into account that non-Kramers ions, such as Tb^{III} and Ho^{III}, present an intrinsic tunnelling gap in the ground state favoring QTM. Moreover, to exhibit an axial bistable ground state these ions require a strict axial symmetry and this is not the case of compounds **3.A.2** and **3.A.4**. Besides, in the case of the Ho^{III} ion, the low anisotropy of the 4f shell makes more difficult the adoption of an axial bistable ground state.

These results show that a good strategy for obtaining Dy^{III} SIMs is that of using tridentate ligands bearing two neutral donor atoms (either nitrogen or oxygen) and a phenol group. This is because the coordination of two of this type of ligands to the

Dy^{III} ions can lead to a distribution of donor atoms where the phenoxide oxygen atoms, which have by far the shortest Dy–O distances, can be located in almost opposite sides of the Dy^{III} coordination sphere. This disposition creates a sufficient axial ligand field so as to favor an axial ground KD and then the SIM behavior.

3.A.4 CONCLUSIONS

In conclusion, we have shown a design synthetic strategy to isolate mononuclear lanthanide complexes by the utilization of a tridentate *NNO* donor ligand bearing one phenolate moiety. The molecular structure of these complexes reveals that the two ligands coordinate to the metal center in a *head* to *tail* fashion which results in the deposition of the two phenolate moieties *trans* to each other. The short Ln–O$_{phenoxide}$ bond distances accompanied by *trans* deposition of the two phenolates creates an approximate strong axial crystal field. Therefore, in this axial crystal field environment the oblate shaped Dy^{III} having the advantage of Kramers degeneracy shows field-induced single-ion magnet behaviour. The dilution study in the Dy^{III} analogue reveals an enhancement in the energy barrier of magnetization reversal, $U_{eff}/k_B = 68(2)$ K compared to the undiluted complex ($U_{eff}/k_B = 56(2)$ K) with concomitant reduction of flipping rate τ_o (from 9.3 x 10^{-7} s^{-1} to 1.8 x 10^{-7} s^{-1}).

3.A.5 REFERENCES

1 (a) N. Ishikawa, M. Sugita, T. Ishikawa, S.-y. Koshihara and Y. Kaizu, *J. Am. Chem. Soc.*, 2003, **125**, 8694-8695; (b) N. Ishikawa, M. Sugita, T. Ishikawa, S.-y. Koshihara and Y. Kaizu, *J. Phys. Chem. B*, 2004, **108**, 11265-11271.

2 (a) A. K. Bar, P. Kalita, M. K. Singh, G. Rajaraman and V. Chandrasekhar, *Coord. Chem. Rev.*, 2018, **367**, 163-216; (b) K. L. M. Harriman and M. Murugesu, *Acc. Chem. Res.*, 2016, **49**, 1158-1167; (c) K. Katoh, T. Komeda and M. Yamashita, *Chem.*

Rec., 2016, **16**, 987-1016; (d) K. Liu, X. Zhang, X. Meng, W. Shi, P. Cheng and A. K. Powell, *Chem. Soc. Rev.*, 2016, **45**, 2423-2439; (e) Z. Zhu, M. Guo, X.-L. Li and J. Tang, *Coord. Chem. Rev.*, 2019, **378**, 350-364.

3 (a) D. N. Woodruff, R. E. P. Winpenny and R. A. Layfield, *Chem. Rev.*, 2013, **113**, 5110-5148; (b) J. Tang and P. Zhang, in *Lanthanide Single Molecule Magnets*, eds. J. Tang and P. Zhang, Springer Berlin Heidelberg, Berlin, Heidelberg, 2015, pp. 41-90.

4 (a) N. F. Chilton, *Inorg. Chem.*, 2015, **54**, 2097-2099; (b) S. K. Singh, T. Gupta, M. Shanmugam and G. Rajaraman, *Chem. Commun.*, 2014, **50**, 15513-15516; (c) L. Ungur and L. F. Chibotaru, *Inorg. Chem.*, 2016, **55**, 10043-10056.

5 J. D. Rinehart and J. R. Long, *Chem. Sci.*, 2011, **2**, 2078-2085.

6 (a) J.-L. Liu, Y.-C. Chen and M.-L. Tong, *Chem. Soc. Rev.*, 2018, **47**, 2431-2453; (b) L. Ungur and L. F. Chibotaru, *Phys. Chem. Chem. Phys.*, 2011, **13**, 20086-20090.

7 (a) G.-J. Chen, Y.-N. Guo, J.-L. Tian, J. Tang, W. Gu, X. Liu, S.-P. Yan, P. Cheng and D.-Z. Liao, *Chem. Eur. J.*, 2012, **18**, 2484-2487; (b) Y.-S. Meng, L. Xu, J. Xiong, Q. Yuan, T. Liu, B.-W. Wang and S. Gao, *Angew. Chem.*, 2018, **130**, 4763-4766; (c) J.-L. Liu, Y.-C. Chen, Y.-Z. Zheng, W.-Q. Lin, L. Ungur, W. Wernsdorfer, L. F. Chibotaru and M.-L. Tong, *Chem. Sci.*, 2013, **4**, 3310-3316; (d) Y.-N. Guo, L. Ungur, G. E. Granroth, A. K. Powell, C. Wu, S. E. Nagler, J. Tang, L. F. Chibotaru and D. Cui, *Sci. Rep.*, 2014, **4**, 5471-5477; (e) K. L. M. Harriman, J. L. Brosmer, L. Ungur, P. L. Diaconescu and M. Murugesu, *J. Am. Chem. Soc.*, 2017, **139**, 1420-1423; (f) S. Zhang, H. Ke, L. Sun, X. Li, Q. Shi, G. Xie, Q. Wei, D. Yang, W. Wang and S. Chen, *Inorg. Chem.*, 2016, **55**, 3865-3871.

8 F.-S. Guo, B. M. Day, Y.-C. Chen, M.-L. Tong, A. Mansikkamäki and R. A. Layfield, *Science*, 2018, **362**, 1400-1403

9 (a) J. Liu, Y.-C. Chen, J.-L. Liu, V. Vieru, L. Ungur, J.-H. Jia, L. F. Chibotaru, Y. Lan, W. Wernsdorfer, S. Gao, X.-M. Chen and M.-L. Tong, *J. Am. Chem. Soc.*, 2016, **138**, 5441-5450; (b) S. K. Gupta, T. Rajeshkumar, G. Rajaraman and R. Murugavel, *Chem. Sci.*, 2016, **7**, 5181-5191; (c) Y.-C. Chen, J.-L. Liu, L. Ungur, J. Liu, Q.-W. Li, L.-F. Wang, Z.-P. Ni, L. F. Chibotaru, X.-M. Chen and M.-L. Tong, *J. Am. Chem. Soc.*, 2016, **138**, 2829-2837.

10 (a) S. Das, A. Dey, S. Biswas, E. Colacio and V. Chandrasekhar, *Inorg. Chem.*, 2014, **53**, 3417-3426; (b) J. Goura, E. Colacio, J. M. Herrera, E. A. Suturina, I. Kuprov, Y. Lan, W. Wernsdorfer and V. Chandrasekhar, *Chem. Eur. J.*, 2017, **23**, 16621-16636.

11 S. Biswas, S. Das, J. Acharya, V. Kumar, J. van Leusen, P. Kögerler, J. M. Herrera, E. Colacio and V. Chandrasekhar, *Chem. Eur. J.*, 2017, **23**, 5154-5170.

12 A. K. Bar, P. Kalita, J.-P. Sutter and V. Chandrasekhar, *Inorg. Chem.*, 2018, **57**, 2398-2401.

13 (a) J. Goura, J. P. S. Walsh, F. Tuna and V. Chandrasekhar, *Inorg. Chem.*, 2014, **53**, 3385-3391; (b) Z.-S. Meng, J.-L. Liu, J.-D. Leng, F.-S. Guo and M.-L. Tong, *Polyhedron*, 2011, **30**, 3095-3099.

14 M. Mohan, N. S. Gupta, L. Chandra, N. K. Jha and R. S. Prasad, *Inorg. Chim. Acta*, 1988, **141**, 185-192.

15 *SMART & SAINT Software Reference manuals*, Bruker Analytical X-ray Systems, Inc., Madison, WI, version 6.45, 2003.

16 G. M. Sheldrick, *SADABS, Program for Empirical Absorption Correction*, University of Gottingen, Germany, 1996.

17 *Bruker APEX2*, Bruker AXS Inc., Madison, Wisconsin, USA, version 2008.1−0, 2008.

18 *CrysAlisPRO*, Oxford Diffraction UK Ltd., Yarnton, England.

19 G. M. Sheldrick, *Acta Cryst. A*, 2015, **71**, 3-8.

20 G. M. Sheldrick, *Acta Cryst. C*, 2015, **71**, 3-8.

21 O. V. Dolomanov, L. J. Bourhis, R. J. Gildea, J. A. K. Howard and H. Puschmann, *J. Appl. Cryst.*, 2009, **42**, 339-341.

22 K. Brandenburg and H. Putz, *DIAMOND*, Crystal Impact GbR, Bonn, Germany, version 3.2, 1997−2014.

23 (a) J. Cirera, E. Ruiz and S. Alvarez, *Organometallics*, 2005, **24**, 1556-1562; (b) *SHAPE: Continuous Shape Measures calculation*, Electronic Structure Group, Universitat de Barcelona, Spain, version 2.1, 2013.

24 N. F. Chilton, R. P. Anderson, L. D. Turner, A. Soncini and K. S. Murray, *J. Comput. Chem.*, 2013, **34**, 1164-1175.

25 (a) J. Ruiz, A. J. Mota, A. Rodríguez-Diéguez, S. Titos, J. M. Herrera, E. Ruiz, E. Cremades, J. P. Costes and E. Colacio, *Chem. Commun.*, 2012, **48**, 7916-7918; (b) Y. Bi , Y.-N. Guo, L. Zhao, Y. Guo, S.-Y. Lin, S.-D. Jiang, J. Tang, B.-W. Wang and S. Gao, *Chem. Eur. J.*, 2011, **17**, 12476-12481; (c) H. L. C. Feltham, Y. Lan, F. Klöwer , L. Ungur, L. F. Chibotaru, A. K. Powell and S. Brooker, *Chem. Eur. J.*, 2011, **17**, 4362-4365.

26 N. F. Chilton, D. Collison, E. J. L. McInnes, R. E. P. Winpenny and A. Soncini, *Nat. Commun.*, 2013, **4**, 2551-2557.

27 N. F. Chilton, S. K. Langley, B. Moubaraki, A. Soncini, S. R. Batten and K. S. Murray, *Chem. Sci.*, 2013, **4**, 1719-1730.

28 P. Panissod and M. Drillon, in *Magnetism: Molecules to Materials IV*, eds. J. S. Miller and M. Drillon, Wiley-VCH Verlag GmbH & Co. KGaA, 2002, ch. 7, p. 235.

29 A. Abragam and B. Bleaney, *Electron paramagnetic resonance of transition ions*, Oxford : Clarendon press, 1970.

30 (a) A. Singh and K. N. Shrivastava, *Phys. Status Solidi B*, 1979, **95**, 273-277; (b) K. N. Shrivastava, *Phys. Status Solidi B*, 1983, **117**, 437-458.

31 (a) I. Oyarzabal, B. Artetxe, A. Rodríguez-Diéguez, J. Á. García, J. M. Seco and E. Colacio, *Dalton Trans.*, 2016, **45**, 9712-9726; (b) P. Kalita, J. Goura, J. Manuel Herrera Martínez, E. Colacio and V. Chandrasekhar, *Eur. J. Inorg. Chem.*, 2019, 212-220.

Mononuclear Ln^{III} Complexes Assembled from a Bulky ^{Mes}Acac Ligand: Luminescence and Magnetism

ABSTRACT: The reaction of a bulky acetyl acetone ligand, 1,3-dimesitylpropane-1, 3-dione (^{Mes}Acac) with hydrated lanthanide chlorides in the presence of tetramethylammonium hydroxide afforded a new family of neutral mononuclear Ln^{III} complexes [Eu(^{Mes}Acac)$_3$(DMF)(EtOH)] (**3.B.1**), [Gd(^{Mes}Acac)$_3$(H$_2$O)] (**3.B.2**) and [Ln(^{Mes}Acac)$_3$(DMF)] (Ln = Tb; (**3.B.3**), Dy; (**3.B.4**), and Er; (**3.B.5**)). The molecular structures of the complexes were confirmed by single crystal X-ray diffraction studies. The coordination geometries of the Ln^{III} center were analyzed by SHAPE analysis which revealed triangular dodecahedron geometry in **3.B.1**, capped trigonal prism geometry in **3.B.2** and capped octahedron geometry in **3.B.3**-**3.B.5**. Photoluminescence studies show ligand-sensitized red and green emissions for **3.B.1** and **3.B.3** with quantum yields (absolute) 58% and 74% respectively. Static (dc) and dynamic (ac) magnetic studies were performed on the complex **3.B.4**. The dynamic magnetic study reveals field-induced single-ion magnet behaviour in the Dy^{III} derivative with an effective energy barrier, U_{eff}/k_B = 70(3) K (diluted) and pre-exponential parameter of τ_0 = 2.7 x 10^{-7} s, respectively.

3.B.1 INTRODUCTION

Single-molecule- and single-ion magnets (SMMs and SIMs) have been receiving a lot of attention in recent years.[1] These are molecular systems that once magnetized, retain their magnetization indefinitely, below certain critical temperatures.[2] While most of the initial efforts were devoted to mainly polynuclear 3d complexes[3], soon this phenomenon was also observed in heterometallic 3d/4f complexes.[4] In a seminal

discovery in 2003, slow magnetic relaxation and magnetic hysteresis was observed for the first time in a mononuclear *bis*(phthalocyanine)Tb^{III} complex, [TBA][Tb(Pc)$_2$] (TBA = tetrabutylammonium and pc = phthalocyanine).[5] This discovery opened up a new direction of utilizing the 4f-ions in the construction of molecular magnets. Recent advancements in this field reveal that mononuclear complexes could exhibit promising SIM behaviour provided the following two criteria are met: (*a*) the complex should have a bistable spin ground state with high magnitude of $|M_J|$ and should possess (*b*) well isolated excited states with magnetic moments co-linear with the ground state.[6] The 4f-ions are considered as suitable candidates for the design and assembly of molecular magnets due to the fact that many of them possess a fairly large ground state spin, *S*, and also, in addition, have intrinsic magnetic anisotropy arising from a large unquenched orbital angular momentum and strong spin-orbit coupling. One important drawback of some of the 4f complexes, however, is the significant contribution of temperature independent zero field quantum tunneling mechanism (QTM) that causes a fast magnetization reversal.[7] Indeed, such relaxation mechanisms short cut the thermal barrier to the effective barrier (U_{eff}) for the reversal of magnetization. However, the QTM process is formally forbidden in the case of 4f ions having half-integer spins (Kramers ions) whereas in the case of integer spins (non-Kramers ions) it can be present in a significant way.[8] One of the ways of effectively reducing these effects and having some control on such deleterious relaxation mechanisms is to use strategic ligand fields which can provide appropriate coordination environment and local symmetry to the 4f complex.[9] In the literature, low coordination numbers around the Ln^{III} center are reported to be capable of inducing axiality as well as large crystal field splitting of the crystal field doublets.[6a, 10] However, at the same time, low-coordinate lanthanide complexes are extremely

sensitive towards air and moisture which limits their practical applicability. Recently

outstanding examples involving organometallic lanthanide complexes, $[Dy(Cp^{ttt})_2][B(C_6F_5)_4]$ ($Cp^{ttt} = \{C_5H_2{}^tBu_3\text{-}1,2,4\}$ and $^tBu = C(CH_3)_3$) and $[(\eta^5\text{-}Cp^*)Dy(\eta^5\text{-}Cp^{iPr5})][B(C_6F_5)_4]$ have been reported with U_{eff} values of 1223 cm^{-1} and 1541 cm^{-1} and blocking temperatures of 60 K and 80 K.[11] However, these complexes also are extremely air-sensitive. Among the air- and moisture-stable mononuclear complexes important examples include seven-coordinate pentagonal bipyramidal Dy^{III} complexes with high energy barriers and high blocking temperatures.[12]

In the literature, a diverse range of ligand systems such as macrocyclic ligands,[13] organometallic ligands,[14] and chelating ligands[15] are known to produce monometallic complexes. We also have been using various kinds of multidentate ligands for preparing both mono- and dinuclear lanthanide complexes that have been shown to possess interesting magnetic properties.[16] In this quest, we wished to explore the well-known β-diketonato family for the synthesis of mononuclear lanthanide complexes. In the literature, there have been precedents on the use of such ligands (Figure 3.B.1) to afford mononuclear complexes of the type $[Ln(\beta\text{-diketonato})_3(AB)]$, (where AB can be two monodente ligands or a bidentate chelating ligand) and $[Ln(\beta\text{-diketonato})_4]$.[17] However, in both these instances, the lanthanide ions are eight-coordinate. In fact, there has been only one report of a seven-coordinate lanthanide complex known with the β-diketone ligand (EIFD see Figure 3.B.1).[18] Other mononuclear Ln^{III} complexes with less than three β-diketonate ligands and β-diketonate as co-ligands are also known.[19] Interestingly, all the Dy^{III} derivatives prepared from the EFID ligand showed SIM behaviour due to the effective suppression of QTM.[18] We were intrigued by the possibility of increasing the steric encumbrance around the acetyl acetonate

ligand to check if such a ligand design can lead to a decrease in the coordination number around the lanthanide ions.
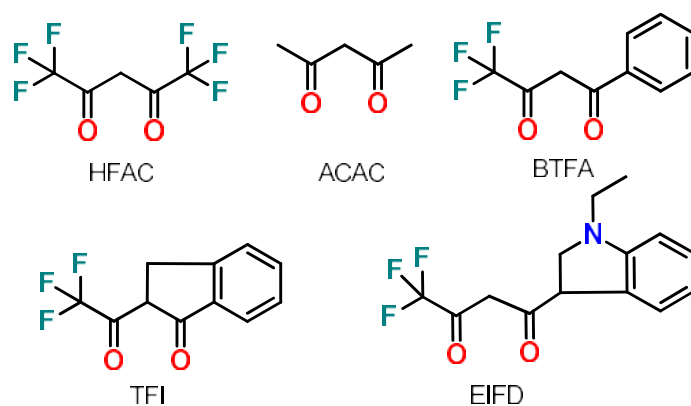
Figure 3.B.1. Selected β-diketonate ligands utilized for the synthesis of mononuclear Ln[III] SIMs/SMMs.

An important reason for the interest in β-diketonate Ln[III] complexes is their photophysical properties.[20] Many lanthanide complexes, particularly those involving Eu[III] and Tb[III] ions with β-diketonate ligands show interesting photoluminescence, however, this property can be tuned by functionalization of the ligand such that the energy transfer process can be accentuated.[20e] Also, mononuclear Ln[III] complexes with dual magnetic and luminescence properties are of considerable interest.[21] Accordingly, we have prepared a sterically bulky and flexible acetylacetone ligand, ^{Mes}Acac by the Friedel-Crafts acylation reaction of malonyl chloride with mesitylene. The reaction of ^{Mes}Acac with hydrated lanthanide chloride metal salts in the presence of Me$_4$NOH in 1:1:3 stoichiometric ratio afforded a new family of eight- and seven-coordinate mononuclear lanthanide complexes [Eu(^{Mes}Acac)$_3$(DMF)(EtOH)] (**3.B.1**), [Gd(^{Mes}Acac)$_3$(H$_2$O)] (**3.B.2**) and [Ln(^{Mes}Acac)$_3$(DMF)] (Ln = Tb; (**3.B.3**), Dy; (**3.B.4**), and Er; (**3.B.5**)) (Scheme 3.B.1). Herein, we report the synthesis, structure, photophysical and magnetic properties of these complexes.
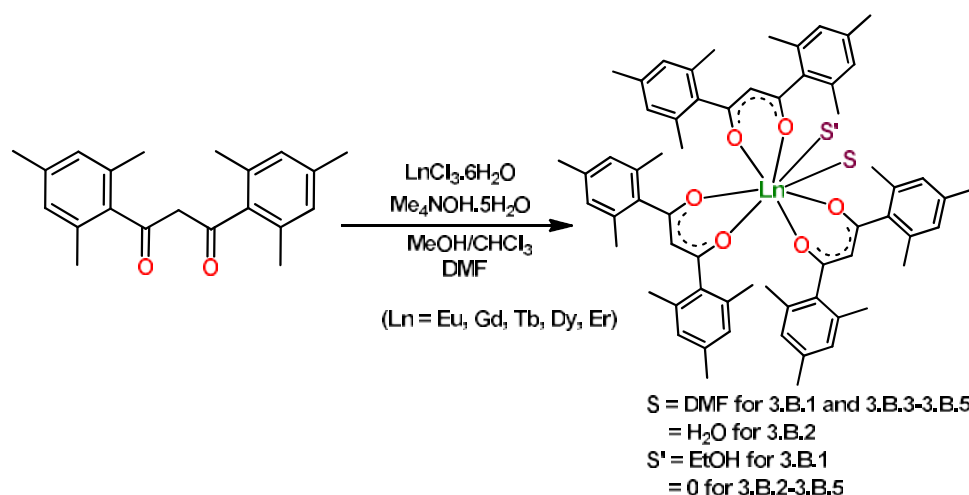
Scheme 3.B.1. Reaction scheme for the synthesis of the mononuclear complexes **3.B.1-3.B.5**.

3.B.2 EXPERIMENTAL SECTION

3.B.2.1 Materials and Methods. The solvents and other general reagents used in this work were received from commercial sources and used without further purification. Mesitylene and malonyl Chloride were obtained from TCI chemicals (India) Pvt. Ltd. Tetramethylammonium hydroxide, Aluminium Chloride, and carbon disulphide was obtained from Spectrochem Chemicals India. $LnCl_3 \cdot 6H_2O$ (Ln = Y, Eu, Gd, Dy, Tb, Er) were obtained from Sigma Aldrich Chemical Co. (India) and used as obtained. The ligand, 1,3-dimesitylpropane-1,3-dione (^{Mes}Acac) was prepared by a previously reported procedure and well characterized (see section 3.B.2.5).[22]

3.B.2.2 Instrumentation. Melting points were measured using a Stuart™ melting point apparatus SMP10 and are uncorrected. ^1H NMR and $^{13}C\{^1H\}$ NMR spectra were recorded on a Bruker Ascend-700 (^1H: 700 MHz; $^{13}C\{^1H\}$: 175 MHz) and were referenced to the resonances of the solvent used. IR spectra were recorded with a PerkinElmer FT-IR spectrometer. Elemental analyses of the compounds were obtained from a Euro Vector EA elemental analyser (CHNS-O, Model EA3000).

3.B.2.3 Photophysical Characterization. Absorption data were measured on an Agilent Cary 60 UV-Vis spectrophotometer at room temperature. Photoluminescence (PL) spectra were recorded on a Spex-Fluorolog FL22 spectrofluorimeter. The latter was equipped with a double grating 0.22 m Spex 1680 monochromator and a 450 W Xe lamp as the excitation source and a Hamamatsu R928P photomultiplier tube detector. Corrections were applied to the emission and excitation spectra regarding source intensity (lamp and grating) by using standard correction curves.

3.B.2.4 Magnetic Measurements. Direct (dc) and alternating (ac) current susceptibility measurements on **3.B.4** and **3.B.4'** were performed with a Quantum Design SQUID MPMS XL-5 device. The ac experiments were performed using an oscillating ac field of 3.5 Oe and frequencies ranging from 1 to 1500 Hz. The experimental susceptibilities were corrected for the sample holder and diamagnetic contributions. Pellets of the different samples were cut into small pieces and placed in the sample holder to avoid any orientation of the microcrystals by the magnetic field.

3.B.2.5 X-ray Crystallography. The single crystal X-ray diffraction data of compound **3.B.1** and **3.B.4'** were collected on a Rigaku Xtal LAB X-ray diffractometer system equipped with a CCD area detector and operated at 30 W power (50 kV, 0.6 mA) to generate MoKα radiation (λ = 0.71073 Å) at 120 K. Data were integrated using CrysAlis[Pro] software with a narrow frame algorithm.[23] Data were subsequently corrected for absorption by the program SCALE3 ABSPACK scaling algorithm.[23] Single crystal X-ray structural studies of **3.B.2**, **3.B.3**, **3.B.4** and **3.B.5** were performed on a Bruker Apex II CCD diffractometer equipped with graphite-monochromated MoKα radiation (λ_α = 0.71073 Å) at 296 K. The SMART and SAINT software package[24] were used for collecting frames of data, indexing reflections, determining lattice parameters, integration of the intensity of reflections

and scaling. A multi-scan absorption correction was performed using SADABS.[25] Space groups were determined using XPREP implemented in APEX2.[26] All the structures were solved with the ShelXT[27] structure solution program using Intrinsic Phasing and refined with the ShelXL[28] refinement package using Least Squares minimisation in the Olex-2[29] software. All the non-hydrogen atoms were refined with anisotropic thermal parameters. Hydrogen atoms were placed in either geometrically calculated positions or found in the Fourier difference map and included in the refinement process using riding model. All the complexes crystallized without any co-crystallized solvent molecule(s). For compound **3.B.4'**, the Dy population was determined by positional disorder treatments. All the mean plane analyses and crystallographic figures have been generated using DIAMOND software (version 3.2).[30] The crystal data and refinement parameters for **3.B.1-3.B.3** are summarized in Table 3.B.1 and those of **3.B.4-3.B.5** are summarized in Table 3.B.2.

Table 3.B.1. Data collection and refinement parameters for compounds **3.B.1-3.B.3**.

	3.B.1	**3.B.2**	**3.B.3**
Chemical formula	$C_{67}H_{79}Eu_1N_1O_8$	$C_{63}H_{71}Gd_1O_7$	$C_{66}H_{76}Tb_1N_1O_7$
M_w (g mol^{-1})	1178.27	1097.44	1154.19
Crystal system, Space group	Monoclinic, $P21/c$	Monoclinic, $P21/n$	Triclinic, P-1
Temperature (K)	120(2)	296(2)	296(2)
a, b, c (Å)	12.283(3) 21.545(8) 23.226(5)	15.262(5), 18.030(6), 23.730(8)	12.233(3) 13.840(3) 19.675(5)
α, β, γ (°)	90 95.053(2) 90	90 108.593(2) 90	94.666(10) 99.170(10) 106.000(10)
V (Å^3)	6123.1(3)	6189.7(4)	3133.6(13)
Z	4	4	2
Radiation type	MoKα (λ = 0.71073)	MoKα (λ = 0.71073)	MoKα (λ = 0.71073)
μ (mm^{-1})	1.078	1.118	1.178

Crystal size (mm)	0.23 × 0.17 × 0.12	0.27 × 0.19 × 0.12	0.3 × 0.24 × 0.2
Reflections collected	73862	86920	54629
GOF on F^2	1.058	1.077	1.029
Independent reflections [R$_{int}$]	12014 [R$_{int}$ = 0.0453]	11769 [R$_{int}$ = 0.052]	19073 [R$_{int}$ = 0.028]
Data/restraints/parameters	12014/23/731	11769/0/557	19073/0/696
Δρ$_{max}$, Δρ$_{min}$ (e Å^{-3})	2.52, -5.61	1.73, -1.07	0.81, -0.57
Density(ρ$_{calc}$, g/cm^3)	1.278	1.178	1.223
Completeness to θ	99% (25.99)	99% (25.73)	99% (30.53)
Limiting indices	-15 ≤ h ≤ 15, -26 ≤ k ≤ 25, -28 ≤ l ≤ 28	-18 ≤ h ≤ 18, -21 ≤ k ≤ 21, -28 ≤ l ≤ 28	-17 ≤ h ≤ 17, -19 ≤ k ≤ 19, -28 ≤ l ≤ 28
2θ range (°)	5.054 to 51.998	2.89 to 51.46	3.50 to 61.06
F (000)	2460.0	2276.0	1200.0
Final R indices [I>2σ (I)]	R$_1$ = 0.0694, wR$_2$ = 0.1590	R$_1$ = 0.059, wR$_2$ = 0.175	R$_1$ = 0.030, wR$_2$ = 0.070
R indices (all data)	R$_1$ = 0.0860, wR$_2$ = 0.1717	R$_1$ = 0.080, wR$_2$ = 0.193	R$_1$ = 0.041, wR$_2$ = 0.075
$R_1 = \sum |F_0 - F_c| / \sum F_0$; $wR_2 = \sum [w(F_0^2 - F_0^2)]^2 / [w(F_0^2)^2]^{\frac{1}{2}}$			

Table 3.B.2. Data collection and refinement parameters for compounds **3.B.4-3.B.5**.

	3.B.4	**3.B.4'**	**3.B.5**
Chemical formula	C$_{66}$H$_{76}$Dy$_1$N$_1$O$_7$	C$_{66}$H$_{76}$Dy$_{0.09}$N$_1$O$_7$Y$_{0.91}$	C$_{66}$H$_{76}$Er$_1$N$_1$O$_7$
M$_w$ (g mol^{-1})	1157.77	1090.81	1162.53
Crystal system, space group	Triclinic, *P*-1	Monoclinic, *P*21/*c*	Triclinic, *P*-1
Temperature (K)	296(2)	120.02(10)	296(2)
a, b, c (Å)	12.220(4) 13.799(4) 19.728(7)	12.5954(4) 23.3723(7) 20.4784(6)	12.532(2) 19.835(3) 25.806(4)
α, β, γ (°)	94.577(2) 99.474(2) 105.841(2)	90 99.867(3) 90	106.578(10) 94.751(10) 91.386(10)
V (Å^3)	3129.7(18)	5939.3(3)	6119.6(17)
Z	2	4	4

Radiation type	MoKα (λ = 0.71073)	MoKα (λ = 0.71073)	MoKα (λ = 0.71073)
μ (mm^{-1})	1.243	1.059	1.422
Crystal size (mm)	0.3 × 0.15 × 0.09	0.25 × 0.16 × 0.1	0.2 × 0.17 × 0.15
Reflections collected	72393	72077	94211
GOF on F^2	1.017	1.078	1.008
Independent reflections [R$_{int}$]	19102 [R$_{int}$ = 0.045]	13979 [R$_{int}$ = 0.0895]	24124 [R$_{int}$ = 0.049]
Data/restraints/ parameters	19102/0/696	13979/0/697	24124/0/1391
Δρ$_{max}$, Δρ$_{min}$ (e Å^{-3})	0.65, -0.68	0.55, -0.69	0.65, -0.48
Density(ρ$_{calc}$, g/cm^3)	1.229	1.220	1.262
Completeness to θ	99% (30.60)	99% (25.24)	99% (26.06)
Limiting indices	-17 ≤ h ≤ 17, -18 ≤ k ≤ 19, -28 ≤ l ≤ 28	-14 ≤ h ≤ 17, -31 ≤ k ≤ 30, -27 ≤ l ≤ 26	-15 ≤ h ≤ 15, -20 ≤ k ≤ 24, -31 ≤ l ≤ 31
2θ range (°)	2.11 to 61.21	5.05 to 57.98	2.14 to 52.12
F (000)	1202.0	2306.0	2412.0
Final R indices [I>2σ (I)]	R$_1$ = 0.036, wR$_2$ = 0.078	R$_1$ = 0.062, wR$_2$ = 0.111	R$_1$ = 0.036, wR$_2$ = 0.076
R indices (all data)	R$_1$ = 0.054, wR$_2$ = 0.088	R$_1$ = 0.105, wR$_2$ = 0.118	R$_1$ = 0.061, wR$_2$ = 0.086
$R_1 = \sum|F_0 - F_c|/\sum F_0$; $wR_2 = \sum[w(F_0^2 - F_0^2)]^2/[w(F_0^2)^2]^{\frac{1}{2}}$			

3.B.2.6 Synthesis of ^{Mes}Acac. The ^{Mes}Acac ligand was prepared by the Friedel-Crafts acylation reaction of malonyl dichloride and mesitylene using anhydrous aluminum chloride as catalyst (Scheme 3.B.2). In a typical procedure, malonyl dichloride (1.41 g, 0.01 mol) was added dropwise to a mixture of mesitylene (6 ml, 0.04 mol) and anhydrous aluminum chloride (6.0 g, 0.045 mol) in 50 ml of carbon disulfide cooled with an ice bath. After the addition was complete, the reaction mixture was stirred at 60 °C for 3 h and then poured into 5 ml of concentrated HCl and 20 g of ice with vigorous stirring. The carbon disulfide solution was separated from the aqueous layer

and washed several times with water. The solvent was removed, and the residue was washed several times with ether to give an off-white solid corresponding to the *tris*(1,3-dimesityl-propane-1,3-dionato)aluminum(III) [AlL$_3$] complex. The solid of [AlL$_3$] complex (2.63 g, 6.25 mmol) was then dissolved in CHCl$_3$ and added 5 ml of conc. HCl. The mixture was refluxed for 24 h to yield the ^{Mes}Acac ligand, which was recrystallized from ethanol as colorless crystalline solids. Yield: 2.1 g (75%) M.P.: 105 °C. ESI-MS: 309.1784 [M + H]$^+$. ^{1}H NMR (CDCl$_3$, 700 MHz, δ = ppm): 2.28-2.32 (d, 18H, CH$_3$), 5.75 (s, 1H, enol CH), 6.88 (s, 4H, ArH). ^{13}C{^{1}H} NMR (CDCl$_3$, 175 MHz, δ = ppm): 19-21 (CH$_3$), 105 (CH$_2$), 128-139 (Ar C=C), 191 (C=O). IR (KBr, υ = cm^{-1}), 3431 (OH), 3107 (C=C−H), 2955 (CH$_2$), 2915 (CH$_3$), 1618(C=O), 1433 (C=C), 1374 (C−H), 1271 (C-O).
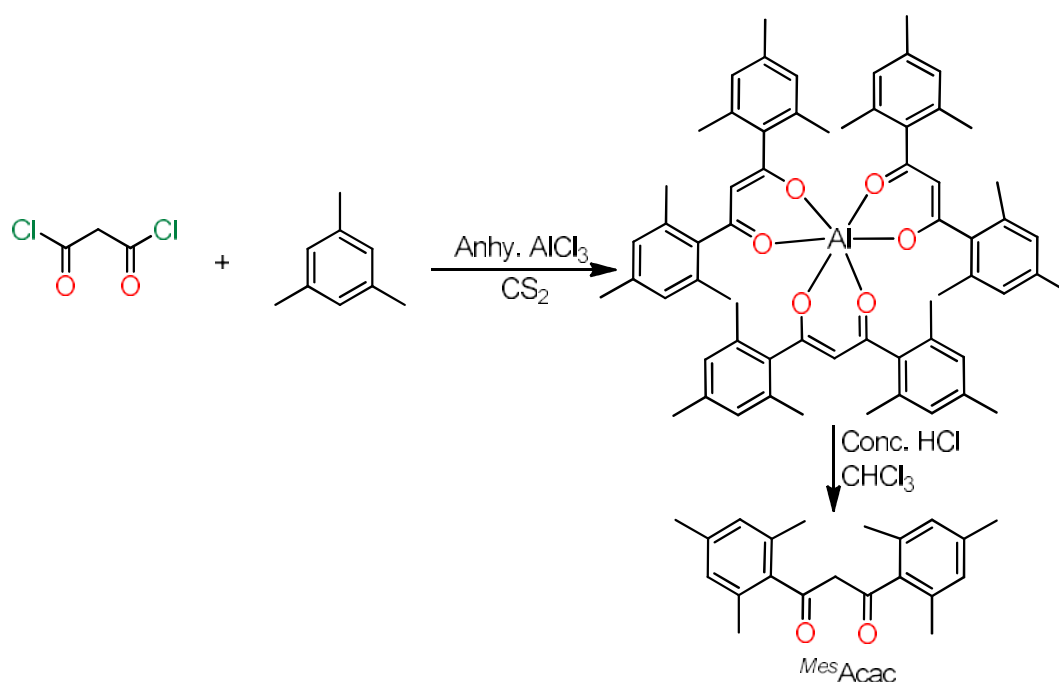
Scheme 3.B.2. Reaction scheme for the synthesis of ^{Mes}Acac.
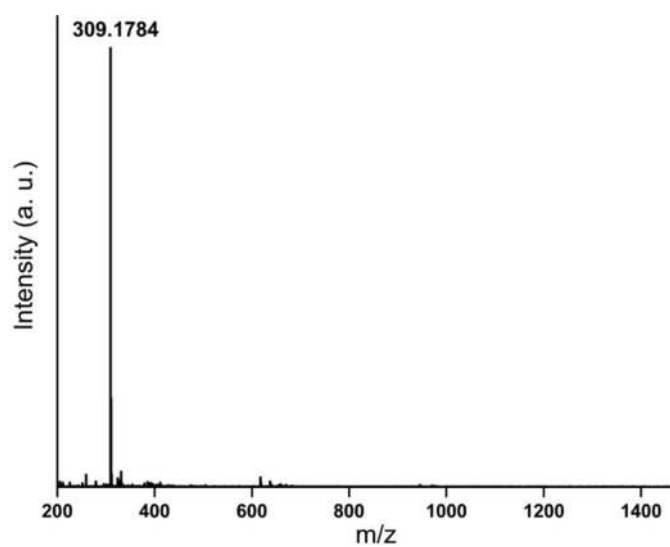
Figure 3.B.2. ESI-MS of ^{Mes}Acac.
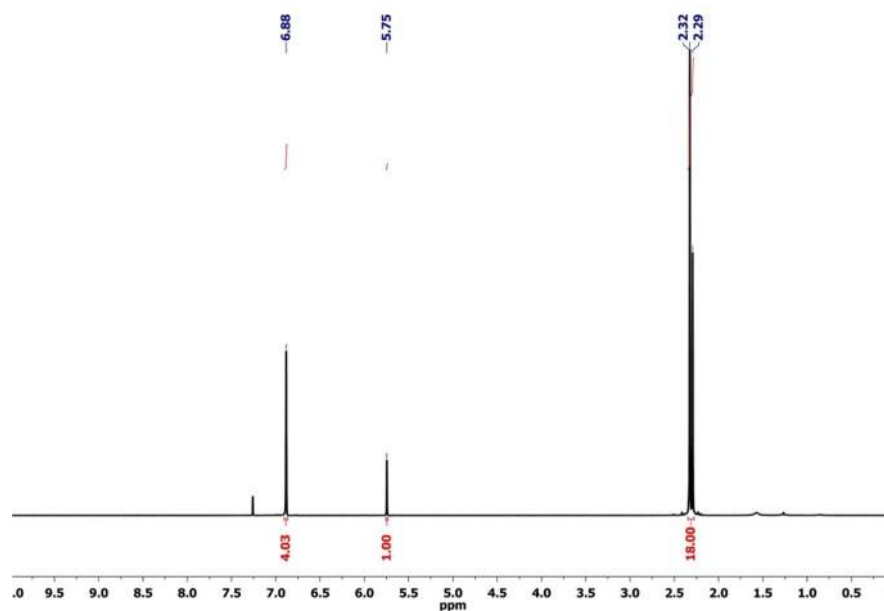
Figure 3.B.3. ^{1}H NMR spectra of ^{Mes}Acac in CDCl$_3$. (The peak at 7.26 is due to the

residual solvent)
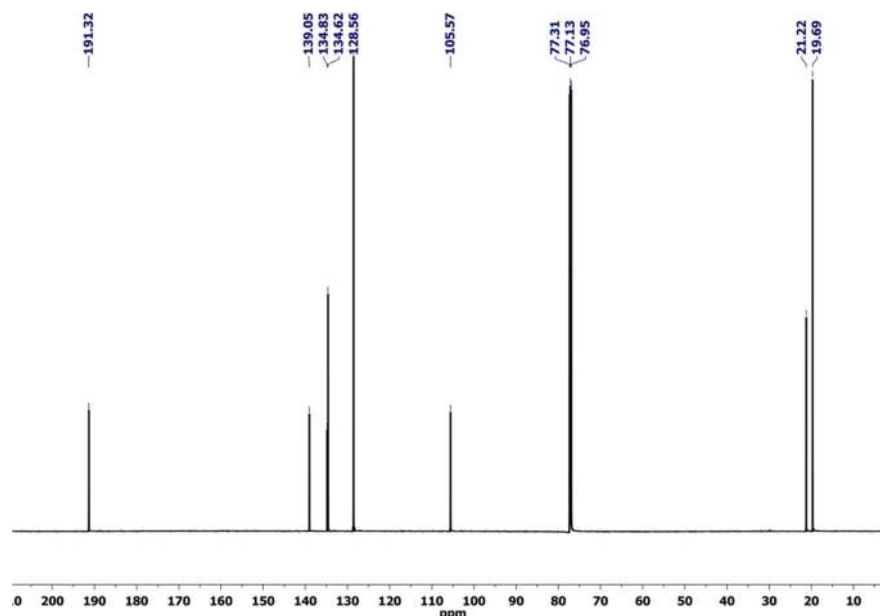
Figure 3.B.4. $^{13}C\{^1H\}$ NMR spectra of ^{Mes}Acac in CDCl$_3$. (The peaks at 76-77 is due to the residual solvent)

3.B.2.7 Synthesis of complexes 3.B.1-3.B.5. A general synthetic protocol was used for the preparation of the metal complexes as follows: ^{Mes}Acac (3 eq.) was taken in ethanol/chloroform solvent mixture (20 mL) and to it 1 mL of DMF was added along with LnCl$_3\cdot$6H$_2$O (1 eq.). To this solution tetramethyl ammonium hydroxide was added (3 eq.). The resulting reaction mixture was heated under reflux for a period of 6 h and brought to ambient temperature. The volume of the solution was reduced to 10 mL, filtered, and kept undisturbed for crystallization under ambient conditions. Slow evaporation of the solvent afforded colorless (for **3.B.1-3.B.4**) and pink (**3.B.5**), block-shaped crystals suitable for single crystal X-ray analysis after one week. The stoichiometry of the reactants involved in each reaction, yield of the products, and their characterization data are provided below:

[Eu(^{Mes}Acac)₃(DMF)] (**3.B.1**). ^{Mes}Acac (0.196 g, 0.636 mmol), EuCl₃·6H₂O (0.058 g, 0.212 mmol), and Me₄NOH (0.115 g, 0.634 mmol) were used. Yield: 0.143 g, 57% (based on Eu). M.P.: >250 °C. Anal. Calcd for $C_{66}H_{85}N_1O_7Er$ (1179.50): C, 68.24; H, 6.84; N, 1.19. Found: C, 68.16; H, 6.63; N, 1.11.

[Gd(^{Mes}Acac)₃(H₂O)] (**3.B.2**). ^{Mes}Acac (0.196 g, 0.636 mmol), GdCl₃·6H₂O (0.079 g, 0.212 mmol), and Me₄NOH (0.115 g, 0.634 mmol) were used. Yield: 0.139 g, 48% (based on Gd). M.P.: >250°C. IR (KBr ν/cm⁻¹): 3447(br), 2994(w), 2949(w),2917(m), 2855(w), 2729(w), 1652(s), 1613(s), 1552(s), 1507(s), 1472(m), 1387(s), 1366(s), 1301(w), 1164(m), 1107(m), 1052(m), 1032(w), 956(w), 850(m), 801(w), 777(w), 722(m), 677(w). Anal. Calcd for $C_{63}H_{71}Gd_1O_7$ (1097.44): C, 68.94; H, 6.52. Found: C, 68.87; H, 6.44.

[Tb(^{Mes}Acac)₃(DMF)] (**3.B.3**). ^{Mes}Acac (0.196 g, 0.636 mmol), TbCl₃·6H₂O (0.079 g, 0.212 mmol), and Me₄NOH (0.115 g, 0.634 mmol) were used. Yield: 0.118 g, 48% (based on Tb). M.P.: >250 °C.IR (KBr ν/cm⁻¹): 3443(br), 2998(w), 2949(m), 2917(m), 2857(w), 2731(w), 1660(s), 1611(s), 1554(s), 1505(s), 1472(m), 1401(s), 1386(s), 1301(m), 1162(m), 1107(m), 1054(m), 1030(w), 958(w), 848(m), 797(w), 777(w), 728(m), 679(w).Anal. Calcd for $C_{66}H_{76}Tb_1N_1O_7$ (1154.19): C, 68.67; H, 6.63; N, 1.21. Found: C, 68.61; H, 6.71; N, 1.16.

[Dy(^{Mes}Acac)₃(DMF)] (**3.B.4**). ^{Mes}Acac (0.196 g, 0.636 mmol), DyCl₃·6H₂O (0.080 g, 0.212 mmol), and Me₄NOH (0.115 g, 0.634 mmol) were used. Yield: 0.132 g, 51% (based on Dy). M.P.: >250 °C.IR (KBr ν/cm⁻¹): 3445(br), 2998(w), 2949(w), 2919(m),2857(w), 2733(w), 1660(s), 1611(s), 1554(s), 1505(s), 1472(m), 1401(s), 1370(s), 1301(m), 1162(m), 1107(m), 1054(m), 1032(w), 958(w), 848(m), 799(w),

777(w), 726(m), 679(w).Anal. Calcd for $C_{66}H_{76}Dy_1N_1O_7$ (1157.77): C, 68.46; H, 6.61; N, 1.21. Found: C, 68.39; H, 6.55; N, 1.17.

[Dy$_{0.09}$Y$_{0.91}$(^{Mes}Acac)$_3$(DMF)] (**3.B.4'**). ^{Mes}Acac (0.196 g, 0.636 mmol), $DyCl_3 \cdot 6H_2O$ (0.008 g, 0.021 mmol), $YCl_3 \cdot 6H_2O$ (0.058 g, 0.191mmol) and Me_4NOH (0.115 g, 0.634 mmol) were used. Yield: 0.112 g, 54% (based on Y). Anal. Calcd for $C_{66}H_{76}N_1O_7Dy_{0.09}Y_{0.91}$ (1090.81): C, 72.60; H, 7.01; N, 1.28. Found: C, 72.56; H, 7.12; N, 1.21.

[Er(^{Mes}Acac)$_3$(DMF)] (**3.B.5**). ^{Mes}Acac (0.196 g, 0.636 mmol), $ErCl_3 \cdot 6H_2O$ (0.081 g, 0.212 mmol), and Me_4NOH (0.115 g, 0.634 mmol) were used. Yield: 0.127 g, 57% (based on Er). M.P.: >250 °C.IR (KBr ν/cm^{-1}): 3445(br), 3006(w), 2949(w), 2917(m), 2855(w), 2731(w), 1662(s), 1613(s), 1556(s), 1505(s), 1472(m), 1405(s), 1370(s), 1301(m), 1162(m), 1107(m), 1054(m), 1032(w), 958(w), 848(m), 797(w), 777(w), 728(m), 681(w).Anal. Calcd for $C_{66}H_{76}Er_1N_1O_7$ (1162.53): C, 68.18; H, 6.58; N, 1.20. Found: C, 68.09; H, 6.50; N, 1.13.

3.B.3 RESULTS AND DISCUSSION

3.B.3.1 Molecular Structures. The molecular structures of complexes **3.B.1**-**3.B.5** were confirmed by single crystal X-ray diffraction studies. The complexes **3.B.1**, **3.B.2** and **3.B.4'** crystallized in the monoclinic crystal system with space groups $P2_1/c$ (for **3.B.1** and **3.B.4'**) and $P2_1/n$ (for **3.B.2**). On the other hand, complexes **3.B.3**, **3.B.4** and **3.B.5** crystallized in the triclinic P-1 space group. All the complexes are formed by the coordination action of three monoanionic ^{Mes}Acac ligands with additional coordination sites occupied by the solvent molecule(s). The complex **3.B.1** is eight-coordinate and the coordinating solvent molecules are EtOH and DMF. The

molecular structure of complex **3.B.1** and its coordination geometry around the Eu^{III} center is shown in Figure 3.B.5.
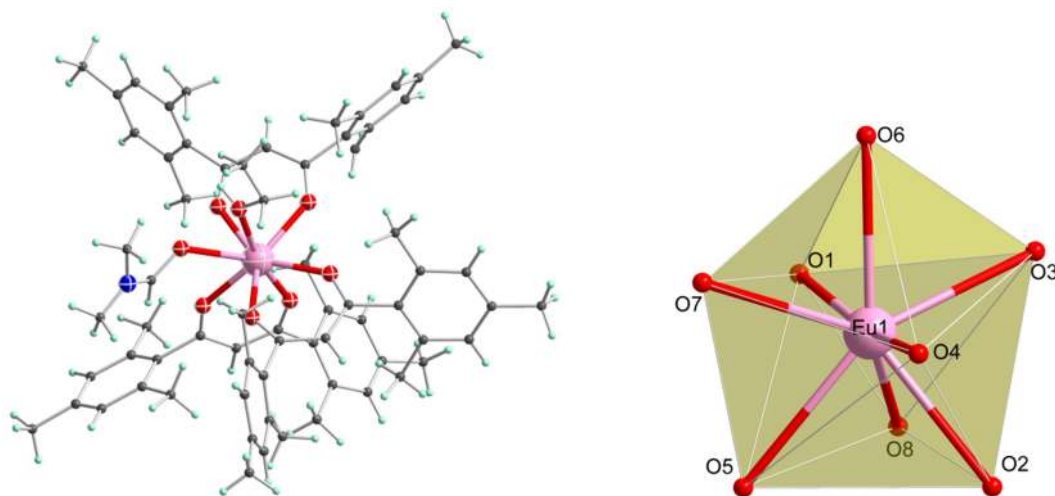
Figure 3.B.5. (*left*) Molecular structure of complex **3.B.1**; (*right*) coordination geometry around the Eu^{III} center. Colour codes: N = blue; O = red; Eu = pink; H = pale blue.

The complexes **3.B.2-3.B.5** are seven-coordinate and the coordinating solvent molecules are H_2O (for **3.B.2**), and DMF (for **3.B.2-3.B.4**). In view of the overall structural similarity present in all the complexes, we choose the complex **3.B.4** as the representative example to elucidate the common structural features present in them. A perspective view of the molecular structure of **3.B.4** is shown in Figure 3.B.6, while those of **3.B.2**, **3.B.3**, **3.B.4'** and **3.B.5** are given in Figures 3.B.8-3.B.11.
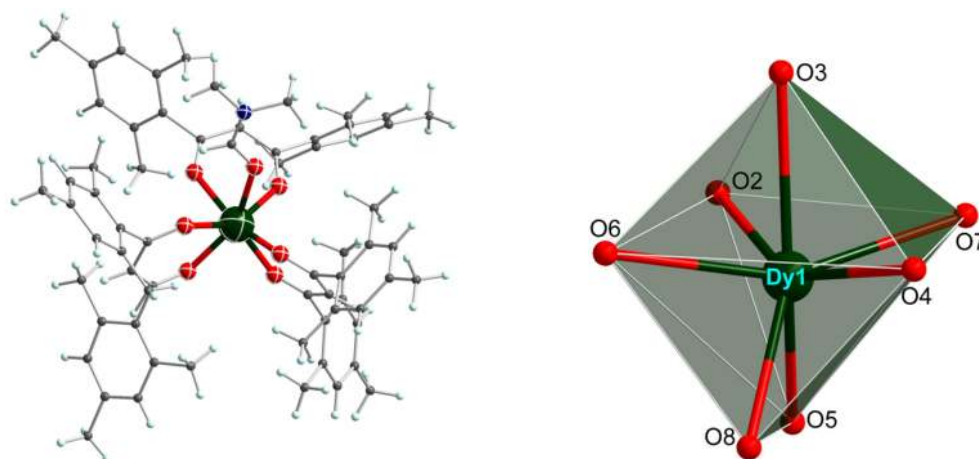
Figure 3.B.6. Molecular structure of complex **3.B.4** (*left*) and the coordination geometry (*right*). Colour codes: N = blue; O = red; Dy = green; H = pale blue.

The seven-coordinate central Dy^{III} in **3.B.4** is coordinated to six oxygen atoms from three ^{Mes}Acac ligands in the η^1:η^1 chelating coordination mode and one oxygen atom from DMF. The cumulative coordination action of all the ligands resulted in a distorted capped octahedron geometry (C_{3v}) around the Dy^{III} center as confirmed by SHAPE analysis (see Table 3.B.3).[31] It is worth mentioning here is that the coordination geometry around the Eu^{III} in complex **3.B.1** is distorted triangular dodecahedron (D_{2d}) (see Table 3.B.4) while the coordination geometry around the Gd^{III} in complex **3.B.2** is distorted capped trigonal prism (C_{2v}) (see Table 3.B.4). The average Dy−O distance for the ^{Mes}Acac ligand is 2.281(2) Å which is comparatively shorter than the Dy−O$_{DMF}$ distance 2.3833(17) Å (see Table 3.B.9). This is primarily due to a strong electrostatic interaction of the highly charged Dy^{III} ion with the anionic ligands. The selected bond distance and angle parameters of **3.B.1**-**3.B.5** are given in the Tables 3.B.6-3.B.11. The crystal packing diagram reveals that the paramagnetic centers are physically far apart with the shortest intermolecular Dy···Dy separation being 9.539 Å (see Figure 3.B.7 (*left*)). The SHAPE analyses of all the complexes are given in the Table 3.B.3 (for **3.B.1**) and Table 3.B.4 (for **3.B.2**-

3.B.5).[31-32] The coordination polyhedra of the Ln[III] center in complexes **3.B.2**, **3.B.3**, **3.B.4'** and **3.B.5** are given in Figure 3.B.12.
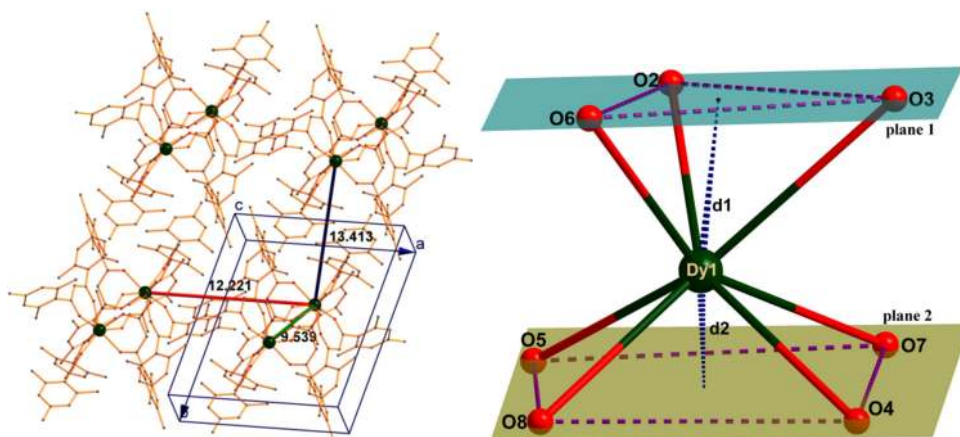
Figure 3.B.7. The solid-state crystal packing diagram of complex **3.B.4** (*left*) and the 3:4 piano stool coordination geometry around Dy[III] (*right*).

The coordination geometry around the Dy[III] can also be viewed as an interesting 3:4 *pseudo*-sandwich conformation where the metal center is sandwiched between a triangular plane and a trapezoid plane (see Figure 3.B.7(*right*)). The triangular plane (*plane 1*) is composed of three oxygen atoms (O2, O3, and O6) of which two are from the ^{Mes}Acac ligand (O2, O6) and the remaining one belongs to the coordinated DMF molecule (O3). The trapezoid plane (*plane 2*) is composed of four oxygen atoms (O4, O5, O7, and O8) which belong to two ^{Mes}Acac ligands. It is to be noted that the distances of *plane 1* and *plane 2* from the Dy[III] centers is quite different. The distance between the Dy[III] and *plane 2* is shorter compared to the *plane 1* because of high negative charge present in the coordinating atoms in that plane. Detailed structural parameters about the plane distances (d1 and d2) from the Ln[III] center, inter-planar distances (*l*), bending angle of the centroid of *plane 1*−Ln[III]−centroid of *plane 2* (α) for complexes **3.B.3** and **3.B.4** are given in Table 3.B.5. These two complexes show comparatively short inter-planar distances compared to the reported complexes which

are expected to stabilize the oblate shaped single-ion anisotropies of the Dy^{III} and Tb^{III} ions.

Table 3.B.3. Continuous Shape Measures (CShM) for Eu^{III} atom in **3.B.1**.

Polyhedron	Eu1
OP-8	32.610
HPY-8	21.940
HBPY-8	14.019
CU-8	12.735
SAPR-8	4.686
TDD-8	**2.218**
JGBF-8	10.571
JETBPY-8	25.668
JBTPR-8	3.263
BTPR-8	3.166
JSD-8	3.286
TT-8	13.352
ETBPY-8	21.911

†*OP-8 = Octagon (D_{8h}); HPY-8 = Heptagonal pyramid (C_{7v}); HBPY-8 = Hexagonal bipyramid (D_{6h}); CU-8 = Cube (O_h); SAPR-8 = Square antiprism (D_{4d}); TDD-8 = Triangular dodecahedron (D_{2d}); JGBF-8 = Johnson gyrobifastigium J26 (D_{2d}); JETBPY-8 = Johnson elongated triangular bipyramid J14 (D_{3h}); JBTPR-8 = Biaugmented trigonal prism J50 (C_{2v}); BTPR-8 = Biaugmented trigonal prism (C_{2v}); JSD-8 = Snub diphenoid J84 (D_{2d}); TT-8 = Triakis tetrahedron (T_d); ETBPY-8 = Elongated trigonal bipyramid (D_{3h})*

Table 3.B.4. Continuous Shape Measures (CShM) for Ln^{III} atom in **3.B.2-3.B.5**.

Complex	Structure†						
	HP-7	HPY-7	PBPY-7	**COC-7**	**CTPR-7**	JPBPY-7	JETPY-7
3.B.2_Gd CShM	34.425	20.755	5.128	1.591	**0.781**	8.661	18.857
3.B.3_Tb CShM	33.050	21.423	6.185	**0.712**	1.533	9.626	16.300
3.B.4_Dy CShM	33.207	21.365	6.096	**0.675**	1.506	9.512	16.499
3.B.4'_Y CShM	33.906	21.193	6.279	**0.620**	1.162	9.969	16.768
3.B.5_Er1 CShM	35.253	19.894	5.631	**0.646**	1.604	9.321	19.036

† HP-7 = Heptagon (D$_{7h}$); HPY-7 = Hexagonal pyramid (C$_{6v}$); PBPY-7 = Pentagonal bipyramid (D$_{5h}$); COC-7 = Capped octahedron (C$_{3v}$); CTPR-7 = Capped trigonal prism (C$_{2v}$); JPBPY-7 = Johnson pentagonal bipyramid J13 (D$_{5h}$); JETPY-7 = Johnson elongated triangular pyramid J7 (C$_{3v}$)

Table 3.B.5. A summary of the *pseudo*-sandwich geometry

	3.B.3	**3.B.4**	**Dy(EIFD)$_3$(H$_2$O)**	**Dy(EIFD)$_3$(DMSO)**	**[(L$_{OEt}$)Dy(L)]**
distance between Ln and centroid of *plane 1* (d1, Å)	1.552	1.544	1.5647	1.5926	1.549
distance between Ln and centroid of *plane 2* (d2, Å)	1.047	1.048	1.0768	1.0856	1.222
distance between *plane 1* and *plane 2* (*l*, Å)	2.593	2.5870	2.6368	2.6561	2.749
bending angle (α, º)	172.23	172.519	173.072	175.278	165.30
Reference	this work	this work	[18]	[18]	[33]
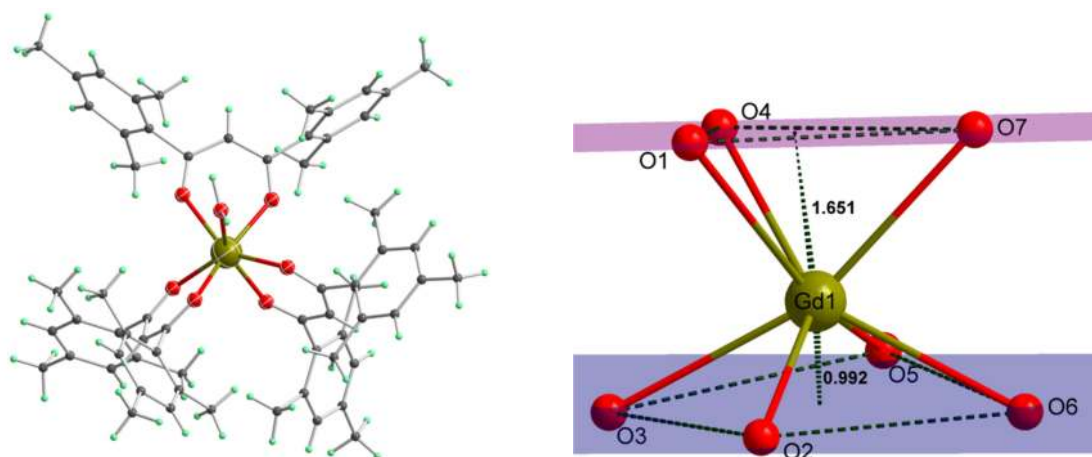
Figure 3.B.8. (*left*) Molecular structure of complex **3.B.2**; (*right*) piano stool coordination geometry around the Gd^{III} center. Colour codes: N = blue; O = red; Gd = dark yellow; H = pale blue.
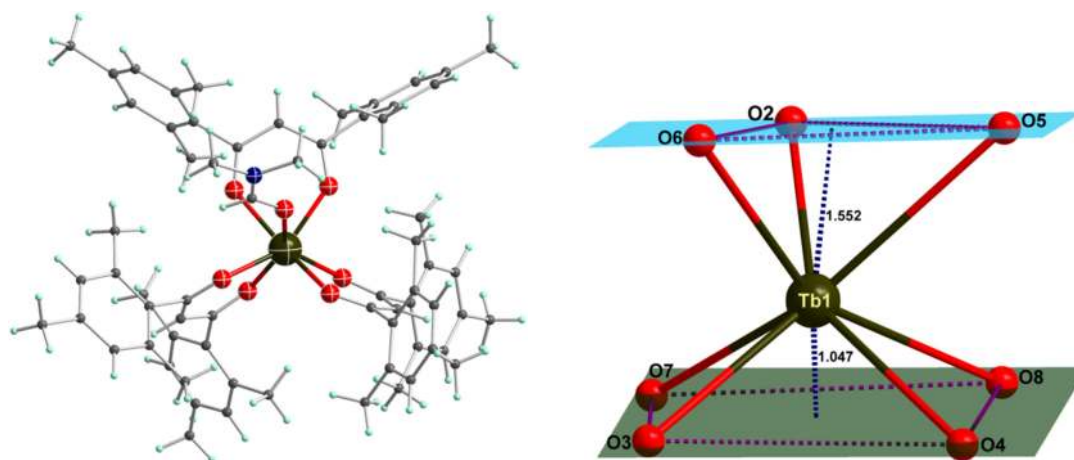
Figure 3.B.9. (*left*) Molecular structure of complex **3.B.3**; (*right*) piano stool coordination geometry around the Tb^{III} center. Colour codes: N = blue; O = red; Gd = olive green; H = pale blue.
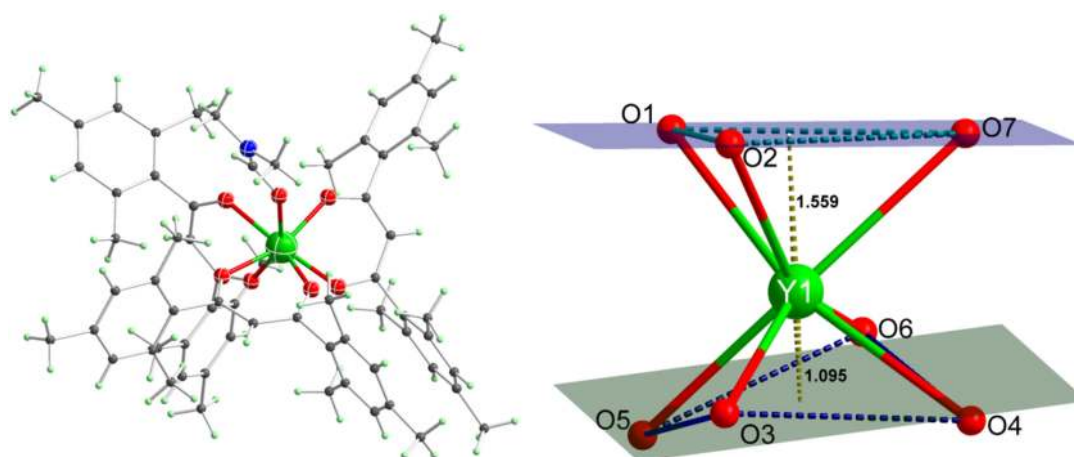
Figure 3.B.10. (*top*) Molecular structure of complex **3.B.4'**; (*bottom*) piano stool coordination geometry around the $(Y_{0.09}/Dy_{0.91})^{III}$ center. Colour codes: N = blue; O = red; $Y_{0.09}Dy_{0.91}$ = bright green; H = pale blue.
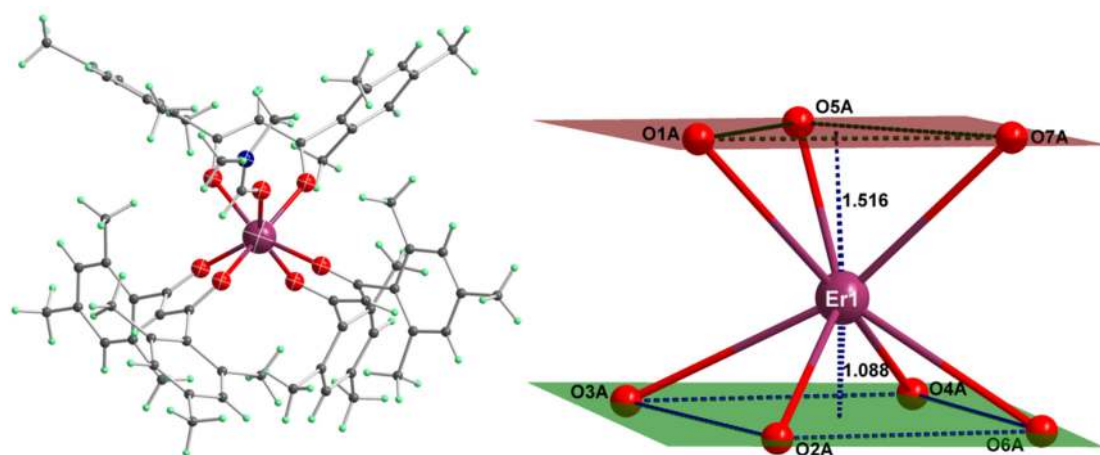
Figure 3.B.11. (*left*) Molecular structure of complex **3.B.5**; (*right*) piano stool coordination geometry around the Er^{III} center. Colour codes: N = blue; O = red; Er = plum; H = pale blue.

(a)

(b)

(c)

(d)
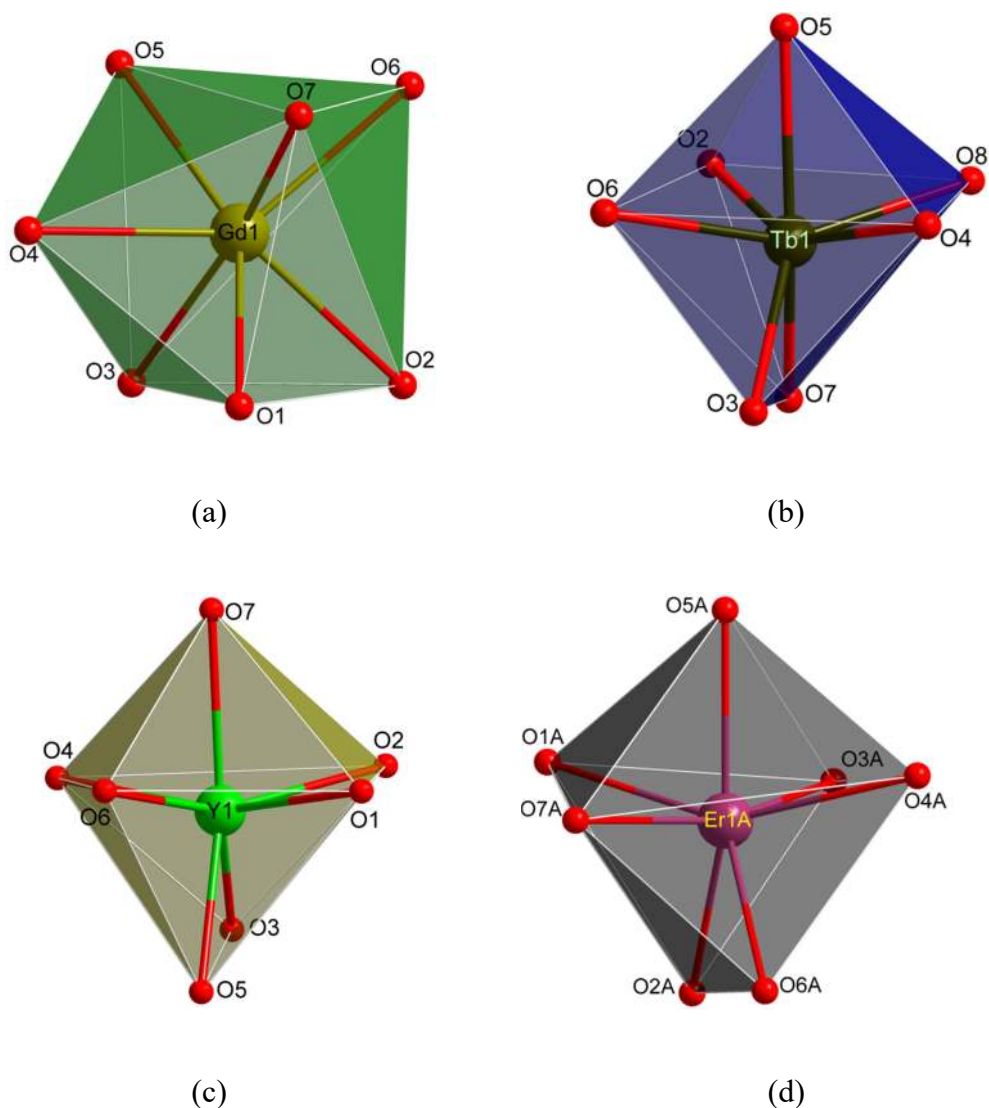
Figure 3.B.12. (a) Distorted capped trigonal prism geometry of Gd1 in complex **3.B.2**. (b-d) Distorted capped octahedron geometry of Ln[III] in complexes **3.B.3**, **3.B.4'** and **3.B.5**.

Table 3.B.6. Selected bond lengths (Å) and angles (°) of complex **3.B.1**.

Bond lengths (Å)		**Bond angles** (°)		
Eu1−O1	2.395(4)	O6−Eu1−O1	139.70(14)	O6−Eu1−O3 133.47(16)
Eu1−O2	2.358(4)	O6−Eu1−O7	70.70(17)	O6−Eu1−O8 120.1(3)
Eu1−O3	2.364(5)	O2−Eu1−O4	144.17(15)	O2−Eu1−O1 71.71(14)
Eu1−O4	2.389(4)	O2−Eu1−O3	140.69(14)	O2−Eu1−O7 74.84(19)
Eu1−O5	2.298(4)	O5−Eu1−O1	85.41(15)	O5−Eu1−O3 77.56(19)
Eu1−O6	2.350(4)	O5−Eu1−O7	142.64(18)	O5−Eu1−O8 167.8(3)

Eu1−O7	2.713(7)	O4−Eu1−O1	139.56(15)	O4−Eu1−O8	85.8(3)
Eu1−O8	2.454(10)	O3−Eu1−O4	72.85(15)	O3−Eu1−O1	69.01(15)

Table 3.B.7. Selected bond lengths (Å) and angles (°) of complex **3.B.2**.

Bond lengths (Å)		Bond angles (°)			
Gd1–O1	2.449(5)	O2–Gd1–O4	140.17(15)	O3–Gd1–O1	89.80(20)
Gd1–O2	2.320(4)	O3–Gd1–O4	82.33(14)	O4–Gd1–O1	72.03(18)
Gd1–O3	2.326(4)	O5–Gd1–O1	146.42(18)	O5–Gd1–O2	133.52(17)
Gd1–O4	2.333(4)	O6–Gd1–O1	129.18(19)	O6–Gd1–O2	79.40(15)
Gd1–O5	2.305(4)	O6–Gd1–O3	124.81(15)	O6–Gd1–O4	140.05(14)
Gd1–O6	2.317(4)	O7–Gd1–O1	76.20(20)	O7–Gd1–O2	113.67(17)
Gd1–O7	2.309(4)	O7–Gd1–O3	161.49(16)	O7–Gd1–O4	81.91(15)

Table 3.B.8. Selected bond lengths (Å) and angles (°) of complex **3.B.3**.

Bond lengths (Å)		Bond angles (°)			
Tb1–O2	2.308(2)	O2–Tb1–O3	134.99(5)	O2–Tb1–O5	76.94(5)
Tb1–O3	2.316(2)	O2–Tb1–O8	82.11(5)	O3–Tb1–O5	134.19(5)
Tb1–O4	2.285(2)	O3–Tb1–O8	128.18(5)	O4–Tb1–O2	148.64(5)
Tb1–O5	2.395(2)	O4–Tb1–O6	105.35(5)	O4–Tb1–O7	123.20(5)
Tb1–O6	2.292(2)	O4–Tb1–O8	73.78(5)	O6–Tb1–O2	88.37(5)
Tb1–O7	2.287(2)	O6–Tb1–O8	155.39(6)	O7–Tb1–O2	74.22(5)
Tb1–O8	2.320(2)	O7–Tb1–O3	75.13(5)	O7–Tb1–O5	149.52(5)

Table 3.B.9. Selected bond lengths (Å) and angles (°) of complex **3.B.4**.

Bond lengths (Å)		Bond angles (°)			
Dy1−O2	2.292 (2)	O2−Dy1−O3	77.06(6)	O2−Dy1−O8	135.00(7)
Dy1−O3	2.383 (2)	O4−Dy1−O2	148.85(6)	O4−Dy1−O3	78.94(7)
Dy1−O4	2.273(2)	O4−Dy1−O5	122.99(7)	O4−Dy1−O7	74.18(6)
Dy1−O5	2.279(2)	O4−Dy1−O8	76.14(6)	O5−Dy1−O3	149.85(6)
Dy1−O6	2.275(2)	O5−Dy1−O7	86.65(7)	O5−Dy1−O8	74.85(6)
Dy1−O7	2.304(2)	O6−Dy1−O2	87.88(6)	O6−Dy1−O5	111.96(7)
Dy1−O8	2.307(2)	O6−Dy1−O7	155.79(7)	O6−Dy1−O8	74.08(6)

Table 3.B.10. Selected bond lengths (Å) and angles (°) of complex **3.B.4'**.

Bond lengths (Å)		Bond angles (°)			
Y1–O1	2.336(2)	O3–Y1–O6	138.03(8)	O3–Y1–O7	132.75(8)
Y1–O2	2.270(2)	O6–Y1–O1	79.27(7)	O2–Y1–O3	72.30(8)
Y1–O3	2.306(2)	O2–Y1–O6	149.07(8)	O2–Y1–O7	81.95(8)
Y1–O4	2.262(2)	O4–Y1–O6	86.34(8)	O4–Y1–O2	113.79(8)
Y1–O5	2.255(2)	O4–Y1–O7	81.63(8)	O4–Y1–O1	160.02(8)
Y1–O6	2.329(2)	O5–Y1–O3	75.07(8)	O5–Y1–O6	75.09(7)
Y1–O7	2.336(2)	O5–Y1–O2	118.07(8)	O5–Y1–O7	151.55(8)

Table 3.B.11. Selected bond lengths (Å) and angles (°) of complex **3.B.5**.

Bond lengths (Å)		Bond angles (°)			
Er1A–O1A	2.335(2)	O2A–Er1A–O1A	77.51(9)	O2A–Er1A–O3A	74.78(8)
Er1A–O2A	2.268(2)	O2A–Er1A–O4A	122.54(9)	O3A–Er1A–O1A	84.62(9)
Er1A–O3A	2.278(2)	O4A–Er1A–O1A	151.16(9)	O4A–Er1A–O3A	81.81(9)
Er1A–O4A	2.274(2)	O5A–Er1A–O3A	87.82(8)	O5A–Er1A–O4A	74.24(8)
Er1A–O5A	2.260(2)	O6A–Er1A–O1A	131.77(9)	O6A–Er1A–O2A	73.87(9)
Er1A–O6A	2.266(2)	O6A–Er1A–O3A	122.78(8)	O6A–Er1A–O4A	76.59(8)
Er1A–O7A	2.256(2)	O7A–Er1A–O1A	79.26(9)	O7A–Er1A–O2A	107.63(9)

3.B.3.2 Photophysical studies. The UV-Visible absorption spectra of complexes **3.B.1-3.B.5** and ^{Mes}Acac were recorded in the DMF solvent (c = 1 x 10^{-5} M) at 298 K (Figure 3.B.13). The absorption properties of ^{Mes}Acac and complexes **3.B.1-3.B.5** are summarized in Table 3.B.12.
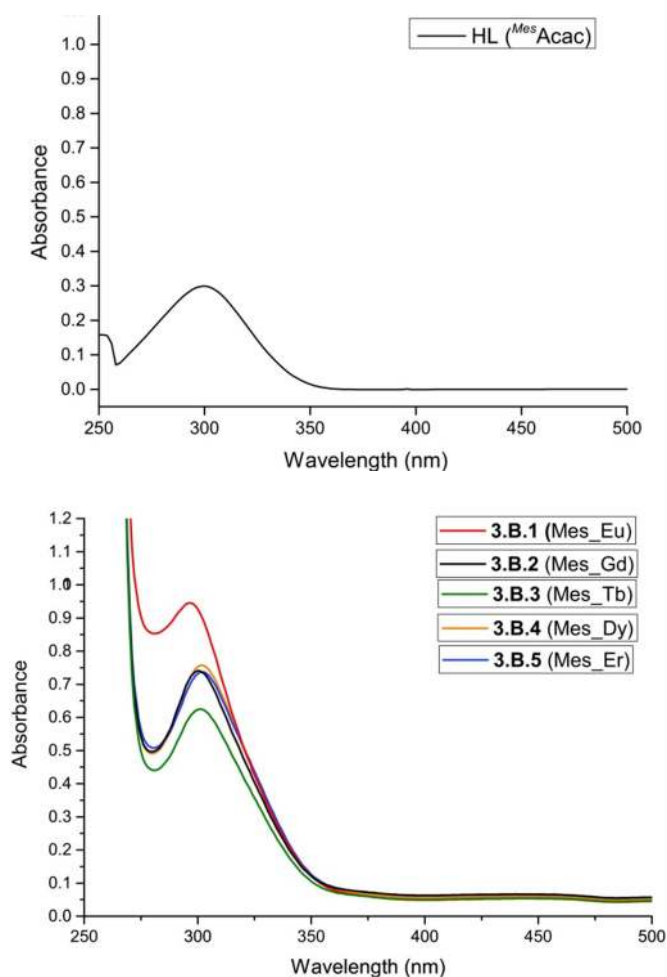
Figure 3.B.13. Absorption spectra of free ligand, ^{Mes}Acac (*top*) and complexes **3.B.1**-**3.B.5** (*bottom*) in DMF (~10^{-5} M).

Table 3.B.12. Absorption properties of ^{Mes}Acac and the complexes (**3.B.1-3.B.5**) in DMF at 298 K

Compound	Absorbance λ [nm] (ε_{max} [1 x 10^3 M^{-1} cm^{-1}]) in solution
^{Mes}Acac	300 (14.99)
3.B.1	297 (47.25)
3.B.2	303 (37.01)
3.B.3	307 (31.24)
3.B.4	306 (37.84)
3.B.5	307(36.86)

The ligand (^{Mes}Acac) displays only one absorption maxima at 300 nm corresponding to the spin-allowed singlet $\pi \rightarrow \pi^*$ transition. In all the complexes this band is shifted to slightly lower or higher wavenumbers (Table 3.B.12) consistent with coordination of the ligand to the metal centers (Figure 3.B.13). The molar absorption coefficients are calculated and tabulated in the Table 3.B.12. The high molar absorption coefficients in the complexes suggest that the ligand could be involved for sensitization of the lanthanide luminescence.

The emission spectrum of free ligand is shown in Figure 3.B.14 (*top*). The free ligand exhibits four emission bands at 360 nm, 407 nm, 492 nm, 547 nm respectively. Among all the complexes studied only the Eu^{III} and Tb^{III} derivatives (**3.B.1** and **3.B.3**) show strong metal-centered red and green luminescence in 5 μM solution in DMF solvent media respectively. Thus, upon excitation at the ligand energy level (λ_{ex}= 300 nm), the {Eu^{III}} complex **3.B.1** exhibits sharp emission bands at 593 nm and 616 nm Figure 3.B.14 (*bottom*). These are characteristic of Eu^{III} emission resulting from the deactivation of $^5D_4$ excited state to ^7F_J ground state ($J = 1, 2$).[34] Among the emission peaks the most intense emission at 616 nm corresponds to the $^5D_0 \rightarrow {}^7F_2$ transition.[34] This intense peak points to a highly polarizable chemical environment around the Eu^{III} ion and is responsible for the observed characteristics red emission.
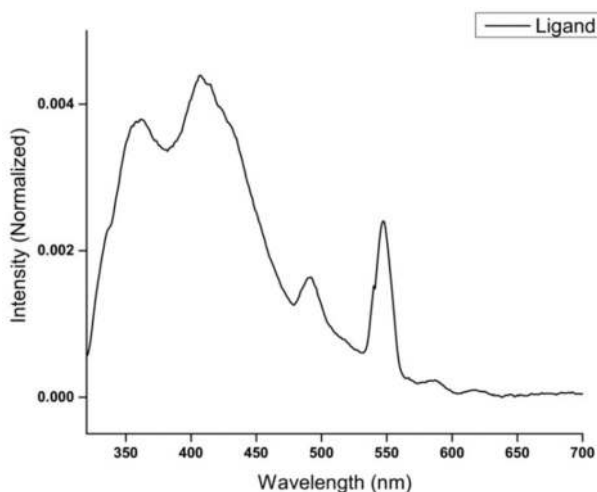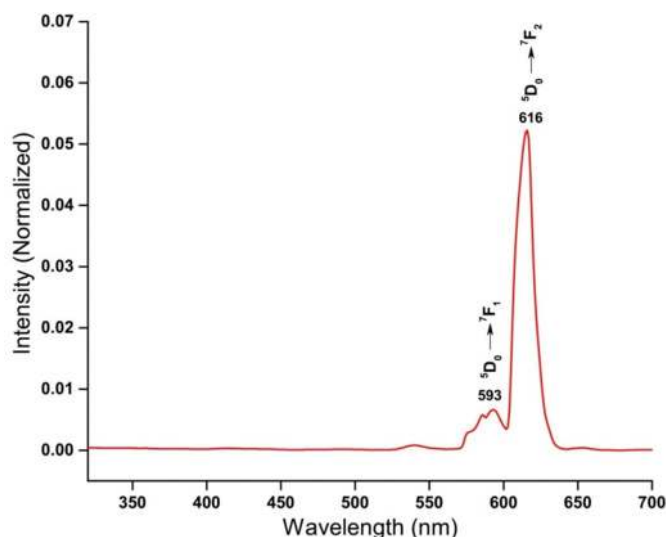
Figure 3.B.14. Emission spectrum of ^{Mes}Acac (*top*) and the Eu^{III} complex **3.B.1** (*bottom*) (excitation at 300 nm; DMF solution 5 μM) at room temperature.

In the case of Tb^{III} complex **3.B.3**, upon excitation at the ligand energy level ($\lambda_{ex} =$ 300 nm), exhibits sharp emission bands 493 nm, 548 nm, 586 nm, and 621 nm (Figure 3.B.15). These are characteristic of Tb^{III} emission resulting from the deactivation of $^5D_4$ excited state to ^7F_J ground state ($J =$ 6, 5, 4, 3).[35] Among the emission peaks the most intense emission at 548 nm corresponds to the $^5D_4 \rightarrow {}^7F_5$ transition.
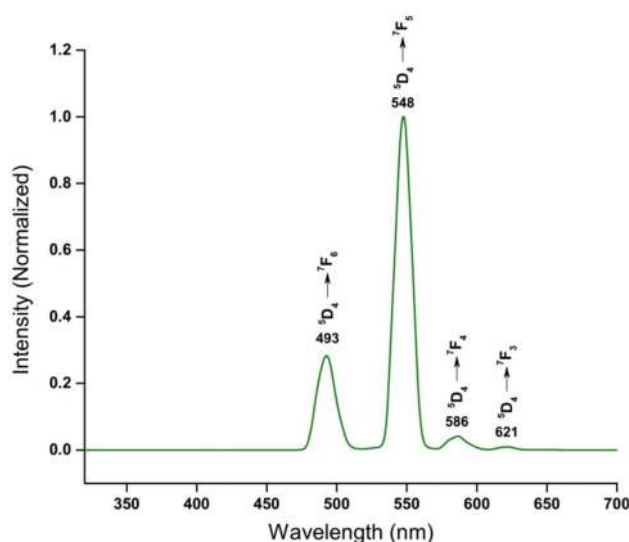
Figure 3.B.15. Emission spectrum of the Tb^{III} complex **3.B.3** (excitation at 300 nm; DMF solution 5 μM) at room temperature.

In the case of Dy^{III} complex **3.B.4**, upon excitation at the ligand energy level (λ_{ex} = 300 nm), two weak emission bands at 485 nm and 577 nm was observed (Figure 3.B.16). These are characteristic of Dy^{III} emission resulting from the deactivation of $^4F_{9/2}$ excited state to ^6H_J ground state (J = 15/2, 13/2).[35a] However, in this case a shoulder peak is observed at 492 nm corresponding to the ligand centered emissions.
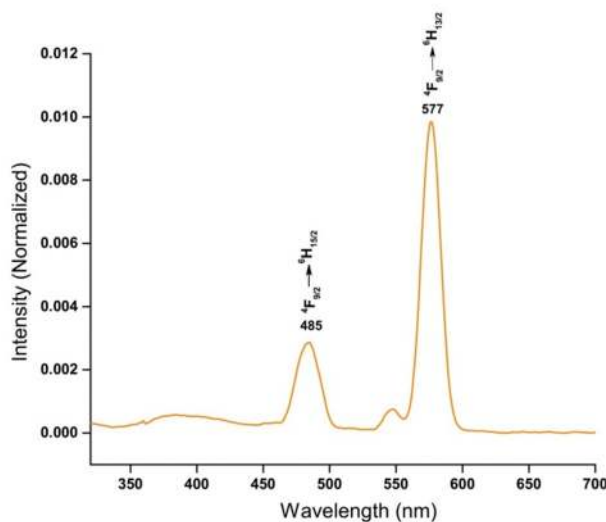
Figure 3.B.16. Emission spectrum of the Dy^{III} complex **3.B.4** (excitation at 300 nm; DMF solution 5 μM) at room temperature.

In view of the strong emission characteristics of the Eu^{III} and Tb^{III} derivatives, solution-state relative luminescence quantum efficiencies of **3.B.1** and **3.B.3** were calculated by comparing the emission intensities of the standard sample and the unknown sample according to following equation

$$\Phi_{unk} = \Phi_{std}(I_{unk}/I_{std})(A_{std}/A_{unk})(\eta_{unk}/\eta_{std})^2$$

Where Φ_{unk} and Φ_{std} are the luminescence quantum yields of the unknown sample and the standard sample, respectively, and I_{unk} and I_{std} are the integrated emission intensities of the unknown sample and standard sample solution, respectively. A_{unk} and A_{std} are the absorbances of the unknown sample and standard sample solution at their excitation wavelengths, respectively. The η_{unk} and η_{std} terms represent the

refractive indices of the corresponding solvents (pure solvents were assumed). Quinine sulfate monohydrate in 0.5 M H_2SO_4 was used as the standard. The absolute quantum yields of **3.B.1** and **3.B.3** were measured on a Spex-Fluorolog FL22 spectrofluorimeter and the results are tabulated in Table 3.B.14.

Table 3.B.13. Relative quantum yields of complexes **3.B.1** and **3.B.3**.

Complex	I_{unk}	I_{std}	A_{unk}	A_{std}	η_{unk} (DMF)	η_{std} (water)	Φ_{std}	Φ_{unk}	% Φ_{unk}
3.B.1 (Eu)	5979.5	8331071.5	0.0646	0.0646	1.4305	1.33	0.546	0.00049	0.045
3.B.3 (Tb)	123085.2	9323545.5	0.0693	0.0693	1.4305	1.33	0.546	0.00833	0.830

Table 3.B.14. Table of absolute quantum yields for **3.B.1** and **3.B.3**.

Sl. No.	Complex	Quantum Yield (%)
1.	**3.B.1** (Eu)	0.58
2.	**3.B.3** (Tb)	0.74

3.B.3.3 Magnetic properties.

Direct current (dc) magnetic susceptibility measurements were carried out on a polycrystalline sample of **3.B.4** in the 290-2 K temperature range in an applied magnetic field of 1000 Oe. The dependence on temperature of $\chi_M T$ product for **3.B.4** (χ_M is the molar magnetic susceptibility per mononuclear Dy^{III} unit) is given in Figure 3.B.17. The $\chi_M T$ value at room temperature (14.05 cm^3 mol^{-1} K) agrees well with that expected for an isolated Dy^{III} ion in the free ion approximation (14.18 cm^3 mol^{-1} K). Upon cooling, $\chi_M T$ decreases slowly until ~125 K and then decreases more rapidly to reach a value of 9.74 cm^3 mol^{-1} K at 2 K. This behaviour is mainly due to the depopulation of the M_J sublevels of the Dy^{III} ions, which arise from the splitting of the $^6H_{15/2}$ ground term by the ligand field, as well as Zeeman effects and possible intermolecular dipolar interactions (which must be very small due to the large

Dy···Dy distance of 9.538 Å). The field dependence of the magnetization at $T = 2$ K (Figure 3.B.17 inset) exhibits a fast increase of the magnetization up to ~ 1 T and then a very slow increase to reach almost saturation at 5 T, thus indicating a well isolated ground state. The fact that the magnetization values at the highest applied dc magnetic field of 5 T ($M = 5.10$ Nμ_B) is rather lower than that calculated for an isolated Dy^{III} ion in the free-ion approximation ($M = 7.10$ Nμ_B), is due to crystal-field effects giving rise to significant magnetic anisotropy.
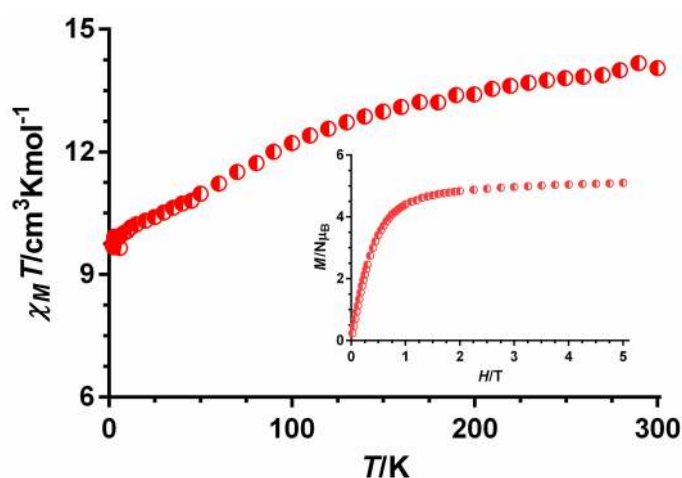
Figure 3.B.17. Temperature dependence of the $\chi_M T$ product and field dependence of the magnetization for compounds **3.B.4**.

It should be noted that low-symmetry Dy^{III} complexes, like **3.B.4**, generally exhibit axial crystal fields, which lead to axial anisotropy with a $M_J = \pm 15/2$ Ising ground Kramers doublet. Assuming the axiality of the ground state, we have calculated the direction of the anisotropy axes of the Dy^{III} ions by using the electrostatic Chilton's method (Figure 3.B.18).[36] As indicated elsewhere,[18, 33] the Dy^{III} coordination sphere can be described as a *pseudo*-sandwich conformation where the metal center is sandwiched between a triangular plane and a trapezoid plane. The trapezoid plane is made of four oxygen atoms belonging to two diketonate ligands, whereas the triangular plane if formed by two oxygen atoms from a diketonate ligand and the

oxygen atom of the DMF molecule. The average Dy–O bond distance in the trapezoid plane is larger than that in the triangular plane, and, moreover, the distance between the trapezoid plane and the Dy^{III} ion is shorter than that to the triangular plane. Considering these considerations, is not surprising that the axial anisotropic axis lies in between these two planes and close to that containing the average shortest Dy–O distance (trapezoid plane).
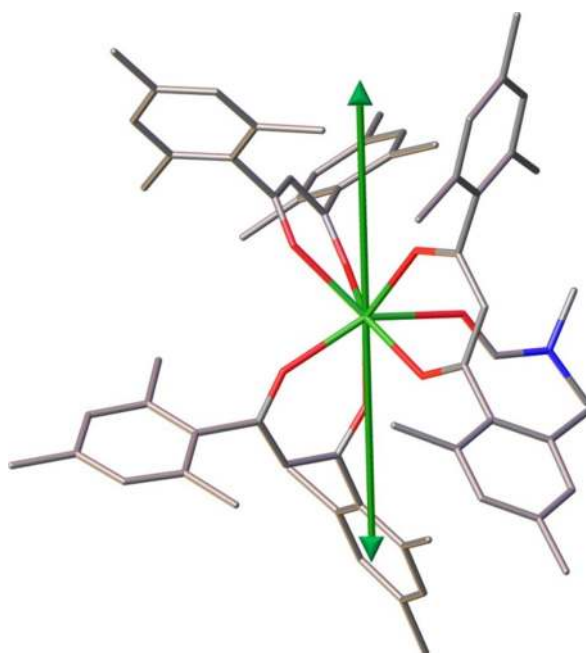
Figure 3.B.18. Quantitative calculation of the anisotropic axes orientation (green arrows) using the Chilton's method.[36]

Preliminary temperature dependent dynamic ac magnetic susceptibility measurements at a frequency of 1400 Hz were carried out to know if **3.B.4** exhibited slow relaxation of the magnetization and SIM behaviour. At zero dc field, complex **3.B.4** shows an out-of-phase (χ''_M) signal below 15 K with an intense tail below 5 K. This tail, which is due to fast resonant zero-field quantum tunneling of the magnetization (QTM), avoids the observation of a clear peak around 5 K. This behaviour can be due to the existence of dipolar and/or hyperfine interactions opening new relaxation pathways for QTM process. When the ac measurements were carried out in the presence of a

small external field of 1000 Oe (this is the field leading to the slower relaxation) compound **3.B.4** showed a well-defined out-of-phase (χ''_M) signal with a maximum at 10 K (Figure 3.B.19, inset). This result clearly points out that the application of a small dc field is enough to suppress QTM.
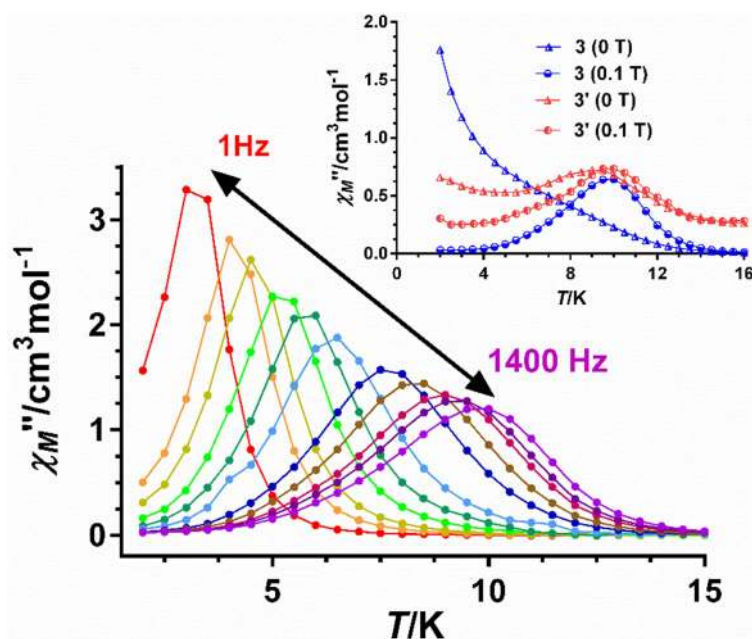
Figure 3.B.19. Temperature dependence of the out-of-phase χ''_M component of the ac susceptibility for **3.B.4** at 0.1 T. (Inset) Temperature dependence of the out-of-phase χ''_M for **3.B.4** and **3.B.4'** at 1400 Hz and under zero and 0.1 T magnetic field (*left*).

In order to know the effect of the magnetic dilution on the slow relaxation of the magnetization, we prepared a magnetic diluted sample of **3.B.4** by substituting Dy^{III} ions by Y^{III} to achieve a Dy^{III}/Y^{III} molar ratio 1/9 (this ratio was estimated from the susceptibility and magnetization data for **3.B.4'** at room temperature compared to those for **3.B.4**). The temperature dependence of out-of-phase (χ''_M) at 1400 Hz and under zero field for **3.B.4'** shows a clear maximum centered at 10 K and a low intensity tail below 5 K, thus pointing out that the QTM has been almost completely suppressed. Moreover, when the results for **3.B.4** at 0.1 T are compared to those of

3.B.4' at zero field, one realizes that the effect of the dilution appears to be a little bit less effective in suppressing QTM than the effect of the field (Figure 3.B.19, inset). As expected, at 0.1 T the results for the **3.B.4** and **3.B.4'** are coincident. Considering this, the complete set of ac measurements on the diluted complex **3.B.4'** were carried out under a field of 0.1 T. The results show a strong frequency dependence of the ac susceptibility signals with maxima in the 10 (1400 Hz)-3 K (1 Hz) temperature range.

The relaxation times (τ) for **3.B.4'** were extracted from the fitting of the frequency dependence of χ''_M at each temperature to the generalized Debye model (Figure 3.B.20). The fit of the relaxation times to the Arrhenius equation in the 8-10 K temperature range afforded the following values of the effective energy barrier for the reversal of the magnetization and the pre-exponential factor, U_{eff} = 70(3) K and τ_0 = 2.7 x 10^{-7} s respectively. The deviation of the data from the Arrhenius law below 8 K is a clear sign that either the magnetic relaxation takes place through a relaxation process other than Arrhenius or there is coexistence of several competing relaxation processes. In the studied temperature range (T > 4 K) and at 0.1 T direct and QTM relaxation processes for **3.B.4'** are almost negligible, and therefore the relaxation times were fitted to the following equation:

$$\tau^{-1} = BT^n + \tau_0^{-1}\exp(-U_{eff}/k_BT)$$

which contemplates that Raman (first term) and Orbach (second term) processes contribute concurrently to the relaxation of the magnetization. It should be noted that all attempts to fit the data to this equation were unsuccessful. However, fixing the U_{eff} and τ_0 values to those extracted from the Arrhenius plot for the Orbach process a very good fit was obtained with B = 0.04 s^{-1} K^n and n = 6.11. It is worth mentioning that n = 9 is expected for Kramers ions like Dy^{III}.[37] Nevertheless, values between n = 2 to 7

are also are realistic when both acoustic and optical phonons are active.[38] Similar values have been previously reported for other Dy^{III} containing complexes.[39]
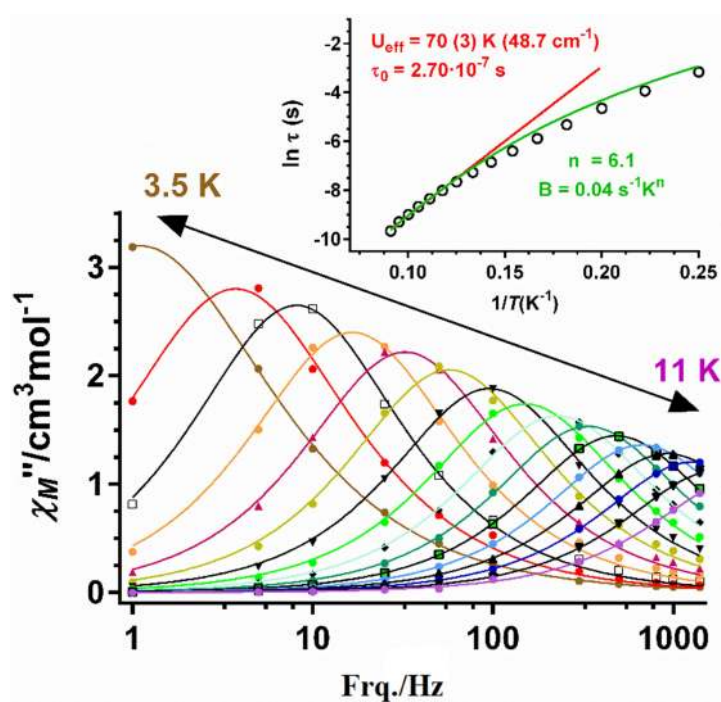
Figure 3.B.20. Frequency dependence of the χ''_M at different temperatures for **3.B.4'** at 0.1 T. (Inset) Temperature dependence of the relaxation time τ for complex **3.B.4'**. The red line represents the best fits of the experimental data to the Arrhenius equation whereas the green violet lines correspond to the best fit to Raman relaxation process.

The ongoing and previous results[40] show that a good approach for obtaining Dy^{III} SIMs is that of using *tris(β-diketonates)* Dy complexes, already formed or prepared *in situ*, with neutral monodentate, bidentate or *bis*(bidentante) ligands (such as water, DMF, pyridine, 2, 2'-bipyridine derivatives, *bis*-bipyrimidine, etc). This is because the Dy–$O_{diketonate}$ bond distances are shorter than either the Dy–N or the Dy–O bond distances of the neutral ligands and therefore the former have larger electron density than the latter. Considering this, the two acetyl acetonato ligands at opposite sides of

each Dy atom, create an appropriate axial crystal field an enough axial ligand field as to favor an axial ground KD and then the SIM behavior.

3.B.4 CONCLUSIONS

In conclusion, we have successfully prepared a new series of neutral mononuclear Ln^{III} complexes by utilizing a flexible and bulky bidentate acetyl acetone ligand (^{Mes}Acac). The solid-state structures of these complexes revealed eight-coordinate triangular dodecahedron geometry for Eu^{III} while for other Ln^{III} ions (Ln = Y, Gd, Tb, and Er) a seven-coordinate capped octahedron/trigonal prism geometry was observed. The different coordination numbers could be attributed to the ionic radii of Ln^{III} ions which undergoes a steady decrease across the period due to lanthanide contraction. Interestingly, the Eu^{III} (**3.B.1**) and Tb^{III} (**3.B.3**) derivatives showed ligand sensitized red and green luminescence characteristics of the Ln^{III} metal center. In view of the axial nature of the ligand field with a *pseudo*-sandwich geometry, dynamic ac susceptibility measurements was performed on Dy^{III} (**3.B.4**) derivative which show well-defined peaks in the frequency dependence out-of-phase susceptibility characteristics of SMM behavior under a biased field of 1000 Oe. In order to know the effect of the magnetic dilution on the slow relaxation of the magnetization, dynamic ac susceptibility measurements were performed on a diluted sample $Y^{III}_{0.09}Dy^{III}_{0.91}$ (**3.B.4'**). In the presence of a dc field (1000 Oe), complex **3.B.4'** revealed SIM behavior with an anisotropic energy barrier of 70 K ($\tau_0 = 2.7 \times 10^{-7}$ s).

3.B.5 REFERENCES

1 (a) K. Katoh, T. Komeda and M. Yamashita, *Chem. Rec.*, 2016, **16**, 987-1016; (b) S. G. McAdams, A.-M. Ariciu, A. K. Kostopoulos, J. P. S. Walsh and F. Tuna, *Coord. Chem. Rev.*, 2017, **346**, 216-239; (c) M. Feng and M.-L. Tong, *Chem. Eur. J.*, 2018, **24**, 7574-7594; (d) R. A. Layfield, *Organometallics*, 2014, **33**, 1084-1099; (e) D. N. Woodruff, R. E. P. Winpenny and R. A. Layfield, *Chem. Rev.*, 2013, **113**, 5110-5148; (f) L. Escalera-Moreno, J. J. Baldoví, A. Gaita-Ariño and E. Coronado, *Chem. Sci.*, 2018, **9**, 3265-3275.

2 (a) A. Caneschi, D. Gatteschi, R. Sessoli, A. L. Barra, L. C. Brunel and M. Guillot, *J. Am. Chem. Soc.*, 1991, **113**, 5873-5874; (b) R. Sessoli, D. Gatteschi, A. Caneschi and M. A. Novak, *Nature*, 1993, **365**, 141-143.

3 (a) A. G. and B. E. K., *Synthesis of 3d Metallic Single-Molecule Magnets* in *Single-Molecule Magnets and Related Phenomena. Structure and Bonding*, ed. W. R., Springer, Berlin, Heidelberg, vol. 122; (b) L. K. Thompson and L. N. Dawe, *Coord. Chem. Rev.*, 2015, **289-290**, 13-31; (c) C. Papatriantafyllopoulou, E. E. Moushi, G. Christou and A. J. Tasiopoulos, *Chem. Soc. Rev.*, 2016, **45**, 1597-1628.

4 (a) K. Liu, W. Shi and P. Cheng, *Coord. Chem. Rev.*, 2015, **289-290**, 74-122; (b) L. Rosado Piquer and E. C. Sañudo, *Dalton Trans.*, 2015, **44**, 8771-8780; (c) A. Chakraborty, J. Goura, P. Kalita, A. Swain, G. Rajaraman and V. Chandrasekhar, *Dalton Trans.*, 2018, **47**, 8841-8864.

5 N. Ishikawa, M. Sugita, T. Ishikawa, S.-y. Koshihara and Y. Kaizu, *J. Am. Chem. Soc.*, 2003, **125**, 8694-8695.

6 (a) L. Ungur and L. F. Chibotaru, *Phys. Chem. Chem. Phys.*, 2011, **13**, 20086-20090; (b) L. Ungur and L. F. Chibotaru, *Inorg. Chem.*, 2016, **55**, 10043-10056.

7 (a) R. J. Blagg, L. Ungur, F. Tuna, J. Speak, P. Comar, D. Collison, W. Wernsdorfer, E. J. L. McInnes, L. F. Chibotaru and R. E. P. Winpenny, *Nat. Chem.*, 2013, **5**, 673-678; (b) M. Guo, Y. Wang, J. Wu, L. Zhao and J. Tang, *Dalton Trans.*, 2017, **46**, 564-570; (c) E. Bartolomé, A. Arauzo, J. Luzón, J. Bartolomé and F. Bartolomé, *Magnetic Relaxation of Lanthanide-Based Molecular Magnets* in *Handbook of Magnetic Materials*, 2017, vol. 26, pp. 1-289.

8 J. D. Rinehart and J. R. Long, *Chem. Sci.*, 2011, **2**, 2078-2085.

9 (a) J.-L. Liu, Y.-C. Chen and M.-L. Tong, *Chem. Soc. Rev.*, 2018, **47**, 2431-2453; (b) S. K. Gupta and R. Murugavel, *Chem. Commun.*, 2018, **54**, 3685-3696.

10 A. K. Bar, P. Kalita, M. K. Singh, G. Rajaraman and V. Chandrasekhar, *Coord. Chem. Rev.*, 2018, **367**, 163-216.

11 (a) C. A. P. Goodwin, F. Ortu, D. Reta, N. F. Chilton and D. P. Mills, *Nature*, 2017, **548**, 439-442; (b) F.-S. Guo, B. M. Day, Y.-C. Chen, M.-L. Tong, A. Mansikkamäki and R. A. Layfield, *Angew. Chem. Int. Ed.*, 2017, **56**, 11445-11449; (c) F.-S. Guo, B. M. Day, Y.-C. Chen, M.-L. Tong, A. Mansikkamäki and R. A. Layfield, *Science*, 2018, **362**, 1400-1403.

12 (a) Y.-C. Chen, J.-L. Liu, L. Ungur, J. Liu, Q.-W. Li, L.-F. Wang, Z.-P. Ni, L. F. Chibotaru, X.-M. Chen and M.-L. Tong, *J. Am. Chem. Soc.*, 2016, **138**, 2829-2837; (b) Y.-S. Ding, N. F. Chilton, R. E. P. Winpenny and Y.-Z. Zheng, *Angew. Chem. Int. Ed.*, 2016, **55**, 16071-16074; (c) S. K. Gupta, T. Rajeshkumar, G. Rajaraman and R. Murugavel, *Chem. Sci.*, 2016, **7**, 5181-5191; (d) J. Liu, Y.-C. Chen, J.-L. Liu, V. Vieru, L. Ungur, J.-H. Jia, L. F. Chibotaru, Y. Lan, W. Wernsdorfer, S. Gao, X.-M. Chen and M.-L. Tong, *J. Am. Chem. Soc.*, 2016, **138**, 5441-5450.

13 (a) V. E. Pushkarev, L. G. Tomilova and V. N. Nemykin, *Coord. Chem. Rev.*, 2016, **319**, 110-179; (b) Y. Chen, F. Ma, X. Chen, B. Dong, K. Wang, S. Jiang, C.

Wang, X. Chen, D. Qi, H. Sun, B. Wang, S. Gao and J. Jiang, *Inorg. Chem.*, 2017, **56**, 13889-13896.

14 (a) M. Xémard, S. Zimmer, M. Cordier, V. Goudy, L. Ricard, C. Clavaguéra and G. Nocton, *J. Am. Chem. Soc.*, 2018, **140**, 14433-14439; (b) B. M. Day, F.-S. Guo, S. R. Giblin, A. Sekiguchi, A. Mansikkamäki and R. A. Layfield, *Chem. Eur. J.*, 2018, **24**, 16779-16782; (c) K. R. McClain, C. A. Gould, K. Chakarawet, S. J. Teat, T. J. Groshens, J. R. Long and B. G. Harvey, *Chem. Sci.*, 2018, **9**, 8492-8503; (d) A. F. R. Kilpatrick, F.-S. Guo, B. M. Day, A. Mansikkamäki, R. A. Layfield and F. G. N. Cloke, *Chem. Commun.*, 2018, **54**, 7085-7088.

15 (a) X. Liu, X. Ma, W. Yuan, P. Cen, Y.-Q. Zhang, J. Ferrando-Soria, G. Xie, S. Chen and E. Pardo, *Inorg. Chem.*, 2018, **57**, 14843-14851; (b) F. Ma, Q. Chen, J. Xiong, H.-L. Sun, Y.-Q. Zhang and S. Gao, *Inorg. Chem.*, 2017, **56**, 13430-13436; (c) L. Sun, S. Zhang, Z. Jiang, Q. Yang, S. Chen, Y. Zhang, W. Wang, Q. Wei and G. Xie, *Dalton Trans.*, 2017, **46**, 11159-11165; (d) D.-P. Lyu, J.-Y. Zheng, Q.-W. Li, J.-L. Liu, Y.-C. Chen, J.-H. Jia and M.-L. Tong, *Inorg. Chem. Front.*, 2017, **4**, 1776-1782.

16 (a) S. Biswas, K. S. Bejoymohandas, S. Das, P. Kalita, M. L. P. Reddy, I. Oyarzabal, E. Colacio and V. Chandrasekhar, *Inorg. Chem.*, 2017, **56**, 7985-7997; (b) A. K. Bar, P. Kalita, J.-P. Sutter and V. Chandrasekhar, *Inorg. Chem.*, 2018, **57**, 2398-2401; (c) P. Bag, C. K. Rastogi, S. Biswas, S. Sivakumar, V. Mereacre and V. Chandrasekhar, *Dalton Trans.*, 2015, **44**, 4328-4340.

17 (a) J. Sun, M. Yang, L. Xi, Y. Ma and L. Li, *Dalton Trans.*, 2018, **47**, 8142-8148; (b) P. Cen, X. Liu, J. Ferrando-Soria, Y.-Q. Zhang, G. Xie, S. Chen and E. Pardo, *Chem. Eur. J.*, 2019, **25**, 3884-3892; (c) S. Zhang, W. Mo, B. Yin, G. Zhang, D.

Yang, X. Lü and S. Chen, *Dalton Trans.*, 2018, **47**, 12393-12405; (d) J. Zhu, C. Wang, F. Luan, T. Liu, P. Yan and G. Li, *Inorg. Chem.*, 2014, **53**, 8895-8901.

18 Y. Dong, P. Yan, X. Zou, T. Liu and G. Li, *J. Mater. Chem. C*, 2015, **3**, 4407-4415.

19 (a) D. N. Bazhin, Y. S. Kudyakova, A. S. Bogomyakov, P. A. Slepukhin, G. A. Kim, Y. V. Burgart and V. I. Saloutin, *Inorg. Chem. Front.*, 2019, **6**, 40-49; (b) Y.-Z. Tong, C. Gao, Q.-L. Wang, B.-W. Wang, S. Gao, P. Cheng and D.-Z. Liao, *Dalton Trans.*, 2015, **44**, 9020-9026; (c) Y. Bi, Y.-N. Guo, L. Zhao, Y. Guo, S.-Y. Lin, S.-D. Jiang, J. Tang, B.-W. Wang and S. Gao, *Chem. Eur. J.*, 2011, **17**, 12476-12481; (d) M. R. Silva, P. Martín-Ramos, J. T. Coutinho, L. C. J. Pereira and J. Martín-Gil, *Dalton Trans.*, 2014, **43**, 6752-6761; (e) W.-M. Wang, S.-Y. Wang, H.-X. Zhang, H.-Y. Shen, J.-Y. Zou, H.-L. Gao, J.-Z. Cui and B. Zhao, *Inorg. Chem. Front.*, 2016, **3**, 133-141; (f) W.-B. Sun, B. Yan, Y.-Q. Zhang, B.-W. Wang, Z.-M. Wang, J.-H. Jia and S. Gao, *Inorg. Chem. Front.*, 2014, **1**, 503-509; (g) J.-R. Jiménez, I. F. Díaz-Ortega, E. Ruiz, D. Aravena, S. J. A. Pope, E. Colacio and J. M. Herrera, *Chem. Eur. J.*, 2016, **22**, 14548-14559.

20 (a) E. A. Varaksina, I. V. Taydakov, S. A. Ambrozevich, A. S. Selyukov, K. A. Lyssenko, L. T. Jesus and R. O. Freire, *J. Lumin.*, 2018, **196**, 161-168; (b) Z. Ahmed and K. Iftikhar, *Dalton Trans.*, 2019, **48**, 4973-4986; (c) F. P. Aguiar, I. F. Costa, J. G. P. Espínola, W. M. Faustino, J. L. Moura, H. F. Brito, T. B. Paolini, M. C. F. C. Felinto and E. E. S. Teotonio, *J. Lumin.*, 2016, **170**, 538-546; (d) Z. Li, P. Li, Q. Xu and H. Li, *Chem. Commun.*, 2015, **51**, 10644-10647; (e) J.-C. G. Bünzli, *Coord. Chem. Rev.*, 2015, **293-294**, 19-47; (f) L. Sun, Y. Qiu, T. Liu, J. Feng, W. Deng and L. Shi, *Luminescence*, 2015, **30**, 1071-1076.

21 J.-H. Jia, Q.-W. Li, Y.-C. Chen, J.-L. Liu and M.-L. Tong, *Coord. Chem. Rev.*, 2019, **378**, 365-381 and references therein.

22 C. Zhang, P. Yang, Y. Yang, X. Huang, X.-J. Yang and B. Wu, *Synth. Commun.*, 2008, **38**, 2349-2356.

23 F. M. Wang, *Acta Cryst. E*, 2012, **68**, m26-m27.

24 *SMART & SAINT Software Reference manuals*, Bruker Analytical X-ray Systems, Inc., Madison, WI, version 6.45, 2003.

25 G. M. Sheldrick, *SADABS, Program for Empirical Absorption Correction*, University of Gottingen, Germany, 1996.

26 *Bruker APEX2*, Bruker AXS Inc., Madison, Wisconsin, USA, version 2008.1−0, 2008.

27 G. M. Sheldrick, *Acta Cryst. A*, 2015, **71**, 3-8.

28 G. M. Sheldrick, *Acta Cryst. C*, 2015, **71**, 3-8.

29 O. V. Dolomanov, L. J. Bourhis, R. J. Gildea, J. A. K. Howard and H. Puschmann, *J. Appl. Cryst.*, 2009, **42**, 339-341.

30 K. Brandenburg and H. Putz, *DIAMOND*, Crystal Impact GbR, Bonn, Germany, version 3.2, 1997−2014.

31 *SHAPE: Continuous Shape Measures calculation*, Electronic Structure Group, Universitat de Barcelona, Spain, version 2.1, 2013.

32 J. Cirera, E. Ruiz and S. Alvarez, *Organometallics*, 2005, **24**, 1556-1562.

33 F. Gao, L. Cui, W. Liu, L. Hu, Y.-W. Zhong, Y.-Z. Li and J.-L. Zuo, *Inorg. Chem.*, 2013, **52**, 11164-11172.

34 (a) T. V. Usha Gangan and M. L. P. Reddy, *Dalton Trans.*, 2015, **44**, 15924-15937; (b) V. Divya, R. O. Freire and M. L. P. Reddy, *Dalton Trans.*, 2011, **40**, 3257-

3268; (c) G. Shao, H. Yu, N. Zhang, Y. He, K. Feng, X. Yang, R. Cao and M. Gong, *Phys. Chem. Chem. Phys.*, 2014, **16**, 695-702.

35 (a) S. Biju, N. Gopakumar, J. C. G. Bünzli, R. Scopelliti, H. K. Kim and M. L. P. Reddy, *Inorg. Chem.*, 2013, **52**, 8750-8758; (b) A. R. Ramya, S. Varughese and M. L. P. Reddy, *Dalton Trans.*, 2014, **43**, 10940-10946.

36 N. F. Chilton, D. Collison, E. J. L. McInnes, R. E. P. Winpenny and A. Soncini, *Nat. Commun.*, 2013, **4**, 2551-2557.

37 A. Abragam and B. Bleaney, *Electron Paramagnetic Resonance of Transition Ions*, Clarendon Press. Oxford, 1970.

38 (a) K. N. Shrivastava, *Phys. Status Solidi B*, 1983, **117**, 437-458; (b) A. Singh and K. N. Shrivastava, *Phys. Status Solidi B*, 1979, **95**, 273-277.

39 I. Oyarzabal, B. Artetxe, A. Rodríguez-Diéguez, J. Á. García, J. M. Seco and E. Colacio, *Dalton Trans.*, 2016, **45**, 9712-9726.

40 I. F. Díaz-Ortega, J. M. Herrera, Á. Reyes Carmona, J. R. Galán-Mascarós, S. Dey, H. Nojiri, G. Rajaraman and E. Colacio, *Front Chem.*, 2018, **6**, 537-553.

Homodinuclear {Ln^{III}$_2$} (Ln = Gd, Tb, Dy, and Ho) Complexes: Field-Induced SMM Behavior of the Tb^{III} and Dy^{III} Analogues

ABSTRACT: A family of four dinuclear complexes, [NHEt$_3$]$_2$[Ln$_2$(μ-NO$_3$)$_2$(NO$_3$)$_2$(HL)$_2$] (Ln = Gd^{III} (**4.A.1**), Tb^{III} (**4.A.2**), Dy^{III} (**4.A.3**), Ho^{III} (**4.A.4**)), were synthesized by the reaction of an enolizable multidentate Schiff base ligand H$_3$L (H$_3$L = *N'*-(2-hydroxy-3-methoxy-5-nitrobenzylidene)-2-(hydroxyimino)propane-hydrazide) with hydrated lanthanide nitrates in the presence of NEt$_3$. The molecular structure of complexes **4.A.1**-**4.A.4** was confirmed by single crystal XRD analysis. All of the centrosymmetric complexes are dianionic, isostructural and each of the Ln^{III} centers is nine-coordinate and adopts *muffin*-like coordination geometry as indicated by SHAPE analysis. The dynamic magnetization studies revealed that the compounds **4.A.2** and **4.A.3** are field-induced single-molecule magnets with effective energy barriers, U_{eff}/k_B = 34(2) K (for **4.A.2**) and 80(3) K (for **4.A.3**) and pre-exponential factors, τ_o = 1.1 x 10^{-8} (for **4.A.2**) and 1.15 x 10^{-7} (for **4.A.3**).

4.A.1 INTRODUCTION

Single-molecule magnets based on lanthanide complexes are of considerable interest in view of the unquenched spin-orbit angular momentum present among lanthanide ions leading to an inherent magnetic anisotropy in many of them particularly in ions such as Dy^{III}, Tb^{III}, Ho^{III}, Er^{III} etc.[1] Various types of lanthanide complexes containing diverse features such as varying nuclearity and structural topology have been investigated revealing a rich magnetochemistry.[2] Among all the lanthanide ion-containing single molecule magnets investigated thus far, the complex [(Cp^{iPr5})Dy(Cp*)][B(C$_6$F$_5$)$_4$] possesses the highest blocking temperature, 80 K, below

which the complex once magnetized retains its magnetization for long periods of time.[3] While such single ion magnets are certainly of considerable interest there is also substantial interest in dinuclear complexes because of several reasons. One, such complexes serve as the simplest models to understand inter-lanthanide interactions mediated through ligands.[4] Second, the pioneering work of Long and co-workers has revealed that having appropriate bridging ligands between the lanthanide centers allows a favorable electronic communication between them.[5] Thus, the complex, [K(18-crown-6)(THF)$_2$] [{[(Me$_3$Si)$_2$N]$_2$(THF)Tb}$_2$(μ-η^2 :η^2 N$_2$)], where the lanthanide centers are connected to each other by the radical ligand [N$_2$]$^{3-}$ shows an effective barrier for magnetization reversal U_{eff} = 227 cm^{-1} and a blocking temperature of 14 K.[5] Spurred by this exciting result there have been many efforts to study dinuclear complexes.[6] While a large number of ligands have been used for assembling such complexes, ligand design that can lead to the exclusive isolation of dinuclear complexes still is an important issue. Oxo-ligand systems have been shown to be quite effective in the synthesis of such complexes, besides providing an opportunity to effect slight structural variations which in turn can bring a change in the magnetic interaction between the lanthanide centers.[6g, 7] Also, studies on dinuclear lanthanide complexes reveal that a number of strategies can be employed to enhance the energy barriers of magnetization reversal. The commonly employed methods are tuning terminal ligands[8], tuning local coordination geometries[9] and tuning ligand fields[4g].

We have been utilizing multi-dentate hydrazone ligands, for some time, to assemble lanthanide complexes.[10] In this context, we wished to explore an *o*-vanillin supported multidentate ligand, *N'*-(2-hydroxy-3-methoxy-5-nitrobenzylidene)-2-hydroxyimino-propanehydrazide (H$_3$L) to prepare dinuclear Ln^{III} complexes. Based on our previous understanding of such ligand systems we intuited that keto-enol tautomerism would

allow H_3L to be present in an enol form and when deprotonated the enolate oxygen can be profitably used to bridge two lanthanide ions. Accordingly, we have isolated a family of dinuclear Ln^{III}_2 complexes, $[NHEt_3]_2[Ln_2(\mu\text{-}NO_3)_2(NO_3)_2(HL)_2]$ (Ln = Gd^{III} **(4.A.1)**, Tb^{III} **(4.A.2)**, Dy^{III} **(4.A.3)**, Ho^{III} **(4.A.4)**). The synthesis, structure and magnetic properties of these complexes are revealed herein.

4.A.2 EXPERIMENTAL SECTION

4.A.2.1 Materials and Methods. Solvents and other general reagents used in this work were obtained from commercial sources and used without further purification. 3-Methoxy-5-nitrosalicylaldehyde, triethylamine, hydroxylamine hydrochloride, $Ln(NO_3)_3 \cdot xH_2O$ were obtained from Sigma Aldrich Chemical Co. (India). Ethyl pyruvate was obtained from Spectrochem Pvt. Ltd., Mumbai, India. All these reagents were used as obtained without further purification. Ethyl 2-(hydroxyimino)propanoate and 2-(hydroxyimino)-propanehydrazide were prepared by a previously reported procedure.[11, 12]

4.A.2.2 Instrumentation. Melting points were measured using a JSGW melting point apparatus and are uncorrected. ^1H NMR and $^{13}C\{^1H\}$ NMR spectra were recorded on a Bruker Ascend-700 (^1H: 700 MHz; $^{13}C\{^1H\}$: 175 MHz) and were referenced to the resonances of the solvent used. IR spectra were recorded with a PerkinElmer FT-IR spectrometer. Mass spectra were recorded with a Bruker micrOTOF-Q II spectrometer. Elemental analyses of the compounds were obtained from a Euro Vector EA elemental analyzer (CHNS-O, Model EA3000). Powder X-ray diffraction data of all the complexes were collected with a Bruker D8 Advance X-ray Powder Diffractometer using CuKα radiation (λ = 1.5418 Å).

4.A.2.3 Magnetic Measurements. Field dependence of the magnetization at different temperatures and variable temperature (2-300 K) magnetic susceptibility measurements on polycrystalline samples were carried out with a Quantum Design SQUID MPMS XL-5 device operating at different magnetic fields. Ac susceptibility measurements were performed using an oscillating ac field of 3 Oe and ac frequencies ranging from 1 to 1500 Hz. The experimental susceptibilities were corrected for the sample holder and diamagnetism of the constituent atoms by using Pascal's tables. A pellet of the sample cut into very small pieces was placed in the sample holder to prevent any torquing of the microcrystals.

4.A.2.4 X-ray Crystallography. Single crystal X-ray structural studies of complexes **4.A.1-4.A.4** were performed on a Bruker Apex II CCD diffractometer system equipped with graphite-monochromated MoK_α radiation (λ_α = 0.71073 Å) at 298(2) K. We did not observe degradation/decomposition of the crystals during data collection. The frames were indexed, integrated, and scaled using the SMART and SAINT software package.[13] Absorption correction was performed by multi-scan method implemented in SADABS.[14] Space groups were determined using XPREP implemented in APEX2.[15] The structures were solved with the ShelXT[16] structure solution program using Direct Methods and refined by the full-matrix least-squares method on F^2(ShelXL-2014)[17] using the Olex-2[18] software. All the non-hydrogen atoms were refined with anisotropic thermal parameters. All the hydrogen atoms were placed in geometrically calculated positions or found in the Fourier difference map and included in the refinement process using riding model. The crystallographic figures have been generated using DIAMOND software.[19]

4.A.4.5 Synthesis of the ligand H₃L. The ligand H_3L was prepared by the condensation of 3-methoxy-5-nitrosalicylaldehyde (1.34 g, 6.83 mmol) with

2-(hydroxyimino)propanehydrazide (0.80 g, 6.83 mmol) in methanol (50 mL) under reflux conditions for 2 h. During this time an off-white precipitate was formed, which was filtered, washed with cold methanol and diethyl ether, and subsequently dried under vacuum for 4 h. Yield: 1.9 g (94%). M. P.: 236 °C. FT-IR (KBr) cm^{-1}: 3743 (m), 3568 (m), 3479 (w), 3439 (w), 3137 (w), 3101 (w), 3028 (m), 2840 (m), 1636 (s), 1530 (s), 1483 (s), 1441 (m), 1351 (s), 1282 (s), 1184 (s), 1100 (m), 1069 (m), 1010 (s), 961 (m), 883 (w), 849 (m), 791 (m), 736 (m), 624 (m). ^{1}H NMR (DMSO-d_6, δ, ppm): 11.97 (s, 1H, enol H), 11.91 (s, 1H, oxime H), 8.74 (s, 1H, imine H), 8.16 (s, 1H, Ar-H), 7.76 (s, 1H, Ar-H), 3.95 (s, 3H, -OCH$_3$), 1.97 (s, 3H, -CH$_3$). Anal. Calcd for $C_{11}H_{12}N_4O_6$ (296.07): C, 44.60; H, 4.08; N, 18.91. Found: C, 44.39; H, 3.89; N, 18.79. ESI-MS, m/z = 297.0809 for (M + H)$^+$.
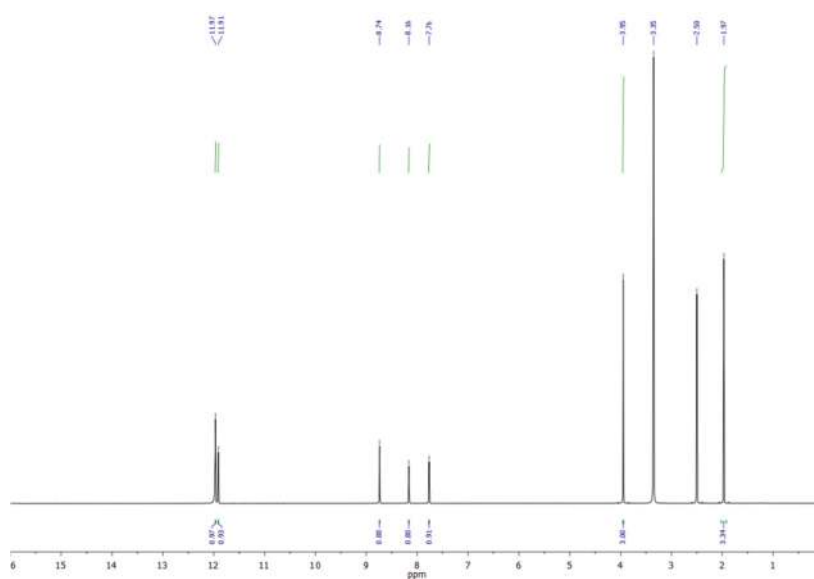
Figure 4.A.1. ^{1}H NMR spectra of ligand H$_3$L in a DMSO-d_6 solvent. (The peaks observed at 3.35 ppm and 2.50 ppm is due to the residual solvents)
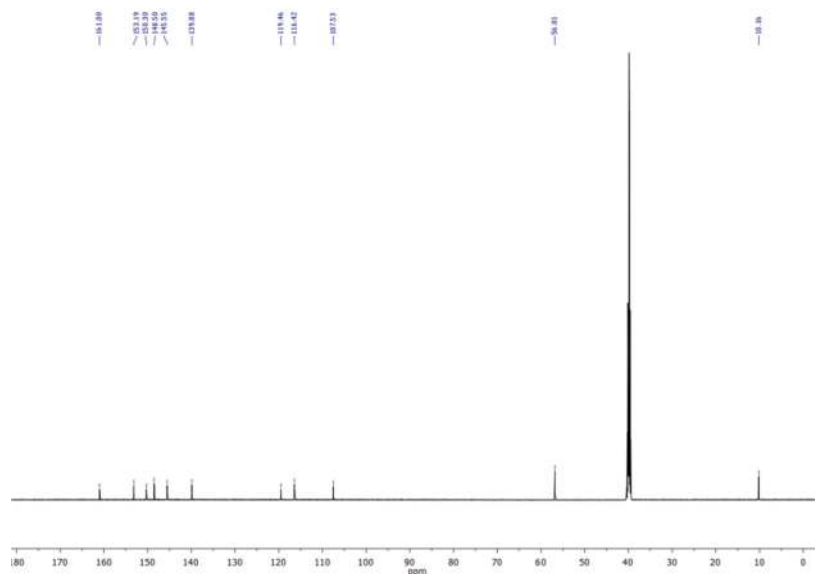
Figure 4.A.2. $^{13}C\{^1H\}$ NMR spectra of ligand H_3L in a DMSO-d_6 solvent. (The peak observed at 40 ppm is due to the residual solvent)
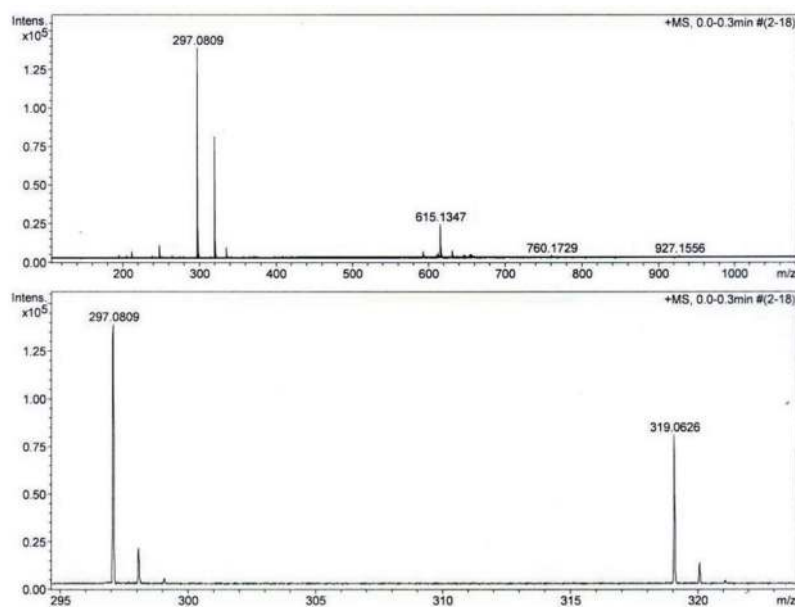
Figure 4.A.3. ESI-MS spectra of ligand H_3L in a CH_3CN solvent.

4.A.4.6 Syntheses of metal complexes. The general synthetic protocol used for the preparation of the dinuclear metal complexes (**4.A.1-4.A.4**) was as follows:

$Ln(NO_3)_3.xH_2O$ (1 eq.), was added to an acetonitrile solution (15 mL) of H_3L (1 eq.), with constant stirring which resulted in a yellow solution. After stirring for 5 min,

NEt$_3$ (2 eq.) was added dropwise to it and the reaction mixture was allowed to stir for a period of 12 h. The yellow solution was filtered, and vapor diffusion of the resultant filtrate with diethyl ether afforded yellow, block-shaped crystals, suitable for X-ray diffraction analysis, after one week. The stoichiometry of the reactants involved in each reaction, yield of the products and their characterization data are provided below.

[NHEt$_3$]$_2$[Gd$_2$(μ-NO$_3$)$_2$(NO$_3$)$_2$(HL)$_2$] (**4.A.1**). H$_3$L (0.060 g, 0.202 mmol), Gd(NO$_3$)$_3$·6H$_2$O (0.091 g, 0.202 mmol), and NEt$_3$ (0.041 g, 0.405 mmol)) were used. Yield: 0.083 g, 67% (based on Gd metal salt). M.P.: >250 °C. IR (KBr v/cm^{-1}): 3412(b), 3079(w), 2989(w), 1602(s), 1564(w), 1497(w), 1427(w), 1384(s), 1307(s), 1255(m), 1199(m), 1104(s), 1054(s), 967(w), 907(s), 839(m), 780(m), 744(m), 638(w), 555(m). Anal. Calcd for C$_{34}$H$_{52}$Gd$_2$N$_{14}$O$_{24}$ (1356.18): C, 30.13; H, 3.87; N, 14.47. Found: C, 29.89; H, 3.65; N, 14.33. ESI-MS, m/z = 1262.0375, [C$_{22}$H$_{20}$Gd$_2$N$_{12}$O$_{24}$ + 2H$_2$O + CH$_3$OH + CH$_3$CN + H]$^-$.

[NHEt$_3$]$_2$[Tb$_2$(μ-NO$_3$)$_2$(NO$_3$)$_2$(HL)$_2$] (**4.A.2**). H$_3$L (0.060 g, 0.202 mmol), Tb(NO$_3$)$_3$·5H$_2$O (0.088 g, 0.202 mmol), and NEt$_3$ (0.041 g, 0.405 mmol)) were used. Yield: 0.091 g, 69% (based on Tb metal salt). M.P.: >250 °C. IR (KBr v/cm^{-1}): 3402(b), 3079(w), 2987(w), 1601(s), 1565(w), 1498(w), 1446(w), 1384(s), 1303(s), 1254(m), 1197(m), 1101(s), 1054(s), 970(w), 907(s), 840(m), 783(m), 745(m), 641(w), 560(m). Anal. Calcd for C$_{34}$H$_{52}$Tb$_2$N$_{14}$O$_{24}$ (1358.18): C, 30.06; H, 3.86; N, 14.43. Found: C, 29.83; H, 3.63; N, 14.26. ESI-MS, m/z = 1262.0253, [C$_{22}$H$_{20}$Tb$_2$N$_{12}$O$_{24}$ + 3H$_2$O + CH$_3$OH + Na]$^-$.

[NHEt$_3$]$_2$[Dy$_2$(μ-NO$_3$)$_2$(NO$_3$)$_2$(HL)$_2$] (**4.A.3**). H$_3$L (0.060 g, 0.202 mmol), Dy(NO$_3$)$_3$·5H$_2$O (0.089 g, 0.202 mmol), and NEt$_3$ (0.041 g, 0.405 mmol)) were used. Yield: 88 g, 64% (based on Dy metal salt). Mp: >250 °C. IR (KBr v/cm^{-1}): 3415(b),

3091(w), 2988(w), 1603(s), 1566(w), 1498(w), 1451(w), 1384(s), 1305(s), 1255(m), 1197(m), 1103(s), 1055(s), 971(w), 909(s), 839(m), 780(m), 746(m), 653(w), 562(m). Anal. Calcd for $C_{34}H_{52}Dy_2N_{14}O_{24}$ (1365.18): C, 29.90; H, 3.84; N, 14.36. Found: C, 29.74; H, 3.66; N, 14.18. ESI-MS, m/z = 1269.9931, $[C_{22}H_{20}Dy_2N_{12}O_{24} + 3H_2O + CH_3OH + Na]^-$.

[NHEt₃]₂[Ho₂(μ-NO₃)₂(NO₃)₂(HL)₂] (**4.A.4**). H_3L (0.060 g, 0.202 mmol), $Ho(NO_3)_3 \cdot 5H_2O$ (0.090 g, 0.202 mmol), and NEt_3 (0.041 g, 0.405 mmol)) were used. Yield: 0.087 g, 62% (based on Ho metal salt). Mp: >250 °C. IR (KBr v/cm^{-1}): 3428(b), 3089(w), 2994(w), 1603(s), 1564(w), 1499(w), 1450(w), 1384(s), 1304(s), 1255(m), 1197(m), 1102(s), 1057(s), 971(w), 910(s), 840(m), 780(m), 748(m), 663(w), 563(m). Anal. Calcd for $C_{34}H_{52}Ho_2N_{14}O_{24}$ (1370.19): C, 29.79; H, 3.82; N, 14.31. Found: C, 29.58; H, 3.65; N, 14.16. ESI-MS, m/z = 1274.9899, $[C_{22}H_{20}Ho_2N_{12}O_{24} + 3H_2O + CH_3OH + Na]^-$.

4.A.3 RESULTS AND DISCUSSION

4.A.3.1 Synthetic Aspects. The ligand H_3L was prepared by a condensation reaction of 5-nitro substituted *o*-vanillin with 2-(hydroxyimino)propanehydrazide. This ligand upon complete deprotonation is trianionic and contains six potential coordination sites (Scheme 4.A.1). Further, the ligand is endowed with the possibility of keto-enol tautomerism thus allowing functional flexibility. The ligand was well characterized by NMR and ESI-MS techniques (Figures 4.A.1-4.A.3) The reaction of H_3L with hydrated lanthanide nitrate metal salts in the presence of triethylamine in a 1:1:2 stoichiometric ratio afforded the dinuclear Ln^{III} complexes, $[NHEt_3]_2[Ln_2(\mu-NO_3)_2(NO_3)_2(HL)_2]$ where Ln = Gd^{III} (**4.A.1**), Tb^{III} (**4.A.2**), Dy^{III} (**4.A.3**) and Ho^{III} (**4.A.4**) (Scheme 4.A.2).
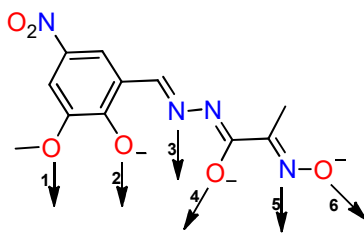
Scheme 4.A.1. Six potential coordination sites of the trianionic ligand $[L]^{3-}$
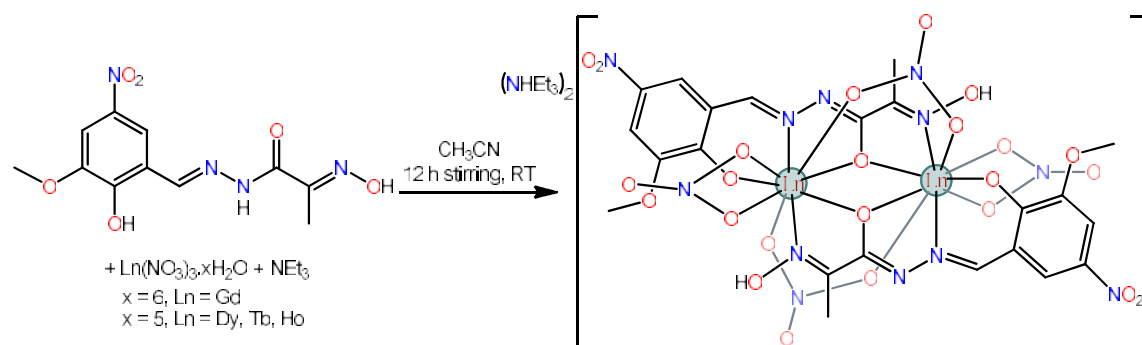
Scheme 4.A.2. Synthesis of dinuclear complexes $[NHEt_3]_2[Ln_2(\mu\text{-}NO_3)_2(NO_3)_2(HL)_2]$ (**4.A.1-4.A.4**).

A keto-enol tautomerization pathway of the free ligand and its corresponding binding mode is shown in Scheme 4.A.3. The keto form of the free ligand in the solid state is detected by IR stretch bands at 3480 and 3441 cm^{-1}, due to the amide ν(N–H) stretching frequencies. On the other hand ν(C=N) stretching absorption bands are observed in the metal complexes at 1603 cm^{-1} instead of 1665 and 1636 cm^{-1} as observed in the free ligand (see Figure 4.A.4). Upon metalation of the ligand the ν(N–H) absorption band in the IR spectrum of complexes **4.A.1-4.A.4** vanishes which implies that the enol form is predominant (Figure 4.A.4 (b); the IR spectra of complex **4.A.2** is given as a representative example). The presence of the enolate form in the metal complexes is further confirmed by a single crystal X-ray analysis which revealed that the C–O single bond lengths are 1.296-1.311 Å and the C=N double bond lengths are 1.291-1.303 Å respectively.
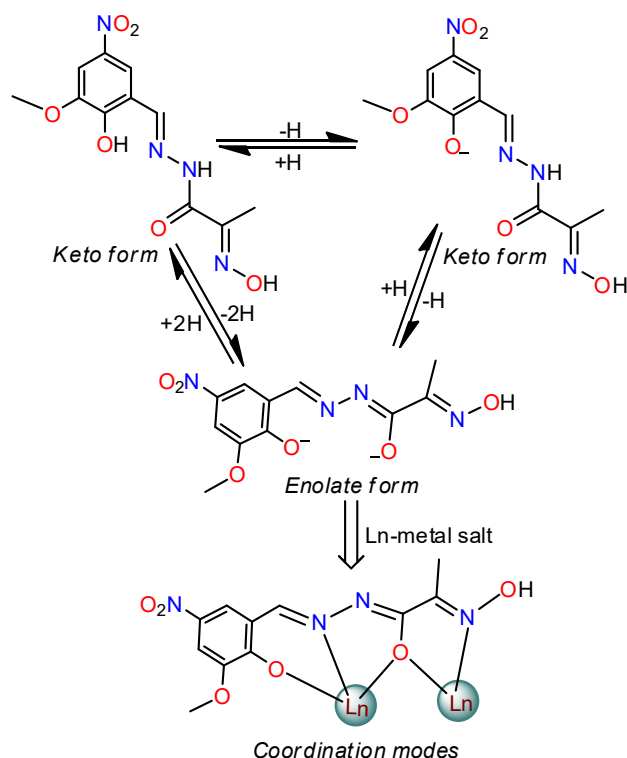
Scheme 4.A.3. Base-assisted reversible keto-enol tautomerization of the ligand H$_3$L and its coordination mode in the complexes **4.A.1-4.A.4**
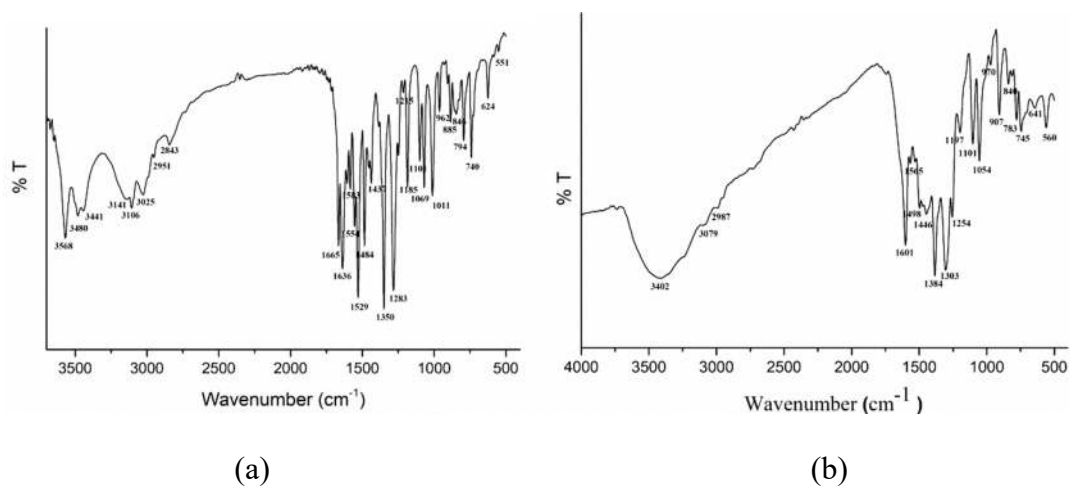
Figure 4.A.4. IR spectra of H$_3$L (a) and complex **4.A.2** (b).

The structural integrity of **4.A.1-4.A.4** in solution was probed by ESI-MS studies in CH$_3$OH/CH$_3$CN solvent (1:1 v/v) which revealed peaks at m/z = 1262.0375, 1262.0253, 1274.9899, and 1269.9931 corresponding to the mono-anionic species; [C$_{22}$H$_{20}$Gd$_2$N$_{12}$O$_{24}$ + 2H$_2$O + CH$_3$OH + CH$_3$CN + H]$^-$ (Figure 4.A.5),

$[C_{22}H_{20}Tb_2N_{12}O_{24} + 3H_2O + CH_3OH + Na]^-$ (Figure 4.A.6), $[C_{22}H_{20}Dy_2N_{12}O_{24} + 3H_2O + CH_3OH + Na]^-$ (Figure 4.A.7), and $[C_{22}H_{20}Ho_2N_{12}O_{24} + 3H_2O + CH_3OH + Na]^-$ (Figure 4.A.8) respectively. These results suggest that the dinuclear motif is quite stable in the solution phase.

(a)

(b)

(c)
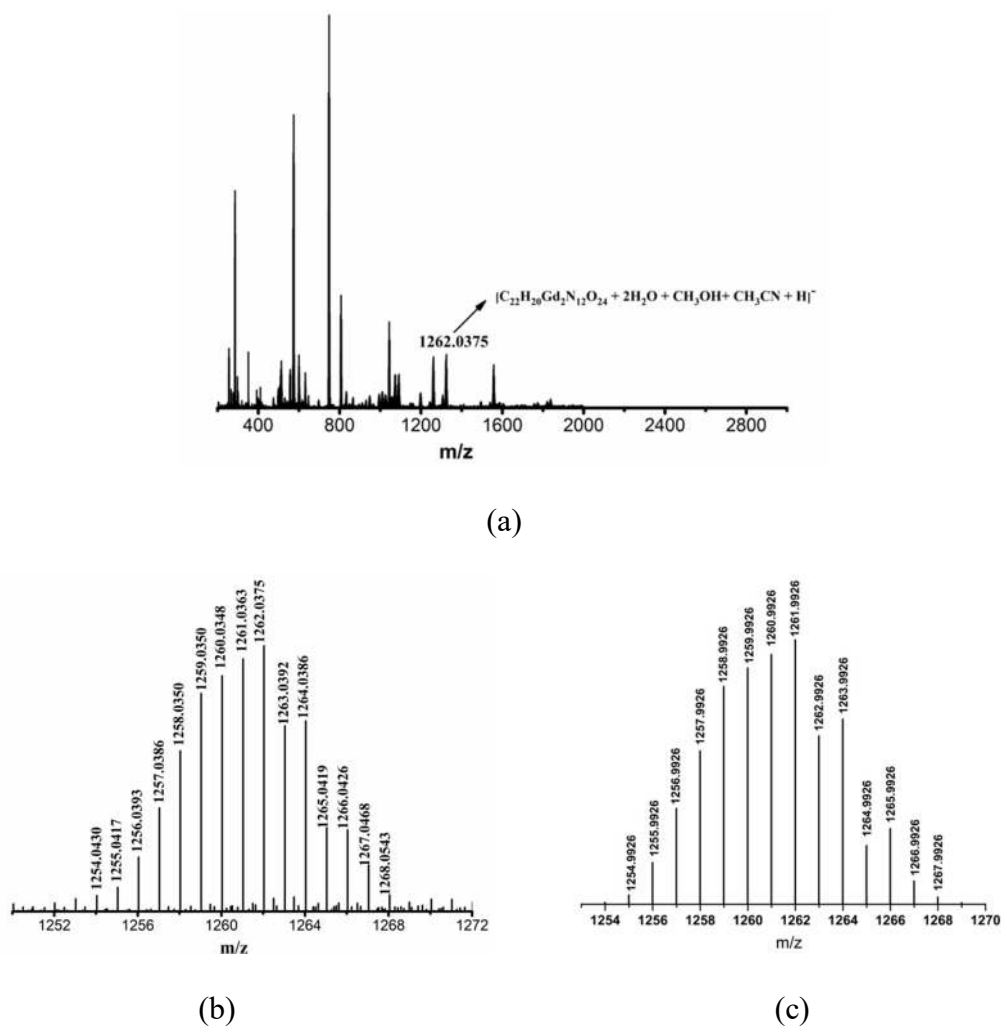
Figure 4.A.5. (a) Full range ESI-MS spectrum of complex **4.A.1**. (b) Experimental and (c) Simulated pattern of $[C_{22}H_{20}Gd_2N_{12}O_{24} + 2H_2O + CH_3OH + CH_3CN + H]^-$.

(a)

(b)   (c)
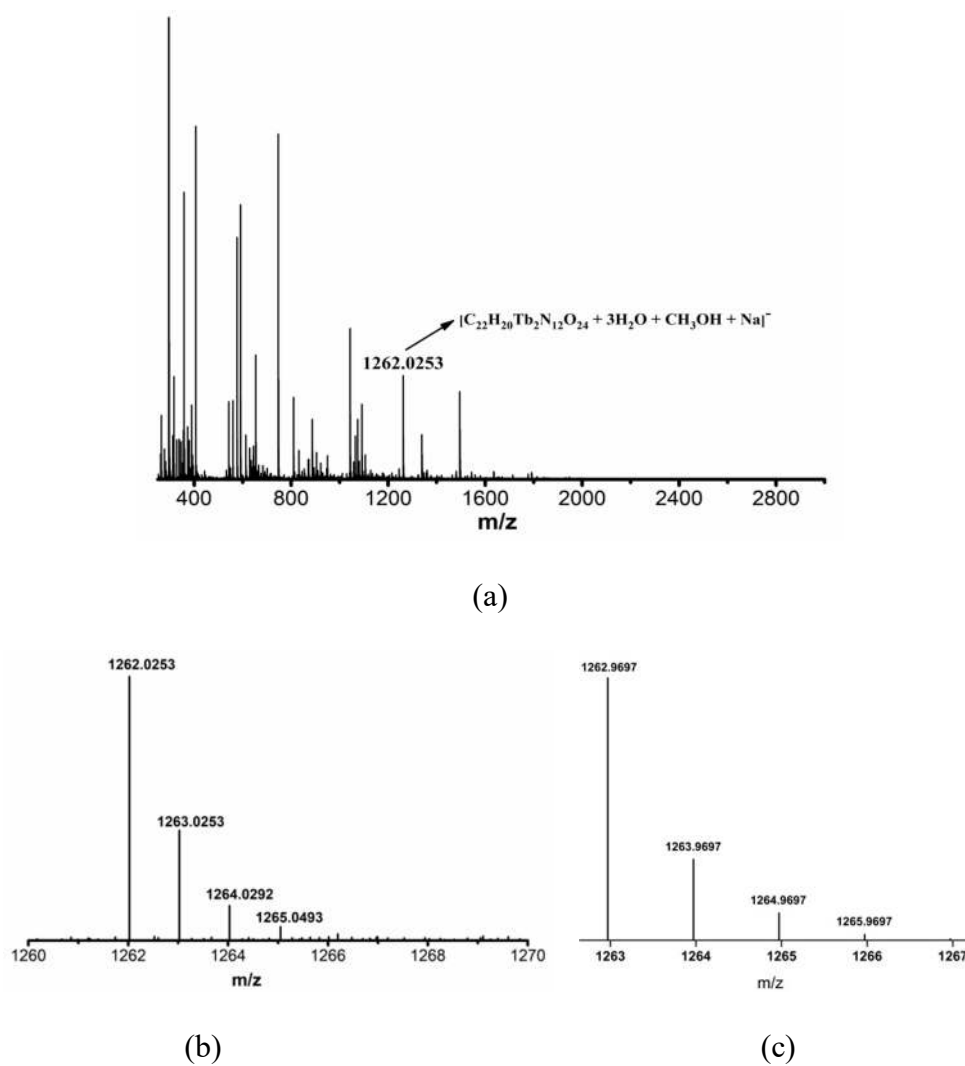
Figure 4.A.6. (a) Full range ESI-MS spectrum of complex **4.A.2**. (b) Experimental and (c) Simulated pattern of $[C_{22}H_{20}Tb_2N_{12}O_{24} + 3H_2O + CH_3OH + Na]^-$.

(a)

(b)

(c)
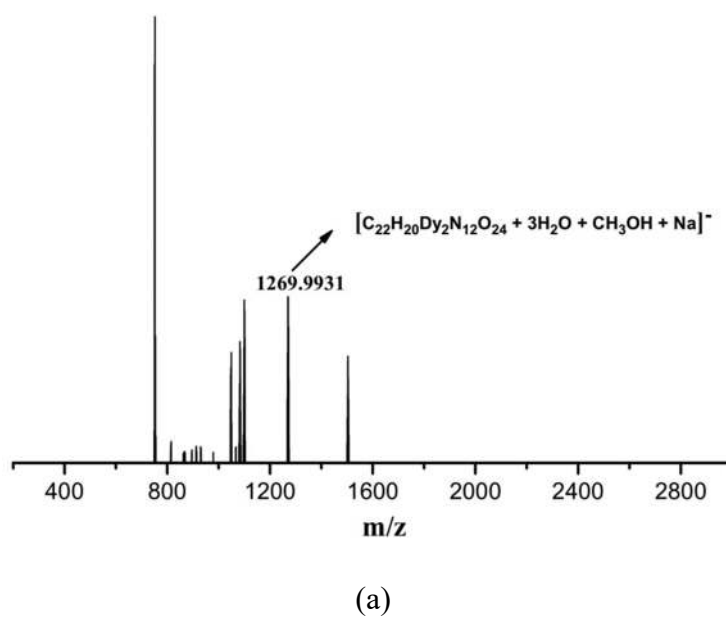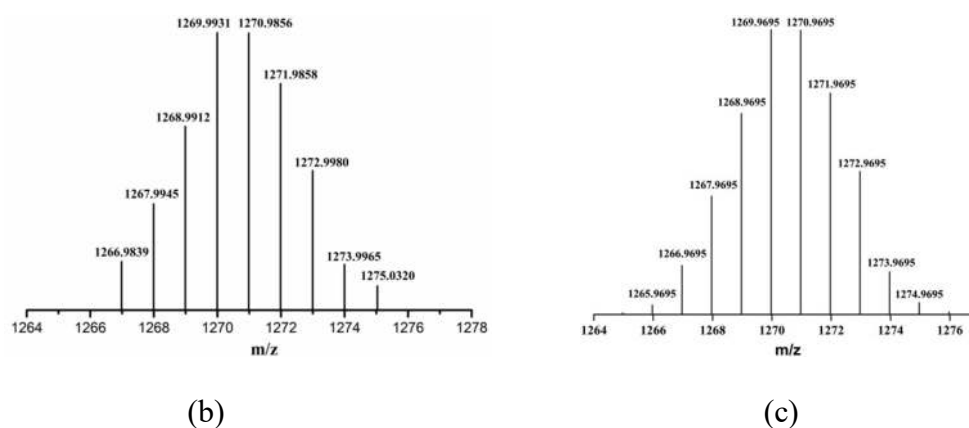
Figure 4.A.7. (a) Full range ESI-MS spectrum of complex **4.A.3**. (b) Experimental and (c) Simulated pattern of $[C_{22}H_{20}Dy_2N_{12}O_{24} + 3H_2O + CH_3OH + Na]^-$.

$[C_{22}H_{20}Ho_2N_{12}O_{24} + 3H_2O + CH_3OH + Na]^-$

1274.9899

(a)

(b)

(c)
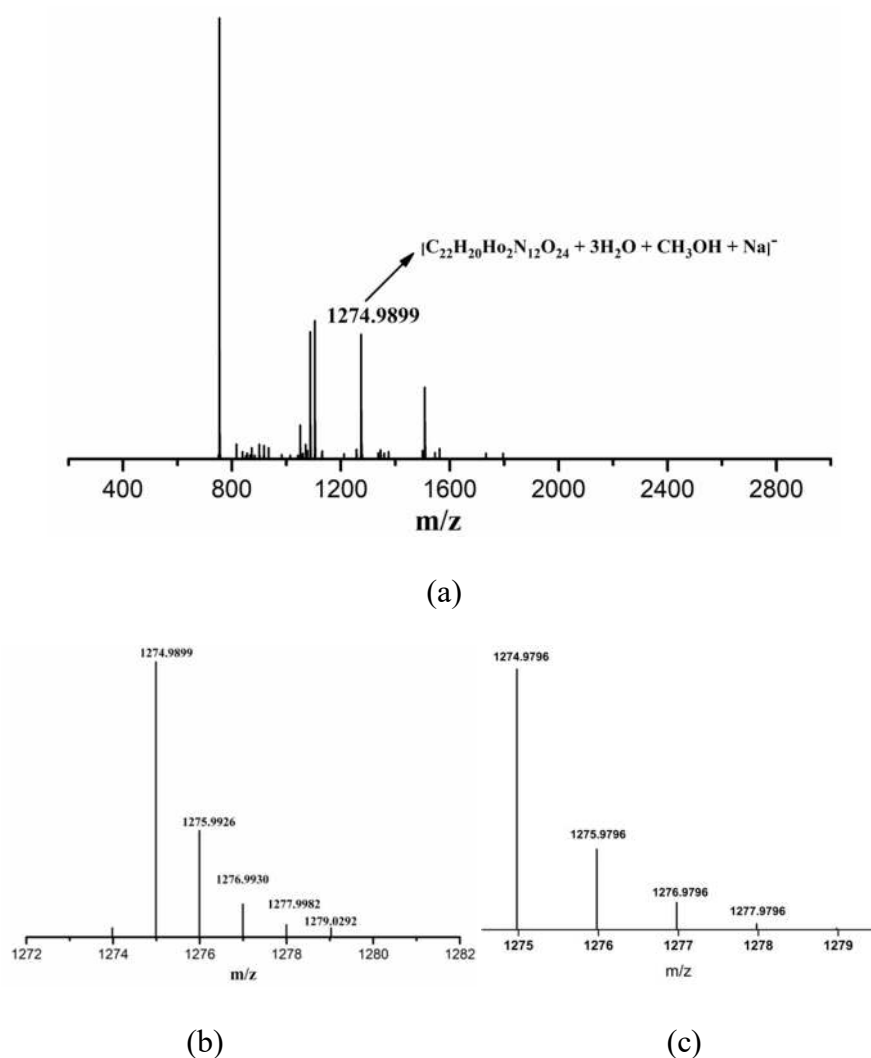
Figure 4.A.8. (a) Full range ESI-MS spectrum of complex **4.A.4**. (b) Experimental and (c) Simulated pattern of $[C_{22}H_{20}Ho_2N_{12}O_{24} + 3H_2O + CH_3OH + Na]^-$.

4.A.3.2 Molecular Structure. The molecular structures of complexes **4.A.1-4.A.1.4** were determined by a single crystal X-ray analysis. The crystal data and refinement parameters for **4.A.1-4.A.4** are summarized in Table 4.A.1.

Table 4.A.1. Details of the data collection and refinement parameters

	4.A.1	4.A.2	4.A.3	4.A.4
Chemical formula	$C_{34}H_{52}Gd_2N_{14}O_{24}$	$C_{34}H_{52}Tb_2N_{14}O_{24}$	$C_{34}H_{52}Dy_2N_{14}O_{24}$	$C_{34}H_{52}Ho_2N_{14}O_{24}$
M_w (g/mol)	1355.39	1358.73	1365.89	1370.75
Temperature (K)	298(2)	298(2)	298(2)	298(2)
Crystal system	Triclinic	Triclinic	Triclinic	Triclinic
Space group	P-1	P-1	P-1	P-1
a, b, c (Å)	8.1915(2) 12.3709(3) 13.1913(3)	8.1877(3) 12.3718(4) 13.1796(4)	8.1692(6) 12.3599(9) 13.1414(11)	8.1598(3) 12.3391(4) 13.1141(5)
α, β, γ (°)	70.3530(10) 82.9060(10) 86.1670(10)	70.427(2) 83.027(2) 86.244(2)	70.482(5) 83.102(5) 86.233(5)	70.625(2) 83.201(2) 86.283(2)
V (Å^3)	1248.84(5)	1248.16(7)	1241.13(17)	1236.39(8)
Z	1	1	1	1
ρ_{calc} (g{cm^3)	1.802	1.808	1.825	1.830
μ (mm^{-1})	2.729	2.907	3.084	3.273
F(000)	674.0	676.0	676.0	672.0
Crystal size (mm)^3	0.17 × 0.14 × 0.12	0.16 × 0.13 × 0.11	0.17 × 0.15 × 0.12	0.16 × 0.15 × 0.12
Radiation	MoK$_\alpha$ (λ = 0.71073)	MoK$_\alpha$ (λ = 0.71073)	MoK$_\alpha$ (λ = 0.71073)	MoK$_\alpha$ (λ = 0.71073)
2θ range (°)	3.298 to 60.154	3.496 to 56.674	5.024 to 56.834	5.55 to 61.354
Index ranges	$-10 \le h \le 11$ $-17 \le k \le 17$ $-17 \le l \le 18$	$-10 \le h \le 10$ $-16 \le k \le 16$ $-17 \le l \le 17$	$-10 \le h \le 10$ $-16 \le k \le 16$ $-17 \le l \le 17$	$-11 \le h \le 11$ $-17 \le k \le 17$ $-18 \le l \le 18$
Reflections collected	23468	22259	18765	25706
Independent reflections	7297	6171	6154	7579
Data/restraints/ parameters	7297/0/316	6171/0/310	6154/0/310	7579/0/309
Goodness-of-fit on F^2	1.052	1.046	1.054	1.040
Completeness to 2θ	99.3 % (60.154)	99.1 % (56.674)	98.6 % (56.834°)	98.9 % (61.354)
Final R indexes [I>=2σ (I)]	$R_1 = 0.0315$, $wR_2 = 0.0764$	$R_1 = 0.0293$, $wR_2 = 0.0737$	$R_1 = 0.0509$, $wR_2 = 0.1257$	R1 = 0.0416, $wR_2 = 0.1051$
Final R indexes [all data]	$R_1 = 0.0376$, $wR_2 = 0.0797$	$R_1 = 0.0331$, $wR_2 = 0.0757$	$R_1 = 0.0614$, $wR_2 = 0.1333$	$R_1 = 0.0499$, $wR_2 = 0.1108$

$R_1 = \sum|F_0 - F_c|/\sum F_0; wR_2 = \sum[w(F_0^2 - F_0^2)]^2/[w(F_0^2)^2]^{\frac{1}{2}}$

All the complexes are isostructural and crystallized in the triclinic system in the space group *P*-1. The asymmetric unit of all these complexes contains one-half of the molecule consisting of one lanthanide ion, one dianionic ligand $[HL]^{2-}$, and two coordinating nitrate anions. The asymmetric unit as shown in Figure 4.A.9 (a) in the case of **4.A.3** carries a unit negative charge counter-balanced by a triethylammonium cation which is hydrogen bonded with the bridging nitrate ligand (Figure 4.A.9 (a)). Intermolecular hydrogen bonding parameters for compounds **4.A.1-4.A.4** are given in the Table 4.A.2. In the view of structural similarity of these complexes, we have chosen complex **4.A.3** (Figure 4.A.9 (b)) as a representative example to elucidate the common structural features present in these complexes. The molecular structures of complexes **4.A.1**, **4.A.2**, and **4.A.4** are given in the Figures 4.A.13-4.A.15.
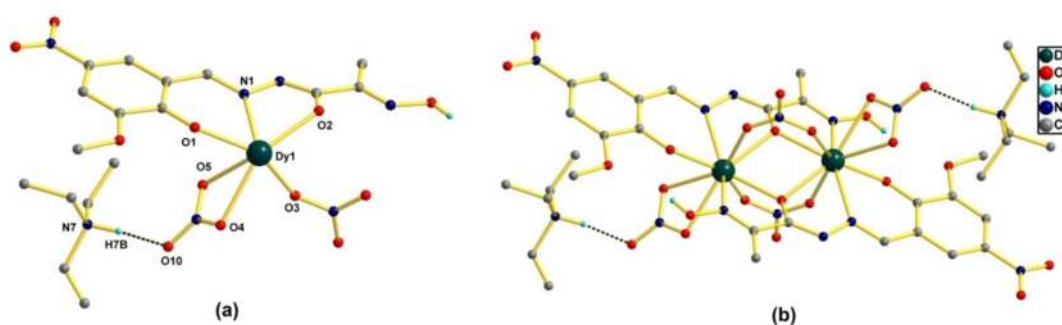
Figure 4.A.9. (a) Asymmetric unit and (b) molecular structure of complex **4.A.3**. (Hydrogen atoms, except selected are omitted for the sake of clarity). *atoms are generated by the symmetry operation 1-X, 1-Y, and 2-Z

Table 4.A.2. Intermolecular hydrogen bonding parameters

Sl. No.	D H A	d(D−H)/Å	d(H−A)/Å	d(D−A)/Å	D−H−A/°
4.A.1	N7 H7B O10	0.98	1.90	2.836(10)	157.9
4.A.2	N7 H7B O10	0.98	1.91	2.841(6)	157.4
4.A.3	N7 H7B O10	0.98	1.91	2.839(6)	157.4
4.A.4	N7 H7B O10	0.98	1.91	2.839(7)	156.8

The crystal structure of **4.A.3** consists of the dianionic complex, $[C_{22}H_{20}Dy_2N_{12}O_{24}]^{2-}$ and two triethylammonium counter cations. Complex **4.A.3** consists of two Dy^{III} ions, two $[HL]^{2-}$ ligands and four nitrate ligands. Two $[HL]^{2-}$ ligands hold the two dysprosium ions in a "head-to-tail" fashion utilizing a tridentate (O1, N1, and O2) and a bidentate (N3 and O2) coordinating motifs. The enolate oxygen atoms (O2 and O2*) of the ligand bridge the two metal centers affording an approximate rhomboidal-shaped four-membered Dy_2O_2 core (Figure 4.A.10 (a)). The $Dy\cdots Dy$ distance and the two $Dy-O-Dy$ angles in the central Dy_2O_2 cores are found to be 3.729 (5) Å and 108.25° (15) respectively. The coordination requirements of the Dy^{III} are met by the nitrate ligands giving an overall 2N, 7O coordination environment around each Dy^{III} center. Among the four nitrate ligands two are bridging ligands while two others are chelating.
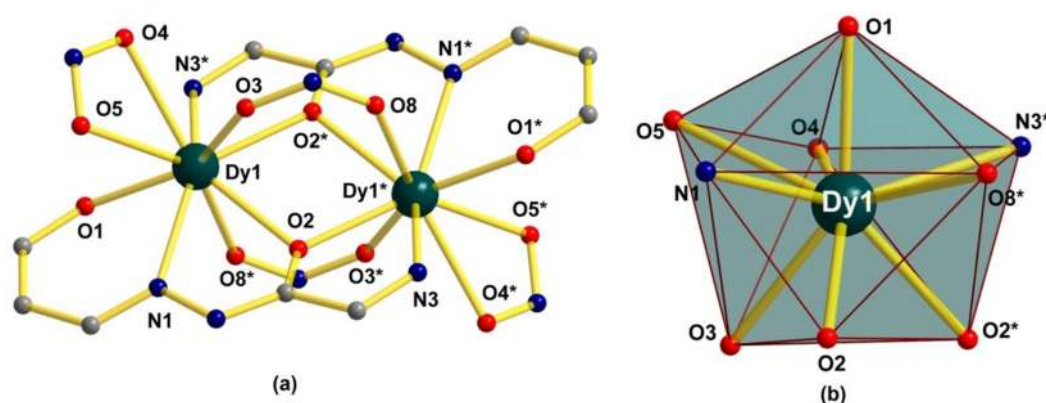
Figure 4.A.10. (a) View of the central Dy_2 core and (b) The distorted *muffin*-like coordination environment around the Dy^{III} center. *atoms are generated by the symmetry operation 1-X, 1-Y, and 2-Z

The two Dy^{III} centers in **4.A.3** are both nine-coordinate and are equivalent and adopt a distorted *muffin*-like geometry as confirmed by SHAPE analysis (Figure 4.A.10 (b), Table 4.A.3).[20] The distorted *muffin*-like coordination geometry consists of two

nitrogen atoms (N1, N3*; Dy−N average distance 2.489 (5) Å) and three oxygen

atoms (O1, O2, O2*; Dy−O2, 3.301 (4) Å; Dy−O1, 2.188 (4) Å) from the two $[HL]^{2-}$

ligands, two oxygen atoms (O4, O5; Dy−O average distance 2.560 (4) Å) from the

chelating nitrates, and two oxygen atoms (O3, O8*; Dy−O average distance 2.544 (5)

Å) from the bridging nitrate ligands. The shortest intermolecular Dy···Dy distance in

complex **4.A.3** is found to be quite large, 8.169 Å (see Figure 4.A.11). A view of the

crystal packing diagram is shown in Figure 4.A.11. We have checked the phase purity

of complex **4.A.3** by using powder X-ray diffraction analysis (Figure 4.A.12), which

shows good agreement with the simulated patterns generated from the SCXRD data.

The CShM values of **4.A.1**-**4.A.4** are given in the Table 4.A.3. The coordination

geometries of **4.A.1**, **4.A.2**, and **4.A.4** are shown in Figure 4.A.16 and the bond

parameters of all the complexes are summarized in Table 4.A.4.
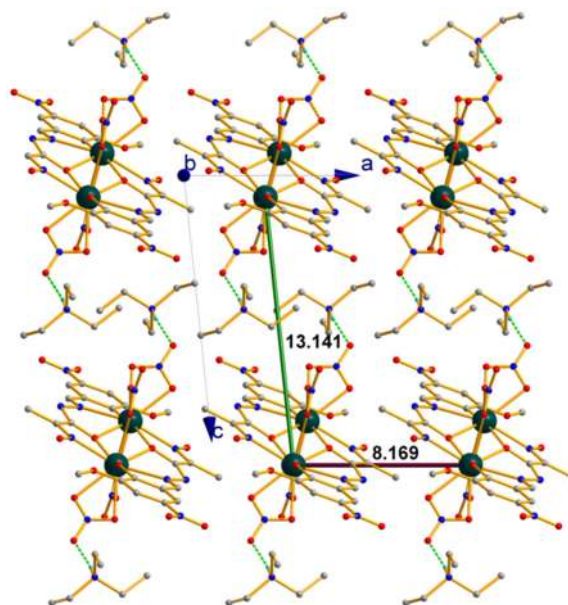
Figure 4.A.11. A perspective view (along the *b* direction) of the crystal packing

diagram of complex **4.A.4**. (H atoms, except those of the protonated NEt_3 groups are

omitted for the sake of clarity)

Table 4.A.3. SHAPE calculation results for selected geometries.

Complex	CShM		
	CSAPR-9	TCTPR-9	**MFF-9**
4.A.1	2.656	2.742	**2.385**
4.A.2	2.611	2.704	**2.390**
4.A.3	2.556	2.633	**2.335**
4.A.4	2.477	2.527	**2.266**

CSAPR-9 (C_{4v}); Spherical capped square antiprism, TCTPR-9 (D_{3h}); Spherical tricapped trigonal prism, MFF-9 (C_s); Muffin.
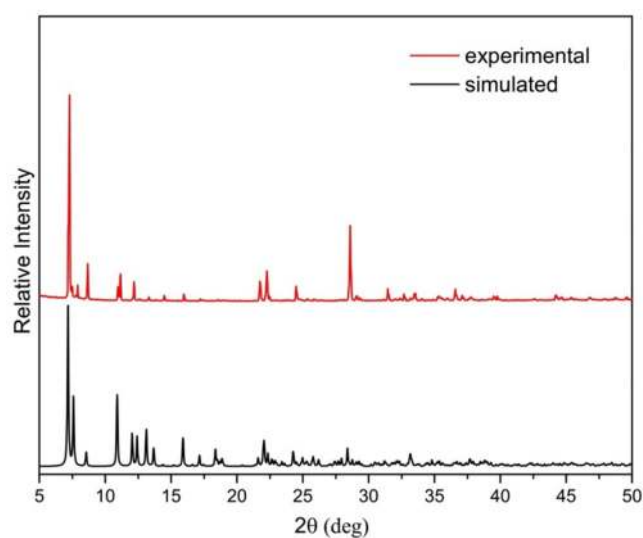
Figure 4.A.12. Powder XRD pattern of $\{Dy^{III}\}_2$ (**4.A.3**) complex.
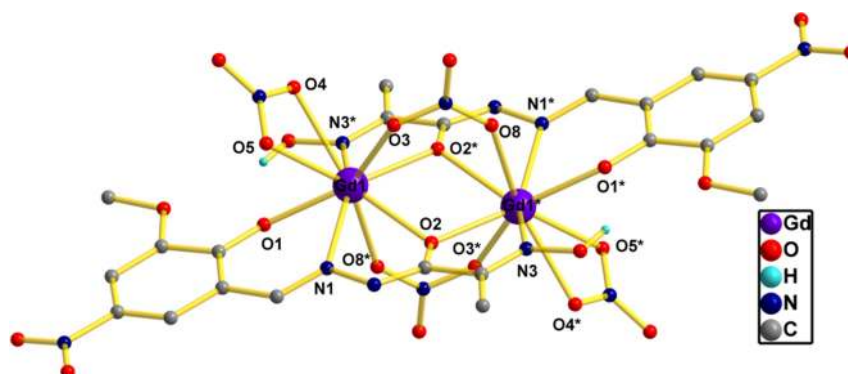
Figure 4.A.13. Molecular structure of complex **4.A.1.** (Hydrogen atoms and the counter cations are omitted for sake of clarity).
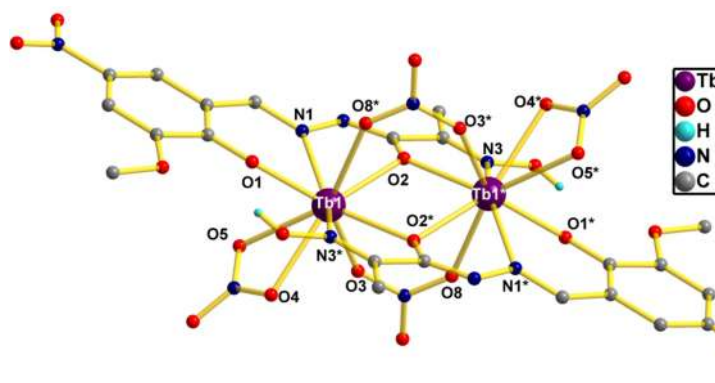
Figure 4.A.14. Molecular structure of complex **4.A.2.** (Hydrogen atoms and the counter cations are omitted for sake of clarity).
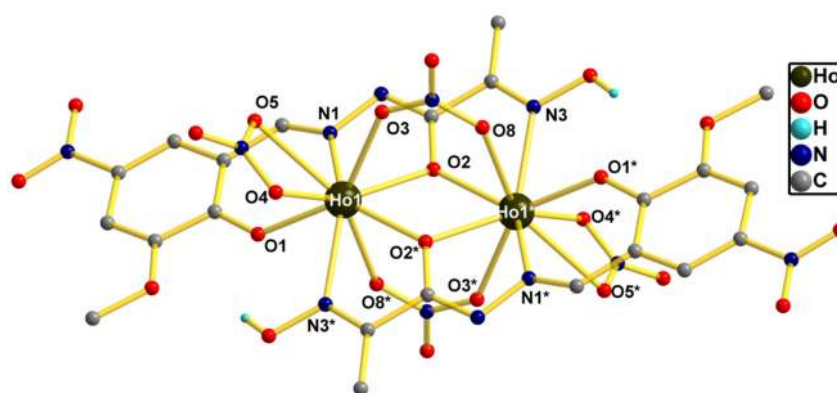
Figure 4.A.15. Molecular structure of complex **4.A.4.** (Hydrogen atoms and the counter cations are omitted for sake of clarity).
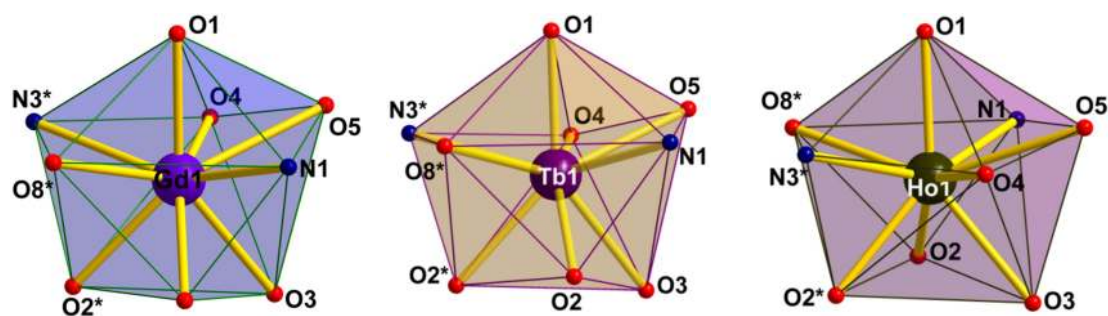
Figure 4.A.16. Coordination geometries of **4.A.1** (*left*), **4.A.2** (*middle*) and **4.A.4** (*right*)

Table 4.A.4. Selected bond length and angle parameters for compounds **4.A.1-4.A.4**

Complex	Bond lengths (Å)	Bond angles (°)			
4.A.1	Gd1−O1 2.222(2)	O1−Gd1−O8*	73.45(8)	O1−Gd1−N31	77.90(8)
	Gd1−O2* 2.309(2)	O1−Gd1−N4	76.38(10)	O2*−Gd1−O2	72.13(8)
	Gd1−O2 2.344(2)	O2−Gd1−O3	74.92(9)	O2*−Gd1−O4	96.36(8)
	Gd1−O3 2.441(3)	O2−Gd1−O5	122.22(8)	O2*−Gd1−O5	136.93(9)
	Gd1−O4 2.503(3)	O2−Gd1−O8*	70.14(8)	O2* Gd1 O8*	76.71(8)
	Gd1−O5 2.614(3)	O2−Gd1−N1	62.57(7)	O2*−Gd1−N1	134.70(8)
	Gd1−O8* 2.536(2)	O2−Gd1−N3*	124.75(8)	O2*−Gd1−N3*	62.52(7)
	Gd1−N1 2.489(2)	O4−Gd1−O8*	135.86(9)	N1−Gd1−O5	73.96(9)
	Gd1−N3* 2.555(2)	O3−Gd1−N3*	121.04(9)	O4−Gd1−O5	49.35(9)
4.A.2	Tb1−O1 2.207(2)	O1−Tb1−O2*	136.59(8)	O1−Tb1−O3	141.81(9)
	Tb1−O2 2.332(2)	O1−Tb1−O8*	73.59(9)	O3−Tb1−O4	74.96(11)
	Tb1−O2* 2.291(2)	O2*−Tb1−O8*	76.99(8)	O1−Tb1−O4	83.73(11)
	Tb1−O5 2.611(3)	O2*−Tb1−N3*	62.95(8)	N1−Tb1−O5	73.96(10)
	Tb1−O4 2.494(3)	O2*−Tb1−O8*	76.99(8)	O1−Tb1−N1	74.79(9)
	Tb1−O3 2.433(3)	O2−Tb1−O5	122.27(9)	O3−Tb1−O8*	141.92(9)
	Tb1−O8* 2.533(3	O2*−Tb1−N3*	62.95(8)	O2−Tb1−O5	122.27(9)
	Tb1−N1 2.476(3)	O2*−Tb1−O3	77.94(9)	O1−Tb1−N1	74.79(9)
	Tb1−N3* 2.544(3)	O1−Tb1−N3*	77.37(9)	O1−Tb1−O5	73.19(10)
4.A.3	Dy1−O1 2.189(4)	O1−Dy1−O2*	136.78(14)	O1−Dy1−O2	125.35(15)
	Dy1−O2 2.324(4)	O1−Dy1−O3	141.50(16)	O1−Dy1−O4	83.85(17)
	Dy1−O4 2.482(5)	O1−Dy1−O5	73.28(16)	O2−Dy1−O4	148.53(17)
	Dy1−O5 2.608(5)	O1−Dy1−O8*	73.86(15)	O2−Dy1−O5	121.85(15)
	Dy1−O3 2.413(4)	O1−Dy1−N1	75.06(15)	O2*−Dy1−O5	136.14(15)
	Dy1−N1 2.461(5)	O1−Dy1−N3*	77.19(14)	O2*−Dy1−O8*	77.37(14)
	Dy1−O8* 2.512(4)	O2*−Dy1−O2	71.75(15)	O2−Dy1−O8*	70.62(14)
	Dy1−O2* 2.277(4)	O2*−Dy1−O3	77.76(15)	O2*−Dy1−N1	135.04(15)
	Dy1−O8* 2.512(4)	O2−Dy1−O3	74.58(16)	O2−Dy1−N1	63.29(14)
	Ho1−O1 2.187(3)	O1−Ho1−O2	125.92(12)	O1−Ho1−O2*	36.69(11)
	Ho1−O2* 2.261(3)	O2−Ho1−O8*	70.58(10)	O4−Ho1−O5	50.00(12)
	Ho1−O2 2.312(3)	O2*−Ho1−N3*	63.51(11)	O2−Ho1−O2	71.59(11)
	Ho1−O3 2.412(4)	O2*−Ho1−N3*	63.51(11)	O1−Ho1−O4	83.74(14)

4.A.4	Ho1−O4 2.462(4)	O2*−Ho1−O8* 77.88(11)	O1−Ho1−O4 83.74(14)
	Ho1−O5 2.594(4)	O2*−Ho1−O8* 77.88(11)	O2−Ho1−O3 74.65(12)
	Ho1−O8* 2.492(3)	O2*−Ho1−O8* 77.88(11)	O2−Ho1−O2 71.59(11)
	Ho1−N1 2.448(4)	O2*−Ho1−N1 135.23(11)	O1−Ho1−O5 73.01(13)
	Ho1−N3* 2.514(3)	O1−Ho1−O4 83.74(14)	N1−Ho1−N3* 148.09(12)

4.A.3.3 Magnetic properties. The temperature dependence of $\chi_M T$ for complexes **4.A.1-4.A.4** (χ_M is the molar magnetic susceptibility per Ln_2^{III} unit) in the temperature range 300-2 K were measured with an applied magnetic field of 0.1 T and are shown in Figure 4.A.17 for complex **4.A.1** and in Figure 4.A.18 for complexes **4.A.2-4.A.4**.
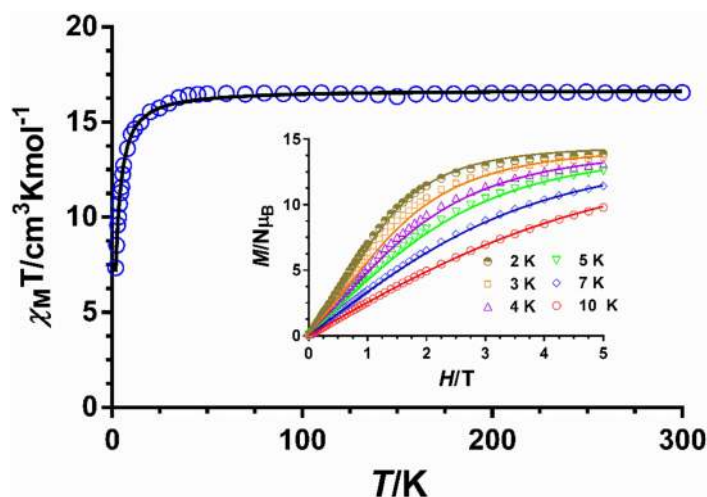
Figure 4.A.17. Temperature dependence of the $\chi_M T$ for compound **4.A.1**. Inset: Field dependence of the magnetization at the indicated temperatures. Solid lines represent the best fit of the experimental data

Let us start with the Gd_2^{III} complex **4.A.1**. The $\chi_M T$ value of **4.A.1** at room temperature (16.56 cm^3 mol^{-1} K) is close to that expected for two independent Gd^{III} ions (15.75 cm^3 mol^{-1} K, with $S = 7/2$ and $g = 2$). As the temperature decreases, $\chi_M T$ remains constant until ~ 50 K and then shows a rapid decrease to reach a value of 7.47

$cm^3 \ mol^{-1}$ K at 2 K. This behavior is mainly due to intramolecular antiferromagnetic interactions between the Gd^{III} ions.

The magnetic properties of **4.A.1** were analyzed using following isotropic Hamiltonian:

$$H = -J(S_{Gd1} + S_{Gd2}) + g\beta H(S_{Gd1} + S_{Gd2})$$

Where J represents the magnetic exchange coupling between the Gd^{III} ions and the rest of parameters have their usual meaning. The axial zero-field splitting parameter, D_{Gd}, was considered to be negligible because this ion is largely isotropic. The temperature dependence of the $\chi_M T$ product and the field dependence of the magnetization at different temperatures were simultaneously fitted with the above Hamiltonian using the PHI program.[21] The best fit led to the following set of parameters: J = -0.19 cm^{-1} and g = 2.059 and R = 1.1 x 10^{-4} (R = $\Sigma(\chi_{obs}T\chi_{calc}T)^2/\Sigma(\chi_{obs}T)^2$), where χ_{calc} and χ_{obs} denote calculated and observed molar magnetic susceptibilities, respectively. The obtained values are in good agreement with the reported coupling constants for other oxo-bridged Gd_2^{III} dinuclear complexes.[5, 22] Roy et al.[22b] carried out a DFT study on bis(oxo)bridged dinuclear Gd_2 complexes, which revealed a correlation between the structural parameters in the Gd_2O_2 fragment and the sign and magnitude of the magnetic exchange coupling. These results indicate that the decrease of the Gd−O−Gd angle (θ), with the concomitant reduction of the Gd$\cdots$Gd distance, produces a decrease of the magnetic coupling, which becomes antiferromagnetic for θ angles lower than approximately 112° (and Gd$\cdots$Gd distances below approximately 4.0 Å). In the case of compound **4.A.1**, the θ angle and the Gd$\cdots$Gd distances are is 108.24° and 3.279 Å. Taking into account the above magneto-structural correlation, an antiferromagnetic coupling is

expected for compound **4.A.1**, which matches well with the experimentally observed magnetic coupling.

The values of $\chi_M T$ at room temperature for complexes **4.A.2-4.A.4** (22.96, 30.3 and 28.76 cm^3 mol^{-1} K, respectively) are close to the expected theoretical values for two non-interacting lanthanide ions using the free ion approximation (23.64, 28.24 and 28.14 cm^3 mol^{-1} K for **4.A.2-4.A.4**, respectively). On lowering the temperature, the χT product decreases first slowly down to ~75 K and then abruptly down to 2.0 K to reach values of 8.5, 7.49 and 20.7 cm^3 mol^{-1} K, for **4.A.2-4.A.4** respectively. This behavior is due to the combined action of the thermal depopulation of the M_J sublevels of the Ln^{III} ion ground term, which is split by the ligand crystal field, and weak Ln^{III}···Ln^{III} antiferromagnetic interactions. The existence of very weak antiferromagnetic interactions in these complexes is not unexpected in view of the fact that isostructural Gd^{III}, Tb^{III}, Dy^{III} and Ho^{III} complexes generally display magnetic exchange interactions of the same nature.[23]
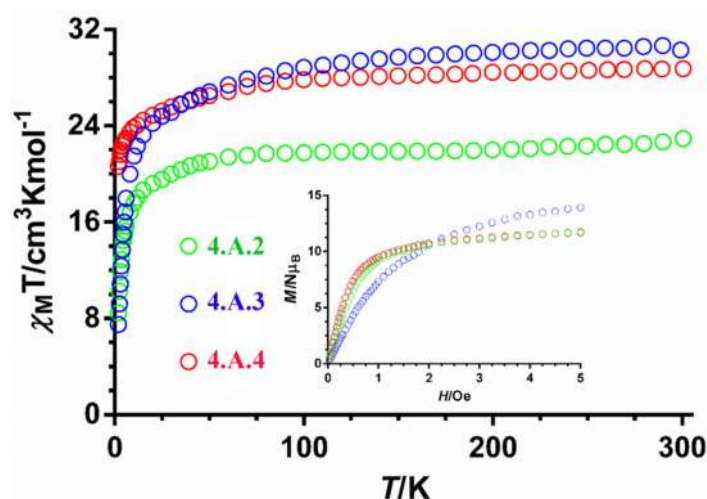
Figure 4.A.18. Temperature dependence of the $\chi_M T$ and field dependence of the magnetization (inset) for compounds **4.A.2-4.A.4**

The field dependence of the magnetization at 2 K for compounds **4.A.2-4.A.4** (Figure 4.A.18, inset) shows a rapid increase of the magnetization at low field (less abrupt for compound **4.A.3**) and a linear increase at high field to reach values of 11.75, 13.93 and 11.69 Nμ_B, respectively. These values are substantially smaller than the expected saturation magnetization values, $M_s/N\mu_B = 2g_JJ$, for two Ln^{III} ions (18, 20 and 20 Nμ_B, respectively), which is more likely due to the presence of a significant magnetic anisotropy arising from ligand-field effects.
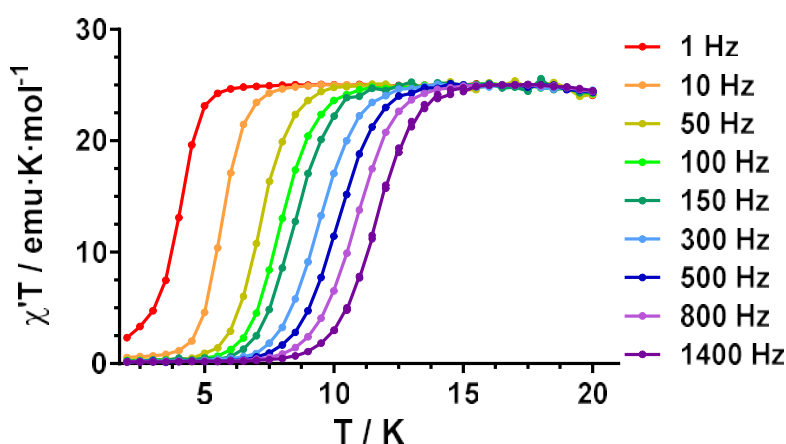
Figure 4.A.19. Temperature dependence of the $\chi'_M T$ product for **4.A.3**

It is worth mentioning at this point that the value of $\chi'_M T$ (χ'_M is the in-phase ac susceptibility, (Figure 4.A.19) at low temperature for **4.A.3**, when all the lines are coincident, is 25.2 cm^3 mol^{-1} K, which agrees rather well with that expected for randomly oriented crystals with a $M_J = \pm15/2$ *Ising* ground Kramers doublet (25 cm^3 mol^{-1} K). In view of the axial nature of the ground Kramers doublet, we have calculated the direction of the anisotropy axes of the Dy^{III} ions by using the Chilton's method,[24] which is based on electrostatic arguments. The results show that the anisotropy axis on the centrosymmetrically related Dy^{III} ions is located close to the Dy−O$_{phenoxide}$ bond, which presents by far the shortest Dy−O distance (2.186 Å). This orientation of the magnetic moment can be properly explained by taking into account

the simple oblate-prolate model.[25] The 4f electron density of the $M_J= \pm15/2$ ground Kramers doublet of the Dy^{III} center has an oblate shape.[25] Thus, in order to reduce the repulsion with the closest coordinated atom (bearing the large negative charge), the electron density disc is situated almost perpendicular to the shortest Dy−O bond, so that the resulting magnetic moment, which is perpendicular to the electron density disc, lies in the direction of the shortest Dy−O bond (see Figure 4.A.20). The presence of a short Dy−O distance like in the case of compound **4.A.3**, is enough to create an axial ligand field around the Dy^{III} ion,[26] leading to axiality in the ground KD and eventually to SMM behaviour.

For centrosymmetric complexes such as **4.A.2-4.A.4**, where the local anisotropy axes of the Dy^{III} ions are parallel, the orientation of the magnetic moments with regard to the line connecting the Dy^{III} ions (angle θ) determines the sign of the magnetic dipolar interaction.[27] It should be noted that the major contribution to the magnetic coupling in these type of oxo-bridged systems with Dy···Dy distances of approximately 3.8 Å comes from magnetic dipolar coupling rather than from magnetic exchange coupling. The dipolar contribution to the magnetic coupling can be calculated by the following equation for the energy of the dipole-dipole interaction:[27]

$$E_{dip} = \frac{-\mu_o}{4\pi} \frac{\mu_i \mu_j}{r^3} (3cos^2\theta - 1)$$

Where r is their distance, $\mu_{i,j}$ are the magnetic moments of centers i and j and μ_0 is the vacuum permittivity. This expression leads to antiferromagnetic coupling for angles between the magnetic moments and the molecular plane larger than 54.7° and ferromagnetic coupling for angles lower than 54.7°, respectively. For compound **4.A.3**, with θ = 64.4° an antiferromagnetic interaction, as in the case of compound **4.A.1**, can be anticipated.
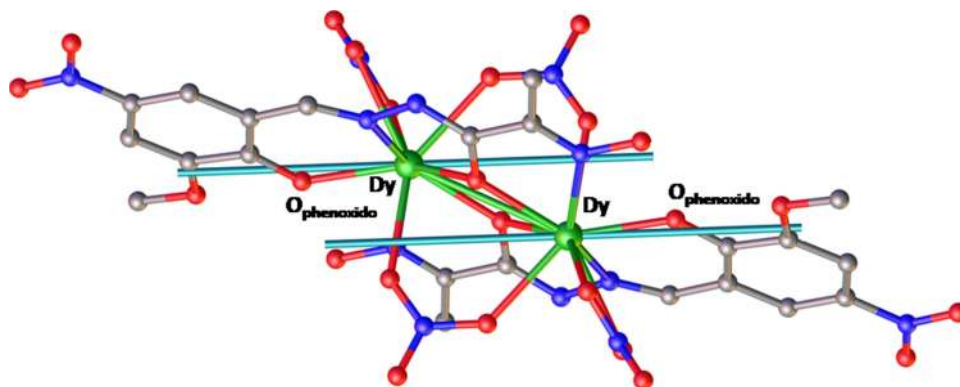
Figure 4.A.20. Quantitative calculation of the anisotropic axes orientation (green lines) using the Chilton´s method.[24]

In view of the above considerations, it is more than probable that compound **4.A.3** exhibits slow relaxation of the magnetization. In order to probe this and to study whether or not compounds **4.A.2**-**4.A.4** show slow relaxation of magnetization, temperature and frequency dependent dynamic ac magnetic susceptibility measurements were carried out on microcrystalline powder samples of complexes **4.A.2**-**4.A.4**. None of the compounds exhibited out-of-phase (χ''_M) signals under zero external dc field, which is most likely due to the existence of QTM promoted by transverse anisotropy in the ground state, intermolecular and hyperfine interactions. However, in the presence of an optimal magnetic field of 1000 Oe, to fully or partly quench QTM, compounds **4.A.2** and **4.A.3** present slow relaxation of the magnetization, which is slower for the latter complex than for the former one. The field dependence of rate of relaxation for the compound **4.A.3** is shown in Figure 4.A.21 which reveal slowest relaxation rate at an optimum field of 1000 Oe.
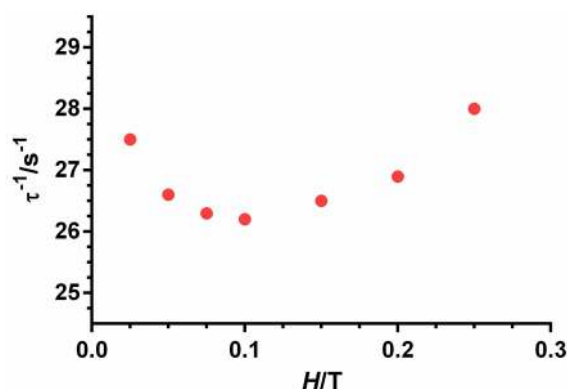
Figure 4.A.21. Field dependence of τ^{-1} for **4.A.3**.

Complex **4.A.2**, however, shows slow relaxation of magnetization (SRM) (Figure 4.A.22) below 8 K under a 1000 Oe dc field with out-of-phase peaks in the 2.5 K (10 Hz)-3.5 K (800 Hz) range. The fit of the frequency dependence of χ''_M at different temperatures to the generalized Debye model allowed extracting the temperature dependence of the relaxation times for magnetization reversal (τ). Fitting the extracted relaxation times to the Arrhenius equation in the high temperature region (2.5-3.5 K), afforded an effective energy barrier for the reversal of the magnetization $U_{eff} = 34(2)$ K and a pre-exponential factor $\tau_o = 1.1 \times 10^{-8}$ s (Figure 4.A.22 inset).
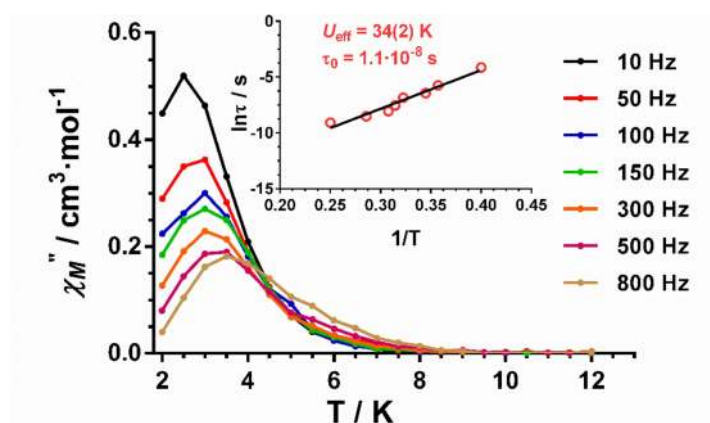
Figure 4.A.22. Temperature dependence of the out-of-phase ac signals (χ''_M) under a magnetic field of 0.1 T for **4.A.2**. Inset: Temperature dependence of the relaxation times for complex **4.A.2**. The black solid line corresponds to the Arrhenius plots for data at 0.1 T.

As for complex **4.A.3**, it shows frequency and temperature dependence of the out-of-phase magnetic susceptibility (χ''_M) under a magnetic field of 1000 Oe below 16 K (Figure 4.A.23) with maxima in the 11.5 K (1400 Hz)-3.5 K (1 Hz) temperature range. This behaviour indicates slow relaxation of the magnetization and field induced SMM behaviour. The temperature dependence of the relaxation times for magnetization reversal (τ) was obtained from the fit of the frequency dependence of χ''_M at different temperatures to the generalized Debye model (Figure 4.A.24). Fitting the extracted relaxation times to the Arrhenius equation in the high temperature region (10-12 K), afforded an effective energy barrier for the reversal of the magnetization U_{eff} = 80(3) K and a pre-exponential factor τ_o = 2.2 x 10^{-6} s. The deviation of the data from the Arrhenius law below 10 K is a clear indication of the coexistence of several competing relaxation processes. Owing to the fact that in the studied temperature range (T > 4.5 K and 0.1 T) direct and QTM relaxation processes should be almost negligible, we have fitted the magnetic data to the following equation:

$$\tau^{-1} = BT^n + \tau_0^{-1}exp(-U_{eff}/k_BT)$$

which considers that Raman (first term) and Orbach processes (second term) contribute simultaneously to the relaxation of the magnetization. However, all attempts to fit the data to this equation were unsuccessful. Nevertheless, to estimate the values of the parameters for the Raman process we have fixed U_{eff} and τ_0 values to those extracted from the Arrhenius plot for the Orbach process. The best fit was obtained for n = 7.4 and B = 0.0012 s^{-1} $K^{7.4}$. Although for a Kramers ion like Dy^{III} an n value equal to 9 is expected,[28] however, values between 2 and 7 are also are realistic when both acoustic and optical phonons are present.[29] The extracted values of n and B points out a significant contribution of the Raman process to the whole relaxation

mechanism in complex **4.A.3**. Similar values have been previously reported for other Dy[III] containing complexes.[30]
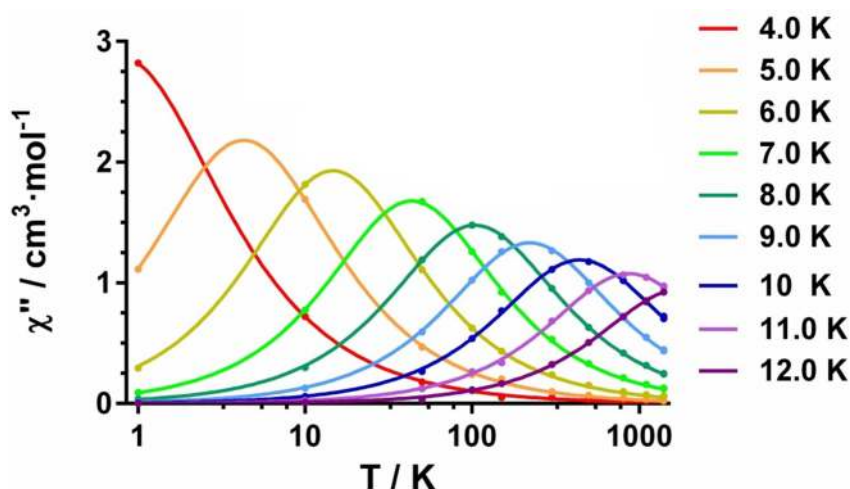
Figure 4.A.23. Frequency dependence of the out-of-phase ac signals (χ''_M) at different temperatures and under a magnetic field of 0.1 T for **4.A.3**.
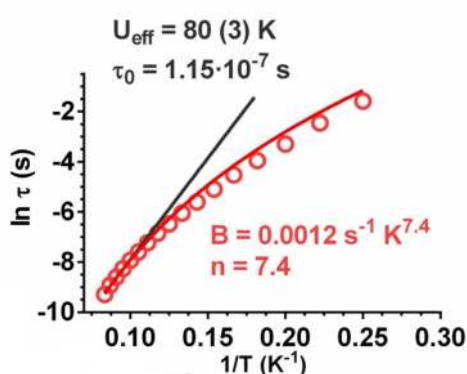
Figure 4.A.24. Temperature dependence of the relaxation times for complex **4.A.3**. The black solid line corresponds to the Arrhenius plots for data at 0.1 T. The red solid line represents the best fit of the temperature dependence of the relaxation times at 0.1 T to a combination of Orbach and Raman relaxation processes with the indicated parameters.

It should be noted at this point that intra- and intermolecular Ln···Ln interactions generally favor fast QTM, which suppress or reduce the thermal energy barrier (U) to

a much smaller effective value, U_{eff}.[31] However, in dinuclear Ln_2 complexes with radical bridging ligands, which provide a strong interaction between the lanthanides, the QTM is not operative leading to zero field SMM behaviour.[4a] In addition, it has been demonstrated that the combination of magnetic exchange and a parallel disposition of the principal anisotropy axes favors the quenching of the QTM and the observation of SMM at zero field.[31] In view of the above considerations and taking into account that **4.A.3** have parallel anisotropy axes, it would be reasonable to anticipate SMM for this compound. However, it does not present SMM at zero field. This fact could be due to the weakness of the Dy···Dy interaction, which is not enough strong to suppress QTM at zero field. In these circumstances, the low symmetry distribution of charges and bond lengths on the DyO_7N_2 coordination sphere must introduce some transverse anisotropy, which favors QTM and inhibit zero-field SMM behaviour. The non-Kramers Tb^{III} and Ho^{III} ions are also oblate ions[4a] and therefore require an axial crystal field to reach an axial bistable ground state and then to exhibit SMM behaviour. However, for it these ions must maintain a rigorous axial symmetry, which is not an easy task. Moreover, non-Kramers ions possess an intrinsic tunnelling gap that favors QTM at zero field. In view of this, the lack of SMM at zero field in **4.A.2** and **4.A.4** is not unexpected.

4.A.4 CONCLUSIONS

In conclusion, we have isolated and structurally characterized a series of centrosymmetric dinuclear lanthanide complexes by the utilization of an enolizable multipocket Schiff base ligand. All the complexes are isostructural and have a comparably short $Ln–O_{phenoxide}$ bond in the coordination sphere. Magnetic studies reveal that the two lanthanide ions are weakly antiferromagnetically coupled to each other. The strength of coupling constant in the complex **4.A.1** was calculated to be

-0.19 cm^{-1} by fitting of the experimental data. Quantitative calculation of the anisotropic axes in the complex **4.A.3** shows parallel orientation of two anisotropy axes in both the Dy^{III} centers passing closely through the shortest Dy–O$_{phenoxide}$ bond. While the complexes **4.A.2** and **4.A.3** show slow relaxation of magnetization under an applied magnetic field, complex **4.A.4** does not exhibit slow relaxation. The energy barriers of magnetization reversal for complex **4.A.2** and complex **4.A.3** were found to be 34(3) K and 80(3) K respectively. It may be noted that in the current dinuclear complexes the oxime –OH groups are *free* and can therefore be in principle utilized to proliferate the dinuclear assembly into a one-dimensional polymeric system.

4.A.5 REFERENCES

1 (a) Y.-C. Chen, J.-L. Liu, L. Ungur, J. Liu, Q.-W. Li, L.-F. Wang, Z.-P. Ni, L. F. Chibotaru, X.-M. Chen and M.-L. Tong, *J. Am. Chem. Soc.*, 2016, **138**, 2829-2837; (b) N. Ishikawa, M. Sugita, T. Ishikawa, S.-y. Koshihara and Y. Kaizu, *J. Am. Chem. Soc.*, 2003, **125**, 8694-8695; (c) T. Kajiwara, *Angew. Chem. Int. Ed.*, 2017, **56**, 11306-11308; (d) A. J. Brown, D. Pinkowicz, M. R. Saber and K. R. Dunbar, *Angew. Chem. Int. Ed.*, 2015, **54**, 5864-5868.

2 (a) J. Liu, Y.-C. Chen, J.-L. Liu, V. Vieru, L. Ungur, J.-H. Jia, L. F. Chibotaru, Y. Lan, W. Wernsdorfer, S. Gao, X.-M. Chen and M.-L. Tong, *J. Am. Chem. Soc.*, 2016, **138**, 5441-5450; (b) F. Tuna, C. A. Smith, M. Bodensteiner, L. Ungur, L. F. Chibotaru, E. J. L. McInnes, R. E. P. Winpenny, D. Collison and R. A. Layfield, *Angew. Chem. Int. Ed.*, 2012, **51**, 6976-6980; (c) L. F. Chibotaru, L. Ungur and A. Soncini, *Angew. Chem. Int. Ed.*, 2008, **47**, 4126-4129; (d) R. J. Blagg, L. Ungur, F. Tuna, J. Speak, P. Comar, D. Collison, W. Wernsdorfer, E. J. L. McInnes, L. F. Chibotaru and R. E. P. Winpenny, *Nat. Chem.*, 2013, **5**, 673-678; (e) X.-L. Li, J. Wu, L. Zhao, W. Shi, P. Cheng and J. Tang, *Chem. Commun.*, 2017, **53**, 3026-3029; (f) S.-

Y. Lin, W. Wernsdorfer, L. Ungur, A. K. Powell, Y.-N. Guo, J. Tang, L. Zhao, L. F. Chibotaru and H.-J. Zhang, *Angew. Chem. Int. Ed.*, 2012, **51**, 12767-12771; (g) R. J. Blagg, C. A. Muryn, E. J. L. McInnes, F. Tuna and R. E. P. Winpenny, *Angew. Chem. Int. Ed.*, 2011, **50**, 6530-6533.

3 (a) F.-S. Guo, B. M. Day, Y.-C. Chen, M.-L. Tong, A. Mansikkamäki and R. A. Layfield, *Science*, 2018, **362**, 1400-1403; (b) F.-S. Guo, B. M. Day, Y.-C. Chen, M.-L. Tong, A. Mansikkamäki and R. A. Layfield, *Angew. Chem. Int. Ed.*, 2017, **56**, 11445-11449; (c) C. A. P. Goodwin, F. Ortu, D. Reta, N. F. Chilton and D. P. Mills, *Nature*, 2017, **548**, 439-442.

4 (a) J. D. Rinehart, M. Fang, W. J. Evans and J. R. Long, *Nat. Chem.*, 2011, **3**, 538-542; (b) F. Habib and M. Murugesu, *Chem. Soc. Rev.*, 2013, **42**, 3278-3288; (c) F. Pointillart, Y. Le Gal, S. Golhen, O. Cador and L. Ouahab, *Chem. Eur. J*, 2011, **17**, 10397-10404; (d) X. Yi, K. Bernot, F. Pointillart, G. Poneti, G. Calvez, C. Daiguebonne, O. Guillou and R. Sessoli, *Chem. Eur. J*, 2012, **18**, 11379-11387; (e) C. Y. Chow, H. Bolvin, V. E. Campbell, R. Guillot, J. W. Kampf, W. Wernsdorfer, F. Gendron, J. Autschbach, V. L. Pecoraro and T. Mallah, *Chem. Sci.*, 2015, **6**, 4148-4159; (f) X. Yi, K. Bernot, O. Cador, J. Luzon, G. Calvez, C. Daiguebonne and O. Guillou, *Dalton Trans.*, 2013, **42**, 6728-6731; (g) F. Habib, G. Brunet, V. Vieru, I. Korobkov, L. F. Chibotaru and M. Murugesu, *J. Am. Chem. Soc.*, 2013, **135**, 13242-13245; (h) K. Zhang, D. Liu, V. Vieru, L. Hou, B. Cui, F.-S. Guo, L. F. Chibotaru and Y.-Y. Wang, *Dalton Trans.*, 2017, **46**, 638-642.

5 J. Long, F. Habib, P.-H. Lin, I. Korobkov, G. Enright, L. Ungur, W. Wernsdorfer, L. F. Chibotaru and M. Murugesu, *J. Am. Chem. Soc.*, 2011, **133**, 5319-5328.

6 (a) F. Pointillart, K. Bernot, G. Poneti and R. Sessoli, *Inorg. Chem.*, 2012, **51**, 12218-12229; (b) P.-H. Lin, T. J. Burchell, R. Clérac and M. Murugesu, *Angew.*

Chem. Int. Ed., 2008, **47**, 8848-8851; (c) F. Habib, J. Long, P.-H. Lin, I. Korobkov, L. Ungur, W. Wernsdorfer, L. F. Chibotaru and M. Murugesu, *Chem. Sci.*, 2012, **3**, 2158-2164; (d) G. Poneti, K. Bernot, L. Bogani, A. Caneschi, R. Sessoli, W. Wernsdorfer and D. Gatteschi, *Chem. Commun.*, 2007, 1807-1809; (e) E. C. Mazarakioti, J. Regier, L. Cunha-Silva, W. Wernsdorfer, M. Pilkington, J. Tang and T. C. Stamatatos, *Inorg. Chem.*, 2017, **56**, 3568-3578; (f) H. Zhang, S.-Y. Lin, S. Xue, C. Wang and J. Tang, *Dalton Trans.*, 2014, **43**, 6262-6268; (g) K. Zhang, C. Yuan, F.-S. Guo, Y.-Q. Zhang and Y.-Y. Wang, *Dalton Trans.*, 2017, **46**, 186-192.

7 (a) W.-M. Wang, S.-Y. Wang, H.-X. Zhang, H.-Y. Shen, J.-Y. Zou, H.-L. Gao, J.-Z. Cui and B. Zhao, *Inorg. Chem. Front.*, 2016, **3**, 133-141; (b) Y.-N. Guo, X.-H. Chen, S. Xue and J. Tang, *Inorg. Chem.*, 2011, **50**, 9705-9713.

8 Y. Qin, H. Zhang, H. Sun, Y. Pan, Y. Ge, Y. Li and Y.-Q. Zhang, *Chem. Asian J.*, 2017, **12**, 2834-2844.

9 S. Mukherjee, J. Lu, G. Velmurugan, S. Singh, G. Rajaraman, J. Tang and S. K. Ghosh, *Inorg. Chem.*, 2016, **55**, 11283-11298.

10 (a) S. Biswas, S. Das, G. Rogez and V. Chandrasekhar, *Eur. J. Inorg. Chem.*, 2016, **2016**, 3322-3329; (b) V. Chandrasekhar, P. Bag and E. Colacio, *Inorg. Chem.*, 2013, **52**, 4562-4570; (c) V. Chandrasekhar, S. Das, A. Dey, S. Hossain and J.-P. Sutter, *Inorg. Chem.*, 2013, **52**, 11956-11965.

11 I. V. Nikolayenko, C. Bazzicalupi, G. P. Thubron and C. Grimmer, *Acta Cryst. E*, 2010, **66**, o887-o888.

12 I. O. Fritsky, H. Kozłowski, P. J. Sadler, O. P. Yefetova, J. Świątek-Kozłowska, V. A. Kalibabchuk and T. Głowiak, *J. Chem. Soc., Dalton Trans.*, 1998, 3269-3274.

13 *SMART & SAINT Software Reference manuals*, Bruker Analytical X-ray Systems, Inc., Madison, WI, version 6.45, 2003.

14 G. M. Sheldrick, *SADABS, Program for Empirical Absorption Correction*, University of Gottingen, Germany, 1996.

15 *Bruker APEX2*, Bruker AXS Inc., Madison, Wisconsin, USA, version 2008.1−0, 2008.

16 G. M. Sheldrick, *Acta Cryst. A*, 2015, **71**, 3-8.

17 G. Sheldrick, *Acta Cryst. C*, 2015, **71**, 3-8.

18 O. V. Dolomanov, L. J. Bourhis, R. J. Gildea, J. A. K. Howard and H. Puschmann, *J. Appl. Cryst.*, 2009, **42**, 339-341.

19 K. Brandenburg and H. Putz, *DIAMOND*, Crystal Impact GbR, Bonn, Germany, version 3.2, 1997−2014.

20 (a) J. Cirera, E. Ruiz and S. Alvarez, *Organometallics*, 2005, **24**, 1556-1562; (b) *SHAPE: Continuous Shape Measures calculation*, Electronic Structure Group, Universitat de Barcelona, Spain, version 2.1, 2013.

21 N. F. Chilton, R. P. Anderson, L. D. Turner, A. Soncini and K. S. Murray, *J. Comput. Chem.*, 2013, **34**, 1164-1175.

22 (a) M. Machata, R. Herchel, I. Nemec and Z. Trávníček, *Dalton Trans.*, 2017, **46**, 16294-16305; (b) L. E. Roy and T. Hughbanks, *J. Am. Chem. Soc.*, 2006, **128**, 568-575; (c) N. C. Anastasiadis, D. A. Kalofolias, A. Philippidis, S. Tzani, C. P. Raptopoulou, V. Psycharis, C. J. Milios, A. Escuer and S. P. Perlepes, *Dalton Trans.*, 2015, **44**, 10200-10209.

23 (a) E. Colacio, J. Ruiz, A. J. Mota, M. A. Palacios, E. Cremades, E. Ruiz, F. J. White and E. K. Brechin, *Inorg. Chem.*, 2012, **51**, 5857-5868; (b) V. Chandrasekhar, B. M. Pandian, J. J. Vittal and R. Clérac, *Inorg. Chem.*, 2009, **48**, 1148-1157.

24 N. F. Chilton, D. Collison, E. J. L. McInnes, R. E. P. Winpenny and A. Soncini, *Nat. Commun.*, 2013, **4**, 2551-2557.

25 J. D. Rinehart and J. R. Long, *Chem. Sci.*, 2011, **2**, 2078-2085.

26 M. M. Hänninen, A. J. Mota, D. Aravena, E. Ruiz, R. Sillanpää, A. Camón, M. Evangelisti and E. Colacio, *Chem. Eur. J*, 2014, **20**, 8410-8420.

27 P. Panissod and M. Drillon, in *Magnetism: Molecules to Materials IV: Nanosized Magnetic Materials*, eds. J. S. Miller and M. Drillon, Wiley-VCH Verlag GmbH & Co. KGaA, 2003, ch. 7, pp. 233-270.

28 A. Abragam and B. Bleaney, *Electron paramagnetic resonance of transition ions*, Oxford : Clarendon press, 1970.

29 (a) A. Singh and K. N. Shrivastava, *Phys. Status Solidi B*, 1979, **95**, 273-277; (b) K. N. Shrivastava, *Phys. Status Solidi B*, 1983, **117**, 437-458.

30 I. Oyarzabal, B. Artetxe, A. Rodríguez-Diéguez, J. Á. García, J. M. Seco and E. Colacio, *Dalton Trans.*, 2016, **45**, 9712-9726.

31 E. Moreno Pineda, N. F. Chilton, R. Marx, M. Dörfel, D. O. Sells, P. Neugebauer, S.-D. Jiang, D. Collison, J. van Slageren, E. J. L. McInnes and R. E. P. Winpenny, *Nat. Commun.*, 2014, **5**, 5243-5249.

Non-planar Octanuclear {Ln$_8$} Complexes: Magneto-Caloric Effect in the {Gd$_8$} Analogue

ABSTRACT: Neutral isostructural octanuclear Ln^{III} complexes, [Ln$_8$(HL)$_6$(L)$_2$(μ_3-OH)$_4$(μ_2-OH)$_2$(H$_2$O)$_4$] (Ln = Gd^{III}, (**4.B.1**), Tb^{III}, (**4.B.2**), Dy^{III}, (**4.B.3**), and Er^{III}, (**4.B.4**)) have been synthesized using Ln^{III} nitrate salts and an *o*-vanillin supported multidentate ligand, *N'*-(2-hydroxy-3-methoxy-5-nitrobenzylidene)-2-hydroxyamino-propanehydrazide (H$_3$L) in the presence of tetramethyl ammonium hydroxide. The complexes were structurally characterized by single crystal X-ray diffraction studies. The complexes are held by the cumulative coordination action of six [HL]$^{2-}$ doubly deprotonated ligands, two [L]$^{3-}$ triply deprotonated chelating ligands, H$_2$O and hydroxide ligands. The magneto-structural analysis in complexes **4.B.1** and **4.B.3** reveals the presence of intramolecular antiferromagnetic interactions between the Ln^{III} ions possibly mediated by the bridging groups. The magneto-caloric effect was analyzed for the complex **4.B.1** which shows a maximum in the change of molar entropy (-ΔS_m) of magnitude 25.5 J kg^{-1} K^{-1} at T = 3 K and applied field change ΔB = 5 T.

4.B.1 INTRODUCTION

Rare earth compounds have been explored in recent years owing to their interesting magnetic[1], optical[2], and catalytic properties[3]. Among lanthanide complexes, polynuclear complexes are formed usually as a result of the bridging coordination action of the hydroxide ligand.[4] Such complexes have been of interest in the field of molecular magnetism.[4b, 4c, 5] However, the synthesis of such complexes is fraught with some challenges. One difficulty is the formation of intractable polymeric complexes

as a result of the ready deprotonation of the coordinated water molecules around the lanthanide ions. The formation of discrete complexes becomes feasible if controlled deprotonation of the coordinated water molecules can be achieved.[4a] This is often feasible by having an appropriate multi-site coordinating ligand to bind to lanthanide ions so that the available coordination sites are reduced and the chances for the formation of a discrete complex increased. In our lab, multi-pocket multidentate hydrazone ligands have been extensively used for the synthesis of discrete polynuclear lanthanide complexes.[6]

In order to take this further and to explore the quest of studying $Ln^{III} \cdots Ln^{III}$ exchange interactions mediated by an enolate oxygen atom, we have designed a multi-pocket hydrazone ligand to isolate dinuclear Ln^{III} complexes. The $\{Dy^{III}\}_2$ and $\{Tb^{III}\}_2$ derivatives showed field induced SMM behaviour. In these dinuclear complexes, we have observed uncoordinated free oxime $-OH$ groups which could be deprotonated so that these dinuclear complexes can proliferate to discrete multinuclear complexes. These aspects have been discussed in Chapter 4A. We were interested in modifying the reaction conditions to examine the possibility of increasing the nuclearity of the complexes. Accordingly, in this chapter, we discuss the *non*-planar octanuclear complexes, $[Ln_8(HL)_6(L)_2(\mu_3\text{-}OH)_4(\mu_2\text{-}OH)_2(H_2O)_4]$ (Ln = Gd^{III}; (**4.B.1**), Tb^{III}; (**4.B.2**), Dy^{III}; (**4.B.3**), and Er^{III}; (**4.B.4**)). Compared to the dinuclear complexes, in these complexes, the ligand is involved in binding to the metal centers in both the dianionic and trianionic charge states with additional coordination modes (Scheme 4.B.1). Interestingly, we did not use any additional co-ligand in isolating the discrete molecular species which are often required to isolate such multinuclear Ln^{III} complexes. In this chapter, the synthesis and solid-state structures of the complexes

4.B.1-**4.B.4** are discussed in detail. The magnetic properties of complexes **4.B.1** and **4.B.3** were analyzed and discussed herein.

4.B.2 EXPERIMENTAL SECTION

4.B.2.1 Materials and Methods. Solvents and other general reagents used in this work were obtained from commercial sources and used without further purification. 3-Methoxy-5-nitrosalicylaldehyde, hydroxylamine hydrochloride and lanthanide nitrate hydrates were obtained from Sigma Aldrich Chemical Co. (India), Ethyl pyruvate and tetramethylammonium hydroxide pentahydrate were obtained from Spectrochem Pvt. Ltd., Mumbai, India. All these reagents were used as obtained without further purification. Ethyl 2-(hydroxyimino)propanoate, 2-(hydroxyimino)-propanehydrazide and the ligand H_3L were prepared by a previously reported procedure as described in Chapter 4A.

4.B.2.2 Instrumentation. Melting points were measured using a Stuart^{TM} SMP10 melting point apparatus and are uncorrected. IR spectra were recorded on a Perkin Elmer FT-IR spectrometer. Mass spectra were recorded with a Bruker micrOTOF-Q II spectrometer. Elemental analyses of the compounds were obtained from a Euro Vector EA instrument (CHNS-O, model EuroEA3000).

4.B.2.3 Magnetic Measurements. Field dependence of the magnetization at different fields and variable temperature (2-300 K) magnetic susceptibility measurements were carried out on polycrystalline samples with a Quantum Design SQUID MPMS XL-5 device operating at different magnetic fields. Ac susceptibility measurement of **4.B.3** was performed using an oscillating ac field of 3 Oe and in the ac frequency 1400 Hz. The static experimental susceptibilities were corrected for the diamagnetism of the constituent atoms (using Pascal's constants) and for the sample holder. In order to

avoid any torquing of the microcrystals, a pellet of the sample cut into very small fragments were introduced in the sample holder.

4.B.2.4 X-ray Crystallography. The molecular structures of complexes **4.B.1**, **4.B.3**, and **4.B.4** were analyzed by single crystal X-ray diffraction studies performed on a Bruker APEX-II CCD diffractometer system equipped with an Oxford low temperature attachment. The crystals were kept at 120 K during data collection. The frames were indexed, integrated, and scaled using the SMART and SAINT software package.[7] Absorption correction was performed by a multiscan method implemented in SADABS.[8] Space groups were determined using XPREP implemented in APEX-II.[9] The single crystal X-ray diffraction data of **4.B.2** was collected on a Rigaku XtaLAB X-ray diffractometer system equipped with a CCD area detector and operated at 30 W power (50 kV, 0.6 mA) to generate MoKα radiation ($\lambda = 0.71073$ Å) at 120(2) K. Data were integrated using CrysAlis[Pro] software with a narrow frame algorithm.[10] Data were subsequently corrected for absorption by the program SCALE3 ABSPACK scaling algorithm.[10] The crystal data and the cell parameters for **4.B.1-4.B.4** are summarized in Table 4.B.1. The structures were solved by ShelXT[11] structure solution programme using Intrinsic Phasing and refined with the ShelXL[12] refinement package using Least Squares minimization on F^2 in the Olex-2 software[13]. All of the non-hydrogen atoms were refined anisotropically using full-matrix least-square procedures. Hydrogen atoms on all the bridging hydroxides were not observed in the diffraction pattern and therefore omitted entirely, although their oxidation states were confirmed by BVS calculations (see Table 4.B.2).[14] The structures also contain heavily disordered solvents of crystallization which couldn't be modelled satisfactorily. Therefore, the PLATON/SQUEEZE programme was used to get rid of the contributions of the disordered solvent molecules.[15] All of the mean plane

analyses and molecular drawings were produced using the DIAMOND software (version 3.2).[16]

Table 4.B.1. Crystallographic details for complexes **4.B.1-4.B.4**.

	4.B.1	4.B.2	4.B.3	4.B.4
Empirical formula*	$C_{88}H_{86}Gd_8N_{32}O_{58}$	$C_{88}H_{88}Tb_8N_{32}O_{59}$	$C_{88}H_{86}Dy_8N_{32}O_{58}$	$C_{88}H_{86}Er_8N_{32}O_{58}$
M_w* /gmol^{-1}	3777.88	3809.26	3819.88	3857.96
Temperature/K	120 (2)	119.99(10)	120(0)	120(0)
Crystal system	Monoclinic	Monoclinic	Monoclinic	Monoclinic
Space group	$C2/c$	$P21/c$	$C2/c$	$C2/c$
a/Å	19.1263(18)	19.0208(3)	18.9896(19)	18.8768(8)
b/Å	31.7579(18)	31.6554(6)	31.583(3)	31.5079(8)
c/Å	25.4695(16)	25.2299(5)	25.239(3)	25.2367(7)
α/°	90	90	90	90
β/°	98.198(5)	95.255(2)	98.325(5)	97.065(3)
γ/°	90	90	90	90
Volume/Å^3	15312.4(19)	15127.4(5)	14978(3)	14896.0(8)
Z	4	4	4	4
ρ^{calc} g/cm^3	1.639	1.673	1.694	1.720
μ/mm^{-1}	3.500	3.776	4.027	4.543
F(000)	7256.0	7328.0	7320.0	7384.0
Crystal size/mm^3	0.21 × 0.15 × 0.11	0.25 × 0.18 × 0.12	0.13 × 0.11 × 0.08	0.15 × 0.14 × 0.11
Radiation	MoKα (λ = 0.71073)	MoKα (λ = 0.71073)	MoKα (λ = 0.71073)	MoKα (λ = 0.71073)
2θ range for data collection/°	2.504 to 51.332	5.032 to 53	3.052 to 57.938	2.53 to 56.808
Index ranges	-22 ≤ h ≤ 23, -38 ≤ k ≤ 38, -30 ≤ l ≤ 24	-23 ≤ h ≤ 23, -37 ≤ k ≤ 39, -31 ≤ l ≤ 31	-25 ≤ h ≤ 25, -42 ≤ k ≤ 41, -30 ≤ l ≤ 33	-25 ≤ h ≤ 24, -41 ≤ k ≤ 42, -33 ≤ l ≤ 33
Reflections collected	85743	193424	114164	139038
Independent reflections	14325 [R_{int} = 0.1923]	31280 [R_{int} = 0.0828]	18900 [R_{int} = 0.2075]	18554 [R_{int} = 0.1837]
Data/restraints/parameters	14325/1/630	31280/0/1699	18900/2/797	18554/0/716
GOF on F^2	1.029	1.045	0.948	0.928
Final R indexes [I>=2σ (I)]	R_1 = 0.1065, wR_2 = 0.2123	R_1 = 0.0701, wR_2 = 0.1517	R_1 = 0.0660, wR_2 = 0.1317	R_1 = 0.0650, wR_2 = 0.1420
Final R indexes [all data]	R_1 = 0.2235, wR_2 = 0.2758	R_1 = 0.1027, wR_2 = 0.1778	R_1 = 0.1692, wR_2 = 0.1690	R_1 = 0.1535, wR_2 = 0.1777
$R_1 = \sum\lvert F_0 - F_c\rvert/\sum F_0$; $wR_2 = \sum[w(F_0^2 - F_0^2)]^2/[w(F_0^2)^2]^{\frac{1}{2}}$				

*including H atoms of the bridging hydroxyl groups as confirmed by BVS calculations.

Table 4.B.2. Bond Valence Sum (BVS) and assignment of bridging O atoms in **4.B.1**

Atoms	BVS	Assignment
O1F	1.069	HO^-
O1G	1.131	HO^-
O1E	0.807	HO^-

4.B.4.5 Synthesis of the metal complexes. A general synthetic protocol was utilized for preparation of the octanuclear metal complexes as follows:

To a solution of H_3L in 20 mL of acetonitrile, tetramethylammonium hydroxide was added. After stirring for half an hour $Ln(NO_3)_3 \cdot xH_2O$ (for **4.B.1**, x = 6, for **4.B.2-4.B.4**, x = 5) was added to this solution which resulted in a clear yellow colored solution. The solution was stirred for another 12 h at room temperature. The reaction mixture was filtered and kept undisturbed for crystallization under ambient conditions. Slow evaporation of the filtrate resulted in the formation of yellow block-shaped crystals suitable for X-ray diffraction after two weeks. The specific quantities of the reactants involved in each reaction, yields of the products, and their characterization data are given below.

$[Gd_8(HL)_6(L)_2(\mu_3\text{-}OH)_4(\mu_2\text{-}OH)_2(H_2O)_4] \cdot 2CH_3CN \cdot 4H_2O$ (**4.B.1**). Quantities: H_3L (0.061 g, 0.205 mmol), $Gd(NO_3)_3 \cdot 6H_2O$ (0.092 g, 0.205 mmol), Me_4NOH (0.112 g, 0.616 mmol). Yield: 0.046 g (46% based on Gd). M.P.: >250 $^\circ$C. IR (KBr) (cm^{-1}): 3425(br), 3245(br, w), 2941(w), 2839(w), 1605(s), 1570(m), 1493(s), 1383(s), 1360(w), 1305(s), 1256(m), 1203(m), 1101(s), 1060 (m), 975(w), 911(s), 842(w), 777(m), 746(m), 725(w), 707(w), 552(w). Calcd elemental analysis for $C_{92}H_{106}Gd_8N_{34}O_{62}$ (M_W = 3938.01): C, 28.06; H, 2.71; N, 12.09; found: C, 27.89; H, 2.56; N, 11.82. ESI-MS: m/z = 1868.9176, $[Gd_8(HL)_6(L)_2(OH)_6 + Na^+ + H^+]^{2+}$.

[Tb$_8$(HL)$_6$(L)$_2$(μ_3-OH)$_4$(μ_2-OH)$_2$(H$_2$O)$_4$]·CH$_3$CN·7H$_2$O (**4.B.2**). Quantities: H$_3$L (0.061 g, 0.205 mmol), Tb(NO$_3$)$_3$·5H$_2$O (0.089 g, 0.205 mmol), Me$_4$NOH (0.111 g, 0.616 mmol). Yield: 0.051 g (52% based on Tb). M.P.: >250 $^{\circ}$C. IR (KBr) (cm^{-1}): 3409(br), 3213(br, w), 2931(w), 2835(w), 1603(s), 1564(m), 1493(s), 1387(s), 1305(s), 1254(m), 1201(m), 1101(s), 1056(m), 973(w), 909(s), 818(w), 777(m), 744(m), 728(w), 707(w), 554(w). Calcd elemental analysis for C$_{90}$H$_{109}$Tb$_8$N$_{33}$O$_{65}$ (M$_W$ = 3964.41): C, 27.27; H, 2.77; N, 11.66; found: C, 27.16; H, 2.86; N, 11.41. ESI-MS: m/z = 1875.4216, [Tb$_8$(HL)$_6$(L)$_2$(OH)$_6$ + Na$^+$ + H$^+$]$^{2+}$.

[Dy$_8$(HL)$_6$(L)$_2$(μ_3-OH)$_4$(μ_2-OH)$_2$(H$_2$O)$_4$]·2CH$_3$CN·3H$_2$O (**4.B.3**). H$_3$L (0.061 g, 0.205 mmol), Dy(NO$_3$)$_3$·5H$_2$O (0.090 g, 0.205 mmol), Me$_4$NOH (0.111 g, 0.616 mmol). Yield: 0.049 g (48% based on Dy). M.P.: >250 $^{\circ}$C. IR (KBr) (cm^{-1}): 3417(br), 3235(br, w), 2939(w), 2837(w), 1603(s), 1568(m), 1491(s), 1381(s), 1360(w), 1306(s), 1254(m), 1201(m), 1101(s), 1058(m), 975(w), 909(s), 842(w), 777(m), 746(m), 726(w), 705(w), 552(w). Calcd elemental analysis for C$_{92}$H$_{104}$Dy$_8$N$_{34}$O$_{61}$ (M$_W$ = 3962.00): C, 27.89; H, 2.65; N, 12.02; found: C, 27.73; H, 2.47; N, 11.91. ESI-MS: m/z = 1889.9365, [Dy$_8$(HL)$_6$(L)$_2$(OH)$_6$ + Na$^+$ + H$^+$]$^{2+}$.

[Er$_8$(HL)$_6$(L)$_2$(μ_3-OH)$_4$(μ_2-OH)$_2$(H$_2$O)$_4$]·3CH$_3$CN·4H$_2$O (**4.B.4**). H$_3$L (0.061 g, 0.205 mmol), Er(NO$_3$)$_3$·5H$_2$O (0.091 g, 0.205 mmol), Me$_4$NOH (0.111 g, 0.616 mmol). Yield: 0.053 g (51% based on Er). M.P.: >250 $^{\circ}$C. IR (KBr) (cm^{-1}): 3425(br), 3237(br, w), 2933(w), 2837(w), 1605(s), 1570(m), 1493(s), 1383(s), 1362(w), 1305(s), 1254(s), 1203(m), 1101(s), 1060(m), 971(w), 911(s), 840(w), 779(m), 746(m), 726(w), 707(w), 554(w). Calcd elemental analysis for C$_{94}$H$_{109}$Er$_8$N$_{35}$O$_{62}$ (M$_W$ = 4059.14): C, 27.81; H, 2.71; N, 12.08; found: C, 27.66; H, 2.59; N, 12.22. ESI-MS: m/z = 1908.9526, [Er$_8$(HL)$_6$(L)$_2$(OH)$_6$ + Na$^+$ + H$^+$]$^{2+}$.

4.B.3 RESULTS AND DISCUSSION

4.B.3.1 Synthetic Aspects. The Schiff base hydrazone ligand, *N'*-(2-hydroxy-3-methoxy-5-nitrobenzylidene)-2-(hydroxyamino)propanehydrazide (H$_3$L), contains six potential coordinating sites capable of binding to multiple lanthanide metal ions in different coordination modes as shown in Scheme 4.B.1. The role of the hydroxide base is crucial not only in deprotonating H$_3$L but also for being a source of hydroxide ligands essential for stitching the multiple metal centers together in the complexes without the additional co-ligands. Hence the reaction of H$_3$L with hydrated Ln(NO$_3$)$_3$.xH$_2$O and Me$_4$NOH.5H$_2$O in the 1:1:3 molar ratio in MeOH/CH$_3$CN (v/v) solvent mixture allowed isolation of [Ln$_8$(HL)$_6$(L)$_2$(μ_3-OH)$_4$(μ_2-OH)$_2$(H$_2$O)$_4$] complexes (Scheme 4.B.2).

μ_2–η^1:η^1:η^2:η^1 μ_3–η^1:η^1:η^2:η^1:η^1 μ_3–η^2:η^1:η^1:η^2:η^1
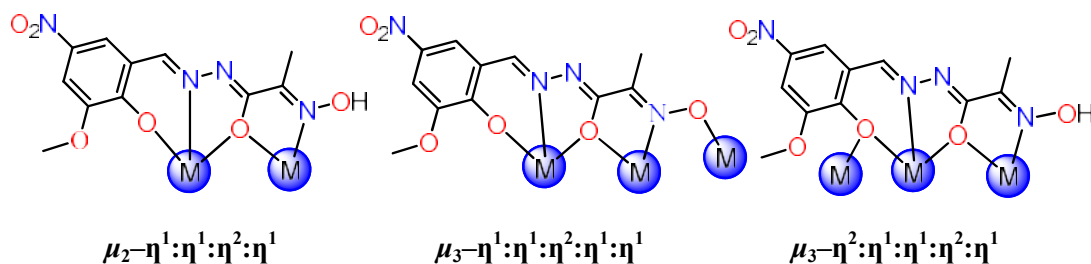
Scheme 4.B.1. The coordination modes of the ligand H$_3$L.

ESI-MS studies on **4.B.1-4.B.4** revealed that all the complexes retain molecular ion peaks at m/z = 1868.9176, 1875.4216, 1889.9365, and 1908.9526 corresponding to the dicationic fragments [Gd$_8$(HL)$_6$(L)$_2$(OH)$_6$ + Na$^+$ + H$^+$]$^{2+}$, [Tb$_8$(HL)$_6$(L)$_2$(OH)$_6$ + Na$^+$ + H$^+$]$^{2+}$, [Dy$_8$(HL)$_6$(L)$_2$(OH)$_6$ + Na$^+$ + H$^+$]$^{2+}$, and [Er$_8$(HL)$_6$(L)$_2$(OH)$_6$ + Na$^+$ + H$^+$]$^{2+}$ (Figures 4.B.1-4.B.4).
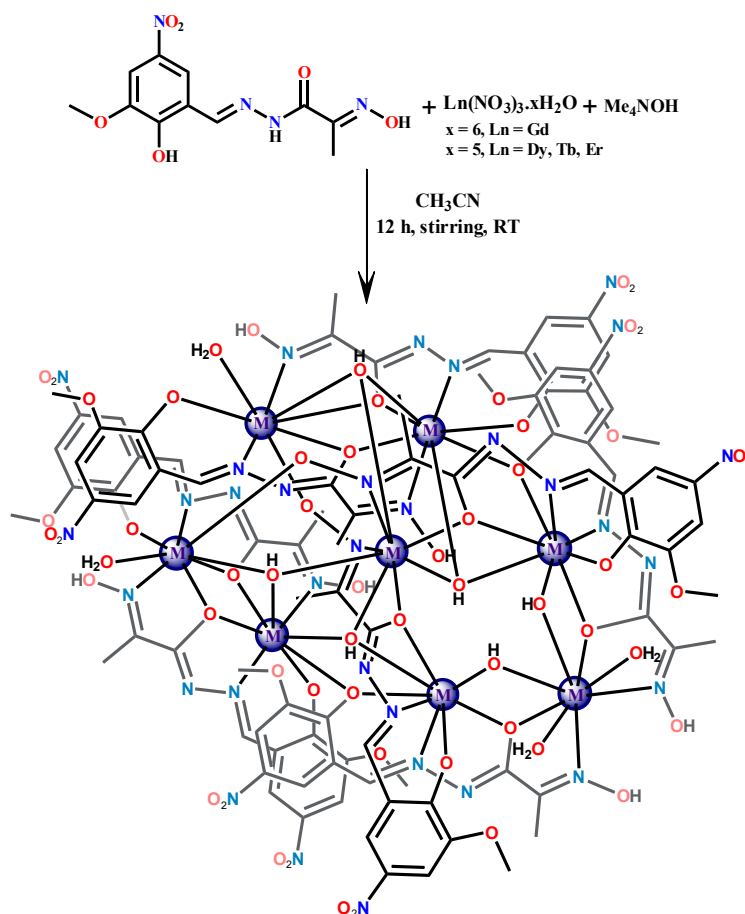
Scheme 4.B.2. The reaction scheme for the synthesis of complexes **4.B.1-4.B.4**.

(a)

(b)   (c)
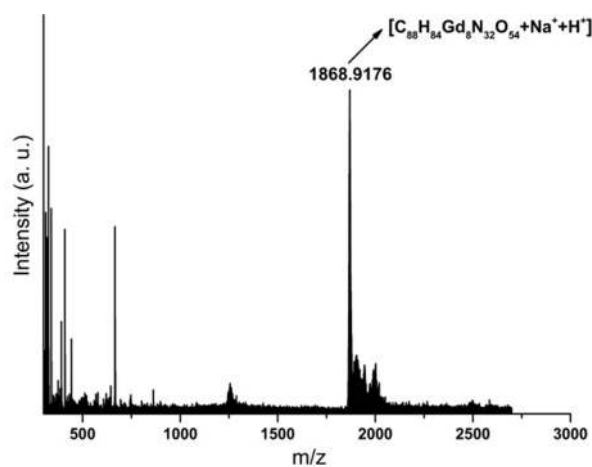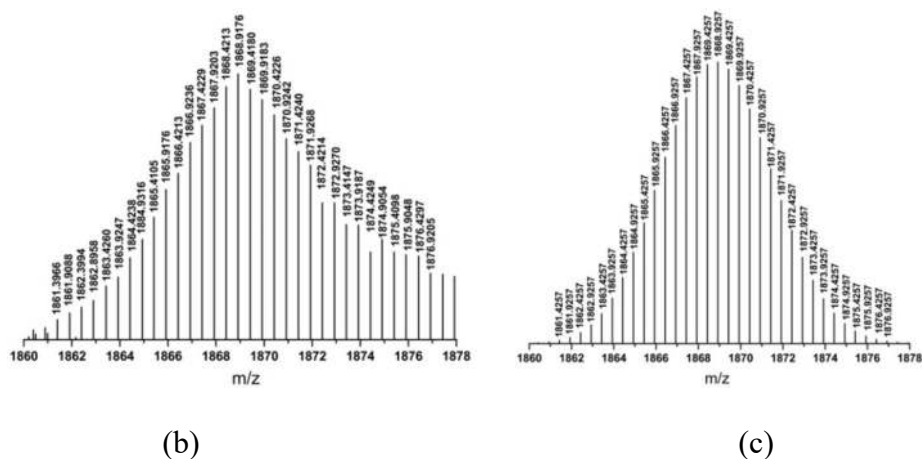
Figure 4.B.1. (a) Full range ESI-MS spectrum of complex **4.B.1**. (b) Experimental and (c) Simulated pattern of $[Gd_8(HL)_6(L)_2(OH)_6 + Na^+ + H^+]^{2+}$.

$[C_{88}H_{84}Tb_8N_{32}O_{54} + Na^+ + H^+]$

1875.4216

(a)

(b)   (c)
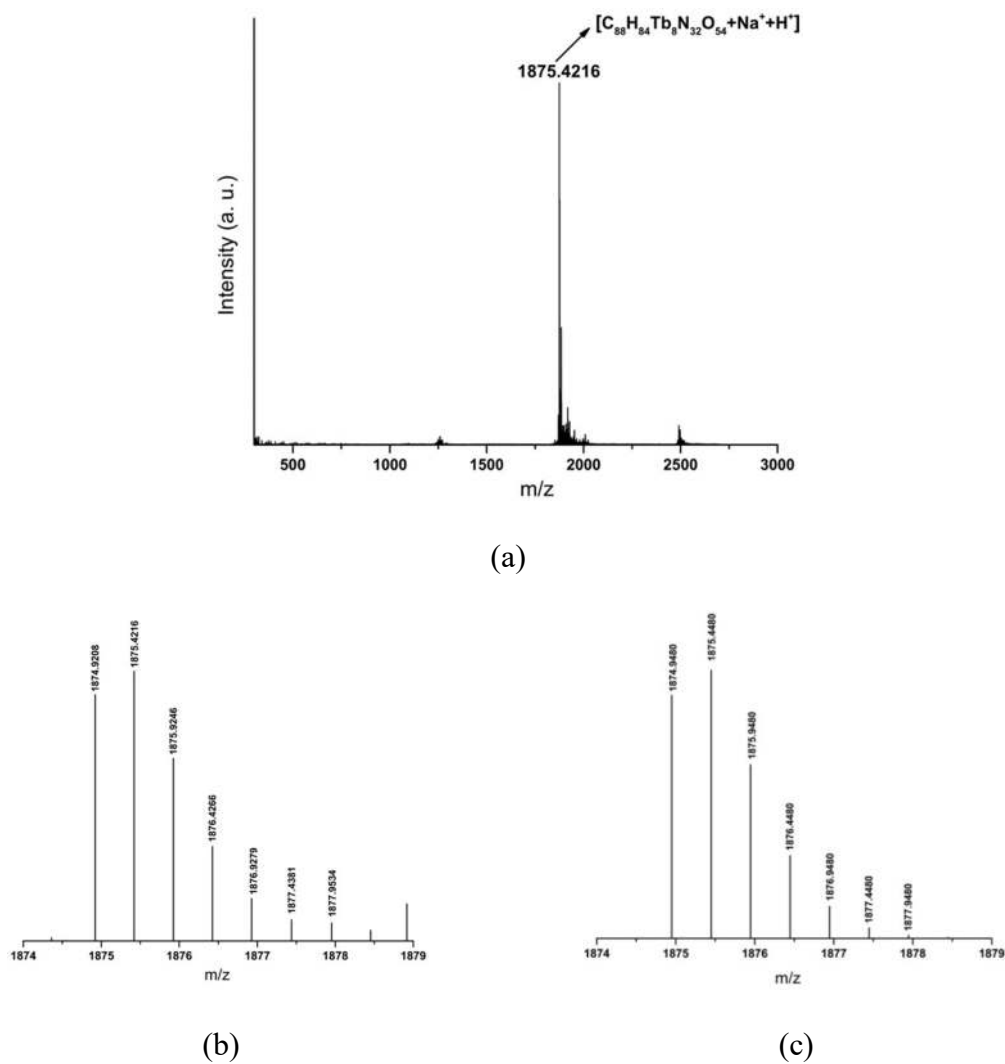
Figure 4.B.2. (a) Full range ESI-MS spectrum of complex **4.B.2**. (b) Experimental and (c) Simulated pattern of $[Tb_8(HL)_6(L)_2(OH)_6 + Na^+ + H^+]^{2+}$.
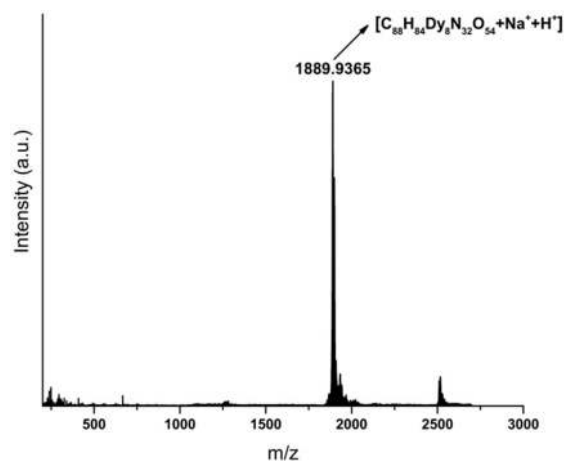
(a)
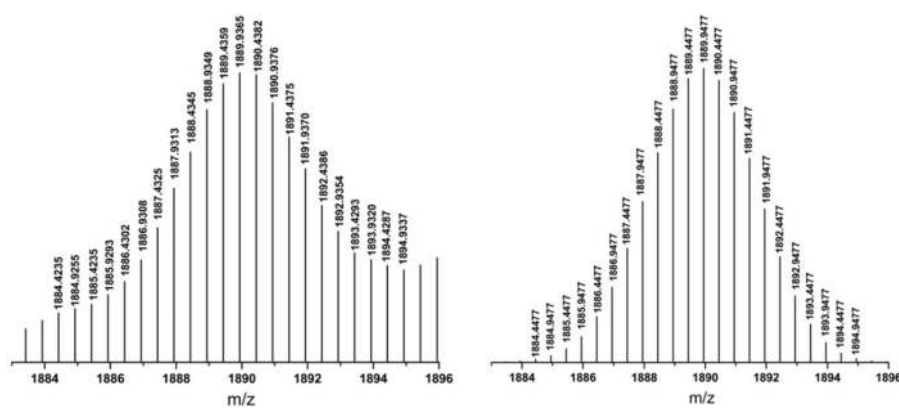
(b)

(c)

Figure 4.B.3. (a) Full range ESI-MS spectrum of complex **4.B.3**. (b) Experimental and (c) Simulated pattern of $[Dy_8(HL)_6(L)_2(OH)_6 + Na^+ + H^+]^{2+}$.

(a)

(b)   (c)
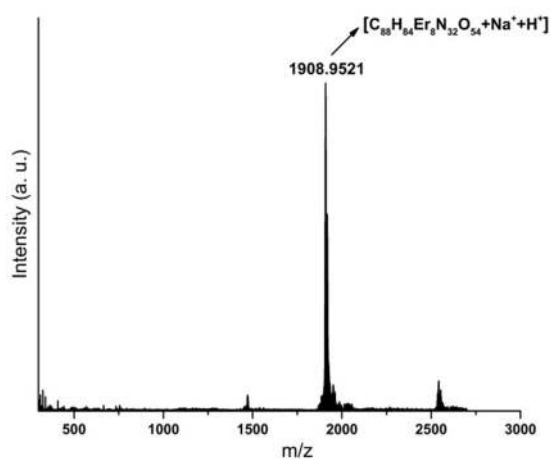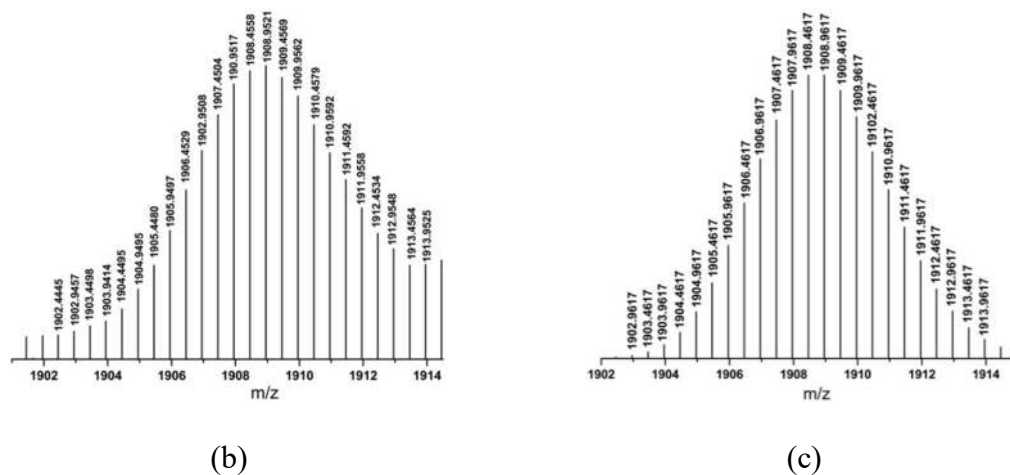
Figure 4.B.4. (a) Full range ESI-MS spectrum of complex **4.B.4**. (b) Experimental and (c) Simulated pattern of $[Er_8(HL)_6(L)_2(OH)_6 + Na^+ + H^+]^{2+}$.

4.B.3.2 Molecular Structures. The molecular structures of the complexes **4.B.1-4.B.4** were confirmed by the single crystal X-ray studies. All the complexes are charge neutral and crystallized in the monoclinic crystal system with the $C2c$ space group in the case of **4.B.1**, **4.B.3**, **4.B.4** (Z = 4) and $P2_1/c$ space group for **4.B.2** (Z = 4).

(a)   (b)
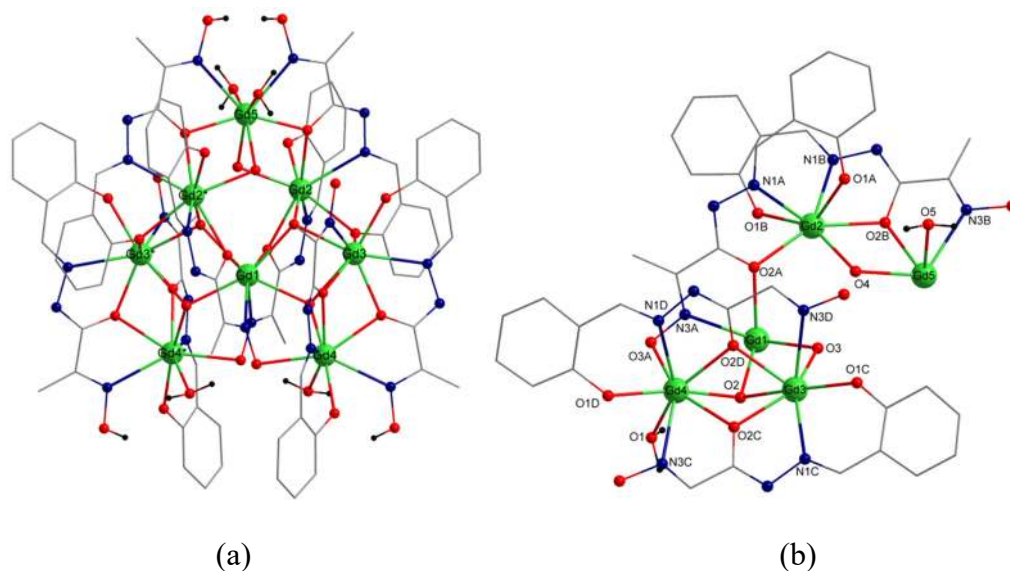
Figure 4.B.5. (a) The molecular structure (−OMe, −NO$_2$ groups, and H atoms except in the water molecules are omitted for clarity) and (b) the asymmetric unit of complex **4.B.1**. Color scheme: Gd^{III}, light green; O, red; N, blue; C, gray.

The octanuclear complexes comprise of eight Ln^{3+} cations, six $[LH]^{2-}$, two $[L]^{3-}$, four $[\mu_3\text{-}OH]^{-}$, two $[\mu_2\text{-}OH]^{-}$ anions and four H_2O molecules (Figure 4.B.5). Considering the overall structural similarity possesses these complexes, we choose the complex **4.B.1** to elucidate the common structural features present in them. The molecular structure of **4.B.1** and its asymmetric unit is shown in Figure 4.B.5. A C_2 axis of symmetry passes through the line connecting the Gd1 and Gd5 atoms which equally divides the whole molecule into two halves generating the asymmetric unit. The asymmetric unit comprise of five Gd^{3+} cations, three $[HL]^{2-}$, one $[L]^{3-}$, one $[\mu_3\text{-}OH]^{-}$, two $[\mu_2\text{-}OH]^{-}$ anions and two H_2O molecules as shown in Figure 4.B.5 (b). The formation of this octanuclear complex can be understood as follows. The whole molecular structure can be viewed as being composed of (*i*) a tetranuclear core motif (Figure 4.B.6 (a)) and (b) two structurally same dinuclear core motifs Figure (4.B.6 (b)). In the dinuclear cores, the two $[HL]^{2-}$ ligands hold two Gd^{III} ions in a "head-to-tail" fashion utilizing a tridentate (O, N, O) and a bidentate (N, O) coordinating motif. The enolate oxygen atoms (O2 and O2*) of the ligand bridge the two metal centers affording an approximate rhomboidal-shaped four-membered Gd_2O_2 core. The average Gd···Gd distance and average $Gd\text{−}O_{enol}\text{−}Gd$ angle in the Gd_2O_2 cores are found to be 3.677(19) Å and 103.365(62)° respectively. Each of the Gd^{III} ions in the dinuclear units is eight-coordinate with an overall 2N, 6O coordination environment. In the tetranuclear core unit, one $[HL]^{2-}$ ligand and one $[L]^{3-}$ ligand hold three Gd^{III} ions in a "head-to-head" fashion. The bridging coordination action of the enolate oxygen atoms and the hydroxyl atoms between the four metal centers results in a Gd_4O_8 core where the four metal ions represent a *kite*-shaped geometry. The average Gd···Gd distance and average $Gd\text{−}O_{enol}\text{−}Gd$ angle in this core are found to be 3.831(18) Å and 107.071(59)° respectively. The overall coordination environment

around the metal ions in this core is also 2N, 6O type similar to the coordination environment observed in the dinuclear units. The cumulative coordination action of the hydroxyl anions and the ligand oxime oxygen atoms connects the two dinuclear units with the tetranuclear unit completing the octanuclear Gd_8 complex. Selected interatomic distances and bond angle parameters of complex **4.B.1** are given in Table 4.B.3.

(a)	(b)
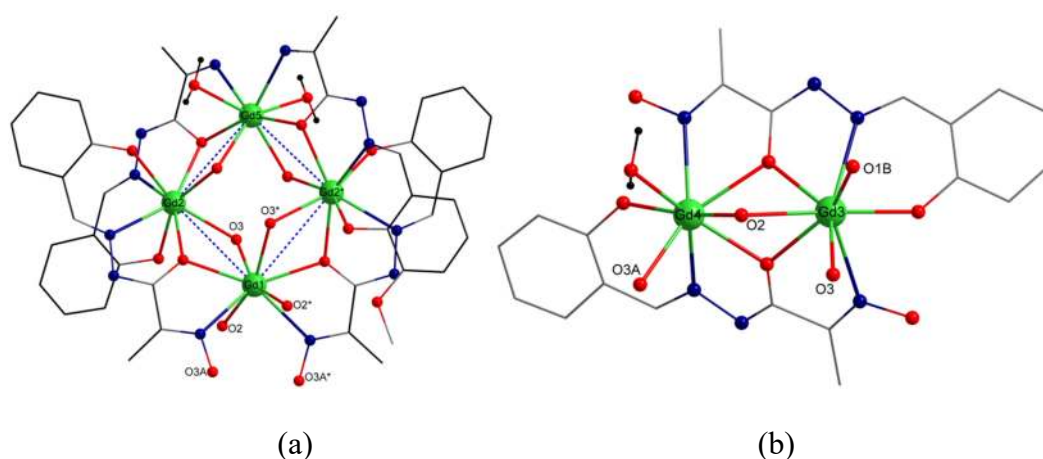
Figure 4.B.6. Structure of (a) the tetranuclear core motif and (b) the dinuclear core motifs.

A view of the Gd_8 core with only the bridging atoms is shown in Figure **4.B.7** (*left*). Mean plane analysis reveals that the *kite*-shaped {Gd_4} unit is perfectly planar comprising the Gd1, Gd2, Gd2*, and Gd5 atoms (*plane 1*). Another two planes corresponding to the dinuclear units i.e. *plane 2* (Gd1, Gd3, Gd4) and *plane 3* (Gd1, Gd3*, Gd4*) pass are at a dihedral angle of 62.97(3)° with respect to *plane* 1 while the *plane 2* and *plane 3* bisects one another with a dihedral angle of 33.57(5)° (Figure **4.B.7** (*right*))
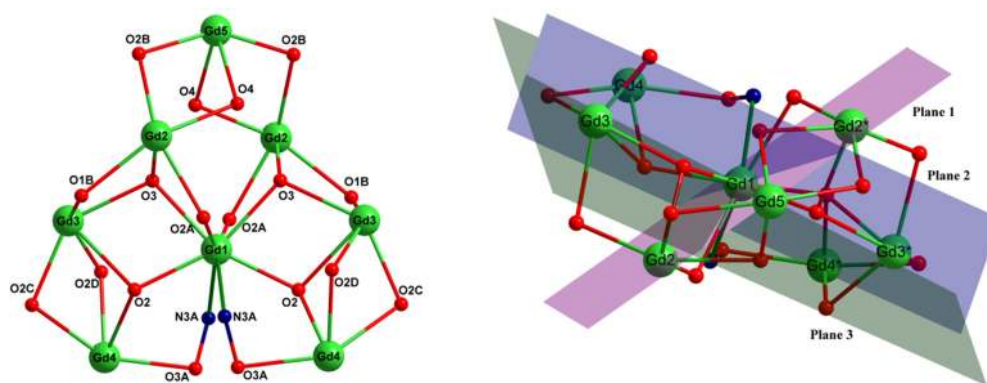
Figure 4.B.7. (l*eft*) The structure of the {Gd₈} core motif and (*right*) the mean planes in the structure of complex **4.B.1**.

Table 4.B.3. Selected interatomic distances (Å) and angles (°) for complex **4.B.1**

Intermetallic distances			
Gd1···Gd2	3.892(2)	Gd1···Gd4	4.076(2)
Gd1···Gd3	3.822(2)	Gd1···Gd5	5.519(2)
Bond distances					
Gd1−O2*	2.349(16)	Gd1−O2	2.349(16)	Gd1−O2A	2.445(12)
Gd2−O1B	2.427(19)	Gd2−O4*	2.347(16)	Gd2−O1A	2.313(16)
Gd2−O2A	2.376(14)	Gd2−O3	2.406(14)	Gd2−N1A	2.511(19)
Gd3−O1C	2.232(19)	Gd3−O2*	2.497(16)	Gd3−O3	2.365(16)
Gd3−N3D	2.592(18)	Gd4−O2*	2.423(15)	Gd4−O1D	2.256(18)
Gd4−O1	2.438(17)	Gd5−O4	2.369(14)	Gd5−O4*	2.369(14)
Gd5−O5*	2.435(19)	Gd5−O5	2.435(19)	Gd5−O2B*	2.300(19)

Bond angles					
O31−Gd1−O2A*	69.7(5)	O3−Gd1−O2A	69.7(5)	O3*−Gd1−O2A	82.9(5)
O3−Gd1−O2A*	82.9(5)	O3−Gd1−O3*	86.0(7)	O3−Gd1−N3A	121.5(6)
O4*−Gd2−O1B	152.5(5)	O1A−Gd2−O3	158.4(6)	O2A−Gd2−O3	70.4(5)
O2D−Gd3−O3	89.5(6)	N3D−Gd3−N1C	124.4(8)	O2C−Gd3−N3D	116.3(7)
O1D−Gd4−O2D	129.8(6)	O21−Gd4−O1	76.9(5)	O1−Gd4−N3A*	93.5(6)
O3A*−Gd4−O2C	151.3(6)	O2C−Gd4−O2*	68.5(6)	N1D−Gd4−N3C	116.5(7)
O41−Gd5−O4	76.5(7)	O4−Gd5−N3B	127.2(8)	O5*−Gd5−N3B*	79.0(8)
O2B*−Gd5−O5	86.9(6)	N3B−Gd5−N3B*	84.0(13)	O2B−Gd5−O4	82.6(5)

*1-X, +Y, 3/2-Z

The immediate coordination geometries around all the eight Gd atoms were confirmed by the SHAPE analysis programme.[17] The geometries were obtained as square antiprism (Gd1, Gd2, Gd2*), Johnson gyrobifastigium (Gd3, Gd3*), biaugmented trigonal prism (Gd4, Gd4*), and triangular dodecahedron (Gd5) (Figure 4.B.8 and Tables 4.B.4 and 4.B.5). Similar types of coordination environments were also observed in the complexes **4.B.2-4.B.4**. The packing diagram (Figure 4.B.9) shows that the shortest Gd···Gd separation between two adjacent {Gd$_8$} molecules is 9.215 Å.
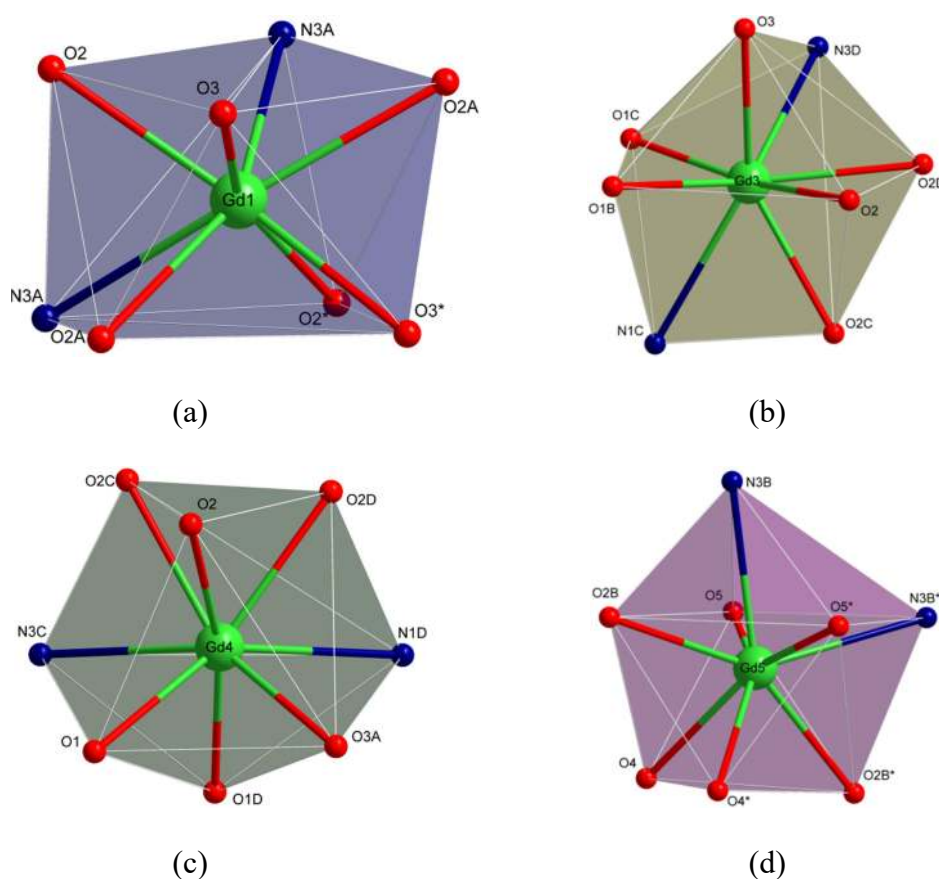
Figure 4.B.8. (a) Square antiprism (Gd1), (b) Johnson gyrobifastigium (Gd3), (c) biaugmented trigonal prism (Gd4), and (d) triangular dodecahedron (Gd5) geometries of the Gd atoms in the structure of complex **4.B.1**.

Table 4.B.4. Continuous Shape Measures (CShM) calculations for Gd^{III} atoms in 4.B.1.

Polyhedron‡	Gd1	Gd2
OP-8	30.152	31.350
HPY-8	23.228	21.581
HBPY-8	11.707	12.980
CU-8	5.299	7.225
SAPR-8	**2.374**	**1.810**
TDD-8	3.009	3.025
JGBF-8	14.447	13.671
JETBPY-8	24.785	23.526
JBTPR-8	5.030	4.385
BTPR-8	4.540	3.914
JSD-8	6.709	6.315
TT-8	5.646	7.546
ETBPY-8	18.744	17.702

‡ *OP-8 = Octagon (D_{8h}); HPY-8 = Heptagonal pyramid (C_{7v}); HBPY-8 = Hexagonal bipyramid (D_{6h}); CU-8 = Cube (O_h); SAPR-8 = Square antiprism (D_{4d}); TDD-8 = Triangular dodecahedron (D_{2d}); JGBF-8 = Johnson gyrobifastigium J26 (D_{2d}); JETBPY-8 = Johnson elongated triangular bipyramid J14 (D_{3h}); JBTPR-8 = Biaugmented trigonal prism J50 (C_{2v}); BTPR-8 = Biaugmented trigonal prism (C_{2v}); JSD-8 = Snub diphenoid J84 (D_{2d}); TT-8 = Triakis tetrahedron (T_d); ETBPY-8 = Elongated trigonal bipyramid (D_{3h})*

Table 4.B.5. Continuous Shape Measures (CShM) calculations for Gd^{III} atoms in **4.B.1**.

Polyhedron†	Gd3	Gd4	Gd5
OP-8	31.765	31.585	30.590
HPY-8	19.841	21.324	24.080
HBPY-8	12.972	13.342	15.516
CU-8	16.767	13.551	8.507
SAPR-8	11.337	9.036	2.329
TDD-8	9.376	6.546	**0.830**
JGBF-8	**7.207**	7.588	14.661
JETBPY-8	23.830	24.431	27.915
JBTPR-8	9.694	7.741	3.296
BTPR-8	8.340	**6.527**	2.843
JSD-8	10.903	9.296	3.330
TT-8	16.405	13.724	8.871
ETBPY-8	19.145	19.349	20.714

† OP-8 = Octagon (D$_{8h}$); HPY-8 = Heptagonal pyramid (C$_{7v}$); HBPY-8 = Hexagonal bipyramid (D$_{6h}$); CU-8 = Cube (O$_h$); SAPR-8 = Square antiprism (D$_{4d}$); TDD-8 = Triangular dodecahedron (D$_{2d}$); JGBF-8 = Johnson gyrobifastigium J26 (D$_{2d}$); JETBPY-8 = Johnson elongated triangular bipyramid J14 (D$_{3h}$); JBTPR-8 = Biaugmented trigonal prism J50 (C$_{2v}$); BTPR-8 = Biaugmented trigonal prism (C$_{2v}$); JSD-8 = Snub diphenoid J84 (D$_{2d}$); TT-8 = Triakis tetrahedron (T$_d$); ETBPY-8 = Elongated trigonal bipyramid (D$_{3h}$)

The molecular structures of complexes **4.B.2**-**4.B.4** are given in Figures 4.B.10-4.B.12 and the selected metric parameters are given in Tables 4.B.6-4.B.8.
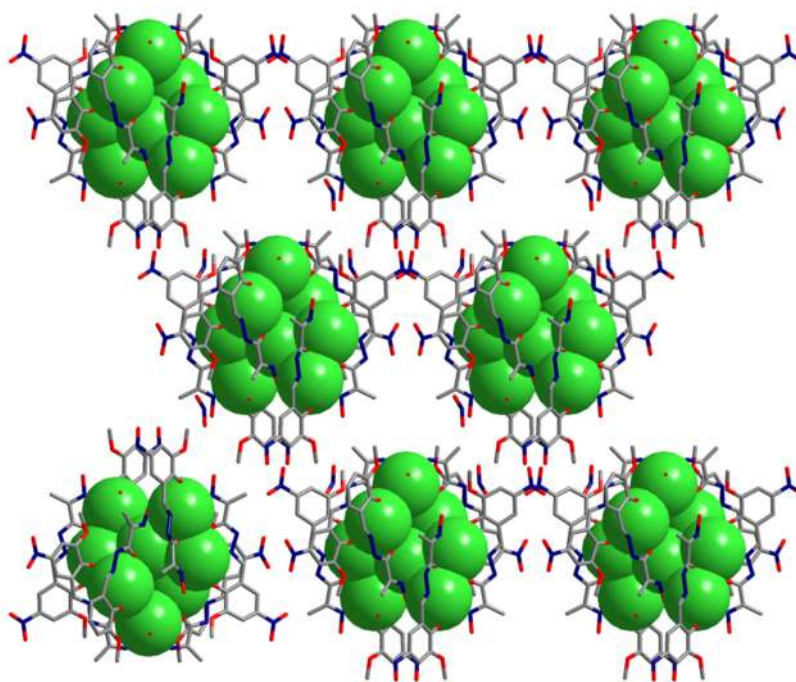
Figure 4.B.9. The solid state packing diagram of complex **4.B.1** viewed along the crystallographic *c* axis. The central metal atoms are shown in the *space fill* model while the other atoms are shown in the *capped stick* model.
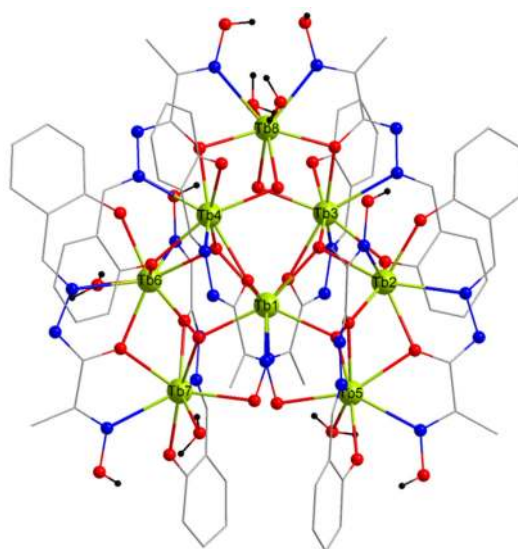
Figure 4.B.10. The molecular structure complex **4.B.2** (−OMe, −NO$_2$ groups, and H atoms except selected are omitted for clarity). Color scheme: Tb^{III}, lime; O, red; N, blue; C, gray.

Table 4.B.6. Selected interatomic distances (Å) and angles (°) for complex **4.B.2**

Intermetallic distances					
Tb1···Tb2	3.755(7)	Tb1···Tb3	3.876(5)	Tb1···Tb4	3.848(5)
Tb1···Tb5	4.537(7)	Tb1···Tb6	3.762(7)	Tb1···Tb7	4.075(6)
Bond distances					
Tb1−O2	2.319(8)	Tb1−O3	2.379(7)	Tb2−O4	2.325(8)
Tb2−N1B	2.593(10)	Tb3−O3A	2.354(8)	Tb3−N1A	2.473(11)
Tb4−O2D	2.357(8)	Tb4−N1D	2.475(10)	Tb5−O1E	2.272(9)
Tb6−O2F	2.307(9)	Tb7−O1G	2.252(9)	Tb8−N3H	2.502(11)
Bond angles					
O2−Tb1−O3	129.8(3)	O3A-Tb1-N3D	153.1(3)	O2E-Tb2-N3E	60.9(3)
O2B−Tb2−O1C	112.6(3)	O6−Tb3−O2C	72.0(3)	O5−Tb4−O1H	152.1(3)
O2H−Tb4−N1D	145.6(3)	O3−Tb5−N3B	108.7(3)	O1E−Tb5−O2B	119.4(3)
O1−Tb6−N1F	143.3(3)	O4A−Tb7−O2F	148.7(3)	O2C−Tb8−N3C	65.3(3)
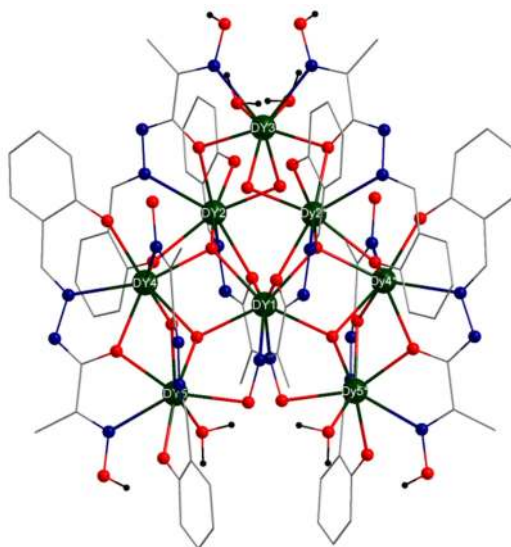
Figure 4.B.11. The molecular structure complex **4.B.3** (−OMe, −NO$_2$ groups, and H atoms except selected are omitted for clarity) Color scheme: Dy^{III}, dark green; O, red; N, blue; C, gray.

Table 4.B.7. Selected interatomic distances (Å) and angles (°) for complex **4.B.3**

Intermetallic distances			
Dy1···Dy2	3.854(8)	Dy1···Dy3	5.465(10)
Dy1···Dy4	3.754(7)	Dy1···Dy5	4.043(8)
Bond distances					
Dy1−O1G	2.379(7)	Dy1−O1F*	2.344(7)	Dy1−N3A	2.545(10)
Dy2−N1B	2.505(10)	Dy2−O1E	2.331(7)	Dy3−O1E*	2.338(7)
Dy3−O1H	2.429(9)	Dy4−O1D	2.238(9)	Dy4−N3C	2.575(11)
Dy5−O1F*	2.393(7)	Dy5−N1C	2.528(10)	Dy1−O2A*	2.406(7)
Bond angles					
O1F*−Dy1−O1G* 156.7(2)	O2A−Dy1−N3A 62.1(3)	O1F*−Dy1−N3A* 69.9(3)
O2A−Dy2−N1B 146.1(3)	O1A−Dy2−O1G* 157.2(3)	O1E−Dy3−N3B 125.5(3)
O1E*−Dy3−O1H* 70.6(3)	O2C-Dy4-O1B* 146.3(3)	N1D-Dy4-N3C 120.1(4)
O1F*−Dy5−O1I 76.4(3)	O2C−Dy5−O3A 95.0(3)	O1I−Dy5−N3D 75.9(3)

*1-X, +Y, 3/2-Z
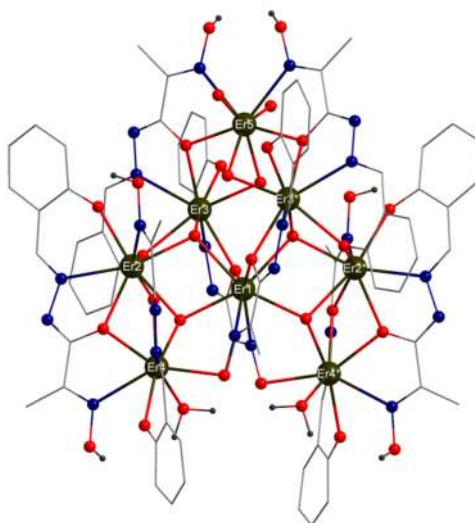
Figure 4.B.12. The molecular structure of complex **4.B.4** (−OMe, −NO$_2$ groups, and H atoms except selected are omitted for clarity). Color scheme: Er^{III}, olive green; O, red; N, blue; C, gray.

Table 4.B.8. Selected interatomic distances (Å) and angles (°) for complex **4.B.4**

Intermetallic distances					
Er1···Er2	3.722(2)		Er1···Er3	4.076(2)	
Er1··· Er4	4.026(2)		Er1···Er5	5.416(3)	
Bond distances					
Er1−O3	2.375(6)	Er1−O3*	2.375(6)	Er1−N3A	2.520(8)
Er2−O2D	2.299(7)	Er2−N1B	2.543(10)	Er2−O1C*	2.347(7)
Er3−O1	2.312(7)	Er3−N1A	2.419(9)	Er4−O5*	2.360(7)
Er4−N3A	2.845(9)	Er5−O2*	2.382(9)	Er5−O1	2.304(7)
Bond angles					
O2A−Er1−N3A*	153.9(2)	O5−Er1−N3A	70.8(2)	O3*−Er1−O2A*	82.1(15)
O5*−Er2−N3D	116.6(2)	O1C*−Er2−N1B 78.1(3)		O1B−Er2−O2D	127.0(3)
O3*−Er3−O1C	70.00(2)	O1−Er3−O1C 152.60(2)		O2D−Er4−N1D	62.6(3)
N3B−Er4−N3A	170.3(3)	O1*−Er5−O1	77.6(3)	O2C*−Er5−N3C*	65.9(3)

*1-X, +Y, 3/2-Z

4.B.3.3 Magnetic properties. The temperature dependence of $\chi_M T$ for complexes **4.B.1** and **4.B.3** (χ_M is the molar magnetic susceptibility per {Ln$_8$} unit) in the range 2-300 K were measured under a magnetic field of 0.1 T (Figure 4.B.13).
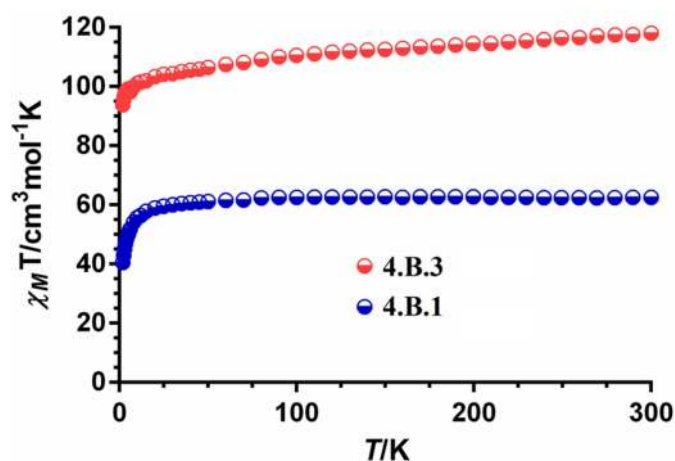
Figure 4.B.13. Temperature dependence of the $\chi_M T$ product for complexes **4.B.1** and **4.B.3**.

The $\chi_M T$ product for **4.B.1** at room temperature (62.60 cm^3 K mol^{-1}) agrees well with that expected for eight isolated Gd^{III} ions with $g = 2$ and $S = 7/2$. By lowering the temperature, the $\chi_M T$ product remains almost constant until $\sim$ 100 K and then decreases sharply down to 2 K to reach a value of (39.40 cm^3 K mol^{-1}). The decrease of the $\chi_M T$ product at low temperature is mainly due to an overall weak antiferromagnetic interaction between the Gd^{III} ions, combined with very small ZFS of the ground state (the Gd^{III} ion is an essentially isotropic ion) and Zeeman effects. The magnitude of the antiferromagnetic exchange interaction in **4.B.1** could not be determined by diagonalization matrix methods because the extremely high dimension of the matrices to be diagonalized for a {Gd$_8$} system.

The existence of antiferromagnetic interactions between the Gd^{III} ions is supported by the field dependence of the magnetization at 2 K which is well below the Brillouin function for eight non-interacting Gd^{III} ions, respectively (Figure 4.B.14). At high field the saturation of the magnetization is almost complete at 5 T (54 μ_B), reaching values that agree well with the theoretical saturation values for eight Gd^{III} ions (56 μ_B).

Experimental and theoretical studies[18, 19] carried out on oxygen-bridged Gd$_2$ complexes (alkoxido, phenoxido and carboxylate) have suggested that J becomes more antiferromagnetic as the Gd−O−Gd angle (θ), and consequently the Gd$\cdots$Gd distance, decrease, and the Gd−O distances become more equal. The crossing point between antiferromagnetic and ferromagnetic interactions occurs approximately at θ and Gd$\cdots$Gd values of 112° and 4.0 Å, respectively. The global antiferromagnetic interaction observed in complex **4.B.1** is not unexpected because, with the exception of one angle (117.39°) and one distance (4.076 Å), in the asymmetric unit all the θ

angles (in the 3.677-3.887 Å range) and Gd···Gd distances (in the 96.70-109.02°) are below the above values.

It is worth mentioning that low temperature molecular magnetic coolers (MMCs) based on Gd^{III} complexes can exhibit higher magneto-caloric effects (MCEs), that is to say, an important change of magnetic entropy upon application of a magnetic field. This effect is of great interest because Gd^{III} complexes with high MCE could be potentially employed for refrigeration applications via adiabatic demagnetisation.[3] We have studied the MCE properties of **4.B.1** because: (*i*) the Gd^{III} ion exhibits negligible anisotropy due to the absence of orbital contribution and the largest single-ion spin ($S = 7/2$) arising from the 4f^7 electron configuration. Both factors (small anisotropy and large spin ground state) favor an enhanced MCE. (*ii*) the weak antiferromagnetic interactions between the Gd^{III} ions give rise to multiple low-lying excited and field-accessible spin states, very close in energy with respect to each other, each of which can contribute to the magnetic entropy of the system. In view of the above considerations, a significant magneto-caloric effect is expected for **4.B.1**. The magnetic entropy changes (-ΔS_m) that characterize the magneto-caloric properties of **4.B.1** were calculated from the experimental isothermal field dependent magnetization data (Figure 4.B.15) by making use of the Maxwell relation:

$$\Delta S_M = (T, \Delta B) = \int_{B_i}^{B_f} \left[\frac{\partial M(T,B)}{dT} \right]_B dB$$

where B_i and B_f are the initial and final applied magnetic fields. The values of -ΔS_m for **4.B.1** (Figure 4.B.15) under all magnetic fields increase with decreasing temperature from 7 to 3 K. The maximum value of -ΔS_m achieved for **4.B.1** is 25.5 J kg^{-1} K^{-1} at $T = 3$ K and applied field change $\Delta B = 5$ T (Figure 4.B.15). In spite of the antiferromagnetic interactions between the Gd^{III} ions in **4.B.1**, there is an important

change in $-\Delta S_m$, which is due to the easy spin polarization at relatively low magnetic field. The extracted $-\Delta S_m$ value at $T = 3$ K is lower than that calculated for the full magnetic entropy content per mole $nR\ln(2S_{Gd} + 1) = 16.6$ R $= 35.1$ J kg^{-1} K^{-1}. This fact is essentially due to the existence of antiferromagnetic interactions between the Gd^{III} ions. It should be noted that the extracted ΔS_m value at 5T for **4.B.1** is close to those found for alkoxido/hydroxo bridged {Gd$_8$} complexes with antiferromagnetic interaction between the Gd^{III} ions and possessing similar molecular weight (M$_w$),[20] but lower than those found other much more magnetic dense Gd^{III} complexes (M$_w$/N, where N = number of Gd^{III} ions).[21, 22]
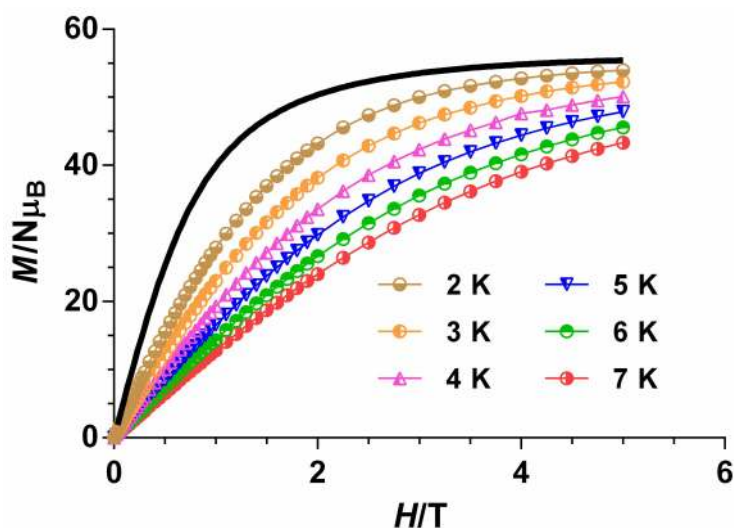
Figure 4.B.14. The field dependence of the magnetization plots for **4.B.1** between 2 and 7 K. The black solid line corresponds to the Brillouin function for eight uncoupled Gd^{III} ions.
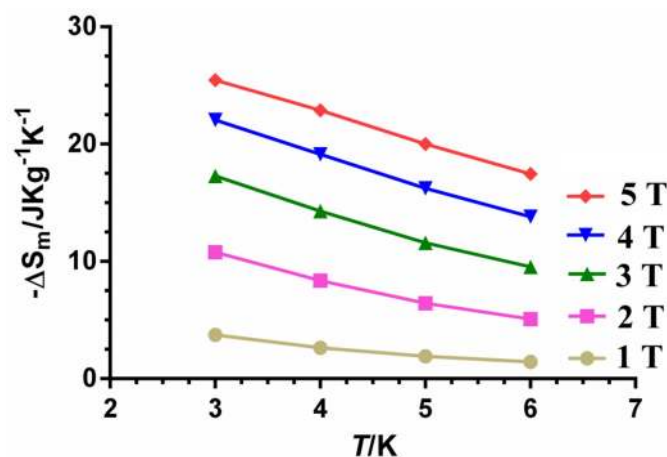
Figure 4.B.15. The magnetic entropy changes ($-\Delta S_m$) calculated using the magnetization data for **4.B.1** from 1 to 5 T and temperatures from 3 to 7 K.

It is well known that Dy^{III} complexes are good candidates to exhibit slow relaxation of the magnetization because the Dy^{III} is a Kramers ion with a bistable ground state (electronic structure composed of Kramers doublets, KDs) and a large magnetic moment. In addition to this, to observe slow magnetization relaxation, the ground state must be axial, that is to say to possess the largest value of M_J ($\pm 15/2$). This KD can be stabilized by an axial crystal field, because the repulsive interactions between the ligands and its disc shape charge cloud is minimized.[23] It is worth noting that the axial ligand field can be attained by serendipity in low symmetry Dy^{III} complexes and, therefore, they often exhibit slow relaxation of the magnetization and SMM behavior.

In view of the above considerations, we have performed ac magnetic susceptibility measurements under zero and with a small-applied magnetic dc field to know if complex **4.B.3** exhibits slow relaxation of the magnetization. The results of these measurements demonstrate that compound **4.B.3** does not exhibit any maximum above 2 K in the out-of-phase (χ''_M) signals even at the highest used frequency of 1400 Hz (Figure 4.B.16). This behavior could be due to a fast relaxation of the magnetization through quantum tunneling (QTM) and/or to the existence of a very

small effective energy barrier that is not able to trap the magnetization in one of the two equivalent orientations at temperatures above 2 K. When the ac measurements were carried out in the presence of a small external dc field of 1000 Oe (Figure 4.B.16), to fully or partly suppress the possible fast quantum tunneling relaxation, the temperature dependence of χ''_M for **4.B.3** at 1400 Hz did not significantly change. This fact either supports a very small height of anisotropic energy barrier (typically below 5 K) or suggests that the strong QTM process, leading to apparently lower U_{eff} values, is not effectively suppressed by the field and therefore should have its origin in hyperfine and intramolecular/intermolecular magnetic interactions.
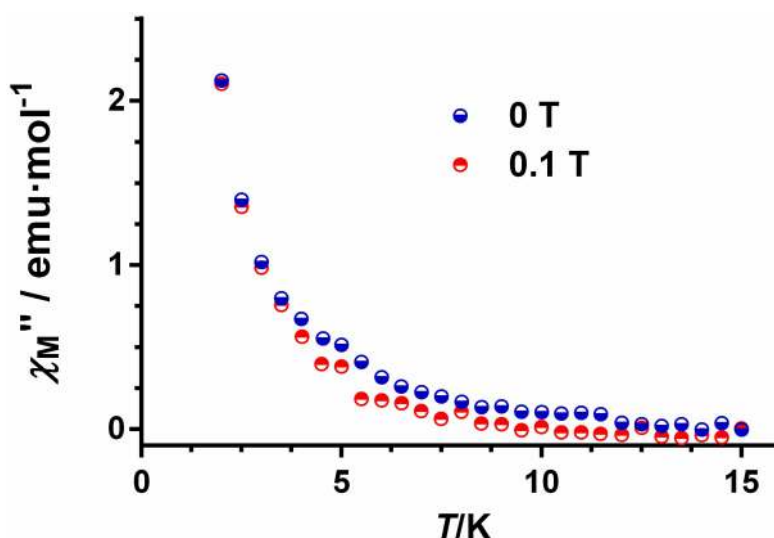
Figure 4.B.16. Temperature dependence of the out-of-phase (χ''_M) ac component of the susceptibility for **4.B.3** under zero and 0.1 T applied fields at 1400 Hz.

4.B.4 CONCLUSIONS

In conclusion, we have shown a cluster expansion method of generating discrete multinuclear Ln^{III} complexes by tuning the reaction conditions. In the present study, we have synthesized four octanuclear $\{Ln_8\}$ complexes and their structures were analyzed by single crystal X-ray diffraction studies. The structural topology of these complexes are quite unprecedented and don't match with literature reported $\{Ln_8\}$

topologies. The complexes are also quite stable in the solution phase as confirmed by the ESI-MS studies. We have studied the magnetic properties of the Gd^{III} and Dy^{III} derivatives. Although the Dy^{III} derivative shows a slow magnetic relaxation at very low temperature and at a high frequency in the ac susceptibility measurements a clear maxima was not observed. The Gd^{III} derivative being isotropic and the Gd^{III} ions interacting in a weakly antiferromagnetic manner magneto-caloric effect in this complex was studied from the magnetization vs field data at different temperatures. This study reveals a maximum in the change of molar entropy ($-\Delta S_m$) of magnitude 25.5 J kg^{-1} K^{-1} at $T = 3$ K and an applied field change $\Delta B = 5$ T.

4.B.5 REFERENCES

1 (a) D. N. Woodruff, R. E. P. Winpenny and R. A. Layfield, *Chem. Rev.*, 2013, **113**, 5110-5148; (b) A. K. Bar, P. Kalita, M. K. Singh, G. Rajaraman and V. Chandrasekhar, *Coord. Chem. Rev.*, 2018, **367**, 163-216; (c) Y.-S. Ding, N. F. Chilton, R. E. P. Winpenny and Y.-Z. Zheng, *Angew. Chem. Int. Ed.*, 2016, **55**, 16071-16074; (d) F. Pointillart, O. Cador, B. Le Guennic and L. Ouahab, *Coord. Chem. Rev.*, 2017, **346**, 150-175; (e) C. A. Gould, L. E. Darago, M. I. Gonzalez, S. Demir and J. R. Long, *Angew. Chem. Int. Ed.*, 2017, **56**, 10103-10107; (f) C. A. P. Goodwin, F. Ortu, D. Reta, N. F. Chilton and D. P. Mills, *Nature*, 2017, **548**, 439-442; (g) T. P. Latendresse, N. S. Bhuvanesh and M. Nippe, *J. Am. Chem. Soc.*, 2017, **139**, 8058-8061; (h) F.-S. Guo, B. M. Day, Y.-C. Chen, M.-L. Tong, A. Mansikkamäki and R. A. Layfield, *Science*, 2018, **362**, 1400-1403; (i) K. L. M. Harriman, J. L. Brosmer, L. Ungur, P. L. Diaconescu and M. Murugesu, *J. Am. Chem. Soc.*, 2017, **139**, 1420-1423; (j) K. S. Pedersen, A.-M. Ariciu, S. McAdams, H. Weihe, J. Bendix, F. Tuna and S. Piligkos, *J. Am. Chem. Soc.*, 2016, **138**, 5801-5804.

2 (a) Y. Ning, S. Cheng, J.-X. Wang, Y.-W. Liu, W. Feng, F. Li and J.-L. Zhang, *Chem. Sci.*, 2019, **10**, 4227-4235; (b) J.-C. G. Bünzli, *Chapter 287 - Lanthanide Luminescence: From a Mystery to Rationalization, Understanding, and Applications* in *Handbook on the Physics and Chemistry of Rare Earths*, eds. J.-C. G. Bünzli and V. K. Pecharsky, Elsevier, 2016, vol. 50, pp. 141-176; (c) J.-C. G. Bünzli, *J. Lumin.*, 2016, **170**, 866-878; (d) L. D. Carlos, R. A. S. Ferreira, V. de Zea Bermudez, B. Julián-López and P. Escribano, *Chem. Soc. Rev.*, 2011, **40**, 536-549; (e) P. Chen, Q. Li, S. Grindy and N. Holten-Andersen, *J. Am. Chem. Soc.*, 2015, **137**, 11590-11593; (f) U. Cho, D. P. Riordan, P. Ciepla, K. S. Kocherlakota, J. K. Chen and P. B. Harbury, *Nat. Chem. Biol.*, 2017, **14**, 15-21; (g) N. Wartenberg, O. Raccurt, E. Bourgeat-Lami, D. Imbert and M. Mazzanti, *Chem. Eur. J.*, 2013, **19**, 3477-3482; (h) L.-J. Xu, G.-T. Xu and Z.-N. Chen, *Coord. Chem. Rev.*, 2014, **273-274**, 47-62; (i) Y.-Y. Xu, P. Chen, T. Gao, H.-F. Li and P.-F. Yan, *CrystEngComm*, 2019, **21**, 964-970; (j) X. Yang, X. Lin, Y. Zhao, Y. S. Zhao and D. Yan, *Angew. Chem. Int. Ed.*, 2017, **56**, 7853-7857; (k) Y. Zhou, H.-Y. Zhang, Z.-Y. Zhang and Y. Liu, *J. Am. Chem. Soc.*, 2017, **139**, 7168-7171.

3 (a) T. C. Jenks, M. D. Bailey, Jessica L. Hovey, S. Fernando, G. Basnayake, M. E. Cross, W. Li and M. J. Allen, *Chem. Sci.*, 2018, **9**, 1273-1278; (b) J. Qin, B. Xu, Y. Zhang, D. Yuan and Y. Yao, *Green Chem.*, 2016, **18**, 4270-4275; (c) N. Kazeminejad, D. Munzel, M. T. Gamer and P. W. Roesky, *Chem. Commun.*, 2017, **53**, 1060-1063; (d) S. Dochain, F. Vetica, R. Puttreddy, K. Rissanen and D. Enders, *Angew. Chem. Int. Ed.*, 2016, **128**, 16387-16389; (e) H. Nagae, R. Aoki, S.-n. Akutagawa, J. Kleemann, R. Tagawa, T. Schindler, G. Choi, T. P. Spaniol, H. Tsurugi, J. Okuda and K. Mashima, *Angew. Chem. Int. Ed.*, 2018, **57**, 2492-2496; (f) S. Chen, D. Yan, M. Xue, Y. Hong, Y. Yao and Q. Shen, *Org. Lett.*, 2017, **19**, 3382-3385; (g) Q. Han, L.

Wang, Z. Shi, C. Xu, Z. Dong, Z. Mou and W. Liu, *Chem. Asian J.*, 2017, **12**, 1364-1373; (h) D. P. Halter, C. T. Palumbo, J. W. Ziller, M. Gembicky, A. L. Rheingold, W. J. Evans and K. Meyer, *J. Am. Chem. Soc.*, 2018, **140**, 2587-2594; (i) C. Pagis, M. Ferbinteanu, G. Rothenberg and S. Tanase, *ACS Catal.*, 2016, **6**, 6063-6072.

4 (a) Z. Zhang, Y. Zhang and Z. Zheng, *Lanthanide Hydroxide Cluster Complexes via Ligand-Controlled Hydrolysis of the Lanthanide Ions* in *Recent Development in Clusters of Rare Earths and Actinides: Chemistry and Materials*, ed. Z. Zheng, Springer, Berlin, Heidelberg, 2016, vol. 173; (b) F. Le Natur, G. Calvez, J.-P. Guégan, L. Le Pollès, X. Trivelli, K. Bernot, C. Daiguebonne, C. Neaime, K. Costuas, F. Grasset and O. Guillou, *Inorg. Chem.*, 2015, **54**, 6043-6054; (c) Y. Zhou, X.-Y. Zheng, J. Cai, Z.-F. Hong, Z.-H. Yan, X.-J. Kong, Y.-P. Ren, L.-S. Long and L.-S. Zheng, *Inorg. Chem.*, 2017, **56**, 2037-2041; (d) T.-Y. Luo, C. Liu, S. V. Eliseeva, P. F. Muldoon, S. Petoud and N. L. Rosi, *J. Am. Chem. Soc.*, 2017, **139**, 9333-9340; (e) F.-S. Guo, Y.-C. Chen, L.-L. Mao, W.-Q. Lin, J.-D. Leng, R. Tarasenko, M. Orendáč, J. Prokleška, V. Sechovský and M.-L. Tong, *Chem. Eur. J.*, 2013, **19**, 14876-14885; (f) D. T. Thielemann, A. T. Wagner, Y. Lan, P. Oña-Burgos, I. Fernández, E. S. Rösch, D. K. Kölmel, A. K. Powell, S. Bräse and P. W. Roesky, *Chem. Eur. J.*, 2015, **21**, 2813-2820; (g) W.-M. Wang, Z.-L. Wu, Y.-X. Zhang, H.-Y. Wei, H.-L. Gao and J.-Z. Cui, *Inorg. Chem. Front.*, 2018, **5**, 2346-2354; (h) X.-Y. Zheng, J.-B. Peng, X.-J. Kong, L.-S. Long and L.-S. Zheng, *Inorg. Chem. Front.*, 2016, **3**, 320-325; (i) G. Calvez, F. Le Natur, C. Daiguebonne, K. Bernot, Y. Suffren and O. Guillou, *Coord. Chem. Rev.*, 2017, **340**, 134-153; (j) S. Omagari, T. Nakanishi, Y. Kitagawa, T. Seki, K. Fushimi, H. Ito, A. Meijerink and Y. Hasegawa, *Scientific Reports*, 2016, **6**, 37008; (k) X.-Y. Zheng, J. Xie, X.-J. Kong, L.-S. Long and L.-S. Zheng, *Coord. Chem. Rev.*, 2019, **378**, 222-236.

5 (a) J. Xiong, H.-Y. Ding, Y.-S. Meng, C. Gao, X.-J. Zhang, Z.-S. Meng, Y.-Q. Zhang, W. Shi, B.-W. Wang and S. Gao, *Chem. Sci.*, 2017, **8**, 1288-1294; (b) L. Qin, Y.-Z. Yu, P.-Q. Liao, W. Xue, Z. Zheng, X.-M. Chen and Y.-Z. Zheng, *Adv. Mater.*, 2016, **28**, 10772-10779; (c) G. Wang, Y. Wei and K. Wu, *Dalton Trans.*, 2016, **45**, 12734-12738; (d) M. Ibrahim, V. Mereacre, N. Leblanc, W. Wernsdorfer, C. E. Anson and A. K. Powell, *Angew. Chem. Int. Ed.*, 2015, **54**, 15574-15578; (e) R. An, X.-L. Chen, H.-M. Hu, Y.-L. Ren, Q.-R. Wu and G.-L. Xue, *Inorg. Chem. Commun.*, 2015, **61**, 177-180; (f) H.-Y. Wong, W. T. K. Chan and G.-L. Law, *Inorg. Chem.*, 2018, **57**, 6893-6902.

6 (a) J. Acharya, S. Biswas, J. van Leusen, P. Kumar, V. Kumar, R. S. Narayanan, P. Kögerler and V. Chandrasekhar, *Cryst. Growth Des.*, 2018, **18**, 4004-4016; (b) S. Das, S. Hossain, A. Dey, S. Biswas, J.-P. Sutter and V. Chandrasekhar, *Inorg. Chem.*, 2014, **53**, 5020-5028; (c) S. Biswas, S. Das, G. Rogez and V. Chandrasekhar, *Eur. J. Inorg. Chem.*, 2016, **2016**, 3322-3329; (d) S. Biswas, S. Das, T. Gupta, S. K. Singh, M. Pissas, G. Rajaraman and V. Chandrasekhar, *Chem. Eur. J.*, 2016, **22**, 18532-18550; (e) S. Biswas, S. Das, S. Hossain, A. K. Bar, J.-P. Sutter and V. Chandrasekhar, *Eur. J. Inorg. Chem.*, 2016, **2016**, 4683-4692.

7 *SMART & SAINT Software Reference manuals*, Bruker Analytical X-ray Systems, Inc., Madison, WI, version 6.45, 2003.

8 G. M. Sheldrick, *SADABS, Program for Empirical Absorption Correction*, University of Gottingen, Germany, 1996.

9 *Bruker APEX2*, Bruker AXS Inc., Madison, Wisconsin, USA, version 2008.1−0, 2008.

10 *CrysAlisPRO*, Oxford Diffraction UK Ltd., Yarnton, England.

11 G. M. Sheldrick, *Acta Cryst. A*, 2015, **71**, 3-8.

12 G. M. Sheldrick, *Acta Cryst. C*, 2015, **71**, 3-8.

13 O. V. Dolomanov, L. J. Bourhis, R. J. Gildea, J. A. K. Howard and H. Puschmann, *J. Appl. Cryst.*, 2009, **42**, 339-341.

14 (a) I. D. Brown, *Chem. Rev.*, 2009, **109**, 6858-6919; (b) A. Trzesowska, R. Kruszynski and T. J. Bartczak, *Acta Cryst. B*, 2004, **60**, 174-178.

15 A. Spek, *Acta Cryst. C*, 2015, **71**, 9-18.

16 K. Brandenburg and H. Putz, *DIAMOND*, Crystal Impact GbR, Bonn, Germany, version 3.2, 1997−2014.

17 (a) *SHAPE: Continuous Shape Measures calculation*, Electronic Structure Group, Universitat de Barcelona, Spain, version 2.1, 2013; (b) J. Cirera, E. Ruiz and S. Alvarez, *Organometallics*, 2005, **24**, 1556-1562.

18 (a) J.-P. Costes, A. Dupuis and J.-P. Laurent, *Inorg. Chim. Acta*, 1998, **268**, 125-130; (b) D. John and W. Urland, *Eur. J. Inorg. Chem.*, 2006, **2006**, 3503-3509 and references therein.

19 L. E. Roy and T. Hughbanks, *J. Am. Chem. Soc.*, 2006, **128**, 568-575.

20 (a) S. Bala, A. Adhikary, S. Bhattacharya, M. S. Bishwas, P. Poddar and R. Mondal, *ChemistrySelect*, 2017, **2**, 11341-11345; (b) C. Cui, W. Ju, X. Luo, Q. Lin, J. Cao and Y. Xu, *Inorg. Chem.*, 2018, **57**, 8608-8614; (c) K. H. Zangana, E. M. Pineda, J. Schnack and R. E. P. Winpenny, *Dalton Trans.*, 2013, **42**, 14045-14048.

21 (a) M. Evangelisti and E. K. Brechin, *Dalton Trans.*, 2010, **39**, 4672-4676; (b) J. W. Sharples and D. Collison, *Polyhedron*, 2013, **66**, 15-27; (c) R. Sessoli, *Angew. Chem. Int. Ed.*, 2012, **51**, 43-45; (d) L. Fernando and E. Marko, in *Molecular Nanomagnets and Related Phenomena*, ed. S. Gao, Springer-Verlag Berlin Heidelberg, 2015, vol. 164, pp. 431-460; (e) M. Evangelisti, *Molecular Magnets Physics and Applications* in *Molecular Magnets Physics and Applications*, eds. J.

Bartolomé, F. Luis and J. F. Fernández, 2014, pp. 365–385; (f) J.-L. Liu, Y.-C. Chen, F.-S. Guo and M.-L. Tong, *Coord. Chem. Rev.*, 2014, **281**, 26-49.

22 (a) Y.-C. Chen, L. Qin, Z.-S. Meng, D.-F. Yang, C. Wu, Z. Fu, Y.-Z. Zheng, J.-L. Liu, R. Tarasenko, M. Orendáč, J. Prokleška, V. Sechovský and M.-L. Tong, *J. Mater. Chem. A*, 2014, **2**, 9851-9858; (b) S.-D. Han, X.-H. Miao, S.-J. Liu and X.-H. Bu, *Inorg. Chem. Front.*, 2014, **1**, 549-552.

23 J. D. Rinehart and J. R. Long, *Chem. Sci.*, 2011, **2**, 2078-2085.

Synthesis, Structure, and Magnetic Properties of Heterometallic Octanuclear $Ni^{II}_4Ln^{III}_4$ (Ln = Y, Gd, Tb, Dy, Ho, Er) Complexes Containing $Ni^{II}_2Ln^{III}_2O_4$ Distorted Cubane Motifs

ABSTRACT: The reaction of 2-methoxy-6-[2-(2-hydroxyethylamino)ethylimino}-methyl] phenol (H_2L), with lanthanide metal salts followed by addition of nickel acetate allowed isolation of a family of heterometallic octanuclear Ni^{II}-Ln^{III} coordination complexes, $[Ni_4Ln_4(\mu_2\text{-}OH)_2(\mu_3\text{-}OH)_4(\mu\text{-}OOCCH_3)_8(HL)_4]\cdot(OH)_2\cdot xH_2O$. Single crystal X-ray diffraction studies of these complexes reveal that their central metallic core consists of two tetranuclear $[Ni_2Ln_2O_4]$ cubane sub-units fused together by acetate and hydroxide bridges. The magnetic study of these complexes reveals a ferromagnetic interaction between the Ln^{III} and the Ni^{II} centers mediated by the *O*-centered bridges. The magnitude of exchange coupling between the Ni^{II} and Ln^{III} centers, parametrized from magnetic data of the Gd analogue gives $J = +0.86$ cm^{-1}. The magneto caloric effect, studied for the $Ni^{II}_4Gd^{III}_4$ complex shows a maximum of magnetic entropy change, $-\Delta S_m = 22.58$ J kg^{-1} K^{-1} at 3 K for an applied external field of 5 T.

5.1 INTRODUCTION

The discovery of single-molecule magnets is now nearly two decades old, yet this field continues to grow unabated with several contributions each year. The first example of a SMM is a Mn_{12} complex and this spurred interest in polynuclear transition metal complexes.[1] The cumulative understanding as a result of studies on several such complexes leads to the understanding that in polynuclear transition metal complexes a high spin ground state (*S*) and a negative magnetic anisotropy (*D*) should

be present to achieve high anisotropic energy barriers (U_{eff}) for magnetization reversal.[2] Although a large spin ground state can be achieved in exchange coupled polynuclear transition metal complexes, the S and D parameters are found to be inversely proportional to each other and therefore there appears to be a limit to the extent of increasing U_{eff} by modulating S.[3] It was soon realized that the single-ion anisotropies, particularly of lanthanide ions might be gainfully harnessed for achieving interesting magnetic properties in molecular complexes.[4] One of the approaches to take advantage of the lanthanide anisotropy is to design molecular magnets containing heterometallic 3d-4f complexes.[5] We have been working in assembling and studying various types of 3d-4f complexes.[6] Among the numerous 3d-4f complexes reported in the literature, including from our lab, polynuclear Ni^{II}-Ln^{III} complexes are gaining interest because of the ferromagnetic exchange interaction that is often seen between the lanthanide and nickel center.[7] In view of this interest we were interested in exploring new Ni^{II}-Ln^{III} complexes. In an earlier study from our laboratory, we have used 2-methoxy-6-[2-(2-hydroxyethylamino)-ethylimino}methyl] phenol (H_2L) ligand to assemble the heterometallic Fe^{III}-Ln^{III} and $Co^{III}_2Dy^{III}$ complexes (Scheme 5.1).[8] The latter was found to be an SMM even at zero applied magnetic field with the highest reversal of energy barrier so far reported in the literature for such type of complexes.[8a]

Further, it was of interest to us to study the coordination behaviour of H_2L towards the assembly of Ni^{II}-Ln^{III} complexes. Accordingly, herein, we report a series of Ni_4Ln_4 complexes (Ln = Y, (**5.1**); Gd, (**5.2**); Tb, (**5.3**); Dy, (**5.4**); Er, (**5.5**); Ho, (**5.6**)). These complexes are composed of two heterometallic $Ni^{II}_2Ln^{III}_2O_4$ distorted cubes connected to each other by acetate and hydroxide bridging ligands. The synthesis, characterization and magnetism of these complexes are discussed herein.
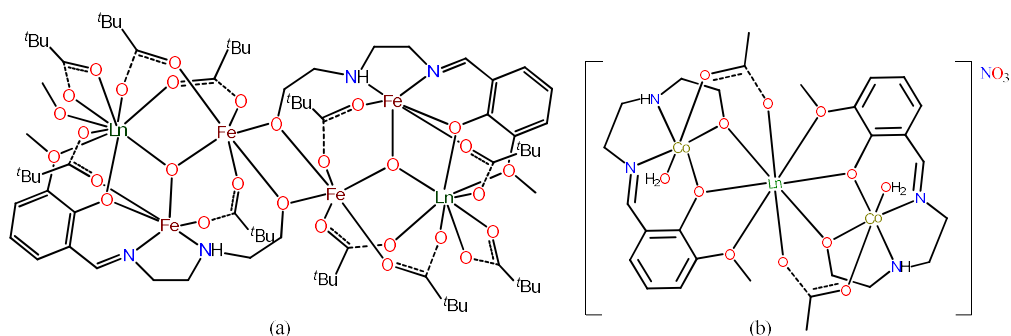
Scheme 5.1. (a) Heterometallic hexanuclear Fe^{III}-Ln^{III} complexes. (b) Heterometallic trinuclear Co^{III}-Ln^{III} complexes.

5.2 EXPERIMENTAL SECTION

5.2.1 Materials and Methods. Solvents and other general reagents used in this work were purified according to standard procedures.[9, 10] *o*-Vanillin, nickel acetate tetrahydrate, and tetramethyl ammonium hydroxide pentahydrate were obtained from Spectrochem Pvt. Ltd., Mumbai, India. *N*-(2-hydroxyetyhyl)ethylenediamine, Ln(NO$_3$)$_3$.xH$_2$O (x = 6, for Ln = Y, and Gd; x = 5 for Ln = Dy, Tb, Ho, and Er) were obtained from Sigma Aldrich Chemical Co. (India). All these chemicals were used as obtained without further purification. The ligand 2-methoxy-6-[2-(2-hydroxyethylamino)ethylimino}methyl] phenol (H$_2$L) was prepared following a previously reported procedure.[11]

5.2.2 Instrumentation. Melting points were measured using a JSGW melting point apparatus and are uncorrected. IR spectra were recorded with a Perkin Elmer FT-IR spectrometer. Mass spectra were recorded with a Bruker micrOTOF-Q II spectrometer. Powder X-ray diffraction data of all the complexes were collected with a Bruker D8 Advance X-ray Powder Diffractometer using CuKα radiation (λ = 1.5418 Å). Elemental analyses of the compounds were obtained from a Euro Vector EA instrument (CHNS-O, Model EuroEA3000).

5.2.3 Magnetic Measurements. Static magnetic properties were measured on polycrystalline samples of the complexes in the temperature range 2-300 K under an applied field of 1000 Oe using a Quantum Design SQUID MPMS XL-5 magnetometer. Field dependence of the dynamic (ac) susceptibility measurements were carried out using an alternating ac field of 3.5 Oe in the frequency range 1-1500 Hz. The static experimental susceptibilities were corrected for the diamagnetism of the constituent atoms (using Pascal's constants) and for the sample holder. In order to avoid any torquing of the microcrystals, a pellet of the sample cut into very small fragments was introduced in the sample holder.

5.2.4 X-ray Crystallography. Single crystal X-ray structural studies of **5.1-5.6** were performed on a Bruker Apex II CCD diffractometer system equipped with graphite-monochromated MoKα radiation (λ_α = 0.71073 Å) at 100(2) K. The crystals did not degrade/decompose during data collection. The frames were indexed, integrated, and scaled using the SMART and SAINT software package.[12] Absorption correction was performed by a multi-scan method implemented in SADABS.[13] Space groups were determined using XPREP implemented in APEX2.[14] The structures were solved with the ShelXT[15] structure solution program using Intrinsic Phasing and refined with the ShelXL[16] refinement package using Least Squares minimization in the Olex-2[17] software. All the non-hydrogen atoms were refined with anisotropic thermal parameters. All the hydrogen atoms except the bridging –OH atoms were included in idealized positions and a riding model was used. Lattice solvent molecules could not be satisfactorily modelled by the present analysis due to heavy disorder associated with it. Therefore, the "PLATON/SQUEEZE" program[18] was used to remove those disordered solvent molecules. All the mean plane analyses and crystallographic figures have been generated using the DIAMOND software (version 3.2).[19]

5.4.5 Synthesis of Complexes 5.1-5.6. The general synthetic protocol that was used for the preparation of the metal complexes (**5.1-5.6**) is as follows: A methanolic solution (5 mL) of $Ln(NO_3)_3 \cdot xH_2O$ (1 eq.) (where x = 6 for **5.1** and **5.2**, and x = 5 for **5.3-5.6**) was added drop wise to a 15 mL methanolic solution containing a mixture of H_2L (1 eq.) and tetramethyl ammonium hydroxide (2 eq.) with constant stirring. To this reaction mixture, solid $Ni(CH_3COO)_2 \cdot 4H_2O$ (1 eq.) was added and the resulting deep orange-colored solution stirred further for 12 h. The volume of the solution was reduced to ~10 mL by rotary evaporation, filtered, and kept undisturbed for crystallization under ambient conditions. Slow evaporation of the solvent afforded green, block-shaped crystals suitable for X-ray analysis after two weeks. The stoichiometry of the reactants involved in each reaction, yield of the products, and their characterization data are provided below:

[Ni₄Y₄(μ₂-OH)₂(μ₃-OH)₄(μ-OOCCH₃)₈(HL)₄]·(OH)₂·4H₂O (**5.1**). H_2L (0.050 g, 0.209 mmol), $Y(NO_3)_3 \cdot 6H_2O$ (0.094 g, 0.209 mmol), $Ni(CH_3COO)_2 \cdot 4H_2O$ (0.052 g, 0.209 mmol), and $Me_4NOH \cdot 5H_2O$ (0.076 g, 0.419 mmol) were used. Yield: 0.051 g, 42% (based on Y). M.P.: >230 °C. IR (KBr ν/cm^{-1}): 3404(br), 2943(m), 2881(w), 1655(s), 1613(s), 1573(s), 1434(s), 1381(s), 1267 (s), 1224(s), 1173(w), 1142(w), 1075(s), 1041(m), 985(w), 954(m), 846(w), 784(w), 745(s), 655(m), 615(w), 541(w), 515(w), 426(m). Anal. Calcd (%) for $C_{64}H_{108}Y_4N_8Ni_4O_{40}$: C, 34.63; H, 4.90; N, 5.05. Found: C, 34.41 H, 4.76; N, 4.88.

[Ni₄Gd₄(μ₂-OH)₂(μ₃-OH)₄(μ-OOCCH₃)₈(HL)₄]·(OH)₂·H₂O (**5.2**). H_2L (0.050 g, 0.209 mmol), $Gd(NO_3)_3 \cdot 6H_2O$ (0.094 g, 0.209 mmol), $Ni(CH_3COO)_2 \cdot 4H_2O$ (0.052 g, 0.209 mmol), and $Me_4NOH \cdot 5H_2O$ (0.076 g, 0.419 mmol) were used. Yield: 0.035 g, 46% (based on Gd). M.P.: >230 °C. IR (KBr ν/cm^{-1}): 3402(br), 2946(m), 2880(w),

1653(s), 1612(s), 1572(s), 1434(s), 1384(s), 1268 (s), 1224(s), 1170(w), 1139(w), 1073(s), 1041(m), 984(w), 954(m), 849(w), 787(w), 746(s), 657(m), 615(w), 542(w), 512(w), 424(m). Anal. Calcd (%) for $C_{64}H_{102}Gd_4N_8Ni_4O_{37}$: C, 31.51; H, 4.21; N, 4.59. Found: C, 31.35; H, 4.08; N, 4.41.

[Ni₄Tb₄(μ₂-OH)₂(μ₃-OH)₄(μ-OOCCH₃)₈(HL)₄]·(OH)₂·5H₂O (**5.3**). H_2L (0.050 g, 0.209 mmol), $Tb(NO_3)_3·6H_2O$ (0.091 g, 0.209 mmol), $Ni(CH_3COO)_2·4H_2O$ (0.052 g, 0.209 mmol), and $Me_4NOH·5H_2O$ (0.076 g, 0.419 mmol) were used. Yield: 0.042 g, 49% (based on Tb). M.P.: >230 °C. IR (KBr ν/cm⁻¹): 3401(br), 2945(m), 2881(w), 1656(s), 1610(s), 1570(s), 1433(s), 1384(s), 1268(s), 1223(s), 1173(w), 1140(w), 1070(s), 1040(m), 986(w), 953(m), 848(w), 784(w), 749(s), 659(m), 616(w), 540(w), 511(w), 423(m). Anal. Calcd (%) for $C_{64}H_{110}Tb_4N_8Ni_4O_{41}$: C, 30.53; H, 4.40; N, 4.45. Found: C, 30.26; H, 4.17; N, 4.20.

[Ni₄Dy₄(μ₂-OH)₂(μ₃-OH)₄(μ-OOCCH₃)₈(HL)₄]·(OH)₂·6H₂O (**5.4**). H_2L (0.050 g, 0.209 mmol), $Dy(NO_3)_3·5H_2O$ (0.092 g, 0.209 mmol), $Ni(CH_3COO)_2·4H_2O$ (0.052 g, 0.209 mmol), and $Me_4NOH·5H_2O$ (0.076 g, 0.419 mmol) were used. Yield: 0.041 g, 54% (based on Dy). M.P.: >230 °C. IR (KBr ν/cm⁻¹): 3401(br), 2947(m), 2884(w), 1657(s), 1610(s), 1570(s), 1433(s), 1384(s), 1268 (s), 1225(s), 1172(w), 1140(w), 1075(s), 1039(m), 986(w), 955(m), 848(w), 789(w), 744(s), 657(m), 614(w), 541(w), 514(w), 425(m). Anal. Calcd (%) for $C_{64}H_{112}Dy_4N_8Ni_4O_{42}$: C, 30.14; H, 4.43; N, 4.39. Found: C, 29.86; H, 4.59; N, 4.11.

[Ni₄Ho₄(μ₂-OH)₂(μ₃-OH)₄(μ-OOCCH₃)₈(HL)₄]·(OH)₂·6H₂O (**5.5**). H_2L (0.050 g, 0.209 mmol), $Ho(NO_3)_3·5H_2O$ (0.092 g, 0.209 mmol), $Ni(CH_3COO)_2·4H_2O$ (0.052 g, 0.209 mmol), and $Me_4NOH·5H_2O$ (0.076 g, 0.419 mmol) were used. Yield: 0.040 g, 53% (based on Ho). M.P.: >230 °C. IR (KBr ν/cm⁻¹): 3403(br), 2946(m), 2879(w),

1652(s), 1614(s), 1576(s), 1432(s), 1384(s), 1268 (s), 1225(s), 1172(w), 1138(w), 1075(s), 1039(m), 983(w), 955(m), 850(w), 786(w), 744(s), 660(m), 614(w), 541(w), 514(w), 426(m). Anal. Calcd (%) for $C_{64}H_{112}Ho_4N_8Ni_4O_{42}$: C, 30.03; H, 4.41; N, 4.38. Found: C, 29.77; H, 4.20; N, 4.08.

[Ni₄Er₄(μ₂-OH)₂(μ₃-OH)₄(μ-OOCCH₃)₈(HL)₄]·(OH)₂·4H₂O (**5.6**). H_2L (0.050 g, 0.209 mmol), $Er(NO_3)_3\cdot5H_2O$ (0.093 g, 0.209 mmol), $Ni(CH_3COO)_2\cdot4H_2O$ (0.052 g, 0.209 mmol), and $Me_4NOH\cdot5H_2O$ (0.076 g, 0.419 mmol) were used. Yield: 0.044 g, 57% (based on Er). M.P.: >230 °C. IR (KBr ν/cm^{-1}): 3414(br), 2944(m), 2881(w), 1656(s), 1611(s), 1573(s), 1435(s), 1384(s), 1267 (s), 1225(s), 1169(w), 1139(w), 1073(s), 1041(m), 983(w), 955(m), 848(w), 786(w), 743(s), 658(m), 618(w), 542(w), 513(w), 427(m). Anal. Calcd (%) for $C_{64}H_{108}Er_4N_8Ni_4O_{40}$: C, 30.34; H, 4.30; N, 4.42. Found: C, 30.06; H, 4.11; N, 4.21.

5.3 RESULTS AND DISCUSSION

5.3.1 Synthetic Aspects. Polyfunctional compartmental ligands with *O*-donor and *N*-donor atoms are the most commonly used ligands for the construction of heterometallic 3d-4f complexes many of which exhibit interesting magnetic properties.[20] Appropriate design of ligands with specific binding compartments that can selectively coordinate to lanthanide and transition metal ions allows the preparation of 3d-4f heterometallic compounds. We have been involved in the design of such ligands for some time and have successfully assembled many 3d-4f complexes. In this context, we have prepared a multipocket compartmental Schiff base ligand based on an ethylene diamine central motif flanked by two unsymmetrical *O*-donor functional units. Previously, we have used this ligand to prepare a Co_2Dy complex which revealed a zero-field SMM behaviour.[8a] In view of this, we were

interested to explore if this ligand could be used for preparing other heterometallic 3d-4f complexes containing Ni^{II}. Accordingly, the ligand 2-methoxy-6-[2-(2-hydroxy-ethylamino)ethylimino}methyl] phenol (H_2L) was allowed to react with nickel acetate and lanthanide metal salts in the presence of tetramethyl ammonium hydroxide in a 1:1.1:2 stoichiometric ratio to afford dicationic octanuclear complexes, **5.1-5.6** (Scheme 5.2).
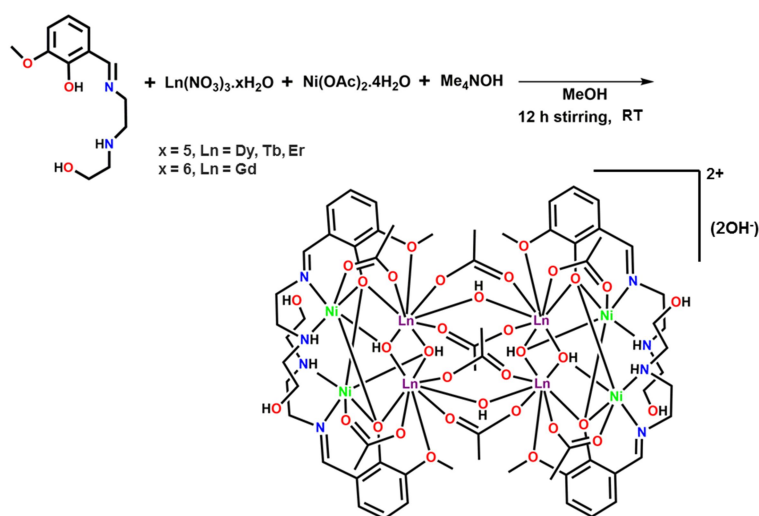
Scheme 5.2. Synthetic scheme for the preparation of $Ni^{II}_4Ln^{III}_4$ complexes.

5.3.2 Molecular Structure. The molecular structures of the complexes **5.1-5.6** were confirmed by single crystal X-ray crystallography. All the complexes are isostructural and crystallized in the monoclinic crystal system with the $P2_1/n$ space group. The crystal data and refinement parameters for **5.1-5.6** are summarized in Table 5.1 and Table 5.2. In view of the overall structural similarity of the complexes the molecular structure of $[Ni_4Gd_4(\mu_2\text{-}OH)_2(\mu_3\text{-}OH)_4(\mu\text{-}OOCCH_3)_8(HL)_4]\cdot(OH)_2$ (**5.2**) is described herein, as a representative example, to illustrate the common structural features of these complexes (Figure 5.1). The coordination modes of all the participating ligands are summarized in Scheme 5.3. The molecular structures of all the other complexes are given in the Figure 5.3 (a-e).
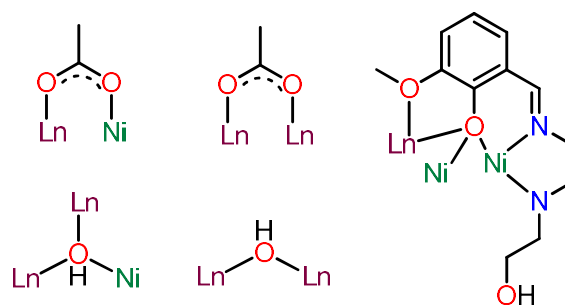
Scheme 5.3. The coordination modes of the different ligands.

Table 5.1. Crystal data and refinement parameters for complexes **5.1-5.3**

	5.1	5.2	5.3
Chemical formula	$C_{64}H_{98}Y_4N_8Ni_4O_{34}\cdot2(OH)$	$C_{64}H_{98}Gd_4N_8Ni_4O_{34}\cdot2(OH)$	$C_{64}H_{98}Tb_4N_8Ni_4O_{34}\cdot2(OH)$
M_w (g mol^{-1})	2147.99	2421.35	2428.03
Crystal system, Space group	Monoclinic, $P2_1/n$	Monoclinic, $P2_1/n$	Monoclinic, $P2_1/n$
Temperature (K)	100(2)	100(2)	100(2)
a, b, c (Å)	12.9768 (12), 15.5079 (15), 23.549 (2),	12.8381 (6), 15.4317 (6), 23.4889 (10)	12.9219 (6), 15.516 (1), 23.5346 (13)
β (°)	96.737 (1)	96.593 (3)	96.576 (3)
V (Å^3)	4706.3(8)	4622.7(3)	4687.6(5)
Z	2	2	2
Radiation type	MoKα	MoKα	MoKα
μ (mm^{-1})	3.298	3.704	3.840
Crystal size (mm^3)	0.17 x 0.15 x 0.11	0.15 x 0.12 x 0.10	0.16 x 0.13 x 0.11
Reflections collected	32167	70774	71751
GOF on F^2	1.012	1.046	1.058
Unique reflections [R$_{int}$]	10018 [R$_{int}$ = 0.0653]	11503 [R$_{int}$ = 0.0595]	11609 [R$_{int}$ = 0.0814]
No. of parameters	531	540	504
No. of restraints	4	5	4
Δρ$_{max}$, Δρ$_{min}$ (e Å^{-3})	1.28, -0.94	1.92, -1.34	2.01, -1.37
Density (g cm^{-3})	1.516	1.740	1.720
Completeness to θ	99.6 % (26.799°)	99.5 % (28.365°)	99.6 % (28.295°)
Limiting	$-16 \leq h \leq 16$	$-17 \leq h \leq 17$	$-17 \leq h \leq 17$

indices	$-17 \leq k \leq 19$	$-20 \leq k \leq 20$	$-20 \leq k \leq 14$
	$-29 \leq l \leq 28$	$-31 \leq l \leq 31$	$-31 \leq l \leq 31$
θ range (°)	2.627 to 26.799	1.582 to 28.365	2.059 to 28.295
F (000)	2192.0	2392	2400
Final R indices [I>2σ (I)]	$R_1 = 0.0457$, $wR_2 = 0.0959$	$R_1 = 0.0349$, $wR_2 = 0.0833$	$R_1 = 0.0520$, $wR_2 = 0.1333$
R indices [all data]	$R_1 = 0.0920$, $wR_2 = 0.1098$	$R_1 = 0.0439$, $wR_2 = 0.0866$	$R_1 = 0.0900$, $wR_2 = 0.1574$
$R_1 = \sum |F_0 - F_c| / \sum F_0$; $wR_2 = \sum [w(F_0^2 - F_0^2)]^2 / [w(F_0^2)^2]^{\frac{1}{2}}$			

Table 5.2. Crystal data and refinement parameters for complexes **5.4-5.6**

	5.4	5.5	5.6
Chemical formula	$C_{64}H_{98}Dy_4N_8Ni_4O_{34} \cdot 2(OH)$	$C_{64}H_{98}Ho_4N_8Ni_4O_{34} \cdot 2(OH)$	$C_{64}H_{98}Er_4N_8Ni_4O_{34} \cdot 2(OH)$
M_w (g mol^{-1})	2442.35	2452.07	2461.39
Crystal system, space group	Monoclinic, $P2_1/n$	Monoclinic, $P2_1/n$	Monoclinic, $P2_1/n$
Temperature (K)	100(2)	100(2)	100(2)
a, b, c (Å)	12.832 (3), 15.413 (3), 23.419 (5)	12.9771 (7), 15.5019 (8), 23.5655 (13)	12.9222 (3), 15.4758 (3), 23.46589 (4)
β (°)	96.765(4)	96.714 (3)	96.601 (1)
V (Å^3)	4599.6(16)	4708.2(4)	4661.61(16)
Z	2	2	2
Radiation type	MoKα	MoKα	MoKα
μ (mm^{-1})	4.088	4.180	4.428
Crystal size (mm^3)	0.14 x 0.11 x 0.08	0.14 x 0.12 x 0.09	0.15 x 0.13 x 0.10
Reflections collected	24420	34917	86231
GOF on F^2	1.052	0.978	1.007
Unique reflections [R$_{int}$]	8541 [R$_{int}$ = 0.0633]	10164 [R$_{int}$ = 0.0545]	14305 [R$_{int}$ = 0.0833]
No. of parameters	536	539	536
No. of restraints	4	3	5
$\Delta\rho_{max}$, $\Delta\rho_{min}$ (e Å^{-3})	1.70, -1.43	1.30, -1.06	1.65, -1.36
Density (g cm^{-3})	1.763	1.730	1.753

Completeness to θ	99.6 % (25.449°)	99.1 % (26.978°)	99.7 % (30.592°)
Limiting indices	$-14 \leq h \leq 15$ $-18 \leq k \leq 18$ $-28 \leq l \leq 21$	$-16 \leq h \leq 16$ $-19 \leq k \leq 16$ $-29 \leq l \leq 28$	$-18 \leq h \leq 18$ $-22 \leq k \leq 21$ $-33 \leq l \leq 33$
θ range (°)	1.585 to 25.499	2.63 to 26.978	1.897 to 30.592
F (000)	2408	2416	2424
Final R indices [I>2σ (I)]	$R_1 = 0.0472$ $wR_2 = 0.1115$	$R_1 = 0.0357,$ $wR_2 = 0.0757$	$R_1 = 0.0430,$ $wR_2 = 0.0977$
R indices [all data]	$R_1 = 0.0694,$ $wR_2 = 0.1300$	$R_1 = 0.0542,$ $wR_2 = 0.0831$	$R_1 = 0.0844,$ $wR_2 = 0.1159$
$R_1 = \sum|F_0 - F_c|/\sum F_0; wR_2 = \sum[w(F_0^2 - F_0^2)]^2/[w(F_0^2)^2]^{\frac{1}{2}}$			

The various aspects of the structural details of **5.2** are given in Figure 5.1 (a-d). The crystal structure of **5.2** reveals it to be a dicationic complex, $[Ni_4Gd_4(\mu_2\text{-}OH)_2(\mu_3\text{-}OH)_4(\mu\text{-}OOCCH_3)_8(HL)_4]^{2+}$, containing two counter hydroxide ions that are involved in a hydrogen-bonded interaction with the complex. The structure of the complex can be understood in the following way. The whole complex can be structurally decomposed into two $Ni^{II}_2Ln^{III}_2$ sub-units which are interconnected by hydroxide and acetate bridges. Two [HL]⁻ units are involved in binding and assembling the $Ni^{II}_2Ln^{III}_2$ motifs. The two Ln^{III}s present in the sub-unit are bridged to each other by a pair of hydroxide ligands affording four-membered $Ln^{III}_2O_2$ ring. Each of the bridging OH groups is also involved in binding to a Ni^{II}. The phenolate unit of a [HL]⁻ is involved in bridging Ni^{II} and Ln^{III} and is also involved in interaction with an additional Ni^{II}. The imino nitrogen and the free NH of the ethylenediamine motif are involved in a chelating coordination action to Ni^{II}. Interestingly, the N-CH_2CH_2OH unit does not take part in coordination and is unutilized; however, the OH group is involved in hydrogen bonding to the counter hydroxide ions (Figure 5.1 (a) and 5.1 (b)). Each of the methoxy groups on the aromatic scaffold are involved in a terminal coordination to the lanthanide ions. Finally, the two sub-units are linked to each other

by a pair of hydroxide ligands and four acetate ligands. The nature of the bridging hydroxylato ligand present in all the complexes has been confirmed by BVS calculations (Table 5.3)

(a)   (b)

(c)   (d)
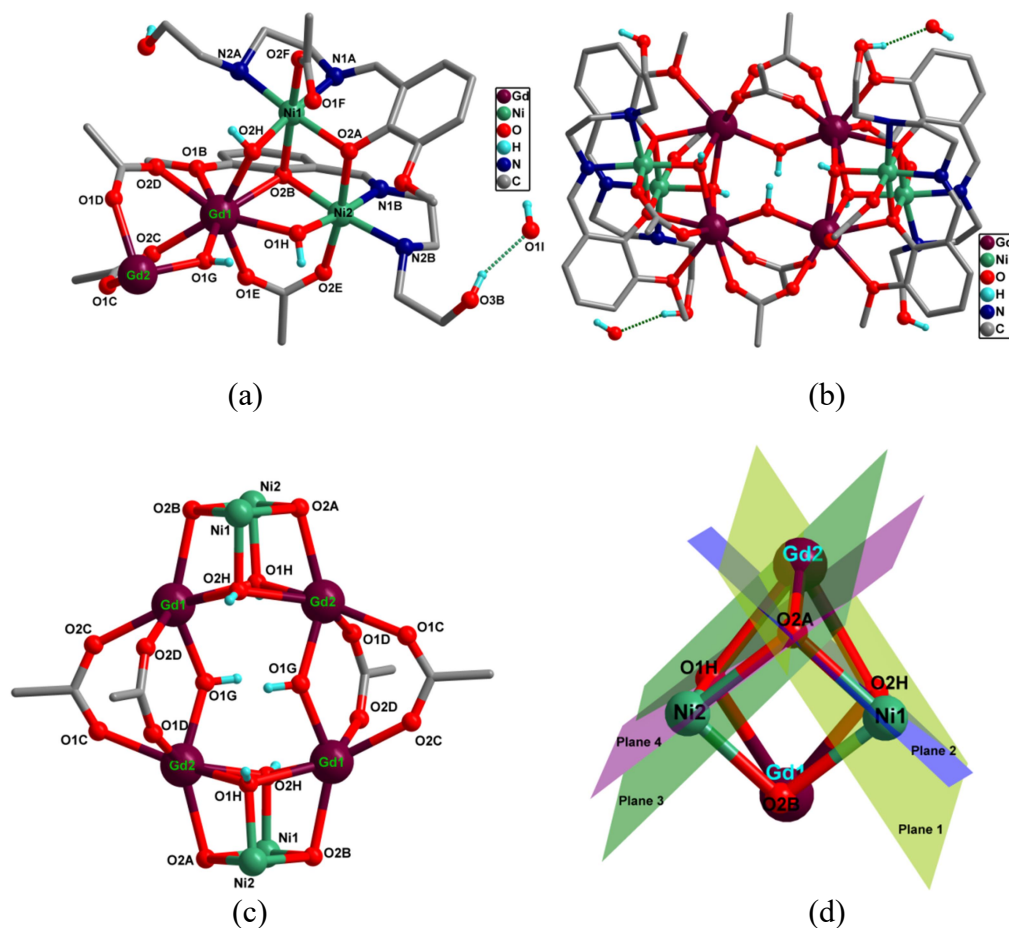
Figure 5.1. (a) Asymmetric unit of **5.2** with the Ni_2Ln_2 sub-unit; (b). Molecular structure of **5.2**; **(c)** Octanuclear core of **5.2**; **(d)** Dihedral angle between the $O-Ni^{II}-O$ and $O-Gd^{III}-O$ planes.

Table 5.3. Bond Valence Sum (BVS) calculations for bridging O atoms of **5.2**

Atoms	BVS	Assignment
O1H	1.127	HO^-
O2H	1.148	HO^-
O1G	1.070	HO^-

As a result of the cumulative coordination interaction described above, the complex contains two tetranuclear $Ni^{II}_2Ln^{III}_2O_4$ cubane cores (containing μ_2-acetate and hydroxide ligands). As mentioned above the acetate ligands bridge the Gd^{III} ions of two different cubane cores in a *syn-syn* μ-η^1:η^1 fashion to form the heterometallic octanuclear core. A perspective view of the octanuclear core structure is shown in Figure 5.1 (c).

(a)   (b)
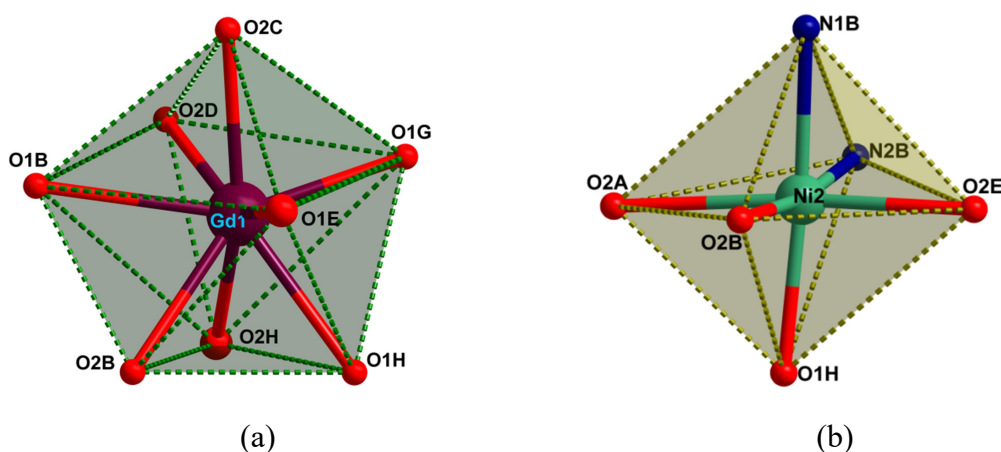
Figure 5.2. (a) Coordination environment/geometry around Gd^{III} showing a distorted trigonal dodecahedron geometry and (b) Coordination environment/geometry of Ni^{II} showing a distorted octahedral geometry.

The Gd^{III} ions are all equivalent and have an 8O coordination environment in a trigonal dodecahedron geometry as confirmed by SHAPE analysis[21] (Figure 5.2 (a) and Table 5.4). Three oxygen atoms of the 8O coordination environment are from the bridging carboxylate groups (O2C, O2D, and O1E; Gd−O average distance 2.359(4) Å), three from hydroxide ligands (O1H, O2H, and O1G; Gd−O average distance 2.353(3) Å), and two O atoms (Gd−O1B distance 2.581(3) Å and Gd−O2B distance 2.482(3) Å) from phenoxide motif of the ligand.

Table 5.4. Continuous Shape Measures (CShM) calculations for Ln^{III}

Complex _Metal centre	Structure[†]								
	CU-8	SAPR-8	**TDD-8**	JGBF-8	JETBP Y-8	JBTP R-8	BTPR -8	JSD-8	TT-8
5.1_Y1 CShM	10.463	2.789	**0.793**	14.056	28.927	2.458	1.961	3.170	11.282
5.2_Gd1 CShM	10.697	2.748	**0.833**	13.857	29.037	2.473	1.975	3.158	11.498
5.3_Tb1 CShM	10.649	2.750	**0.801**	13.840	28.872	2.468	2.013	3.134	11.448
5.4_Dy1 CShM	10.555	2.709	**0.829**	13.890	28.916	2.420	1.944	3.197	11.355
5.5_Ho1 CShM	10.493	2.760	**0.791**	14.078	28.942	2.477	1.961	3.212	11.340
5.6_Er1 CShM	10.449	2.771	**0.794**	14.017	28.849	2.445	1.963	3.175	11.264

†*CU-8 = Cube (O_h); SAPR-8 = Square antiprism (D_{4d}); TDD-8 = Triangular dodecahedron (D_{2d}); JGBF-8 = Johnson gyrobifastigium J26 (D_{2d}); JETBPY-8 = Johnson elongated triangular bipyramid J14 (D_{3h}); JBTPR-8 = Biaugmented trigonal prism J50 (C_{2v}); BTPR-8 = Biaugmented trigonal prism (C_{2v}); JSD-8 = Snub diphenoid J84 (D_{2d}); TT-8 = Triakis tetrahedron (T_d)*

The Ni^{II} centers in the complex are equivalent and are hexa-coordinate (2N, 4O) in a distorted octahedral geometry with the nitrogen atoms occupying the *cis* positions (Figure 5.2 (b) and Table 5.5). The coordination sphere consists of two oxygen atoms from the phenolates of two different ligands (O2B and O2A; Ni−O average distance 2.140(3) Å), one oxygen atom from the hydroxide ligand (Ni−O1H distance 2.018(3) Å), one oxygen atom from the acetate ligand (Ni−O2E distance 2.083(3) Å), and two N atoms of the same ligand (N1B and N2B; average distance 2.060(4) Å). The average Gd−O$_{oph}$−Ni bond angle is 98.35(10)° while the average Ni⋯Gd separation is 3.502(6) Å. The dihedral angles in the bridging fragment were obtained through mean plane analysis shown in Figure 5.1 (d). The dihedral angle containing *plane* 1 (O2A–

Gd2–O2H) and *plane* 2 (O2A–Ni1–O2H) is 16.0˚; however, a value of 21.1˚ is obtained when *plane* 3 and *plane* 4 were considered.

Table 5.5. Continuous Shape Measures (CShM) calculations for Ln^{III}

Metal center	Structure†				
	HP-6	PPY-6	**OC-6**	TPR-6	JPPY-6
5.1_Ni1	31.179	27.792	**0.754**	14.256	30.833
5.2_Ni1	31.515	27.207	**0.759**	13.337	30.949
5.3_Ni1	31.378	27.563	**0.728**	14.418	30.533
5.4_Ni1	31.378	27.341	**0.793**	13.425	30.784
5.5_Ni1	31.322	27.439	**0.797**	14.238	30.385
5.6_Ni1	31.185	27.437	**0.794**	14.311	30.411

† *HP-6 = Hexagon (D$_{6h}$); PPY-6 = Pentagonal pyramid (C$_{5v}$); OC-6 = Octahedron (O$_h$); TPR-6 = Trigonal prism (D$_{3h}$); JPPY-6 = Johnson pentagonal pyramid J2 (C$_{5v}$)*

Analysis of the crystal packing diagram reveals that the shortest distance between two Ln^{III} centers of the neighboring molecule is 9.714 Å. (Figure 5.4). The intermolecular hydrogen bonding parameters and matric parameters of complexes **5.1-5.6** are given in Table 5.6 and Table 5.7 respectively. We have also checked the phase purity of all the complexes (**5.1-5.6**) using powder X-ray diffraction analysis (Figures 5.5), which shows good agreement with the simulated patterns generated from the SCXRD data.

Table 5.6. Intermolecular hydrogen bonding parameters for compounds **5.1-5.6**

Complex No.	D H A	d(D–H)/Å	d(H–A)/Å	d(D–A)/Å	D–H–A/°
5.1	O2B H2BA O1H	0.84	2.02	2.754(9)	144.8
5.2	O3B H3B O1I	0.84	1.93	2.723(8)	157.4
5.3	O3B H3B O4	0.82	1.99	2.745(18)	153.5
5.4	O3A H3A O4	0.84	1.92	2.743(12)	165.9
5.5	O4 H4 O2D	0.85	2.11	2.923(5)	159.7
5.6	O1G H1G O2F	0.85	2.08	2.925(6)	167.7

(a)

(b)

(c)

(d)

(e)
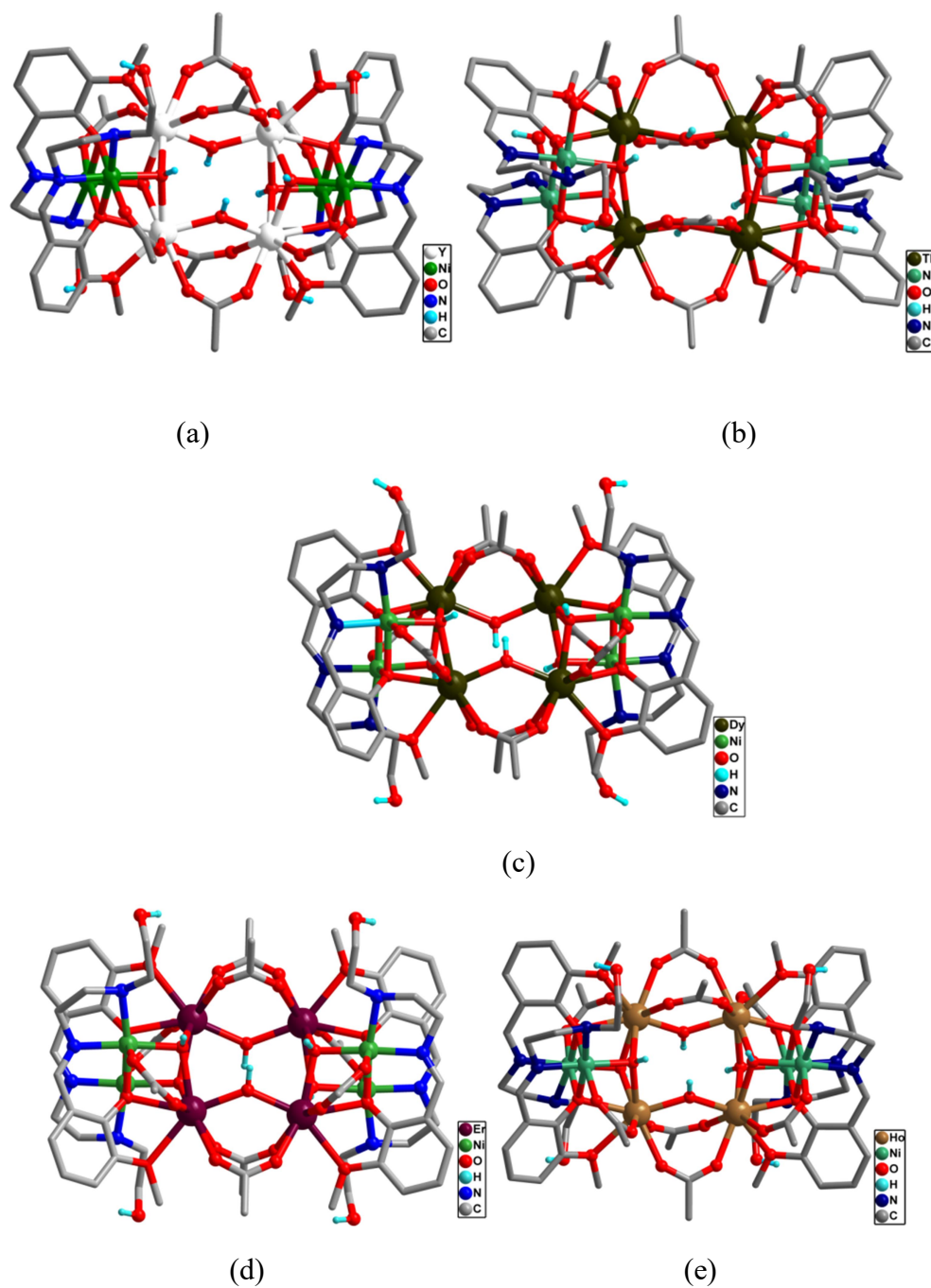
Figure 5.3. The molecular structures of complexes **5.1**, (a); **5.3**, (b); **5.4**, (c); **5.5**, (d); and **5.6**, (e) with selected H atoms. The counter anions and hydrogen atoms have been omitted for clarity
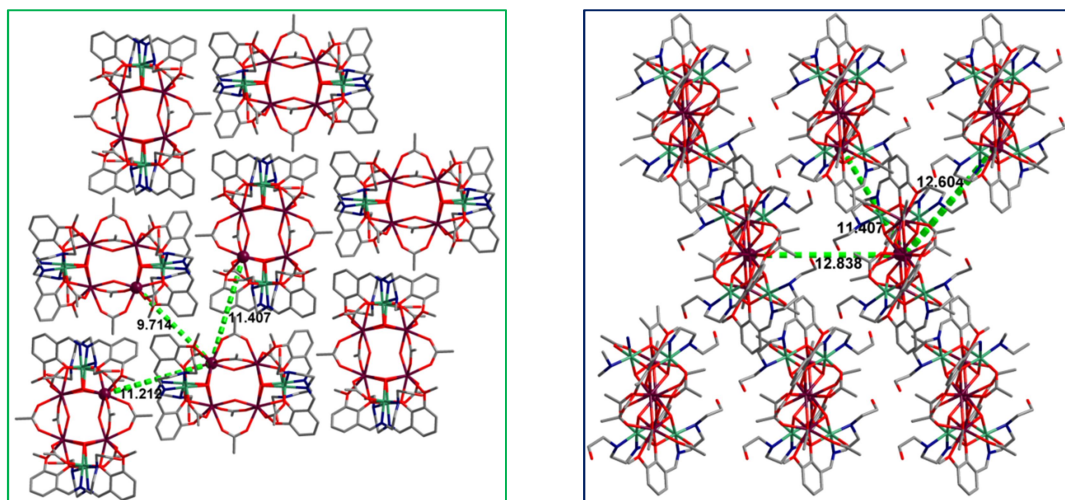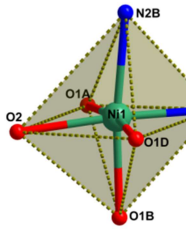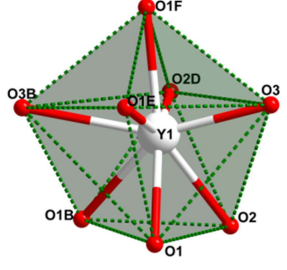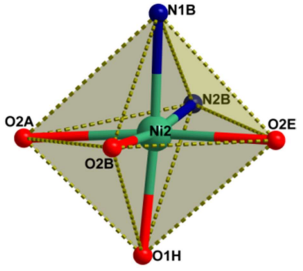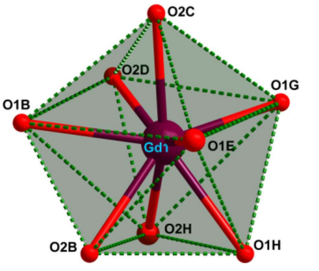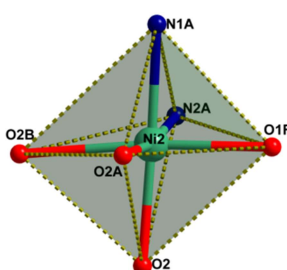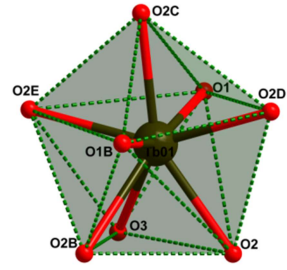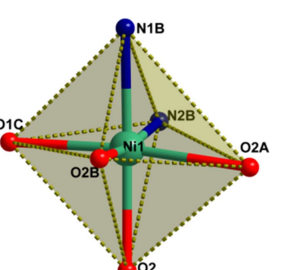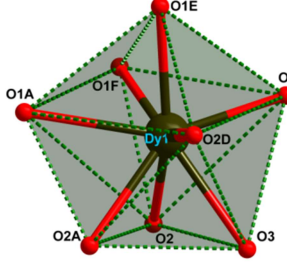
Figure 5.4. (*left*) Crystal packing diagram of **5.2** viewed along the *a* direction; (*right*) Crystal packing diagram of **5.2** viewed along the *b* direction (the counter anions and H-atoms are removed for clarity)
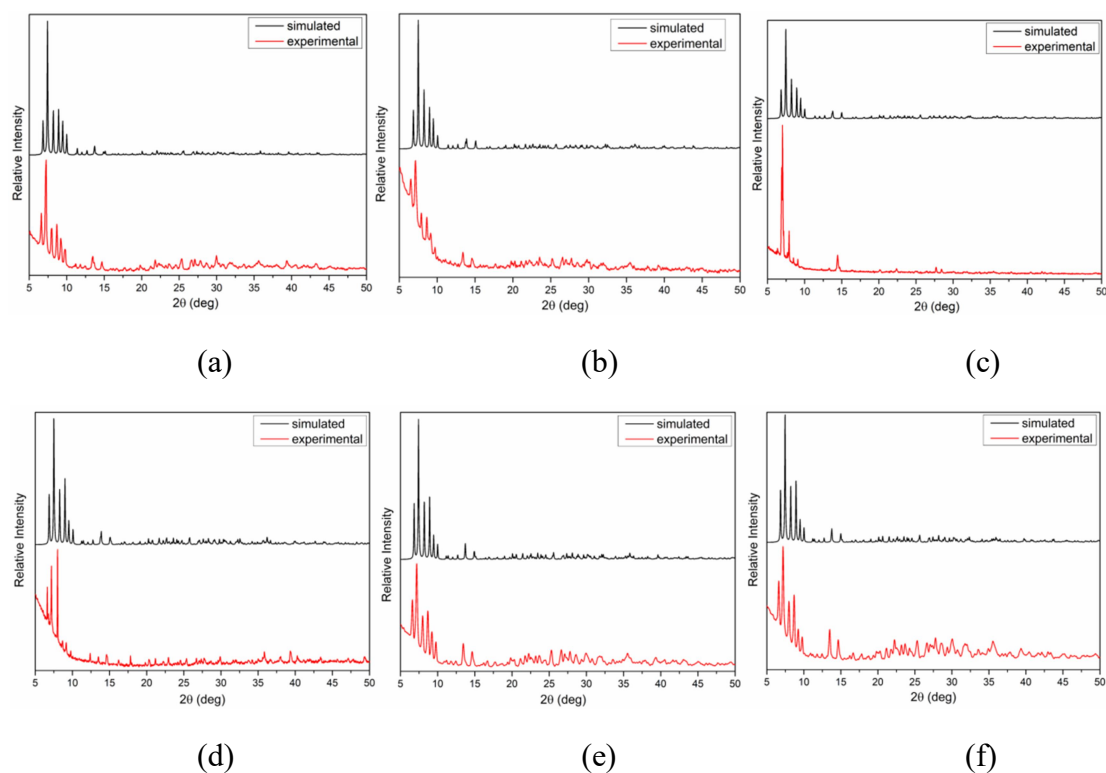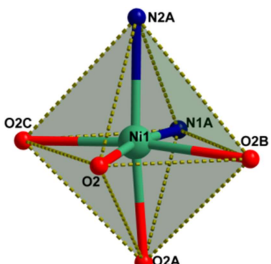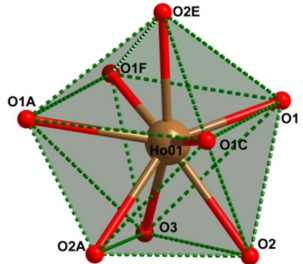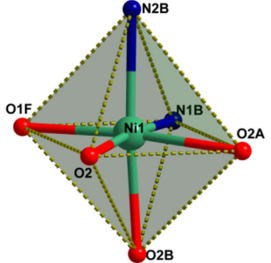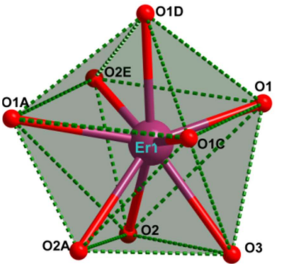
Figure 5.5. Powder XRD pattern of complexes **5.1** (a), **5.2** (b), **5.3** (c), **5.4** (d), **5.5** (e), and **5.6** (f).

Table 5.7. Selected bond lengths and bond angles for **5.1-5.6.**

Coordination environment around metal ion	Bond lengths (Å)	Bond angles (°)
Complex **5.1**. Distorted octahedron	Ni1–O2 2.011(3) Ni1–O1B 2.077(3) Ni1–O1A 2.218(3) Ni1–O1D 2.077(3) Ni1–N1B 2.000(4) Ni1–N2B 2.134(4)	N1B–Ni1–O2 173.96(14) N1B–Ni1–O1B 90.18(13) O2–Ni1–N2B 102.08(13) O1D–Ni1–O1B 92.36(11) O1D–Ni1–O1A 172.52(11) O1D–Ni1–N2B 89.44(13) O1B–Ni1–O1A 81.74(10) O1B–Ni1–N2B 172.92(12) N2B–Ni1–O1A 96.97(12)
Complex **5.1**.Triangular dodecahedron	Y1–O3 2.224(3) Y1–O1 2.338(3) Y1–O2 2.407(3) Y1–O1B 2.456(3) Y1–O3B 2.569(3) Y1–O1F 2.344(3) Y1–O1E 2.319(3) Y1–O2D 2.305(3)	O3–Y1–O1E 86.39(11) O1–Y1–O2D 95.23(11) O2D–Y1–O1 138.73(11) O2D–Y1–O2 76.67(10) O2D–Y1–O1B 78.46(10) O2D–Y1–O3B 88.75(10) O1E–Y1–O1F 75.49(11) O1–Y1–O2 67.37(10) O1–Y1–O3B 130.31(10)
Complex **5.2**. Distorted octahedron	Ni2–O1H 2.018(3) Ni2–O2A 2.202(3) Ni2–O2B 2.075(3) Ni2–O2E 2.083(3) Ni2–N1B 1.993(4) Ni2–N2B 2.127(4)	O1H–Ni2–O2E 93.34(12) O2A–Ni2–O2B 81.62(11) O2A–Ni2–N2B 96.38(14) O2B–Ni2–N2B 172.91(14) N1B–Ni2–N2B 83.22(16) O1H–Ni2–O2A 81.74(11) O1H–Ni2–N1B 174.75(14) O2A–Ni2–O2E 172.77(12)
Complex **5.2**. Triangular dodecahedron	Gd1–O1B 2.581(3) Gd1–O1E 2.349(4) Gd1–O1G 2.267(3) Gd1–O2B 2.482(3) Gd1–O2C 2.377(3) Gd1–O2D 2.352(4)	O1E–Gd1–O1G 94.91(12) O1E–Gd1–O2D 147.14(11) O1G–Gd1–O2B 144.64(11) O1G–Gd1–O1H 76.07(11) O2B–Gd1–O2D 116.90(10) O2C–Gd1–O2D 75.53(12) O2D–Gd1–O1H 135.71(10) O1B–Gd1–O2B 61.38(10)

	Gd1–O1H 2.432(3)	O1B–Gd1–O1H	129.69(10)
	Gd1–O2H 2.361(3)	O1E–Gd1–O2B	78.57(10)
 Complex **5.3**. Distorted octahedron	Ni2–O2 2.028(5) Ni2–O2B 2.215(5) Ni2–O1F 2.037(5) Ni2–O2A 2.080(5) Ni2–N1A 2.015(7) Ni2–N2A 2.115(7)	O2B–Ni2–O2A O2B–Ni2–N1A O2B–Ni2–N2A O1F–Ni2–O2A O2A*–Ni2–N1A O2A–Ni2–N2A N1A–Ni2–N2A O2–Ni2–O2B	80.94(19) 97.1(2) 97.7(2) 94.4(2) 89.8(2) 171.8(2) 82.4(3) 81.55(19)
 Complex **5.3**. Triangular dodecahedron	Tb01–O1 2.256(5) Tb01–O1B 2.588(5) Tb01–O2 2.357(5) Tb01–O2B 2.468(5) Tb01–O2C 2.372(5) Tb01–O2D 2.337(5) Tb01–O2E 2.326(6) Tb01–O3 2.434(5)	O2–Tb01–O2C O2–Tb01–O2E O2–Tb01–O3 O2B–Tb01–O2C O2B–Tb01–O2D O2C–Tb01–O2D O2C–Tb01–O2E O2C–Tb01–O3 O2D–Tb01–O2E O2D–Tb01–O3	148.60(19) 138.75(17) 75.94(17) 127.32(16) 117.32(18) 75.6(2) 72.45(19) 139.70(19) 147.18(18) 134.82(18)
 Complex **5.4**. Distorted octahedron	Ni1–O2 2.026(5) Ni1–O2A 2.198(4) Ni1–O1C 2.046(5) Ni1–O2B 2.087(5) Ni1–N1B 2.003(7) Ni1–N2B 2.121(7)	O2–Ni1–O1C O2–Ni1–O2B O2A–Ni1–N2B O1C–Ni1–O2B O2B–Ni1–N2B N1B–Ni1–N2B O2–Ni1–O2A	92.92(19) 85.81(19) 97.4(2) 94.3(2) 172.1(2) 82.7(3) 82.00(19)
 Complex **5.4**. Triangular dodecahedron	Dy1–O1 2.245(5) Dy1–O1A 2.560(5) Dy1–O1E 2.356(5) Dy1–O1F 2.317(5) Dy1–O2 2.329(5) Dy1–O2A 2.455(5) Dy1–O2D 2.326(5) Dy1–O3 2.418(5)	O1A–Dy1–O2 O1A–Dy1–O2A O1A–Dy1–O2D O1A–Dy1–O3 O1E–Dy1–O1F O1E–Dy1–O1A O1E–Dy1–O2 O1E–Dy1–O2D O1E–Dy1–O3 O1)–Dy1–O2	99.69(16) 61.71(15) 88.54(16) 130.45(15) 75.91(17) 149.02(17) 127.00(16) 71.92(17) 139.16(17) 73.20(17)

 Complex **5.5**. Distorted octahedron	Ni1–O2 2.018(3) Ni1–O2A 2.076(3) Ni1–O2C 2.078(4) Ni1–N1A 1.993(4) Ni1–N2A 2.133(4) Ni1–O2B 2.224(3)	O2–Ni1–O2C O2–Ni1–N1A O2–Ni1–N2A O2–Ni1–O2B O2C–Ni1–N2A N1A–Ni1–O2B N2A–Ni1–O2B O2–Ni1–O2A	93.91(12) 173.45(14) 102.38(15) 80.80(11) 89.70(16) 94.99(14) 97.10(14) 84.51(11)
 Complex **5.5.** Triangular dodecahedron	Ho01–O1 2.224(3) Ho01–O1A 2.574(3) Ho01–O1C 2.324(4) Ho01–O1F 2.310(3) Ho01–O2 2.407(3) Ho01–O2A 2.459(3) Ho01–O2E 2.342(3) Ho01–O3 2.336(3)	O1–Ho01–O1A O1–Ho01–O1C O1–Ho01–O1F O1–Ho01–O2 O1–Ho01–O2A O1–Ho01–O2E O1–Ho01–O3 O1A–Ho01–O1C O1A–Ho01–O1F O1A–Ho01–O2	152.31(12) 95.48(13) 86.36(13) 76.89(11) 145.77(11) 81.36(11) 95.56(11) 88.66(12) 75.64(11) 130.54(11)
 Complex **5.6**. Distorted octahedron	Ni1–O2 2.020(4) Ni1–O2A 2.200(4) Ni1–O1F 2.020(4) Ni1–O2B 2.080(4) Ni1–N1B 2.010(5) Ni1–N2B 2.130(5)	O2–Ni1–O2A O2A–Ni1–O1F O2A–Ni1–O2B O2A–Ni1–N1B O2A–Ni1–N2B O1F–Ni1–O2B O1F–Ni1–N1B N1B–Ni1–N2B	81.35(15) 173.43(16) 81.73(15) 97.18(17) 97.64(18) 4.03(17) 7.79(19) 82.8(2)
 Complex **5.6**. Triangular dodecahedron	Er1–O1 2.208(4) Er1–O1A 2.560(4) Er1–O1C 2.303(4) Er1–O1D 2.337(4) Er1–O2 2.323(4) Er1–O2A 2.445(4) Er1–O2E 2.306(4) Er1–O3 2.398(4)	O1–Er1–O2E O1–Er1–O3 O1A–Er1–O1C O1A–Er1–O1D O1A–Er1–O2 O1A–Er1–O2A O1A–Er1–O2E O1A–Er1–O3 O1C–Er1–O1D	86.57(15) 76.76(13) 88.69(14) 73.69(15) 99.30(14) 61.78(12) 75.54(15) 130.70(12) 72.36(16)

5.3.3 Magnetic properties. The temperature dependence of the $\chi_M T$ product for complexes **5.1-5.6** (χ_M being the molar magnetic susceptibility per mononuclear $Ni^{II}_4Ln^{III}_4$ unit) in the 2-300 K temperature range was measured with an applied magnetic field of 0.1 T and are given in Figures 5.6 and 5.7 for complexes **5.1** and **5.2**, respectively, and in Figure 5.10 for complexes **5.3-5.6**.
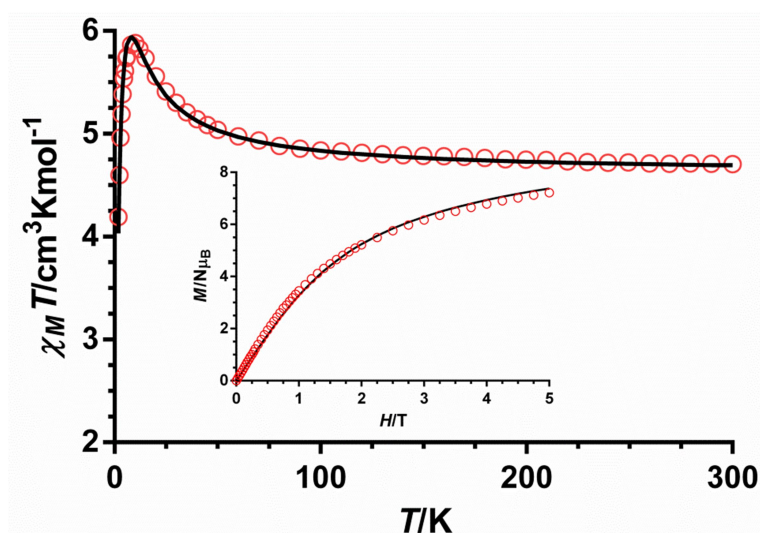
Figure 5.6. Temperature dependence of the $\chi_M T$ product and field dependence of magnetization for compound **5.1**. The solid lines represent the best fit of the experimental data.

At room temperature, the observed $\chi_M T$ values for **5.1-5.6** are close to those calculated for four independent Ni^{II} and Ln^{III} (Y^{III}) ions in the free ion approximation (Table 5.8). We are going to start the discussion with the Ni_4Y_4 (**5.1**) and Ni_4Gd_4 (**5.2**) complexes. On lowering the temperature, the $\chi_M T$ slowly increases from room temperature to 50 K (5.03 cm^3 K mol^{-1}) for **5.1** and 30 K (42.1 cm^3 K mol^{-1}) for **5.2** and then in a more abrupt way to reach values of 5.88 cm^3 K mol^{-1} at 10 K and 65.7 cm^3 K mol^{-1} at 2 K, for **5.1** and **5.2**, respectively. These behaviors are due to a ferromagnetic interaction between the Ni^{II} ions in the case of **5.1** and between the Ni^{II} ions and the Ni^{II} and Gd^{III}

ions in the case of **5.2**. In the case of **5.1**, the $\chi_M T$ decreases below 10 K up to 2 K, which is probably associated to the zero-field splitting effect of the Ni^{II} ions.

Table 5.8. Direct current magnetic data for the complexes **5.1-5.6**

Compound	Theoretical $\chi_M T_{300K}$ value (cm^3 K mol^{-1})^b	Experimental $\chi_M T_{300K}/\chi_M T_{2K}$ (cm^3 K mol^{-1})	Experimental M_{sat} value (T =2 K, H = 5 T) (Nμ_B)	Theoretical M_{sat} value (Nμ_B)^c
5.1	4.6 (g = 2.15)	4.7 / 4.19	7.21	8.6
5.2	39.1 (g =2.10)	40.3/ 67.5	37.5	37.8
5.3	51.3^a	52.5 / 98.3	25.9	44
5.4	60.7^a	61.4 / 55.1	30.7	48
5.5	60.3^a	61.6 / 36.2	31.0	48
5.6	49.9^a	51.6/37.3	29.1	44

$^a g_{Ni} = 2$; $^b \chi_M T = \frac{N\beta^2}{3k}\{g_J^2 J(J+1)$; $^c M = N J g_J \mu_B$;$J = L + S$; $g_J = \frac{3}{2} + \frac{S_T(S_T+1)-L(L+1)}{2J(J+1)}$

The magnetic properties of **5.1** have been modelled by using the following Hamiltonian:

$$H = -J(S_{Ni1}S_{Ni2} + S_{Ni1'}S_{Ni2'}) - J_a(S_{Ni1}S_{Ni2} + S_{Ni1'}S_{Ni2'}) + \sum_{i=1}^{4} D_{Ni\,i}S_{Niiz}^{2} \qquad (eq.\ 5.1)$$

where J accounts for the magnetic exchange coupling between Ni^{II} ions, J_a represents the magnetic exchange coupling between Ni^{II} ions through the shorter Ni1-Y3-Y3'-Ni1' and Ni2-Y4-Y4'-Ni2' pathways and D_{Ni} accounts for the axial single ion zero-field splitting parameter of the Ni^{II} ions, which are equivalent (see Figure 5.8). The simultaneous fit of the experimental susceptibility and magnetization data with the above Hamiltonian using the PHI program[22] afforded the following set of parameters: J = 5.2 cm^{-1}, J_a = -0.09 cm^{-1}, g = 2.15, D = 5.6 cm^{-1} and R = 4.3 x 10^{-7}. The very weak

antiferromagnetic interaction described by J_a must be taken into account, because when J_a is fixed to zero the quality of the fit got rather worse.

The ferromagnetic coupling exhibited by complex **5.1** can be justified by analyzing the structural parameters of dinuclear Ni_2 complexes with diphenoxido bridging group connecting octahedral Ni^{II} ions. Experimental and theoretical magneto-structural correlations[23] have shown that the Ni–O–Ni bridging angle (θ) is the major issue influencing the nature of the magnetic coupling in hydroxido-, alkoxido- and phenoxido- $Ni(O)_2Ni$ complexes. Thus, for Ni–O–Ni angles close to 90°, a ferromagnetic coupling is expected. As the Ni-O-Ni angle increases from 90°, the ferromagnetic coupling diminished and becomes antiferromagnetic (AF) at values of ~ 96-98°. Moreover, it has been shown from theoretical studies[23a] that the AF interaction increases when τ (the out-of-plane displacement of the phenyl carbon atom from the Ni_2O_2 plane) diminishes. Taking into account this, $Ni(O)_2Ni$ diphenoxo-bridging fragment in complex **5.1**, with mean θ and τ angles of 98.6° and 46.7° should transmit either weak F or AF interactions between the Ni^{II} ions, which is in good agreement with the observed values.

The magnetic data for such an intricate system as the Ni_4Gd_4 complex (**5.2**) were modelled in a crude manner with the following Hamiltonian:

$$H = -J(S_{Ni1}S_{Ni2} + S_{Ni1'}S_{Ni2'}) - J'\sum_{i=1}^{8}(S_{Nii}S_{Gdi}) - J''(Gd_3Gd_4 + Gd_{3'}Gd_{4'}) + \sum_{i=1}^{8}D_{Nii}S_{Niiz}^2 - zJ'\langle S_z\rangle S_z$$

$$(eq.\ 5.2)$$

Where the interactions between the Gd^{III} and Ni^{II} ions connected by two μ_3-O bridging atoms of the two cubane units are assumed to be equal, J'' represents the Gd···Gd interactions inside the cubane units and zJ' accounts for the intercubane interactions between the Gd^{III} using the molecular field approach (see Figure 5.8).

Taking into account that the structural parameters affecting the dinuclear Ni_2 units inside the cubane units are almost identical for the isostructural complexes **5.1** and **5.2**, and to avoid over parametrization, the values of J and D were fixed to those extracted for compound **5.1**. Considering the above approximations, the best fit of the magnetic data with the above Hamiltonian led to the following magnetic parameters:

$J' = 0.86$ cm^{-1}, $J'' = -0.0034$ cm^{-1}, $g = 2.10$, $zJ' = -0.0002$ cm^{-1} and R = 1.2 x 10^{-5}.
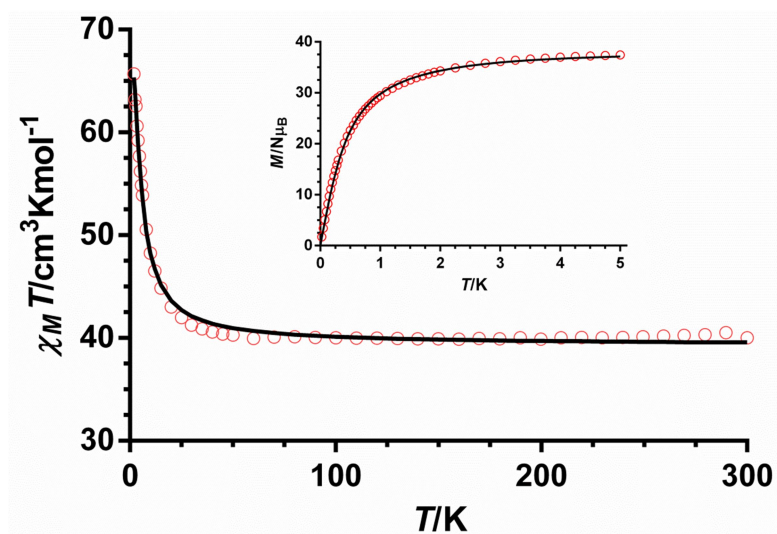
Figure 5.7. Temperature dependence of the $\chi_M T$ product and field dependence of magnetization for compound **5.2**. The solid lines represent the best fit of the experimental data.
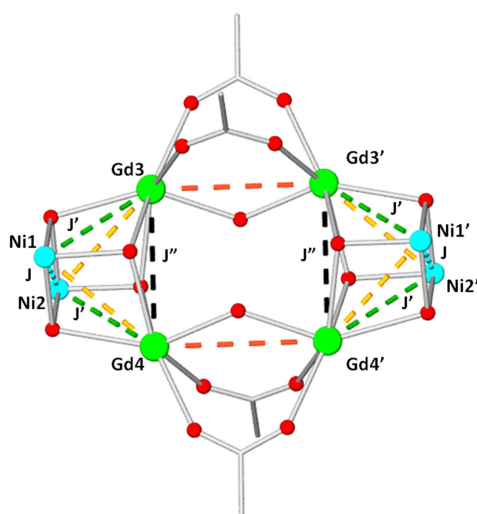
Figure 5.8. Scheme of magnetic coupling pathways in the complex **5.2**

Experimental and theoretical studies on diphenoxide-bridged Gd-Ni dinuclear complexes[6b, 24] have shown that the ferromagnetic interaction between Ni^{II} and Gd^{III} ions increases mainly with the increase of the Ni–O–Gd angle (θ) and with the planarity of the Ni–O_2–Gd fragment. Complex **5.2** has average values of the θ angle and the hinge angle β (the dihedral angle between the O–Ni–O and O–Gd–O planes in the bridging fragment) of 102.1° and 18.6°, respectively. For these values, and according to the magneto-structural correlations a $J_{NiGd} \sim +1$ cm^{-1} is expected, which agrees well with the J'_{NiGd} value extracted for **5.2**. It is worth noting that the magnetic coupling constants for the Ni$\cdots$Gd and Gd$\cdots$Gd intra-cubane interactions agree in sign and magnitude with those found for other $Ni_2Gd_2O_4$ cubane complexes.[25] As the Gd^{III} ion does not have first order angular momentum and almost a negligible zero field splitting, the dipolar interactions are expected to be very weak, so that the experimentally observed Gd$\cdots$Gd interactions are due mainly to exchange coupling between the Gd^{III} ions. Experimental and theoretical studies have shown that with diphenoxo-, dialkoxo-, two oxo-carboxylate and two carboxylate-acetate bridging groups smaller values of the Gd–O–Gd, and consequently of the Gd$\cdots$Gd distance, favour an antiferromagnetic interaction.[26] For some of these compounds antiferromagnetic interactions are predicted for Gd–O–Gd angles smaller than 110°. In view of the above considerations, the fact that the intra-cubane antiferromagnetic interactions (described by J'') are larger than the intercubane ones (described by zJ') is not unexpected as the Gd–O–Gd angles for the former are around 108.5°, whereas the Gd–O–Gd angle for the latter ones is 132.23°. Taking into account only the Gd–O–Gd angle, the intercubane interaction is expected to be ferromagnetic in nature, however, the existence of two additional *syn-syn* acetate bridging groups connecting the Gd^{III} ions lead to the very weak antiferromagnetic interaction found for this triple

bridge. Nevertheless, these assumptions should be taken with caution because of (*i*) the crudeness of the model, (*ii*) the weakness of the magnetic interactions and, (*iii*) the possible existence of ZFS splitting of the Gd^{III} ions.

Previous work has shown that Ni_xGd_y polynuclear complexes can exhibit large magneto-caloric effects (MCE) and therefore can be considered for magnetic refrigeration materials.[27] This is so because, among other factors, the magnetic exchange interaction between the Gd^{III} and Ni^{II} ions is very weak, which generates multiple low-lying excited and field-accessible states, each of which can contribute to the total magnetic entropy of the system. Moreover, if the interaction is ferromagnetic in nature, the low lying states would have a large spin, which also favors larger MCE. In view of this, we decided to evaluate the MCE of **5.2** from magnetization measurements in the 2-6 K temperature range under an applied magnetic field in the range 0-5 T, making use of the Maxwell relation:

$$\Delta S_M = (T, \Delta B) = \int_{B_i}^{B_f} \left[\frac{\partial M(T,B)}{dT} \right]_B dB \quad (eq.\ 5.3)$$

where B_i and B_f are the initial and final applied magnetic fields. The integration results show that the $-\Delta S_m$ values for complex **5.2** under all fields (Figure 5.9) increase as the temperature decreases from 5 to 3 K, with a maximum magnetic entropy change ($-\Delta S_m = 22.58$ J kg^{-1} K^{-1}). This value is rather smaller than the full magnetic entropy content per mole for the $Ni_4^{II}Gd_4^{III}$ complex is $2R\ln(2S_{Gd} + 1) + 2R\ln(2S_{Ni} + 1) = 6.08$ R, which corresponds to 36.8 J kg^{-1} K^{-1} for **5.2**. This fact can be mainly due to magnetic anisotropy of the Ni^{II} ions and the intra- and inter-cubane antiferromagnetic interactions between the Gd^{III} ions (both the increase of D and AF interactions diminishes $-\Delta S_m$). The $-\Delta S_m$ value for **5.2** is larger than those observed for complexes with a Gd/Ni = 0.5 but lower than those found for other more dense

complexes with Gd/Ni ratios in the range 1-4.2.[27] The MCE increases with the increase of the Gd/Ni ratio as expected for increasing the spin and decreasing the magnetic anisotropy.
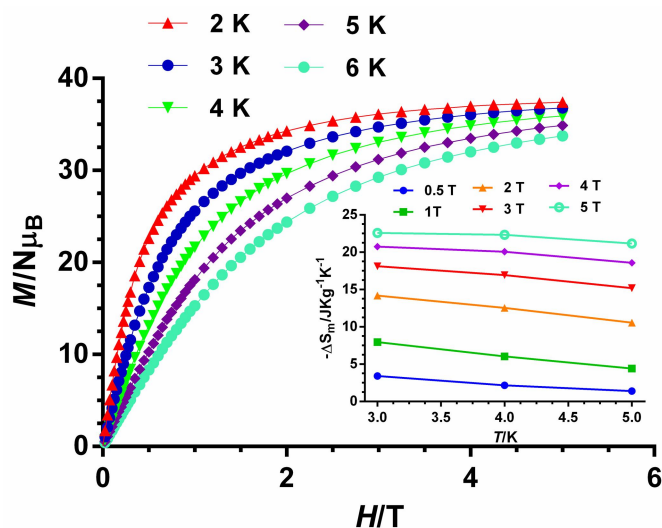
Figure 5.9. Isothermal field dependent curves for **5.2** between 2 and 6 K and magnetic entropy changes (inset) extracted from the experimental magnetization data with the Maxwell equation between 1 to 5 T and temperatures from 3 to 5 K (points).

The $\chi_M T$ product compounds Ni$_4$Tb$_4$ (**5.3**) and Ni$_4$Dy$_4$ (**5.4**) steadily decreases with decreasing temperature to minimum values of 49.1 cm^3 K mol^{-1} at 35 K for **5.3** and 54.74 cm^3 K mol^{-1} at 12 K for **5.4**, then sharply increases at lower temperatures up to 2 K in the case of **5.3** and to reach a maximum value of 55.5 cm^3 K mol^{-1} at 5 K for **5.4**. Below this temperature, the $\chi_M T$ value for **5.4** drops down to 2 K. As usual, the decrease of the $\chi_M T$ product in the high temperature region (above 40 K) is due to the depopulation of the M_J sublevels of the Tb^{III} and Dy^{III} ions, which arise from the splitting of the ground term by the ligand field. The increase of $\chi_M T$ at low temperature is likely to be due to a ferromagnetic interaction between Ni^{II} and Ln^{III}, whereas the decrease of $\chi_M T$ below 5 K for **5.4** is essentially associated with the magnetic anisotropy of the Ni^{II} ions. For complexes **5.5** and **5.6**, the $\chi_M T$ product

decreases steadily with decreasing temperature until approximately 20 K and then more sharply down to 2 K. The observed behavior is mainly due to the depopulation of the M_J sublevels of the Ln^{III} ions, which are able to overcome (together with the effect of the Ni^{II} anisotropy) the effect of the presumable Ni^{II}-Ln^{III} ferromagnetic interactions in the low temperature region. This behaviour is rather common in Ho^{III} and Er^{III} complexes. In the case of complexes **5.3** and **5.4** the opposite situation occurs, so that the Ni^{II}-Ln^{III} ferromagnetic interaction are strong enough as to overcome the effect of the depopulation of the M_J sublevels and an increase in $\chi_M T$ is observed at low temperature. The fact that the $\chi_M T$ for **5.3** reaches a rather larger value than **5.4** at 2 K seems to indicate that the Ni^{II}-Ln^{III} magnetic coupling is stronger for the former.
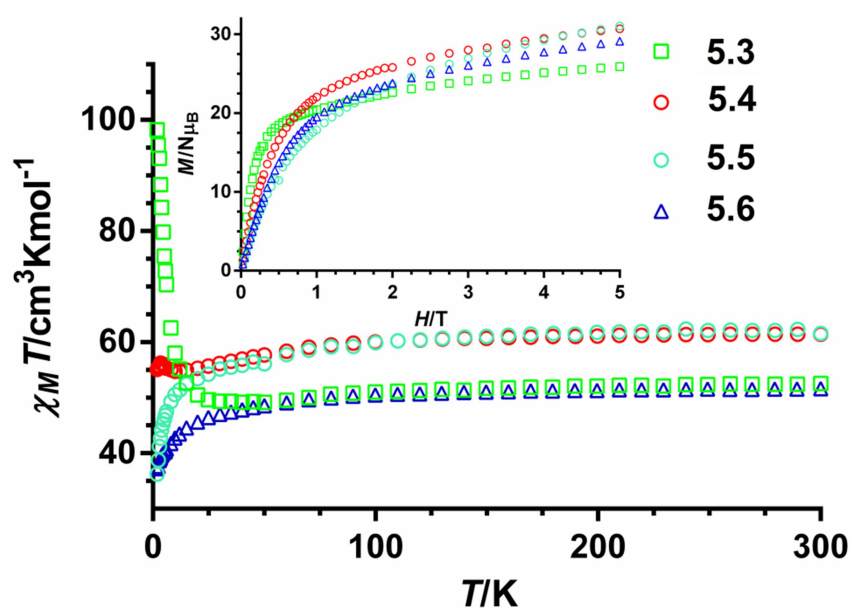
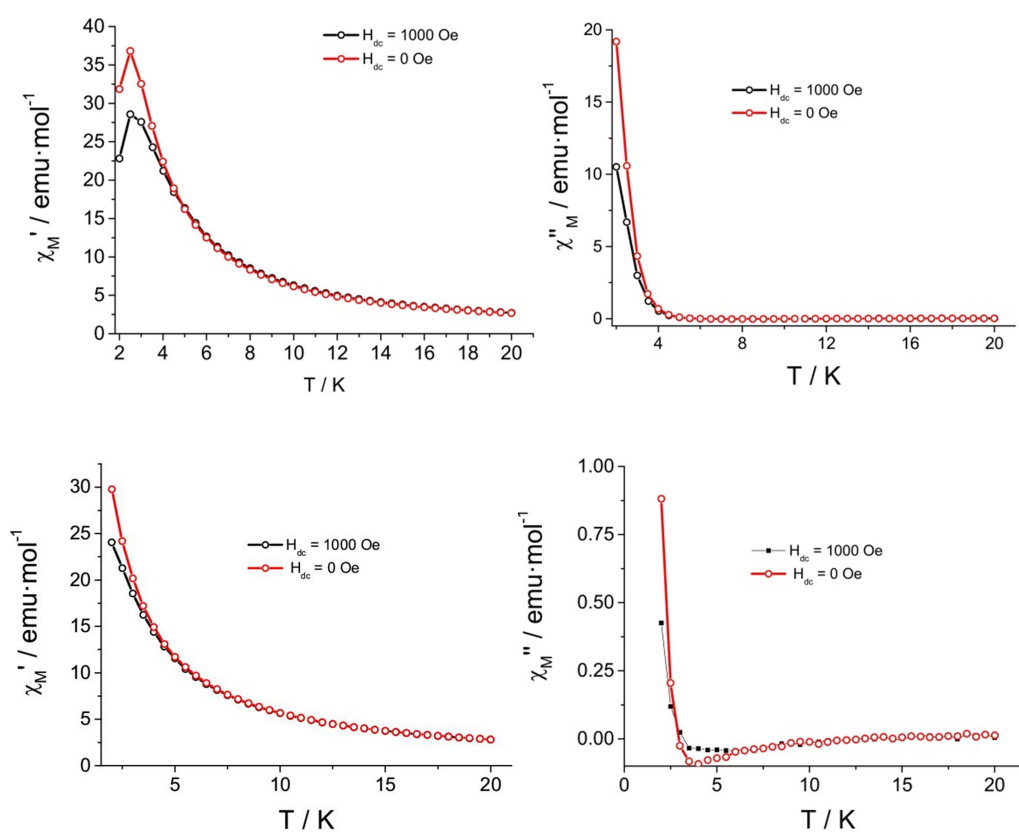**Figure 5.10.** Temperature dependence of the $\chi_M T$ product and field dependence of magnetization (inset) for compound **5.3-5.6**

The magnetization versus field plots for complexes **5.3-5.6** at $T = 2$ K (Figure 5.10) show a fast increase of the magnetization up to ~1 T, which supports the ferromagnetic interaction between Ni^{II} and Ln^{III} in these complexes, and then a slow

increase with the field without reaching saturation at 5 T, which is mainly due to the presence of significant magnetic anisotropy and/or low-lying excited states that are partially populated at this temperature. The presence of low lying excited states is in agreement with the existence of weak Ni···Ln magnetic interactions in these complexes. It should be noted that the magnetization values at the highest applied dc magnetic field of 5 T are however almost the half of those calculated for non-interacting Ni^{II} and Ln^{III} ions (Table 5.8), which is, as usual, mainly attributed to crystal-field effects giving rise to significant magnetic anisotropy.[28] The fact that the slope of the *M* vs *H* plot below 1 T is higher for **5.3** than for **5.4** seems to support a stronger Ni^{II}···Ln^{III} magnetic coupling for the former. The smaller slope for **5.5** and **5.6** could indicate a weaker magnetic coupling than in complexes **5.3** and **5.4**. Nevertheless, these qualitative suggestions should be taken with caution as the crystal field splitting of the ground term by the ligand field is different for each of the complexes **5.3**-**5.6** and therefore their ability for counterbalancing the effect of the Ni^{II}···Ln^{III} ferromagnetic coupling.

In order to know if these complexes exhibit slow relaxation and possible SMM behaviour, dynamic ac magnetic susceptibility measurements as a function of the temperature at different frequencies were performed on complexes **5.1**-**5.6** under zero and 1000 Oe external dc field. Only complexes **5.3** and **5.4** showed out-of-phase (χ''_M) signals below 4 K (Figure 5.11), but none of them exhibited any maximum in the temperature dependence of χ''_M above 2 K at frequencies reaching 1400 Hz, even in the presence of a small dc field to fully or partly suppress the possible quantum tunneling relaxation (this process is able in some cases to prevent the observation of slow relaxation of the magnetization). Therefore, in these two complexes either the energy barrier for the flipping of the magnetization is not enough as to block the

magnetization above 2 K or there exists a very fast resonant zero-field quantum tunnelling of the magnetization (which cannot be eliminated by applying a small dc field) with a flipping rate that is too fast to give rise to a maximum in the χ''_M above 2 K. This behaviour can be related with the existence of very weak Ni···Ln and Ln···Ln magnetic interactions in complexes **5.3**-**5.6**. These interactions generate small separations of the low lying split sublevels, which lead to very small energy barrier for the flipping of the magnetization and, moreover, favor QTM by mixing of low-lying excited states in the ground state.

Figure 5.11. Temperature dependence of the in-phase χ'_M and out-of-phase χ''_M components of the ac susceptibility at 1400 Hz under applied magnetic field of zero and 1000 Oe for complex **5.3** (*top*) and **5.4** (*down*)

5.4 CONCLUSIONS

A compartmental ligand, 2-methoxy-6-[2-(2-hydroxyethylamino)ethylimino}methyl] phenol (H_2L), was utilized to assemble heterometallic octanuclear Ni_4Ln_4 complexes. Structural studies of these complexes reveal that they are made up of two tetranuclear $[Ni_2Ln_2O_4]$ cubane sub-units. The core of the assembly consists of a tetranuclear lanthanide motif, where two four-membered $[Ln_2(\mu\text{-OH})_2]$ sub-units are linked to each other by four acetate and two hydroxide bridging ligands. Magnetic studies on these complexes reveals a ferromagnetic interaction between the lanthanide and the nickel centers, the magnitude of which for the Gd^{III} analogue has been estimated as $J = +0.86$ cm^{-1}. While none of the complexes are single-molecule magnets due to the existence of very weak Ni$\cdots$Ln and Ln$\cdots$Ln magnetic interactions, the $Ni^{II}_4Gd^{III}_4$ complex shows a magneto caloric effect with a maximum magnetic entropy change, $-\Delta S_m = 22.58$ J kg^{-1} K^{-1} at 3 K for an applied external field of 5 T.

5.5 REFERENCES

1 (a) A. Caneschi, D. Gatteschi, R. Sessoli, A. L. Barra, L. C. Brunel and M. Guillot, *J. Am. Chem. Soc.*, 1991, **113**, 5873-5874; (b) R. Sessoli, D. Gatteschi, A. Caneschi and M. A. Novak, *Nature*, 1993, **365**, 141-143; (c) R. Sessoli, H. L. Tsai, A. R. Schake, S. Wang, J. B. Vincent, K. Folting, D. Gatteschi, G. Christou and D. N. Hendrickson, *J. Am. Chem. Soc.*, 1993, **115**, 1804-1816; (d) G. Christou, D. Gatteschi, D. N. Hendrickson and R. Sessoli, *MRS Bull.*, 2000, **25**, 66-71; (e) H. B. Heersche, Z. de Groot, J. A. Folk, H. S. J. van der Zant, C. Romeike, M. R. Wegewijs, L. Zobbi, D. Barreca, E. Tondello and A. Cornia, *Phys. Rev. Lett.*, 2006, **96**, 206801-206804.

2 (a) O. Waldmann, *Inorg. Chem.*, 2007, **46**, 10035-10037; (b) F. Neese and D. A. Pantazis, *Faraday Discuss.*, 2011, **148**, 229-238; (c) J. M. Frost, K. L. M. Harriman and M. Murugesu, *Chem. Sci.*, 2016, **7**, 2470-2491.

3 (a) R. T. W. Scott, S. Parsons, M. Murugesu, W. Wernsdorfer, G. Christou and E. K. Brechin, *Angew. Chem., Int. Ed.*, 2005, **44**, 6540-6543; (b) A. M. Ako, I. J. Hewitt, V. Mereacre, R. Clérac, W. Wernsdorfer, C. E. Anson and A. K. Powell, *Angew. Chem., Int. Ed.*, 2006, **45**, 4926-4929; (c) W. G. Wang, A. J. Zhou, W. X. Zhang, M. L. Tong, X. M. Chen, M. Nakano, C. C. Beedle and D. N. Hendrickson, *J. Am. Chem. Soc.*, 2007, **129**, 1014-1015; (d) E. Ruiz, J. Cirera, J. Cano, S. Alvarez, C. Loose and J. Kortus, *Chem. Commun.*, 2008, 52-54; (e) J. Cirera, E. Ruiz, S. Alvarez, F. Neese and J. Kortus, *Chem.—Eur. J.*, 2009, **15**, 4078-4087.

4 (a) B. Wang, S. Jiang, X. Wang and S. Gao, *Sci. China, Ser. B: Chem.*, 2009, **52**, 1739-1758; (b) J. D. Rinehart and J. R. Long, *Chem. Sci.*, 2011, **2**, 2078-2085; (c) R. J. Blagg, L. Ungur, F. Tuna, J. Speak, P. Comar, D. Collison, W. Wernsdorfer, E. J. L. McInnes, L. F. Chibotaru and R. E. P. Winpenny, *Nat. Chem.*, 2013, **5**, 673-678; (d) D. N. Woodruff, R. E. P. Winpenny and R. A. Layfield, *Chem. Rev.*, 2013, **113**, 5110-5148; (e) J. Tang and P. Zhang, *Lanthanide Single Molecule Magnets*, 2015.

5 (a) C. Papatriantafyllopoulou, W. Wernsdorfer, K. A. Abboud and G. Christou, *Inorg. Chem.*, 2011, **50**, 421-423; (b) S. K. Langley, N. F. Chilton, L. Ungur, B. Moubaraki, L. F. Chibotaru and K. S. Murray, *Inorg. Chem.*, 2012, **51**, 11873-11881; (c) S. K. Langley, D. P. Wielechowski, V. Vieru, N. F. Chilton, B. Moubaraki, B. F. Abrahams, L. F. Chibotaru and K. S. Murray, *Angew. Chem., Int. Ed.*, 2013, **52**, 12014-12019; (d) J. L. Liu, J. Y. Wu, Y. C. Chen, V. Mereacre, A. K. Powell, L. Ungur, L. F. Chibotaru, X. M. Chen and M. L. Tong, *Angew. Chem., Int. Ed.*, 2014, **53**, 12966-12970; (e) S. K. Langley, C. Le, L. Ungur, B. Moubaraki, B. F. Abrahams, L. F. Chibotaru and K. S. Murray, *Inorg. Chem.*, 2015, **54**, 3631-3642; (f) T. Gupta, M. F. Beg and G. Rajaraman, *Inorg. Chem.*, 2016, **55**, 11201-11215.

6 (a) V. Chandrasekhar, B. M. Pandian, J. J. Vittal and R. Clérac, *Inorg. Chem.*, 2009, **48**, 1148-1157; (b) E. Colacio, J. Ruiz, A. J. Mota, M. A. Palacios, E. Cremades, E. Ruiz, F. J. White and E. K. Brechin, *Inorg. Chem.*, 2012, **51**, 5857-5868; (c) S. Das, K. S. Bejoymohandas, A. Dey, S. Biswas, M. L. P. Reddy, R. Morales, E. Ruiz, S. Titos-Padilla, E. Colacio and V. Chandrasekhar, *Chem. Eur. J.*, 2015, **21**, 6449-6464; (d) J. Goura, E. Colacio, J. M. Herrera, E. A. Suturina, I. Kuprov, Y. lan, W. Wernsdorfer and V. Chandrasekhar, *Chem. Eur. J.*, 2017, **23**, 16621-16636.

7 (a) N. Ahmed, C. Das, S. Vaidya, S. K. Langley, K. S. Murray and M. Shanmugam, *Chem. Eur. J.*, 2014, **20**, 14235-14239; (b) T. D. Pasatoiu, A. Ghirri, A. M. Madalan, M. Affronte and M. Andruh, *Dalton Trans.*, 2014, **43**, 9136-9142; (c) S. Biswas, J. Goura, S. Das, C. V. Topping, J. Brambleby, P. A. Goddard and V. Chandrasekhar, *Inorg. Chem.*, 2016, **55**, 8422-8436; (d) W. P. Chen, P. Q. Liao, Y. Yu, Z. Zheng, X. M. Chen and Y. Z. Zheng, *Angew. Chem., Int. Ed.*, 2016, **55**, 9375-9379; (e) D. P. Liu, X. P. Lin, H. Zhang, X. Y. Zheng, G. L. Zhuang, X. J. Kong, L. S. Long and L. S. Zheng, *Angew. Chem., Int. Ed.*, 2016, **55**, 4532-4536.

8 (a) J. Goura, J. Brambleby, P. Goddard and V. Chandrasekhar, *Chem. Eur. J.*, 2015, **21**, 4926-4930; (b) J. Goura, V. Mereacre, G. Novitchi, A. K. Powell and V. Chandrasekhar, *Eur. J. Inorg. Chem.*, 2015, 156-165; (c) J. Goura, J. Brambleby, C. V. Topping, P. A. Goddard, R. S. Narayanan, A. K. Bar and V. Chandrasekhar, *Dalton Trans.*, 2016, **45**, 9235-9249.

9 W. L. E. Armarego and C. L. L. Chai, *Purification of Laboratory Chemicals*, 2003.

10 B. S. Furniss, A. J. Hannaford, P. W. G. Smith and A. R. Tatchell, *Vogel's Textbook of Practical Organic Chemistry*, 1989.

11 (a) F. M. Wang, *Acta Cryst. E*, 2012, **68**, m26-m27; (b) Z. L. You, D. H. Shi, J. C. Zhang, Y. P. Ma, C. Wang and K. Li, *Inorg. Chim. Acta*, 2012, **384**, 54-61.

12 *SMART & SAINT Software Reference manuals*, Bruker Analytical X-ray Systems, Inc., Madison, WI, version 6.45, 2003.

13 G. M. Sheldrick, *SADABS, Program for Empirical Absorption Correction*, University of Gottingen, Germany, 1996.

14 *Bruker APEX2*, Bruker AXS Inc., Madison, Wisconsin, USA, version 2008.1−0, 2008.

15 G. M. Sheldrick, *Acta Cryst. A*, 2015, **71**, 3-8.

16 G. M. Sheldrick, *Acta Cryst. C*, 2015, **71**, 3-8.

17 O. V. Dolomanov, L. J. Bourhis, R. J. Gildea, J. A. K. Howard and H. Puschmann, *J. Appl. Cryst.*, 2009, **42**, 339-341.

18 A. L. Spek, *Acta Cryst. C*, 2015, **71**, 9-18.

19 K. Brandenburg and H. Putz, *DIAMOND*, Crystal Impact GbR, Bonn, Germany, version 3.2, 1997−2014.

20 (a) E. Colacio, J. Ruiz-Sanchez, F. J. White and E. K. Brechin, *Inorg. Chem.*, 2011, **50**, 7268-7273; (b) K. Liu, W. Shi and P. Cheng, *Coord. Chem. Rev.*, 2015, **289–290**, 74-122; (c) L. R. Piquer and E. C. Sañudo, *Dalton Trans.*, 2015, **44**, 8771-8780; (d) J. Wu, L. Zhao, L. Zhang, X. L. Li, M. Guo and J. Tang, *Inorg. Chem.*, 2016, **55**, 5514-5519.

21 (a) J. Cirera, E. Ruiz and S. Alvarez, *Organometallics*, 2005, **24**, 1556-1562; (b) *SHAPE: Continuous Shape Measures calculation*, Electronic Structure Group, Universitat de Barcelona, Spain, version 2.1, 2013.

22 N. F. Chilton, R. P. Anderson, L. D. Turner, A. Soncini and K. S. Murray, *J. Comput. Chem.*, 2013, **34**, 1164-1175.

23 (a) M. A. Palacios, A. J. Mota, J. E. Perea-Buceta, F. J. White, E. K. Brechin and E. Colacio, *Inorg. Chem.*, 2010, **49**, 10156-10165; (b) R. Biswas, S. Giri, S. K. Saha

and A. Ghosh, *Eur. J. Inorg. Chem.*, 2012, 2916-2927; (c) K. K. Nanda, L. K. Thompson, J. N. Bridson and K. Nag, *J. Chem. Soc., Chem. Commun.*, 1994, 1337-1338; (d) M. A. Halcrow, J. S. Sun, J. C. Huffman and G. Christou, *Inorg. Chem.*, 1995, **34**, 4167-4177; (e) J. M. Clemente-Juan, B. Chansou, B. Donnadieu and J. P. Tuchagues, *Inorg. Chem.*, 2000, **39**, 5515-5519; (f) X. H. Bu, M. Du, L. Zhang, D. Z. Liao, J. K. Tang, R. H. Zhang and M. Shionoya, *J. Chem. Soc., Dalton Trans.*, 2001, 593-598.

24 S. K. Singh, N. K. Tibrewal and G. Rajaraman, *Dalton Trans.*, 2011, **40**, 10897-10906.

25 Z. S. Meng, F. S. Guo, J. L. Liu, J. D. Leng and M. L. Tong, *Dalton Trans.*, 2012, **41**, 2320-2329.

26 (a) L. E. Roy and T. Hughbanks, *J. Am. Chem. Soc.*, 2006, **128**, 568-575; (b) L. Cañadillas-Delgado, O. Fabelo, J. Pasán, F. S. Delgado, F. Lloret, M. Julve and C. Ruiz-Pérez, *Dalton Trans.*, 2010, **39**, 7286-7293; (c) L. Cañadillas-Delgado, O. Fabelo, J. Cano, J. Pasán, F. S. Delgado, F. Lloret, M. Julve and C. Ruiz-Pérez, *CrystEngComm*, 2009, **11**, 2131-2142.

27 (a) P. F. Shi, C. S. Cao, C. M. Wang and B. Zhao, *Inorg. Chem.*, 2017, **56**, 9169-9176; (b) A. Hosoi, Y. Yukawa, S. Igarashi, S. J. Teat, O. Roubeau, M. Evangelisti, E. Cremades, E. Ruiz, L. A. Barrios and G. Aromí, *Chem. Eur. J.*, 2011, **17**, 8264-8268; (c) Y. Z. Zheng, M. Evangelisti and R. E. P. Winpenny, *Angew. Chem., Int. Ed.*, 2011, **50**, 3692-3695; (d) J. B. Peng, Q. C. Zhang, X. J. Kong, Y. P. Ren, L. S. Long, R. B. Huang, L. S. Zheng and Z. Zheng, *Angew. Chem., Int. Ed.*, 2011, **50**, 10649-10652; (e) P. Wang, S. Shannigrahi, N. L. Yakovlev and T. S. A. Hor, *Chem. Asian J.*, 2013, **8**, 2943-2946; (f) T. N. Hooper, J. Schnack, S. Piligkos, M. Evangelisti and E. K. Brechin, *Angew. Chem., Int. Ed.*, 2012, **51**, 4633-4636; (g) S. Das, A. Dey, S. Kundu,

S. Biswas, A. J. Mota, E. Colacio and V. Chandrasekhar, *Chem. Asian J.*, 2014, **9**, 1876-1887.

28 (a) J. Ruiz, A. J. Mota, A. Rodríguez-Diéguez, S. Titos, J. M. Herrera, E. Ruiz, E. Cremades, J. P. Costes and E. Colacio, *Chem. Commun.*, 2012, **48**, 7916-7918; (b) Y. Bi, Y. N. Guo, L. Zhao, Y. Guo, S. Y. Lin, S. D. Jiang, J. Tang, B. W. Wang and S. Gao, *Chem. Eur. J.*, 2011, **17**, 12476-12481; (c) H. L. C. Feltham, Y. Lan, F. Klöwer, L. Ungur, L. F. Chibotaru, A. K. Powell and S. Brooker, *Chem. Eur. J.*, 2011, **17**, 4362-4365.